USE OF BACKFILL IN NEW BRUNSWICK POTASH MINES

PHASE II

September 1989

Final Report For:

DENISON-POTACAN POTASH COMPANY
Sussex, New Brunswick

Prepared By:

MRAZ PROJECT CONSULTANTS LTD
Saskatoon, Saskatchewan

L1178
D. Z. MRAZ
1989

Work on the project was conducted under the auspices of the Canada Centre for Mineral and Energy Technology, Energy, Mines and Resources Canada as part of the Canada/New Brunswick Mineral Development Agreement.

DSS FILE NO: 14SQ.23440-7-9228

DSS CONTRACT SERIAL NO: 23440-7-9228/01-SQ

CANMET PROJECT NO: 1.4.09.05

CANMET SCIENTIFIC AUTHORITY: Dr. G. Herget

423 pp

MICROMEDIA

ACKNOWLEDGMENTS

This report has been prepared by Mraz Project Consultants Ltd, (MPC) Saskatoon, Saskatchewan, with the help and contributions from the following organizations and individuals:

* All in situ testing and monitoring of rock mechanics instrumentation included in Section 3.0 has been done by S. Munroe and R. Fry under the direction of D.C.E. Waugh, Superintendent of Engineering, Engineering Department of Denison-Potacan Potash Company.

* Laboratory testing programs described in Sections 4.0, 5.0 and 6.0 were performed at WATSALT Laboratory, Department of Earth Sciences, University of Waterloo, Waterloo, Ontario, by C.J. Fordham under the direction of M.B. Dusseault.

* The results of laboratory testing included in Section 5.0 have been extensively used by C.J. Fordham in his 1988 Ph.D. study, which he carried out concurrently with the testing program, and his Ph.D. thesis was used in preparation of Section 5.0.

* The parametric analysis on in situ and laboratory data included in Section 7.0 was performed under the direction of L. Rothenburg, Department of Civil Engineering, University of Waterloo, Waterloo, Ontario.

* The numerical modelling program FLAC, used in Sections 8.0 and 9.0, was purchased from ITASCA Consulting Group, Inc. by MPC. The constitutive laws for intact materials and halite backfill used in this study were incorporated into FLAC under a contract between ITASCA and MPC. The constitutive laws for intact rocks and halite backfill are the result of a joint effort of MPC and the University of Waterloo.

* All three-dimensional analyses included in Section 10.0 were done by L. Rothenburg, Department of Civil Engineering, University of Waterloo, Waterloo, Ontario, using the program VELMINA. VELMINA, written by

L. Rothenburg, utilizes the displacement discontinuity method for modelling visco-elastic media. The technical description of VELMINA included in Appendix A was also written by L. Rothenburg.

TABLE OF CONTENTS

LIST OF FIGURES
LIST OF TABLES
LIST OF PARAMETERS

1.0 EXECUTIVE SUMMARY

1.1 Introduction
1.2 In Situ Testing
1.3 Laboratory Testing
1.4 Parametric Analysis of Data on Salt Rocks
1.5 Two-Dimensional Material Modelling
1.6 Three-Dimensional Numerical Modelling
1.7 Conclusions and Recommendations

2.0 INTRODUCTION

2.1 Background to Mine Development
2.2 Geology
2.3 Description of Mining Methods
2.4 Mine Backfill Operations
2.4.1 Dry Backfill System
2.4.2 Hydraulic Backfill System
2.5 Backfill Research - Summary of Program Under Phase I
2.6 Backfill Research - Summary of Program Under Phase II

3.0 IN SITU TESTING

3.1 Introduction
3.2 Instrumentation Equipment
3.3 Instrumentation Protection
3.4 Underground Rock Mechanics Sites and Records of Data
3.4.1 Panel 11, Stope 11200
3.4.2 Panel 11, Convergence Stations in Stopes 11120 and 11240
3.4.3 Panel 12, Entries 12826/12827/12828
3.4.4 Panel 12, Entry 12831
3.5 Interpretation of Underground Instrumentation Data
3.5.1 Stope 11200, Extensometers
3.5.2 Stope 11200, Pressure Cells
3.5.3 Stope 11120 and 11240, Convergence
3.5.4 Instrumentation in Entry Systems in Panel 12
3.6 Surface Subsidence Monitoring

TABLE OF CONTENTS Continued

4.0 LABORATORY TESTING OF OVERBURDEN ROCKS

4.1 Test Methodology
4.2 Sample Preparation
4.3 Test Results
4.3.1 Strength Tests
4.3.2 Elastic Constants

5.0 LABORATORY TESTING OF BACKFILL

5.1 Overview of Laboratory Testing Programs
5.2 Testing Methodology of Granular Halite Backfill
5.3 Granular Backfill Characterization
5.3.1 Moisture Content
5.3.2 Long Term Moisture Content of DPPC Halite Backfill
5.3.3 Grain Size Analysis
5.3.4 Mineralogy
5.3.5 Standard Proctor Compaction Tests
5.4 Compaction Creep Testing on Granular Backfill
5.4.1 Specimen Preparation
5.4.2 Constant Stress Compaction Creep Tests
5.4.3 Constant Strain Rate Compaction Creep Tests
5.4.4 Effect of Moisture and Initial Porosity
5.5 Brittle Strength Testing
5.6 Results
5.6.1 Moisture Content
5.6.2 Grain Size Analysis
5.6.3 Mineralogy
5.6.4 Standard Proctor Compaction Tests
5.6.5 Overview of Compaction Creep Tests
5.6.6 Overview of Brittle Strength Tests
5.7 Evaluation of Tests on Granular Halite Backfill
5.7.1 Compaction Creep Behaviour of Halite Backfill
5.7.2 Proposed Behaviourial Model for Compaction Creep
5.7.3 In Situ Compaction Creep Behaviour
5.7.4 Applicability to Other Halite Backfills
5.7.5 Compacted Backfill Under Shear Stress
5.7.6 Uniaxial Brittle Strength (σ_c) of Halite Backfill
5.7.7 Uniaxial Brittle Strength of Fully Compacted Halite Backfill
5.7.8 Apparent Stiffness of Halite Backfill

TABLE OF CONTENTS Continued

6.0 LABORATORY TESTING OF ENGINEERED BACKFILL

6.1 Previous Work
6.2 Materials
6.3 Test Program
6.4 Results
6.4.1 Mixture of Backfill and Sand
6.4.2 Mixture of Backfill, Brine and Cement
6.5 Conclusions

7.0 PARAMETRIC ANALYSIS OF IN SITU AND LABORATORY DATA ON SALT ROCKS

7.1 Introduction
7.2 Definition of Shear Stress Criterion
7.3 Re-evaluation of Original Parameters
7.4 Determination of Exponent "n_2"
7.5 Determination of Reference Parameters
7.6 Determination of Properties for Remaining Materials
7.7 Summary of Parametric Analysis

8.0 NUMERICAL MODELLING OF DPPC MINE USING THE PROGRAM FLAC WITHOUT BACKFILL

8.1 Introduction
8.2 Computational Procedure Used in FLAC to Predict Behaviour of Visco-Elastic/Plastic Material
8.3 Capabilities of FLAC
8.4 Verification of FLAC
8.4.1 Comparison of Analytical and Numerical Solutions
8.4.2 Benchmark Against Numerical Models
8.5 Calibration of FLAC
8.5.1 Calibration Against the Virgin Ground Test Room
8.5.2 Calibration Against the Three Room Entry (12826/12827/12828) System
8.6 FLAC Outputs and Analyses
8.6.1 Two Room Sequence (Stopes 1120 and 11240)
8.7 Results of FLAC Numerical Simulations

9.0 NUMERICAL MODELLING OF DPPC MINE USING THE PROGRAM FLAC WITH BACKFILL

9.1 Introduction
9.2 Computational Procedure in FLAC to Predict Behaviour of Halite Backfill
9.3 Analysis of Backfilling Method
9.4 Numerical Simulation of Second Pass Mining
9.5 Results of FLAC Numerical Simulations with Backfill

TABLE OF CONTENTS Continued

10.0 NUMERICAL MODELLING OF DPPC MINE USING COMPUTER PROGRAM VELMINA

10.1 Introduction
10.2 Simulation of 1988 Mining Layout
10.3 Verification of Input Parameters
10.4 Simulation of Combined Excavation of Panels 10, 11 and 12
10.5 Simulation of Backfill in Panels 10, 11 and 12
10.6 Simulation of Secondary Mining in Panels 10, 11 and 12

11.0 CONCLUSIONS AND RECOMMENDATIONS

11.1 Conclusions
11.2 Recommendations

12.0 REFERENCES

APPENDIX A TECHNICAL ASPECTS OF VELMINA CODE

A.1 Technical Aspects of VELMINA Code
A.1.1 The Velocity Discontinuity Method
A.1.2 Mathematical Model of Pillars
A.1.3 Determination of Equivalent Linear Viscosity
A.2 Test Problem

APPENDIX B NUMERICAL MODELLING WITH VISCOT

B.1 Introduction
B.2 Finite Element Method of Numerical Modelling
B.3 Technical Limitations
B.4 Verification of VISCOT (Comparison of Analytic and Numerical Solutions)

LIST OF FIGURES

FIGURE 1.1 LOCATION OF MINE SITE

FIGURE 1.2 GEOLOGY OF THE MONCTON SUBBASIN IN NEW BRUNSWICK (After Waugh and Urquhart, 1983)

FIGURE 1.3 CLOVER HILL MINE, GENERAL MINE PLAN

FIGURE 1.4 PANEL 11, TYPICAL GEOLOGICAL CROSS-SECTION

FIGURE 1.5 HALITE BACKFILL EMPIRICAL CREEP LAW FIT

FIGURE 1.6 UNCONFINED COMPRESSIVE STRENGTH VS. COMPACTION STRESS FOR TEST SPECIMENS AT POROSITIES OF 0.14, 0.18, 0.22 AND 0.26

FIGURE 1.7 'ZERO COMPACTION STRESS' σ_c AS A FUNCTION OF FRACTIONAL DENSITY FOR DPPC HALITE BACKFILL

FIGURE 1.8 STRESS/STRAIN DIAGRAM FOR HALITE BACKFILL COMPACTED TO $n = 0.22$, CONFINING STRESS 1.03 MPa, AXIAL STRAIN RATE 10^{-4} sec^{-1}

FIGURE 1.9 DEFORMATION MECHANISM MAP FOR SALT (After Munson, 1979)

FIGURE 1.10 DPPC PANEL 11, MINING PATTERN

FIGURE 1.11 DPPC PANELS 10 - 11 - 12 MINING PATTERN

FIGURE 1.12 DPPC PANELS 10 - 11 - 12 NORMAL STRESS

FIGURE 1.13 DPPC PANELS 11 12 13 BACKFILLED, AFTER 11 YEARS DENSITY

FIGURE 1.14 DPPC PANELS 10 11 12 BACKFILLED MINING PATTERN

FIGURE 1.15 DPPC PANELS 10 - 11 - 12 BACKFILL DENSITY

FIGURE 1.16 DPPC PANELS 10 11 12 CONVERGENCE RATE

FIGURE 1.17 DPPC PANELS 10 11 12, SECONDARY EXCAVATION CONVERGENCE RATE

FIGURE 2.1 LOCATION OF MINE SITE

LIST OF FIGURES Continued

FIGURE 2.2	GEOLOGY OF THE MONCTON SUBBASIN IN NEW BRUNSWICK (After Waugh and Urquhart, 1983)
FIGURE 2.3	STRATIGRAPHIC COLUMN MARCHBANK SYNCLINE (After Waugh and Urquhart, 1983)
FIGURE 2.4	SCHEMATIC OF CASSIDY LAKE FORMATION POTASH MEMBER (After Waugh and Urquhart, 1983)
FIGURE 2.5	CLOVER HILL MINE, GENERAL MINE PLAN
FIGURE 2.6	PANEL 11, TYPICAL GEOLOGICAL CROSS-SECTION
FIGURE 2.7	SCHEMATIC OF MINE BACKFILL SYSTEM
FIGURE 3.1	ROCK MECHANICS INSTRUMENTATION SITES
FIGURE 3.2	PANEL 11 (11200), INSTRUMENTATION STATION
FIGURE 3.3	PHOTOGRAPH SHOWING 6-POINT WALL EXTENSOMETER
FIGURE 3.4	PHOTOGRAPH SHOWING PRESSURE TRANSDUCER INTERFACE
FIGURE 3.5	STOPE 11200, REMOTE READOUT LAYOUT
FIGURE 3.6	STOPE 11200, REMOTE READOUT CONFIGURATION
FIGURE 3.7	PANEL 11, STOPE 11200 ROCK MECHANICS STATION CHRONOLOGY OF EVENTS
FIGURE 3.8	STOPE 11200 - ROOF EXTENSOMETER PANEL #11 - ROCK MECHANICS STATION
FIGURE 3.9	STOPE 11200 - PILLAR EXTENSOMETER PANEL #11 - ROCK MECHANICS STATION
FIGURE 3.10	STOPE 11200 - ROOF LATERAL PRESSURE PANEL #11 - ROCK MECHANICS STATION
FIGURE 3.11	STOPE 11200 - ROOF TANGENTIAL PRESSURE PANEL #11 - ROCK MECHANICS STATION
FIGURE 3.12	STOPE 11200 - PILLAR VERTICAL PRESSURE PANEL #11 - ROCK MECHANICS STATION
FIGURE 3.13	STOPE 11200 - PILLAR LATERAL PRESSURE PANEL #11 - ROCK MECHANICS STATION

LIST OF FIGURES Continued

FIGURE 3.14 STOPE 11200 - PILLAR RADIAL PRESSURE
PANEL #11 - ROCK MECHANICS STATION

FIGURE 3.15 STOPE 11200 - BACKFILL PRESSURE CELLS
PANEL #11 - ROCK MECHANICS STATION

FIGURE 3.16 PANEL 11, TOTAL CLOSURE STATIONS

FIGURE 3.17 STOPE 11120 - TOTAL CLOSURE
PANEL #11 - TOTAL CLOSURE STATIONS

FIGURE 3.18 STOPE 11120 - TOTAL CLOSURE RATES
PANEL #11 - RATES SINCE INSTALLATION

FIGURE 3.19 STOPE 11240 - TOTAL CLOSURE
PANEL #11 - TOTAL CLOSURE STATIONS

FIGURE 3.20 STOPE 11240 - TOTAL CLOSURES RATES
PANEL #11 - RATES SINCE INSTALLATION

FIGURE 3.21 PANEL 12, SOUTH THREE-ENTRY INSTRUMENTATION STATION

FIGURE 3.22 12826 AND 12827 - VERTICAL CLOSURES
PANEL #12 - SOUTH THREE-ENTRY STATION

FIGURE 3.23 12826 AND 12827 - HORIZONTAL CLOSURES
PANEL #12 - SOUTH THREE-ENTRY STATION

FIGURE 3.24 12826 - PILLAR EXTENSOMETERS
PANEL #12 SOUTH THREE-ENTRY SYSTEM

FIGURE 3.25 12826/12827 PILLAR EXTENSOMETERS
PANEL #12 SOUTH THREE-ENTRY SYSTEM

FIGURE 3.26 12826 3-ENTRY PRESSURE CELLS
DENISON-POTACAN ROCK MECHANICS

FIGURE 3.27 12826 3-ENTRY PRESSURE CELLS
DENISON-POTACAN ROCK MECHANICS

FIGURE 3.28 12826 - PILLAR PRESSURE CELLS
PANEL #12 - SOUTH THREE-ENTRY STATION

FIGURE 3.29 12826 - PILLAR PRESSURE CELLS
PANEL #12 - SOUTH THREE-ENTRY STATION

FIGURE 3.30 12826/12827 - PILLAR PRESSURE CELLS
PANEL #12 - SOUTH THREE ENTRY STATION

LIST OF FIGURES Continued

FIGURE 3.31	12827/12828 - PILLAR PRESSURE CELLS PANEL #12 - SOUTH THREE-ENTRY STATION
FIGURE 3.32	12827 RELATIVE CLOSURE YIELD PILLAR
FIGURE 3.33	12827 TOTAL CLOSURE DPPC ROCK MECHANICS
FIGURE 3.34	PANEL 12, WEST THREE-ENTRY INSTRUMENTATION STATIONS
FIGURE 3.35	12831 (175 M) RELATIVE CLOSURE DPPC ROCK MECHANICS
FIGURE 3.36	12831 (350 M) RELATIVE CLOSURE DPPC ROCK MECHANICS
FIGURE 3.37	12831/12832 - PILLAR PRESSURE CELL 175 m PANEL #12 - WEST THREE-ENTRY STATION
FIGURE 3.38	12831/12832 - PILLAR PRESSURE CELL 350 m PANEL #12 - WEST THREE-ENTRY STATION
FIGURE 3.39	STOPE 11200, STRAIN RATES IN ROOF
FIGURE 3.40	STOPE 11200, STRAIN RATES IN WALL
FIGURE 3.41	STOPE 11200, PRESSURE CELLS IN PILLAR
FIGURE 3.42	CONCEPTUAL INTERPRETATION OF FULLY GROUTED BOREHOLE PRESSURE CELLS
FIGURE 3.43	ANNUALIZED SUBSIDENCE RATE CONTOURS FOR 1987-1988 IN MILLIMETERS PER YEAR
FIGURE 3.44	SUBSIDENCE RATE, 1987-88 NORTH-SOUTH SECTION, PANEL 11
FIGURE 3.45	SUBSIDENCE RATE, 1987-88 EAST-WEST SECTION, PANEL 10 & 11
FIGURE 4.1	SOURCE OF CORE SAMPLES TESTED IN LABORATORY RELATIVE TO ORE HORIZON (After Waugh and Urquhart, 1983)
FIGURE 4.2	MOHR-COULOMB DIAGRAM FOR POODIAC SANDSTONE
FIGURE 4.3	MOHR-COULOMB DIAGRAM FOR POODIAC SILTSTONE

LIST OF FIGURES Continued

FIGURE 4.4 MOHR-COULOMB DIAGRAM FOR FRACTURED POODIAC SANDSTONE

FIGURE 4.5 MOHR-COULOMB DIAGRAM FOR SILTSTONE CAPROCK BRECCIA

FIGURE 4.6 FRACTURED POODIAC SANDSTONE ENVELOPE

FIGURE 4.7 SILTSTONE CAPROCK BRECCIA ENVELOPE

FIGURE 4.8 POODIAC SANDSTONE FAILURE ENVELOPE

FIGURE 4.9 POODIAC SILTSTONE FAILURE ENVELOPE

FIGURE 5.1 RESULTS OF STANDARD PROCTOR COMPACTION TESTS

FIGURE 5.2 TESTING OEDOMETERS

FIGURE 5.3 GRAIN SIZE DISTRIBUTION OF DPPC HALITE BACKFILL

FIGURE 5.4 OPTICAL MICROGRAPH OF UNCOMPACTED DPPC HALITE BACKFILL

FIGURE 5.5 X-RAY DIFFRACTION TRACE, DPPC HALITE BACKFILL

FIGURE 5.6 STANDARD PROCTOR COMPACTION TEST RESULTS

FIGURE 5.7 TYPICAL HIGH STRESS COMPACTION CREEP TEST RESULTS

FIGURE 5.8 TYPICAL MEDIUM STRESS COMPACTION CREEP TEST RESULTS

FIGURE 5.9 TYPICAL LOW STRESS COMPACTION CREEP TEST RESULTS

FIGURE 5.10 EFFECT OF MOISTURE CONTENT ON COMPACTION CREEP UNDER 10 MPa

FIGURE 5.11 UNCONFINED COMPRESSIVE STRENGTH VS. POROSITY FOR TEST SPECIMENS COMPACTED UNDER 50, 40, 30, 20 AND 10 MPa

FIGURE 5.12 UNCONFINED COMPRESSIVE STRENGTH VS. COMPACTION STRESS FOR TEST SPECIMENS AT POROSITIES OF 0.14, 0.18, 0.22 AND 0.26

FIGURE 5.13 APPARENT STIFFNESS VS. POROSITY FOR TEST SPECIMENS COMPACTED AT 50, 40, 30 AND 20 MPa

LIST OF FIGURES Continued

FIGURE 5.14 RESULTS OF TRIAXIAL COMPRESSION TESTS ON DPPC HALITE BACKFILL AT POROSITIES OF 0.26, 0.22, 0.18 AND 0.14

FIGURE 5.15 VOLUMETRIC CREEP RATE VERSUS COMPACTION STRESS

FIGURE 5.16 CRUSHED GRAIN CONTACT IN HALITE BACKFILL COMPACTED UNDER 0.5 MPa FOR ABOUT 7 DAYS

FIGURE 5.17 GRAIN INDENTATION IN COMPACTED HALITE BACKFILL

FIGURE 5.18 PRECIPITATE IN PORE OF COMPACTED HALITE BACKFILL

FIGURE 5.19 LOG $\dot{\epsilon}$/LOG n CURVES FOR MEDIUM STRESS COMPACTION CREEP TESTS

FIGURE 5.20 $\dot{\epsilon}_{os}$ VS. INITIAL POROSITY (n_i)

FIGURE 5.21 DIFFERENCE BETWEEN INITIAL POROSITY (n_i) AND n_c VS. APPLIED STRESS

FIGURE 5.22 SLOPES OF HIGH CREEP RATE REGIME CURVES (1_1) ON LOG $\dot{\epsilon}$/LOG n PLOTS

FIGURE 5.23 SLOPES OF LOW CREEP RATE REGIME CURVES (1_2) ON LOG $\dot{\epsilon}$/ LOG n PLOTS

FIGURE 5.24 CONCEPTUAL DIAGRAM OF BEHAVIOURIAL MODEL FOR DPPC HALITE BACKFILL AT CONSTANT STRESS

FIGURE 5.25 LOG $\dot{\epsilon}$/ LOG n CURVES FOR HALITE BACKFILL AT 2.5% w_{ct} AND OVEN DRIED, COMPACTED UNDER 10 MPa

FIGURE 5.26 LOG $\dot{\epsilon}$/ LOG n CURVES FOR HALITE BACKFILL COMPACTED UNDER 0.5 MPa AT DIFFERENT INITIAL POROSITIES

FIGURE 5.27a SCANNING ELECTRON MICROGRAPHS OF HALITE BACKFILL COMPACTED UNDER 0.5 MPa WITH AN INITIAL POROSITY OF 0.477

FIGURE 5.27b SCANNING ELECTRON MICROGRAPHS OF HALITE BACKFILL COMPACTED UNDER 0.5 MPa WITH AN INITIAL POROSITY OF 0.477

FIGURE 5.28 SCANNING ELECTRON MICROGRAPH OF HALITE BACKFILL COMPACTED UNDER 0.5 MPa WITH AN INITIAL POROSITY OF 0.439

FIGURE 5.29 STRESS EXPONENT PLOT

LIST OF FIGURES Continued

FIGURE 5.30 HALITE BACKFILL EMPIRICAL CREEP LAW FIT

FIGURE 5.31 CRITICAL STRESS VERSUS DENSITY

FIGURE 5.32 CREEP OF FULLY COMPACTED BACKFILL AND UPPER HALITE UNDER A SHEAR STRESS

FIGURE 5.33 PHOTOMICROGRAPH OF DPPC HALITE BACKFILL COMPACTED TO A POROSITY OF 0.26 UNDER 20 MPa

FIGURE 5.34 PHOTOMICROGRAPH OF DPPC HALITE BACKFILL COMPACTED TO A POROSITY OF 0.26 UNDER 34 MPa

FIGURE 5.35 PHOTOMICROGRAPH OF DPPC HALITE BACKFILL COMPACTED TO A POROSITY OF 0.14 UNDER 20 MPa

FIGURE 5.36 PHOTOMICROGRAPH OF DPPC HALITE BACKFILL COMPACTED TO A POROSITY OF 0.14 UNDER 50 MPa

FIGURE 5.37 UNCONFINED COMPRESSIVE BRITTLE STRENGTH AS A FUNCTION OF POROSITY

FIGURE 5.38 'ZERO COMPACTION STRESS' σ_c AS A FUNCTION OF FRACTIONAL DENSITY OF DPPC HALITE BACKFILL

FIGURE 5.39 STRESS/STRAIN DIAGRAM FOR HALITE BACKFILL COMPACTED TO $n = 0.22$, CONFINING STRESS 1.03 MPa, AXIAL STRAIN RATE 10^{-4} $\sec^{-1}$

FIGURE 5.40 MOHR COULOMB DIAGRAM FOR HALITE BACKFILL COMPACTED TO $n = 0.22$

FIGURE 5.41 EXPONENTIAL FAILURE ENVELOPE FOR HALITE BACKFILL COMPACTED TO $n = 0.22$, $R = 0.06$, $M = 43$

FIGURE 6.1 GRAIN SIZE DISTRIBUTIONS OF DPPC HALITE BACKFILL, FULL SILICA SAND MIXTURE, AND TESTED SILICA SAND MIXTURE

FIGURE 6.2 1-D OEDOMETER USED FOR COMPACTION TESTING OF DPPC BACKFILL AND HALITE BACKFILL/SAND MIXES

FIGURE 6.3 POROSITIES OF DPPC HALITE BACKFILL/SAND MIXES BEFORE (INITIAL) AND AFTER (FINAL) VIBRO-COMPACTING FOR 1 MINUTE

LIST OF FIGURES Continued

FIGURE 6.4	COMPACTION CURVES FOR DPPC HALITE BACKFILL AND HALITE BACKFILL WITH 5 AND 10% SAND ADDED. ALL TESTS WERE PERFORMED WITH MATERIAL AT 2.5% MOISTURE CONTENT UNDER 0.5 MPa
FIGURE 6.5	STRENGTH DEVELOPMENT OF DPPC HALITE BACKFILL WITH 3, 5 AND 10% TYPE 10 CEMENT ADDED
FIGURE 6.6	UNCONFINED COMPRESSIVE STRENGTH AS A FUNCTION OF CEMENT CONTENT, DPPC HALITE BACKFILL
FIGURE 6.7	UNCONFINED COMPRESSIVE STRENGTH AS A FUNCTION OF CEMENT AND FLY ASH CONTENT, DPPC HALITE BACKFILL
FIGURE 7.1	DPPC VIRGIN GROUND OPENING
FIGURE 7.2	DEFORMATION MECHANISM MAP FOR SALT
FIGURE 7.3	COMPONENTS OF CREEP AT HIGH AND LOW TEMPERATURES PALO DURO SALT, UNITS 4 AND 5
FIGURE 7.4	EXPONENTIAL FIT OF ROCANVILLE POTASH TESTS
FIGURE 7.5	DPPC VIRGIN GROUND OPENING ROOF TO FLOOR CONVERGENCE RATES
FIGURE 7.6	DPPC VIRGIN GROUND OPENING VERTICAL STRESS ALONG MID-HEIGHT OF PILLAR
FIGURE 7.7	DPPC VIRGIN GROUND OPENING HORIZONTAL STRESS ALONG MID-HEIGHT OF PILLAR
FIGURE 7.8	DPPC VIRGIN GROUND OPENING EFFECTIVE STRESS ALONG MID-HEIGHT OF PILLAR
FIGURE 7.9	PARAMETRIC COMPARISON SYLVINITE BED
FIGURE 7.10	PARAMETRIC COMPARISON LOWER GRADATIONAL BED
FIGURE 7.11	PARAMETRIC COMPARISON UPPER HALITE
FIGURE 8.1	FLAC VERIFICATION RUN CLOSURE RATE OF CIRCULAR OPENING
FIGURE 8.2	FLAC VERIFICATION RUN RADIAL STRESS AROUND OPENING

LIST OF FIGURES Continued

FIGURE 8.3 FLAC VERIFICATION RUN CIRCUMFERENTIAL STRESS AROUND OPENING

FIGURE 8.4 DPPC NUMERICAL MODELLING - VIRGIN GROUND (APPLIED LOAD, LARGE STRAIN MODE) GRID PLOT

FIGURE 8.5 DPPC NUMERICAL MODELLING - VIRGIN GROUND (APPLIED LOAD, LARGE STRAIN MODE) GRID PLOT

FIGURE 8.6 DPPC NUMERICAL MODELLING - VIRGIN GROUND (APPLIED LOAD, LARGE STRAIN MODE) PLASTICITY INDICATOR

FIGURE 8.7 DPPC NUMERICAL MODELLING - VIRGIN GROUND (APPLIED LOAD, LARGE STRAIN MODE) PRINCIPAL STRESSES

FIGURE 8.8 DPPC NUMERICAL MODELLING - VIRGIN GROUND (APPLIED LOAD, LARGE STRAIN MODE) HORIZONTAL STRESS CONTOURS

FIGURE 8.9 DPPC NUMERICAL MODELLING - VIRGIN GROUND (APPLIED LOAD, LARGE STRAIN MODE) VERTICAL STRESS CONTOURS

FIGURE 8.10 DPPC NUMERICAL MODELLING - VIRGIN GROUND (APPLIED LOAD, LARGE STRAIN MODE) DISPLACEMENT VECTORS

FIGURE 8.11 DPPC NUMERICAL MODELLING - VIRGIN GROUND (APPLIED LOAD, LARGE STRAIN MODE) VELOCITY VECTORS

FIGURE 8.12 DPPC NUMERICAL MODELLING - VIRGIN GROUND (APPLIED LOAD, LARGE STRAIN MODE) ROOF CLOSURE

FIGURE 8.13 DPPC NUMERICAL MODELLING - VIRGIN GROUND (APPLIED LOAD, LARGE STRAIN MODE) FLOOR CLOSURE

FIGURE 8.14 DPPC NUMERICAL MODELLING - VIRGIN GROUND (APPLIED LOAD, LARGE STRAIN MODE) WALL CLOSURE

FIGURE 8.15 FLAC COMPARISON, VERTICAL CLOSURE

FIGURE 8.16 FLAC COMPARISON, HORIZONTAL CLOSURE

LIST OF FIGURES Continued

FIGURE 8.17 FLAC COMPARISON, VERTICAL CLOSURE RATE

FIGURE 8.18 FLAC COMPARISON, HORIZONTAL CLOSURE RATE

FIGURE 8.19 DPPC NUMERICAL MODELLING - THREE ROOM CALIBRATION (STAGE #1) GRID PLOT

FIGURE 8.20 DPPC NUMERICAL MODELLING - THREE ROOM CALIBRATION (FINAL) GRID PLOT

FIGURE 8.21 DPPC NUMERICAL MODELLING - THREE ROOM CALIBRATION (STAGE #1) PLASTICITY INDICATOR

FIGURE 8.22 DPPC NUMERICAL MODELLING - THREE ROOM CALIBRATION (FINAL) PLASTICITY INDICATOR

FIGURE 8.23 DPPC NUMERICAL MODELLING - THREE ROOM CALIBRATION (STAGE #1) PRINCIPAL STRESSES

FIGURE 8.24 DPPC NUMERICAL MODELLING - THREE ROOM CALIBRATION (FINAL) PRINCIPAL STRESSES

FIGURE 8.25 DPPC NUMERICAL MODELLING - THREE ROOM CALIBRATION (STAGE #1) HORIZONTAL STRESS CONTOURS

FIGURE 8.26 DPPC NUMERICAL MODELLING - THREE ROOM CALIBRATION (FINAL) HORIZONTAL STRESS CONTOURS

FIGURE 8.27 DPPC NUMERICAL MODELLING - THREE ROOM CALIBRATION (STAGE #1) VERTICAL STRESS CONTOURS

FIGURE 8.28 DPPC NUMERICAL MODELLING - THREE ROOM CALIBRATION (FINAL) VERTICAL STRESS CONTOURS

FIGURE 8.29 DPPC NUMERICAL MODELLING - THREE ROOM CALIBRATION (STAGE #1) VELOCITY VECTORS

FIGURE 8.30 DPPC NUMERICAL MODELLING - THREE ROOM CALIBRATION (FINAL) VELOCITY VECTORS

FIGURE 8.31 DPPC NUMERICAL MODELLING - THREE ROOM CALIBRATION (STAGE #1) DISPLACEMENT VECTORS

FIGURE 8.32 DPPC NUMERICAL MODELLING - THREE ROOM CALIBRATION (FINAL) DISPLACEMENT VECTORS

FIGURE 8.33 DPPC NUMERICAL MODELLING - THREE ROOM CALIBRATION (FINAL) ROOM 1 - ROOF CLOSURE

LIST OF FIGURES Continued

FIGURE 8.34 DPPC NUMERICAL MODELLING - THREE ROOM CALIBRATION (FINAL) ROOM 1 - FLOOR CLOSURE

FIGURE 8.35 DPPC NUMERICAL MODELLING - THREE ROOM CALIBRATION (FINAL) ROOM 1 - LEFT WALL CLOSURE

FIGURE 8.36 DPPC NUMERICAL MODELLING - THREE ROOM CALIBRATION (FINAL) ROOM 1 - RIGHT WALL CLOSURE

FIGURE 8.37 DPPC NUMERICAL MODELLING - THREE ROOM CALIBRATION (FINAL) VERTICAL STRESS BETWEEN ROOMS 2 AND 3

FIGURE 8.38 DPPC NUMERICAL MODELLING - THREE ROOM CALIBRATION (FINAL) HORIZONTAL STRESS BETWEEN ROOMS 2 AND 3

FIGURE 8.39 DPPC NUMERICAL MODELLING - THREE ROOM CALIBRATION (FINAL) VERTICAL STRESS BETWEEN ROOMS 1 AND 2

FIGURE 8.40 DPPC NUMERICAL MODELLING - THREE ROOM CALIBRATION (FINAL) HORIZONTAL STRESS BETWEEN ROOMS 1 AND 2

FIGURE 8.41 DPPC NUMERICAL MODELLING - THREE ROOM CALIBRATION (FINAL) VERTICAL STRESS IN LEFT ABUTMENT

FIGURE 8.42 DPPC NUMERICAL MODELLING - THREE ROOM CALIBRATION (FINAL) HORIZONTAL STRESS IN LEFT ABUTMENT

FIGURE 8.43 DPPC 12826 3-ENTRY CALIBRATION VERTICAL STRESS IN YIELD PILLAR

FIGURE 8.44 ROOM 12826 3-ENTRY CALIBRATION HORIZONTAL CLOSURE

FIGURE 8.45 ROOM 12826 3-ENTRY CALIBRATION VERTICAL CLOSURE

FIGURE 8.46 DPPC NUMERICAL MODELLING - PILLAR RUN, 10 M X 30 M ROOM, GRID PLOT

FIGURE 8.47 DPPC NUMERICAL MODELLING - PILLAR RUN, 20 M X 30 M ROOM, GRID PLOT

FIGURE 8.48 DPPC NUMERICAL MODELLING - PILLAR RUN, 30 M X 30 M ROOM, GRID PLOT

FIGURE 8.49 DPPC VIRGIN GROUND - 30 M X 30 M PILLAR RUN, GRID PLOT

LIST OF FIGURES Continued

FIGURE 8.50 DPPC NUMERICAL MODELLING - THREE ROOM ENTRY SYSTEM (FINAL) GRID PLOT

FIGURE 8.51 DPPC NUMERICAL MODELLING - NINE ROOM SEQUENCE (STAGE #3) GRID PLOT

FIGURE 8.52 DPPC NUMERICAL MODELLING PROBLEM - TWO 12 M STOPES (STAGE #4)

FIGURE 8.53 DPPC NUMERICAL MODELLING PROBLEM - THREE 10M STOPES (FINAL-STAGE #7)

FIGURE 8.54 DPPC NUMERICAL MODELLING - BAUER FOLD PROBLEM (STAGE #4) GRID PLOT

FIGURE 8.55 DPPC NUMERICAL MODELLING - TWO ROOM SEQUENCE (STAGE #1) GRID PLOT

FIGURE 8.56 DPPC NUMERICAL MODELLING - TWO ROOM SEQUENCE (STAGE #3) GRID PLOT

FIGURE 8.57 DPPC NUMERICAL MODELLING - TWO ROOM SEQUENCE (STAGE #1) PLASTICITY INDICATOR

FIGURE 8.58 DPPC NUMERICAL MODELLING - TWO ROOM SEQUENCE (STAGE #3) PLASTICITY INDICATOR

FIGURE 8.59 DPPC NUMERICAL MODELLING - TWO ROOM SEQUENCE (STAGE #3) PRINCIPAL STRESSES

FIGURE 8.60 DPPC NUMERICAL MODELLING - TWO ROOM SEQUENCE (STAGE #3) PRINCIPAL STRESSES

FIGURE 8.61 DPPC NUMERICAL MODELLING - TWO ROOM SEQUENCE (STAGE #1) HORIZONTAL STRESS CONTOURS

FIGURE 8.62 DPPC NUMERICAL MODELLING - TWO ROOM SEQUENCE (STAGE #3) HORIZONTAL STRESS CONTOURS

FIGURE 8.63 DPPC NUMERICAL MODELLING - TWO ROOM SEQUENCE (STAGE #1) VERTICAL STRESS CONTOURS

FIGURE 8.64 DPPC NUMERICAL MODELLING - TWO ROOM SEQUENCE (STAGE #3) VERTICAL STRESS CONTOURS

FIGURE 8.65 DPPC NUMERICAL MODELLING - TWO ROOM SEQUENCE (STAGE #3) DISPLACEMENT VECTORS

LIST OF FIGURES Continued

FIGURE 8.66 DPPC NUMERICAL MODELLING - TWO ROOM SEQUENCE (STAGE #3) DISPLACEMENT VECTORS

FIGURE 8.67 DPPC NUMERICAL MODELLING - TOW ROOM SEQUENCE (STAGE #3) VELOCITY VECTORS

FIGURE 8.68 DPPC NUMERICAL MODELLING - TWO ROOM SEQUENCE (STAGE #3) VELOCITY VECTORS

FIGURE 8.69 DPPC NUMERICAL MODELLING - TWO ROOM SEQUENCE (STAGE #3) ROOF CLOSURE - ROOM 1

FIGURE 8.70 DPPC NUMERICAL MODELLING - TWO ROOM SEQUENCE (STAGE #3) FLOOR CLOSURE - ROOM 1

FIGURE 8.71 DPPC NUMERICAL MODELLING - TWO ROOM SEQUENCE (STAGE #3) ROOF CLOSURE - ROOM 2

FIGURE 8.72 DPPC NUMERICAL MODELLING - TWO ROOM SEQUENCE (STAGE #3) FLOOR CLOSURE - ROOM 2

FIGURE 8.73 DPPC NUMERICAL MODELLING - TWO ROOM SEQUENCE (STAGE #3) LEFT WALL CLOSURE - ROOM 1

FIGURE 8.74 DPPC NUMERICAL MODELLING - TWO ROOM SEQUENCE (STAGE #3) RIGHT WALL CLOSURE - ROOM 1

FIGURE 8.75 DPPC NUMERICAL MODELLING - TWO ROOM SEQUENCE (STAGE #3) LEFT WALL CLOSURE - ROOM 2

FIGURE 8.76 DPPC NUMERICAL MODELLING - TWO ROOM SEQUENCE (STAGE #3) RIGHT WALL CLOSURE - ROOM 2

FIGURE 9.1 DPPC TEST STOPE PRIOR TO BACKFILL - MESH (T = 1.36 YRS)

FIGURE 9.2 DPPC HYDRAULIC BACKFILL PLACEMENT VERTICAL STRESS 2.5 M INTO PILLAR (T = 21.55 YRS)

FIGURE 9.3 DPPC HYDRAULIC BACKFILL PLACEMENT HORIZONTAL STRESS 2.5 M INTO PILLAR (T = 21.55 YRS)

FIGURE 9.4 DPPC DRY BACKFILL PLACEMENT VERTICAL STRESS 2.5 M INTO PILLAR (T = 21.59 YRS)

LIST OF FIGURES Continued

FIGURE 9.5 DPPC DRY BACKFILL PLACEMENT HORIZONTAL STRESS 2.5 M INTO PILLAR (T = 21.59 YRS)

FIGURE 9.6 DPPC DRY BACKFILL PLACEMENT - ROOF CLOSURE (T = 21.59 YRS)

FIGURE 9.7 DPPC DRY BACKFILL PLACEMENT - FLOOR CLOSURE (T = 21.59 YRS)

FIGURE 9.8 DPPC DRY BACKFILL PLACEMENT - WALL CLOSURE (T = 21.59 YRS)

FIGURE 9.9 DPPC HYDRAULIC BACKFILL PLACEMENT - ROOF CLOSURE (T = 21.55 YRS)

FIGURE 9.10 DPPC HYDRAULIC BACKFILL PLACEMENT - FLOOR CLOSURE (T = 21.55 YRS)

FIGURE 9.11 DPPC HYDRAULIC BACKFILL PLACEMENT - WALL CLOSURE (T = 21.55 YRS)

FIGURE 9.12 STOPE 11200 PRIOR TO BACKFILL - MESH (T = 1.05 YRS)

FIGURE 9.13 2ND PASS MINING AFTER 5 YEARS - MESH (T = 22.56 YRS)

FIGURE 9.14 2ND PASS MINING AFTER 5 YEARS VERTICAL STRESS IN BEARING PILLAR LEFT OF 11200 (T = 22.56 YRS)

FIGURE 9.15 2ND PASS MINING AFTER 5 YEARS HORIZONTAL STRESS IN BEARING PILLAR LEFT OF 11200 (T = 22.56 YRS)

FIGURE 9.16 2ND PASS MINING AFTER 5 YEARS VERTICAL STRESS IN PILLAR LEFT OF 2ND PASS STOPE (T = 22.56 Y)

FIGURE 9.17 2ND PASS MINING AFTER 5 YEARS HORIZONTAL STRESS IN PILLAR LEFT OF 2ND PASS STOPE (T = 22.56 Y)

FIGURE 9.18 2ND PASS MINING AFTER 5 YEARS VERTICAL STRESS IN PILLAR RIGHT OF 2ND PASS STOPE (T = 22.56)

LIST OF FIGURES Continued

FIGURE 9.19 2ND PASS MINING AFTER 5 YEARS HORIZONTAL STRESS IN PILLAR RIGHT OF 2ND PASS STOPE (T = 22.56)

FIGURE 9.20 2ND PASS MINING AFTER 5 YEARS VERTICAL STRESS IN BEARING PILLAR RIGHT OF 11240 (T = 22.56 Y)

FIGURE 9.21 2ND PASS MINING AFTER 5 YEARS HORIZONTAL STRESS IN BEARING PILLAR RIGHT OF 11240 (T = 22.56 Y)

FIGURE 9.22 2ND PASS MINING AFTER 10 YEARS VERTICAL STRESS IN BEARING PILLAR LEFT OF 11200 (T = 28.61 Y)

FIGURE 9.23 2ND PASS MINING AFTER 10 YEARS HORIZONTAL STRESS IN BEARING PILLAR LEFT OF 11200 (T = 28.61 Y)

FIGURE 9.24 2ND PASS MINING AFTER 10 YEARS VERTICAL STRESS IN PILLAR LEFT OF 2ND PASS STOPE (T = 28.61)

FIGURE 9.25 2ND PASS MINING AFTER 10 YEARS HORIZONTAL STRESS IN PILLAR LEFT OF 2ND PASS STOPE (T = 28.61)

FIGURE 9.26 2ND PASS MINING AFTER 10 YEARS VERTICAL STRESS IN PILLAR RIGHT OF 2ND PASS STOPE (T = 28.61)

FIGURE 9.27 2ND PASS MINING AFTER 10 YEARS HORIZONTAL STRESS IN PILLAR RIGHT OF 2ND PASS STOPE (T = 28.61)

FIGURE 9.28 2ND PASS MINING AFTER 10 YEARS VERTICAL STRESS IN BEARING PILLAR RIGHT OF 11240 (T = 28.61)

FIGURE 9.29 2ND PASS MINING AFTER 10 YEARS HORIZONTAL STRESS IN BEARING PILLAR RIGHT OF 11240 (T = 28.61)

FIGURE 9.30 2ND PASS MINING AFTER 5 YEARS - STOPE 11200 ROOF CLOSURE (T = 22.56 YRS)

FIGURE 9.31 2ND PASS MINING AFTER 5 YEARS - STOPE 11200 FLOOR CLOSURE (T = 22.56 YRS)

LIST OF FIGURES Continued

FIGURE 9.32 2ND PASS MINING AFTER 5 YEARS - STOPE 11200 LEFT WALL CLOSURE (T = 22.56 YRS)

FIGURE 9.33 2ND PASS MINING AFTER 5 YEARS - STOPE 11200 RIGHT WALL CLOSURE (T = 22.56 YRS)

FIGURE 9.34 2ND PASS MINING AFTER 5 YEARS - 2ND PASS STOPE ROOF CLOSURE (T = 22.56 YRS)

FIGURE 9.35 2ND PASS MINING AFTER 5 YEARS - 2ND PASS STOPE FLOOR CLOSURE (T = 22.56 YRS)

FIGURE 9.36 2ND PASS MINING AFTER 5 YEARS - 2ND PASS STOPE LEFT WALL CLOSURE (T = 22.56 YRS)

FIGURE 9.37 2ND PASS MINING AFTER 5 YEARS - 2ND PASS STOPE RIGHT WALL CLOSURE (T = 22.56 YRS)

FIGURE 9.38 2ND PASS MINING AFTER 5 YEARS - STOPE 11240 ROOF CLOSURE (T = 22.56 YRS)

FIGURE 9.39 2ND PASS MINING AFTER 5 YEARS - STOPE 11240 FLOOR CLOSURE (T = 22.56 YRS)

FIGURE 9.40 2ND PASS MINING AFTER 5 YEARS - STOPE 11240 LEFT WALL CLOSURE (T = 22.56 YRS)

FIGURE 9.41 2ND PASS MINING AFTER 5 YEARS - STOPE 11240 RIGHT WALL CLOSURE (T = 22.56 YRS)

FIGURE 9.42 2ND PASS MINING AFTER 10 YEARS - STOPE 11200 ROOF CLOSURE (T = 28.61 YRS)

FIGURE 9.43 2ND PASS MINING AFTER 10 YEARS - STOPE 11200 FLOOR CLOSURE (T = 28.61 YRS)

FIGURE 9.44 2ND PASS MINING AFTER 10 YEARS - STOPE 11200 LEFT WALL CLOSURE (T = 28.61 YRS)

FIGURE 9.45 2ND PASS MINING AFTER 10 YEARS - STOPE 11200 RIGHT WALL CLOSURE (T = 28.61 YRS)

FIGURE 9.46 2ND PASS MINING AFTER 10 YEARS - 2ND PASS STOPE ROOF CLOSURE (T = 28.61 YRS)

FIGURE 9.47 2ND PASS MINING AFTER 10 YEARS - 2ND PASS STOPE FLOOR CLOSURE (T = 28.61 YRS)

LIST OF FIGURES Continued

FIGURE 9.48 2ND PASS MINING AFTER 10 YEARS - 2ND PASS STOPE LEFT WALL CLOSURE (T = 28.61 YRS)

FIGURE 9.49 2ND PASS MINING AFTER 10 YEARS - 2ND PASS STOPE RIGHT WALL CLOSURE (T = 28.61 YRS)

FIGURE 9.50 2ND PASS MINING AFTER 10 YEARS - STOPE 11240 ROOF CLOSURE (T = 28.61 YRS)

FIGURE 9.51 2ND PASS MINING AFTER 10 YEARS - STOPE 11240 FLOOR CLOSURE (T = 28.61 YRS)

FIGURE 9.52 2ND PASS MINING AFTER 10 YEARS - STOPE 11240 LEFT WALL CLOSURE (T = 28.61 YRS)

FIGURE 9.53 2ND PASS MINING AFTER 10 YEARS - STOPE 11240 RIGHT WALL CLOSURE (T = 28.61 YRS)

FIGURE 9.54 2ND PASS MINING AFTER 5 YEARS - VELOCITY VECTORS (T = 22.56 YRS)

FIGURE 9.55 2ND PASS AFTER 10 YEARS - VELOCITY VECTORS (T = 28.61 YRS)

FIGURE 9.56 STRESS STATE IN STOPE 11200 2ND PASS - 5 YEARS AFTER BACKFILLING

FIGURE 9.57 STRESS STATE IN STOPE 11240 2ND PASS - 5 YEARS AFTER BACKFILLING

FIGURE 9.58 STRESS STATE IN STOPE 11200 2ND PASS - 10 YEARS AFTER BACKFILLING

FIGURE 9.59 STRESS STATE IN STOPE 11240 2ND PASS - 10 YEARS AFTER BACKFILLING

FIGURE 10.1 CLOVER HILL MINE, GENERAL MINE PLAN

FIGURE 10.2 DPPC PANELS 10 AND 11, 1988 MINING LAYOUT MINING PATTERN

FIGURE 10.3 DPPC PANELS 10 AND 11, 1988 MINING LAYOUT MINING HEIGHT

FIGURE 10.4 DPPC PANELS 10 AND 11, 1988 MINING LAYOUT NORMAL STRESS

LIST OF FIGURES Continued

FIGURE 10.5	DPPC PANELS 10 AND 11, 1988 MINING LAYOUT SHEAR STRESS
FIGURE 10.6	DPPC PANELS 10 AND 11, 1988 MINING LAYOUT CONVERGENCE RATE
FIGURE 10.7	DPPC PANELS 10 AND 11, 1988 MINING LAYOUT CONVERGENCE RATE ALONG X = 716
FIGURE 10.8	DPPC PANELS 10 AND 11, 1988 MINING LAYOUT CONVERGENCE RATE ALONG Y = 555
FIGURE 10.9	DPPC PANEL 11 1988 MINING LAYOUT SHOWING CONVERGENCE STATIONS
FIGURE 10.10	VERTICAL STRESS IN NORTH PILLAR, ROCK MECHANICS STATION IN STOPE 11200
FIGURE 10.11	PANELS 10, 11 AND 12, 1988 MINING LAYOUT SHOWING VELMINA STEADY-STATE SUBSIDENCE RATE FOR LARGE BASE CASE IN MICRO-METRES PER DAY
FIGURE 10.12	SUBSIDENCE RATE, 1987-88 NORTH-SOUTH SECTION
FIGURE 10.13	SUBSIDENCE RATE, 1987-88 EAST-WEST SECTION
FIGURE 10.14	DPPC PANELS 10 - 11 - 12 MINING PATTERN
FIGURE 10.15	DPPC PANEL 11 MINING PATTERN
FIGURE 10.16	DPPC PANEL 12 MINING PATTERN
FIGURE 10.17	DPPC PANEL 12 (DETAIL) MINING PATTERN
FIGURE 10.18	DPPC PANELS 10 - 11 - 12 NORMAL STRESS
FIGURE 10.19	DPPC PANELS 10 - 11 - 12 SHEAR STRESS
FIGURE 10.20	DPPC PANELS 10 - 11 - 12 CONVERGENCE RATE

LIST OF FIGURES Continued

FIGURE 10.21 DPPC PANEL 10 CONVERGENCE RATE

FIGURE 10.22 DPPC PANEL 11 CONVERGENCE RATE

FIGURE 10.23 DPPC PANEL 12 CONVERGENCE RATE

FIGURE 10.24 DPPC PANELS 10 - 11 - 12 CONVERGENCE RATE ALONG X = 1350

FIGURE 10.25 DPPC PANELS 10 - 11 - 12 CONVERGENCE RATE ALONG X = 571

FIGURE 10.26 PANELS 10, 11 AND 12, 1988 MINING LAYOUT SHOWING VELMINA STEADY-STATE SUBSIDENCE RATE IN MICROMETRES PER DAY

FIGURE 10.27 DPPC PANELS 10, 11, 12 BACKFILLED DENSITY AFTER 6 YEARS

FIGURE 10.28 DPPC PANELS 10, 11, 12 BACKFILLED DENSITY AFTER 11 YEARS

FIGURE 10.29 DPPC PANELS 10, 11, 12 BACKFILLED DENSITY AFTER 16 YEARS

FIGURE 10.30 DPPC PANELS 10, 11, 12 BACKFILLED DENSITY AFTER 21 YEARS

FIGURE 10.31 DPPC PANELS 10, 11, 12 BACKFILLED DENSITY AFTER 26 YEARS

FIGURE 10.32 DPPC PANELS 10, 11, 12, BACKFILLED MINING PATTERN

FIGURE 10.33 DPPC PANELS 10 - 11 - 12, BACKFILL DENSITY

FIGURE 10.34 DPPC PANELS 10 - 11 - 12, CONVERGENCE RATE

FIGURE 10.35 DPPC PANELS 10, 11, 12, SECONDARY EXCAVATION MINING PATTERN

FIGURE 10.36 DPPC PANELS 10, 11, 12, SECONDARY EXCAVATION NORMAL STRESS

FIGURE 10.37 DPPC PANELS 10, 11, 12, SECONDARY EXCAVATION SHEAR STRESS

LIST OF FIGURES Continued

FIGURE 10.38 DPPC PANELS 10, 11, 12, SECONDARY EXCAVATION CONVERGENCE RATE

FIGURE 10.39 DPPC PANELS 10, 11, 12 EFFECT OF SECONDARY EXCAVATION

FIGURE 10.40 DPPC PANELS 10, 11, 12 EFFECT OF SECONDARY EXCAVATION

FIGURE 10.41 DPPC PANELS 10, 11, 12 EFFECT OF SECONDARY EXCAVATION

FIGURE A.1 DISTRIBUTION OF HORIZONTAL/VERTICAL STRESS RATIOS PILLARS OF DIFFERENT WIDTH TO HEIGHT RATIOS

FIGURE A.2 DISTRIBUTION OF VERTICAL DEVIATOR/EFFECTIVE STRESS RATIOS PILLARS OF DIFFERENT WIDTH TO HEIGHT RATIOS

FIGURE A.3 AVERAGE EFFECTIVE STRESS IN PILLAR VS. MATCHING EFFECTIVE STRESS

FIGURE A.4 PLAIN STRAIN TEST PATTERN - VISCOT

FIGURE A.5 PLAIN STRAIN TEST PATTERN - VELMINA

FIGURE A.6 TEST PATTERN, VERTICAL STRESS

FIGURE A.7 TEST PATTERN, CONVERGENCE RATE

FIGURE A.8 PLAIN STRAIN TEST PATTERN - VELMINA

FIGURE B.1 VISCOT VERIFICATION RUN, CIRCULAR OPENING IN UNIFORM STRESS FIELD, CLOSURE RATE

FIGURE B.2 VISCOT VERIFICATION RUN, CIRCULAR OPENING IN UNIFORM STRESS FIELD, RADIAL STRESS

FIGURE B.3 VISCOT VERIFICATION RUN, CIRCULAR OPENING IN UNIFORM STRESS FIELD, CIRCUMFERENTIAL STRESS

LIST OF TABLES

TABLE 3.1	SUMMARY OF ROCK MECHANICS INSTRUMENTATION "USE OF BACKFILL IN NEW BRUNSWICK POTASH MINES -PHASE II"
TABLE 3.2	DENISON-POTACAN POTASH MINE STOPE 11200 ROCK MECHANICS STATION ROOM EXTENSOMETER (DAYS 0 TO 200)
TABLE 3.3	DENISON-POTACAN POTASH MINE STOPE 11200 ROCK MECHANICS STATION ROOF EXTENSOMETER (DAYS 200 TO 404)
TABLE 3.4	DENISON-POTACAN POTASH MINE STOPE 11200 ROCK MECHANICS STATION ROOF EXTENSOMETER (DAYS 404 TO 600)
TABLE 3.5	DENISON-POTACAN POTASH MINE STOPE 11200 ROCK MECHANICS STATION ROOF EXTENSOMETER (DAYS 600 TO 801)
TABLE 3.6	DENISON-POTACAN POTASH MINE STOPE 11200 ROCK MECHANICS STATION ROOF EXTENSOMETER (DAYS 801 TO 902)
TABLE 3.7	DENISON-POTACAN POTASH MINE STOPE 11200 ROCK MECHANICS STATION WALL EXTENSOMETER (DAYS 422 TO 600)
TABLE 3.8	DENISON-POTACAN POTASH MINE STOPE 11200 ROCK MECHANICS STATION WALL EXTENSOMETER (DAYS 600 TO 801)
TABLE 3.9	DENISON-POTACAN POTASH MINE STOPE 11200 ROCK MECHANICS STATION WALL EXTENSOMETER (DAYS 801 TO 902)
TABLE 3.10	STOPE 11200, PRESSURE CELL MEASUREMENTS
TABLE 3.11	DENISON POTACAN POTASH MINE PANEL 12 SOUTH 3-ENTRY SYSTEM (12826, 12827 & 12828) ROCK MECHANICS STATION, YIELD PILLAR ROD EXTENSOMETER (DAYS 0 TO 222)
TABLE 3.12	DENISON-POTACAN POTASH MINE PANEL 12 SOUTH 3-ENTRY SYSTEM (12826, 12827 & 12828) ROCK MECHANICS STATION, BARRIER PILLAR ROD EXTENSOMETER (DAYS 0 TO 222)

LIST OF TABLES Continued

TABLE 3.13 SURFACE SUBSIDENCE SURVEY

TABLE 4.1 CONSTANTS "C" AND "Ø" FOR DPPC OVERBURDEN ROCKS

TABLE 4.2 PARABOLIC FAILURE CRITERION CONSTANTS

TABLE 4.3 SHEAR WAVE AND COMPRESSIONAL WAVE VELOCITIES

TABLE 4.4 DYNAMIC AND STATIC ELASTIC MODULUS

TABLE 4.5 AVERAGE ELASTIC CONSTANTS OF OVERBURDEN ROCKS

TABLE 5.1 COMPACTION CREEP TEST MATRIX

TABLE 5.2 MOISTURE CONTENTS OF DRAINED BACKFILL

TABLE 5.3 STANDARD PROCTOR COMPACTION RESULTS

TABLE 5.4 DENSITY/STRAIN RATE DATA, DPPC HALITE BACKFILL COMPACTION CREEP

TABLE 5.5 SLOPES OF σ_c vs. COMPACTION STRESS CURVES

TABLE 5.6 PREDICTED ULTIMATE σ_c VALUES, DPPC HALITE BACKFILL

TABLE 5.7 STIFFNESS DATA, DPPC HALITE BACKFILL

TABLE 5.8 MOHR-COULOMB BRITTLE STRENGTH PARAMETERS

TABLE 6.1 POROSITIES OF BACKFILL/SAND MIXTURES

TABLE 6.2 BACKFILL/SAND AGGREGATE WITH WATER:CEMENT RATIO OF 0.3

TABLE 6.3 BACKFILL AGGREGATE WITH VARIOUS WATER:CEMENT RATIOS

TABLE 6.4 BACKFILL AGGREGATE WITH FLY ASH AND VARIOUS WATER: CEMENT RATIOS

TABLE 6.5 BACKFILL AGGREGATE WITH FLY ASH AND VARIOUS WATER: CEMENT RATIOS

TABLE 7.1 DPPC CREEP PARAMETER DETERMINATION

TABLE 7.2 STEADY-STATE CLOSURE RATES AND REFERENCE CREEP PARAMETERS

LIST OF TABLES Continued

TABLE 7.3 DPPC CREEP PARAMETER DETERMINATION
MATERIAL: SYLVINITE

TABLE 7.4 DPPC CREEP PARAMETER DETERMINATION
MATERIAL: UPPER HALITE

TABLE 7.5 DPPC CREEP PARAMETER DETERMINATION
MATERIAL: LOWER GRADATIONAL BED

TABLE 7.6 SUMMARY OF PARAMETRIC ANALYSIS

TABLE 8.1 COMPARISON OF PREDICTED AND ACTUAL CLOSURE RATES FOR THREE ROOM ENTRY SYSTEM (12826, 12827 & 12828)

TABLE 9.1 SUMMARY OF CLOSURE RATES FOR BACKFILL PLACEMENT METHODS

TABLE 9.2 FAILURE STATE OF HALITE BACKFILL IN TEST STOPE

TABLE 9.3 SUMMARY OF MINING AND BACKFILL SEQUENCE AND SUBSEQUENT CLOSURE RATES

TABLE 9.4 FAILURE STATE OF HALITE BACKFILL PRIOR TO SECOND PASS MINING

TABLE 9.5 FAILURE STATE OF HALITE BACKFILL AFTER SECOND PASS MINING

TABLE 9.6 FAILURE STATE OF HALITE BACKFILL AFTER SECOND PASS MINING

LIST OF PARAMETERS

GENERAL PARAMETERS

ϕ	Angle of Internal Friction
C	Cohesion
τ	Shear Strength
σ_n	Normal Stress
σ_Y	Yield Stress for Parabolic Failure Criterion
σ_c	Unconfined Compressive Strength
σ_t	Tensile Strength
σ_1	Major Principal Stress
σ_2	Intermediate Principal Stress
σ_3	Minor Principal Stress
R	Empirical Constant for Parabolic Failure Criterion
M	Empirical Constant for Parabolic Failure Criterion
E_d	Dynamic Elastic Modulus
ν	Poisson's Ratio
E_s	Static Elastic Modulus
γ	Density
V_s	Shear (s) Wave Velocity
V_p	Compressional (p) Wave Velocity
$\dot{\epsilon}$	Strain Rate
A	Empirical Creep Constant

LIST OF PARAMETERS Continued

BACKFILL PARAMETERS

w_c .... Moisture Content
w_{ct} .... True Moisture Content
m_w .... Mass of Water
m_s .... Mass of Solids
M_b .... Mass of Backfill
M_s .... Mass of Sand
b_c .... Saturated Brine Concentration in Mass of Dissolved Salt Per Volume of Water
V .... Volume
V_t .... Total Volume
V_i .... Volume of Material "i"
n .... Porosity
n_c .... Critical Porosity of Backfill
n_i .... Initial Porosity
n_d .... Difference Between n_i and n_c
G_s .... Specific Gravity of Solids
G_{sb} .... Bulk Specific Gravity of Engineered Backfill
G_{si} .... Specific Gravity of material "i"
i .... Material Number in Backfill Mixture
j .... Number of Materials in Backfill Mixture
r .... Cylinder Radius
h .... Depth of Backfill/Sand Mixture
γ_d .... Dry Density
γ_f .... Full Dry Density
D .... Fractional Density
d .... Grain Size

LIST OF PARAMETERS Continued

A_s	Scaling Constant
C_u	Coefficient of Uniformity
M_{50}	Apparent Stiffness
ϵ_v	Volumetric Strain
$\dot{\epsilon}_v$	Volumetric Strain Rate
$\dot{\epsilon}_{OB}$	Critical Strain Rate of Backfill
A_{B1}	Empirical Constant Lower Regime
A_{B2}	Empirical Constant Upper Regime
l_1	Slope of Curve of High Creep Rate Regime
l_2	Slope of Curve of Low Creep Rate Regime
m	Stress Exponent
m_1	Lower Regime Stress Exponent
m_2	Upper Regime Stress Exponent
m_3	Empirical Exponent
σ	Compaction Stress
σ_m	Hydrostatic Stress
σ_{OB}	Critical Stress corresponding to $\dot{\epsilon}_{OB}$
a_1	Empirical Constant
a_2	Empirical Constant
a_3	Empirical Constant
a_4	Empirical Constant
b_1	Empirical Constant
b_2	Empirical Constant
b_3	Empirical Constant
b_4	Empirical Constant
C_1	Empirical Constant
C_2	Empirical Constant

LIST OF PARAMETERS Continued

INTACT MATERIAL PARAMETERS

σ_s .... Deviatoric Stress (Tresca's Criterion)
σ_{eff} .... Effective Stress (Von Mises Criterion)
J_2 .... Second Invariant of Stress Deviation
σ_o .... Critical Effective Stress
σ_{o1} .... Lower Regime Reference Stress
σ_{o2} .... Upper Regime Reference Stress
$\dot{U}_{ss}$ .... Steady State Closure Rate
$\dot{\epsilon}_{ss}$ .... Steady State Strain Rate
$\dot{\epsilon}_o$ .... Critical Strain Rate of Intact Material
$\dot{\epsilon}_{o1}$ .... Lower Regime Reference Strain Rate
$\dot{\epsilon}_{o2}$ .... Upper Regime Reference Strain Rate
A_1 .... Lower Regime Empirical Creep Constant
A_2 .... Upper Regime Empirical Creep Constant
n_1 .... Lower Regime Exponent
n_2 .... Upper Regime Exponent
Q .... Activation Energy
R_i .... Ideal Gas Constant
T_i .... In Situ Temperature
T_r .... Laboratory Temperature

SECTION 1.0

1.0 EXECUTIVE SUMMARY

1.1 Introduction

The Denison-Potacan Potash Co. mine site is located southwest of Sussex, New Brunswick, as shown in Figure 1.1. The Clover Hill deposit was first identified by surface exploratory drilling conducted in 1973 under the direction of the New Brunswick Department of Natural Resources. It is confined to the Marchbank Syncline, which is the most southerly major structural feature of the Moncton Subbasin shown in Figure 1.2.

The Denison-Potacan potash deposit is at a depth, on average, of 880 metres below surface. It is approximately 10 kilometres in length along the strike and has a maximum plan width of 3.5 kilometres. A mine plan showing the existing mining panels 10, 11 and 12 and a typical section through Panel 11 are included as Figures 1.3 and 1.4. The room and pillar method of mining utilized to extract the potash ore uses mechanical excavation with mining machines as well as drilling and blasting techniques. Conveyor belt systems are used to transport ore from the mining areas to the underground ore storage bin and then the production shaft through which ore is hoisted to surface in 25 tonne skips. The ore is then conveyed to the plant where sylvite is removed from the ore as product and the waste, principally halite, is then either returned underground as backfill or, temporarily, to a surface tailings stockpile.

Halite tailings in the plant circuit are dewatered to approximately 8% moisture by vacuum filtration and then directed to the Service Shaft by conveyor belt. They are discharged from this belt to one of two 200 mm diameter steel pipelines installed in the shaft. The pipelines terminate in a drop box at the main shaft station at the 795 m level where the tailings are directed to a conveyor belt system for transport to the areas in the mine that are being backfilled.

In July 1985, a proposal for research was submitted by Denison-Potacan to the Minister of Supply and Services, bearing the title of "Use of Backfill in New Brunswick Potash Mines Proposal", in response to a request from the

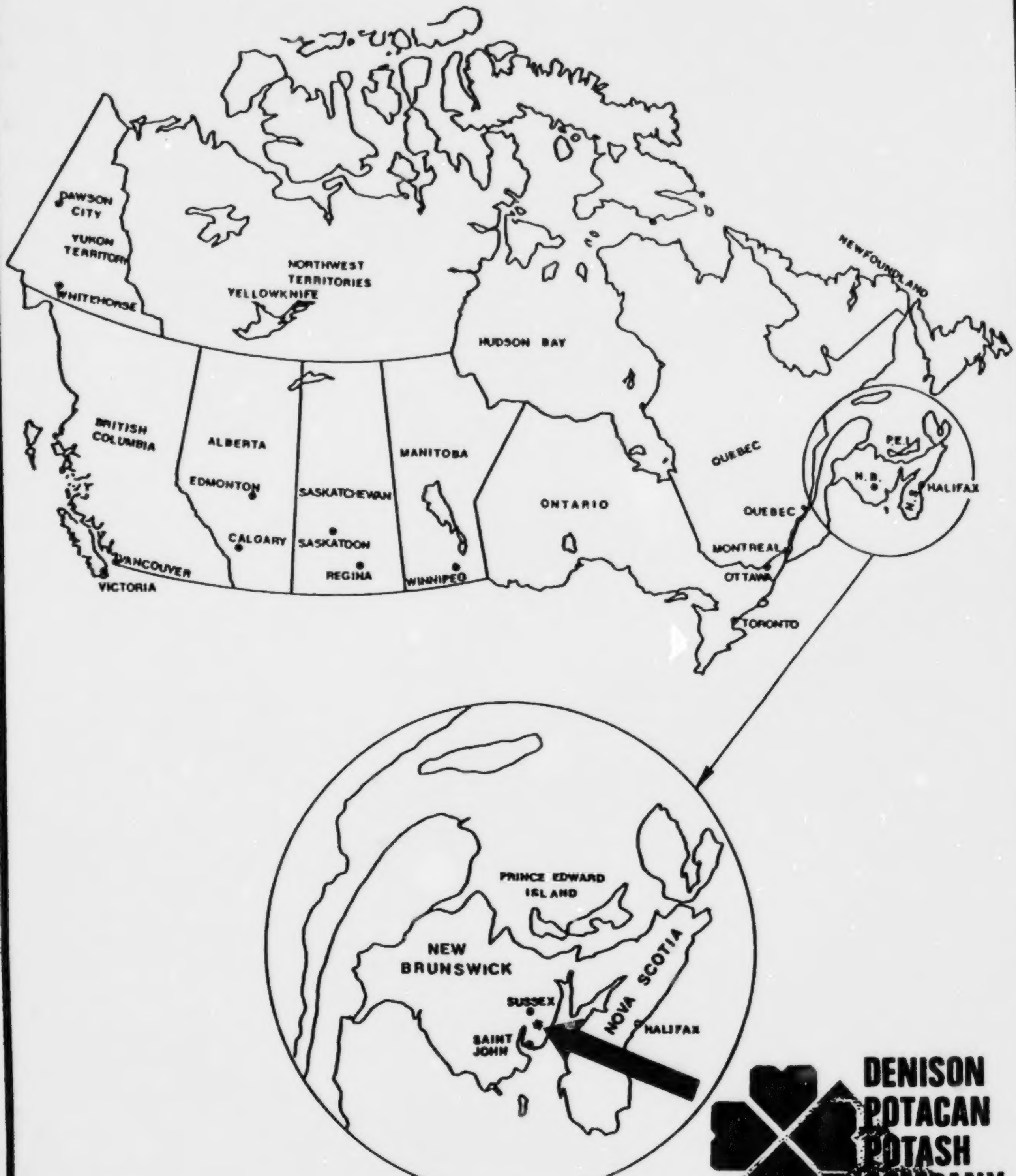

DENISON POTACAN POTASH COMPANY

DENISON POTACAN POTASH COMPANY	TITLE: LOCATION OF MINE SITE	SCALE: N.T.S. FIGURE: 1.1

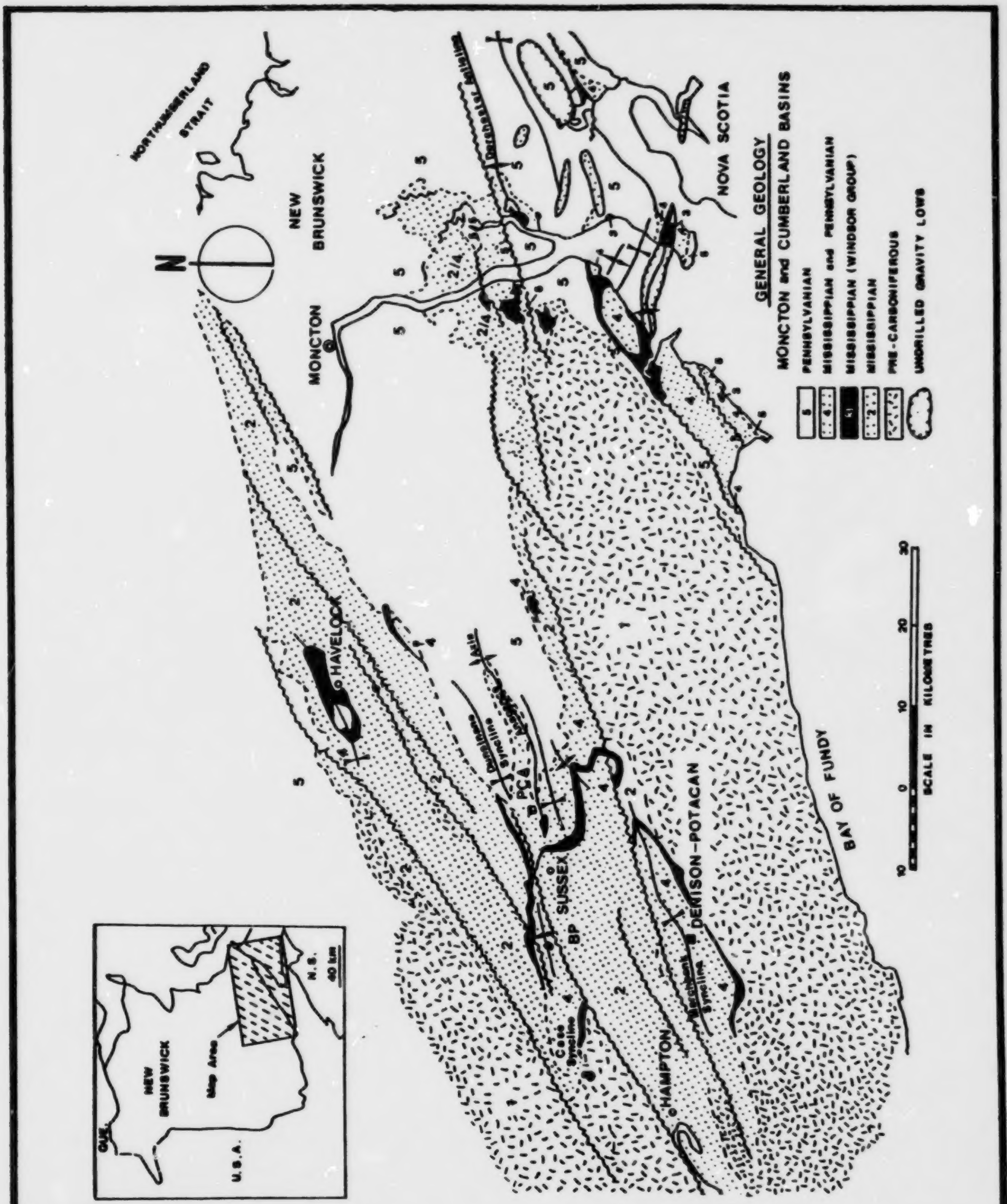

DENISON
POTACAN
POTASH
COMPANY

TITLE:

GEOLOGY OF THE MONCTON
SUBBASIN IN NEW BRUNSWICK
(After Waugh and Urquhart, 1983)

SCALE:
N.T.S.

FIGURE:
1.2

Department of Supply and Services. The goal of the program was to research the behaviour and methods of placement of the tailings from the Denison-Potacan plant with the aim of providing support and stabilization to the mine workings, leading to improved resource recovery mining methods and an environmentally acceptable means of disposal for tailings.

A research contract was awarded to Denison-Potacan entitled "Phase I - Use of Backfill in New Brunswick Potash Mines". Findings of the Phase I of the program were submitted in May 1987 as a Final Report of the work performed under DSS Contract Serial No. 0SQ85-00208/CANMET Project No. 1.4.09.05. Backfilling operations commenced at the Denison-Potacan mine in February 1987. However, several major technical aspects remained to be addressed that had not been included in the Phase I program.

In May 1987, a proposal for further research into the technical aspects identified by Phase I was submitted bearing the title of "Use of Backfill in New Brunswick Potash Mines, Phase II". A contract for Phase II was awarded to Denison-Potacan in January 1988 to proceed with the research work, who retained MPC to carry out some of the work and coordinate the study. The following report is a Final Report of the work performed under DSS Contract Serial No. 23440-7-9228/01-SQ, CANMET project No. 1.4.09.05.

1.2 In Situ Testing

The significance and value of collecting and analyzing in situ rock mechanics data, as to stress and strain distribution surrounding mine openings, was recognized and acted upon by Denison-Potacan as early as 1982. The rock mechanics instrumentation used consisted of equipment to measure displacements and stresses. The equipment ranged from simple inexpensive manual measurement systems to electronic measuring devices and programmable dataloggers.

Prior to the start up of production activities in July 1985, two test sites were excavated to provide virgin ground field data. These sites, the Test Room and Test Stope, were excavated in 1982 and 1983, respectively, and have been discussed in detail in Phase I report. Since July 1985, emphasis

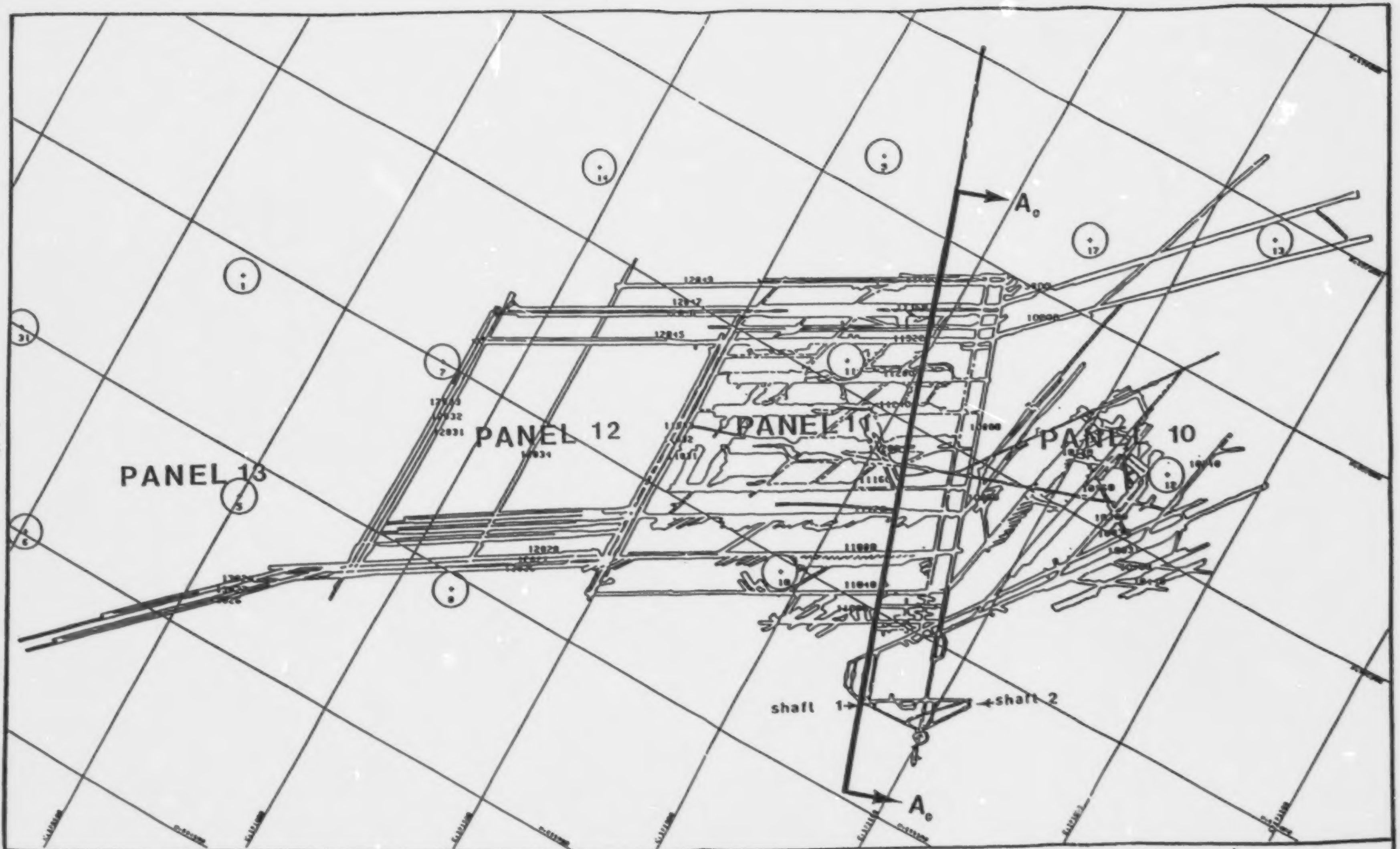

DENISON
POTACAN
POTASH
COMPANY

TITLE:

CLOVER HILL MINE
GENERAL MINE PLAN

SCALE: NTS

FIGURE:
1.3

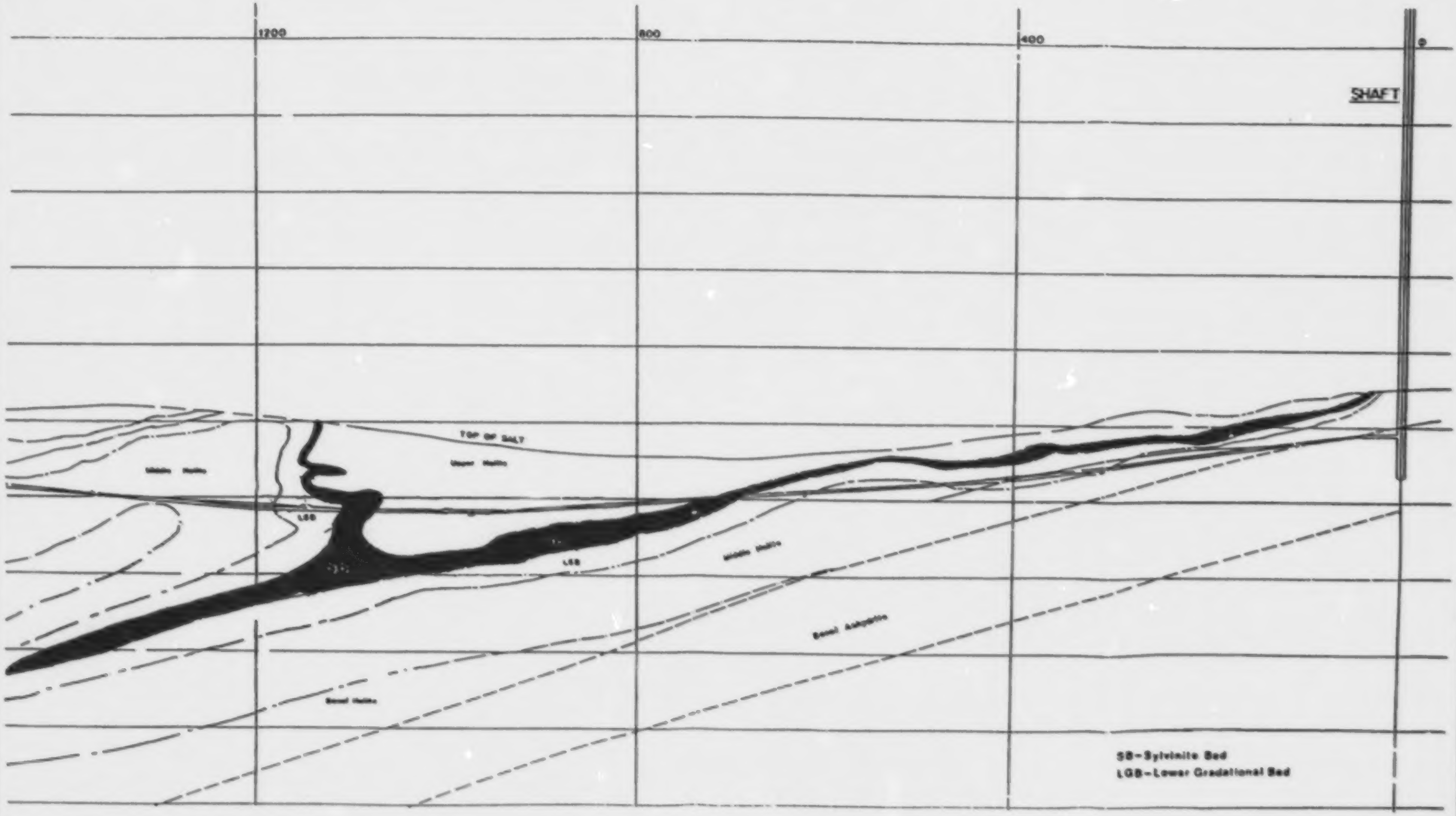

DENISON
POTACAN
POTASH
COMPANY

TITLE:
PANEL 11
TYPICAL GEOLOGICAL CROSS-SECTION

SCALE: N T S

FIGURE:
1.4

has been placed upon the monitoring of active mining sites. A rock mechanics station in Stope 11200 (previously referred to as Stope 1105) was chosen to be the initial backfill monitoring site and was instrumented to monitor the roof and wall behaviour of a full scale backfilled production stope.

Multiple point extensometers and pressure cells were installed in both the roof and wall of Stope 11200 at various depths. It was planned to place instrumentation in the floor of the stope as well however this was prevented by the pooling of brine from a nearby backfilling area. Earth pressure cells were emplaced in the backfill to monitor backfill stress levels. All instrumentation was provided with electronic readout capability to allow monitoring by a programmable datalogger. Various methods were utilized to provide protection to the monitoring equipment and readout cables from impact and corrosion.

Vertical closure stations were installed in stopes to provide calibration data for the numerical modelling runs. The entry systems were used to evaluate instrumentation performances, in particular, various types of pressure cells and to provide field data for comparison and calibration of numerical modelling runs.

A total of 17 subsidence monuments were installed over Panel 10 workings in the summer of 1985. An additional 14 monuments were added in 1987 to monitor mining activity as it progressed.

1.3 Laboratory Testing

A laboratory testing program of overburden core samples was carried out to identify the mechanical properties of rocks within the formations overlying the evaporite interval for the purpose of numerical modelling. Four types of tests were performed on the four materials:

1) Sonic velocity measurements used in the calibration of the dynamic elastic constants.
2) Brazilian tests for tensile strength.
3) Unconfined compressive strength (UCS) tests.
4) Triaxial compressive strength tests.

During most of the UCS tests, unload/reload cycles were performed for determination of the unload moduli.

The backfill testing performed under Phase I of the program was of a preliminary nature. Compaction testing over a period of 90 days supported the initial hypothesis that the emplaced backfill would have limited support capability prior to a substantial elimination of porosity of the backfill during the closure history of the backfilled openings.

The triaxial testing was very limited in scope and insufficient data was generated to warrant the development of stiffness functions and the brittle yield failure criteria of backfill. Hence, additional testing was required under the Phase II program. The scope of the Phase II program was designed to determine the following:

a) Compaction creep behaviour of backfill.
b) Triaxial strength of backfill at various densities.
c) Backfill stiffness as a function of fractional density.
d) Effect of stress, density and time on the microfabric of the backfill.
e) Methods of halite backfill enhancement with additives (engineered backfill).

To limit the number of test variables, the relevance of each of the parameters which have been found to affect the mechanical behaviour of granular halite was examined as it applied to the backfilling of potash mines. Of the external parameters (stress, strain rate and temperature), only stress and strain rate were considered uncontrollable (and variable with time). Temperature was not included as it is unlikely to vary significantly over the life of the mine. Of the material dependent parameters (impurities content, grain size, grain size distribution, moisture content and porosity), only moisture content and porosity were included as test variables.

Material characterization was carried out to determine the physical properties of the backfill to aid in the interpretation of laboratory test results. It included an examination of the grain size, mineralogy and moisture/porosity relationships in the backfill. Compaction creep testing was carried out to examine the effect of stress, strain rate, moisture content and porosity on the rate at which the backfill compacts. The test results were used to develop an empirical relationship describing the time dependent behaviour of halite backfill. The brittle strength of the backfill was examined to determine under what stress conditions the backfill could fail in shear. Two strength properties were investigated:

a) brittle strength development in backfill compacted under different stresses;

b) confined brittle strength at various fractional densities/porosities.

Granular halite backfill crystals are small pieces of intact salt. As such, they are subject to the same creep mechanisms (dislocation creep, diffusion creep, grain boundary sliding and cataclasis). However, in situ conditions (i.e. temperature, stress) and material properties (i.e. moisture content, grain size) will govern which mechanism dominates compaction creep. Pressure solution has been suggested as an important time dependent mechanism at the stresses and temperatures encountered in Canadian potash mines, and it has been identified in this study as one of the dominant mechanisms of compaction creep in pure granular halite. At low stresses, slopes in the range of 1.5 to 2 were similar to those noted by Spiers et al. (1989) and reflect pressure solution dominated creep. At medium stresses, particulate sliding becomes dominant if moisture is present. It can be suggested from the presence of crushed grain contracts that cataclastic deformation also occurred during the compaction of the backfill. This type of deformation is relatively time independent and has an associated stress dependent, finite amount of strain. Cataclastic processes can account for the initial rapid compaction of a granular aggregate after the imposition of an external, compressive stress. Cataclastic processes essentially cease once stresses at grain contacts have dropped below the crushing or fracturing strength of the material. Under in situ conditions, the rapid compaction dominated by cataclasis will be rare. The mechanisms dominating deformation in halite backfill, based on examination of laboratory behaviour were:

a) pressure solution at low stresses (< 2 MPa) and low volumetric strain rates ($<10^{-6}\ s^{-1}$);

b) particulate sliding at volumetric strain rates above $10^{-6}\ s^{-1}$;

c) cataclasis initially at all stresses upon a sudden imposition of a stress, with magnitude being stress dependent.

In situ stresses will be low for long periods of time before room closure begins to transfer roof and pillar loads. Pressure solution will, therefore, be the dominant in situ compaction creep mechanism. An empirical model describing the compaction creep behaviour of halite backfill has been developed based on the following assumptions and observations:

a) a very high rate volumetric compaction creep regime dominated by cataclasis is unlikely to operate in situ and has been disregarded;

b) volumetric compaction creep under in situ conditions will occur in two creep rate regimes; a high rate regime dominated by particulate sliding and a low rate regime dominated by pressure solution;

c) the rates of volumetric strain rate within both regimes are a function of stress, provided that fractional density is greater than 0.6;

d) the volumetric stain rate $\dot{\epsilon}_{os}$ at which high rate processes cease and low rate processes begin to dominate, can be taken as a constant.

e) at fractional densities greater than 0.75, within the range of stresses and strain rates tested, the two creep rate regimes seem to merge into one with a stress dependency exponent of 3, an indication that intragranular processes begin to dominate.

The fit of the proposed empirical creep law (equation 5.10) to the experimental data is shown in Figure 1.5.

The brittle strength of halite backfill is largely a function of its porosity and compaction rate used to achieve that porosity. In situ the backfill will densify slowly under low stress conditions. In the laboratory,

FIGURE 1.5

Halite Backfill Empirical Creep Law Fit

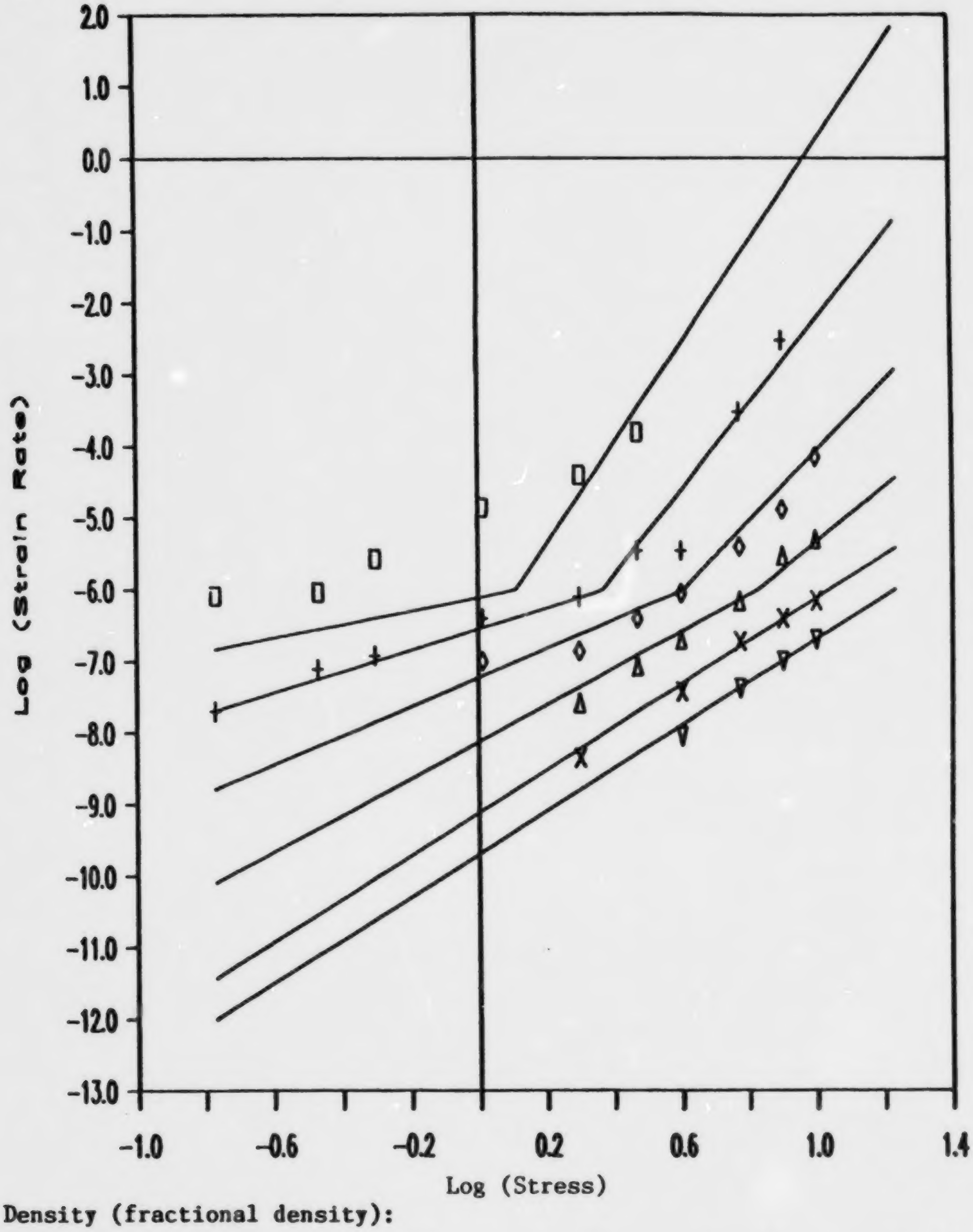

Density (fractional density):

□ 1.2 (0.56) + 1.3 (0.61) ◊ 1.4 (0.65) Δ 1.5 (0.70) X 1.6 (0.75) ∇ 1.7 (0.79) the test specimens must be compacted rapidly relative to in situ. High rate compaction is dominated by cataclasis. As cataclastic processes deform by breaking material (i.e. crushing, fracturing), brittle strength increases are predominantly due to those achieved by increases in frictional surface area between grains. Under the low compaction in situ, pressure solution creep anneals adjacent crystals; the dissolved ions from both grains precipitate together in pores, joining the two grains. This increases the brittle strength of the backfill by making it a rock with porosity rather than a granular mass held together by friction.

Laboratory brittle strength test results were extrapolated to determine approximate in situ values. The curves shown in Figure 1.6 were extrapolated to the left to a 'zero compaction rate' brittle strength. A linear extrapolation of these curves to a backfill with porosity of 0.01 (i.e. fractional density of 0.99) yields UCS values for a compacted DPPC halite backfill (Figure 1.7). It can be suggested that from an extrapolation of the curve in Figure 1.7, backfill with a fractional density of less than 0.7 has little or no brittle strength, and that the uniaxial compressive strength can be defined in terms of fractional density.

The apparent stiffness (M_{50}) was measured from the stress/strain curves of 50% of the UCS during each test. A porous granular material placed under stress undergoes grain crushing, fracture and reorientation (cataclasis) as well as elastic deformation of individual grains. Separating the two types of deformation is difficult. The stiffness of halite backfill is, therefore, a bulk measurement of the total instantaneous deformation, both recoverable elastic and non-recoverable cataclastic, the material undergoes when subjected to a deviatoric stress. The test results tabulated were combined to determine an equation describing the relationship between M_{50} and fractional density "D". This relationship predicts that materials with fractional densities less than 0.7 will have very low stiffness.

Triaxial brittle strength data, plotted on a σ_1/σ_3 diagram, show the failure envelopes to become increasingly linear with decreasing porosity over the range of confining stresses tested. During testing, the specimens were confined and initially underwent a period of compaction before dilating and

FIGURE 1.6

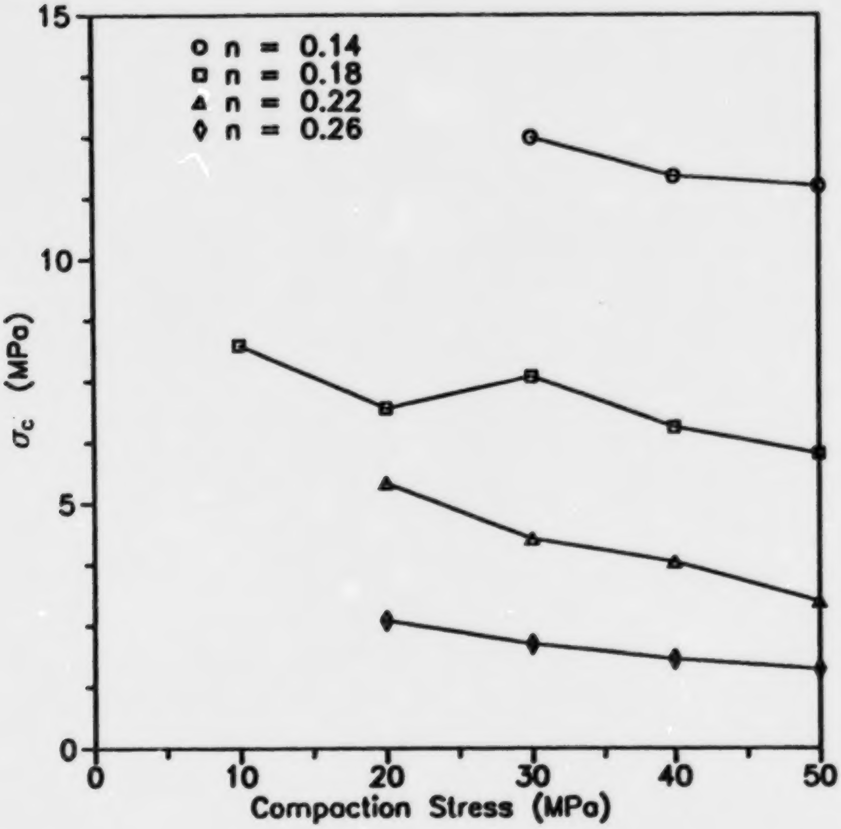

Unconfined compressive strength vs. compaction stress for test specimens at porosities of 0.14, 0.18, 0.22 and 0.26.

FIGURE 1.7

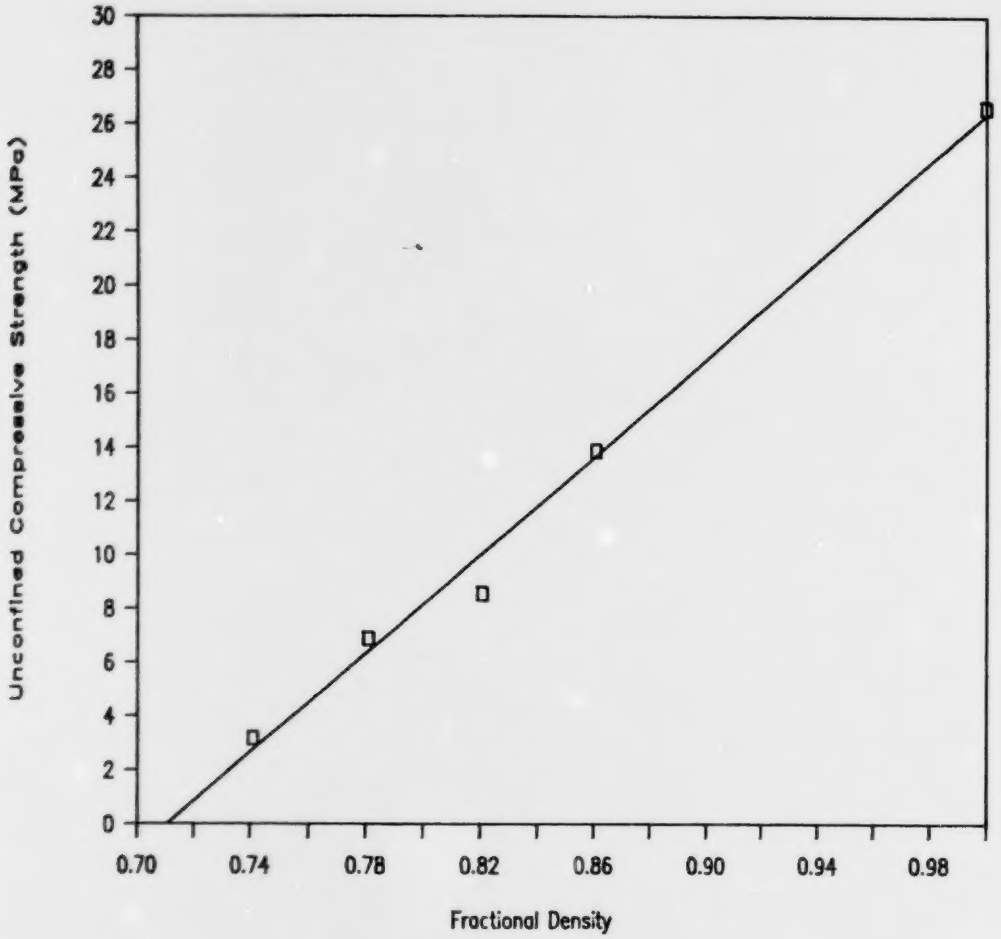

'Zero compaction stress' σ_c as a function of fractional density for DPPC halite backfill.

eventually strain weakening (Figure 1.8). The amount of compaction was dependent on the confining stress and the initial porosity. To determine the true 'zero compaction stress' brittle strength would require several sets of triaxial tests performed on specimens compacted under different stresses, and it was not clear how the triaxial brittle strengths can be extrapolated to in situ values. However, the values obtained from this study can be assumed to be conservative.

A test program was carried out to determine the effects of additives on the strength of DPPC halite backfill. Two types of additives were examined during this study; cements and sand. The sand used in the testing was obtained from the local Sussex Silica quarry near the DPPC mine site. Incorporation of sand into the backfill can reduce its placement porosity, thereby reducing the total amount of closure and time to achieve overburden support. The strength of engineered backfill is primarily a function of its cement content and water:cement ratio. It appears that a 9-10% cement content produces a material with a UCS of 1.3-2 MPa. Additives such as silica sand and fly ash can increase the strength of the backfill provided they are added in high enough proportions.

1.4 Parametric Analysis of Data on Salt Rocks

Since the completion of Phase I of the project, additional research was devoted to the analysis of in situ and laboratory data and the development of parameters for input into the numerical modelling process. Included were:

a) the use of a different shear stress criterion in derivation of creep strain rate;
b) re-evaluation of initial in situ and laboratory data;
c) re-evaluation of parameters derived from in situ and laboratory data;
d) determination of corresponding input parameters.

A shear stress criterion is a mathematical expression giving a specific combination of stress components in a body which will initiate and maintain a specific level of creep strain rate. In Phase I of the research project,

FIGURE 1.8

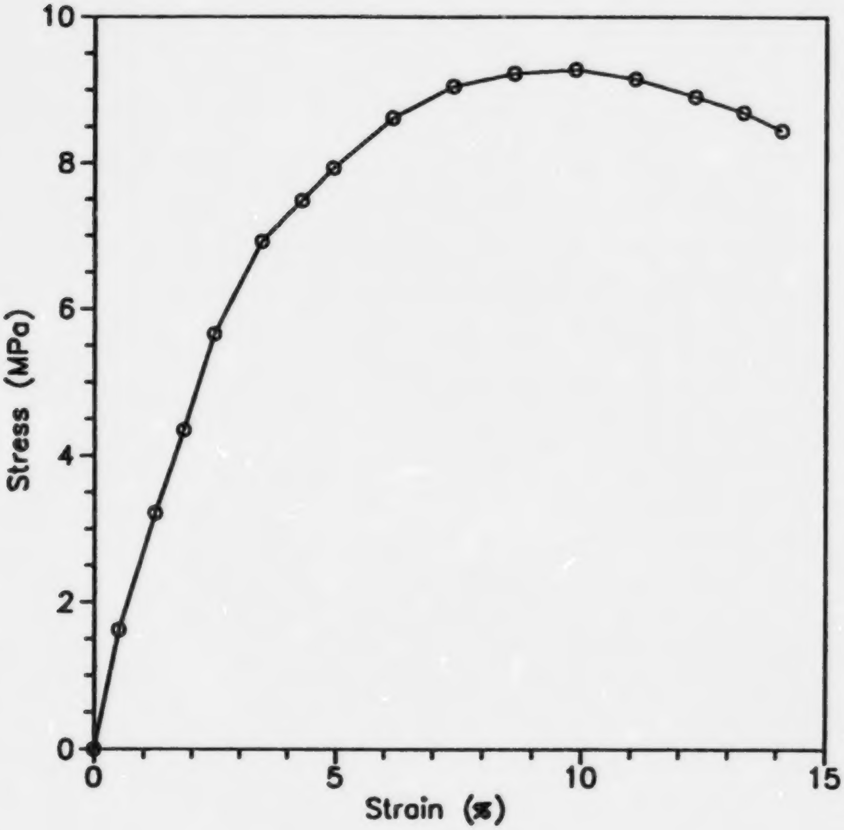

Stress/strain diagram for halite backfill compacted to n = 0.22, confining stress 1.03 MPa, axial strain rate 10^{-4} sec^{-1}.

Tresca's criterion was used. This was changed to **Von Mises criterion** in Phase II. The disadvantage of Tresca's criterion is it implies that stresses in tension and compression have the same effect, which does not hold true for rocks, and the intermediate principal stress (σ_2) has no affect on the criterion. Examination of available published research literature shows that the **Von Mises criterion is more widely accepted compared to Tresca's** criterion when used to predict the in situ behaviour of rock.

The Rock Mechanics Station used for calibration in Phase I of the CANMET study was rerun using the Von Mises definition of effective stress, the same modelling parameters as in Phase I, and a restructured mesh. Upon completion of the rerun, it was found that the predicted closure rates were 5.5 times greater than the measured in situ rates.

As shown in Figure 1.9, only two mechanisms are thought to operate at ambient temperatures and within the regime of stresses under typical mining conditions: mechanism (2) and mechanism (5). This leads to the concept of a two-component creep law, reflecting a change of power law exponent at the level of stress between the two regimes. Mechanism (5) is governed by a power law with an exponent of 3. A new analysis of laboratory data from Phase I resulted in the exponent for mechanism (2) equal to 6.9 compared to the previous value of 5.8.

The next step taken in the revaluation was to determine the values of the reference stress and strain rate that would reproduce the in situ closure rate. To accomplish this, a total of three numerical modelling runs were required to determine if a relationship existed between the closure rate and these reference parameters. A linear regression was performed to determine if a relationship exists between the reference stress (σ_0) and the steady-state closure rate. The results have shown a definite exponential trend between the two parameters. The values of the new creep parameters determined by this analysis produced results that were in close agreement with measured in situ behaviour. The statistical fits of the current creep law parameters for the three materials studied also offer much better fits than parameters used in Phase I.

FIGURE 1.9

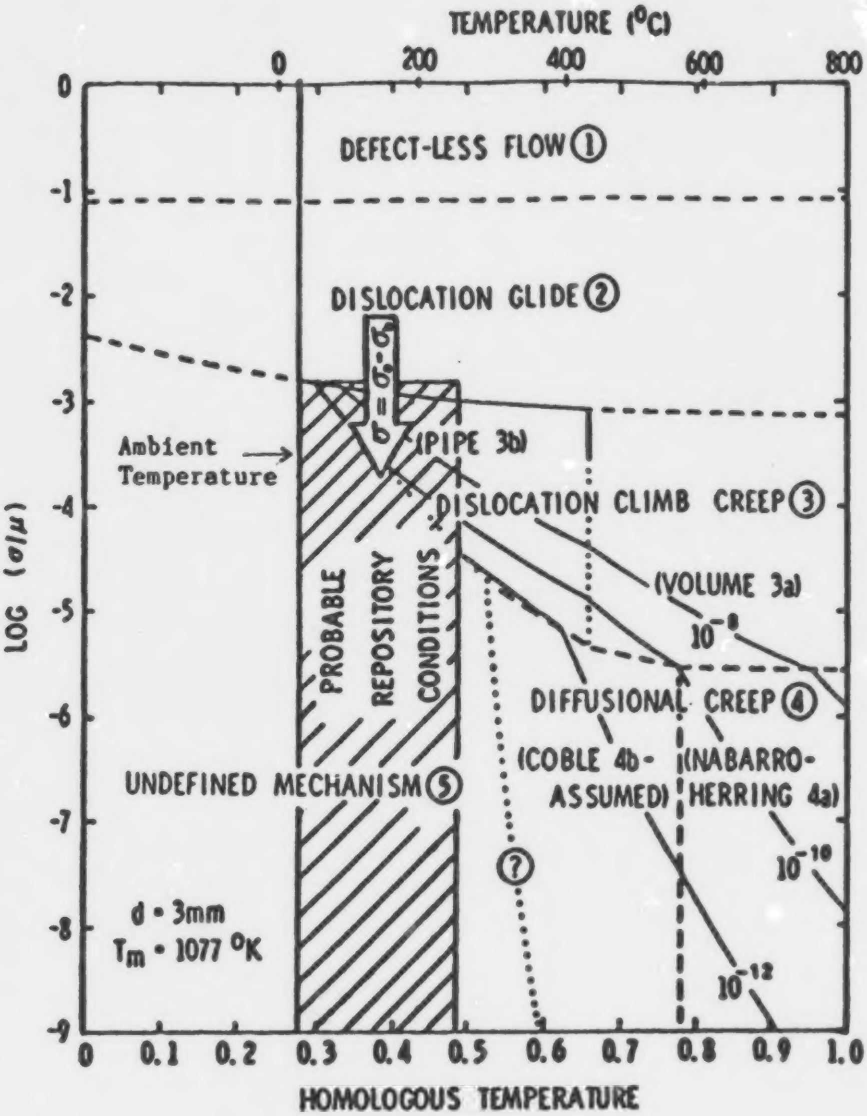

Deformation Mechanism Map for Salt
(After Munson, 1979).

1.5 Two-Dimensional Material Modelling

The program **FLAC** (Fast Langarian Analysis of Continua) written by ITASCA Consulting Group Inc. was used for two-dimensional modelling. The constitutive law used in this study was developed through a joint effort by MPC and the University of Waterloo and incorporated into the program by ITASCA under a contract with Mraz Project Consultants Ltd. FLAC is a two-dimensional microcomputer program that uses the explicit finite difference method to model a variety of geotechnical problems, including large-strain plasticity, time dependent creep, interfaces and support-structure interaction. FLAC is capable of analyzing Plane strain, Plane stress or axisymmetric problems.

A numerical solution obtained using FLAC was compared to the analytical solution for closure of a infinitely long cylindrical cavity. The numerical solution was obtained using a uniform stress field under virgin ground conditions. Sylvinite material properties were used in the analysis. A comparison of the analytical and FLAC solutions has shown very good correlation.

Prior to using FLAC as a predictive tool for mine design, FLAC was calibrated against in situ data from the virgin ground Test Room. Using the material properties and the constitutive law in this study, behaviour of the test room was simulated. A comparison between the in situ data and the numerical solution has shown a good correlation between the in situ measurements and the modelled closures.

Using the computer program FLAC, analysis of existing mining geometries and planned geometries were simulated to evaluate their performance. The analyses were used to identify potentially unfavourable stress conditions and potential failure zones. The amount of closure and the closure rates were used to evaluate the overall behaviour in response to the closure/stress events produced by mining.

Satisfactory agreements between predicted and actual closure measurements in virgin ground openings were obtained using the proposed properties and the constitutive law for intact rock. The convergence rates for high mining stopes were somewhat overpredicted due to the two-dimensional nature of the analysis. Potential problems in regard to failure in the roof were identified if the salt cover was too thin. In every case studied, the need for good roof bolting practices and regular roof inspections was evident. Horizontal and vertical stress levels were found to be at safe levels at the top of the salt in regard to the hydrostatic water pressure of 9 MPa. In none of the cases considered was the stability of the bearing pillars found to be inadequate.

The constitutive law that was developed to predict the behaviour of halite backfill was incorporated into the numerical model FLAC. Using the program FLAC, analysis of the backfilling method and the sequencing of second pass mining was performed. Investigation of backfill placement was performed by varying the initial placement density of the backfill which was placed in the Test Stope geometry. Sequencing of second pass mining was investigated 5 years and 10 years after backfilling Stopes 11200 and 11240. Generally, it can be concluded that stopes should be backfilled using the hydraulic placement method, and second pass mining can be considered after 10 to 15 years following the backfill placement.

1.6 Three-Dimensional Numerical Modelling

The three-dimensional modelling was done using the program VELMINA (Visco-Elastic Mine Analysis) written by Dr. L. Rothenburg. The program is designed for three-dimensional analysis of large-scale mining layouts that involve large numbers of rooms and pillars in visco-elastic rock. The mathematical formulation in the VELMINA is a rigorous implementation of the Displacement Discontinuity method for an anisotropic linearly visco-elastic host rock outside of the mining seam. In-seam rock properties can be described by an arbitrary non-linear steady state creep law. Pillars can be assigned non-linear elasto-visco-plastic properties. Both transient and steady state conditions can be determined. The capability to model sequential excavation includes placement of backfill in selected areas. Relatively thin layered inclusions in the host rock can be accommodated in analysis. The program has a capability of doing an iterative analysis to determine matching equivalent linear properties for a specified non-linear creep law of the host rock. For elements representing pillars with visco-elastic properties, a ratio of vertical to effective stress is assigned. The ratios of vertical to effective stresses are assigned based on finite element analysis of pillars.

In order to reflect the complexity of the ore body correctly in the computer simulation, the **ore thickness** sub-routine has been generated. The ore thickness information has been extracted from a DPPC ore thickness isopach map and entered into the sub-routine for future use. The first geometry investigated was Panels 10 and 11 as they existed in 1988 (Figure 1.10). The mesh consisted of 30,000 elements.

The behavioural laws and input parameters used in VELMINA were the same as those used in FLAC. In order to verify that these were valid for VELMINA runs, the results of the run were compared to the various in situ measurements.

In spite of mining disturbances at the time of measurements, the predicted and measured convergence rates compare well and confirm validity of the input parameters and material laws used. The subsidence rates, and to some extent vertical stress measurements, compare well with the predicted values which increases the level of confidence in this modelling.

The mesh for a combined excavations of Panels 10, 11 and 12 consisted of 60,000 elements. The ultimate mining layout of Panel 12 was based on the current DPPC mining plan for this area. It was determined that the maximum convergence rates in Panel 12 would be about twice the maximum convergence rates currently experienced in Panel 11.

The mesh (Figure 1.11) and the steady state stress conditions (Figure 1.12) from previous analysis were used. The initial backfill placement density was assumed to be 1.4 g/cm^3. Figure 1.13 shows the density distribution at 11 years. The degree of densification at various points (Figure 1.14) within the layout over time is shown in Figure 1.15. The convergence rates at various points over time are shown in Figure 1.16.

FIGURE 1.10

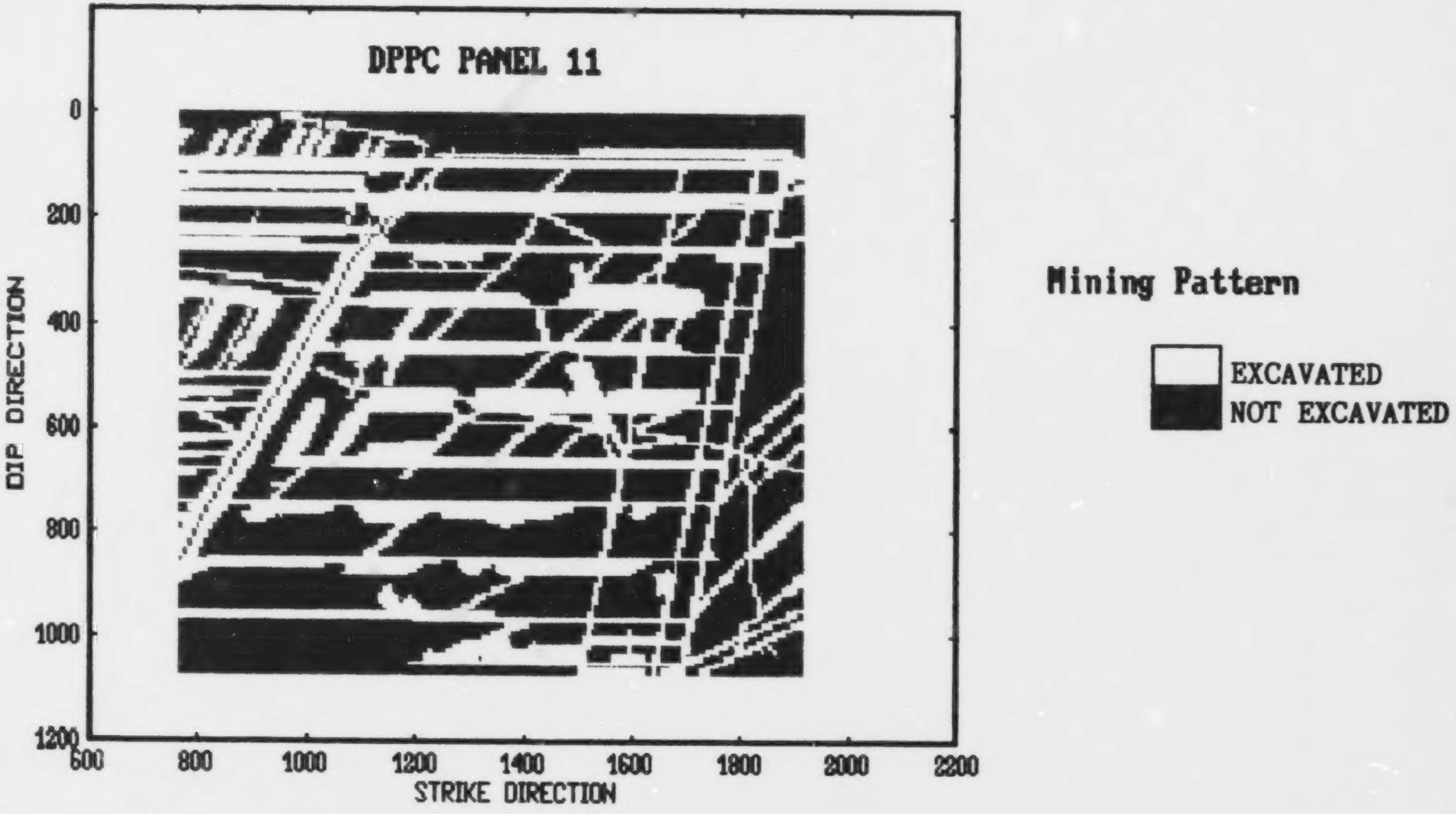
DPPC PANEL 11
DIP DIRECTION
0
200
400
600
800
1000
1200
600
800
1000
1200
1400
1600
1800
2000
2200
STRIKE DIRECTION
Mining Pattern
EXCAVATED
NOT EXCAVATED

FIGURE 1.11

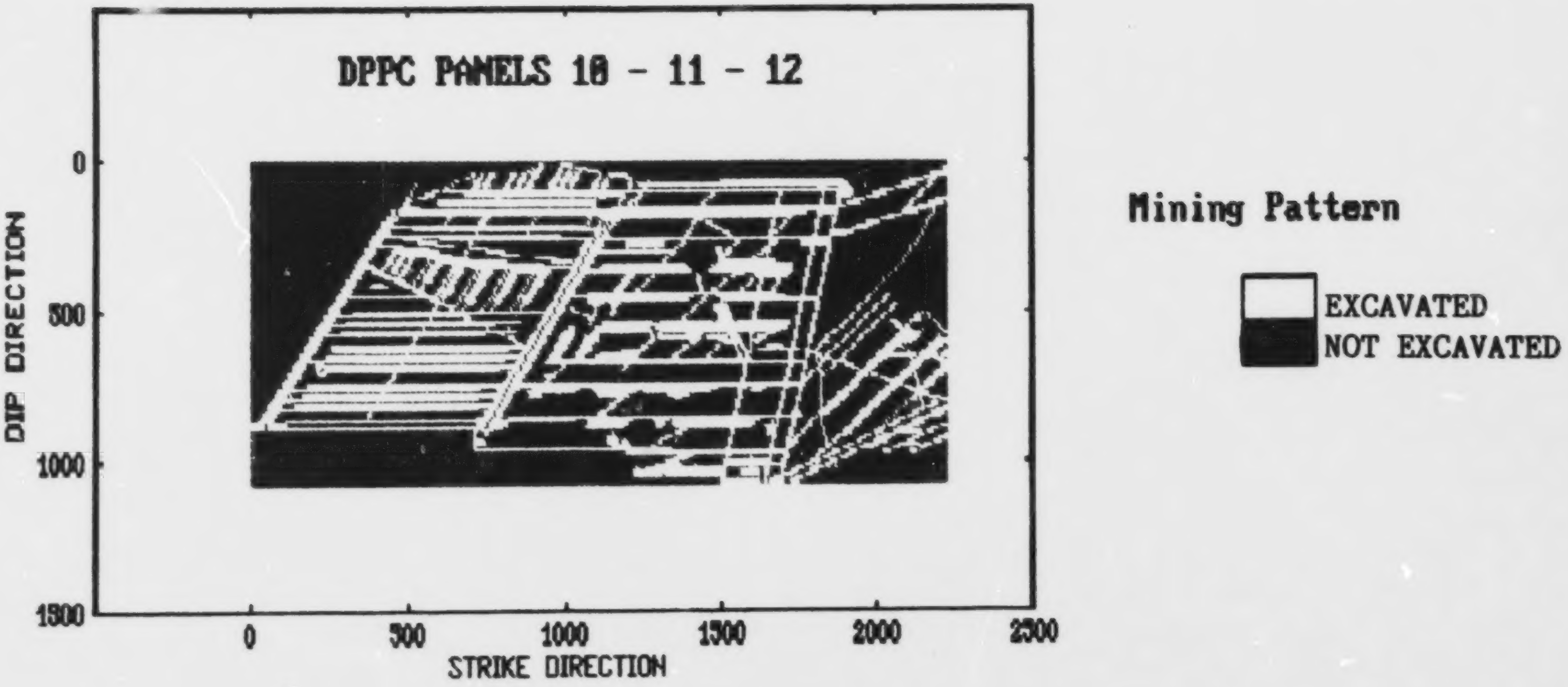

DPPC PANELS 10 - 11 - 12

FIGURE 1.12

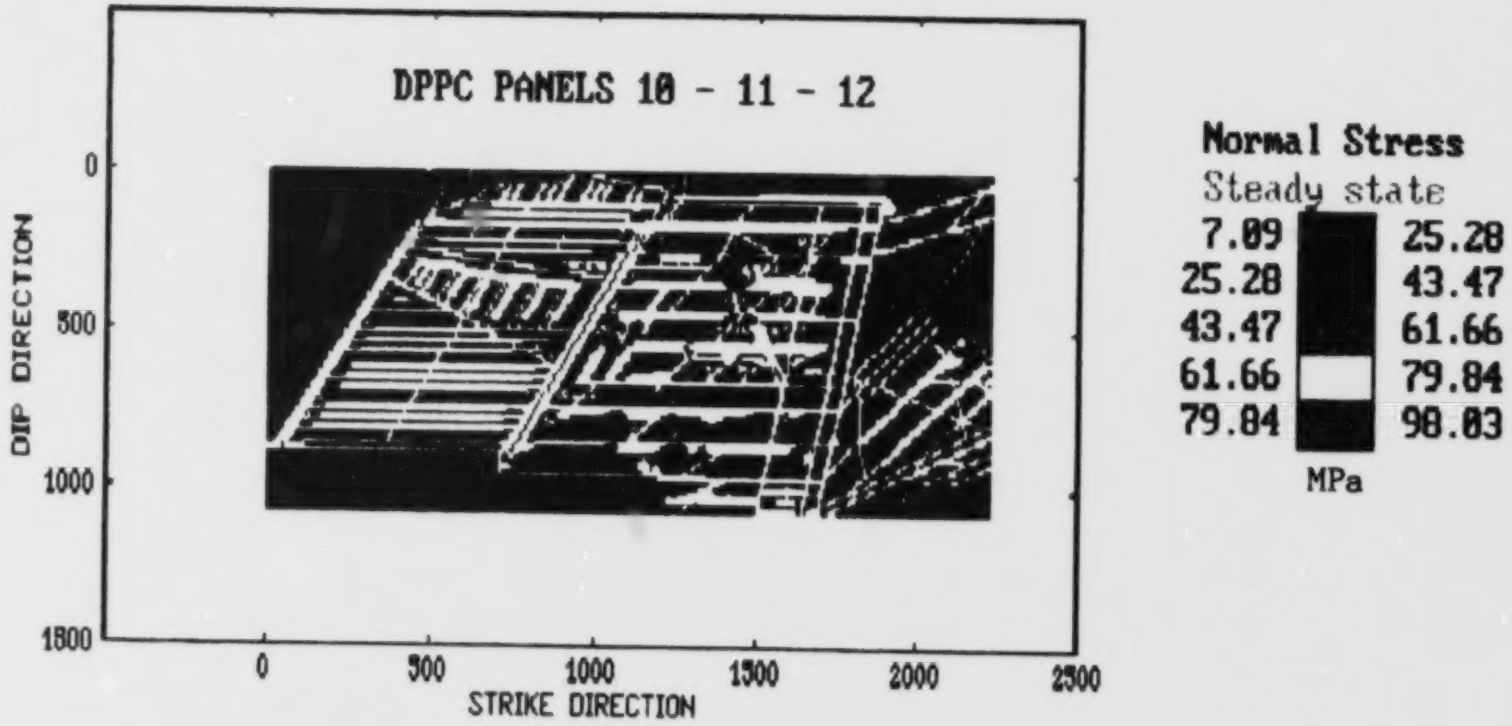
DPPC PANELS 10 - 11 - 12
DIP DIRECTION
0
500
1000
1500
STRIKE DIRECTION
0
500
1000
1500
2000
2500
Normal Stress
Steady state
7.09 25.28
25.28 43.47
43.47 61.66
61.66 79.84
79.84 98.03
MPa

FIGURE 1.13

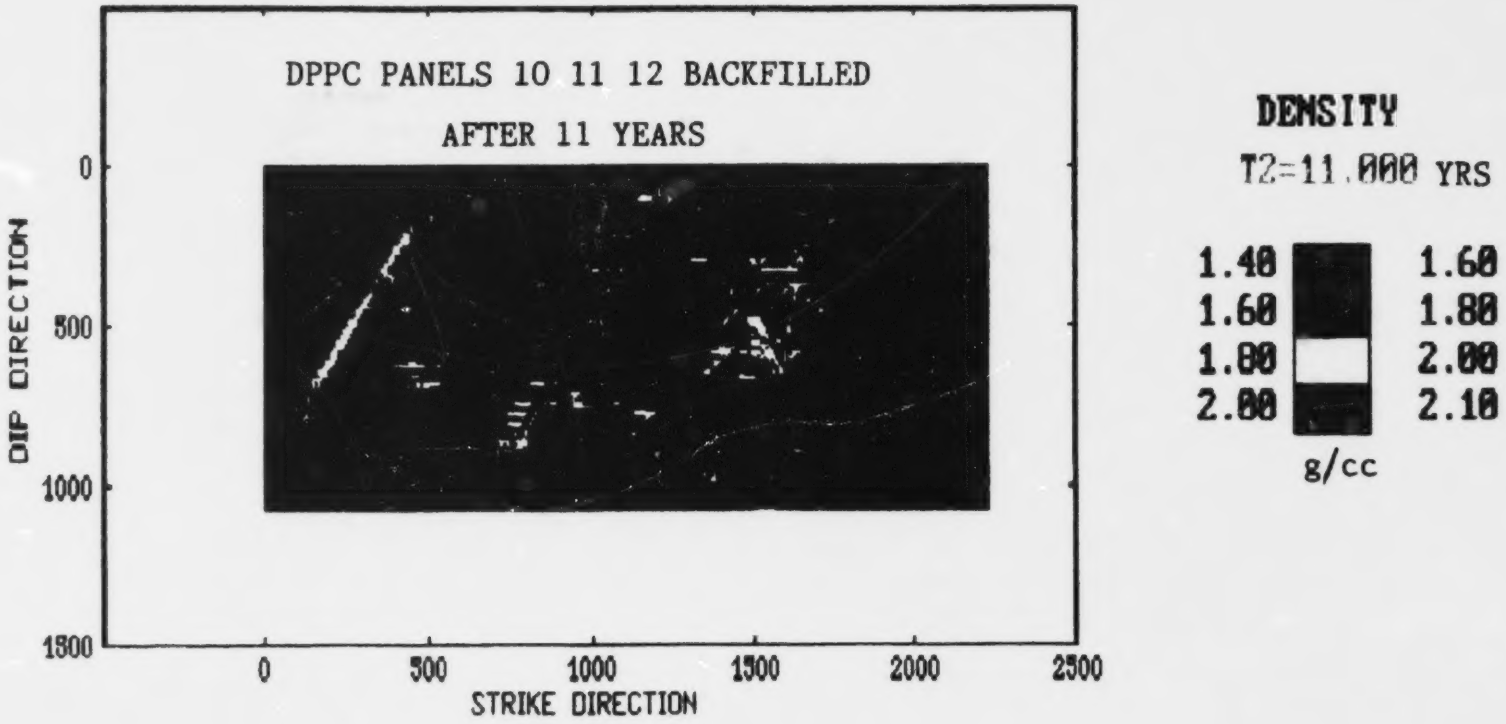
DPPC PANELS 10 11 12 BACKFILLED
AFTER 11 YEARS
DIP DIRECTION
0
500
1000
1500
STRIKE DIRECTION
0
500
1000
1500
2000
2500
DENSITY
T2=11.000 YRS
1.40 1.60
1.60 1.80
1.80 2.00
2.00 2.10
g/cc

FIGURE 1.14

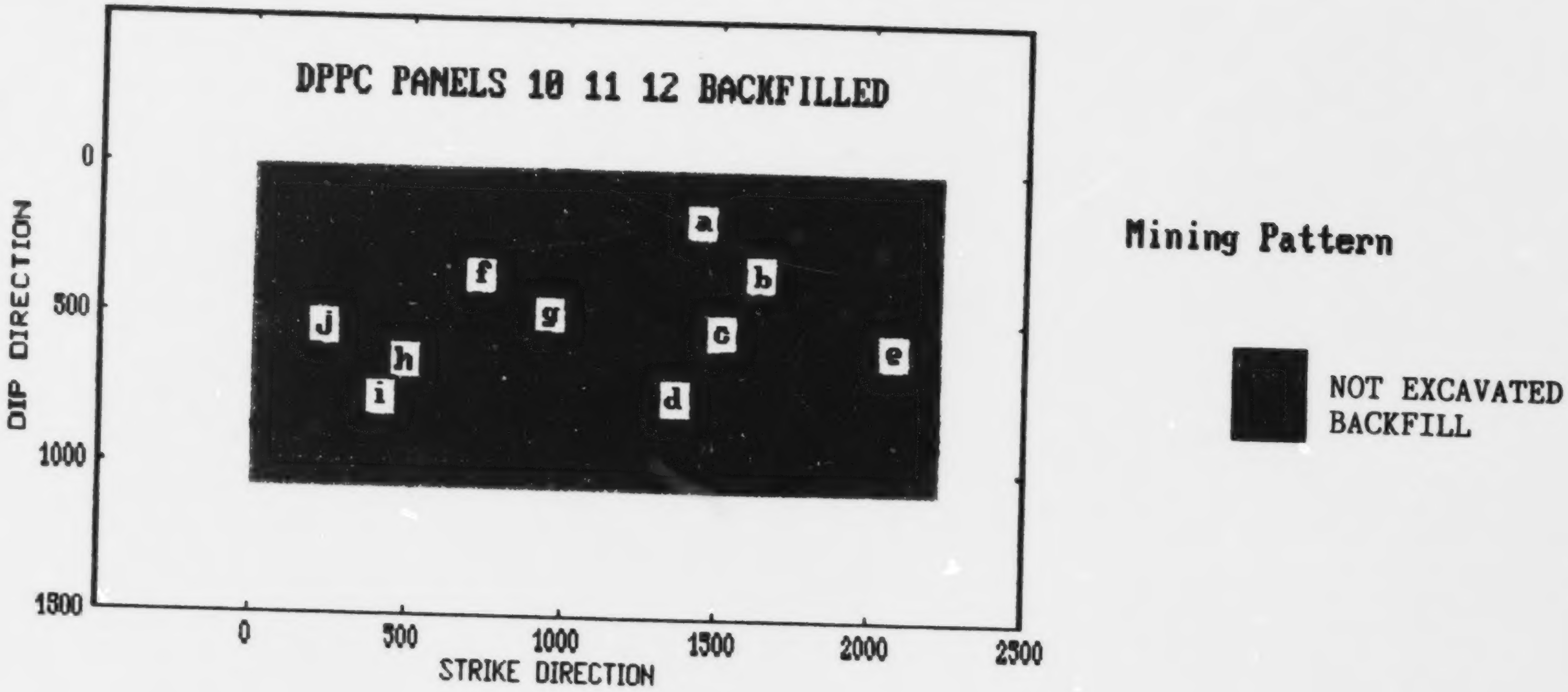
DPPC PANELS 10 11 12 BACKFILLED
DIP DIRECTION
0
500
1000
1500
STRIKE DIRECTION
0
500
1000
1500
2000
2500
a
b
c
d
e
f
g
h
i
j
Mining Pattern
NOT EXCAVATED
BACKFILL

FIGURE 1.15

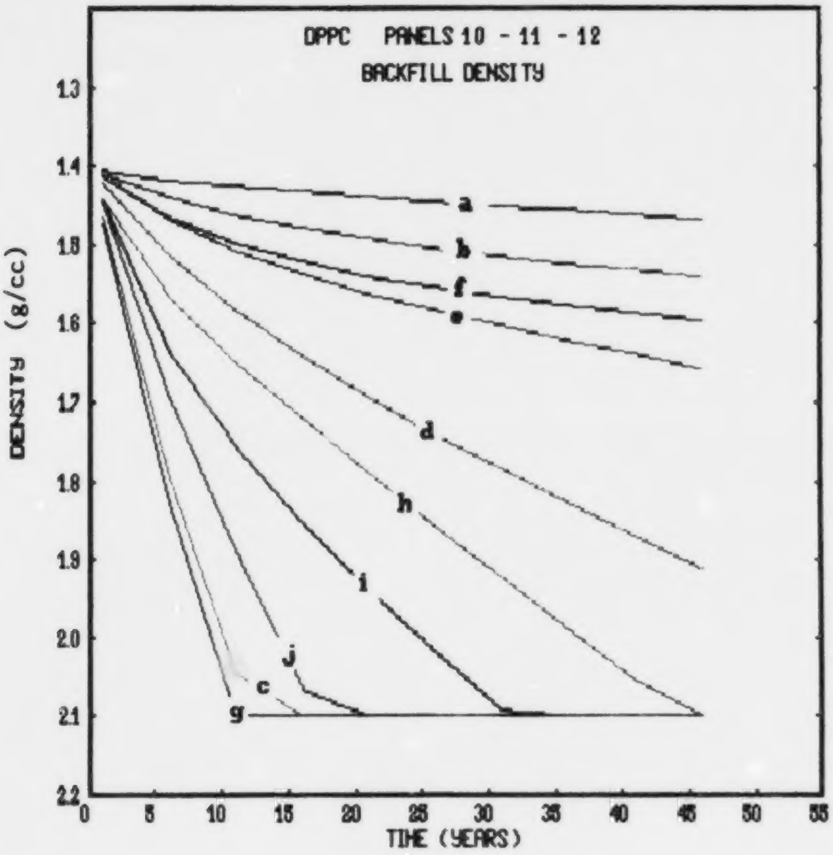
DPPC PANELS 10 - 11 - 12
BACKFILL DENSITY
DENSITY (g/cc)
1.3
1.4
1.5
1.6
1.7
1.8
1.9
2.0
2.1
2.2
a
b
f
e
d
h
i
j
c
g
0
5
10
15
20
25
30
35
40
45
50
55
TIME (YEARS)

FIGURE 1.16

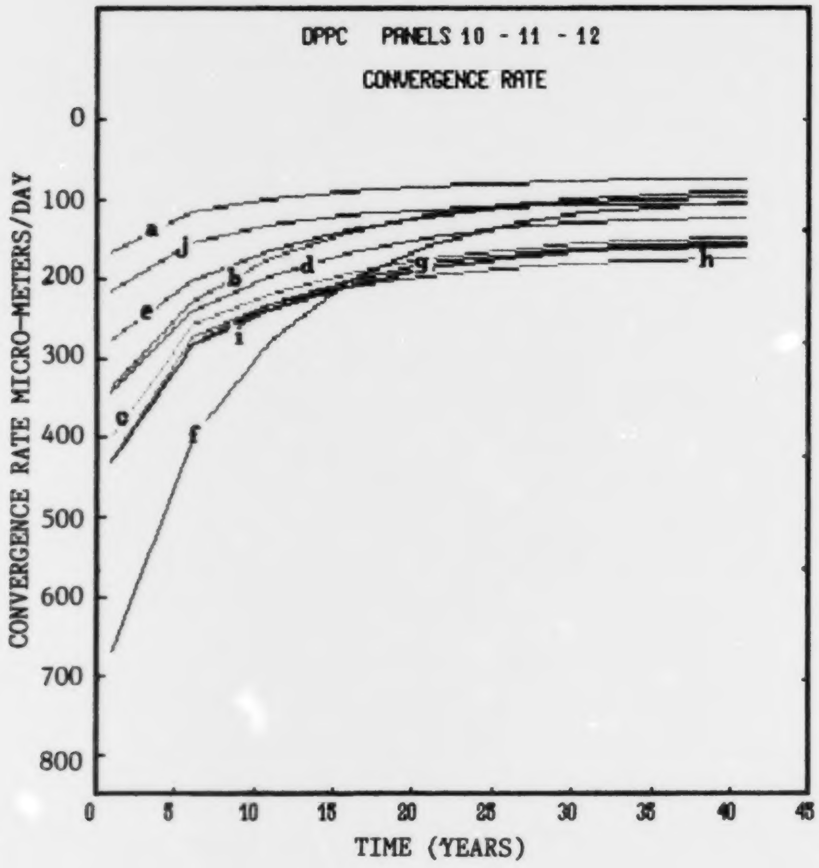
DPPC PANELS 10 - 11 - 12
CONVERGENCE RATE
CONVERGENCE RATE MICRO-METERS/DAY
0
100
200
300
400
500
600
700
800
a
j
e
b
d
g
i
c
f
h
0
5
10
15
20
25
30
35
40
45
TIME (YEARS)

Based on density distribution at various times, it was concluded that the secondary excavation in the pillars would be possible after about 10 years of backfill consolidation. Figure 1.17 shows that the maximum convergence rates after the secondary excavations would be similar to those currently experienced in Panel 11. Thus, it can be concluded that a secondary mining in backfilled Panels 10, 11 and 12, 10 years after backfilling, is feasible.

The effect of modelling backfill placement is negligible because little change in backfill density occurs in the time it takes to backfill a stope. However, gradual excavation in actual mining opposed to instantaneous excavation (i.e. numerical modelling), represents a potential reduction in the time to secondary mining. Gradual excavation of secondary stopes will potentially produce accelerated compaction of backfill resulting in backfilled stopes being capable of supporting overburden at an early time thereby allowing early exploitation of pillars.

1.7 Conclusions and Recommendations

1. The current method of dry backfill placement limits the initial net placement density of 1.26 g/cm^3 (0.6 fraction density), due to the inability to fill the stopes and rooms entirely. The feasibility study prepared by Denison-Potacan and underground trials indicate that the hydraulic backfill placement method is more efficient and that it will provide higher initial placement density. The initial average placement density of backfill in all future stopes should be 1.4 g/cm^3 (0.65 fractional density) or more. Wherever possible the open spaces in the existing backfilled stopes should be hydraulically backfilled to achieve an average backfill density of no less than 1.4 g/cm^3.

2. The backfill pressure cells located within the backfill in Stope 11200 registered only a gravity load indicating that, within the time interval measured, no support was offered by backfill to the mine.

3. The convergence stations installed in Panel 11 recorded an average convergence rate of about 100 millimetres per year. This rate appeared to be quite uniform over the time period monitored indicating that the panel is converging at a steady state rate.

FIGURE 1.17

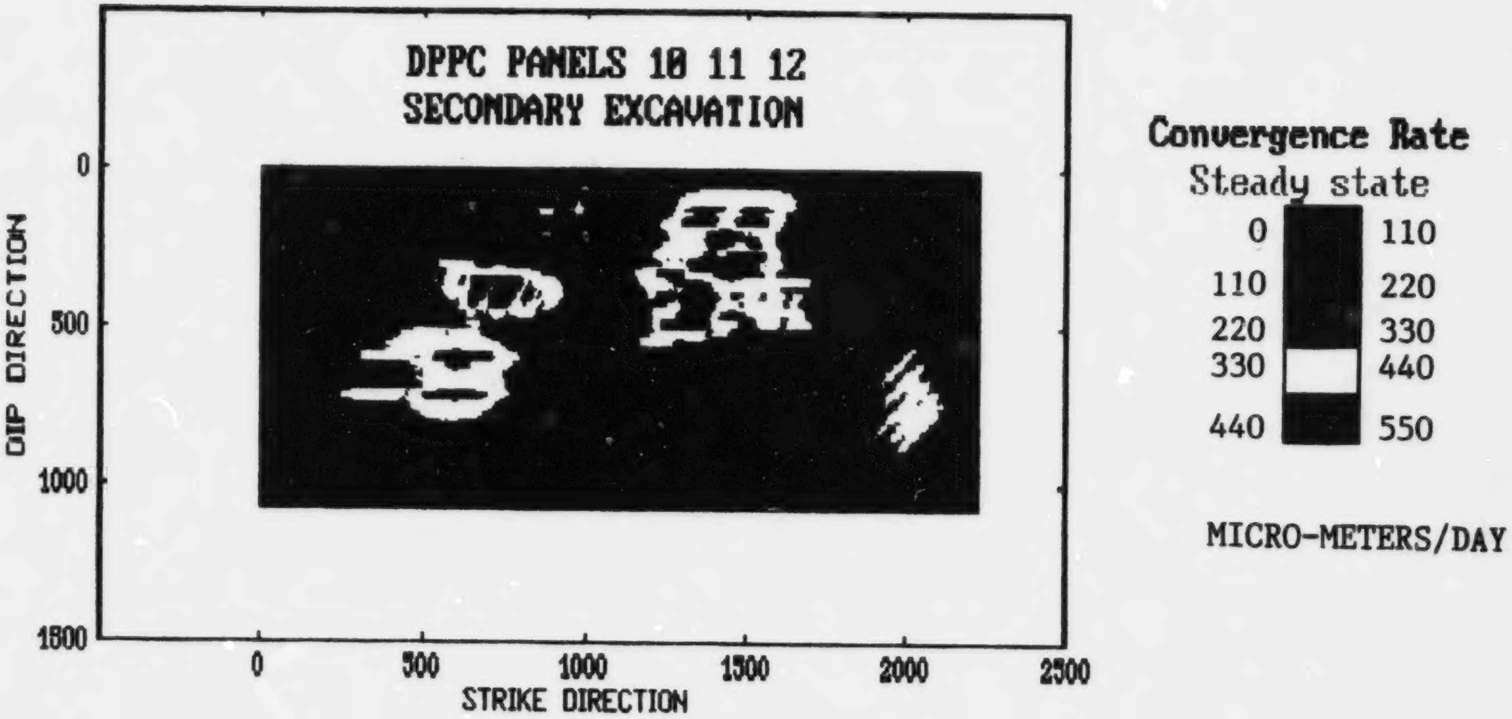
DPPC PANELS 10 11 12
SECONDARY EXCAVATION
DIP DIRECTION
0
500
1000
1500
STRIKE DIRECTION
0
500
1000
1500
2000
2500
Convergence Rate
Steady state
0 110
110 220
220 330
330 440
440 550
MICRO-METERS/DAY

4. The instrumentation installed in the 3-entry system of Panel 12 indicated that the proposed 3-room layout provides a stress relief protection for the centre entry.

5. The maximum surface subsidence rate measured was 33.6 millimetres per year.

6. Based on the examination of laboratory behaviour, the following mechanisms are thought to dominate the volumetric creep deformation in halite backfill:

   (a) pressure solution at stresses of less than 2 MPa and volumetric strain rates of less than $10^{-6}s^{-1}$;
   (b) particulate sliding at volumetric strain rates above $10^{-6}s^{-1}$;
   (c) cataclasis upon a sudden imposition of stress.

   Based on the assumption that cataclasis is unlikely to operate in situ, an empirical two mechanism power law has been proposed and fitted to the experimental data.

7. Based on laboratory experiments, it was concluded that backfill with a fractional density of less than 0.7 has little or no unconfined strength, and that the uniaxial compressive strength of backfill can be defined as a linear function of fractional density.

8. Triaxial brittle strength of backfill increases with density. The Mohr-Coloumb criterion was fitted to the brittle strength data and both the cohesion and the angle of internal friction could be defined as a linear function of density.

9. Mixing of sand into the halite backfill will reduce its initial placement porosity, thereby, reducing the total amount of consolidation required to achieve support. Addition of cement into the halite backfill will decrease initial porosity and achieve early compressive strength of about 2.0 MPa.

10. The two-dimensional microcomputer program FLAC was used for all plane strain analyses. The overall mining geometry was modelled by the three-dimensional program VELMINA and the results compared to the in situ convergence rate measurements. This comparison shows a very good agreement between the in situ convergence rates and the convergence rates predicted by VELMINA.

11. The steady state subsidence rates predicted by VELMINA were compared to the actual subsidence rates measured and a very good correlation was found. This is an indication that the strata over the DPPC mining area are subsiding correctly, without extensive bridging.

12. The results of this study indicate that the secondary mining of pillars in backfilled areas may be possible within 10 to 15 years after the backfill placement. Gradual excavation of secondary mining could potentially lead to even earlier secondary mining of some pillars as a result of an increased backfill compaction rate. It is recommended to confirm this conclusion through the long term monitoring of the backfilled areas. Samples of compacted backfill should be taken from selected locations annually and tested in order to obtain a long term history of in situ backfill behaviour.

SECTION 2.0

2.0 INTRODUCTION

2.1 Background to Mine Development

The Denison-Potacan Potash Company mine site is located southwest of Sussex, New Brunswick, as shown in Figure 2.1. The Clover Hill deposit was first identified by surface exploratory drilling conducted in 1973 under the direction of the New Brunswick Department of Natural Resources.

In 1975, the Government of New Brunswick granted International Minerals and Chemical Corporation (Canada) Limited (IMC) exclusive rights to explore and develop the Clover Hill property. IMC conducted a surface exploration drilling program which defined approximately 200 million tonnes of potash ore grading 28% K_2O, making this deposit one of the world's richest.

In 1979, Denison Mines Limited purchased the Clover Hill property and, in 1980, formed a partnership with the Potash Company of Canada. An extensive underground exploration program led to a decision in 1983 to develop the property into a mine capable of producing 1.3 million tonnes of product per year. Potash production commenced in July 1985.

2.2 Geology

The Clover Hill potash deposit is confined to the Marchbank Syncline, which is the most southerly major structural feature of the Moncton Subbasin shown in Figure 2.2. The potash deposit is part of the Cassidy Lake Evaporite Formation of the Windsor group as shown in the Marchbank Syncline stratigraphic column, Figure 2.3.

The evaporite interval has been sub-divided into four members:

1. Basal Halite;
2. Middle Halite;
3. Potash;
4. Upper Halite.

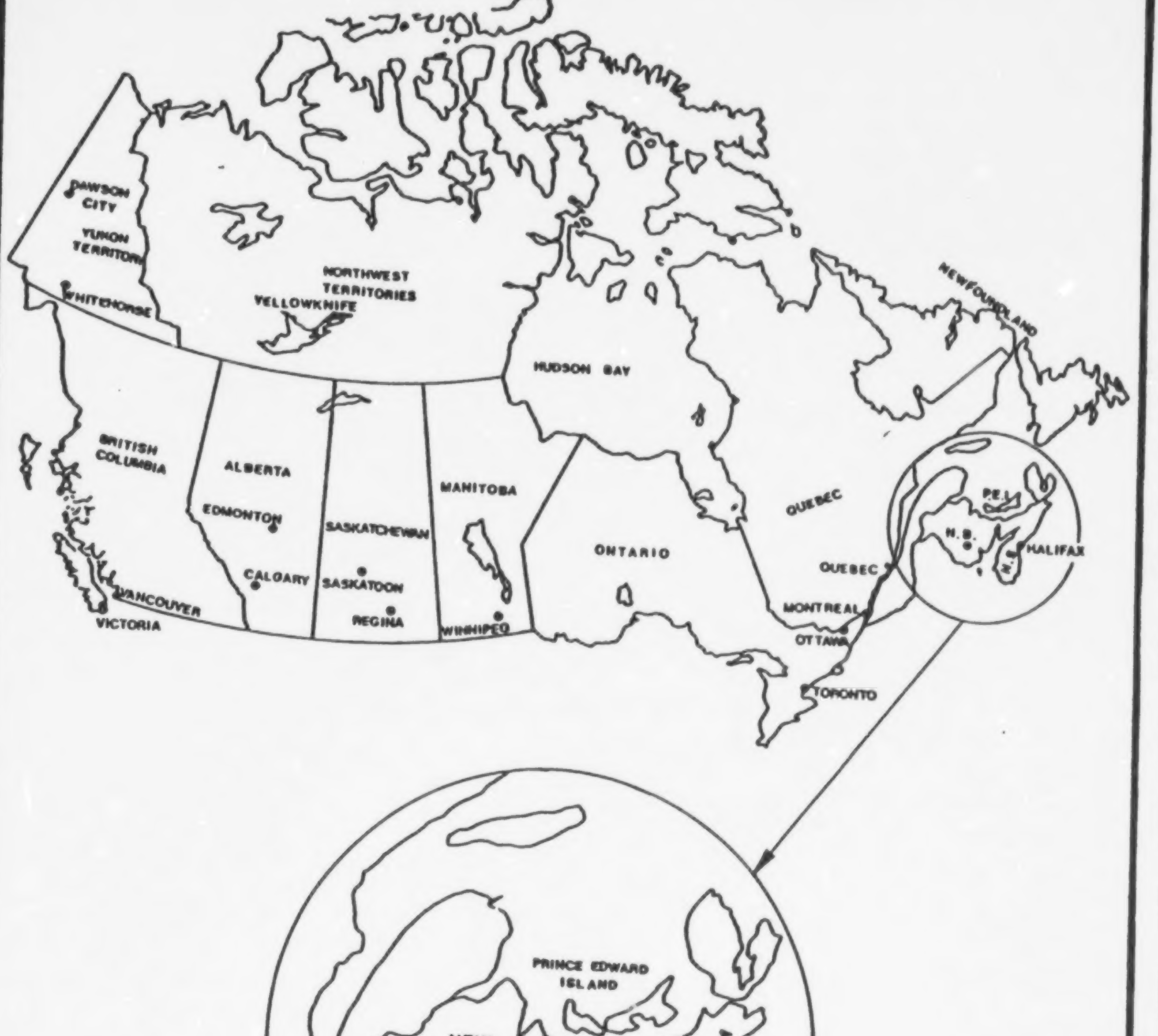

DENISON
POTACAN
POTASH
COMPANY

DENISON POTACAN POTASH COMPANY	TITLE: LOCATION OF MINE SITE	SCALE: N.T.S. FIGURE: 2.1

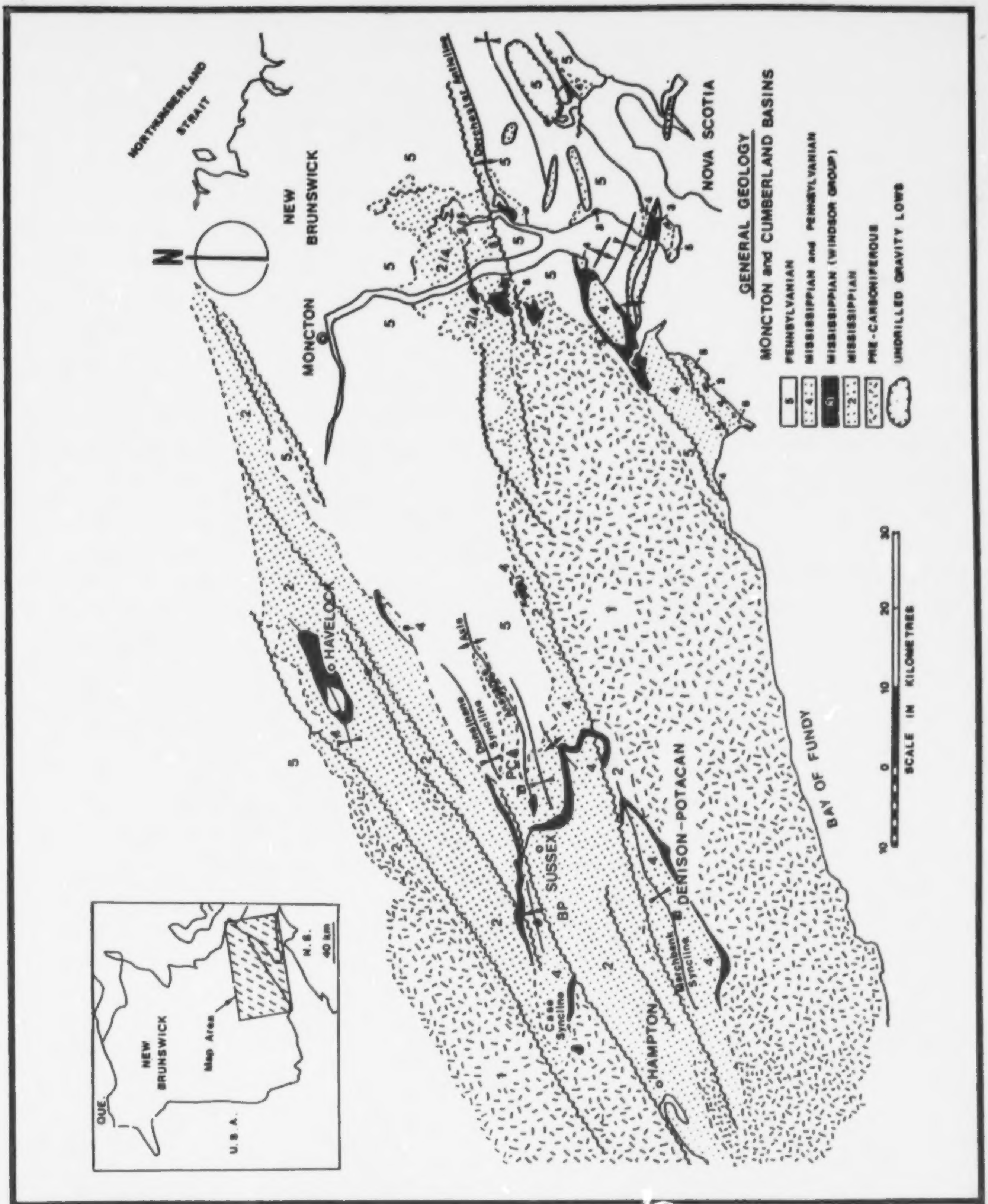

DENISON POTACAN POTASH COMPANY

TITLE:

GEOLOGY OF THE MONCTON SUBBASIN IN NEW BRUNSWICK
(After Waugh and Urquhart, 1983)

SCALE:
N.T.S.

FIGURE:
2.2

MARCHBANK SYNCLINE – STRATIGRAPHIC COLUMN

GROUP	FORMATION	MEMBER	BED		GENERAL LITHOLOGIES
HOPEWELL	Wanamaker	Fowler Brook			Grey red sandstone and siltstone numerous grey limestone nodules
		DeForest Lake			Grey red to grey brown conglomerate and sandstone
		Scoodic Brook			Grey red sandstone and siltstone
					unconformity
	Campbell Settlement				Pale red vuggy siltstone/sandstone
	Poodiac				Grey brown siltstone
					Grey to grey brown sandstone/siltstone
					Grey brown siltstone and sandstone
					Variable collapse breccia
WINDSOR	Plumweseep	Grey Clay			Green grey claystone
		Upper Salt			Not present in Marchbank Syncline
		Upper Anhydrite			Grey to bluish grey anhydrite
	Cassidy Lake	Upper Halite			Fine to medium grain orange to brown halite interbedded with numerous argillaceous and red sylvite beds and borate minerals
		Potash	Sylvinite Bed		Brick red very fine to fine grain sylvinite
			L.G.B.		Light orange halite with sylvite clusters
		Middle Halite			Light brown medium grain halite with irregular bands of dark brown to dark gray argillaceous halite
		Basal Halite			Very light grey to clear medium to coarse grain halite with irregular dark brown black argillaceous halite bands
	Upham	Upperton			Grey anhydrite
		Devine Corner			Light grey to buff limestone

DENISON POTACAN POTASH COMPANY

TITLE:

STRATIGRAPHIC COLUMN
MARCHBANK SYNCLINE
(After Waugh and Urquhart, 1983)

SCALE:
N.T.S.

FIGURE:
2.3

The potash member consists of the **Sylvinite Bed** and the **Lower Gradational Bed.**

The **Sylvinite Bed** is composed of fine-grained sylvite and halite. It is subdivided into five distinct zones based on mineralization, percent insolubles and colour. These have been designated from oldest to youngest as the A, B, C, D and E zones. The B and C zones comprise the main ore bed as shown in Figure 2.4.

The **Lower Gradational Bed** is composed of medium to fine-grained brown to orange halite with sylvite clusters being present.

2.3 Description of Mining Methods

The Denison-Potacan potash deposit averages a thickness of 12.5 meters and a depth of 880 meters below surface. It is approximately 10 kilometres in length along strike and has a maximum plan width of 3.5 kilometres.

The room and pillar method of mining utilized to extract the potash ore uses mechanical excavation with mining machines as well as drilling and blasting techniques. Conveyor belt systems are used to transport ore from the mining areas to the underground ore storage bin and then to the production shaft through which ore is hoisted to surface in 25 tonne skips.

The ore is then conveyed to the plant where the sylvite is removed from the ore as product and the waste, principally halite, is then either returned underground as backfill or, temporarily, to a surface tailings stockpile. The present method of backfilling relies on conveyor belts for transportation and scooptrams or stackers for placement.

A mine plan showing the existing mining panels 10, 11 and 12 and a typical section through Panel 11 are included as Figures 2.5 and 2.6.

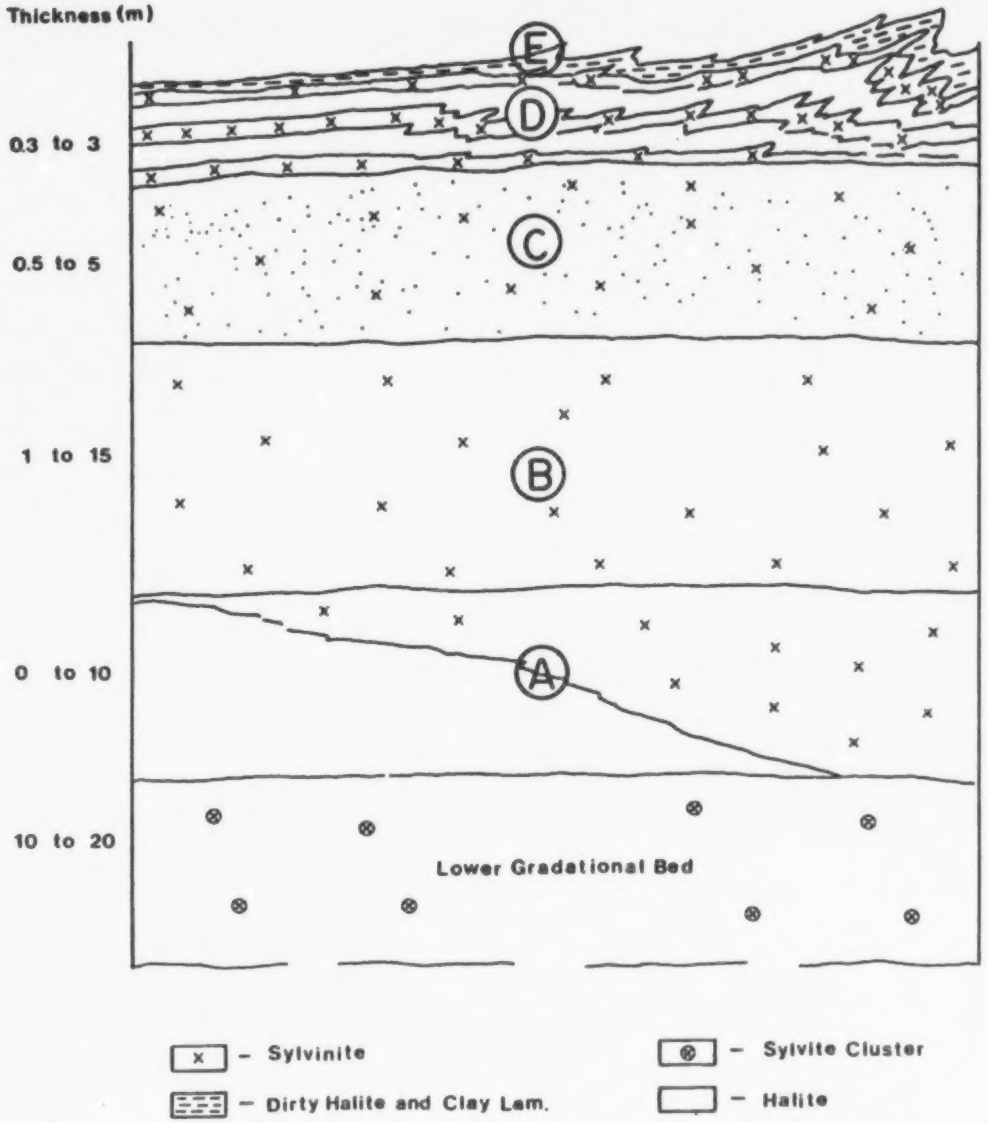

DENISON
POTACAN
POTASH
COMPANY

TITLE:
SCHEMATIC OF CASSIDY LAKE
FORMATION POTASH MEMBER
(After Waugh and Urquhart, 1983)

SCALE:
N.T.S.

FIGURE:
2.4

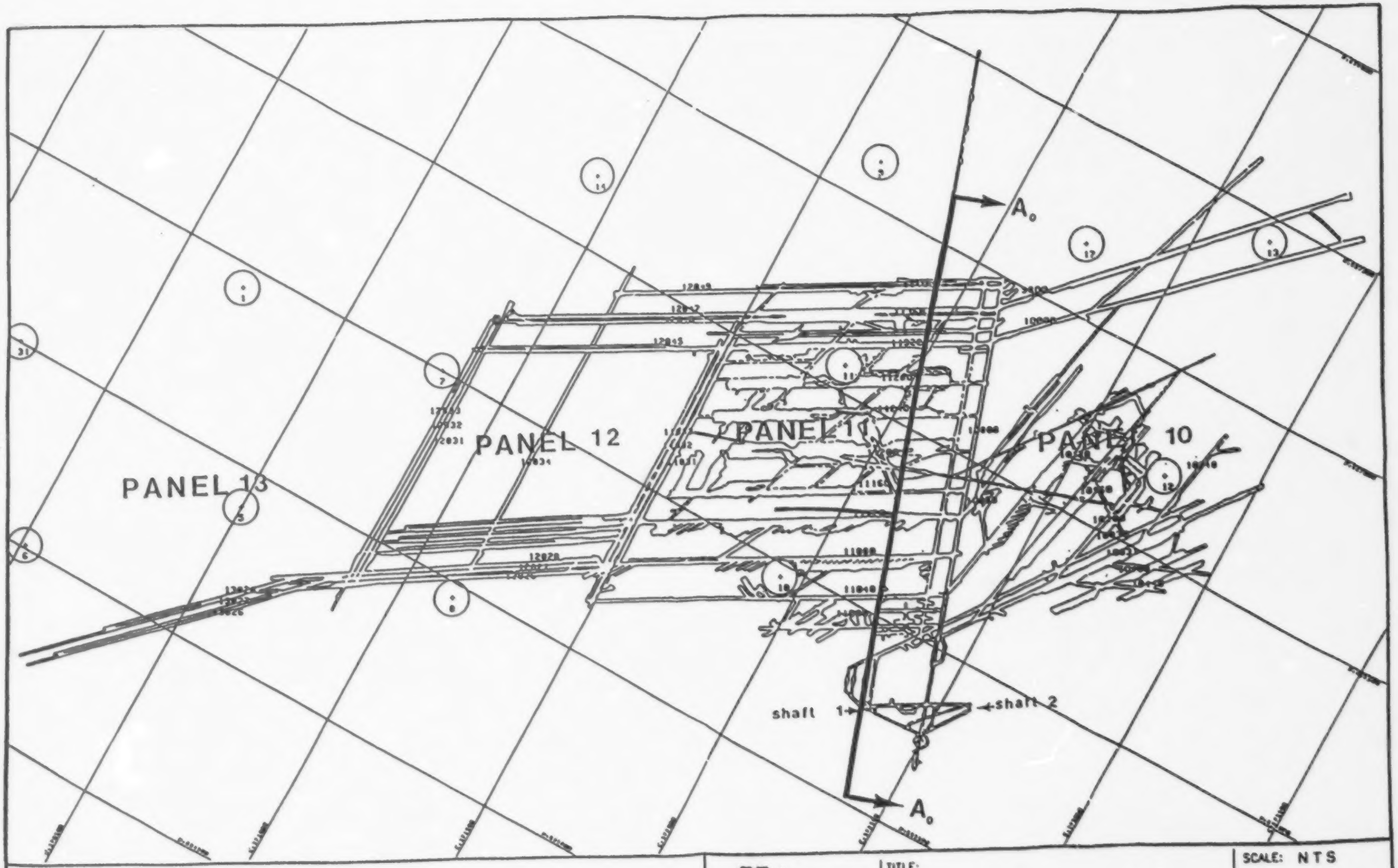

DENISON
POTACAN
POTASH
COMPANY

TITLE:
CLOVER HILL MINE
GENERAL MINE PLAN

SCALE: N T S

FIGURE: 2.5

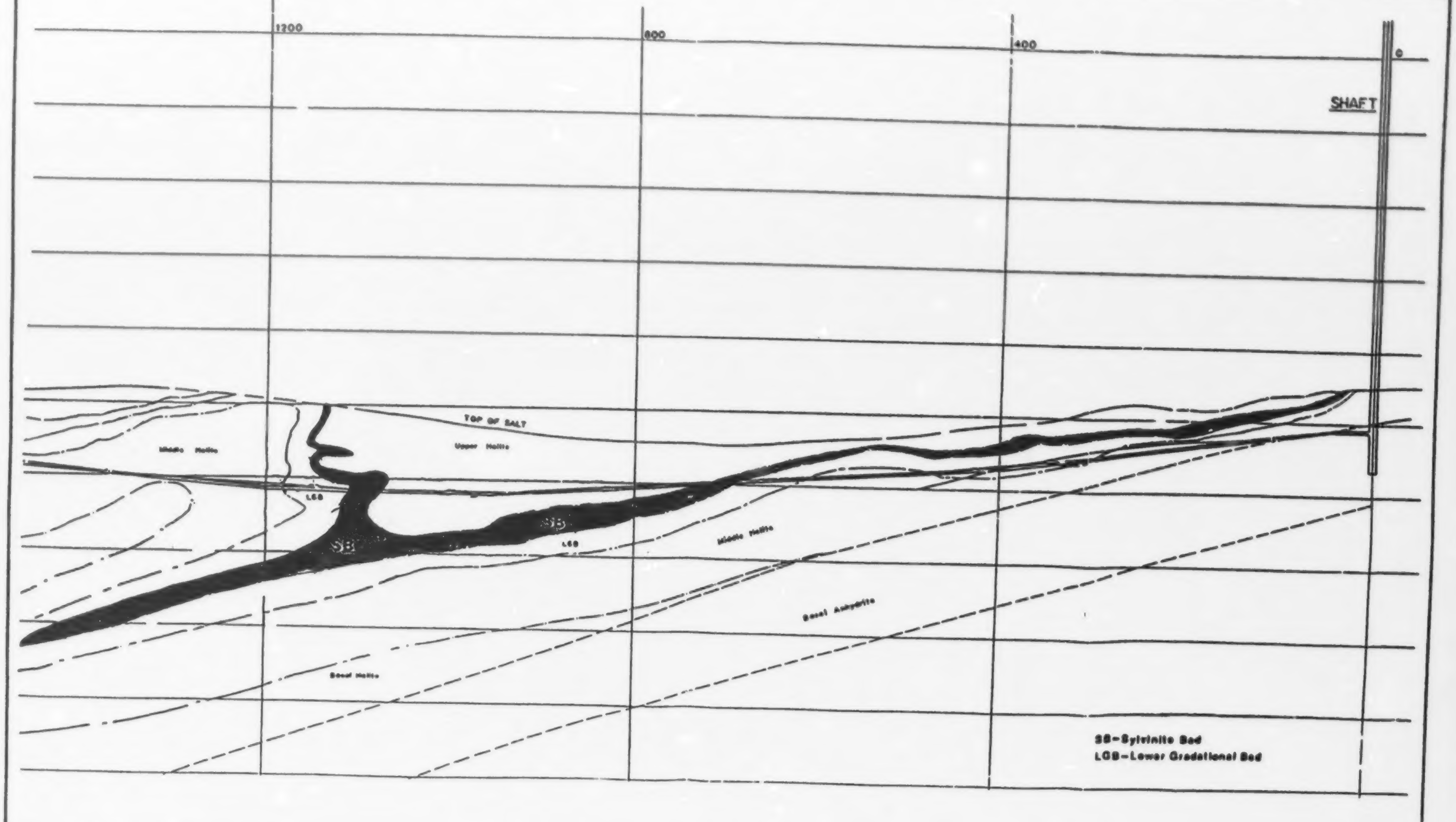

DENISON
POTACAN
POTASH
COMPANY

TITLE:
PANEL 11
TYPICAL GEOLOGICAL CROSS-SECTION

SCALE: N T S

FIGURE: 2.6

2.4 Mine Backfill Operations

Return of the halite tailings as backfill to the mined out underground workings is done for two reasons:

1) To permit environmentally acceptable disposal of the tailings;
2) To potentially increase the recovery of potash reserves through secondary mining of pillars if the backfill can be relied upon for overburden support in the future.

A surface stockpile for halite tailings was established in the development stages of the mine until sufficient underground storage space had been developed to receive the salt tailings on a sustained basis.

2.4.1 Dry Backfill System

In this report, the term "dry" backfill refers to surface stockpile reclaimed halite backfill and halite tailings dewatered in the processing plant to approximately 8% moisture for the purpose of backfilling.

A simplified schematic flowsheet of the dry backfill system which has been in operation since February 1987 is shown in Figure 2.7.

Reclaim of sorted halite backfill from the surface stockpile is done by truck. Salt is loaded into the trucks by a front-end loader at the stockpile and carried to the truck dump at the (No.1) Service Shaft where it is directed through lump breakers to reduce oversize and then onto a "flexwall" belt conveyor. This elevating conveyor feeds onto a transfer conveyor belt which in turn discharges into a diverter chute connected to the pipelines down the shaft.

Halite tailings in the plant circuit are dewatered to approximately 8% moisture by vacuum filtration and then directed to the Service Shaft by conveyor belt. From this belt, they are discharged via a transfer conveyor directly into a diverter chute connected to one of two 200 mm diameter steel pipelines installed in the shaft.

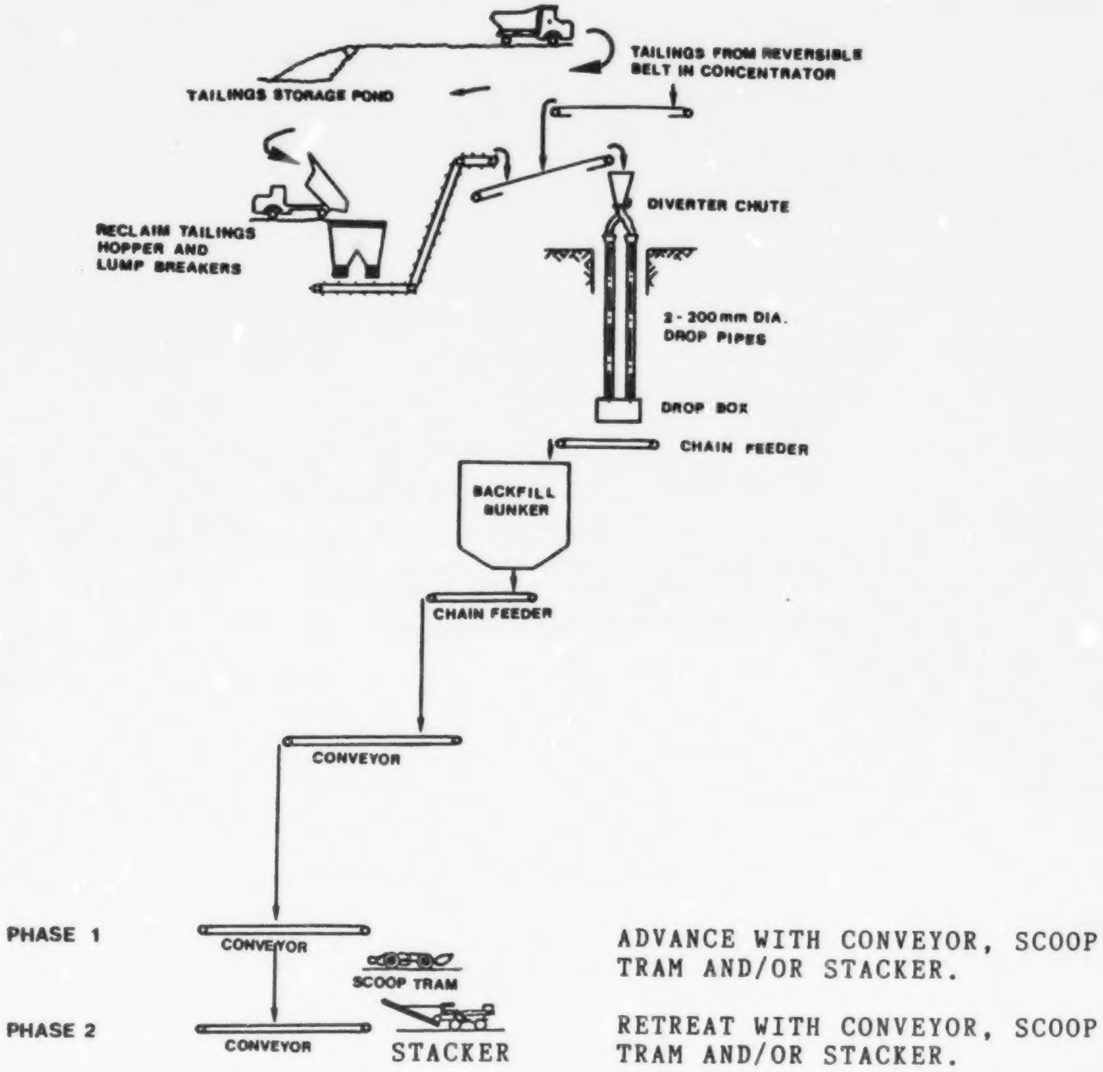

ADVANCE WITH CONVEYOR, SCOOP TRAM AND/OR STACKER.

RETREAT WITH CONVEYOR, SCOOP TRAM AND/OR STACKER.

DENISON
POTACAN
POTASH
COMPANY

TITLE:
SCHEMATIC OF MINE BACKFILL SYSTEM

SCALE:
N.T.S.

FIGURE:
2.7

The pipelines terminate in a drop box at the main shaft station at the 795 m level where the tailings are directed by a short chain feeder/conveyor to a 350 tonne capacity backfill bunker located adjacent to the shaft station. Backfill is reclaimed from this bunker by twin chain feeder/conveyors to a conveyor belt system for transport to the areas in the mine that are being backfilled.

There are two phases in the backfill operation:

Phase 1 - Beginning at the front end of the stope, the backfill delivery conveyor discharge point is advanced dependent upon the rate of backfill discharge from the conveyor. Two predominant methods have been utilized by the scooptrams for backfill placement; placement in lifts with incidental compaction by the scooptrams tires and large lift dumping. The method used is primarily a function of the opening height being backfilled. Large lift dumping is prevalent in higher openings (> 15 m) due to fewer required conveyor relocations. Since 1988 a specially designed backfill stacker with an extensible belt system has been utilized for advancing backfill placement in stopes. The electrically powered stacker greater reduces ventilation requirements which are often an operational constraint for the diesel powered scooptrams.

Phase 2 - Once the full extent of the stope has been filled in advance to within 3 - 5 meters of the roof, the conveyor system is retreated out of the stope. Scooptrams and/or the stacker are used to place the backfill up as close as possible to the roof. Final filling efficiency with the scooptrams is somewhat limited and often requires a travelway or opening to be left for ventilation requirements. A pilot scale pneumatic stower was tried for final tight backfill placement. However, problems encountered primarily with the moist backfill sticking in the unit led to its abandonment.

2.4.2 Hydraulic Backfill System

Experience has shown that the dry backfill system works well when large mine openings of considerable height (such as 30 metre high stopes) are to be filled, because they require fewer conveyor advance/retreat moves per unit volume of backfill placed. However, only 30% to 40% of the Denison-Potacan ore body consists of high stopes.

In addition, the existing method of dry backfilling limits the average placement density to less than 1.3 g/cm^3 (0.6 fractional density) due to the inability to efficiently fill the top lift. It is also susceptible to numerous operational delays.

Hence, Denison-Potacan personnel evaluated the feasibility of introducing a hydraulic backfilling system to the mine. The outcome of the feasibility study combined with underground trials in Stope 11280 led to a decision to immediately proceed with the installation of a hydraulic backfill system. The system is currently being installed and is anticipated to be operational on a permanent basis by November 1989.

The anticipated advantages of a hydraulic backfill system, as opposed to the dry backfill system, are the elimination of dry backfill system malfunctions, conveyor installations and the use of diesel equipment for backfill distribution in stopes, as well as a potential improvement of average placement density to 1.4 g/cm^3 (0.65 fractional density).

No drainage problems are anticipated with hydraulic backfill since the backfill material is relatively coarse and reasonably free of slimes. The natural dip of the ore body and the sloping stopes should assist placement and drainage. However, brine collection sites will have to be selected with care since brine seepage can be expected along separation cracks below the floor.

There may be a noticeable increase in the mine convergence due to increased moisture content in pillars as a result of hydraulic backfilling. This effect, as well as the effects of humidity on the mine ventilation system and problems due to corrosion will have to be closely monitored.

2.5 Backfill Research - Summary of Program Under Phase I

The Denison-Potacan mine is the second potash mine to begin operations in the Province of New Brunswick. The Potash Company of America (PCA) mine currently uses tailings backfill in its mining operations principally as an aid to the mining cycle and not as a means of secondary pillar recovery. No other potash mine in Canada practices backfilling underground in significant quantities. Thus, in planning for the placement of tailings backfill in the mined out underground workings, a number of technical issues required solving prior to the commencement of backfilling.

Denison-Potacan retained the services of Mraz Project Consultants Ltd (MPC) of Saskatoon, Saskatchewan to assist them in solving these technical issues as to the use of backfill underground. A proposal for a research program into the use of backfill was prepared for submission to the Canada Centre of Mineral and Energy Technology (CANMET) and the Province of New Brunswick.

The goal of the program was to research behaviour and methods of placement of the tailings from the Denison-Potacan plant with the aim of providing support and stabilization to the mine workings, leading to improved resource recovery mining methods.

A contract, in the amount of $214,740 was awarded to Denison-Potacan to proceed with the research work. This contract was subsequently entitled "Phase I - Use of Backfill in New Brunswick Potash Mines". Phase I of the research program included:

a) The collection and laboratory analysis of intact salt rock samples.
b) The collection and laboratory analysis of backfill material.
c) The installation and monitoring of in-situ rock mechanics instrumentation.
d) The development of a preliminary constitutive law for the interactive behaviour of backfilled mine openings.

The findings of Phase I of the program were submitted in May 1987 as a Final Report of the work performed under DSS Contract Serial No. OSQ85-00208/CANMET Project No. 1.4.09.05.

Backfilling operations commenced at the Denison-Potacan mine as of February 1987. However, several major technical aspects remained to be addressed that had not been included as part of the Phase I program:

a) The installation, protection and monitoring of in situ instrumentation in a backfilled stope.
b) The analysis of a backfill support capability as a function of backfill density.
c) The feasibility of employing methods of accelerating in situ densification of backfill.
d) The evaluation of alternate backfill density improvement methods.
e) The development of failure criteria for backfill as functions of its density.
f) The optimization of backfill density and mining geometry to achieve safe and cost efficient recovery of reserves through second stage mining.
g) The evaluation of the relationship between the mine convergence and overburden subsidence over the mining area and potential impacts of overburden behaviour on the safety of the mine and its workers.

2.6 Backfill Research - Summary of Program Under Phase II

In May 1987, a proposal for further research into the major outstanding technical aspects identified by Phase I was submitted to the Minister of Supply and Services bearing the title of "Use of Backfill in New Brunswick Potash Mines, Phase II".

The stated goal of the Phase II program was to continue research into the practise of tailings from the Denison-Potacan plant circuit being returned to mined out workings, including:

a) Evaluation of physical properties and creep characteristics of salt/potash intact rock samples and their correlation with in situ measurements.

b) Determination of the physical properties and creep characteristics of halite backfill materials.

c) Development of constitutive laws for intact salt rock and halite backfill.

d) Preliminary assessment of the overburden subsidence and caving mechanisms and their potential impact on the mine and ground surface.

e) Optimization of first and second stage mining geometries and sequential operations, including backfilling, so as to provide guidance to mining operations for timely and efficient recovery of the ore reserves.

f) Installation and ongoing monitoring of rock mechanics instrumentation for providing in situ field data.

The results of the Phase I and Phase II research programs are summarized and presented in two forms:

a) Research results and evaluation
A formal compilation of the testing, analyses and data covered in the research work, which was performed in the laboratory, on the computer, in-situ at the Denison-Potacan mine, and analytically during the correlation of data and assessment of results.

b) Recommendations for mining practices
A practical presentation of the research results in the form of recommendations for backfill placement methods, backfill densities required for optimal layouts of first and second stage mining, sequences of mining operations including backfilling, and specialized instrumentation and rock mechanics practices.

A contract, in the amount of $199,130 was awarded to Denison-Potacan in January 1988 to proceed with the research work, who retained MPC to carry out some of the work and coordinate the study.

The following report is a Final Report of the work performed under DSS Contract Serial No. 23440-7-9228/01-SQ, CANMET project No. 1.4.09.05.

SECTION 3.0

3.0 IN SITU TESTING

3.1 Introduction

The significance and value of collecting and analyzing in situ rock mechanics data, as to stress and strain distributions surrounding mine openings, was recognized and acted upon by Denison-Potacan as early as 1982. This led to the establishment of the Rock Mechanics Station (Test Room) in February, 1983.

Information collected from virgin ground and active mining sites is establishing a valuable data base for evaluating mine design criteria as well as monitoring localized and global mine stability.

3.2 Instrumentation Equipment

The rock mechanics instrumentation used consisted of equipment to measure displacements and stresses. The equipment ranged from simple inexpensive manual measurement systems to electronic measuring devices and programmable dataloggers.

The convergence of mine openings was measured using either a tape extensometer, homemade wire and pulley measurement system, or electronic closure meters.

Roof and wall expansion (relative closure) of the mine openings was measured using either fabricated plate/rod systems or electronic extensometers. Wire extensometers utilizing rotary potentiometers were used where large displacements were anticipated. Rod extensometers utilizing linear potentiometers were also used, primarily for roof installations.

The pressures related to stress around mine openings were measured primarily by unidirectional hydraulic (flatjack) pressure cells. The cells were either grouted in place or encapsulated in potash or epoxy and then inserted into the borehole. Unidirectional borehole strain gauge stressmeters and cylindrical borehole total pressure cells were also utilized. The summary of instrumentation used is included in Table 3.1

3.3 Instrumentation Protection

Various methods were utilized to provide protection to monitoring equipment and readout cables from impact and corrosion.

Stainless steel lines for the hydraulic pressure cells were protected with plastic tubing and sealed with silicone to prevent attack from backfill brine.

Vibrating wire pressure transducers and valve assemblies were protected from impact and corrosion by steel pipe enclosures packed with grease.

Borehole extensometers were protected by steel plating and reinforced concrete frames. The borehole collars were filled with grease to prevent backfill brine drainage into the extensometer housing.

All individual electronic readout cables were run through PVC pipe from the instrument locations to the readout site, often a distance of up to 500 metres. Wherever possible, the PVC pipe containing the readout cables was buried in the backfill for additional protection.

Some instrumentation was lost due to cables being severed as a result of mining activity. The backfill earth pressure cells were particularly prone to accidental damage or destruction as mobile equipment was frequently working in the immediate area.

3.4 Underground Rock Mechanics Sites and Records of Data

The locations of the major underground rock mechanics stations at the Denison-Potacan mine are shown in Figure 3.1. Note revised mine opening numbering system introduced in 1987 as compared to the system used in Phase I.

TABLE 3.1

SUMMARY OF ROCK MECHANICS INSTRUMENTATION
"USE OF BACKFILL IN NEW BRUNSWICK POTASH MINES - PHASE II"

LOCATION	INSTRUMENT/DEVICE	MANUFACTURER	MODEL NO.	READOUT METHOD	COMMENTS
12826/27, 11120, 11240	Tape extensometer	Irad Gage	---	manual	used in accessible areas
Test Stope	Wire/pulley closure meter	D.P.P.C.	---	tape measure	homemade device
Test Stope	Closure meter	S.R.C.	601	S.R.C. Model 400 readout box	rotary potentiometer;1500 mm travel
Test Stope, 12826/27	Plate/rebar extensometer	D.P.P.C.	---	removable dial gauge	homemade device
11200	Wire extensometer	S.R.C.	606	S.R.C. Model 400 readout box	rotary potentiometer;1500 mm travel
11200, 12826	Pressure cell	S.R.C.	---	pressure gauge	flatjack grouted with Sternson M-Bed
12831	Pressure cell	S.R.C.	---	pressure gauge	potash encapsulated flatjack
11200, 12826	Pressure cell	S.R.C.	---	pressure gauge	epoxy encapsulated flatjack
12826, 12831	Borehole pressure cell	S.G.I.	BPC-100	pressure gauge	cylindrical elastomeric membrane
12827	Borehole stress meter	E.I.	PAL	Terrascience uE-350 readout box	strain gauge measuring element
11200	Radial pressure cell	E.I.	---	pressure gauge	packer confined hydraulic oil
11200	Earth pressure cells	Geokon	4800E	Geokon GK-401 readout box	vibrating wire; 0-5000 psi
11200	Pressure transducers	Geokon	4500HC	Geokon GK-401 readout box	vibrating wire; 0-10,000 psi
11200	Datalogger	Geokon	Micro-10	Tandy 102 microcomputer	Tandy 102 downloads to PC on surface

LEGEND:
D.P.P.C. - Denison-Potacan Potash Company
S.R.C. - Saskatchewan Research Council
S.G.I. - Serata Geomechanics Inc.
E.I. - Engineered Instruments Inc.

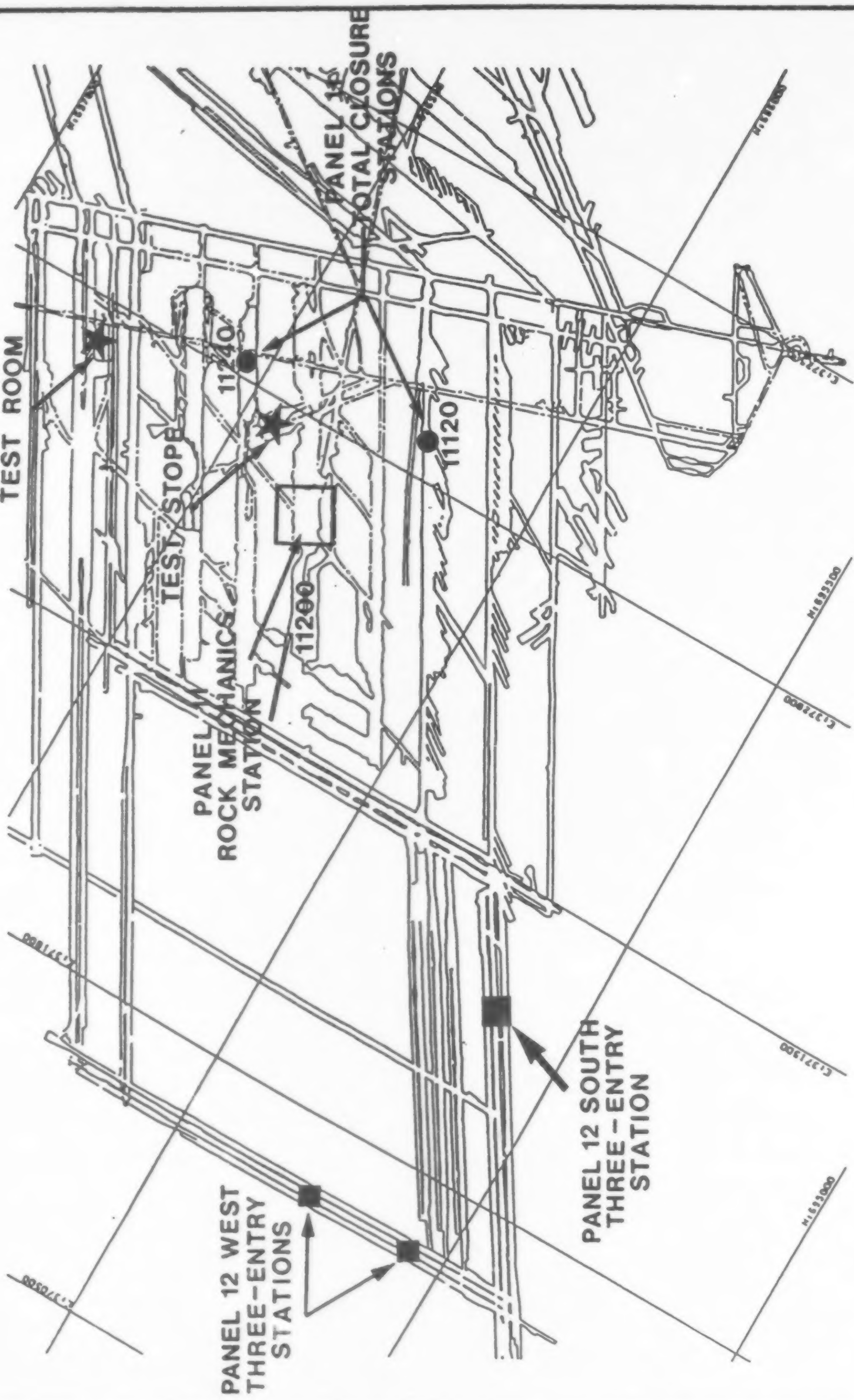
TEST ROOM
TEST STOPE
11240
11120
11200
PANEL 15 TOTAL CLOSURE STATIONS
PANEL ROCK MECHANICS STATION
PANEL 12 SOUTH THREE-ENTRY STATION
PANEL 12 WEST THREE-ENTRY STATIONS

DENISON
POTACAN
POTASH
COMPANY

TITLE:

ROCK MECHANICS
INSTRUMENTATION SITES

SCALE:
1:10000

FIGURE:
3.1

Prior to the start up of production activities in July 1985, two test sites were excavated to provide virgin ground field data. These sites, the Test Room and Test Stope, were excavated in 1982 and 1983, respectively, and have been discussed in detail in the Phase I report (CANMET, 1987).

Since July 1985, emphasis has been placed upon the monitoring of active mining sites. A rock mechanics station in Stope 11200 (previously referred to as Stope 1105) was chosen to be the initial backfill monitoring site and was instrumented to monitor the roof and wall behaviour of a full scale backfilled production stope.

Vertical closure stations were installed in Stopes 11120 and 11240 to provide calibration data for the numerical modelling runs.

The entry systems in 12826/12827/12828 and 12831 were used to evaluate instrumentation performances, in particular, various types of pressure cells and to provide field data for comparison and calibration of numerical modelling runs.

3.4.1 Panel 11, Stope 11200

Stope 11200 (previously referred to as Stope 1105) in Panel 11 was excavated in 1986. This stope was chosen as an instrumentation site as it provided a number of features that were typical in terms of mine layout at that time, such as:

a) a fully excavated mining width of 42 metres
b) an average ore thickness of 15 metres

In addition, the site chosen was readily available for the installation of rock mechanics instrumentation, backfill placement and long term access.

For reference purposes, May 10, 1986, was taken as Day 0 for the date of excavation for the rock mechanics station. This date corresponds to the time at which the hanging wall was excavated to full width (42 metres). A detailed plan of the instrumentation station is shown in section in Figure 3.2.

The placement and commissioning of instrumentation commenced in July 1986 (Day-88) with the installation of the roof extensometer. Some technical and logistical problems occurred with the electronic readout device resulting in an approximate two month gap in readings after the initial readings. Technical problems were also encountered with the 2.5 metre extensometer anchor. These problems were subsequently resolved.

The vertical, lateral and radial pressure cells were installed in the wall and commissioned by June 1987 (Day 404). The wall extensometer was commissioned shortly after in July 1987 (Day 422). A photograph of the 6-channel wall extensometer is shown in Figure 3.3. Note the concrete wall built to provide protection to the unit housing. The steel cover plate that rests on the concrete walls above the unit is not shown.

The original layout for the rock mechanics station proposed installation of instrumentation in the floor. However, large quantities of brine (draining from the backfill being placed to the east of the station) flooded the floor area. Consequently, it was decided to abandon any attempt to install instrumentation in the floor.

The stress within the emplaced backfill was monitored with vibrating wire earth pressure cells. Backfill pressure cells were installed in two phases (in accord with backfill placement); the initial cells were placed in the floor area by August 1987 (Day 457) and the second set by December 1987 (Day 585).

Installations continued with the installation and commissioning of the lateral and tangential pressure cells in the roof by October 1987 (Day 530).

Monitoring of the instrumentation in Stope 11200 required the installation of a remote readout system. This was accomplished using vibrating wire pressure transducers, electrical read-out cables, junction box, multiplexer and a programmable datalogger.

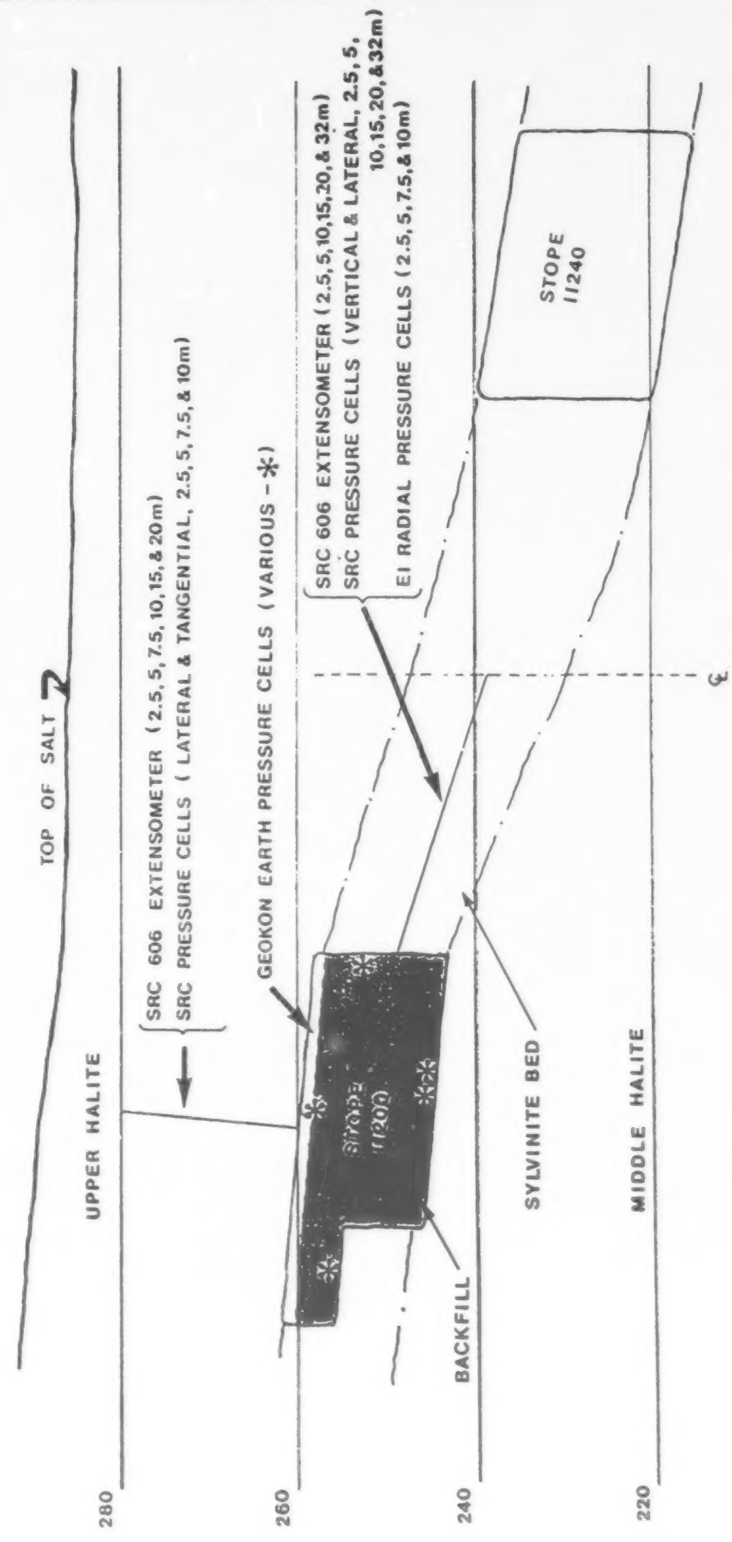
TOP OF SALT
UPPER HALITE
SRC 606 EXTENSOMETER (2.5, 5, 7.5, 10, 15, & 20m)
SRC PRESSURE CELLS (LATERAL & TANGENTIAL, 2.5, 5, 7.5, & 10m)
GEOKON EARTH PRESSURE CELLS (VARIOUS - *)
SRC 606 EXTENSOMETER (2.5, 5, 10, 15, 20, & 32m)
SRC PRESSURE CELLS (VERTICAL & LATERAL, 2.5, 5, 10, 15, 20, & 32m)
EI RADIAL PRESSURE CELLS (2.5, 5, 7.5, & 10m)
STOPE 11200
STOPE 11240
BACKFILL
SYLVINITE BED
MIDDLE HALITE
℄
280
260
240
220

DENISON
POTACAN
POTASH
COMPANY

TITLE:

PANEL 11 (11200)
INSTRUMENTATION STATION

SCALE:
NTS

FIGURE:
3.2

FIGURE 3.3

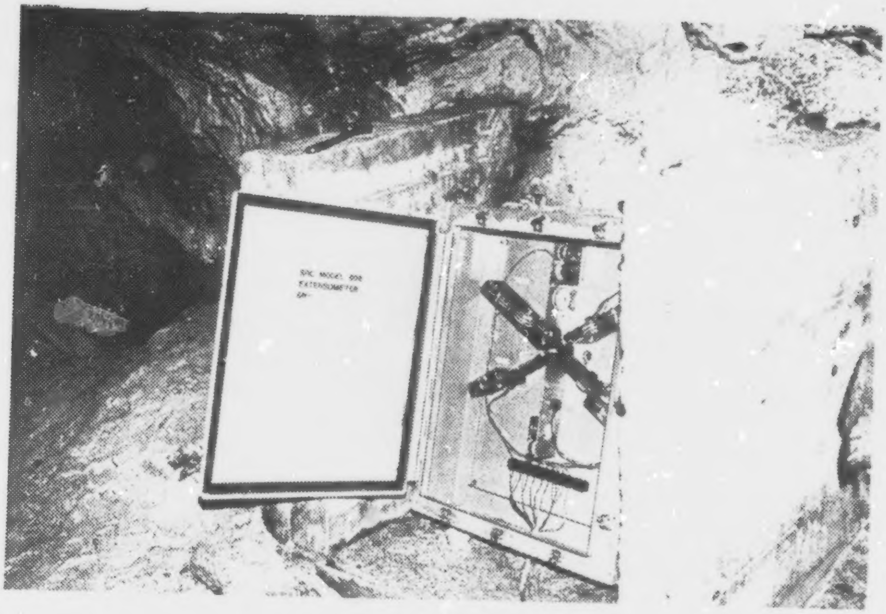

Photograph showing 6-point wall extensometer. Note protective concrete wall - steel cover plate not shown.

FIGURE 3.4

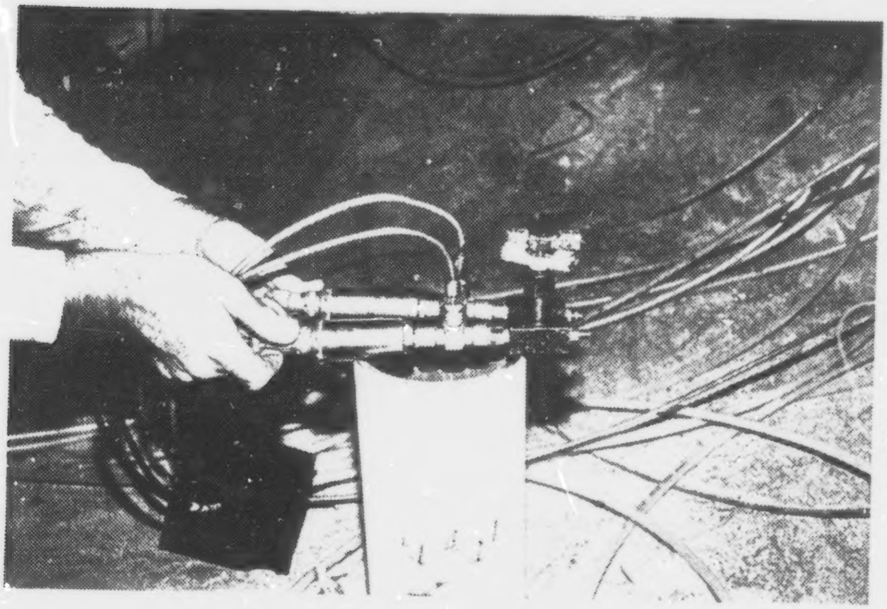

Photograph showing pressure transducer interface. Unit is shown resting on grease-packed protective enclosure into which it is inserted.

The installations of remote readout signal lines and the junction box were completed by August 1987 (Day 455). A photograph of the pressure transducer interface used to convert hydraulic pressure signals to electrical signals, recorded by the datalogger, is shown in Figure 3.4.

The datalogger was hooked up and was operational by December 1987 (Day 580). The Stope 11200 remote readout layout is shown in Figure 3.5. A schematic of the overall remote readout and datalogging system is shown in Figure 3.6.

A roof fall occurred in June 1988 (Day 765) in the immediate vicinity of the rock mechanics station. This resulted in the loss of the following pressure cells:

ROOF - Lateral cells at 2.5, 5, 7.5 and 10 metres.
- Tangential cell at 5 metres.
WALL - Lateral cells at 2.5, 5, 10, 15 and 20 metres.
- Vertical cells at 10, 15 and 29 metres.
- Radial cells at 2.5, 5, 7.5 and 10 metres.
BACKFILL - All backfill pressure cells.

Fortunately, two separate instrumentation signal lines were installed. The second line was not entirely damaged and the following instrumentation continued to be monitored:

ROOF - Extensometer.
- Tangential cells at 7.5 and 10 metres.
WALL - Extensometer.
- Lateral cell at 32 metres.
- Vertical cells at 2.5, 5 and 32 metres.

Logging of data from these installations continued until January 1989 (Day 980) at which time the electrical transformer supplying power to the data acquisition system was lost. Monitoring of the remaining instrumentation can recommence once an electrical power supply has been re-established.

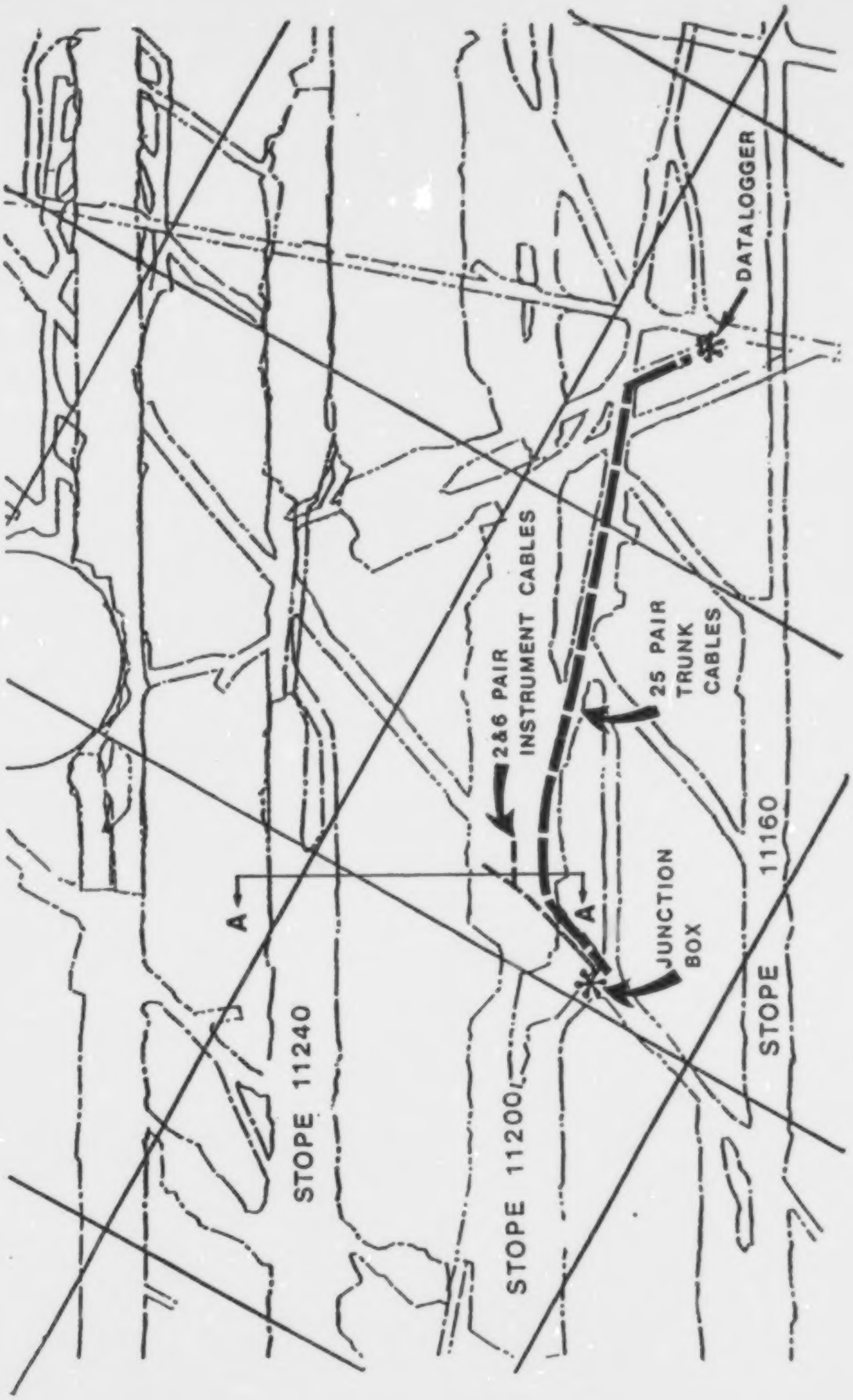

DENISON
POTACAN
POTASH
COMPANY

TITLE:

STOPE 11200
REMOTE READOUT LAYOUT

SCALE:
1:3000

FIGURE:
3.5

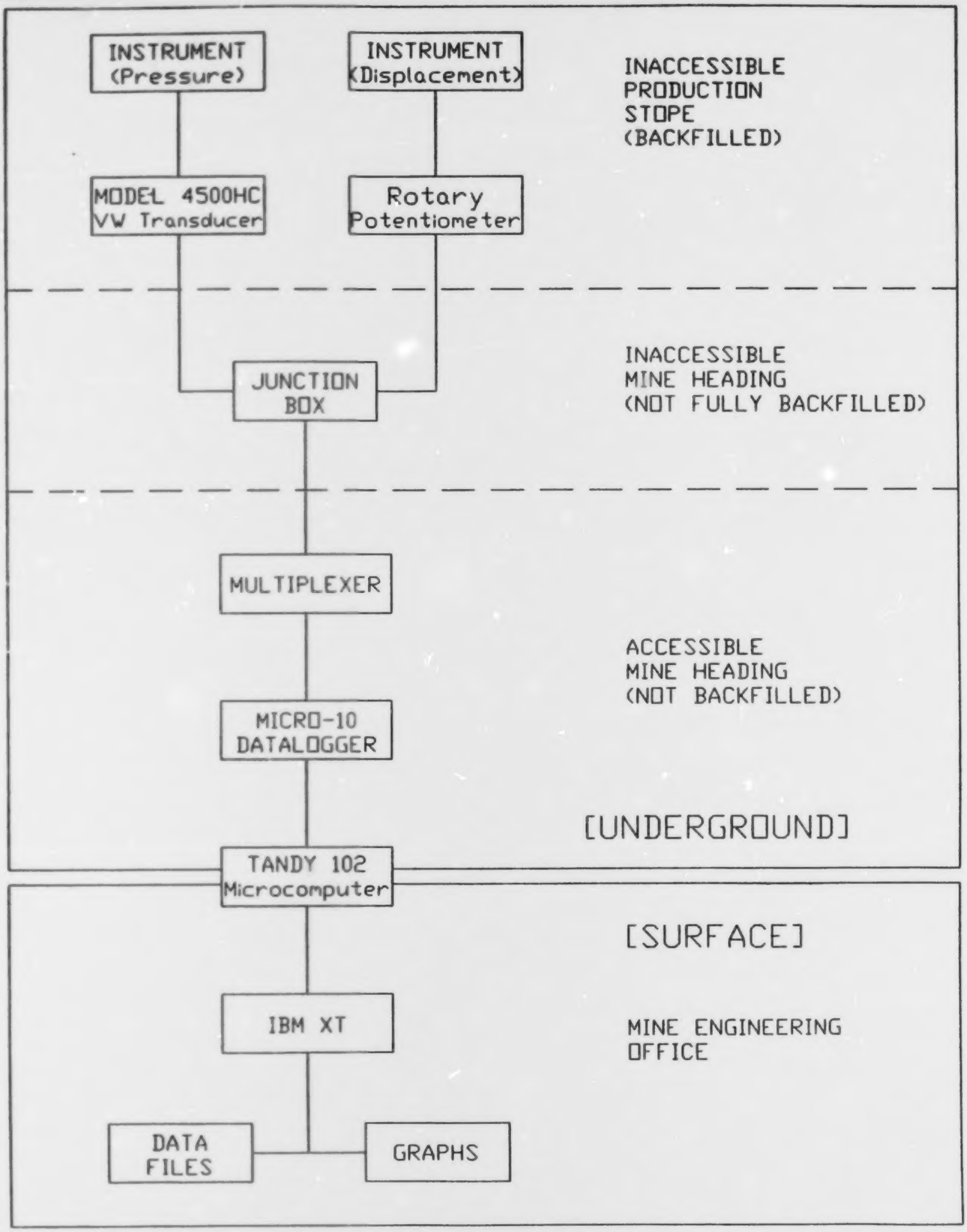
INSTRUMENT (Pressure)
INSTRUMENT (Displacement)
INACCESSIBLE PRODUCTION STOPE (BACKFILLED)
MODEL 4500HC VW Transducer
Rotary Potentiometer
INACCESSIBLE MINE HEADING (NOT FULLY BACKFILLED)
JUNCTION BOX
MULTIPLEXER
ACCESSIBLE MINE HEADING (NOT BACKFILLED)
MICRO-10 DATALOGGER
[UNDERGROUND]
TANDY 102 Microcomputer
[SURFACE]
IBM XT
MINE ENGINEERING OFFICE
DATA FILES
GRAPHS

DENISON
POTACAN
POTASH
COMPANY

TITLE:
STOPE 11200 REMOTE
READOUT CONFIGURATION

SCALE:
NTS

FIGURE:
3.6

A summary of the installation and events that occurred in relationship to the installation of Stope 11200 instrumentation is included as Figure 3.7. A listing of the instrumentation is included as Table 3.1. The results obtained in Stope 11200 are presented in Figures 3.8 to 3.15.

FIGURE 3.7
PANEL 11, STOPE 11200
ROCK MECHANICS STATION

CHRONOLOGY OF EVENTS

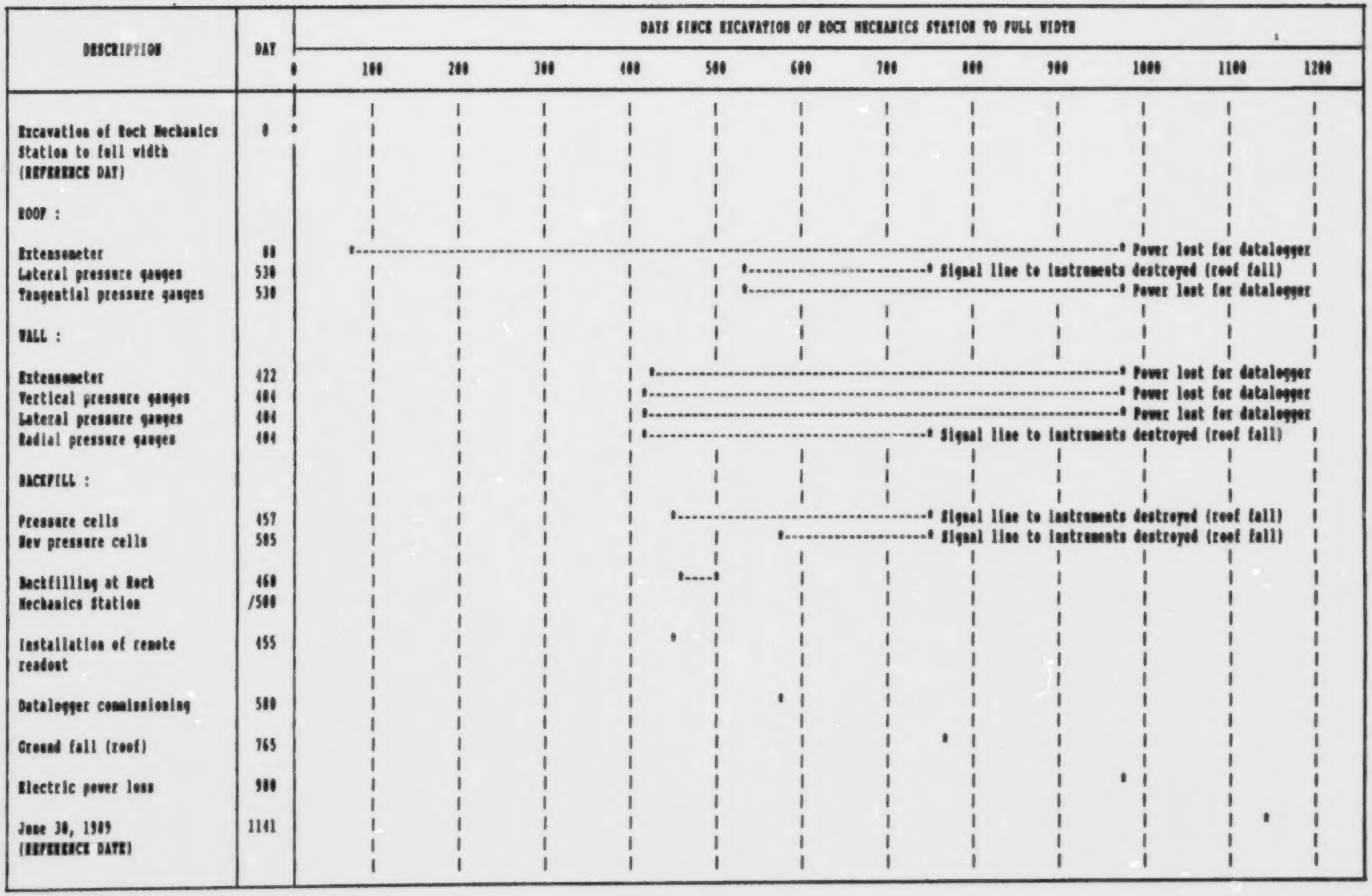

NOTES : (1) The day that excavation was completed to full width (42 metres) is used as the REFERENCE DAY for all events.

(2) June 30, 1989 is used as a REFERENCE DATE for all events.

FIGURE 3.8

STOPE 11200 -- ROOF EXTENSOMETER

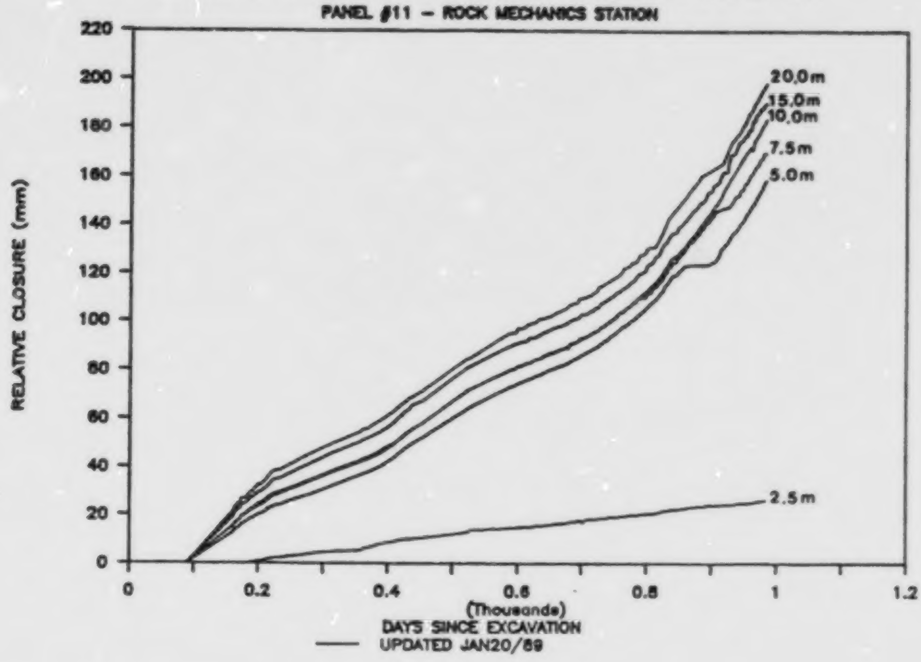

FIGURE 3.9

STOPE 11200 -- PILLAR EXTENSOMETER

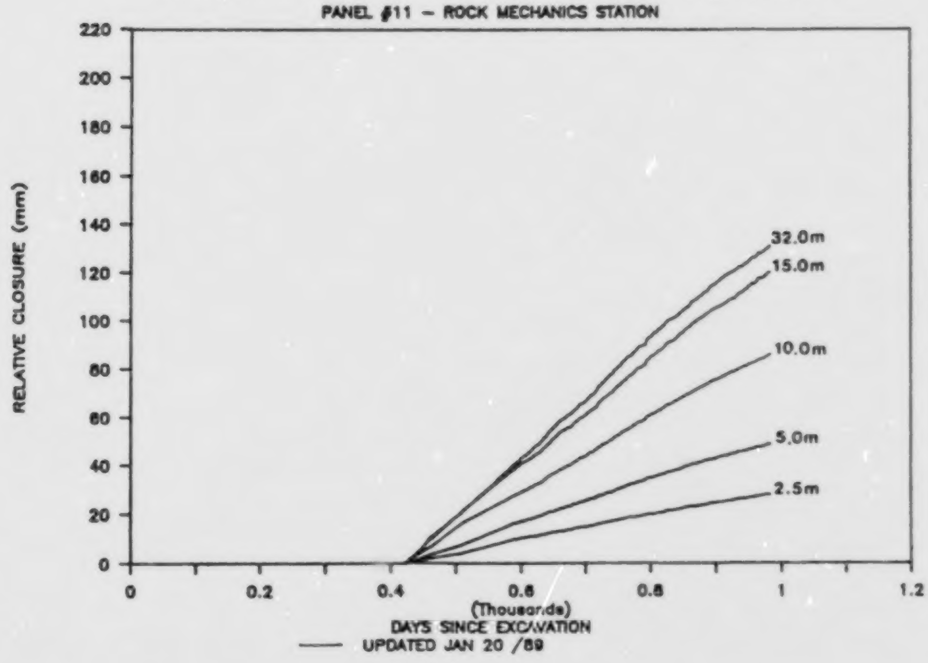

FIGURE 3.10

STOPE 11200 – ROOF LATERAL PRESSURE

PANEL #11 – ROCK MECHANICS STATION

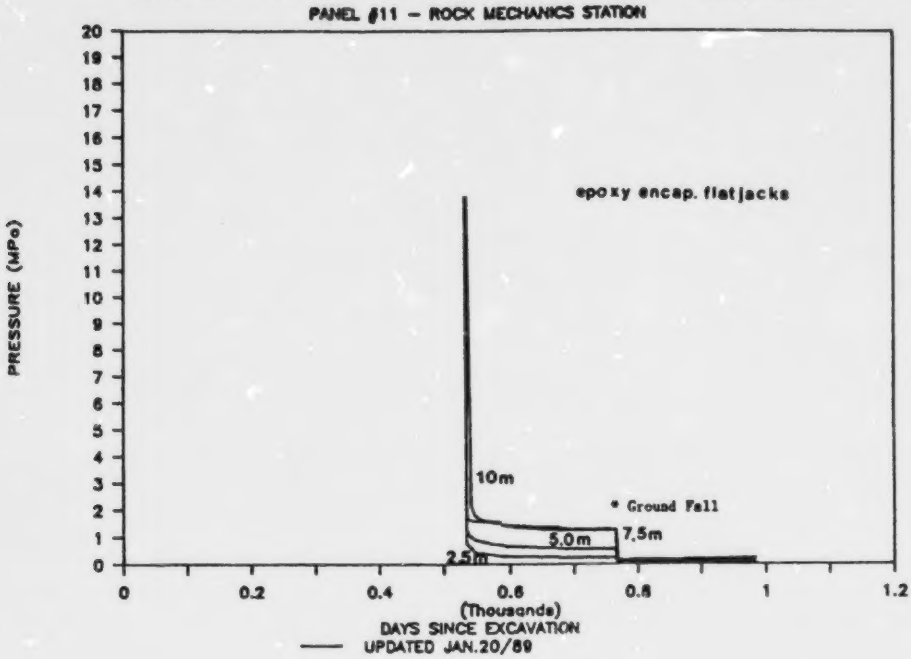

FIGURE 3.11

STOPE 11200 –– ROOF TANGENTIAL PRESSURE

PANEL #11 – ROCK MECHANICS STATION

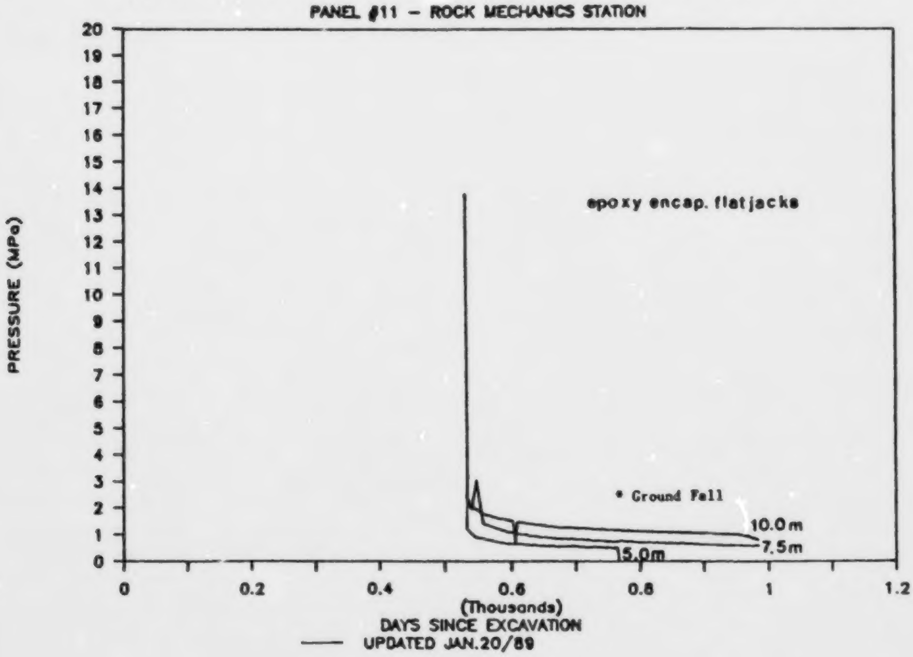

FIGURE 3.12

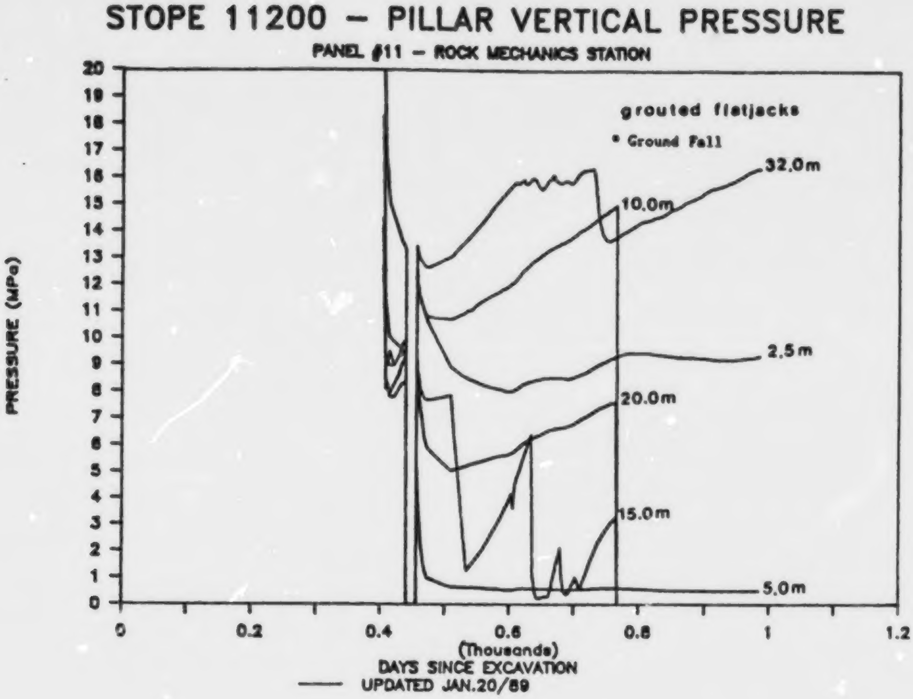

FIGURE 3.13

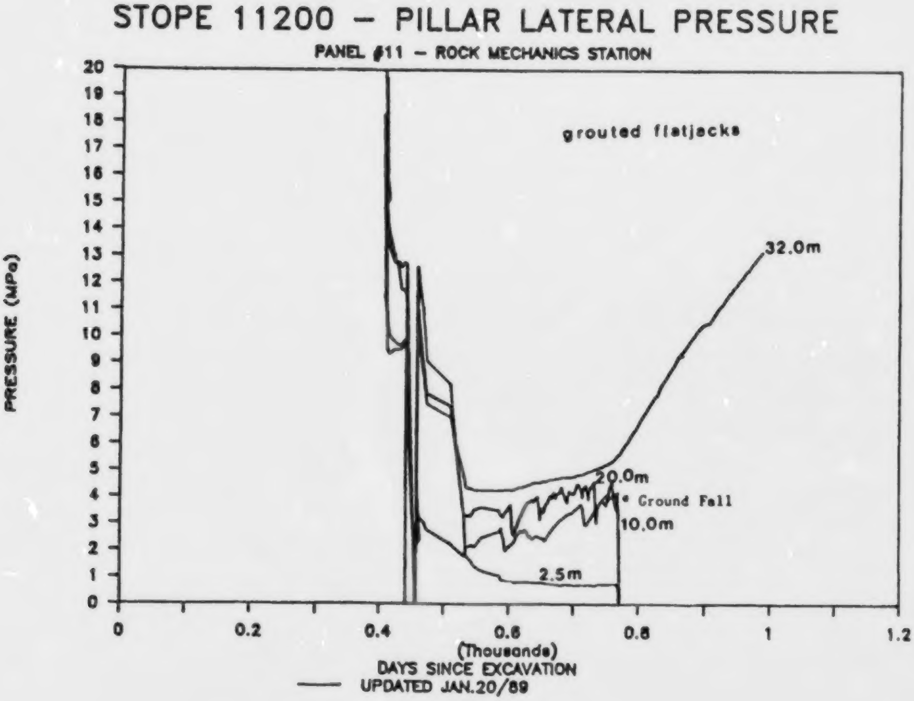

FIGURE 3.14

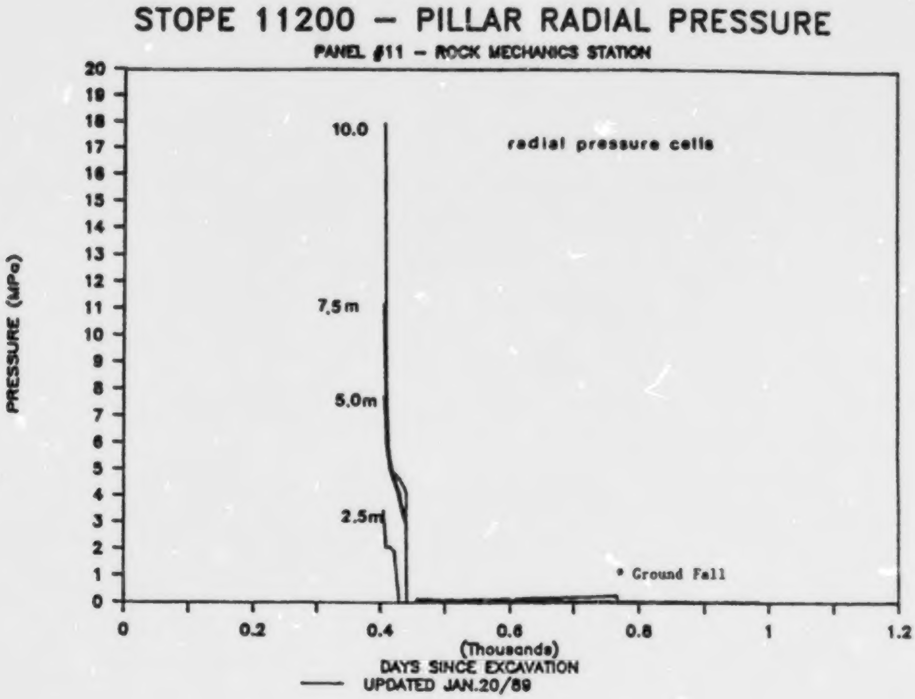

FIGURE 3.15

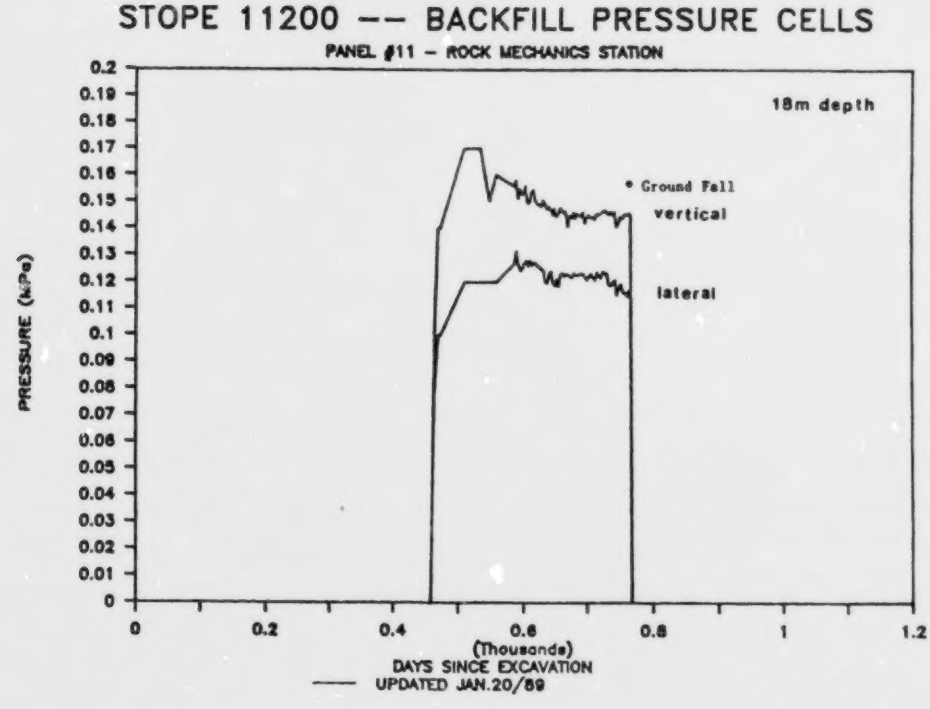

3.4.2 Panel 11, Convergence Stations in Stopes 11120 and 11240

Due to the anticipated difficulties associated with maintenance of total closure (convergence) stations during backfilling operations, the instruments were installed after the stopes had been backfilled to within 4 to 5 metres of the roof. The two selected sites were located about 300 m apart (Figure 3.1) to provide a sufficient calibration base for the numerical program VELMINA (Section 10.3). As can be seen from Figure 3.16, the heights of room cross-sections monitored at the two sites are 8 m in Stope 11120 and 25 m in Stope 11240. The sites continue to be monitored. The graphs of total closures and closure rates recorded to date are included in Figures 3.17 to 3.20.

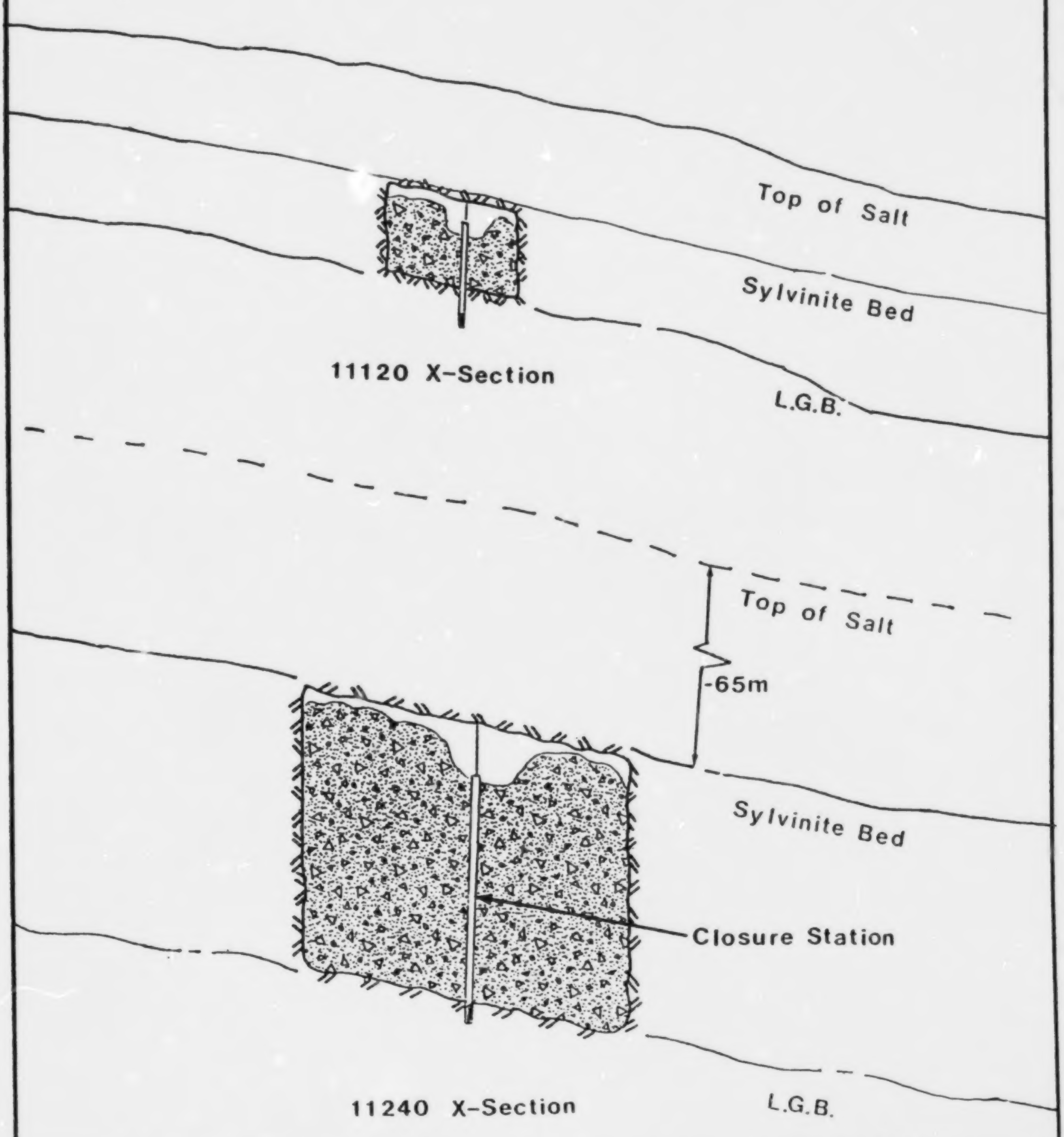

DENISON
POTACAN
POTASH
COMPANY

TITLE:

PANEL 11
TOTAL CLOSURE STATIONS

SCALE:
1:500

FIGURE:
3.16

FIGURE 3.17

STOPE 11120 – TOTAL CLOSURE

PANEL #11 – TOTAL CLOSURE STATIONS

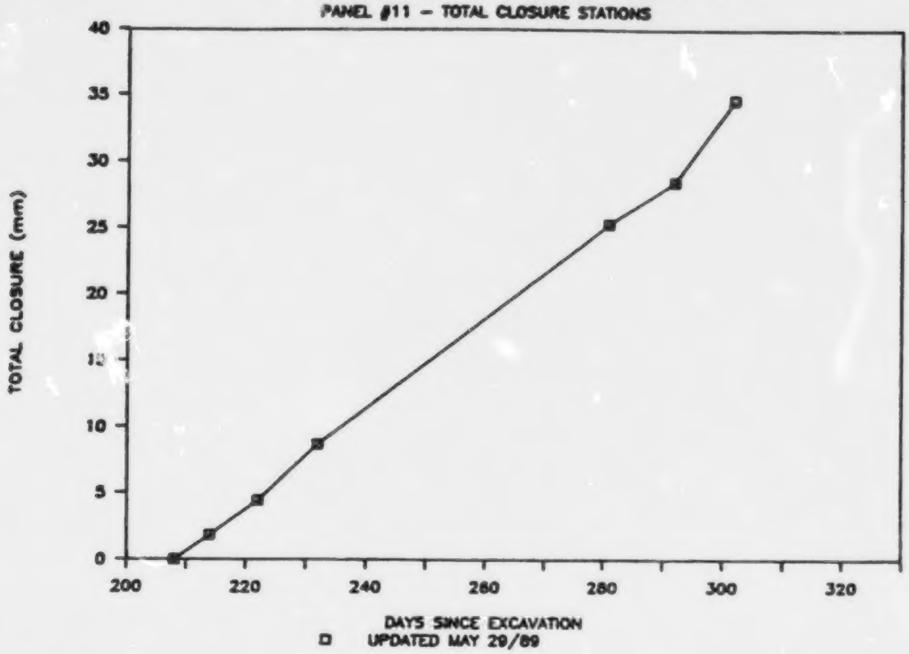

FIGURE 3.18

STOPE 11120 – TOTAL CLOSURE RATES

Panel #11 – RATES SINCE INSTALLATION

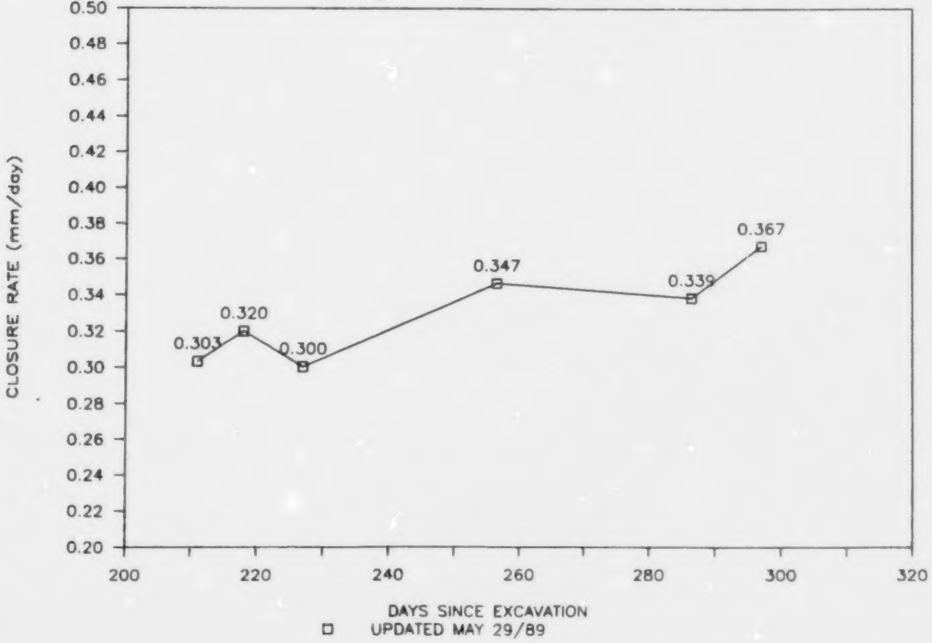

FIGURE 3.19

STOPE 11240 – TOTAL CLOSURE

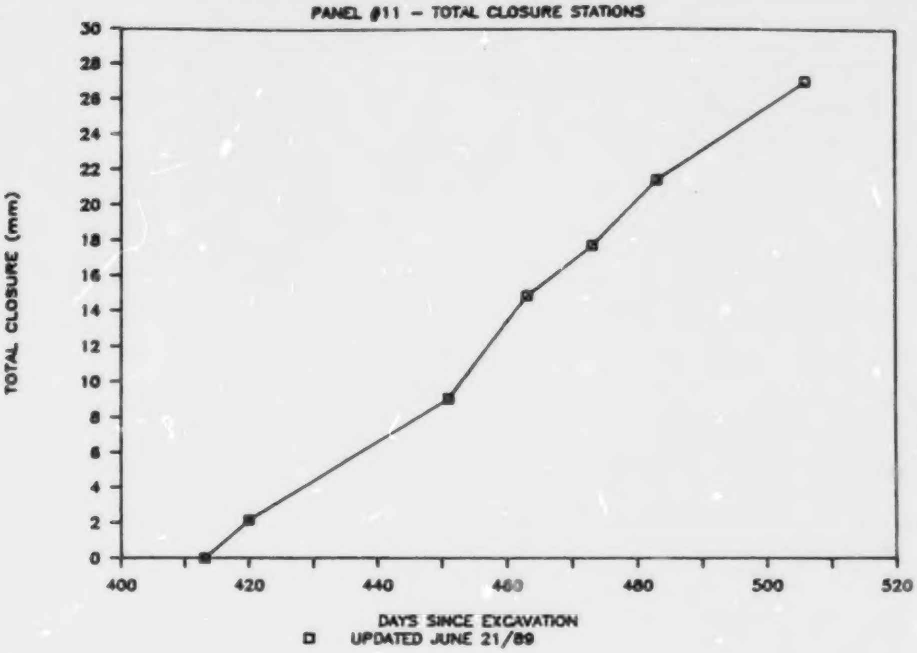

FIGURE 3.20

STOPE 11240 – TOTAL CLOSURE RATES

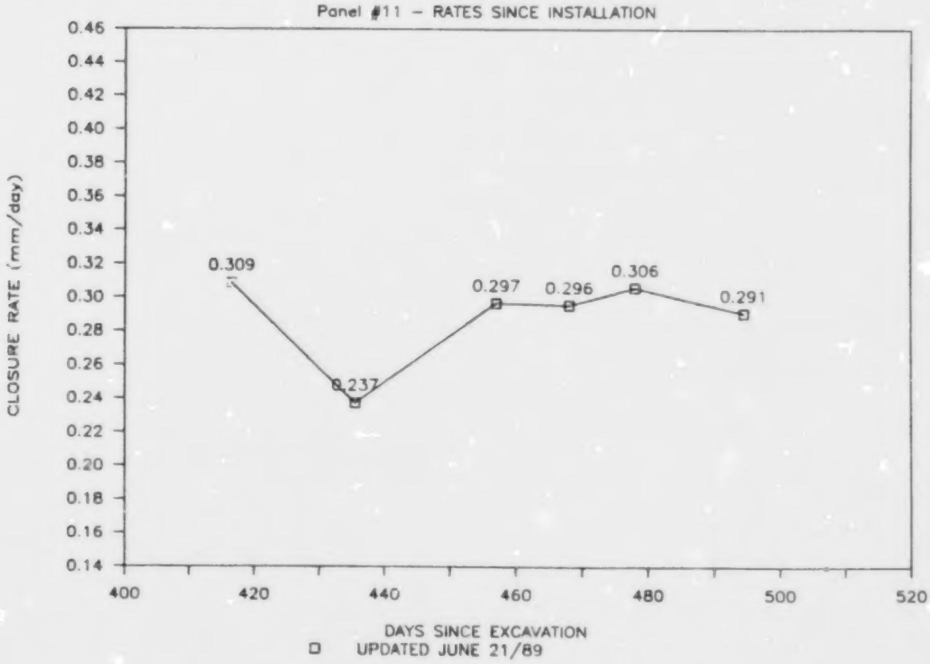

3.4.3 Panel 12, Entries 12826/12827/12828

The location of the rock mechanics station in Entries 12826/12827/12828 is shown in Figure 3.1. The cross-section is shown in Figure 3.21.

This station was installed to provide in situ data for a long term three entry system with particular emphasis on the long term stability of the middle entry (Entry 12827). The data was also used to verify numerical modelling runs of the entry system using the program FLAC (Section 8.5.2).

Included in the instrumentation array were different instrumentation devices such as the S.R.C. epoxy encapsulated "flatjack" unidirectional pressure cells and the Serata Geomechanics Inc. Model BPC-100 pressure cells. These were installed in separate boreholes at the same depths and orientations. They were installed so as to provide a comparison of the relative performance of the cells against each other and against the stress distribution predicted by the numerical modelling runs.

A listing of the instrumentation installed is included in Table 3.1. This instrumentation continues to be monitored. The results obtained to date are presented in Figures 3.22 to 3.33.

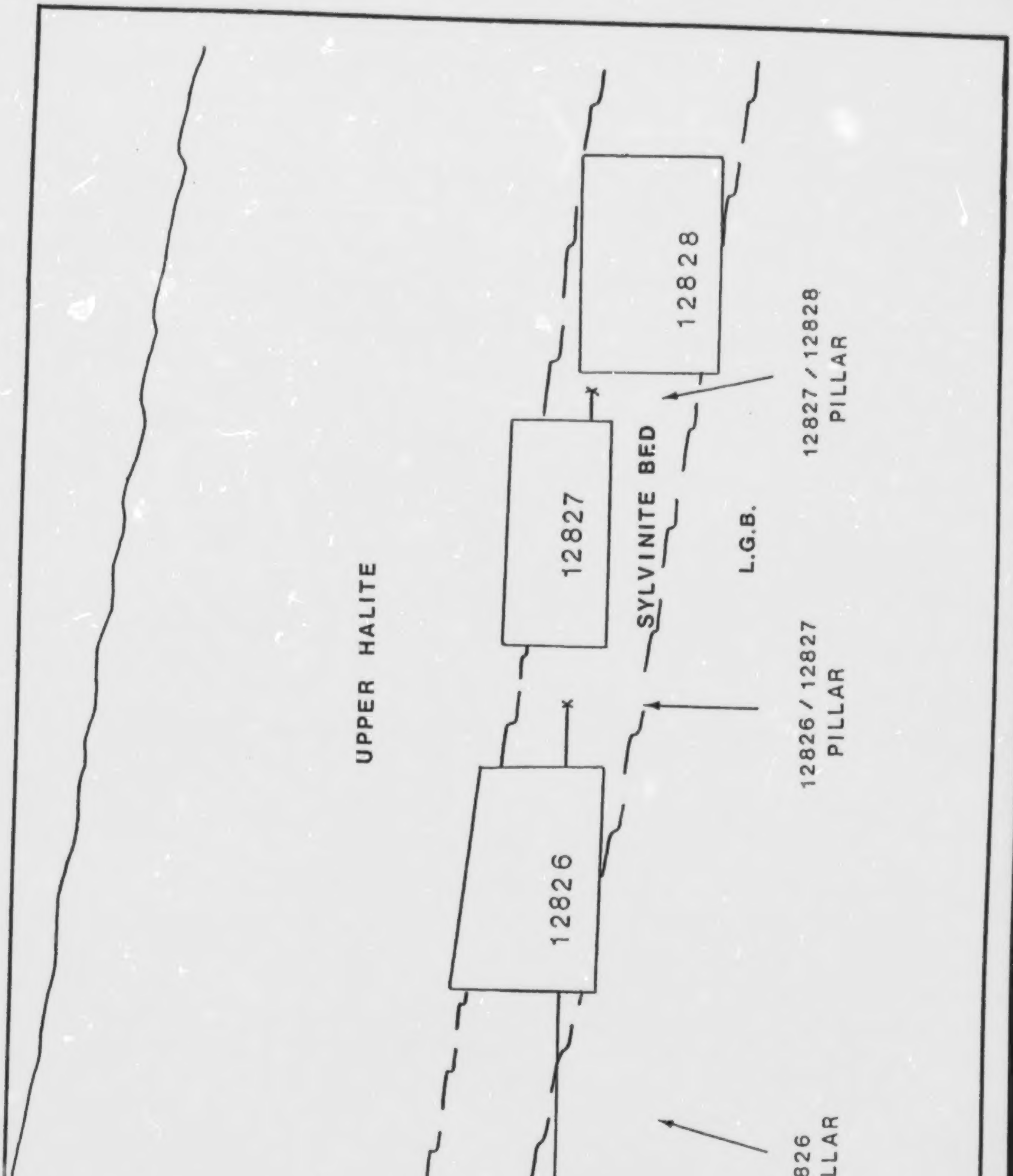

DENISON
POTACAN
POTASH
COMPANY

TITLE:

PANEL 12 SOUTH THREE-ENTRY
INSTRUMENTATION STATION

SCALE:
1:250

FIGURE:
3.21

FIGURE 3.22

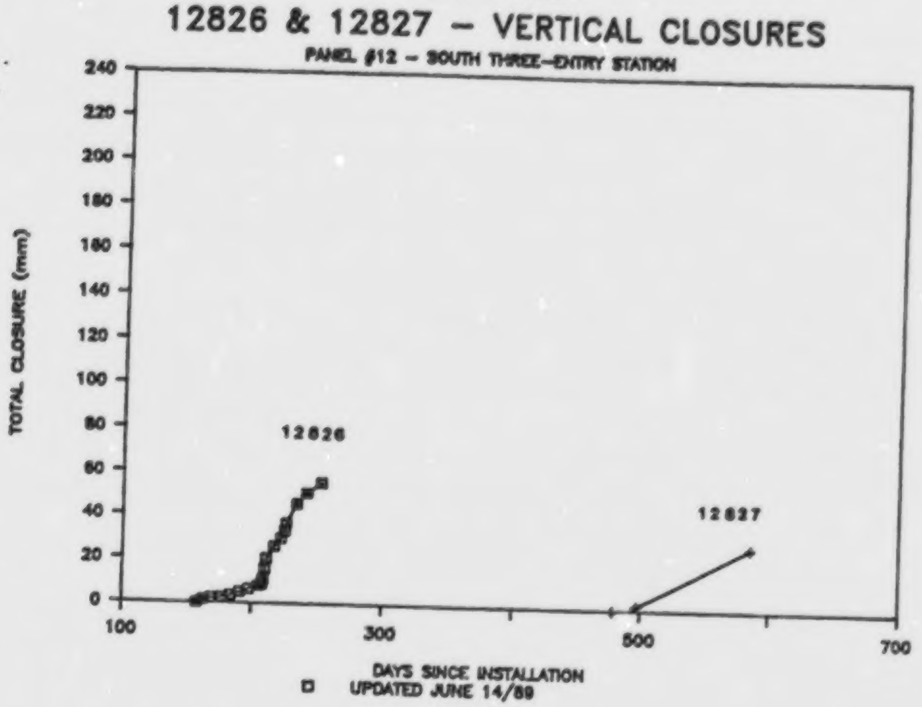

FIGURE 3.23

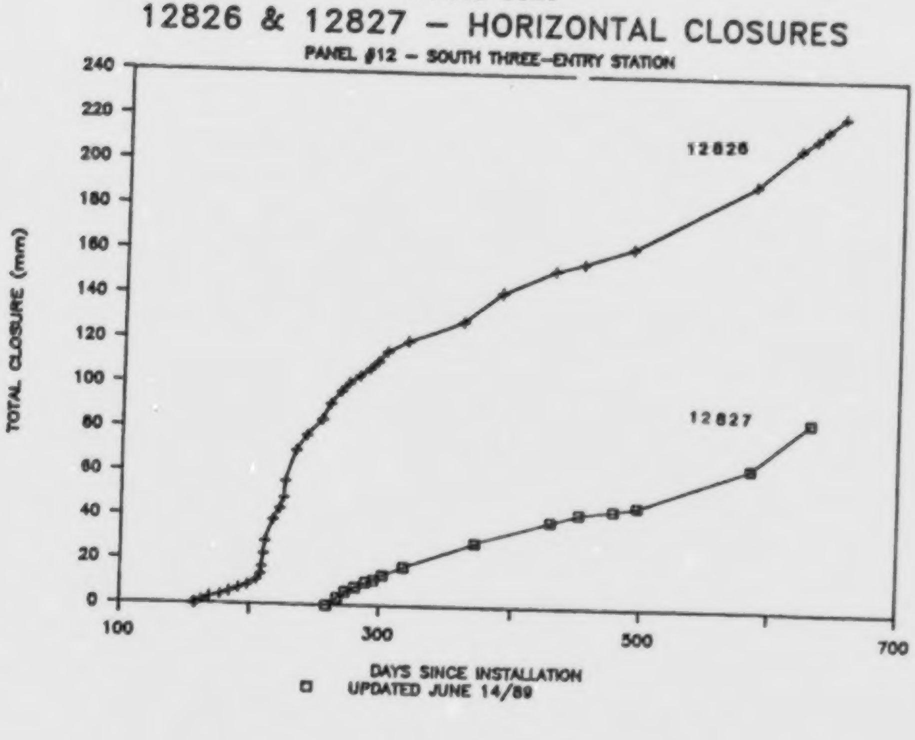

FIGURE 3.24

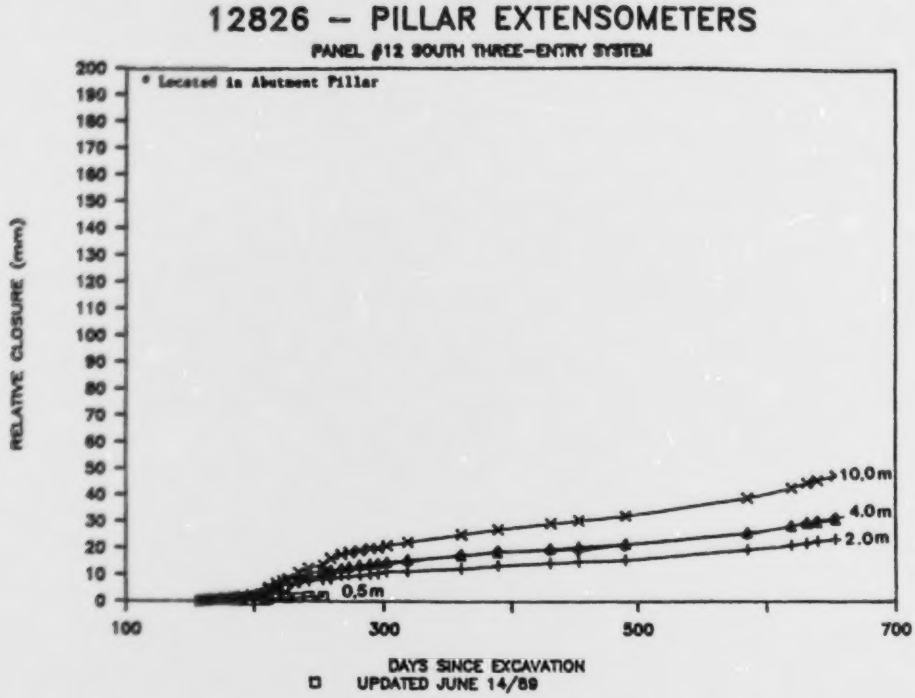

FIGURE 3.25

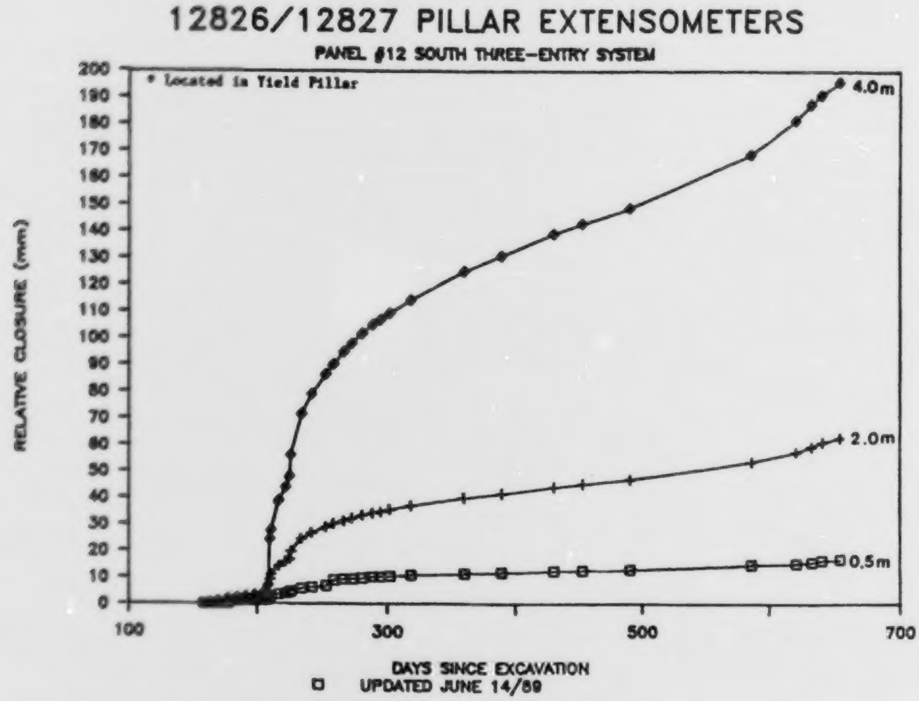

FIGURE 3.26

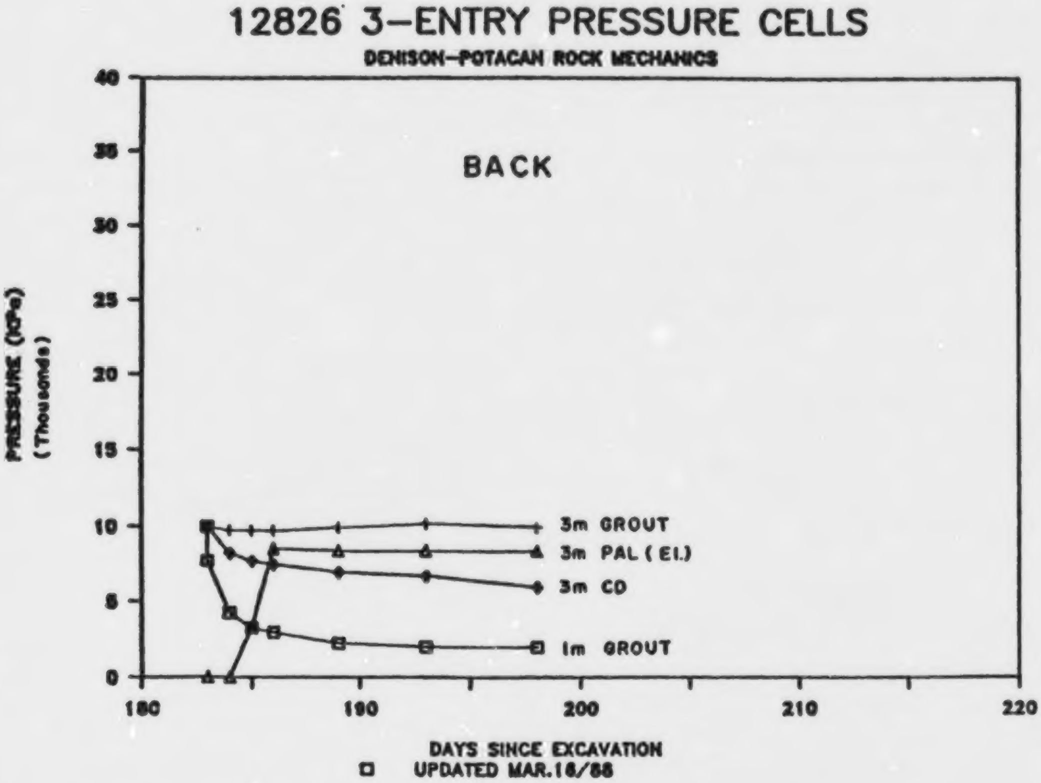

FIGURE 3.27

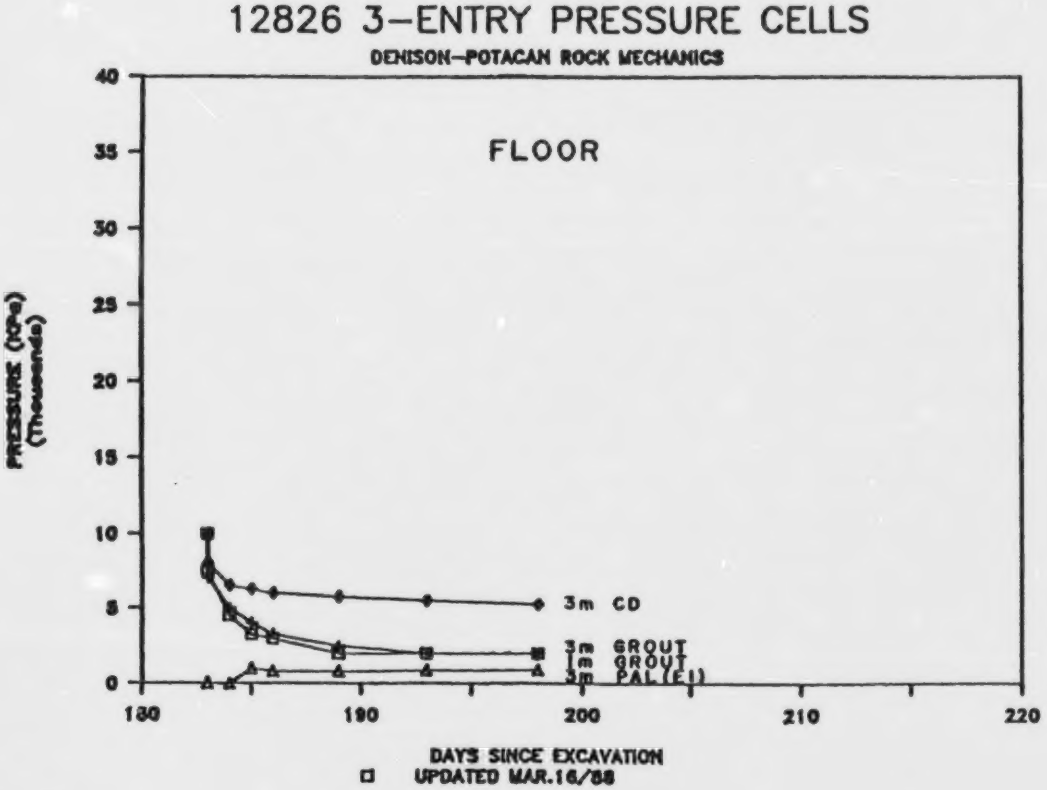

FIGURE 3.28

12826 – PILLAR PRESSURE CELLS

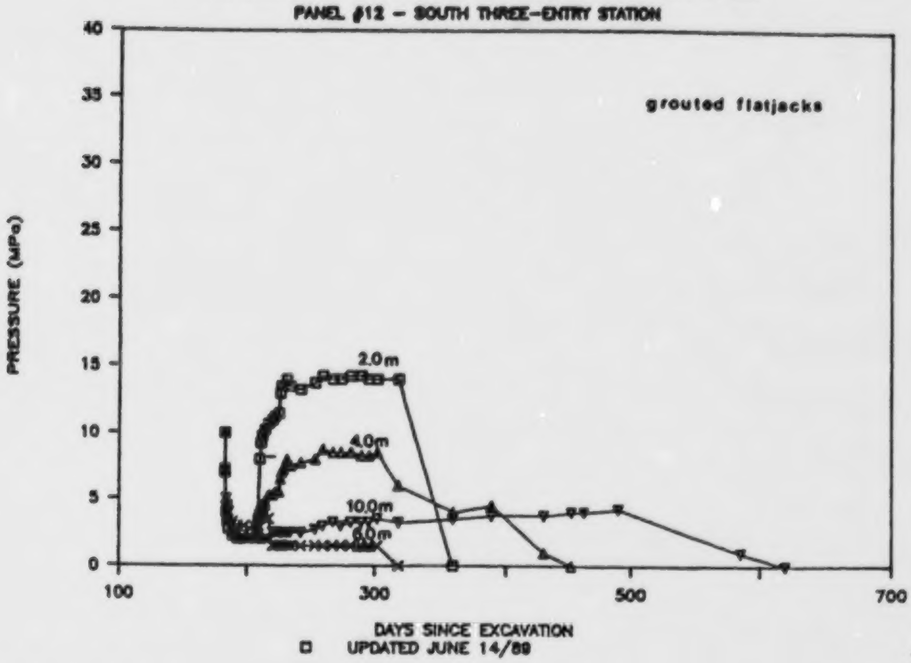

FIGURE 3.29

12826 – PILLAR PRESSURE CELLS

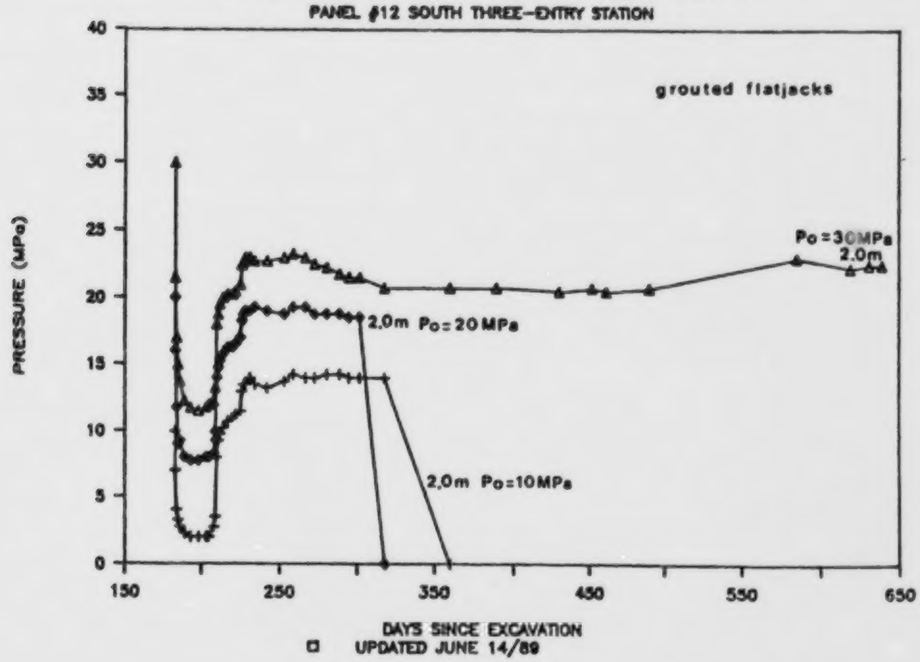

FIGURE 3.30

12826/12827 – PILLAR PRESSURE CELLS

PANEL #12 – SOUTH THREE ENTRY STATION

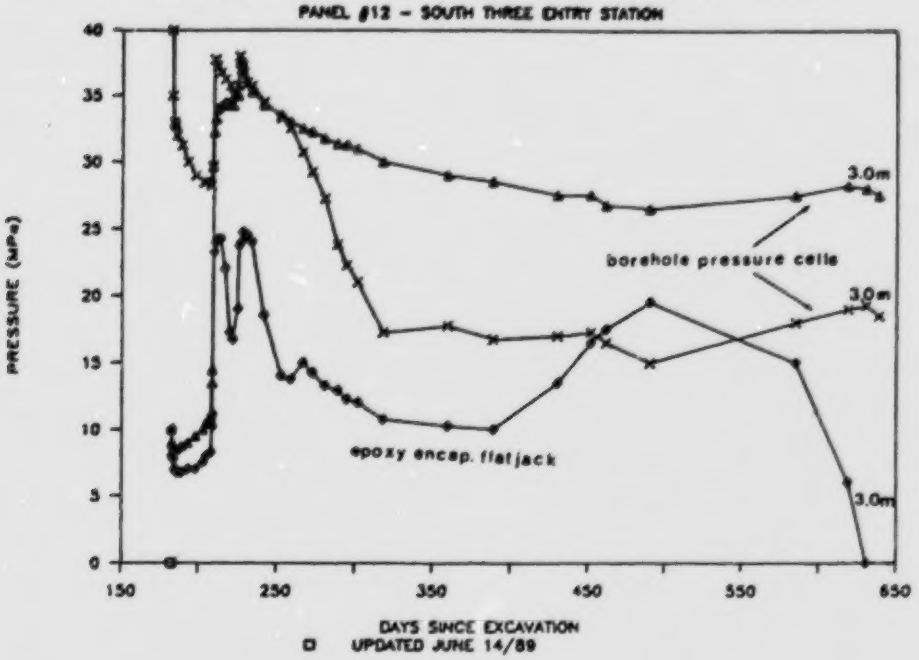

FIGURE 3.31

12827/12828 –PILLAR PRESSURE CELLS

PANEL #12 – SOUTH THREE-ENTRY STATION

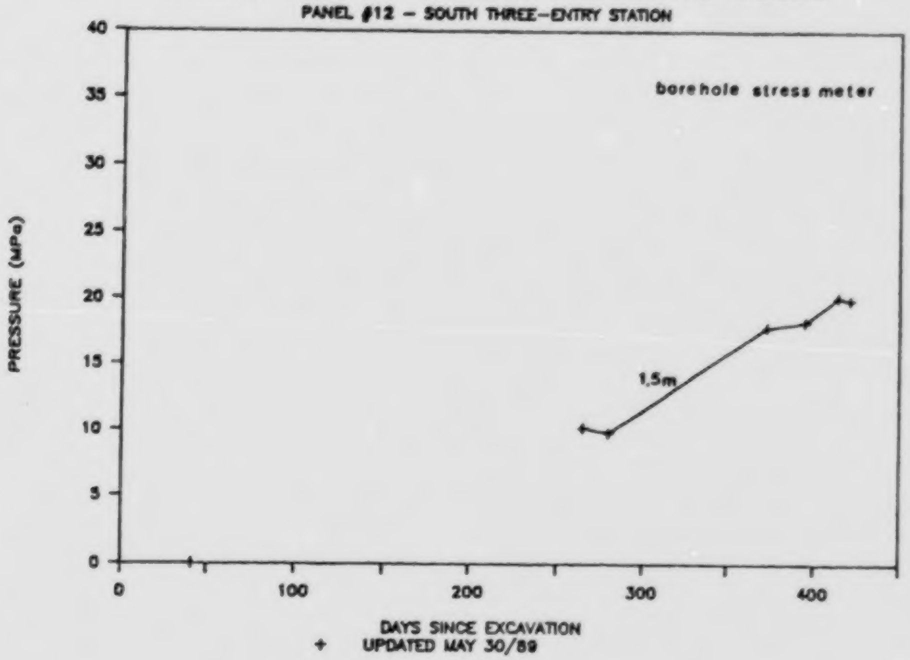

FIGURE 3.32

12827 RELATIVE CLOSURE

YIELD PILLAR

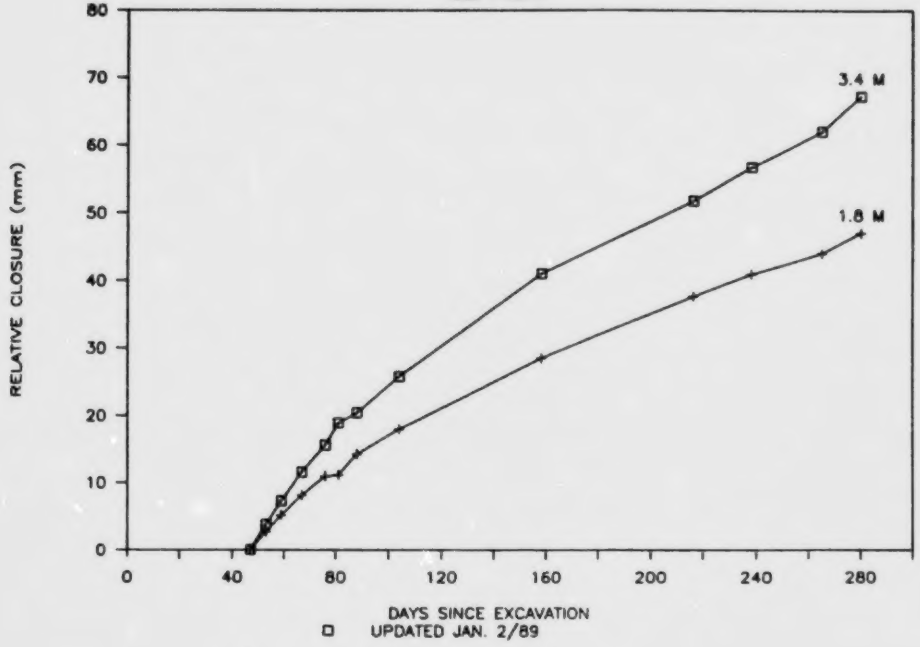

FIGURE 3.33

12827 TOTAL CLOSURE

DPPC ROCK MECHANICS

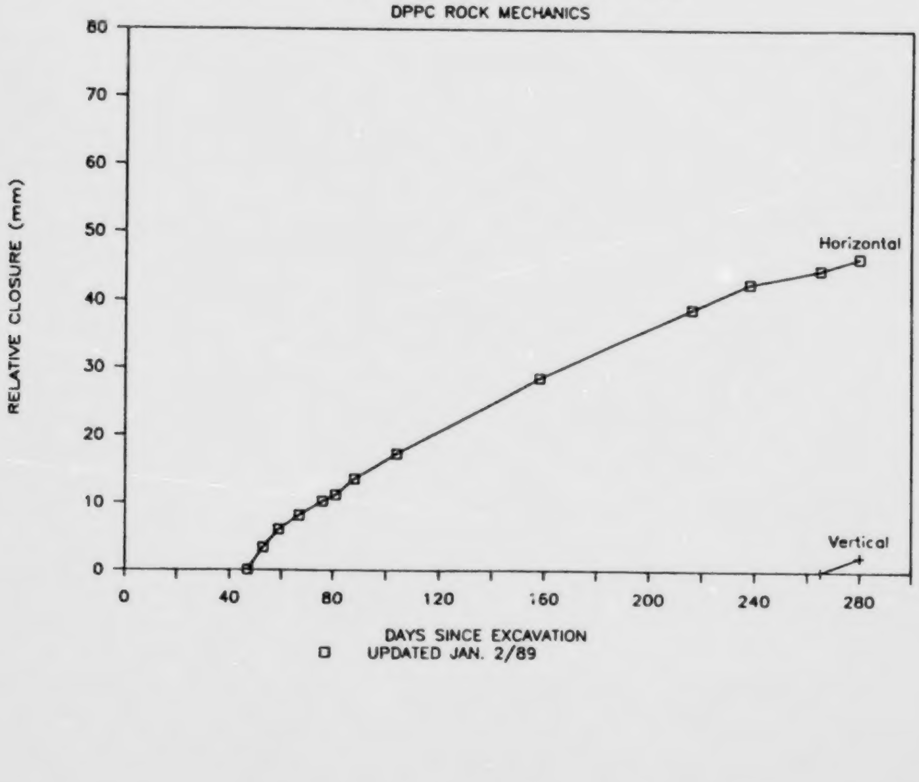

3.4.4 Panel 12, Entry 12831

The location of the rock mechanics stations in Entry 12831 are shown in Figure 3.1. The cross-sections are shown in Figure 3.34.

The instrumentation installed is listed in Table 3.1. The type of instrumentation and the purpose of this station is similar to the rock mechanics station described in Section 3.4.3. This instrumentation continues to be monitored. The results obtained to date are presented in Figures 3.34 to 3.38.

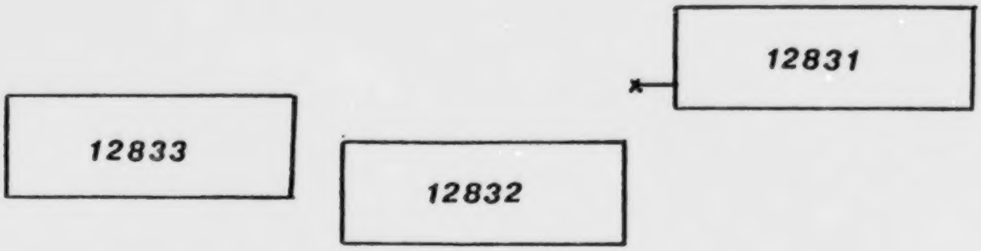

STATION #1 (175m)

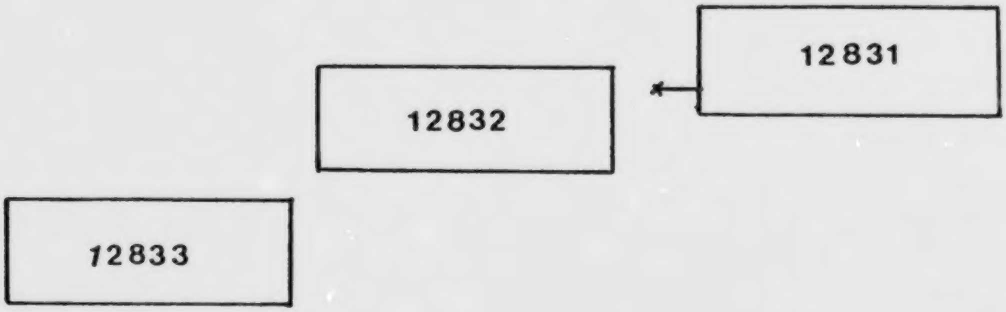

STATION #2 (350m)

DENISON
POTACAN
POTASH
COMPANY

TITLE:

PANEL 12 WEST THREE-ENTRY
INSTRUMENTATION STATIONS

SCALE:
1:250

FIGURE:
3.34

FIGURE 3.35

12831 (175 M) RELATIVE CLOSURE

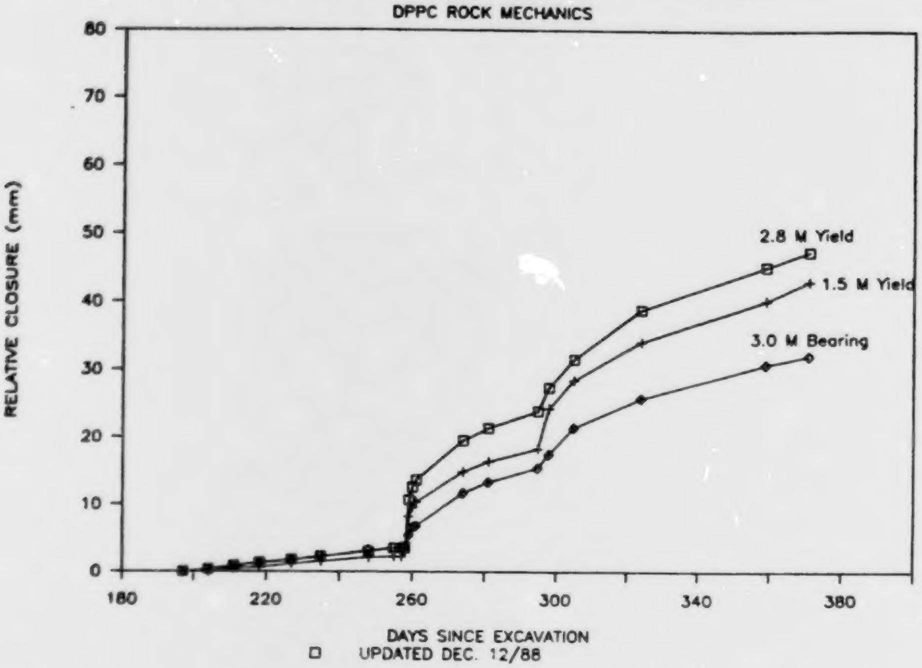

FIGURE 3.36

12831 (350 M) RELATIVE CLOSURE

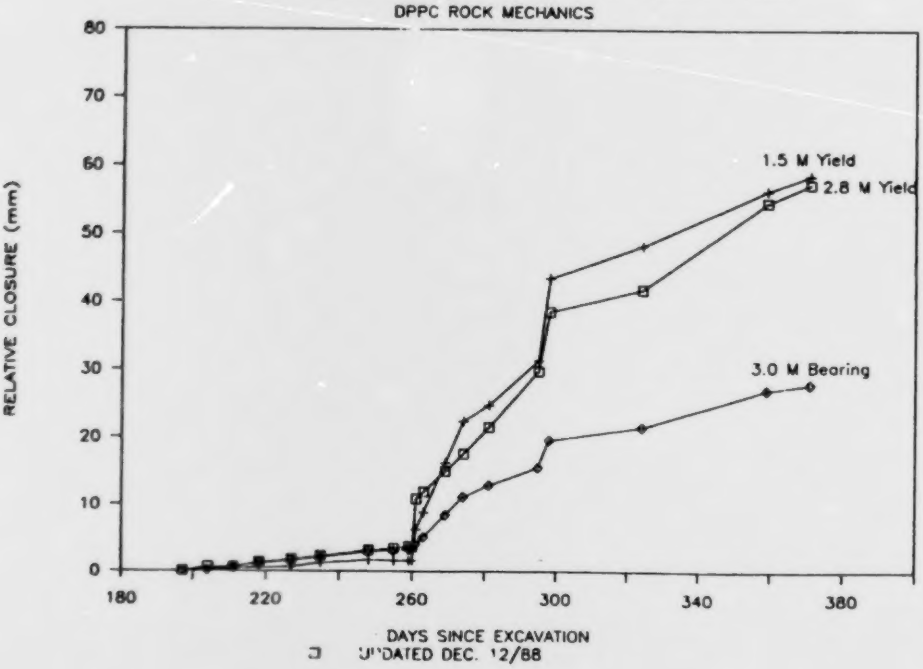

3.5 Interpretation of Underground Instrumentation Data

3.5.1 Stope 11200, Extensometers

The strain rates calculated from the roof extensometer data are plotted in Figure 3.39 and tabulated in Tables 3.2 to 3.6. The strain rates calculated from wall extensometer data are plotted in Figure 3.40 and tabulated in Tables 3.7 to 3.9. Following is the interpretation of these strain rate distributions:

* A fracture developed within the interval of 2.5 to 5.0 m in the roof shortly after the excavation and continued to open up during the monitoring interval.

* A second fracture developed within the interval of 5.0 to 7.5 m in the roof after 800 days. This occurrence could be attributed to the ground fall that occurred on Day 765.

* Average strain rates within the interval of 7.5 to 20.0 m in the roof was about 2.0 x 10^{-11} s^{-1} throughout the monitoring period.

* Fracture and/or dilation occurred within the interval of 0 to 2.5 m in the wall, suggesting the presence of the **active opening**.

* Average strain rates within the interval of 2.5 to 15.0 m in the wall was about 1.5 x 10^{-10} s^{-1}, suggesting that the **high exponent** region of the power law governs creep in this zone of the pillar.

* Average strain rate beyond 15 m was less than 2.0 x 10^{-11} s^{-1}, decreasing towards the center of pillar. This suggests that the **low exponent** region of the power law governs creep in this zone of the pillar.

* The response of the extensometers installed in the roof and wall of Stope 11200 to the backfill from Day 460 to 500 was negligible (Figures 3.8 and 3.9).

3.5.2 Stope 11200, Pressure Cells

Pressure cell measurements are tabulated in Table 3.10. The interpretation of results is as follows:

FIGURE 3.37

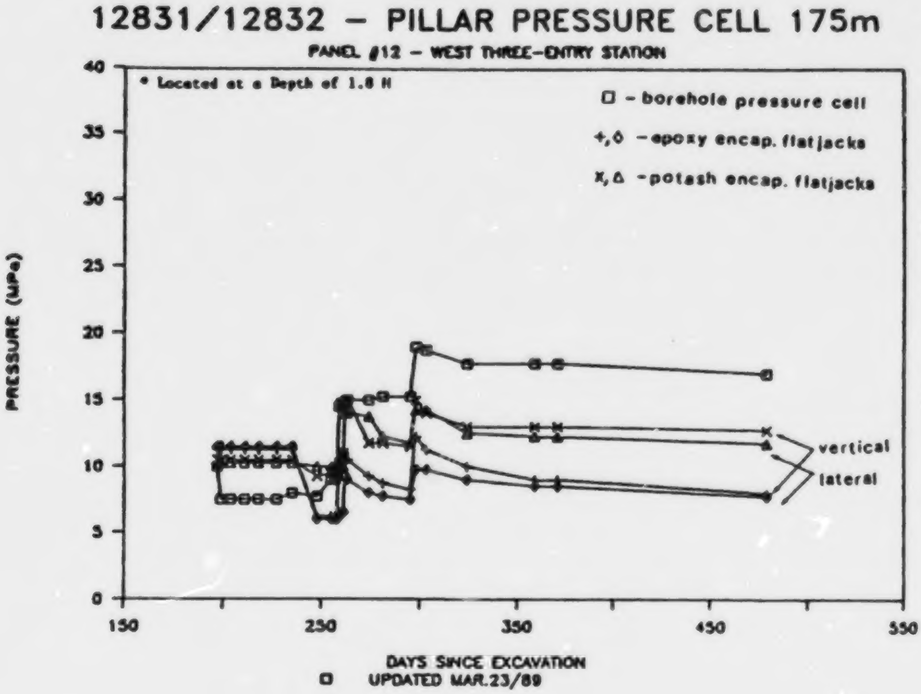

FIGURE 3.38

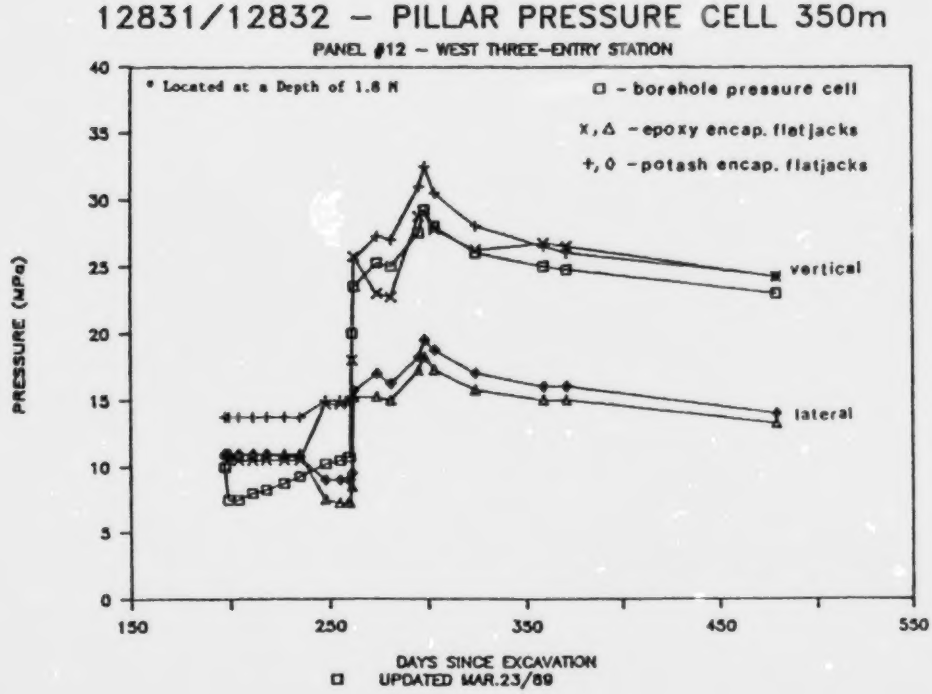

FIGURE 3.39

STOPE 11200

STRAIN RATES IN ROOF

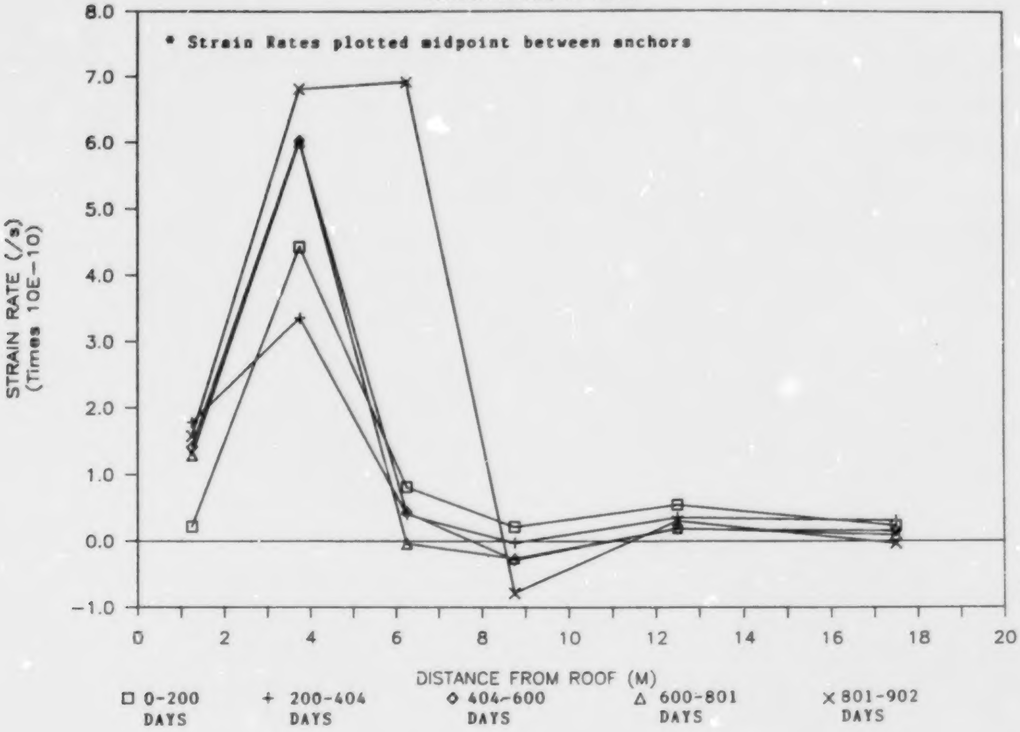

FIGURE 3.40

STOPE 11200

STRAIN RATES IN WALL

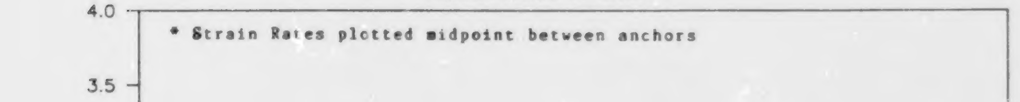

TABLE 3.2

DENISON-POTACAN POTASH MINE

STOPE 11200 ROCK MECHANICS STATION
ROOF EXTENSOMETER (DAYS 0 TO 200)

	R20M (mm)	R15M (mm)	R10M (mm)	R7.5M (mm)	R5M (mm)	R2.5M (mm)
READING ON DAY 200	31.566	29.486	24.670	23.699	20.143	0.972
READING ON DAY 0	0.000	0.000	0.000	0.000	0.000	0.000
DIFFERENCE	31.566	29.486	24.670	23.699	20.143	0.972
20 TO 15M ANCHOR	2.080					
AV.STRAIN (SEC-1)	2.41E-11					
15 TO 10M ANCHOR		4.816				
AV.STRAIN (SEC-1)		5.57E-11				
10 TO 7.5M ANCHOR			0.971			
AV.STRAIN (SEC-1)			2.25E-11			
7.5 TO 5M ANCHOR				3.556		
AV.STRAIN (SEC-1)				8.23E-11		
5 TO 2.5M ANCHOR					19.171	
AV.STRAIN (SEC-1)					4.44E-10	
2.5 TO 0M ANCHOR						0.972
AV.STRAIN (SEC-1)						2.25E-11

TABLE 3.3

DENISON-POTACAN POTASH MINE

STOPE 11200 ROCK MECHANICS STATION
ROOF EXTENSOMETER (DAYS 200 TO 404)

	R20M (mm)	R15M (mm)	R10M (mm)	R7.5M (mm)	R5M (mm)	R2.5M (mm)
READING ON DAY 404	62.071	57.195	49.144	48.267	42.916	8.903
READING ON DAY 200	31.566	29.486	24.670	23.699	20.143	0.972
DIFFERENCE	30.505	27.709	24.474	24.568	22.773	7.931
20 TO 15M ANCHOR	2.796					
AV.STRAIN (SEC-1)	3.17E-11					
15 TO 10M ANCHOR		3.235				
AV.STRAIN (SEC-1)		3.67E-11				
10 TO 7.5M ANCHOR			-0.094			
AV.STRAIN (SEC-1)			-2.13E-12			
7.5 TO 5M ANCHOR				1.795		
AV.STRAIN (SEC-1)				4.07E-11		
5 TO 2.5M ANCHOR					14.842	
AV.STRAIN (SEC-1)					3.37E-10	
2.5 TO 0M ANCHOR						7.931
AV.STRAIN (SEC-1)						1.80E-10

TABLE 3.4

DENISON-POTACAN POTASH MINE

STOPE 11200 ROCK MECHANICS STATION
ROOF EXTENSOMETER (DAYS 404 TO 600)

	R20M (mm)	R15M (mm)	R10M (mm)	R7.5M (mm)	R5M (mm)	R2.5M (mm)
READING ON DAY 600	97.286	91.066	81.419	81.723	74.516	14.917
READING ON DAY 404	62.071	57.195	49.144	48.267	42.916	8.903
DIFFERENCE	35.215	33.871	32.275	33.456	31.600	6.014
20 TO 15M ANCHOR	1.344					
AV.STRAIN (SEC-1)	1.59E-11					
15 TO 10M ANCHOR		1.596				
AV.STRAIN (SEC-1)		1.88E-11				
10 TO 7.5M ANCHOR			-1.181			
AV.STRAIN (SEC-1)			-2.79E-11			
7.5 TO 5M ANCHOR				1.856		
AV.STRAIN (SEC-1)				4.38E-11		
5 TO 2.5M ANCHOR					25.586	
AV.STRAIN (SEC-1)					6.04E-10	
2.5 TO 0M ANCHOR						6.014
AV.STRAIN (SEC-1)						1.42E-10

TABLE 3.5

DENISON-POTACAN POTASH MINE

STOPE 11200 ROCK MECHANICS STATION
ROOF EXTENSOMETER (DAYS 600 TO 801)

	R20M (mm)	R15M (mm)	R10M (mm)	R7.5M (mm)	R5M (mm)	R2.5M (mm)
READING ON DAY 801	130.306	123.297	111.917	113.347	106.303	20.581
READING ON DAY 600	97.286	91.066	81.419	81.723	74.516	14.917
DIFFERENCE	33.020	32.231	30.498	31.624	31.787	5.664
20 TO 15M ANCHOR	0.789					
AV.STRAIN (SEC-1)	9.09E-12					
15 TO 10M ANCHOR		1.733				
AV.STRAIN (SEC-1)		2.00E-11				
10 TO 7.5M ANCHOR			-1.126			
AV.STRAIN (SEC-1)			-2.59E-11			
7.5 TO 5M ANCHOR				-0.163		
AV.STRAIN (SEC-1)				-3.75E-12		
5 TO 2.5M ANCHOR					26.123	
AV.STRAIN (SEC-1)					6.02E-10	
2.5 TO 0M ANCHOR						5.664
AV.STRAIN (SEC-1)						1.30E-10

TABLE 3.6

DENISON-POTACAN POTASH MINE

STOPE 11200 ROCK MECHANICS STATION
ROOF EXTENSOMETER (DAYS 801 TO 902)

	R20M (mm)	R15M (mm)	R10M (mm)	R7.5M (mm)	R5M (mm)	R2.5M (mm)
READING ON DAY 902	163.306	156.437	143.707	146.827	124.663	24.052
READING ON DAY 801	130.306	123.297	111.917	113.347	106.303	20.581
DIFFERENCE	33.000	33.140	31.790	33.480	18.360	3.471
20 TO 15M ANCHOR	-0.140					
AV.STRAIN (SEC-1)	-3.21E-12					
15 TO 10M ANCHOR		1.350				
AV.STRAIN (SEC-1)		3.09E-11				
10 TO 7.5M ANCHOR			-1.690			
AV.STRAIN (SEC-1)			-7.75E-11			
7.5 TO 5M ANCHOR				15.120		
AV.STRAIN (SEC-1)				6.93E-10		
5 TO 2.5M ANCHOR					14.889	
AV.STRAIN (SEC-1)					6.82E-10	
2.5 TO 0M ANCHOR						3.471
AV.STRAIN (SEC-1)						1.59E-10

TABLE 3.7

DENISON-POTACAN POTASH MINE

STOPE 11200 ROCK MECHANICS STATION
WALL EXTENSOMETER (DAYS 422 TO 600)

	R32M (mm)	R17M (mm)	R15M (mm)	R10M (mm)	R5M (mm)	R2.5M (mm)
READING ON DAY 600	42.915	41.273	40.743	29.162	17.381	10.445
READING ON DAY 422	0.000	0.000	0.000	0.000	0.000	0.000
DIFFERENCE	42.915	41.273	40.743	29.162	17.381	10.445
32 TO 17M ANCHOR	1.642					
AV.STRAIN (SEC-1)	7.12E-12					
17 TO 15M ANCHOR		0.530				
AV.STRAIN (SEC-1)		1.72E-11				
15 TO 10M ANCHOR			11.581			
AV.STRAIN (SEC-1)			1.51E-10			
10 TO 5M ANCHOR				11.781		
AV.STRAIN (SEC-1)				1.53E-10		
5 TO 2.5M ANCHOR					6.936	
AV.STRAIN (SEC-1)					1.80E-10	
2.5 TO 0M ANCHOR						10.445
AV.STRAIN (SEC-1)						2.72E-10

TABLE 3.8

DENISON-POTACAN POTASH MINE

STOPE 11200 ROCK MECHANICS STATION
WALL EXTENSOMETER (DAYS 600 TO 801)

	R32M (mm)	R17M (mm)	R15M (mm)	R10M (mm)	R5M (mm)	R2.5M (mm)
READING ON DAY 801	93.590	87.120	85.404	61.287	35.261	20.312
READING ON DAY 600	42.915	41.273	40.743	29.162	17.381	10.445
DIFFERENCE	50.675	45.847	44.661	32.125	17.880	9.867
32 TO 17M ANCHOR	4.828					
AV.STRAIN (SEC-1)	1.85E-11					
17 TO 15M ANCHOR		1.186				
AV.STRAIN (SEC-1)		3.41E-11				
15 TO 10M ANCHOR			12.536			
AV.STRAIN (SEC-1)			1.44E-10			
10 TO 5M ANCHOR				14.245		
AV.STRAIN (SEC-1)				1.64E-10		
5 TO 2.5M ANCHOR					8.013	
AV.STRAIN (SEC-1)					1.85E-10	
2.5 TO 0M ANCHOR						9.867
AV.STRAIN (SEC-1)						2.27E-10

TABLE 3.9

DENISON-POTACAN POTASH MINE

STOPE 11200 ROCK MECHANICS STATION
WALL EXTENSOMETER (DAYS 801 TO 902)

	R32M (mm)	R17M (mm)	R15M (mm)	R10M (mm)	R5M (mm)	R2.5M (mm)
READING ON DAY 902	116.130	108.410	105.57	75.675	43.109	24.832
READING ON DAY 801	93.590	87.120	85.404	61.287	35.261	20.312
DIFFERENCE	22.540	21.290	20.166	14.388	7.848	4.520
32 TO 17M ANCHOR	1.250					
AV.STRAIN (SEC-1)	9.55E-12					
17 TO 15M ANCHOR		1.124				
AV.STRAIN (SEC-1)		6.44E-11				
15 TO 10M ANCHOR			5.778			
AV.STRAIN (SEC-1)			1.32E-10			
10 TO 5M ANCHOR				6.540		
AV.STRAIN (SEC-1)				1.50E-10		
5 TO 2.5M ANCHOR					3.328	
AV.STRAIN (SEC-1)					1.53E-10	
2.5 TO 0M ANCHOR						4.520
AV.STRAIN (SEC-1)						2.07E-10

* The low pressures in the cells located in the roof correctly indicated low stress levels resulting from tension superimposed on horizontal stress in the roof beam.

* The vertical cells in the pillar at depths of 5.0, 15.0 and 20.0 m appear to have been damaged and were disregarded. Remaining vertical and lateral cells followed the expected trends. The pressures measured before the ground fall and damage to the instrumentation cable are shown in Figure 3.41.

* Grouted pressure cells measuring vertical and lateral pressures in the pillar (Figure 3.12 and 3.13) showed poor performance with pressure measurements being highly erratic. Subsequently, potash encapsulated pressure cells were installed in the pillar showing good results to date.

3.5.3 Stopes 11120 and 11240, Convergence

The measurements were taken for the purpose of calibrating the VELMINA program and will be evaluated in Section 10.4.

3.5.4 Instrumentation in Entry Systems in Panel 12

The measurements and observations in the three entry systems indicate that the proposed layout provides a stress relief protection in the center entry in the short term. The strain rates in the yield pillar and in the barrier pillar are tabulated in Tables 3.11 and 3.12. The strain rates in the yield pillar are at least an order of magnitude greater, which is an indication of an effective stress relief performance.

The convergence and stress measurements will be compared to the results of FLAC analysis in Section 8.5.2.

Behaviour of the fully grouted pressure cells illustrated in Figures 3.28 & 3.29, and the other pressure cells shown in Figure 3.30 can be explained by the following interpretation.

TABLE 3.10

STOPE 11200, PRESSURE CELL MEASUREMENTS

Location	Orientation	Depth (m)	Time (Days)	Pressure (MPa)	Remark	Reference Figure No.
Roof	Lateral	2.5	600	0.3	-	3.10
Roof	Lateral	5.0	600	0.6	-	3.10
Roof	Lateral	7.5	600	1.2	-	3.10
Roof	Lateral	10.0	600	1.2	-	3.10
Roof	Tangential	5.0	700	0.5	-	3.11
Roof	Tangential	7.5	700	0.9	-	3.11
Roof	Tangential	10.0	700	1.2	-	3.11
Pillar	Vertical	2.5	700	8.5	-	3.12
Pillar	Vertical	5.0	700	0.6	Damaged	3.12
Pillar	Vertical	10.0	700	13.8	-	3.12
Pillar	Vertical	15.0	700	0.7	Damaged	3.12
Pillar	Vertical	20.0	700	6.8	Damaged	3.12
Pillar	Vertical	32.0	700	15.9	-	3.12
Pillar	Lateral	2.5	700	0.8	-	3.13
Pillar	Lateral	10.0	700	3.3	-	3.13
Pillar	Lateral	20.0	700	4.0	-	3.13
Pillar	Lateral	32.0	700	4.7	-	3.13

FIGURE 3.41

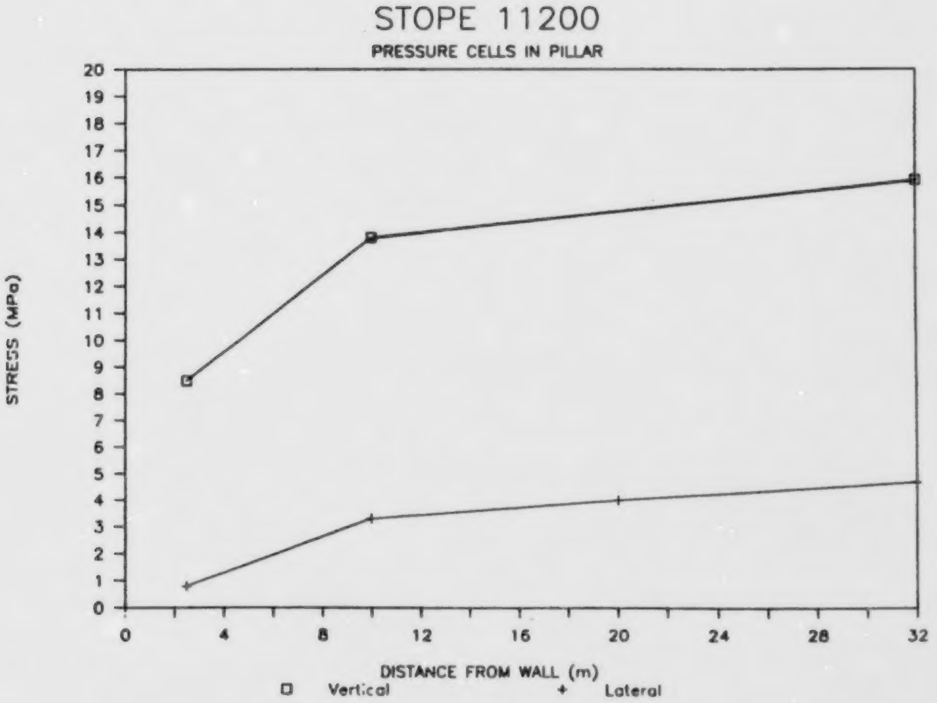

TABLE 3.11

DENISON-POTACAN POTASH MINE

PANEL 12 SOUTH 3-ENTRY SYSTEM (12826.12827 & 12828) ROCK MECHANICS STATION
YIELD PILLAR ROD EXTENSOMETER (DAYS 0 TO 222)

	R4M (mm)	R2M (mm)	R0.5M (mm)
READING ON DAY 222	43.940	15.950	3.900
READING ON DAY 0	0.000	0.000	0.000
DIFFERENCE	43.940	15.950	3.900
4 TO 2M ANCHOR	27.990		
AV.STRAIN (SEC-1)	7.30E-10		
2 TO 0.5M ANCHOR		12.050	
AV.STRAIN (SEC-1)		3.14E-10	
0.5 TO 0M ANCHOR			3.900
AV.STRAIN (SEC-1)			4.07E-10

TABLE 3.12

DENISON-POTACAN POTASH MINE

PANEL 12 SOUTH 3-ENTRY SYSTEM (12826.12827 & 12828) ROCK MECHANICS STATION
BARRIER PILLAR ROD EXTENSOMETER (DAYS 0 TO 222)

	R10M (mm)	R6M (mm)	R4M (mm)	R2M (mm)	R0.5M (mm)
READING ON DAY 222	7.630	6.630	5.610	4.810	1.320
READING ON DAY 0	0.000	0.000	0.000	0.000	0.000
DIFFERENCE	7.630	6.630	5.610	4.810	1.320
10 TO 6M ANCHOR	1.000				
AV.STRAIN (SEC-1)	1.30E-11				
6 TO 4M ANCHOR		1.020			
AV.STRAIN (SEC-1)		2.66E-11			
4 TO 2M ANCHOR			0.800		
AV.STRAIN (SEC-1)			2.09E-11		
2 TO 0.5M ANCHOR				3.490	
AV.STRAIN (SEC-1)				1.21E-10	
0.5 TO 0M ANCHOR					1.320
AV.STRAIN (SEC-1)					1.38E-10

Drilling a borehole follows the same analogy as creating a mine opening, disturbing the stress field and cause a stress relieved zone. When a borehole pressure cell is installed and pressurized its initial response is an immediate drop in pressure. The decrease in pressure is attributed to the pressure cell and the destressed zone coming to equilibrium. When equilibrium is reached pressure will stabilize and begin to increase because the destressed zone and the pressure cell will then accept load from the undisturbed rock mass. As strain continues with time the pressure cell and the destressed zone will approach equilibrium with the undisturbed rock mass. Equilibrium of the entire system is indicated by stable pressure readings.

Behaviour of a pressure cell is highly dependent on several factors. The type of material that encapsulates the cell is a major factor in whether the cell functions properly. Three types of encapsulate were used: potash, epoxy, and grout. Also, the initial setting pressure determines the reliability of a cell and whether the cell will function or fail. Activity in the area of instrumentation will have influence on the behaviour of a pressure cell.

Behaviour of the cells indicated if the encapsulate is too stiff (ie. fully grouted) cell response is slower and stress peaks are missed. This phenomenon is illustrated when comparing the readings between Figures 3.29 and 3.30. Beddoes et al. (1989) found that a cell encapsulated in a material that strains faster (ie. epoxy, potash core) than the surrounding rock mass, results in lower pressure readings because of longitudinal deformation of the cell down the borehole. This phenomenon is reflected in the measurements shown in Figure 3.30. However, if this deformation of the encapsulating material is restrained by fully grouting the cell in the borehole the resulting pressure measurements of a cell are more reliable.

Figure 3.42 illustrates that initial pressurization of a cell determines the amount of time for an entire system to reach equilibrium. It also determines if a cell will function or fail. Excessive initial over-pressurization of a cell leads to immediate failure, and excessive under-pressurization allows large amounts of strain to occur within a cell which

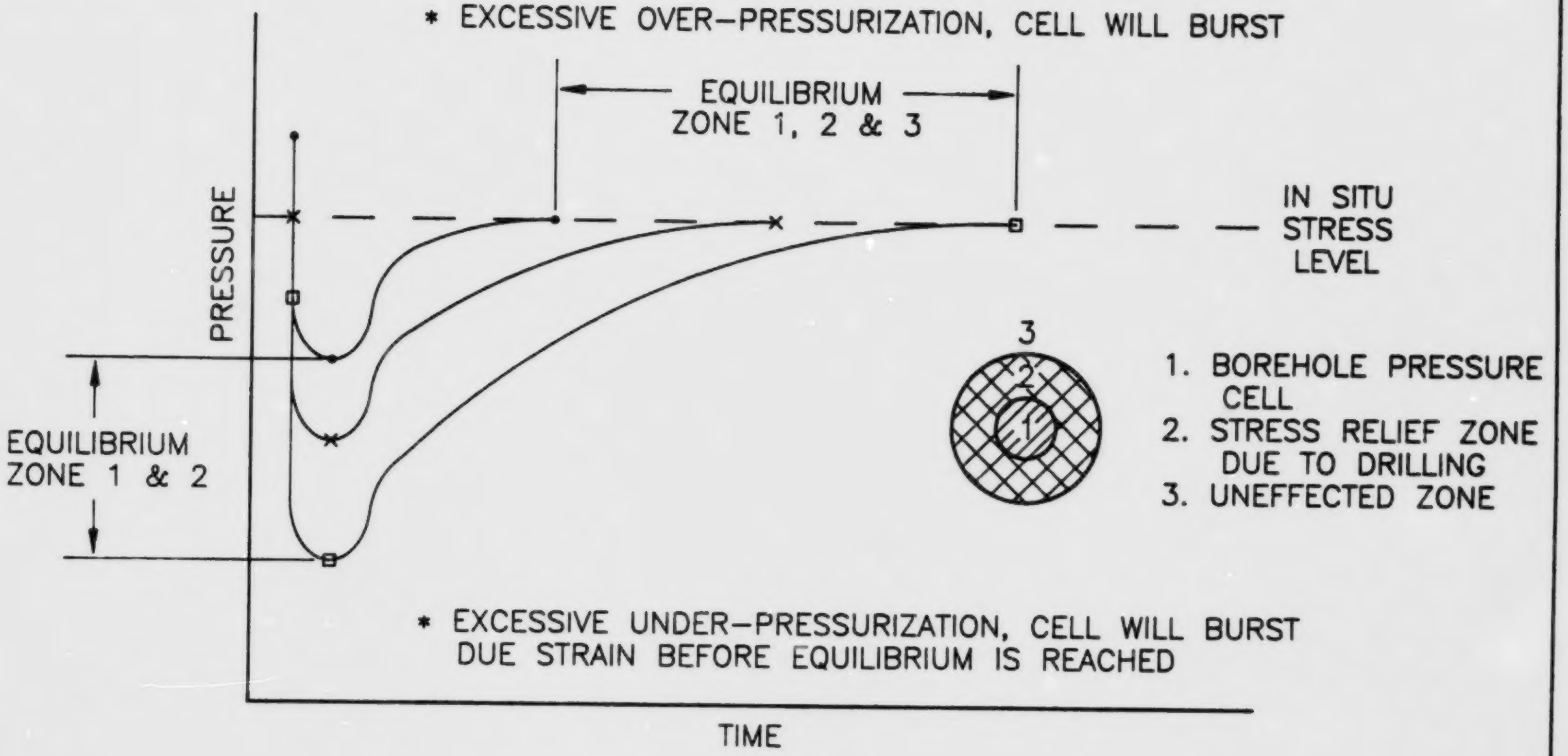
* EXCESSIVE OVER-PRESSURIZATION, CELL WILL BURST
EQUILIBRIUM ZONE 1, 2 & 3
IN SITU STRESS LEVEL
PRESSURE
EQUILIBRIUM ZONE 1 & 2
3
2
1
1. BOREHOLE PRESSURE CELL
2. STRESS RELIEF ZONE DUE TO DRILLING
3. UNEFFECTED ZONE
* EXCESSIVE UNDER-PRESSURIZATION, CELL WILL BURST DUE STRAIN BEFORE EQUILIBRIUM IS REACHED
TIME

FIGURE 3.42
CONCEPTUAL INTERPRETATION OF FULLY
GROUTED BOREHOLE PRESSURE CELLS

leads to failure before system equilibrium is reached. The three conceptual pressure curves of Figure 3.42 illustrate the difference in pressure readings between cells initially set at different pressures. The lower the setting pressure the longer it takes a cell to reach equilibrium with the surrounding rock mass. Figure 3.42 illustrates the following conclusions:

1) Short term error (ie. 1 year) is directly dependent on the difference between the initial setting pressure and the in situ stress level.
2) The probability of cell failure is proportional to the level of difference as a direct result of non-equilibrium and the amount of strain that occurs.
3) It is preferable to initially pressurize a cell at or slightly above the pressure level that is expected because excessive over and under pressurization may lead to cell failure.

Therefore, it can be interpreted that the cells in Figure 3.29 that failed were under-pressurized, and the cell set at 30 MPa reflects a relative pressure (ie. not actual) because of its stiffness, hence a longer time to reach equilibrium. As well, the area of measurement was actively being mined which would effect the response of the pressure cells. The cells illustrated in Figure 3.30 reflect a relative pressure (ie. lower than actual or predicted pressure) because their behaviour is influence by longitudinal strain down the borehole.

The comparative evaluation of various stress measuring instruments continues.

3.6 Surface Subsidence Monitoring

The installation and monitoring of surface subsidence monuments continues to be an essential component of the research program.

Measurement and analysis of the rate of mining induced subsidence provides valuable insight into both the closure of the mine workings, and the response of the main load bearing pillars and the backfilled stopes. Moreover this data, in combination with the in situ convergence data and the VELMINA numerical modelling run (Section 10.3), provided the means for evaluating the response of the overburden to mining activity.

A total of 17 subsidence monuments were installed over Panel 10 workings in the summer of 1985. Fourteen additional monuments were added in 1987 to monitor mining activity as it progressed to Panel 11.

The following observations have been made based on the currently available data:

- a substantial subsidence rate is being detected on surface over and around the Panel 10 and 11 working areas;
- the maximum subsidence recorded at the time of the last surface subsidence survey (November 22, 1988) was over Panel 11 in the area of Stopes 11200 and 11240;
- the maximum 1987-1988 annualized rate of surface subsidence was 33.6 mm per year;
- monuments #9 and #12 appear to have been damaged and the readings have been disregarded;
- monument #17 was damaged and is considered destroyed.

The observations made from the available data indicated the area of influence from subsidence is smaller than the area predicted by VELMINA. However, the predicted location and amount of maximum subsidence corresponded very well with actual subsidence measurements (Figures 10.12 and 10.13). The reason for this is the manner in which VELMINA models overburden strata. Overburden strata is modelled as an elastic beam which does not allow breaking along caving lines to occur. Consequently, subsidence extends further into the abutment pillars. In situ, the overburden strata consists of fractured materials, therefore breaking along caving lines does occur, which is illustrated by the smaller area influenced from subsidence, as well as the size and shape of the subsidence bowl (Figure 3.43). In general, the predicted magnitude of subsidence in the centre of the mining layout compares well with the actual subsidence, however until a function which models caving in overburden strata is available in VELMINA, surface subsidence will be overpredicted on the fringes of the mine.

Initially, the greatest concern was that subsidence of the overburden strata in response to mining would not occur in an orderly fashion. In many other potash mines, substantial delay in subsidence has been observed (Baar, 1977). This is a result of bridging over individual panels, which in turn, reload pillars when stress concentrations are released through strata failure. The shape and size of the actual subsidence bowl at DPPC (Figure 3.43) indicate that the overburden strata is subsiding in an orderly fashion, therefore extensive bridging of strata is not anticipated. However, it is recommended the microseismic monitoring continues, to determine the pattern of microseismicity, and outline in detail the subsidence mechanism.

In the initial design of the mine the angle of draw used for shaft pillar design was 18 degrees (Kilborn, 1982). The actual size of the shaft pillar was established on that basis. The amount of subsidence in the area of the shaft pillar is very small as illustrated in Figure 3.43, and should have no adverse effects on the shaft. Therefore it can be concluded that the angle of draw and the size of the shaft pillar was selected properly.

The locations of the surface subsidence monuments in relationship to the mine workings and an interpretation of the 1987-1988 data are shown in Figure 3.43. The north-south and the east-west cross-sections through the area of maximum recorded subsidence over Panel 11 are included as Figures 3.44 and 3.45. The surface subsidence survey results are tabulated in Table 3.13.

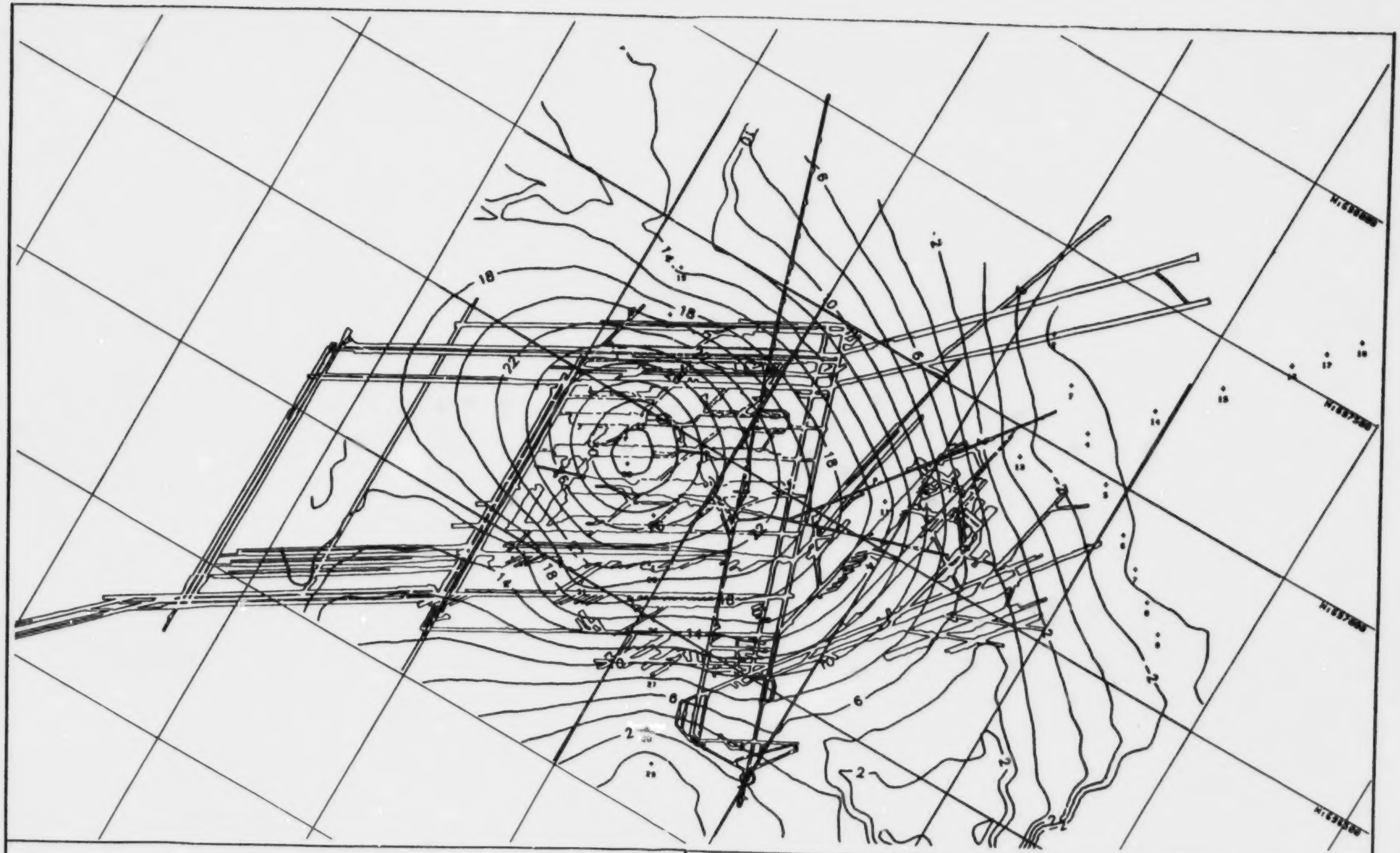

DENISON
POTACAN
POTASH
COMPANY

TITLE:
Annualized Subsidence Rate Contours For
1987 - 1988 in Millimetres Per Year

SCALE: **NTS**

FIGURE:
3.43

FIGURE 3.44

SUBSIDENCE RATE, 1987–88

NORTH–SOUTH SECTION, PANEL 11

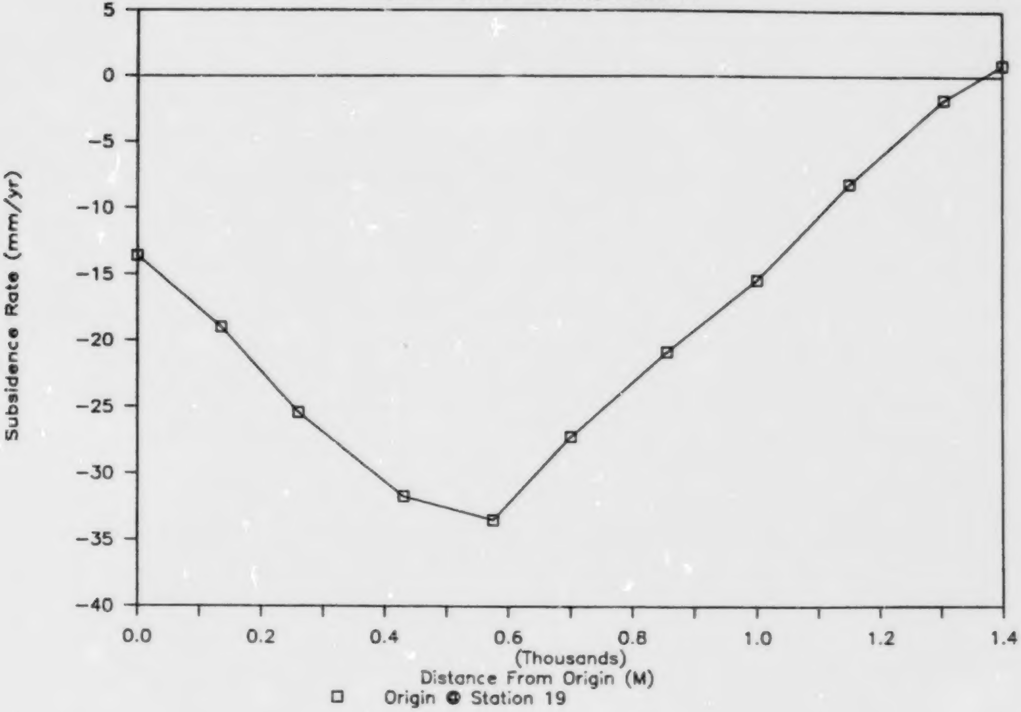

FIGURE 3.45

SUBSIDENCE RATE, 1987–88

EAST–WEST SECTION, PANEL 10 & 11

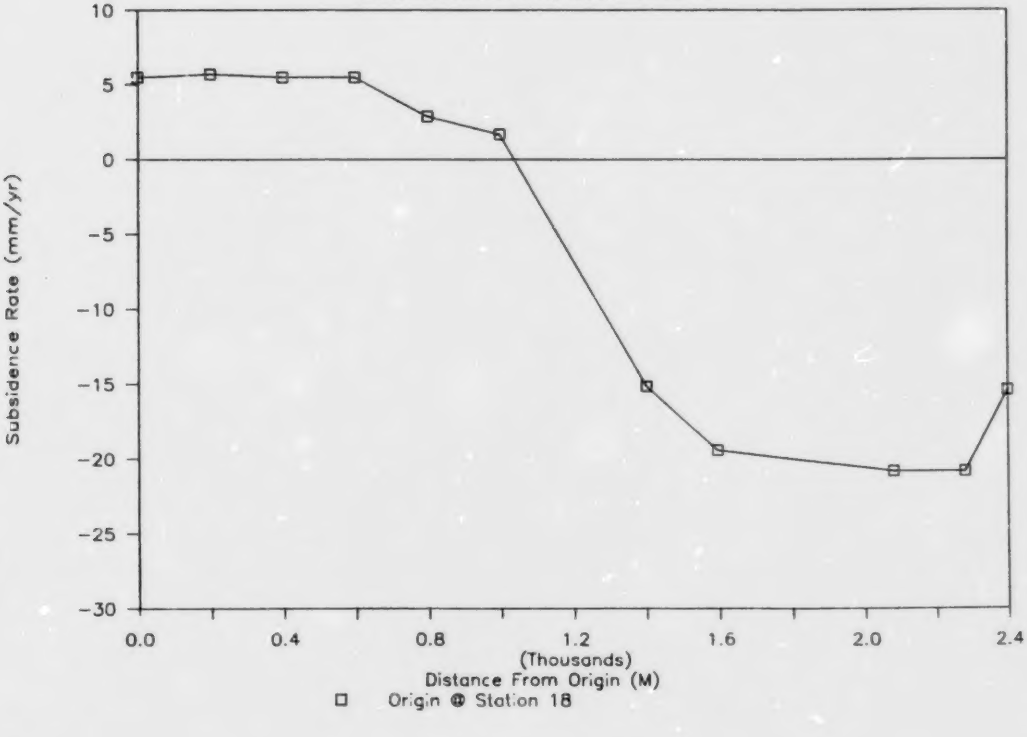

TABLE 3.13

SURFACE SUBSIDENCE SURVEY

SUBSIDENCE MONUMENT NUMBER	SURVEY NOV. 18/86 (M)	SURVEY OCT. 16/87 (M)	SURVEY NOV. 22/88 (M)	TOTAL CHANGE (mm)	1987-1988 ANNUALIZED RATE (mm/Year)	REMARKS
2	67.843	-	67.852	-9	-4.5	-
3	64.992	-	64.998	-6	-3.0	-
4	53.581	-	53.587	-6	-3.0	-
5	47.718	-	47.725	-7	-3.5	-
6	39.874	-	39.881	-7	-3.5	-
7	33.504	-	33.513	-9	-4.5	-
8	31.040	-	31.048	-8	-4.0	-
9	24.705	-	24.727	-22	-11.0	ANOMALOUS
10	47.990	-	47.951	39	19.5	-
11	43.885	-	43.855	30	15.0	-
12	45.085	-	45.125	-40	-20.0	ANOMALOUS
13	51.561	-	51.564	-3	-1.5	-
14	55.680	-	55.691	-11	-5.5	-
15	58.504	-	58.515	-11	-5.5	-
16	53.532	-	53.543	-11	-5.5	-
17	51.605	-	-	-	-	DESTROYED
18	48.862	-	48.873	-11	-5.5	-
19	-	91.102	91.087	15	13.6	-
20	-	91.041	91.020	21	19.1	-
21	-	88.121	88.093	28	25.5	-
22	-	83.408	83.373	35	31.8	-
23	-	76.481	76.444	37	33.6	MAXIMUM
24	-	63.576	63.546	30	27.3	-
25	-	53.437	53.414	23	20.9	-
26	-	48.759	48.742	17	15.5	-
27	-	41.755	41.746	9	8.2	-
28	-	40.474	40.472	2	1.8	-
29	-	38.021	38.022	-1	-0.9	-
30	-	44.541	44.522	19	17.3	-
31	-	51.663	51.640	23	20.9	-
32	-	59.827	59.810	17	15.5	-

SECTION 4.0

4.0 LABORATORY TESTING OF OVERBURDEN ROCKS

A laboratory testing program of overburden core samples was conducted in September and October 1988 to identify the mechanical properties of rocks within the formations overlying the evaporite interval, for the purpose of numerical modelling.

The sediments overlying the evaporites in the area of the South Flank of the Marchbank Syncline (Figure 2.2), which includes current mining areas are, in descending order, as follows:

FORMATION	INTERVAL	THICKNESS (m)	TYPICAL UCS (MPa)
Wanamaker	Sandstone Conglomerates	400	85
Campbell	Siltstone	35	17
Poodiac	Siltstone	60	26
	Sandstone	50	85
	Siltstone	75	10
	Collapse Breccia	75	10
Plumweseep	Caprock Breccia	15	5

The approximate location of the core samples relative to the stratigraphic column and ore horizon are shown in Figure 4.1.

The rocks tested under this program were:

TYPE OF ROCK	FORMATION
Sandstone	Poodiac
Siltstone	Poodiac
Sandstone (Fractured)	Poodiac
Siltstone Breccia	Plumweseep

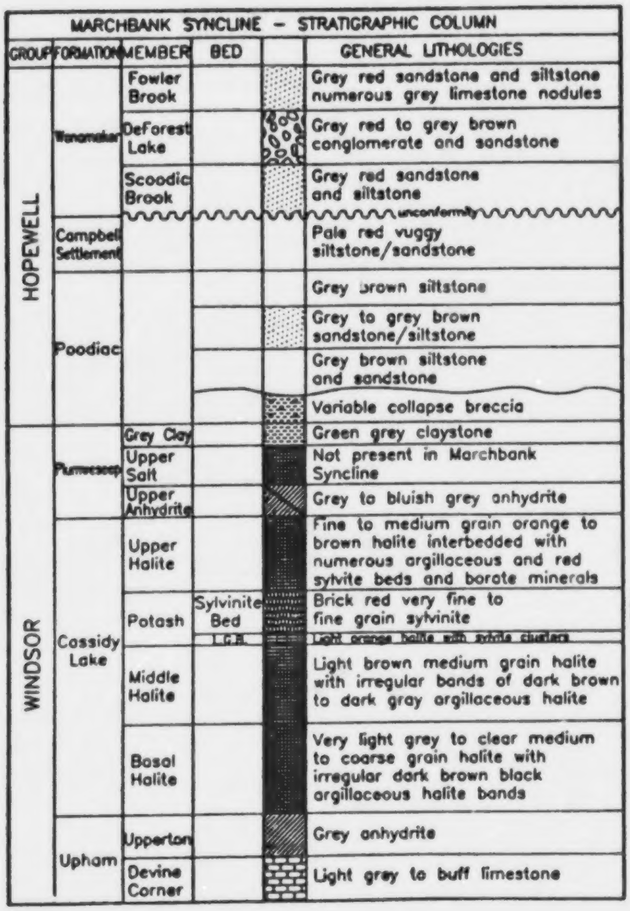

MARCHBANK SYNCLINE – STRATIGRAPHIC COLUMN					
GROUP	FORMATION	MEMBER	BED		GENERAL LITHOLOGIES
HOPEWELL	Wanamaker	Fowler Brook			Grey red sandstone and siltstone numerous grey limestone nodules
		DeForest Lake			Grey red to grey brown conglomerate and sandstone
		Scoodic Brook			Grey red sandstone and siltstone
					unconformity
	Campbell Settlement				Pale red vuggy siltstone/sandstone
	Poodiac				Grey brown siltstone
					Grey to grey brown sandstone/siltstone
					Grey brown siltstone and sandstone
					Variable collapse breccia
WINDSOR	Plumweseep	Grey Clay			Green grey claystone
		Upper Salt			Not present in Marchbank Syncline
		Upper Anhydrite			Grey to bluish grey anhydrite
	Cassidy Lake	Upper Halite			Fine to medium grain orange to brown halite interbedded with numerous argillaceous and red sylvite beds and borate minerals
		Potash	Sylvinite Bed		Brick red very fine to fine grain sylvinite
			L.G.B.		Light orange halite with sylvite clusters
		Middle Halite			Light brown medium grain halite with irregular bands of dark brown to dark gray argillaceous halite
		Basal Halite			Very light grey to clear medium to coarse grain halite with irregular dark brown black argillaceous halite bands
	Upham	Upperton			Grey anhydrite
		Devine Corner			Light grey to buff limestone

CORE SAMPLES FOR LABORATORY TESTING TAKEN FROM THIS INTERVAL

ORE HORIZON

DENISON
POTACAN
POTASH
COMPANY

TITLE:

SOURCE OF CORE SAMPLES TESTED IN LABORATORY RELATIVE TO ORE HORIZON
(After Waugh and Urquhart, 1983)

SCALE:
N.T.S.

FIGURE:
4.1

4.1 Test Methodology

Four types of tests were performed on the four materials:

1) Sonic velocity measurements prior to compressive strength tests used in the calculation of the dynamic elastic constants.
2) Brazilian tests for uniaxial tensile strength.
3) Unconfined compressive strength (UCS) tests.
4) Triaxial compressive strength tests.

During most of the UCS tests, unload/reload cycles were performed for determination of the unload moduli.

The results of the strength tests were plotted on Mohr-Coulomb diagrams.

4.2 Sample Preparation

Representative sections were selected from the Denison-Potacan Clover Hill mine exploration drillhole core stored at the provincial core laboratory storage facilities in Sussex, New Brunswick. These were carefully packed and shipped to WATSALT laboratory at the University of Waterloo, Ontario.

Upon reaching the laboratory, the cores were unpacked, photographed and inspected with reference to the core log identification sheet provided by Denison-Potacan. The core samples were selected for testing on the basis of three criteria:

1) The core had to be at least 2.5 times as long as the core diameter (approx. 12.5 cm or 5 inches).
2) There were no open fractures or other discontinuities.
3) The core was typical (i.e. visibly similar, as to grain size and mineralogy, to other cores of the same type).

The cores selected for specimen preparation were cut on a diamond saw to the required length. They were then placed in a surface grinder and the ends ground flat and perpendicular to the sides of the core.

Both the cutting and grinding equipment used water as a cutting fluid. It was discovered that the siltstone caprock breccia tended to slake when exposed to water. Hence, these specimens were prepared by hand using a dry grinding technique.

The results of the strength tests for the core samples are shown in the following Mohr-Coulomb diagram, Figures 4.2 to 4.5.

4.3 Test Results

4.3.1 Strength Tests

The results were fitted to a Mohr-Coulomb failure criterion of the form:

$$\tau = C + \sigma_n . \tan \phi \tag{4.1}$$

where τ = Shear stress at failure
C = Cohesion
σ_n = Normal Stress
ϕ = Angle of Internal Friction

The Mohr-Coulomb constants C and ϕ for the four materials are listed in Table 4.1.

Table 4.1: Constants "C" and "Ø" for DPPC Overburden Rocks

ROCK TYPE	COHESION "C" (MPa)	ANGLE OF INTERNAL FRICTION (Degrees)
Poodiac Sandstone	15.2	53.5
Poodiac Siltstone	30.5	43.0
Fractured Poodiac Sandstone	27.0	24.5
Siltstone Caprock Breccia	4.7	32.5

FIGURE 4.2
Mohr-Coulomb diagram for Poodiac Sandstone

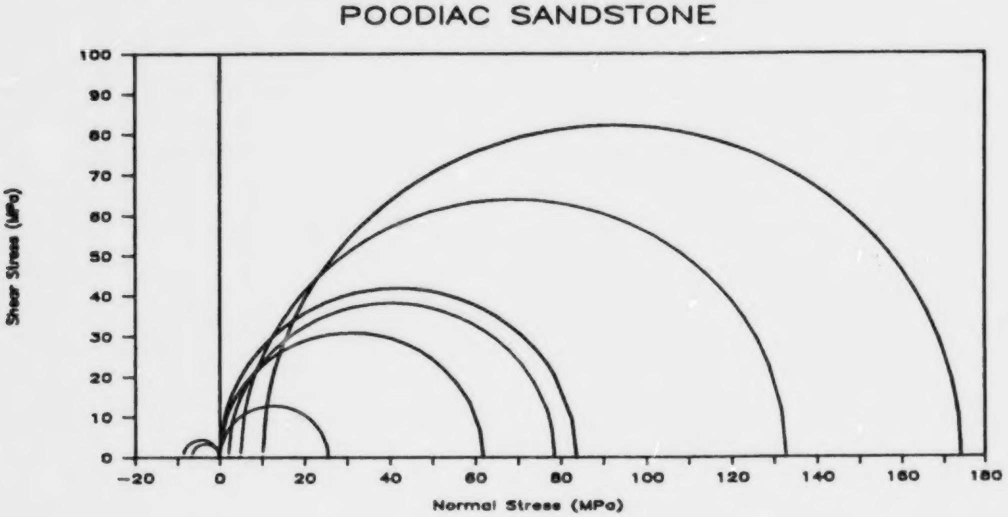

FIGURE 4.3
Mohr-Coulomb diagram for Poodiac Siltstone

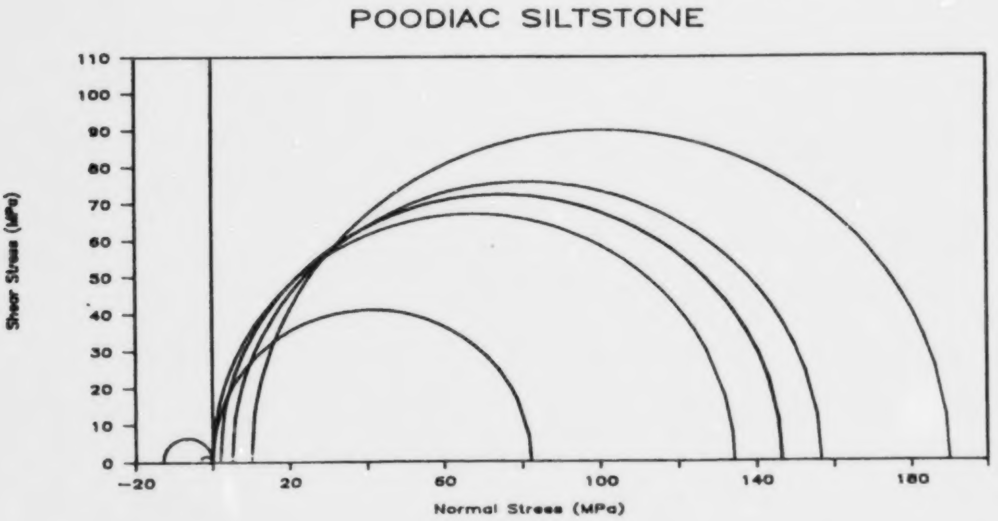

FIGURE 4.4

Mohr-Coulomb diagram for fractured Poodiac Sandstone

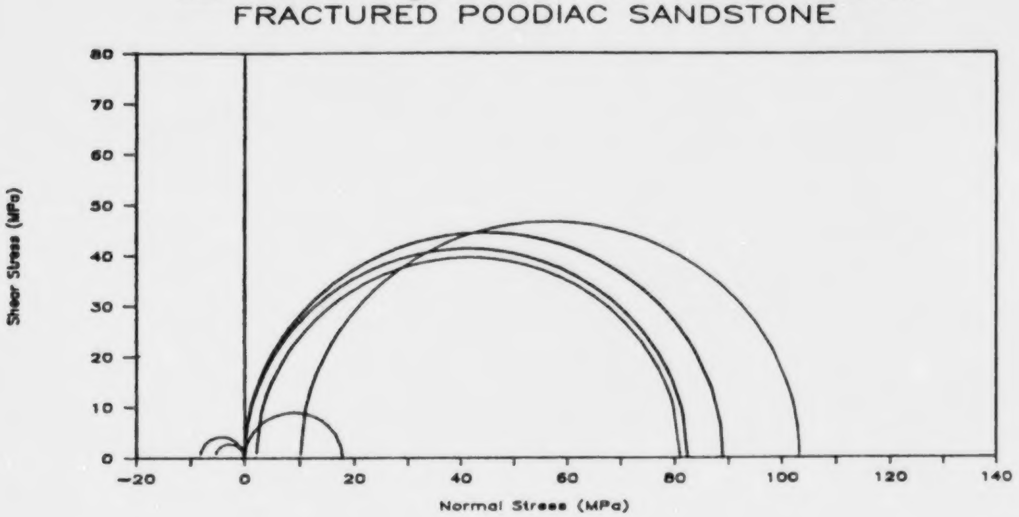

FIGURE 4.5

Mohr-Coulomb diagram for Siltstone Caprock Breccia

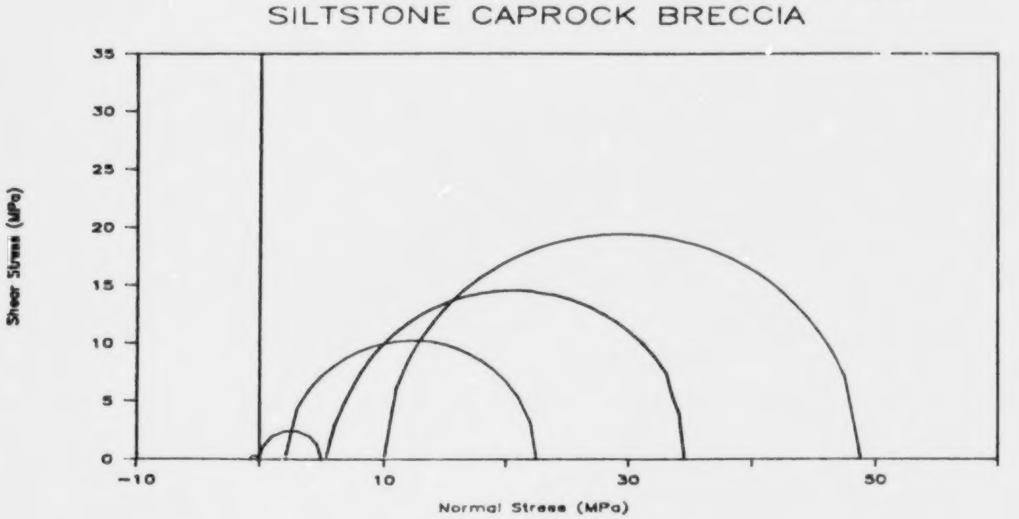

Fits were also obtained for a parabolic failure criterion of the form (Dusseault et al., 1987):

$$\sigma_Y = (\sigma_c/2)\left\{(1-RM) + [(1+RM)^2 + 4M(\sigma_3/\sigma_c)]^{0.5}\right\} \qquad (4.2)$$

where: $R = (\sigma_T/\sigma_c)$
σ_T = Tensile Strength
σ_c = Unconfined Compressive Strength
M = Constant

In order to calculate the constants R and M in equation (4.2), the 'best fit' values of σ_c and σ_T have been used. The values of the σ_c, σ_T, R and M for the four overburden rocks are listed in Table 4.2.

Table 4.2: Parabolic Failure Criterion Constants

ROCK TYPE	σ_c (MPa)	σ_T (MPa)	R	M
Poodiac Sandstone	83.77	-6.71	0.0801	68
Poodiac Siltstone	134.21	-12.95	0.0965	17
Fractured Poodiac Sandstone	82.32	-8.40	0.1020	10
Siltstone Caprock Breccia	5.04	-0.75	0.1488	122

Parabolic failure envelopes are shown in Figures 4.6 to 4.9.

Of the materials tested, the two strongest are the Poodiac sandstone and siltstone.

The strength of fractured Poodiac sandstone is dependent on the strength of the fracture filling as well as the orientation of the fractures relative to the principal stresses.

FIGURE 4.6

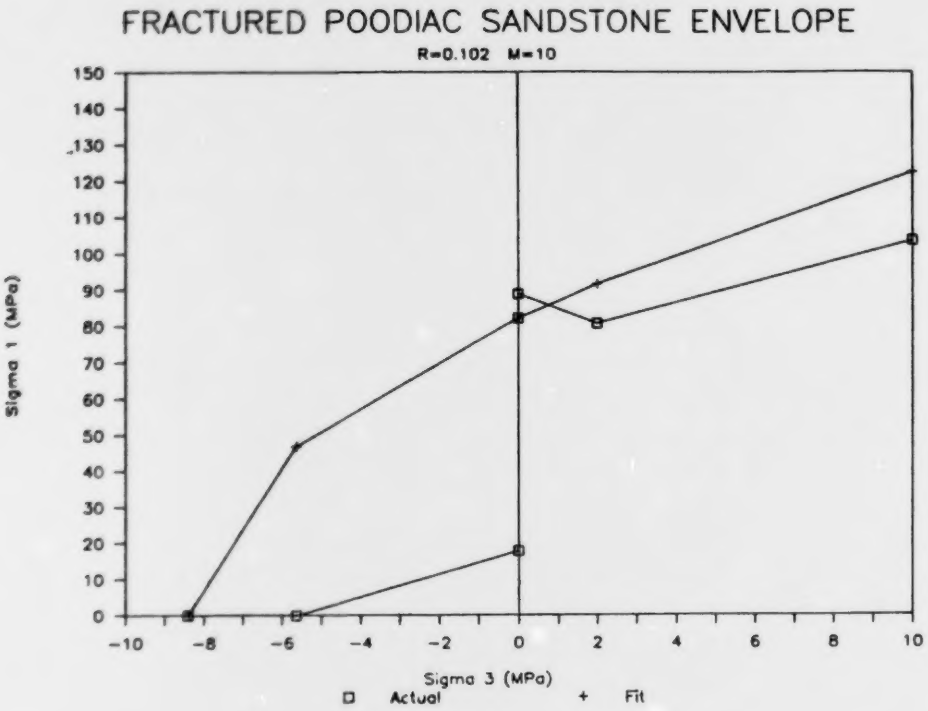

FIGURE 4.7

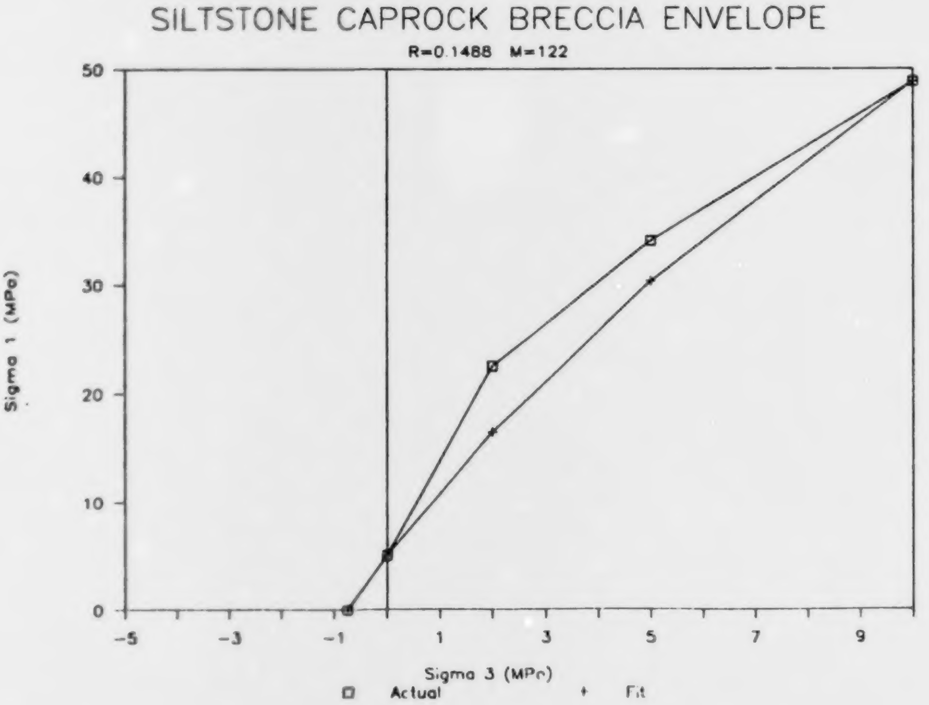

FIGURE 4.8

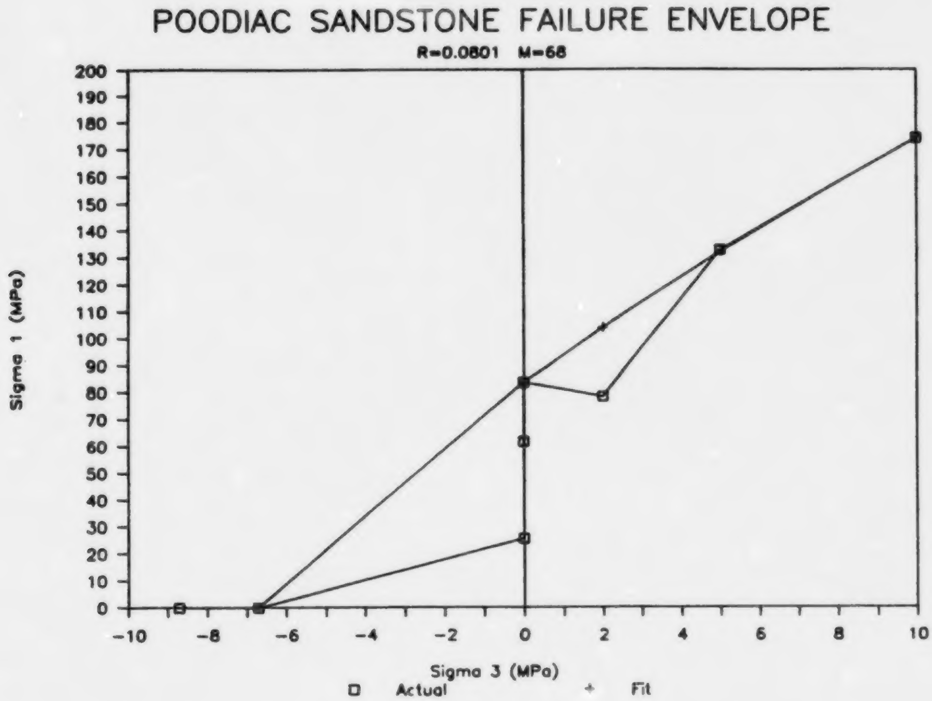

FIGURE 4.9

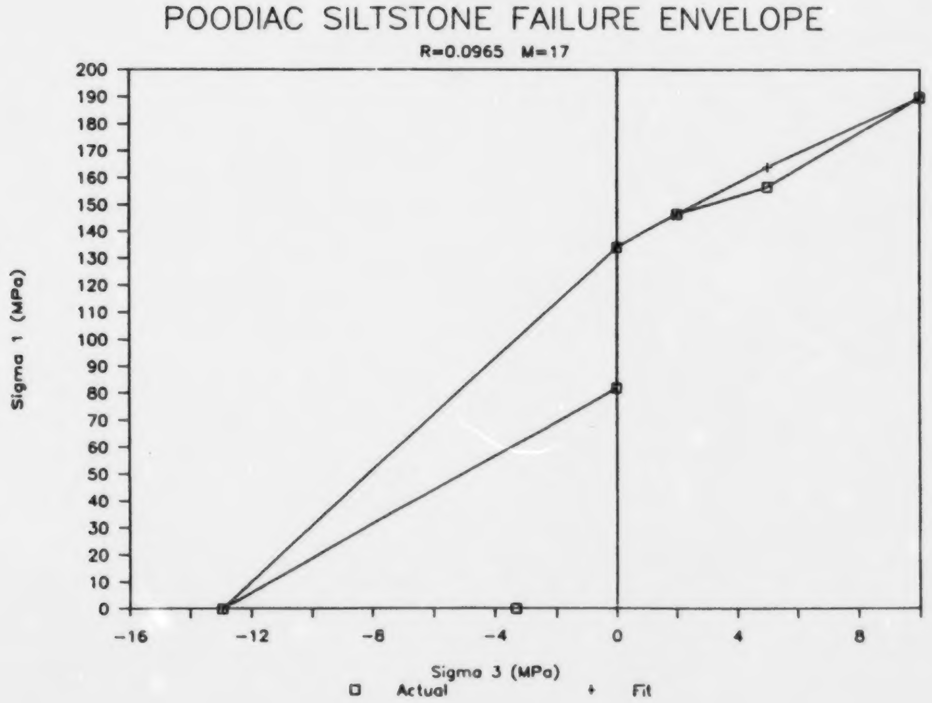

The brecciated rocks are the weakest of the four materials. They tend to slake when exposed to water and behave somewhat more plastically than the other rocks (i.e. they are not as brittle).

4.3.2 Elastic Constants

Two types of elastic parameters were calculated for the four materials; the dynamic elastic modulus (E_d) and Poissons Ratio (ν) from sonic velocity tests.

The static elastic moduli (E_s) were determined from unload/reload curves during uniaxial compressive strength tests. The equations used to calculate the dynamic elastic modulus and Poissons Ratio from sonic velocity data are as follows:

$$E_d = \left\{ \gamma \times V_s^2 \times (3V_p^2 - 4V_s^2) \right\} / (V_p^2 - V_s^2) \qquad (4.3)$$

$$\nu = (V_p^2 - 2V_s^2) / \left\{ 2 \times (V_p^2 - V_s^2) \right\} \qquad (4.4)$$

where: E_d = Dynamic Elastic Modulus
γ = Density
V_s = Shear (s) Wave Velocity
V_p = Compressional (p) Wave Velocity
ν = Poissons Ratio

Compressional (p) and Shear (s) wave velocities are determined by dividing the length of the specimen by the arrival times of the p and s waves. The p wave arrival is measured directly with a Pundit device or as the first deviation from a straight line on the sonic trace. The s-wave arrival is measured as the first deviation from a regular sinusoidal curve on the sonic trace.

The shear wave and compressional wave velocities for the rock samples tested are tabulated in Table 4.3. The average values of the dynamic and static elastic moduli are listed in Table 4.4.

TABLE 4.3: Shear Wave and Compressional Wave Velocities

Sample No.	V_p (m/s)	Vs (m/s)
PSLT1377	4381.25	2804.00
PSLT1378A	4467.78	2792.36
PSLT1357	3932.69	2621.79
PSLT1349	4592.22	2830.82
PSLT1378B	4486.67	2804.17
PSLT1357B	4248.94	2662.67
PSLT1452	4408.51	2877.78
AVG.	4359.72	2770.51
PSS1447A	4071.00	2714.00
PSS1448B	3975.00	2650.00
PSS1257B	4127.00	2751.33
PSS1273A	4007.84	2689.47
PSS1273B	4050.00	2700.00
PSS1257A	4122.45	2693.33
PSS1448A	4080.00	2649.35
PSS1280A	4134.00	2684.42
PSS1280B	4253.06	2778.67
PSS1447B	4021.57	2663.64
AVG.	4084.19	2697.42
F-PSS1868B	3730.00	2471.69
F-PSS1854	3507.89	--
F-PSS1867B	3986.46	--
F-PSS1867A	3921.57	--
F-PSS1868A	3896.15	2383.53
AVG.	3808.42	2427.61
SCAP1805	3125.00	1666.67
SCAP1808.5	3207.26	1529.62
SCAP1803	2886.99	1538.32
SCAP1597	3266.67	1513.24
SCAP1580	3310.77	1582.35
SCAP1802	3014.71	1576.92
AVG.	3135.23	1567.85

PSLT: Poodiac Siltstone
PSS: Poodiac Sandstone
F-PSS: Fracture Poodiac Sandstone
SCAP: Siltstone Caprock Breccia

Table 4.4: Dynamic and Static Elastic Modulus

ROCK TYPE	E_d (GPa)	E_s (GPa)	E_d/E_s
Poodiac Sandstone	40.81	9.94	4.11
Poodiac Siltstone	46.73	24.10	1.94
Fractured Poodiac Sandstone	34.08	14.33*	2.38
Siltstone Caprock Breccia	16.53	0.43*	38.44

* Static moduli obtained from initial loading curves.

The ratio of dynamic to static moduli is generally between 1 and 4. The high ratio reported for siltstone caprock breccia in Table 4.4 may be due to:

a) A low initial loading curve.
b) A weaker than average specimen.

The specimen SCAP1802 (Table 4.3) used to measure the static modulus began to spall shortly after it was loaded. It is possible that unload/reload cycles may have weakened the already weak specimen further.

The dynamic values are all relatively consistent. The average values for Poisson's ratio and the static modulus of Siltstone Caprock Breccia and Fractured Poodiac Sandstone were used in numerical modelling.

The average elastic constants of the four rocks are listed below:

Table 4.5: Average Elastic Constants of Overburden Rocks

ROCK TYPE	E_d (GPa)	ν	E_s (GPa)
Poodiac Sandstone	40.81	0.11	9.94
Poodiac Siltstone	46.73	0.16	24.10
Fractured Poodiac Sandstone	34.08	0.16	14.33
Siltstone Caprock Breccia	16.53	0.33	0.43

SECTION 5.0

5.0 LABORATORY TESTING OF BACKFILL

5.1 Overview of Laboratory Testing Programs

The scope of the Phase I testing program included:

a) Determination of material properties of backfill such as grain size distribution, mineralogy, moisture content and specific gravity.
b) Determination of a range of expected densities according to the placement method used based on both field and laboratory testing of backfill.
c) Backfill compaction (consolidation) tests at various levels of compaction stress.
d) Triaxial strength tests on backfill samples compacted to fractional density of 0.9.

The backfill compaction and the triaxial strength testing performed under Phase I of the program was of a preliminary nature. Compaction testing over a period of 90 days supported the initial hypothesis that the emplaced backfill would have limited support capability prior to a substantial elimination of porosity of the backfill during the closure history of the backfilled openings. As to the stiffness of the backfill in the numerical modelling, it was assumed that the modulus of elasticity of the backfill increases in linear proportion to stress.

The triaxial testing was very limited in scope and insufficient data was generated to warrant the development of stiffness functions and the brittle yield failure criteria of backfill. Hence, additional testing was required under the Phase II program.

The scope of the Phase II program was designed to determine the following:

a) Compaction creep behaviour of backfill.
b) Triaxial strength of backfill at various densities.

c) Backfill stiffness as a function of fractional density (porosity).
d) Effect of stress, density and time on the microfabric of the backfill.
e) Methods of salt backfill enhancement with additives (engineered backfill).

The results of the test program on granular salt backfill, including all of the pertinent test results from Phase I, are presented in Section 5.0. The results of tests on engineered backfill are included in Section 6.0.

5.2 Testing Methodology of Granular Halite Backfill

It was evident from the work performed under Phase I and by others (Beddoes, 1984; Fordham, 1988; Fordham et al., 1988; Holcomb and Hannum, 1982; Holcomb and Shields, 1987; IT Corp., 1987; Kappei, 1986; Pfeifle et al., 1987; Pufahl and Yoshida, 1982; Raj, 1982; Rutter, 1976; Sjaardema and Krieg, 1987; Spiers et al., 1989; Yost and Aronson, 1987) that granular halite backfill:

a) compacts by creep at a rate that is dependent on grain size, stress, fractional density (porosity), and moisture content;
b) has brittle strength properties dependent on fractional density (porosity) and compaction rate.

To limit the number of test variables, the relevance of each of the parameters which have been found to affect the mechanical behaviour of granular halite was examined as it applied to the backfilling of potash mines. To be deemed relevant, a parameter had to:

a) vary its effect on the backfill in situ with time;
b) be uncontrollable in situ;
c) be controllable at essentially no cost.

The parameters examined during this study were:

a) stress;
b) stain rate;

c) fractional density (porosity);
d) moisture content.

Of the external parameters (stress, strain rate and temperature), only stress and strain rate were considered uncontrollable (and variable with time). Temperature was not included as it is unlikely to vary significantly over the life of the mine.

Of the material dependent parameters (impurities content, grain size, grain size distribution, moisture content and fractional density/porosity), only moisture content and fractional density (porosity) were included as test variables. The other three were not included as no impurities were noted in the backfill samples tested and grain size reduction or additives to alter the grain size distribution would likely not be cost effective even though grain size variations have been shown to affect the behaviour of halite backfill.

The effect of moisture content on the compaction creep behaviour of halite backfill was examined as it has been shown to affect the compaction behaviour of pure granular halite (Spiers et al., 1989). Moisture content will vary in situ due to drainage, and it will be altered if additional backfill is placed by slurrying techniques.

Fractional density was included as a test variable as it will increase with time and it also affects the brittle strength of halite backfill (Fordham et al., 1988; Beddoes, 1984).

The test program included:

a) material characterization;
b) compaction creep tests;
c) brittle strength tests.

Material characterization was carried out to determine the physical properties of the backfill to aid in the interpretation of laboratory test results. It included an examination of the grain size, mineralogy and moisture/fractional density relationships in the backfill.

Compaction creep testing was carried out to examine the effect of stress, strain rate, moisture content and fractional density (porosity) on the rate at which the backfill compacts. The test results were used to develop an empirical relationship describing the time dependent behaviour of halite backfill.

The brittle strength of the backfill was examined to determine under what stress conditions the backfill could fail in shear. Two strength properties were investigated:

a) brittle strength development in backfill compacted under different stresses;
b) confined brittle strength at various fractional densities (porosities).

5.3 Granular Backfill Characterization

The tailings were collected from the processing plant over a period of 3 hours during a normal mill run to ensure that test materials were representative of those to be used as backfill. The tailings were shipped in sealed, epoxy lined steel drums. After delivery to the laboratory at University of Waterloo, the backfill was transferred to plastic bags and pails to prevent corrosion and loss of moisture.

The physical examination of the backfill consisted of four parts:

a) moisture content determination;
b) grain size analysis;
c) mineralogy;
d) Standard Proctor compaction tests.

5.3.1 Moisture Content

The standard soil mechanics definition of water content is (Craig 1978):

$$w_c = \frac{m_w}{m_s} \tag{5.1}$$

where: w_c = moisture content
m_w = mass of water
m_s = mass of solids

The high solubility of salts in water causes any water in the tailings to be brine, saturated with respect to both NaCl and KCl. When the water is removed by drying, the dissolved salts precipitate. The dry weight then consists of the original solid phase plus the precipitate from the brine.

The true moisture content of granular halite backfill depends on the amount of water plus the amount of dissolved salts in the brine. The amount of dissolved salts in the processing brine from DPPC is 0.304 per gram of brine or 0.435 g per ml of water.

Hence, the moisture content of halite backfill is:

$$w_{ct} = \frac{m_w}{m_s - [b_c \cdot m_w]} \tag{5.2}$$

where: w_{ct} = true moisture content
m_w = mass of water
b_c = saturated brine concentration in mass of dissolved salt per volume of water

The dry density of halite backfill is:

$$\gamma_d = \frac{m_s}{V} \tag{5.3}$$

where: γ_d = dry density
V = volume

The porosity of halite backfill is:

$$n = \frac{G_s - \gamma_d}{G_s} = 1 - D \tag{5.4}$$

where: n = porosity

γ_d = dry density

G_s = specific gravity of solids

D = fractional density

To prepare test specimens to known moisture contents, the backfill was first oven dried at 50°C for 24 hours. The dried backfill was sieved through a 2 mm sieve to remove all large clumps. Enough process brine was then added to the backfill to give it the desired moisture content (2.5% ± 0.1%).

5.3.2 Long Term Moisture Content of DPPC Halite Backfill

When the backfill leaves the plant, it has a moisture content of about 7-8%. Once it has been placed in the mine, the brine immediately begins to drain. The brine drains both vertically and horizontally as many of the stopes dip 5° - 10°. Although there will be locations within the backfill, such as depressions in the floor, where it may be fully saturated (i.e. all porosity filled with brine), it is expected that most of the placed backfill will lose much of its initial moisture.

In order to determine the final moisture content of the backfill, the moisture contents of drained backfill samples were measured. The first measurements were made on the backfill as it was removed from the shipping drums. Moisture content determinations were made at the top, middle and bottom of the drums. Samples collected from the top of the drums were taken below the dried out crust (about 10 cm). In addition, several drainage tests were performed on the backfill by filling 5 cm x 50 cm plexiglass tubes with brine-saturated backfill and allowing them to gravity drain for 1 to 15 days. The tops of the cylinders were covered with Parafilm to prevent drying in the upper portions of the columns.

5.3.3 Grain Size Analysis

Grain size analysis was performed by wet sieving the tailings in acetone. Dry sieving was not attempted as the grains clump together when allowed to dry, cemented by the precipitate from the brine. Both halite and sylvite are essentially insoluble in acetone. However, the effect of the acetone on the grains was examined during optical mineralogical analysis to ensure it did not alter the grain size distribution.

5.3.4 Mineralogy

The mineralogy of the tailings was studied using an optical microscope and by X-Ray diffraction. Optical microscopy was used to perform a semi-quantitative mineralogical analysis on 7 grain size groups (separated during grain size analysis) in the backfill and to examine the effect on the grains of the acetone used for grain size analysis.

X-Ray diffraction was performed on the same 7 grain size groups examined optically as well as bulk (total tailings) and 'slimes' (fine tailings) samples. The analyses were performed to determine if any other minerals (i.e. clays, anhydride) not noted during optical analysis were present in the backfill.

5.3.5 Standard Proctor Compaction Tests

Standard Proctor Compaction tests were used to examine the relationship between initial density and moisture content. The placement density of the backfill and its moisture content are two important variables governing its behaviour.

The higher the initial density, the more quickly the backfill will accept load and the lower will be the amount of total displacement that occurs in an opening. Increasing the moisture content of a granular material tends to increase its initial density (Terzaghi and Peck, 1967), however, higher moisture contents may also lead to excessive brine drainage (Beddoes, 1984).

Standard Proctor tests are perhaps the most common method of testing the optimum moisture/density relationship for a granular material. This test is used extensively for roadbed and earth filled dam compaction. Test procedures followed those outlined in ASTM D698 Method A.

The Standard Proctor tests have been used previously to determine the optimum moisture content/density relationship for halite backfill (Beddoes, 1984; Johnson et al., 1984; Pufhal and Yoshida, 1982). Its applicability as an index test for halite backfill is unclear, however, it is comparable to other granular materials and widely used (Figure 5.1).

5.4 Compaction Creep Testing on Granular Backfill

5.4.1 Specimen Preparation

Most of the material used for compaction creep tests was first prepared to 2.5% w_{ct} (two of the tests were performed on 0% and 5% w_{ct} material). The backfill was then placed in an oedometer (Figure 5.2) in 1.5-2 cm lifts. Each lift was gently compacted by tamping 25-30 times with the end of a 0.5 cm diameter brass rod. Backfill was added until it was of known depth (i.e. volume) in the oedometer. The mass of backfill placed in the oedometer was then calculated in order to determine the initial fractional density (porosity). This process yielded initial porosities of between 0.54 and 0.42 and initial fractional densities of between 0.46 and 0.58.

After the backfill was added, the piston was replaced and the oedometer attached to a pressure control system or placed in a load frame. The oedometer was then loaded and fractional density (porosity) changes monitored with time. Stresses were maintained to within ±2%. Displacement measurements during long term tests (>10 days) were monitored with LVDT's (resolution 0.001 mm, accuracy ±5%) connected to a data acquisition system. Shorter duration tests were manually monitored with a dial gauge (resolution 0.025 mm).

FIGURE 5.1

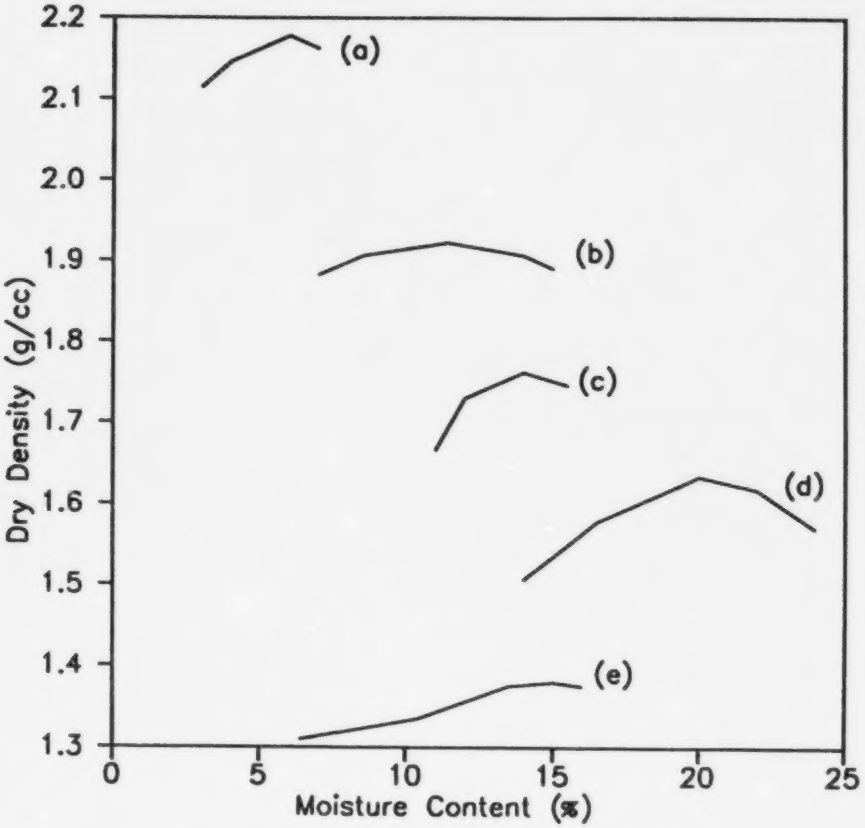

Results of Standard Proctor Compaction tests on (a) well graded sand with small percentage of clay, (b) low plasticity clay, (c) inorganic nonplastic silt, (d) high plasticity clay, and (e) granular halite backfill, Cory potash mine, Sask. (from Terzaghi and Peck, 1967; Johnson et al., 1984)

FIGURE 5.2

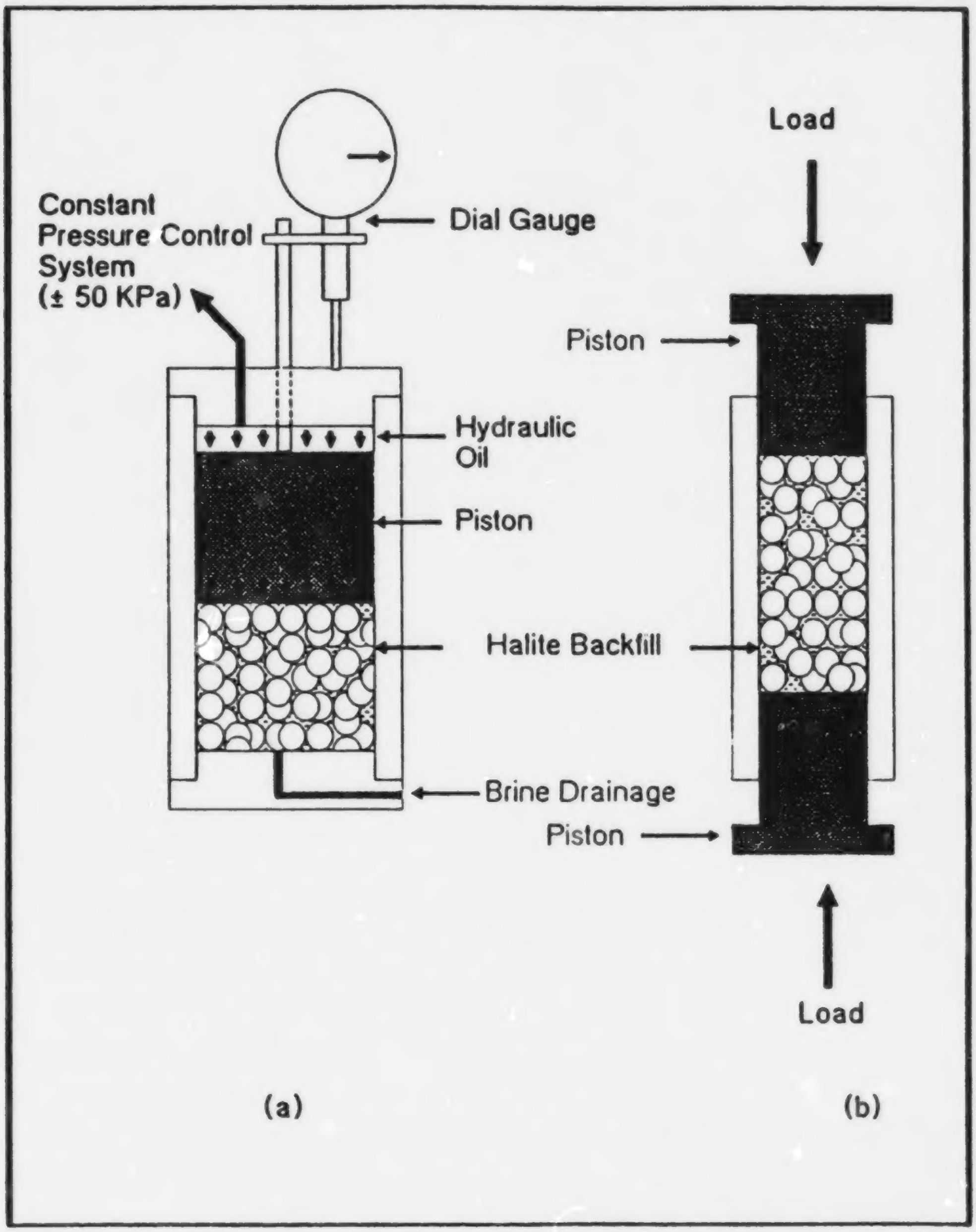

(a) Single piston, internally loaded oedometers used for medium and low stress compaction creep tests and constant strain rate tests.

(b) Double piston oedometer used for high stress compaction creep tests.

5.4.2 Constant Stress Compaction Creep Tests

Constant stress compaction creep tests were carried out primarily to identify the relationship between stress, time and fractional density (porosity) as well as the effects of initial fractional density (porosity) and moisture. During the tests, both stress and volumetric stains were monitored with time.

Three types of constant stress compaction creep tests were carried out:

a) high stress tests (10 - 50 MPa)
b) medium stress tests (1 - 10 MPa)
c) low stress tests (0.17 - 1 MPa)

Table 5.1 lists the compaction creep tests carried out during this study.

High stress compaction creep tests were performed to prepare strength test specimens. The results of these tests were not used in the determination of the behavioural model as:

a) the stresses applied were much higher than those expected in situ (both horizontal and vertical virgin ground stresses are about 20 MPa at DPPC);
b) extensive grain fracture was noted in materials compacted under stresses greater than 10 MPa, altering the grain size.

Table 5.1: Compaction Creep Test Matrix

Test No.	Stress (MPa)	Preparation Moisture Content (o/v) (±.1%)	Initial Porosity (±.005)	Initial Fractional Density
High Stress Tests				
8020	20.00	2.5	0.415	0.585
8030	30.00	2.5	0.425	0.575
8040	34.00	2.5	0.439	0.561
8520	20.00	2.5	0.294	0.706
8530	30.00	2.5	0.435	0.565
8550	47.00	2.5	0.435	0.565
9010	10.00	2.5	---	---
9020	20.00	2.5	0.327	0.673
9030	30.00	2.5	0.411	0.589
9040	40.00	2.5	0.388	0.612
9050	50.00	2.5	0.411	0.589
9520	20.00	2.5	0.304	0.696
9530	30.00	2.5	0.381	0.619
9540	40.00	2.5	0.364	0.636
9550	50.00	2.5	0.313	0.687
Medium Stress Tests				
10	10.00	2.5	0.428	0.572
10A	10.00	2.5	0.421	0.579
5WC	10.00	5.0	0.449	0.551
OWC	10.00	0.0	0.472	0.528
8	8.00	2.5	0.500	0.500
6	6.00	2.5	0.439	0.561
4	4.00	2.5	0.456	0.544
3	3.00	2.5	0.508	0.492
2	2.00	2.5	0.457	0.543
2A	2.00	2.5	0.449	0.551
Low Stress Tests				
150P	1.03	2.5	0.515	0.485
150PA	1.03	2.5	0.509	0.491
500K1	0.50	2.5	0.476	0.524
500K2	0.50	2.5	0.439	0.561
500K3	0.50	2.5	0.472	0.528
500K4	0.50	2.5	0.538	0.462
500K5	0.50	2.5	0.458	0.542
50P	0.34	2.5	0.539	0.461
25P	0.17	2.5	0.492	0.508

High stress tests were carried out in a 54 mm diameter, double piston oedometer, loaded externally (Figure 5.2b). This cell allowed preparation of right circular cylinder backfill specimens of known porosity. After compacting a known amount, the densified backfill was removed and tested for Unconfined Compressive Strength (UCS).

Compaction creep tests under medium and low stresses were carried out to obtain parameters for a material law which could be used to predict in situ behaviour. Although stresses on the backfill may exceed 20 MPa at some time, these stresses will not occur until the backfill has compacted to a low porosity (i.e high fractional density).

Medium and low stress tests were carried out in 101 mm diameter, single piston, internally loaded oedometers (Figure 5.2a). These cells allowed full compaction (i.e. 0% porosity).

No temperature control apparatus was used during testing, although the oedometers were shielded against sudden temperature changes. Average laboratory temperatures were about 19° to 23°C. It was felt that this range of temperature would have a negligible effect on the behaviour of the backfill (Spiers et al., 1989; Holcomb and Hannum, 1982).

5.4.3 Constant Strain Rate Compaction Creep Tests

Constant strain rate compaction creep tests were performed to determine if the backfill displays the same constitutive behaviour under constant stress and constant strain rate. In situ openings at DPPC exhibit constant rates of closure (i.e. steady state creep) after about a year. Because the backfill has little strength initially, it will offer little resistance to room closure and will, therefore, compact under the constant strain rate imposed by room closure. As the backfill densifies, it will gain strength and eventually begin to support load. When this occurs, the backfill will offer resistance to room closure and will begin to compact under conditions of increasing stress.

Constant strain rate tests were performed at strain rates of 10^{-3}, 10^{-4} and 10^{-5} sec^{-1}. Unfortunately, equipment limitations prevented slower tests. The tests were performed using single piston oedometers (Figure 5.2a). However, instead of applying a constant stress to the internal piston, the cell was placed in a servo-controlled loading frame and the piston displaced at a constant rate.

5.4.4 Effect of Moisture and Initial Porosity

The effect of moisture content on compaction behaviour was examined using constant stress compaction creep tests. Three of the 10 MPa tests were performed on backfill with 0% (oven dried), 2.5%, and 5% w_{ct}.

The effect of initial fractional density (porosity) on compaction behaviour was examined by preparing backfill material at 2.5% w_{ct} to five different initial fractional densities between 0.439 and 0.537 and allowing them to compact by creep under 0.5 MPa. Different initial fractional density (porosities) were achieved by varying the amount of tamping during placement of backfill in the oedometer. Two of these specimens were examined under a Scanning Electron Microscope to examine grain contact behaviour.

5.5 Brittle Strength Testing

The brittle strength of compacted granular halite is largely a function of its fractional density (porosity). However, the rate at which the material is densified can also affect its brittle strength. Studies have shown (Fordham et al., 1988; Beddoes, 1984) that samples compacted to the same fractional density (porosity) but at different rates (i.e. under different stresses) have significantly different Unconfined Compressive Strengths (σ_c). The test program was designed to determine the effect of compaction stress, time and fractional density (porosity) on the shear strength.

The test specimens for UCS tests were prepared by taking a known mass of backfill at 2.5% w_{ct} and placing it in the double piston oedometer. The backfill was then compacted under stresses of either 10, 20, 30, 40 or 50 MPa until the shoulders of the pistons rested on the body of the oedometer (Figure 5.2b) where it was of known volume, hence known fractional density (porosity). The amount of backfill placed in the oedometer allowed specimens with porosities of about 0.14, 0.18, 0.22, 0.26 to be prepared. After creep compacting to the desired fractional density (porosity), the backfill specimen was removed from the oedometer, measured and immediately tested for UCS.

The test specimens for triaxial compression tests were prepared by compacting the backfill in the double piston oedometer under a constant stress of 30 MPa to porosities of 0.26, 0.22, 0.18 and 0.14. Tests were performed by placing a specimen in two oil coated, latex membranes in a Wykeham-Farrance triaxial cell. Confining stresses of 0.34, 0.69 and 1.03 MPa were applied with water. Axial stresses were applied by a constant axial strain rate of 10^{-4} sec^{-1}.

5.6 Results

5.6.1 Moisture Content

After free draining for about 10 days during transit, the average corrected moisture contents (using equation 5.2) at the top, middle and bottom of the shipping drums were 2.2%, 7.3% and 22.0% respectively. The average moisture contents of the laboratory drainage columns are listed in Table 5.2.

Table 5.2: Moisture Contents of Drained Backfill

Test	Corrected Moisture Contents (%) Top	Middle	Bottom
Shipping Drums (Avg. of 4 Drums)	2.2	7.3	22.0
1-Day Laboratory Drainage Column	2.5	7.1	9.5
1-Day Laboratory Drainage Column	1.7	4.6	9.3
5-Day Laboratory Drainage Column	2.6	5.0	-

In situ the backfill will be stowed as high at 30 m. Gravity drainage conditions should allow much of the backfill to drain like the upper portions of the drums and test columns. For this reason, most of the test program was conducted on material prepared with a 2.5% moisture content.

5.6.2 Grain Size Analysis

Ninety five percent of the grain sizes of DPPC halite backfill are between 0.125 and 2.0 mm in diameter (Figure 5.3). The coefficient of uniformity (C_u) of DPPC halite backfill is 3.4.

5.6.3 Mineralogy

Microscopic examination showed that most of the sample material is made up of several types of halite: orange, yellow and clear. KCl made up only 5% of grains 1 mm or greater and was not noted in any smaller size fraction. No difference was noted between the surfaces of grains exposed to acetone during grain size analysis and fresh grains (Figure 5.4). It was, therefore, assumed that the acetone had not affected the grain size distribution in the backfill.

Only halite and sylvite appeared on the X-Ray diffraction traces (Figure 5.5). No insolubles were detected in the DPPC tailings tested.

The specific gravity of fully densified DPPC backfill is 2.14. This was calculated from a weighted average of the mineralogy of 7 grain size groups within the backfill assuming the specific gravities of pure NaCl and pure KCl are 2.16 and 1.98, respectively.

5.6.4 Standard Proctor Compaction Tests

The Standard Proctor Compaction test showed that while the wet density (density of backfill grains and brine) of the backfill continues to increase with moisture content up to 16%, the dry density (density of backfill grains alone) changes little but peaks at about 12% (Table 5.3; Figure 5.6).

FIGURE 5.3

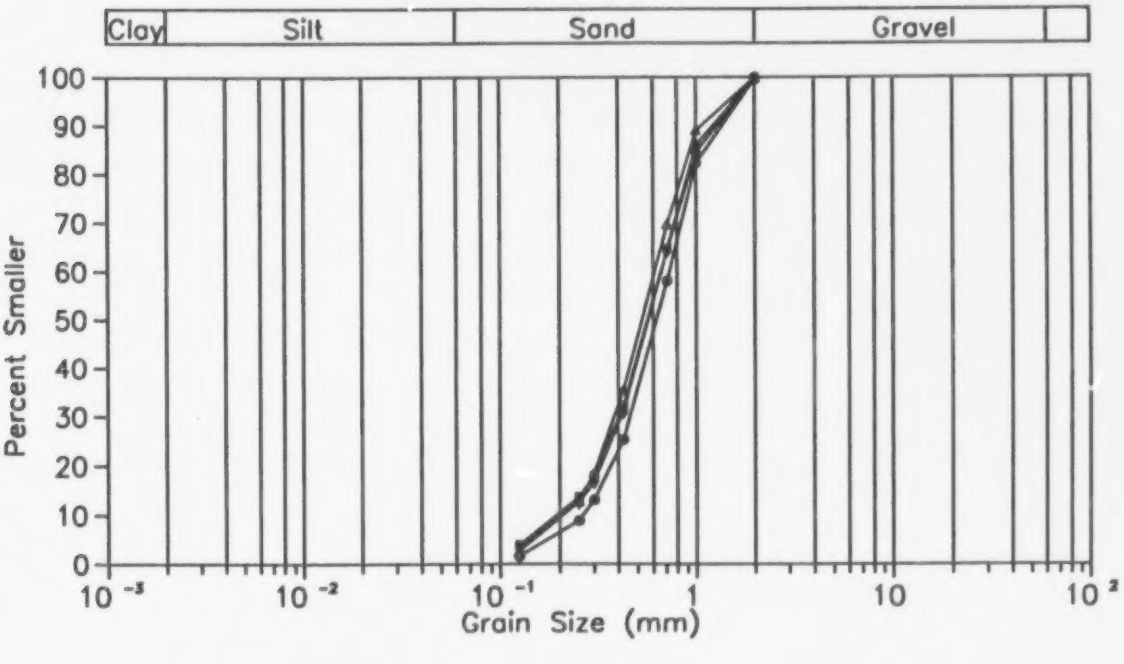

Grain size distribution of DPPC halite backfill.

FIGURE 5.4

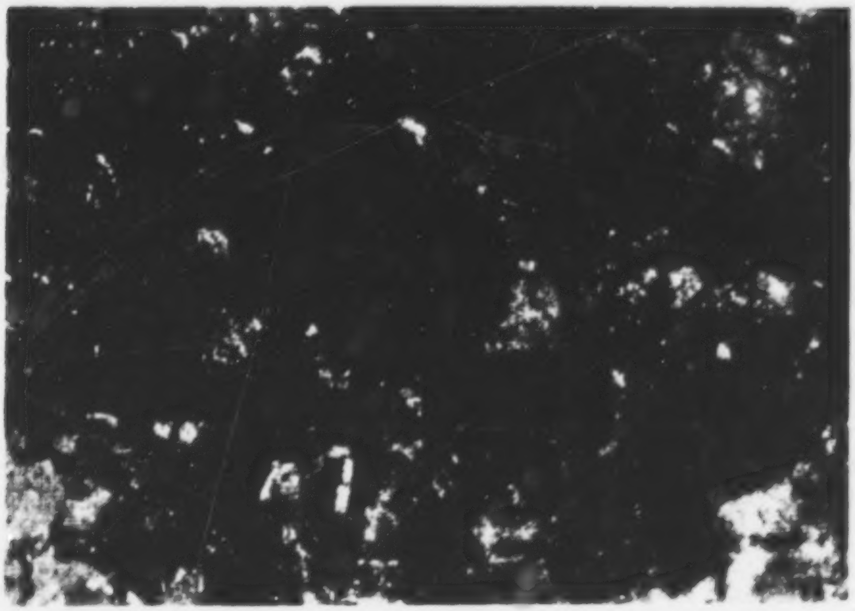

Optical micrograph of uncompacted DPPC halite backfill.

FIGURE 5.5

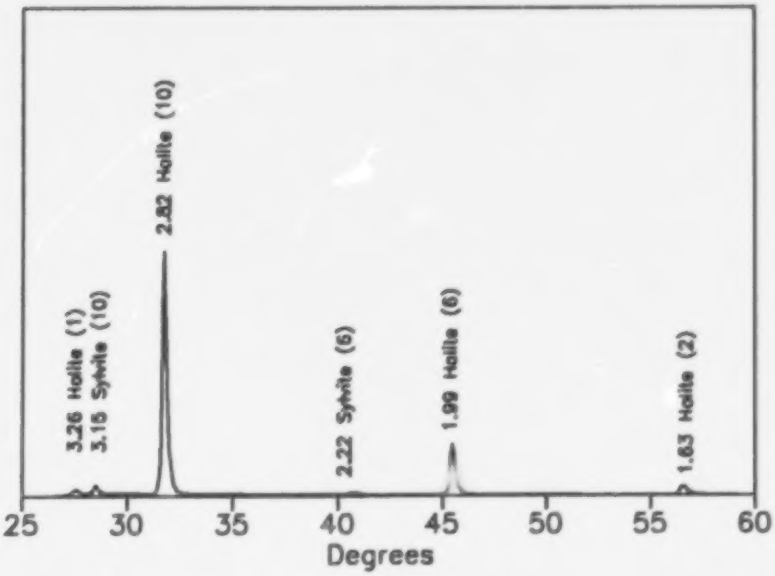

X-Ray diffraction trace, DPPC halite backfill.

FIGURE 5.6

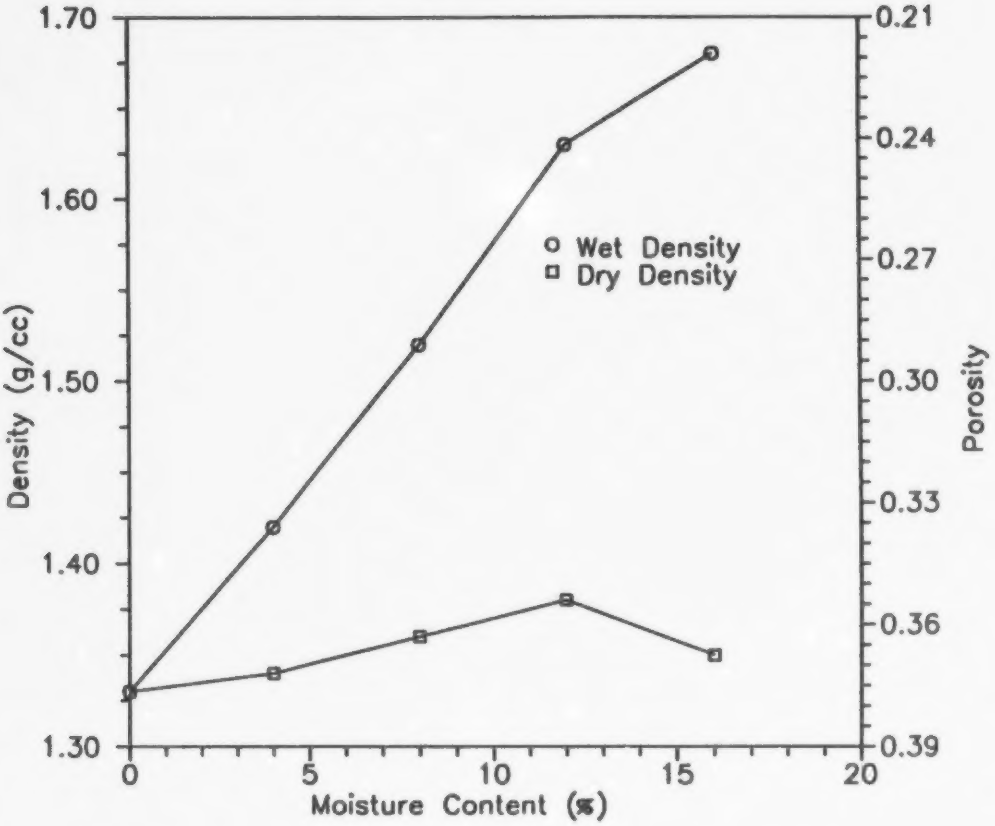

Standard Proctor compaction test results.

The maximum increase in dry density with moisture content over the range 0 to 16% w_{ct} is only about 4%. The addition or removal of brine from the backfill before it is placed will have little effect, and the brine content above 2-3% will drain and require pumping systems to remove it from the mine. This lack of increase in density with moisture content supports the use of moisture contents of 2.5% for the tests.

Table 5.3: Standard Proctor Compaction Results

Moisture Content (%)	Wet Density (g/cc)	Dry Density (g/cc)
0.0	1.33	1.33
4.0	1.42	1.34
8.0	1.52	1.36
12.0	1.63	1.38
16.0	1.68	1.35

5.6.5 Overview of Compaction Creep Tests

The results of the compaction creep tests are plotted as porosity (n) against time. Typical results for 2.5% moisture samples from the high, medium and low stress tests are shown in Figures 5.7, 5.8 and 5.9. In general, the results of the compaction creep tests showed:

a) the higher the applied stress, the faster the compaction rate;
b) the lower the porosity, the slower the compaction rate;

The shapes of the porosity/time curves were similar for all tests. Creep rates slowed rapidly during the first 5-10 minutes of the test to about 10^{-5} to 10^{-6} sec^{-1}. After 10 to 20 days, rate decreased to about 10^{-9} sec^{-1}. At this point, strain rate data often became somewhat scattered due to the precision limits of the measuring equipment.

FIGURE 5.7

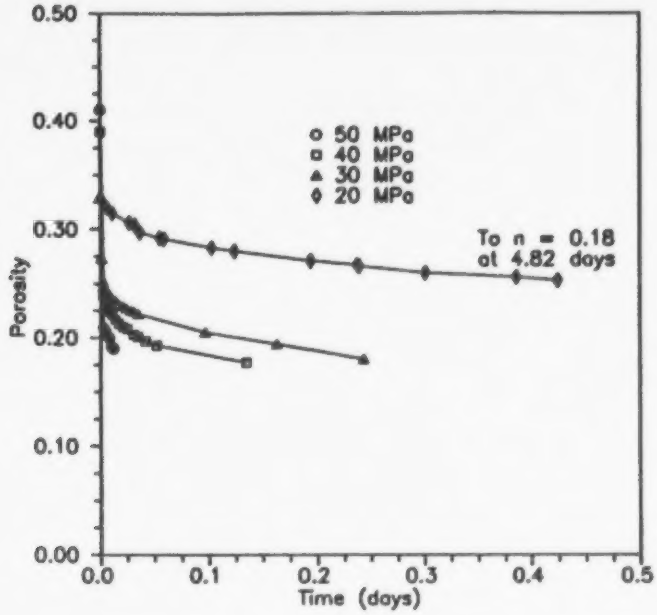

Typical high stress compaction creep test results.

FIGURE 5.8

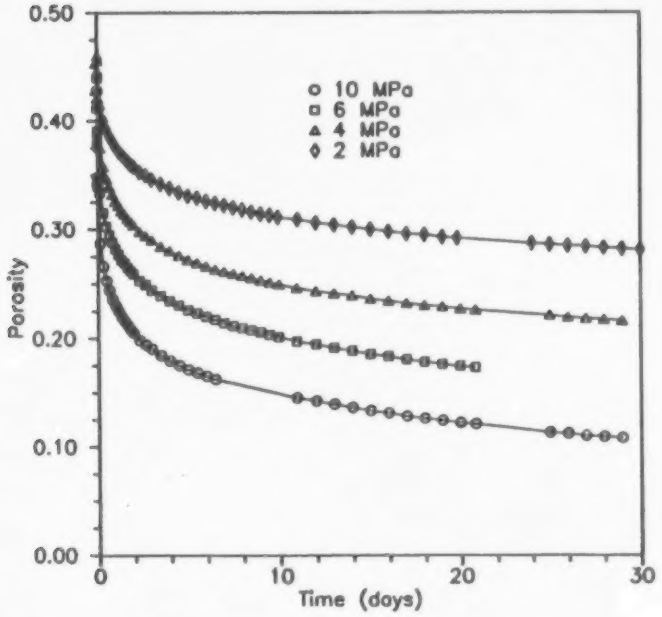

Typical medium stress compaction creep test results.

FIGURE 5.9

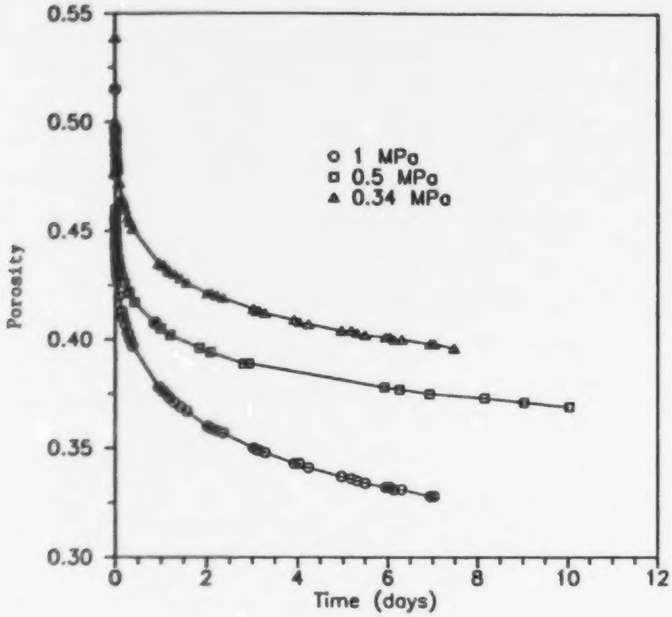

Typical low stress compaction creep test results.

FIGURE 5.10

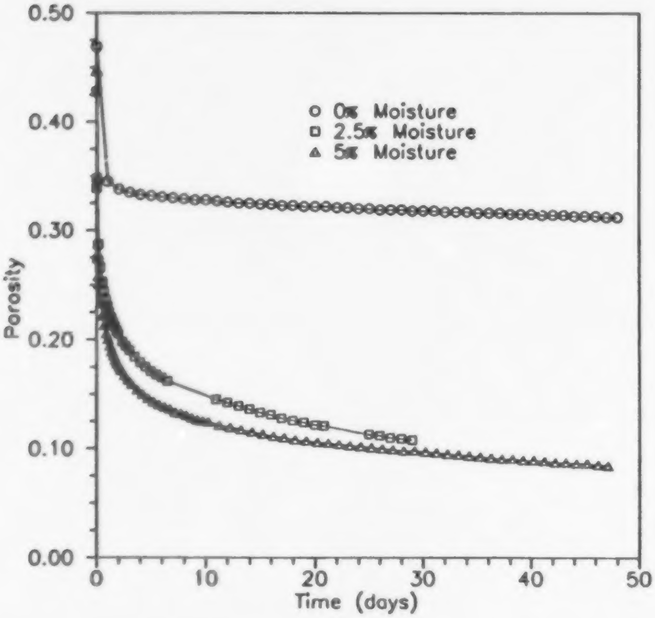

Effect of moisture content on compaction creep under 10 MPa.

The porosity versus time curves for the compaction creep curves performed on material at 0% (oven dried at 50°C for 24 hours), 2.5% and 5% moisture are shown in Figure 5.10. The results of the test indicate that the biggest difference in behaviour is between 0% and 2.5%, increasing the moisture content to 5% has only a small effect.

5.6.6 Overview of Brittle Strength Tests

The Unconfined Compressive Strength (σ_c) of the prepared specimens ranged between 1.6 MPa and 12.5 MPa. The weakest specimens were those compacted to a fractional density of 0.74 (i.e porosity = 0.26) and the strongest those compacted to a fractional density of about 0.86 (i.e. porosity = 0.14) (Figure 5.11). In almost all cases, the lower the stress used to compact a test specimen prior to testing, the greater its unconfined strength (Figure 5.12). The rate of increase in σ_c versus the compaction stress is approximately equal for each fractional density (porosity).

The apparent stiffness (M_{50}) was measured from the stress/strain curves at 50% of the UCS during each test. Figure 5.13 shows an approximately linear increase of M_{50} with decreasing porosity at all stresses.

Triaxial brittle strength data, plotted on a σ_1/σ_3 diagram, show the failure envelopes to become increasingly linear with decreasing porosity over the range of confining stresses tested (Figure 5.14). Included on this plot for comparison, is the failure envelope for Upper Halite, the roof rock at DPPC. This material is mineralogically similar to the backfill but has essentially no porosity (i.e. fractional density = 1.0).

The values of tensile strength (σ_T) for the backfill could not be obtained from tests, rather they were derived as function of σ_c defined by

$$\sigma_T = -0.06 \cdot (\sigma_c) \qquad (5.5)$$

This relationship has been noted in many salt rocks including domal halite, Saskatchewan potash salts, as well as DPPC salts (CANMET, 1987).

FIGURE 5.11

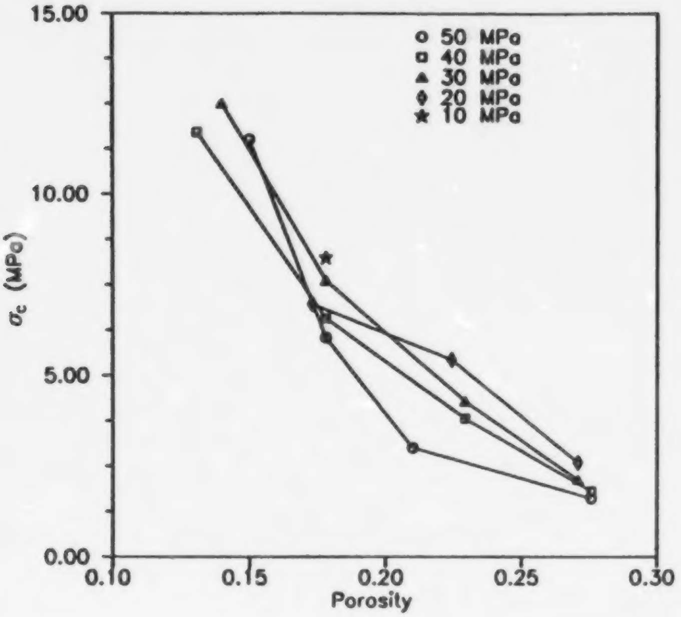

Unconfined compressive strength vs. porosity for test specimens compacted under 50, 40, 30, 20 and 10 MPa.

FIGURE 5.12

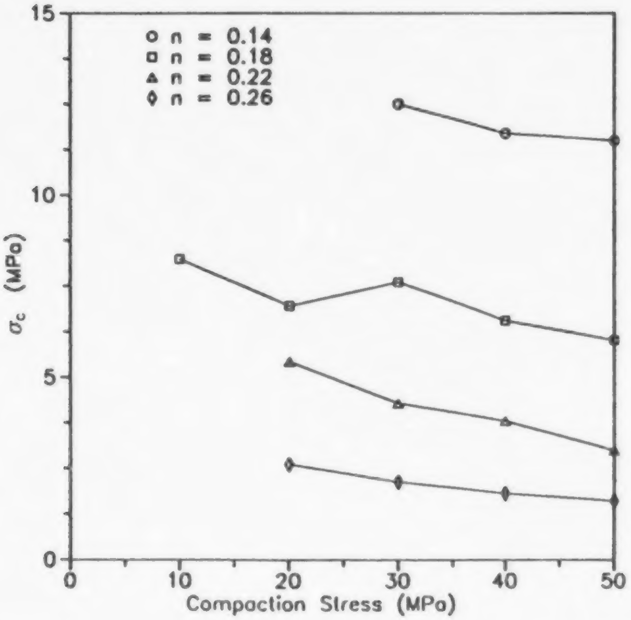

Unconfined compressive strength vs. compaction stress for test specimens at porosities of 0.14, 0.18, 0.22 and 0.26.

FIGURE 5.13

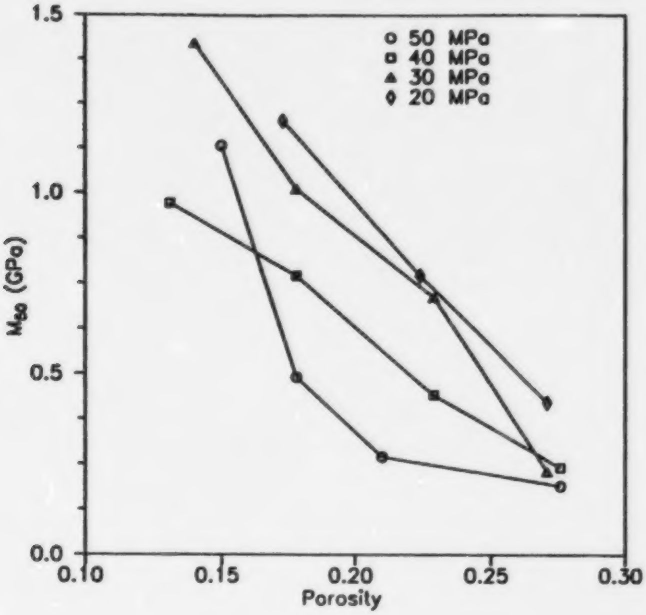

Apparent stiffness vs. porosity for test specimens compacted at 50, 40, 30 and 20 MPa.

FIGURE 5.14

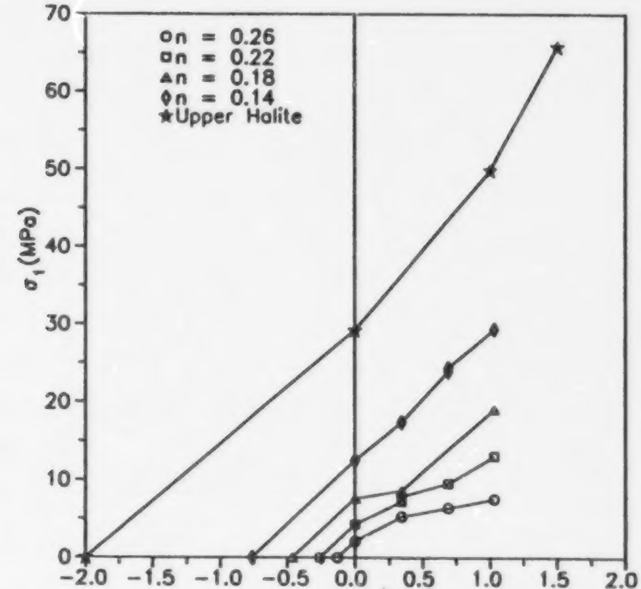

Results of triaxial compression tests on DPPC halite backfill at porosities of 0.26, 0.22, 0.18 and 0.14.

5.7 Evaluation of Tests on Granular Halite Backfill

5.7.1 Compaction Creep Behaviour of Halite Backfill

Granular halite backfill crystals are small pieces of intact salt. As such, they are subject to the same creep mechanisms (dislocation creep, diffusion creep, grain boundary sliding, and cataclasis). However, in situ conditions (i.e. temperature, stress) and material properties (i.e. moisture content, grain size) will govern which mechanism dominates compaction creep.

Pressure solution has been suggested as an important time dependent mechanism at the stresses and temperatures encountered in Canadian potash mines, and it has been identified as the dominant mechanism of compaction creep in pure granular halite (Spiers et al., 1989; Raj, 1982; Raj and Chyung, 1981; Rutter, 1976). Some of the characteristics of pressure solution used by Spiers et al. (1989) to identify it as the dominant mechanism of compaction creep in pure granular halite include:

a) it can only operate in the presence of a fluid (water) capable of dissolving the solid material (salt);

b) creep rates show an exponential stress dependence of between 1 and 2 at low fractional densities (ie. high porosities);

c) microstructural examination of compacted granular halite shows grain-to-grain indentations and changes in grain shape with little plastic deformation;

d) creep rates show a strong dependence on grain size.

Spiers et al. (1989) found that compaction creep rates in pure granular halite had a grain size (d) dependence of about $1/d^3$ and a volumetric strain (ϵ_v)dependence of about $1/\epsilon_v^{2-4}$ from which they inferred pressure solution in pure granular halite to be diffusion controlled.

Although determined to be the dominant mechanism of compaction in pure granular halite, pressure solution must be accompanied by grain boundary sliding in order to accommodate grain shape changes during creep (Burton, 1977; Rutter, 1976). Much of the previous work on grain boundary sliding has been performed on metals which have essentially no porosity. In a granular halite where grains have pores in which to move, it seems likely that grain boundary sliding may play an important role in compaction. Because grain boundary sliding has been identified as a creep mechanism in 'intact' materials, grain boundary sliding in granular halite will, henceforth, be referred to as particulate sliding.

Cataclasis can also occur at mine temperatures and has been suggested as a possible mechanism of deformation in intact salt (Skrotzki and Haasen, 1984; Carter and Hansen, 1983). Although it is unlikely that cataclasis is a compaction creep mechanism (i.e. time dependent), it is probable that cataclasis does occur at high stress locations such as small area contacts (point contacts) within granular halite.

Three aspects of the compaction creep behaviour were examined in order to compare the behaviour of the backfill to the characteristics of the three deformation mechanisms likely to dominate it (pressure solution, particulate sliding, and cataclasis):

a) effect of moisture content on compaction behaviour;
b) stress dependent of compaction creep rates;
c) microstructural effects.

Figure 5.10 shows that oven dried halite backfill does not compact as fast as backfill with 2.5% or 5% moisture. This agrees with the observations of Spiers et al. (1989) and Holcomb and Shields (1987) for pure granular halite and indicates that a creep mechanism requiring the presence of pore fluid (i.e. pressure solution) does occur during compaction creep in halite backfill.

In order to examine the dependence of creep rates on stress, experimental data must be compared at constant structure (i.e. porosity, grain size, moisture content, etc.)(Spiers et al., 1989). Figure 5.15 shows the relationship between stress and strain rate for backfill with fractional densities of 0.56, 0.61, 0.65, 0.70 and 0.79. At high stresses (>2 MPa), the slopes of the lines are between 3 and 6. At lower stresses, the slope

FIGURE 5.15

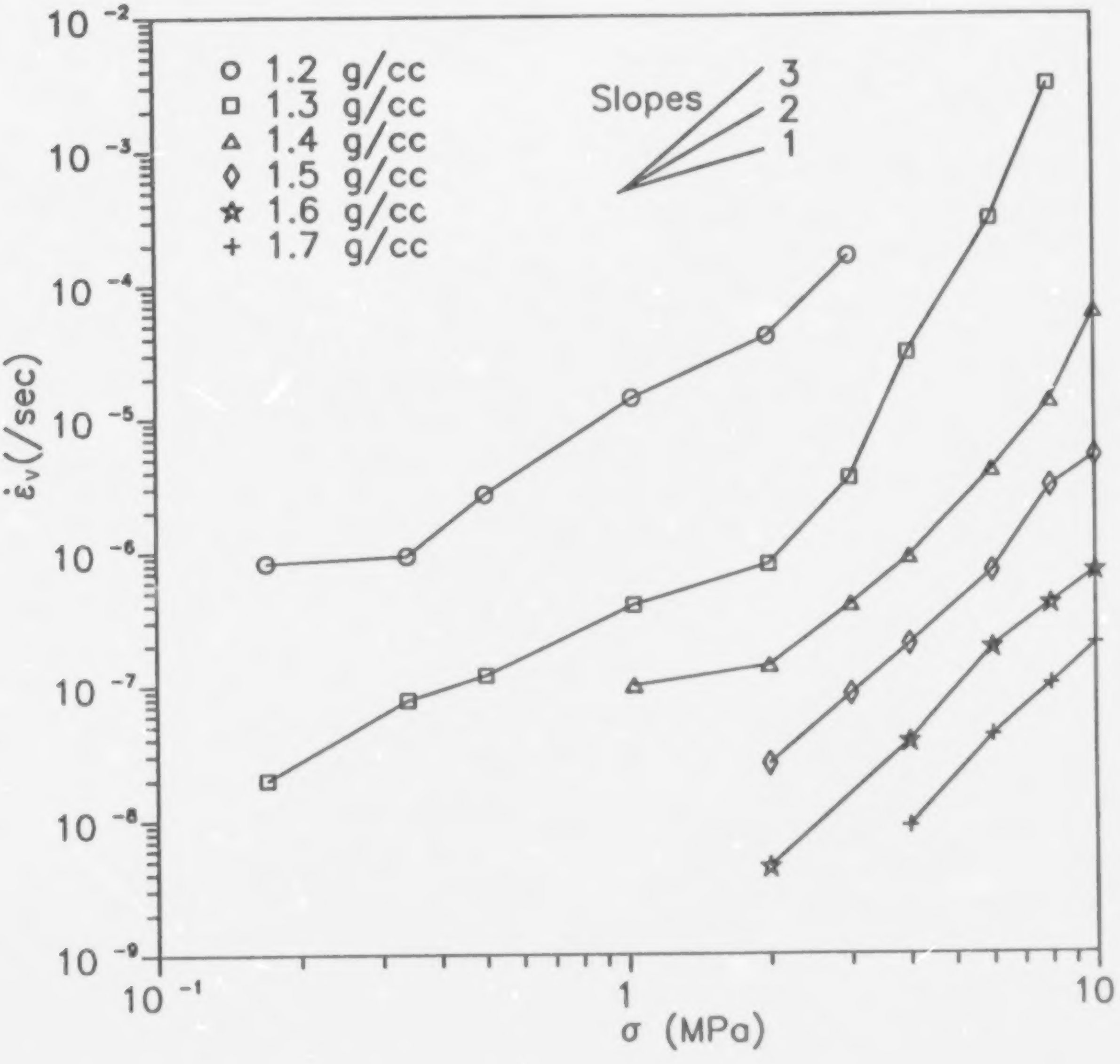

Volumetric creep rate versus compaction stress.

flattens to about 1.5-2. No single mechanism has been identified which exhibits such a wide range of stress dependence. It seems, therefore, that two mechanisms may account for the curves in Figure 5.15.

At low stresses, slopes in the range of 1.5 to 2 were similar to those noted by Spiers et al. (1989) and reflect pressure solution dominated creep. At medium stresses, particulate sliding becomes dominant if moisture is present. The slopes of the lines above stresses of 2-4 MPa are similar to those noted for grain boundary sliding in metals (Evans, 1984; Horton, 1976; Langdon, 1973; Sklenicka et al., 1973).

An examination of the microstructure of compacted halite backfill was performed using a Scanning Electron Microscope (SEM). Two specimens which had each been compacted under 0.5 MPa were examined. Several features were noted:

a) contacts which appeared to have been originally sharp (point contacts) had been flattened by crushing and crushed material was evident around the contact (Figure 5.16);
b) grains had been pushed or indented into one another (Figure 5.17);
c) there appeared to be material precipitated in pores next to grain contacts (Figure 5.18).

It can be suggested from the presence of crushed grain contracts that cataclastic deformation occurred during compaction of the backfill. This type of deformation is relatively time independent and has an associated stress dependent, finite amount of strain. Cataclastic processes can account for the initial rapid compaction of a granular aggregate after the imposition of an external, compressive stress. Cataclastic processes essentially cease once stresses at grain contacts have dropped below the crushing or fracturing strength of the material. Under in situ conditions, the rapid compaction, dominated by cataclasis will be relatively rare.

Grain indentation and precipitation of material in the pores of compacted granular halite has been noted by Spiers et al. (1989). These features are indicative of pressure solution creep.

FIGURE 5.16

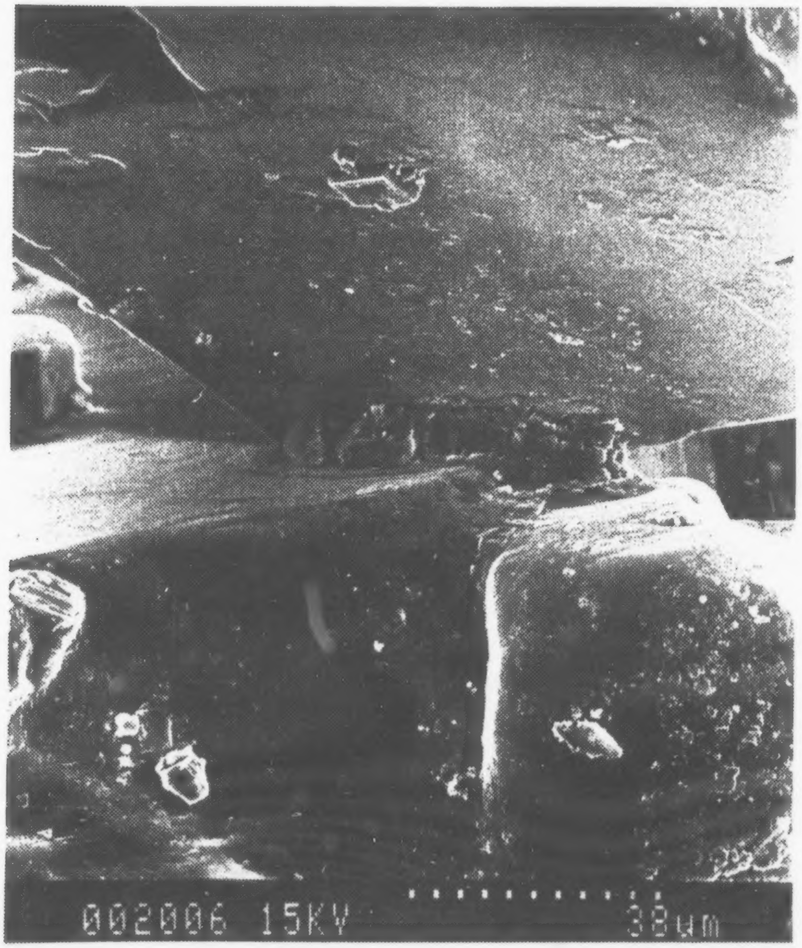

Crushed grain contact in halite backfill compacted under 0.5 MPa for about 7 days.

FIGURE 5.17

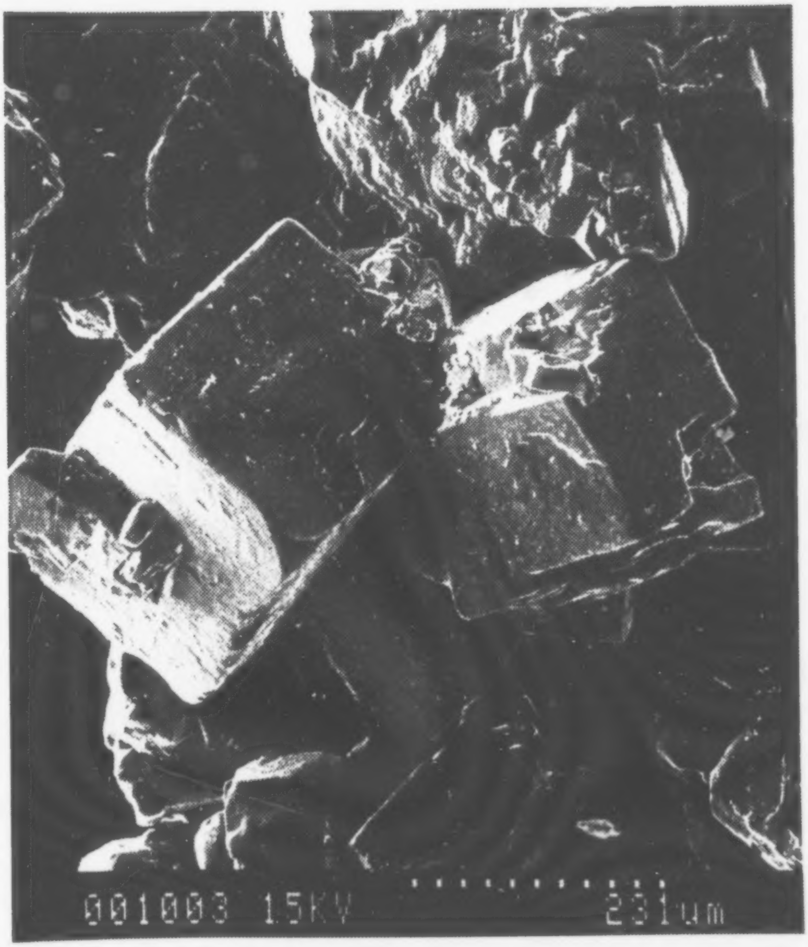

Grain indentation in compacted halite backfill. Note large grain in left centre of micrograph has indented into adjacent grain.

FIGURE 5.18

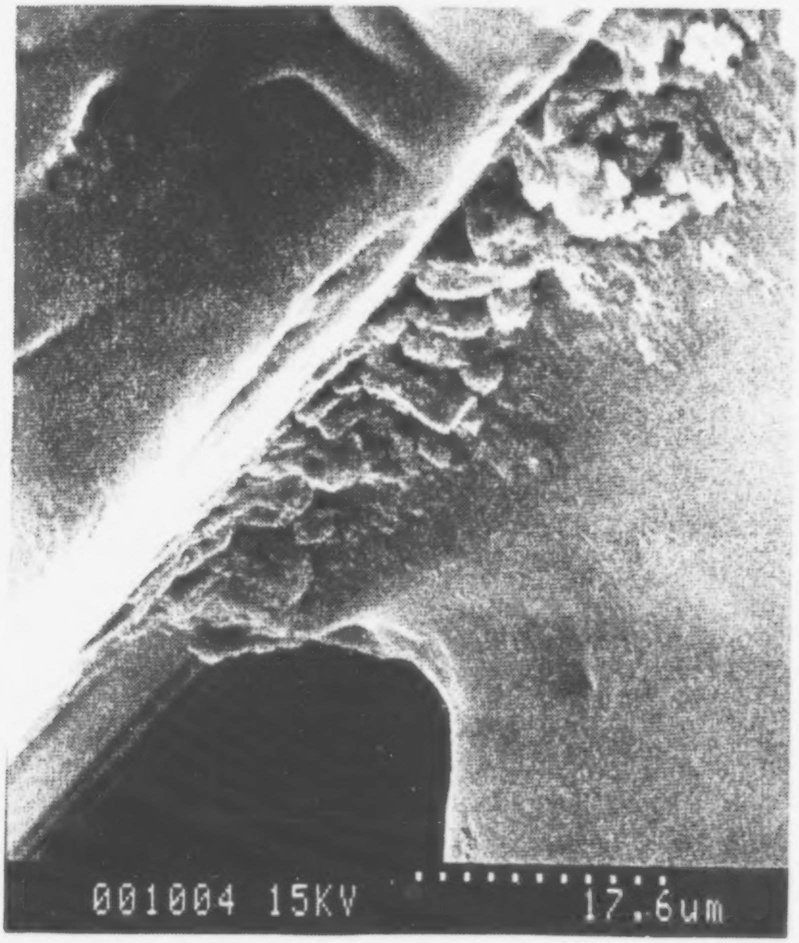

Precipitate in pore of compacted halite backfill. This precipitate material may contain material transported during pressure solution creep and/or material precipitated during drying after compaction testing.

The mechanisms dominating deformation in halite backfill, based on examination of laboratory behaviour, are therefore:

a) pressure solution at low stresses (< 2 MPa) and low volumetric strain rates ($<10^{-6}$ s^{-1});

b) particulate sliding at volumetric strain rates above about 10^{-6} s^{-1};

c) cataclasis initially at all stresses upon a sudden imposition of a stress, with magnitude being stress dependent.

In situ stresses will be low for long periods of time before room closure begins to transfer roof and pillar loads. Pressure solution will, therefore, be the dominant in situ compaction creep mechanism.

At constant grain size and moisture content, creep rates in the halite backfill were found to be primarily dependent on fractional density (porosity) and stress. To examine this dependence, the compaction creep data was plotted on a log $\dot{\epsilon}$ / log n diagram (Figure 5.19). A visual examination suggested the data could be divided into two creep regimes which were characterised as follows:

1) Initially a rapid decrease in creep rate from about 10^{-3} sec^{-1} to about 10^{-6} sec^{-1} (high rate regime). This period usually lasted only about 5 minutes.

2) A period of much slower decreases in creep rate (low rate regime) which lasted for the duration of the test.

A characteristic strain rate ($\dot{\epsilon}_{os}$) and porosity (n_c) separates the two creep rate regimes.

The strain rate $\dot{\epsilon}_{os}$ varied between $1 \cdot 10^{-6}$ sec^{-1} and $4 \cdot 10^{-5}$ sec^{-1}. It was found to be a weak function of initial porosity (n_i), increasing in value with higher initial porosity. The low initial porosity specimens (<0.45) exhibited $\dot{\epsilon}_{os}$ values of about $1\text{-}3 \cdot 10^{-6}$ sec^{-1} (Figure 5.19). The relationship between $\dot{\epsilon}_{os}$ and n_i was found to be (Figure 5.20):

FIGURE 5.19

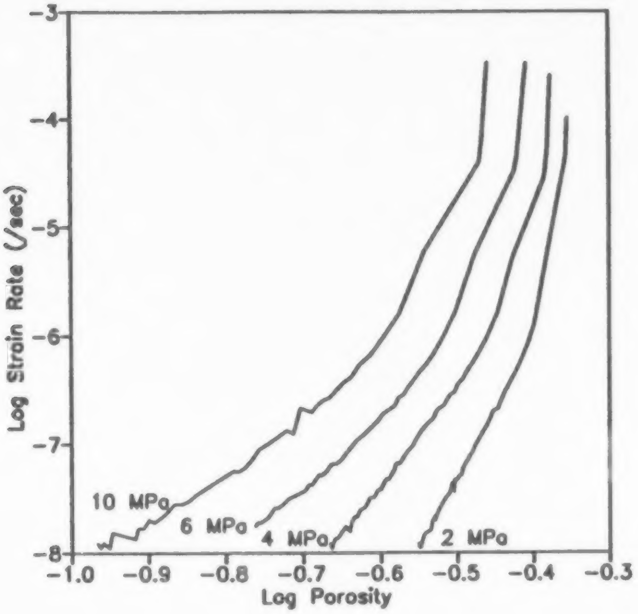

Log $\dot{\epsilon}$/log n curves for medium stress compaction creep tests.

FIGURE 5.20

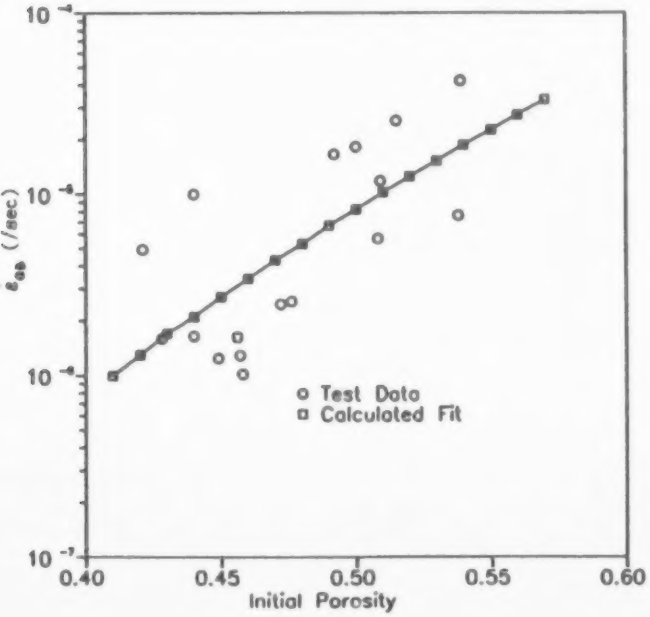

$\dot{\epsilon}_{os}$ vs. initial porosity (n_i)

$$\dot{\epsilon}_{os} = 1.31 \cdot 10^{-2} \cdot n_i^{10.633} \tag{5.6}$$

The porosity n_c is a function of the applied stress and the initial porosity (n_i). The amount of porosity reduction during the high creep rate regime increases with stress. The relationship between stress and (n_i-n_c) was found to be (Figure 5.21):

$$n_d = (n_i - n_c) = 4.87 \cdot 10^{-2} \cdot \sigma^{0.518} \tag{5.7}$$

where: n_d = difference between n_i and n_c
σ = applied stress (MPa)

Although the slopes of curves in Figure 5.19 seem to suggest three creep rate regimes, greater than 5.0×10^{-5}, 1.0×10^{-6} to 5.0×10^{-5}, and less than 1.0×10^{-6}, the curve fitting was done assuming only two creep rate regimes for simplicity. The slopes of the log $\dot{\epsilon}$ /log n curves for the two creep rate regimes (Figure 5.19) were also stress dependent (Figures 5.22 and 5.23). The relationship between the slopes and stress was determined to be (Figure 5.24):

$$l_1 = 105 \cdot \sigma^{-0.725} \tag{5.8}$$

$$l_2 = 18.6 \cdot \sigma^{-0.463} \tag{5.9}$$

where: l_1 = slope of log $\dot{\epsilon}$ /log n curve in the high creep rate regime
l_2 = slope of log $\dot{\epsilon}$ /log n curve in the low creep rate regime

The change in slope of the log $\dot{\epsilon}$ /log n curve at $\dot{\epsilon}_{os}$ /n_c indicates a change in dominant deformation mechanism. Changes in mechanism in intact salt and metals are usually exhibited by changes in stress dependence (exponent 'n_1') at a certain value of stress (Poirier, 1985). Porosity dependent changes in mechanism in halite backfill are also an expression of the stress dependency; as the backfill densifies, grain contact areas increase, reducing stresses between grains even though the external stress is maintained. As intergranular stresses drop, the overall creep rate of the backfill drops from high rate mechanisms to low rate mechanisms.

FIGURE 5.21

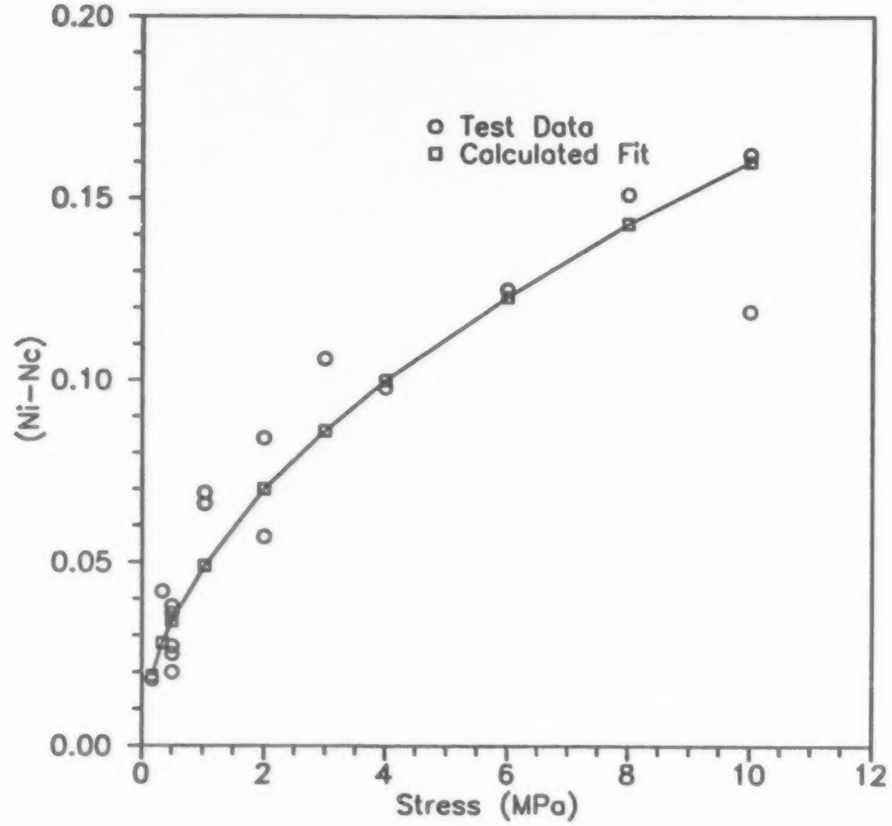

Difference between initial porosity (n_i) and n_c vs. applied stress.

FIGURE 5.22

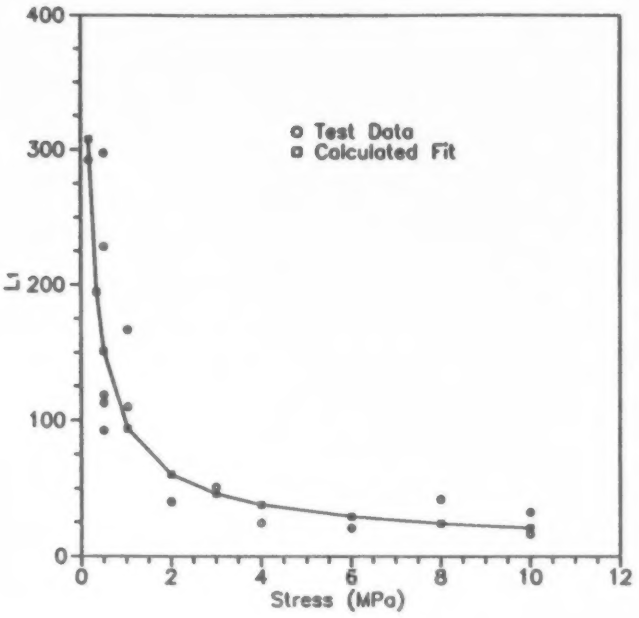

Slopes of high creep rate regime curves (l_1) on log $\dot{\epsilon}$/log n plots.

FIGURE 5.23

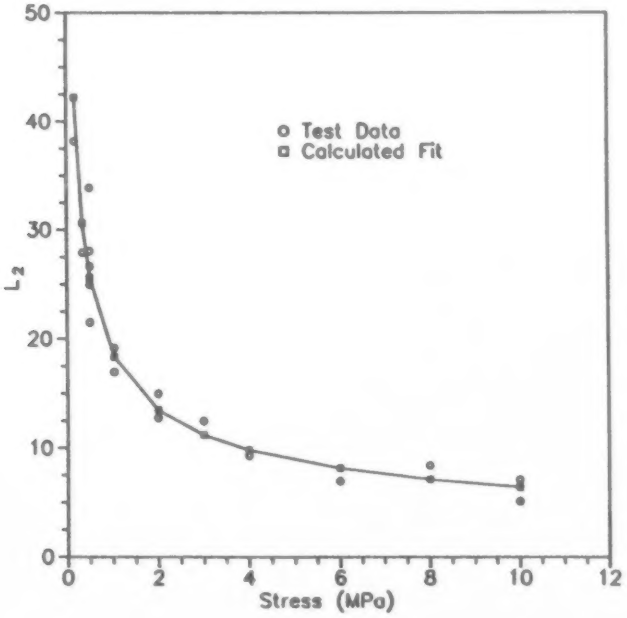

Slopes of low creep rate regime curves (l_2) on log $\dot{\epsilon}$/log n plots.

FIGURE 5.24

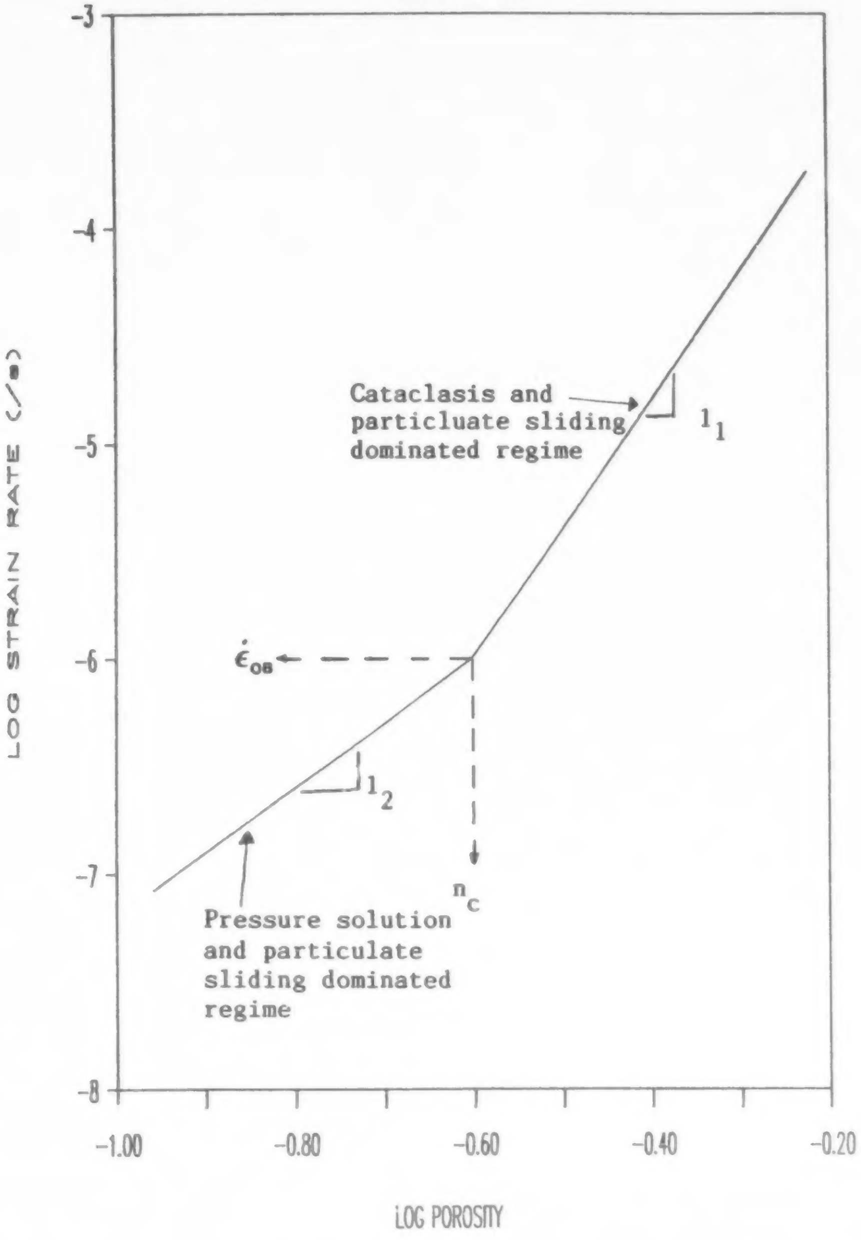

Conceptual diagram of behavioural model for DPPC halite backfill at constant stress. Note the dominant deformation mechanisms in each creep regime (see Figures 5.16 and 5.17).

The very high rate creep regime is attributed to deformation by cataclastic processes. As cataclasis loses its dominance, particulate sliding becomes important. Pressure solution operates at much slower strain rates than cataclasis (< approx. 10^{-6} sec^{-1}), but densification rate decreases are also much slower. A comparison of the creep rates in the oven dried and 2.5% w_{ct} backfill demonstrates this point. The oven dried material, which undergoes little or no pressure solution/particulate sliding creep, does not enter a low creep regime until it is creeping at a rate of about 10^{-8} sec^{-1} (Figure 5.25).

An important side effect of cataclasis is the reduction in grain size which can be achieved. If enough grain fracture occurs, the reduced average grain size can alter the behaviour dramatically. However, the amount of grain fracture, and hence the resulting grain size distribution, is difficult to qualify and compaction by cataclasis at high stresses will not likely occur in New Brunswick potash mines. For these reasons, high stress (>10 MPa) compaction creep data have not been included in this analysis.

Although many of the log $\dot{\epsilon}$ /log n curves show sharp breaks at $\dot{\epsilon}_{os}$ /n_c, the break is likely an artifact of the frequency of data collection rather than true material behaviour. A continuous data curve would show the change from high rate to low rate mechanisms happens gradually as the stress levels at various grain contacts drop below the stress required for cataclastic processes and begin to creep by particulate sliding and pressure solution. At low stresses, where cataclasis is less dominant due to the strength of the grains, the dominance of pressure solution creep and particulate sliding at early stages of the test can make it difficult to determine $\dot{\epsilon}_{os}$ and n_c precisely (Figures 5.20 and 5.21).

Stresses at grain contacts are the primary driving force for compaction creep. It was expected, therefore, that materials with initially high porosities (i.e low fractional densities), which have smaller contact areas and correspondingly higher intergranular stresses than lower porosity material, would show more rapid rates of compaction creep, particularly at early times. However, four of the five tests performed at 0.5 MPa with different initial porosities showed that the higher the initial porosity of a test specimen, the lower the creep rate (Figure 5.26).

FIGURE 5.25

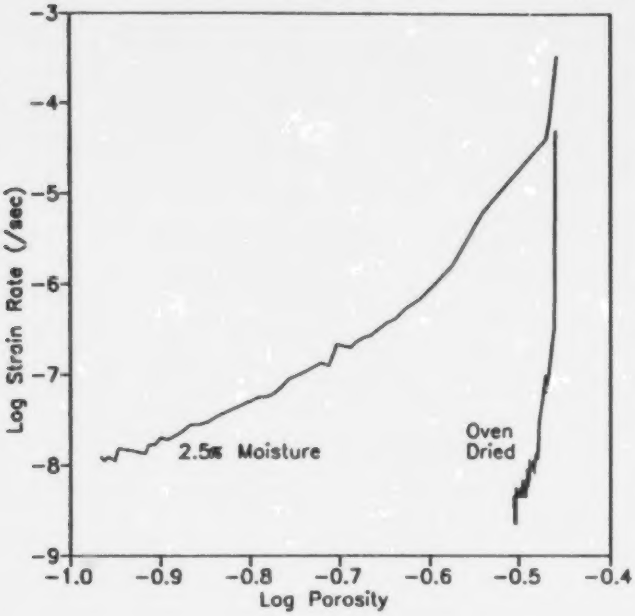

Log $\dot{\epsilon}$ /log n curves for halite backfill at 2.5% w_{ct} and oven dried, compacted under 10 MPa.

FIGURE 5.26

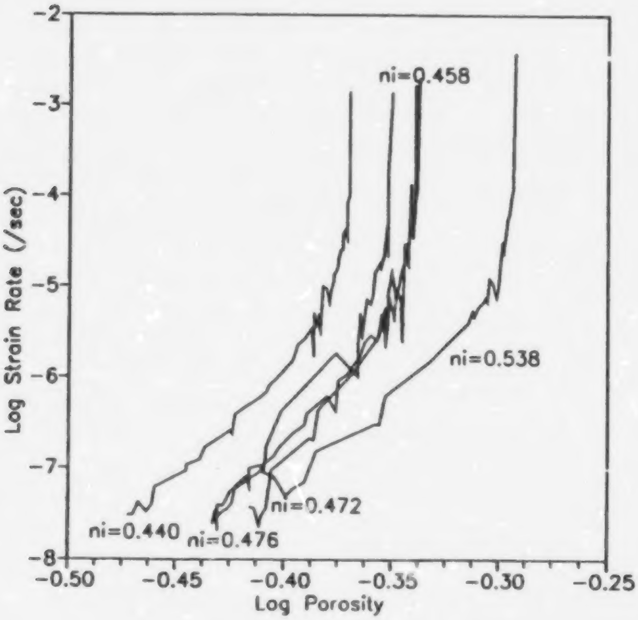

Log $\dot{\epsilon}$ /log n curves for halite backfill compacted under 0.5 MPa at different initial porosities.

In order to resolve this behaviour, scanning electron micrographs were taken of two of the 0.5 MPa test specimens with initial porosities of 0.477 and 0.439 (Figures 5.27 and 5.28). The higher porosity specimen showed at matrix of predominantly large grains (>0.75 mm) (Figure 5.27). The pores between the large grains contained smaller grains which were not in close contact with the surrounding large grains. Hence, a conclusion can be drawn, that at very low compaction stresses (approx. 0.5 MPa) and very high porosities (approx. 0.45) the dominant factor is the number of grain contacts experiencing pressure solution, not the level of stress at these contacts.

5.7.2 Proposed Behavioural Model for Compaction Creep

An empirical model describing the compaction creep behaviour of halite backfill has been developed based on the following assumptions and observations:

a) a very high rate volumetric compaction creep regime dominated by cataclasis is unlikely to operate in situ and has been disregarded;

b) volumetric compaction creep under in situ conditions will occur in two creep rate regimes; a high rate regime dominated by particulate sliding and a low rate regime dominated by pressure solution;

c) the rates of volumetric strain rate within both regimes are a function of stress, provided that porosity is less than 0.4 (i.e. fractional densities > 0.6);

d) the volumetric strain rate $\dot{\epsilon}_{0B}$ at which high rate processes cease and low rate processes begin to dominate can be taken as a constant (Figures 5.15 and 5.19);

e) at porosities of less than 0.25 (i.e. fractional density > 0.75), within the range of stresses and strain rates tested, the two creep rate regimes seem to merge into one with a stress dependency exponent of 3, an indication that intragranular processes begin to dominate.

FIGURE 5.27a

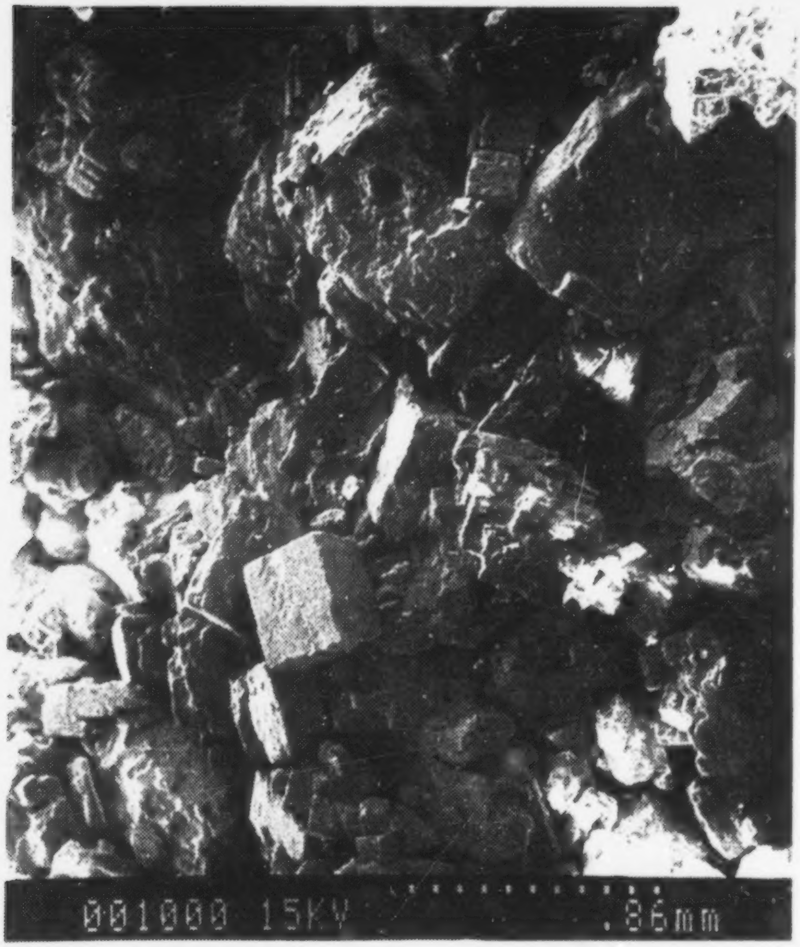

Scanning electron micrographs of halite backfill compacted under 0.5 MPa with an initial porosity of 0.477.

FIGURE 5.27b

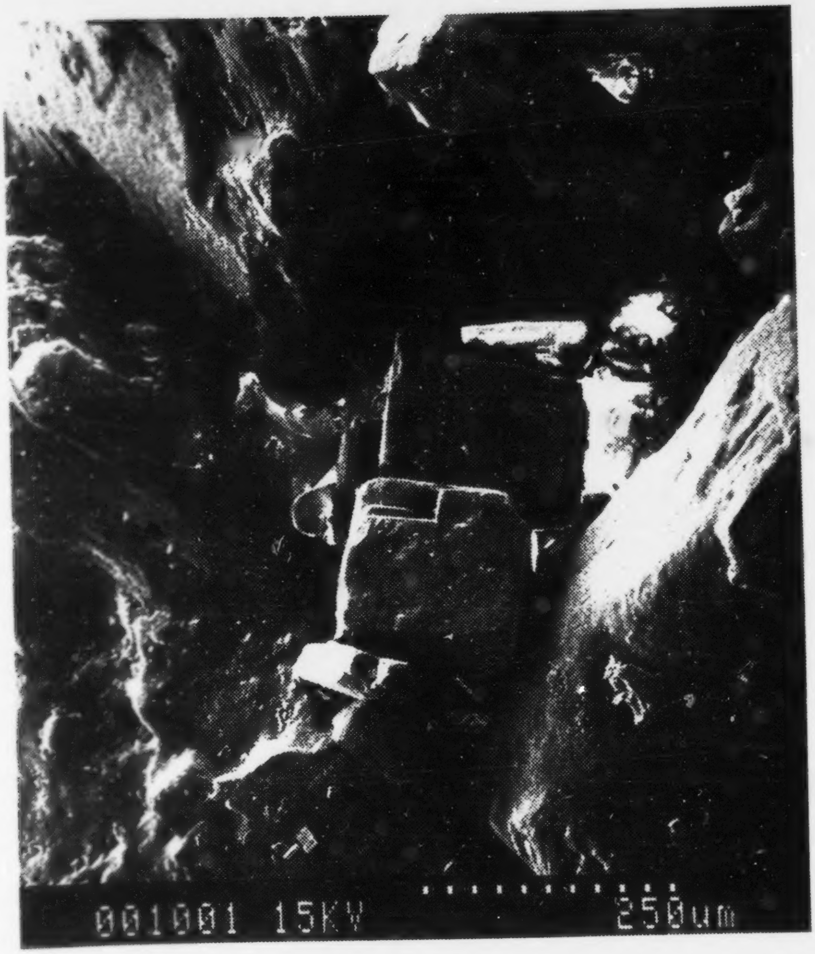

Scanning electron micrographs of halite backfill compacted under 0.5 MPa with an initial porosity of 0.477. Note small non-supporting grains between large grains.

FIGURE 5.28

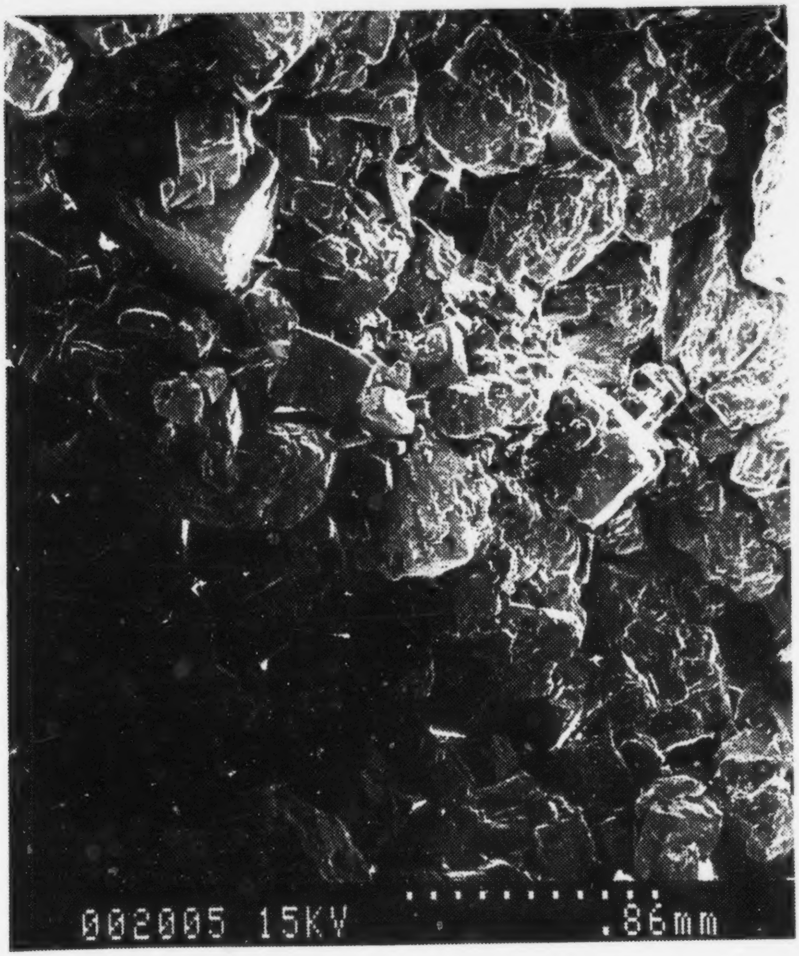

Scanning electron micrograph of halite backfill compacted under 0.5 MPa with an initial porosity of 0.439.

Based on the above assumptions, the following empirical compaction creep law is proposed:

$$\dot{\epsilon}_v = \dot{\epsilon}_{os} \left| \begin{array}{ll} \left(\dfrac{\sigma_m}{\sigma_{os}}\right)^{m_1} & \text{for} \quad \sigma_m \leq \sigma_{os} \\ \left(\dfrac{\sigma_m}{\sigma_{os}}\right)^{m_2} & \text{for} \quad \sigma_m > \sigma_{os} \end{array} \right. \tag{5.10}$$

$\dot{\epsilon}_v$ ...... volumetric strain rate

σ_m ...... hydrostatic stress

$\dot{\epsilon}_{os}$ ...... critical volumetric strain rate at boundary between two volumetric creep rate regimes

σ_{os} ...... reference compaction stress corresponding to $\dot{\epsilon}_{os}$

$$\sigma_{os} = C_1 D^{m_3} \tag{5.11}$$

$$m_1 = a_1 D + b_1 \tag{5.12}$$

$$m_2 = a_2 D + b_2 \quad \text{for } D < 0.74 \tag{5.13}$$

$$m_1 = m_2 = 3.0 \qquad \text{for } D \geq 0.74 \tag{5.14}$$

$$D = \gamma_d / \gamma_f \tag{5.15}$$

D ...... fractional density

γ_d ...... dry density (g/cm^3)

γ_f ...... full dry density (g/cm^3)

$\dot{\epsilon}_{os}$, C_1, m_3, a_1, a_2, b_1, b_2, γ_f ...... constants

The constants derived for DPPC backfill are as follows:

$\dot{\epsilon}_{os}$ = $1.0 \times 10^{-6}\ s^{-1}$
C_1 = 94.6 MPa
m_3 = 7.41
a_1 = 11.5
a_2 = -22.3
b_1 = -5.5
b_2 = 19.5
γ_f = $2.14\ g\ cm^{-3}$

Equations 5.10 to 5.14 can also be written as follows:

$$\dot{\epsilon}_v = \left| \begin{array}{lll} A_{B1}\sigma_m{}^{m_1} & \text{for} & \sigma_m \le \sigma_{oB} \\ A_{B2}\sigma_m{}^{m_2} & \text{for} & \sigma_m > \sigma_{oB} \end{array} \right. \qquad (5.10A)$$

$$\sigma_{oB} = C_2\,\gamma_d{}^{m_3} \qquad (5.11A)$$

$$\left. \begin{array}{ll} m_1 = a_3\gamma_d + b_3 & (5.12A) \\ m_2 = a_4\gamma_d + b_4 & (5.13A) \end{array} \right] \quad \text{for} \quad \gamma_d < 1.58\ \mathrm{g{\cdot}cm^{-3}}$$

$$m_1 = m_2 = 3.0 \qquad \text{for} \quad \gamma_d \ge 1.58\ \mathrm{g{\cdot}cm^{-3}} \qquad (5.14A)$$

and corresponding parameters and constants are:

$$A_{B1} = \dot{\epsilon}_{oB}\,\sigma_{oB}{}^{-m_1} \qquad (5.16)$$

$$A_{B2} = \dot{\epsilon}_{oB}\,\sigma_{oB}{}^{-m_2} \qquad (5.17)$$

$C_2 = 0.337\ \mathrm{MPa} \cdot \mathrm{g}^{-m_3}\ \mathrm{cm}^{3m_3}$

$a_3 = 5.37\ \mathrm{g^{-1}cm^3}$

$a_4 = -10.45\ \mathrm{g^{-1}cm^3}$

$b_3 = -5.52$

$b_4 = 19.47$

The compaction strain rate data with regression constants are tabulated in Table 5.4 and the stress exponent "m" versus fractional density is plotted in Figure 5.29. The fit of the proposed empirical creep law (equation 5.10) to the experimental data is shown in Figure 5.30. The plot of critical stress σ_{oB} versus density, equation (5.11), is shown in Figure 5.31.

The normalized form of this empirical law, as per equations (5.10) and (5.11), is more convenient than equations (5.10A) and (5.11A) and has been used as input in numerical modelling under this program.

Table 5.4: Density/Strain Rate Data, DPPC Halite Backfill Compaction Creep

Density (g/cc)/ Porosity	Stress (MPa)	Strain Rate (sec^{-1})	Regression Constants $\dot{\epsilon} = A^* \sigma_m{}^m$
1.2/0.44	0.17	8.3×10^{-7}	
	0.24	9.4×10^{-7}	
	0.50	2.7×10^{-6}	
	1.03	1.4×10^{-5}	
	2.00	4.0×10^{-5}	
	3.00	1.6×10^{-4}	
1.3/0.39	0.17	2.0×10^{-8}	
	0.34	7.8×10^{-8}	
	0.50	1.2×10^{-7}	$m = 1.49$, $A = 3.2 \times 10^{-7}$
	1.03	4.0×10^{-7}	
	2.00	8.0×10^{-7}	
	3.00	3.5×10^{-6}	
	4.00	3.0×10^{-5}	$m = 6.00$, $A = 8.0 \times 10^{-9}$
	6.00	3.0×10^{-4}	
	8.00	3.0×10^{-3}	
1.4/0.35	1.03	1.0×10^{-7}	
	2.00	1.4×10^{-7}	$m = 1.60$, $A = 7.4 \times 10^{-8}$
	3.00	4.0×10^{-7}	
	4.00	9.0×10^{-7}	
	6.00	4.0×10^{-6}	$m = 4.45$, $A = 1.6 \times 10^{-9}$
	8.00	1.3×10^{-5}	
	10.00	6.0×10^{-5}	
1.5/0.3	2.00	2.6×10^{-8}	
	3.00	8.5×10^{-8}	$m = 3.00$, $A = 3.21 \times 10^{-9}$
	4.00	2.0×10^{-7}	
	6.00	7.0×10^{-7}	
	8.00	3.0×10^{-6}	$m = 3.91$, $A = 7.07 \times 10^{-10}$
	10.00	5.0×10^{-6}	
1.6/0.25	2.00	4.5×10^{-9}	
	4.00	3.8×10^{-8}	
	6.00	1.9×10^{-7}	$m = 3.21$, $A = 4.94 \times 10^{-10}$
	8.00	4.0×10^{-7}	
	10.00	7.0×10^{-7}	
1.7/0.21	4.00	9.0×10^{-9}	
	6.00	4.2×10^{-8}	$m = 3.37$, $A = 8.91 \times 10^{-11}$
	8.00	1.0×10^{-7}	
	10.00	2.0×10^{-7}	
1.8/0.16	6.00	3.1×10^{-8}	
	10.00	5.0×10^{-8}	
1.9/0.11	6.00	5.0×10^{-9}	
	10.00	1.0×10^{-8}	

FIGURE 5.29

Stress Exponent Plot

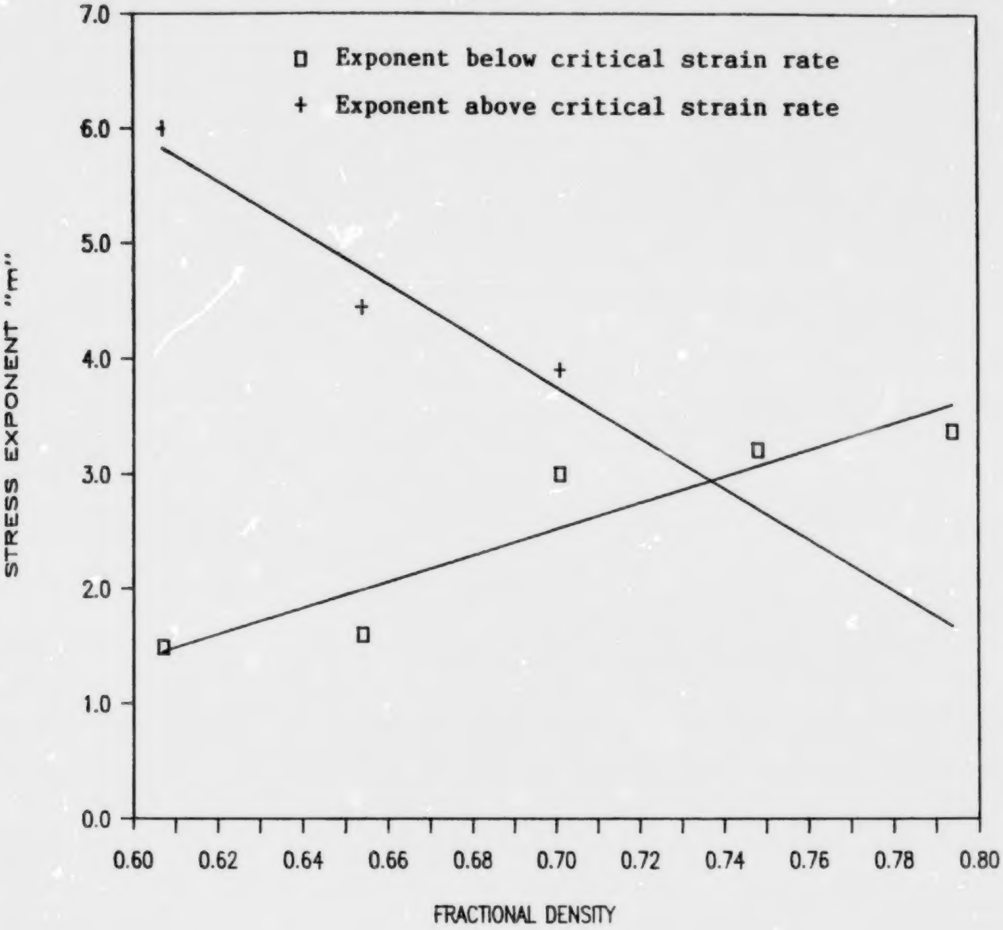

Fractional Density	m below	m above
0.607	1.49	6.00
0.654	1.60	4.45
0.701	3.00	3.91
0.748	3.21	N/A
0.794	3.37	N/A

Regression Equations:

Below $m = 11.485D - 5.515$
Above $m = 19.328 - 22{,}234D$

The two equations become equal at $D = 0.737$

FIGURE 5.30

Halite Backfill Empirical Creep Law Fit

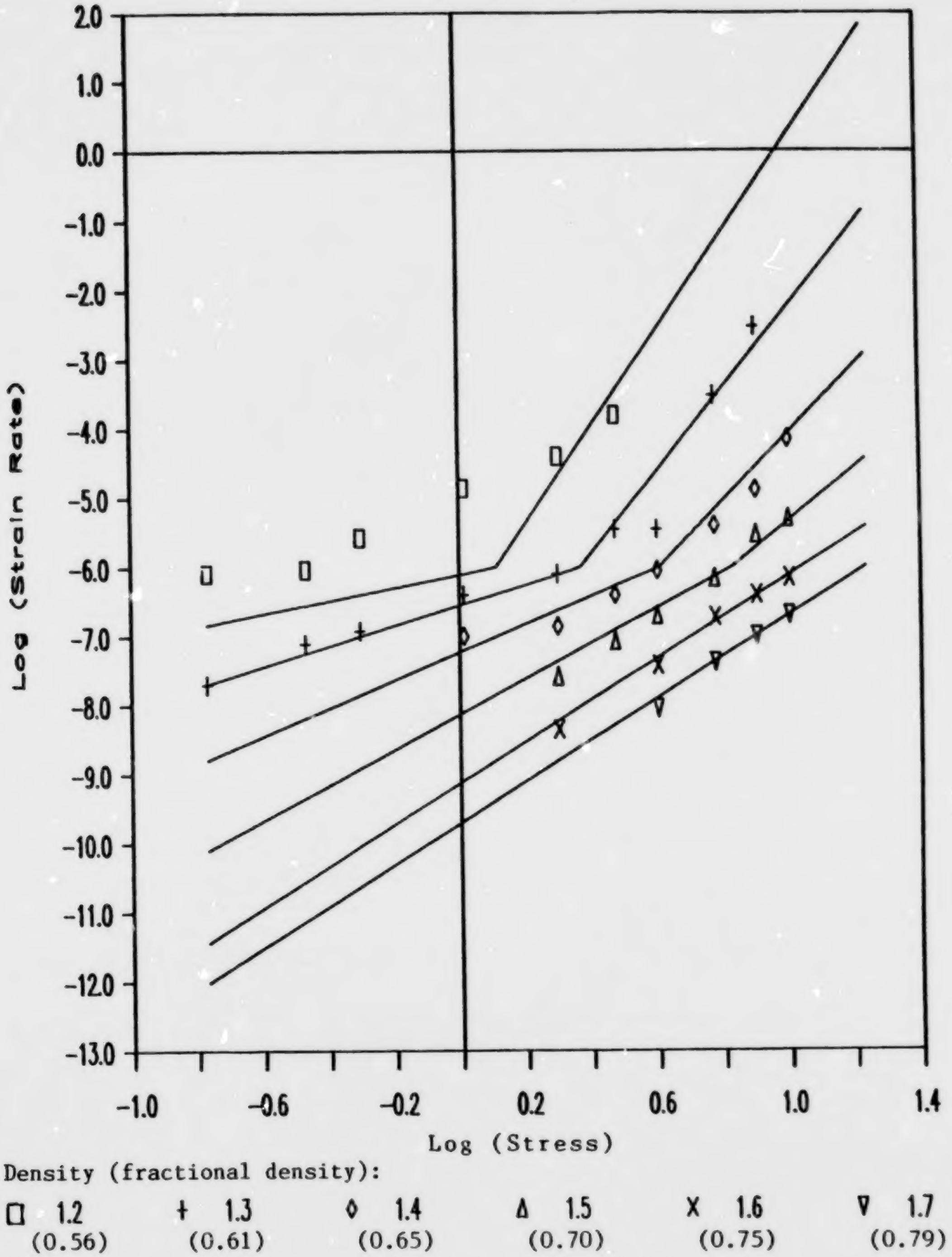

FIGURE 5.31

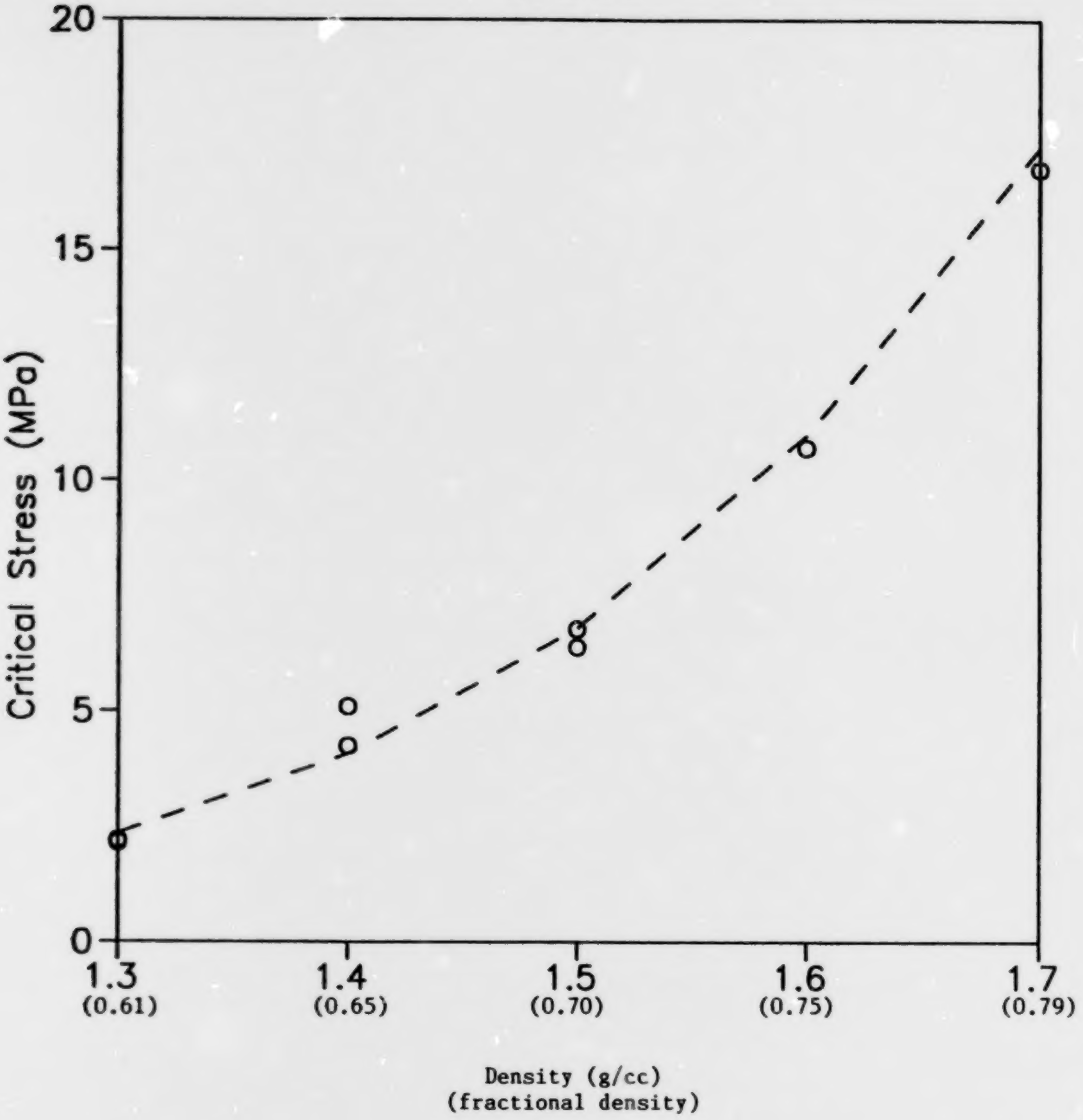

Critical stress versus density

5.7.3 In Situ Compaction Creep Behaviour

In situ conditions will ultimately govern which mechanism dominates the compaction creep of halite backfill. Once placed in the mine, DPPC backfill experiences mine temperatures of about 26°C ± 3°C, and low stress (gravity stresses are about 0.013 MPa per metre of depth of backfill with a fractional density of 0.6) for long periods of time until room closure densifies the backfill to a fractional density of greater than 0.7 where it begins to gain strength. It is currently being placed at relatively low initial fractional density (approx. 0.6). Initially, in situ conditions cover only the low range of stresses and initial densities tested in the laboratory. As such, prediction of in situ behaviour can be somewhat simplified.

The low stresses result in no cataclasis (i.e. n_c approx. n_i), and creep is dominated by pressure solution. This justifies the use of only the low rate regime portion of the compaction creep equation, and a constant value for $\dot{\epsilon}_{OB}$, of approximately 1.0×10^{-6} sec^{-1}.

5.7.4 Applicability to Other Halite Backfills

Halite backfills from other Canadian potash mines (chiefly in Saskatchewan) will experience conditions similar to those at DPPC. Temperatures do vary between mines (approx. 18° to 30°C), however, this is not expected to have a large effect on creep rates. Any behavioural differences noted in other backfills will primarily be backfill dependent.

The empirical model derived from this study can be extrapolated to approximate the behaviour of differently grained material by determining a new value of $\dot{\epsilon}_{OB}$ based on the relationship $\dot{\epsilon}_v \alpha \ 1/d^3$.

Assuming a low initial porosity (i.e. high fractional density) and a constant value for $\dot{\epsilon}_{OB}$ of 1.0×10^{-6} sec^{-1} and using the mean grain size of DPPC backfill (about .0005 m), the following expression can be derived;

$$\dot{\epsilon}_{os} = \frac{A_s}{d^3} \qquad (5.18)$$

where: A_s .... scaling constant
d .... mean grain size

or

$$A_s = \dot{\epsilon}_{os} \cdot d^3$$

All other relationships obtained for DPPC backfill should be relatively applicable to other halite backfills.

5.7.5 Compacted Backfill Under Shear Stress

Under a shear stress, compaction creep can be expected to proceed more slowly as the backfill will dilate as well as densify. The two processes are additive, resulting in net volumetric compaction or dilation depending on the magnitude of the shear stress. At high enough shear stresses, the material will continue to dilate until it undergoes strain weakening. Shear stresses are not likely to substantially affect backfill until its fractional density is high (i.e. low porosity).

In order to determine the creep behaviour of compacted backfill, a specimen was compacted in the double piston oedometer (Figure 5.2b) under 30 MPa until it had a very low porosity (brine was expelled near the end of the compaction). It was then placed in a triaxial cell and loaded hydrostatically (20 MPa) to ensure maximum compaction. After about 10 days, a shear stress was applied to the specimen and it was allowed to creep until it was in steady state. Shear stresses were then altered and a new steady state creep rate achieved (Figure 5.32). Also included on Figure 5.32 is creep behaviour of

FIGURE 5.32

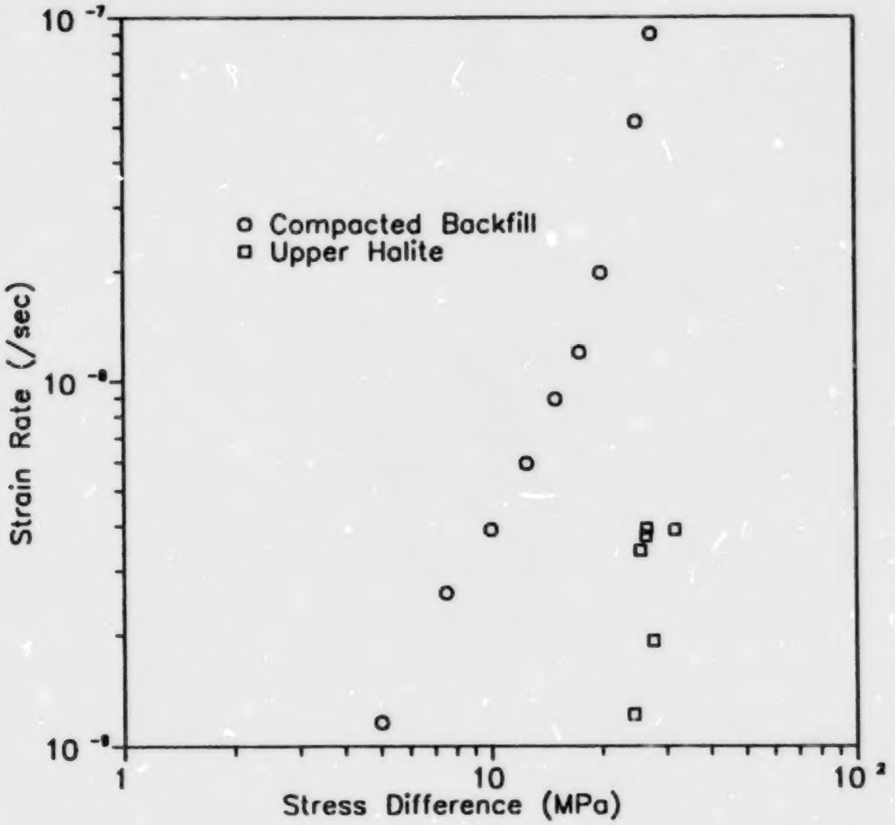

Creep of fully compacted backfill and Upper Halite under a shear stress.

Upper Halite. The compacted backfill creeps about an order of magnitude faster than Upper Halite at a given stress. This is likely due to the higher moisture content of the compacted backfill and a lower grain size.

5.7.6 Uniaxial Brittle Strength (σ_c) of Halite Backfill

The brittle strength of halite backfill is largely a function of its fractional density (porosity) and compaction rate used to achieve that fractional density (porosity). In situ the backfill will densify slowly under low stresses. Gravitational stresses will be the major stresses initially acting on the backfill. At a placement porosity of 0.4 (i.e. fractional density = 0.6), gravitational stresses will average about 0.013 MPa per metre of depth. In 12 m high rooms, the maximum initial stress in the backfill under self-weight will be less than 0.2 MPa. Pressure solution will be the primary densification mechanism.

In the laboratory, the test specimens must be compacted rapidly relative to in situ. It is impractical to try to compact brittle strength test specimens to low porosities (< 0.3) at stresses similar to in situ; specimen 9010 took about 10 days to compact to a porosity of about 0.18 under a stress of 10 MPa. High rate compaction is dominated by cataclasis. As cataclastic processes deform by breaking material (i.e. crushing, fracturing), brittle strength increases are predominantly due to those achieved by increases in frictional surface area between grains.

Under the low rate compaction in situ, pressure solution creep anneals adjacent crystals; the dissolved ions from both grains precipitate together in pores, joining the two grains. This increases the brittle strength of the backfill by making it a rock with porosity rather than a granular mass held together by friction.

The greater the amount of pressure solution creep involved in backfill compaction, or the lower the compaction rate, the higher the brittle strength of the backfill. In situ, where compaction rates are slow, the backfill will achieve maximum strength. Although pressure solution was noted during compaction of many brittle strength tests specimens, the laboratory specimen shows lower strength than equivalent in situ material due to cataclastic deformations during the early stage compaction.

Laboratory brittle strength test results were extrapolated to determine approximate in situ values. The curves shown in Figure 5.12 were extrapolated to the left to a 'zero compaction rate' brittle strength (Table 5.5). These values represent the approximate brittle strength of backfill compacted slowly.

Table 5.5: Slopes of σ_c vs. Compaction Stress Curves

Porosity	Fractional Density	Slope	σ_c @ Zero Compaction Rate (MPa)
0.14	0.86	-0.051	13.86
0.18	0.82	-0.048	8.53
0.22	0.78	-0.078	6.84
0.26	0.74	-0.033	3.19

An assumption has been made in extrapolating the curves in Figure 5.12. It was assumed that the curves remain linear and do not curve upwards (i.e. increased brittle strength) or downwards (i.e. decreased brittle strength) under low compaction rates. It is unlikely that the brittle strength of the material decreases when compacted slowly; the primary low rate compaction mechanism, pressure solution, is a strengthening mechanism. If little or no material breakage occurs, pressure solution creep may develop more brittle strength than the curves in Figure 5.12 predict. In the latter case, the extrapolated brittle strength will be a conservative estimate of the final brittle strength.

In order to examine the effects of high and low rate compaction on halite backfill grains, a set of high stress compaction test specimens was prepared (Table 5.1) and thin sectioned. A qualitative analysis of the thin sections (Figures 5.33, 5.34, 5.35, 5.36) has shown:

a) a possible reduction in overall grain size;
b) grains showing apparent fractures.

The reduction in overall grain size is difficult to quantify. However, very few large grains (> 1 mm) are visible in any of the photomicrographs, suggesting that the large grains originally present in the backfill (Figure 5.3) have been broken into smaller grains. A reduction in grain size due to grain fracture appears to be supported by the number of grains which appear to contain fractures. These grains are predominant in specimens of high fractional density and specimens consolidated under high stress.

The specimens showing the greatest number of fracture grains are the specimens which have either the lowest overall σ_c or the lowest brittle strength for a given porosity. In general, the higher the rate of compaction, the greater the number of fractured grains and the lower the σ_c .

5.7.7 Uniaxial Brittle Strength of Fully Compacted Halite Backfill

In situ, as the stopes close, the backfill will eventually become fully compacted. Figure 5.12 shows the increase in σ_c associated with lower

FIGURE 5.33

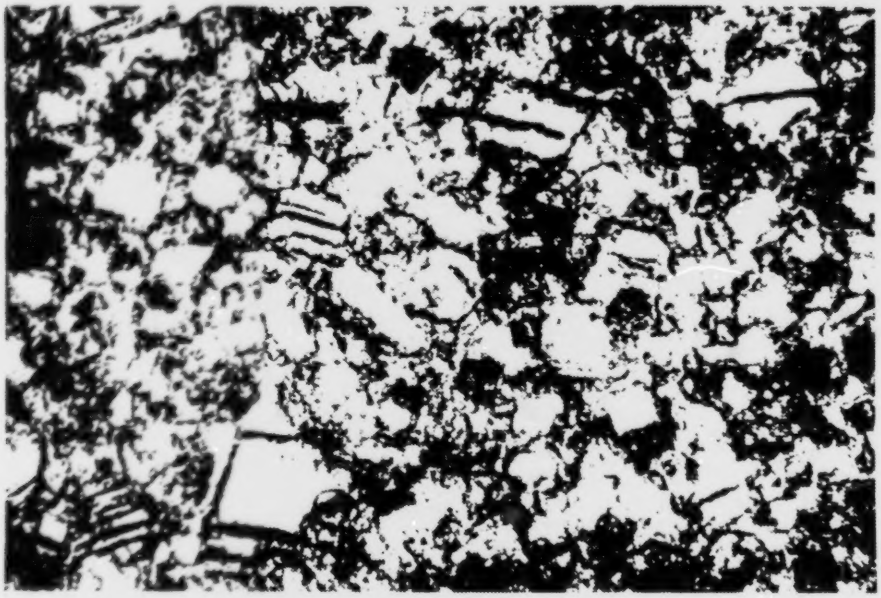

Photomicrograph of DPPC halite backfill compacted to a porosity of 0.26 under 20 MPa. Scale bar is 1 mm.

FIGURE 5.34

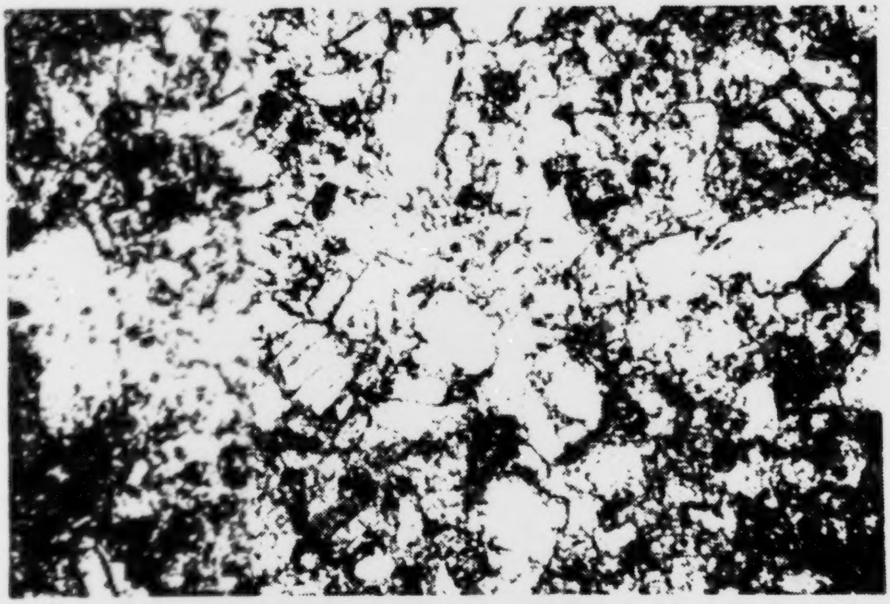

Photomicrograph of DPPC halite backfill compacted to a porosity of 0.26 under 34 MPa. Scale bar is 1 mm.

FIGURE 5.35

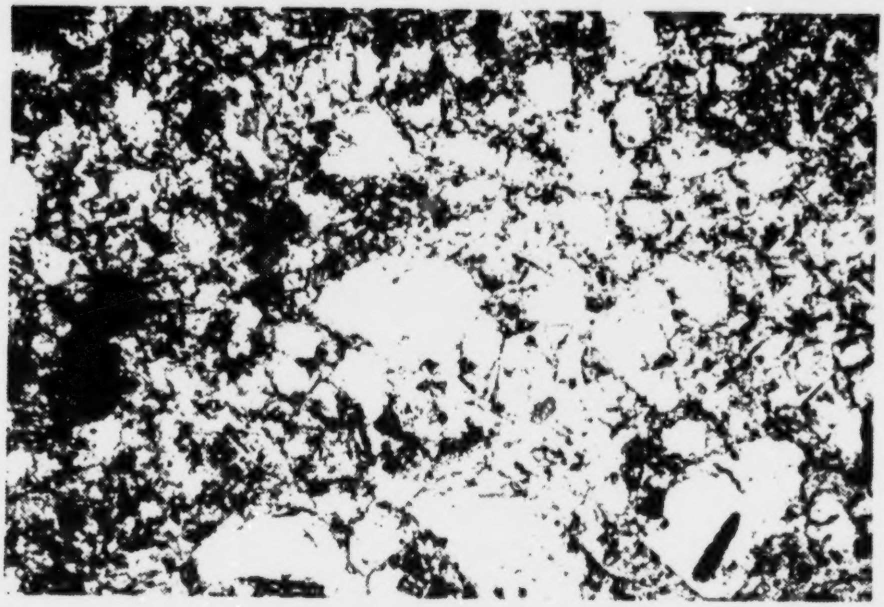

Photomicrograph of DPPC halite backfill compacted to a porosity of 0.14 under 20 MPa. Scale bar is 1 mm.

FIGURE 5.36

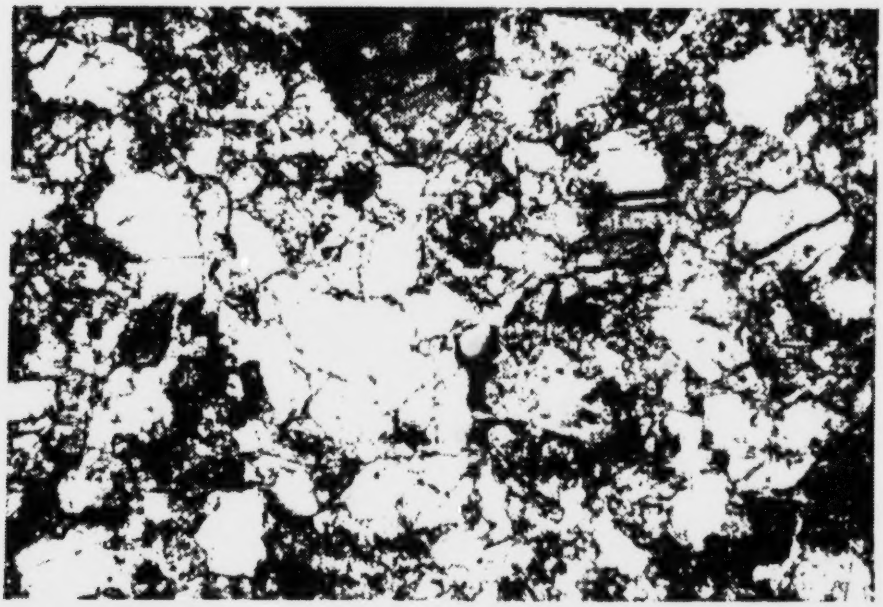

Photomicrograph of DPPC halite backfill compacted to a porosity of 0.14 under 50 MPa. Scale bar is 1 mm.

porosity materials. A linear extrapolation of these curves to a backfill with a porosity of 0.01 (assumes no air porosity and about 1% brine) yields the values listed in Table 5.6. Table 5.6 also includes the predicted values of 1% and 0% porosity backfill based on the 'zero compaction stress' σ_c values listed in Table 5.5 and σ_c of Upper Halite.

Although several of the curves in Figure 5.12 appear to be concave, a linear variation of σ_c with porosity in salt has been noted elsewhere (Figure 5.37) (Kelsall and Nelson, 1983). Similar trends were noted for 'zero compaction stress' σ_c values for DPPC halite backfill (Figure 5.38). It can be suggested from an extrapolation of the curve in Figure 5.38 that backfill with a fractional density of less than 0.7 has little of no brittle strength. Results from a linear regression of Figure 5.38 shows that the uniaxial compressive strength can be defined in terms of fractional density as follows:

$$\sigma_c = 91.15D - 64.81 \qquad (5.19)$$

Table 5.6: Predicted Ultimate σ_c Values, DPPC Halite Backfill

Compaction Stress (MPa)	Predicted σ_c (MPa)
50	19.43
40	18.86
30	21.62
0*	25.71
0**	26.61
Upper Halite (as tested)	29.22

* Linear extrapolation of zero compaction stress σ_c (Table 5.5) @ porosity = 0.01 and a fractional density of 0.99

** Linear extrapolation of zero compaction stress σ_c (Table 5.5) @ porosity = 0 and a fractional density of 1.0

FIGURE 5.37

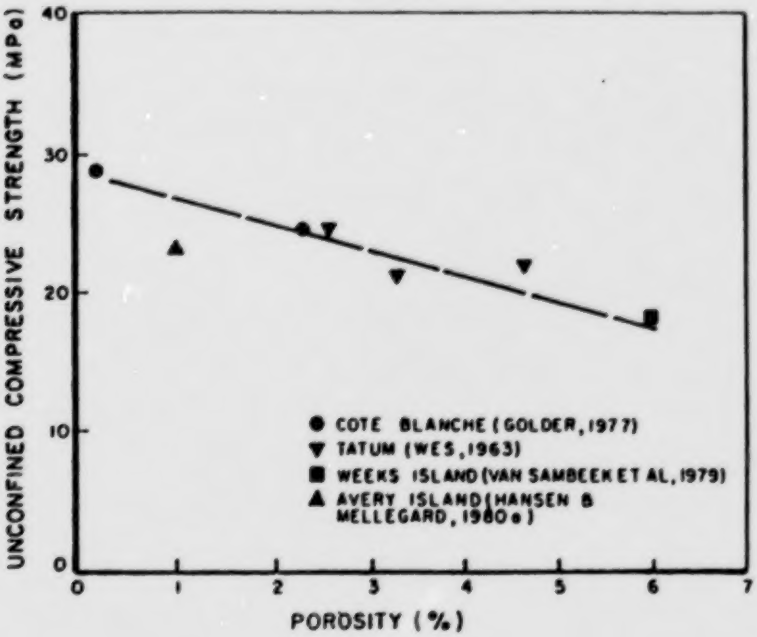

Unconfined compressive brittle strength as a function of porosity (from Kelsall and Nelson, 1983)

FIGURE 5.38

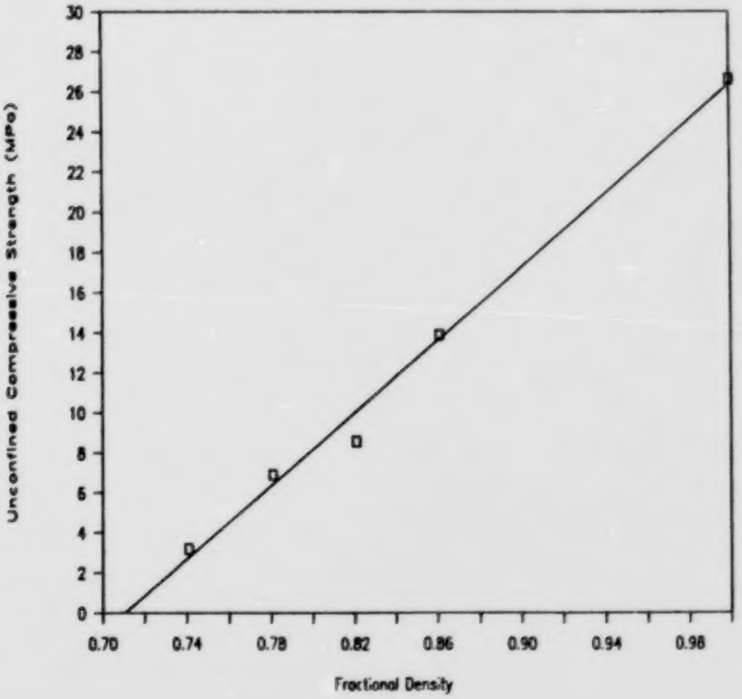

'Zero compaction stress' σ_c as a function of fractional density for DPPC halite backfill.

5.7.8 Apparent Stiffness of Halite Backfill

True linear elastic parameters are time and stress independent. They reflect the instantaneous fully recoverable deformations material undergoes when placed under stress. A porous granular material placed under stress undergoes grain crushing, fracture and reorientation (cataclasis) as well as elastic deformation of individual grains. Separating the two types of deformation is difficult. The stiffness of halite backfill is, therefore, a bulk measurement of the total instantaneous deformation, both recoverable elastic and non-recoverable cataclastic, the material undergoes when subjected to a stress.

The curves shown in Figure 5.13 show less stress dependence than other properties measured during this study. This is due to the near linear relationship of cataclastic processes and the 'elastic' response of the grains to stress. The test results tabulated in Table 5.7 were combined to determine an equation describing the relationship between M_{50} and fractional density "D"

$$M_{50} = 5.4\ D^{9.3} \tag{5.20}$$

This relationship predicts that materials with fractional densities < 0.7 (i.e. porosities >0.3) will have very low stiffness.

No lateral strain measurements were made during UCS testing for determination of Poisson's ratio. Based on the assumption that the Poisson's ratio of fully compacted backfill is the same as for the intact salt (ν = 0.33) The following has been used in the numerical modelling:

$$\nu = 0.33\ D^{-0.77} \tag{5.21}$$

Initially, at a low fractional density, halite backfill will behave similar to a perfectly plastic material with a Poisson's Ratio of approximately 0.5. As the material compacts, Poisson's Ratio will decrease according to equation (5.21).

Table 5.7: Stiffness Data, DPPC Halite Backfill

Test No.	Density (g/cc)/ Porosity	Compaction Stress (MPa)	Stiffness (M_{50}) (GPa)
9550	1.82/0.15	50	1.13
9050	1.76/0.18	50	0.49
8550	1.69/0.21	50	0.27
8050	1.55/0.28	50	0.19
9540	1.86/0.13	40	0.97
9040	1.77/0.18	40	0.77
8540	1.65/0.23	40	0.44
8040	1.55/0.28	40	0.24
9530	1.84/0.14	30	1.42
9030	1.76/0.18	30	1.01
8530	1.65/0.23	30	0.71
8030	1.56/0.27	30	0.23
9020	1.77/0.17	20	1.20
8520	1.66/0.22	20	0.77
8020	1.56/0.27	20	0.42
9010	1.76/0.18	10	2.23

Because brittle strength is a function of compaction stress, it is unclear if triaxial brittle strength test results can be extrapolated in a similar manner to the σ_c values. During testing, the specimens were confined and initially underwent a period of compaction before dilating and eventually strain weakening (Figure 5.39). The amount of compaction was dependent on the confining stress and the initial density. To determine the true 'zero compaction stress' brittle strength, it would require several sets of triaxial tests performed on specimens compacted under other stresses.

Because it was not clear exactly how triaxial brittle strengths can be extrapolated to in situ values, the values obtained from this study were used for analysis. It is felt that these values are conservative. The triaxial brittle strength data were fit to two failure criteria:

FIGURE 5.39

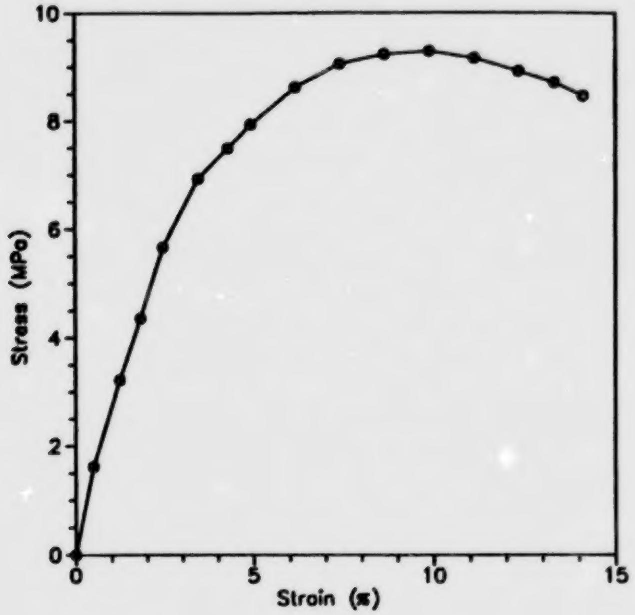

Stress/strain diagram for halite backfill compacted to n = 0.22, confining stress 1.03 MPa, axial strain rate 10^{-4} sec^{-1}.

FIGURE 5.40

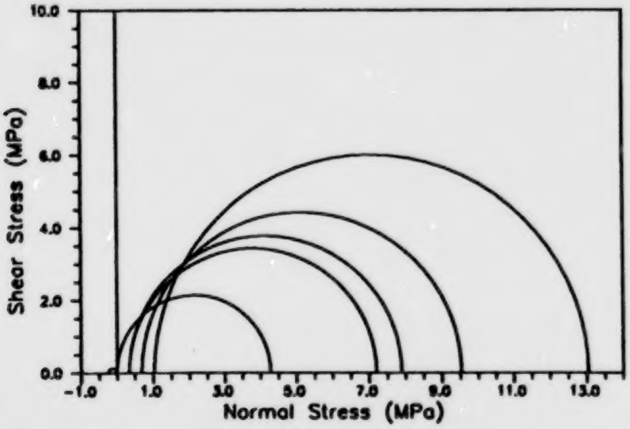

Mohr Coulomb diagram for halite backfill compacted to n = 0.22.

a) a Mohr-Coulomb linear failure criterion;

b) an exponential failure envelope.

The Mohr-Coulomb failure envelope is a linear equation of the form:

$$\tau = C + \sigma_n \cdot \tan \phi \tag{5.22}$$

where:
τ = shear strength
C = cohesion (Y axis intercept)
σ_n = normal stress
ϕ = angle of internal friction (slope)

These fitted constants C and ϕ are listed in Table 5.8. A typical Mohr-Coulomb diagram for DPPC halite backfill is shown in Figure 5.40.

Using the values from Table 5.8, a linear regression indicated that cohesion (C) and the angle of internal fraction (ϕ) could be defined in terms of fractional densities by the following functions:

$$C = 8.25D - 5.31 \tag{5.23}$$

$$\phi = 116.25D - 43.25 \tag{5.24}$$

Table 5.8: Mohr-Coulomb Brittle Strength Parameters

Porosity	C (MPa)	ϕ (°)
0.26	1.15	33.0
0.22	0.80	52.0
0.18	1.25	56.5
0.14	1.90	62.0
Upper Halite	3.00	68.5

An exponential failure envelope for intact salt was developed by Rothenburg (Dusseault et al., 1987). It is an equation of the form:

$$\sigma_Y = (\sigma_C/2) \left\{(1 - RM) + [(1 + MR)^2 + 4M(\sigma_3/\sigma_C)]^{0.5}\right\} \qquad (5.25)$$

where: $R = (\sigma_T/\sigma_C)$
σ_T = tensile strength
σ_C = unconfined compressive strength
M = fitting parameter
σ_3 = minor principal stress

The value of R has been assumed constant at 0.06 (see Section 5.6.6). The fitting parameter M increases in value with increasing fractional density indicating reduction in the curvature of the failure envelopes with increasing density. M has values of 27.5, 43, 47 and 200 for the 0.74, 0.78, 0.82 and 0.86 fractional density test specimens, respectively. Performing a linear regression upon the logarithmic values of the M and the corresponding fractional densities showed that M could be defined by:

$$M = 550\ D^{10.16} \qquad (5.26)$$

The value of M for Upper Halite is 500 (CANMET, 1987). A typical exponential failure envelope is shown in Figure 5.41.

At low porosity, (i.e. high fractional density) both failure criteria adequately describe the behaviour of halite backfill. However, at higher porosities (i.e. low fractional densities), the exponential failure criterion offers a better fit.

FIGURE 5.41

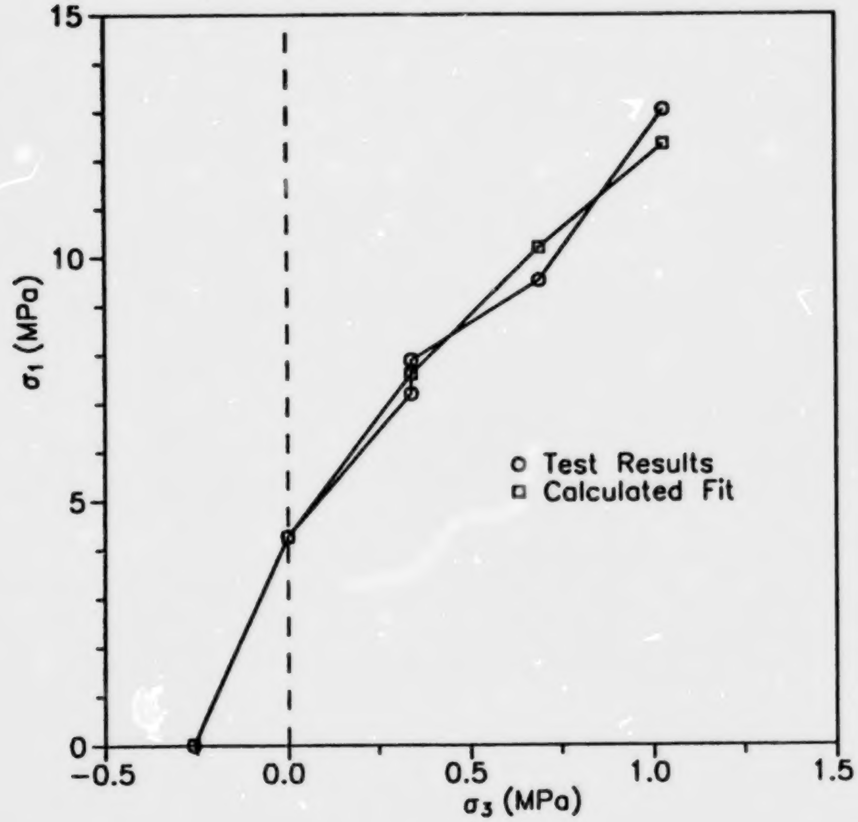

Exponential failure envelope for halite backfill compacted to $n = 0.22$. $R = 0.06$, $M = 43$.

SECTION 6.0

6.0 LABORATORY TESTING OF ENGINEERED BACKFILL

This section outlines the results of a test program carried out to determine the effects of additives on the strength of DPPC halite backfill. Two types of backfill applications were examined:

a) mining applications for supporting overburden in mining panels;
b) structural engineering applications for construction of retaining walls, bulkheads, etc.

Two types of additives were examined during this study; cements (Ordinary Portland cement, Type 10, and cement Fondu, a calcium alumina cement) and sand from the Sussex Silica quarry. Both cement and sand were examined for long term and short term strength development.

6.1 Previous Work

The use of additives to improve backfill performance has been practised for almost as long as backfilling itself (Wayment, 1978). Additives are generally chosen because of their effect on the backfill, as well as their availability and cost. Many materials have been used including cement, sand, blast furnace slag and fly ash. However, because backfilling programs in potash mines are relatively new, there is little data available on the effect of additives on the mechanical behaviour of halite backfill.

Cement is a common additive as in many cases. It yields the greatest strength increase per unit cost, however, there has been little research done into the effect of highly saline brines and aggregates on the behaviour of cement and concrete. Wakely et al. (1981) examined a borehole plug made of salt concrete and determined that, although weak (σ_c approx. 2.59 MPa), it had remained chemically stable with respect to the host rock, a bedded evaporite deposit. Theissing et al. (1978) studied the hydration of brine cement pastes (NaCl and $CaCl_2$) and noted that $CaCl_2$ can speed up the hardening of cement. They also observed that Cl^- ions (particularly from $CaCl_2$) combine with hydrated minerals in hardened cement pastes, however, they did not discuss the effects of this combination on strength properties.

In Germany, nuclear waste is currently being placed in abandoned salt mines for long term disposal. Once the waste has been placed, the rooms are backfilled with crushed salt and sealed with bulkheads made of salt concrete (Kappei, 1986). These bulkheads are hydraulically placed and effectively seal the room. Unfortunately, Kappei (1986) does not describe the salt concrete 'recipe', however, he notes that the rapid increase in stress in the bulkheads indicates that they are probably stiffer than the surrounding rock. Generally, the effect of salts such as halite and sylvite on cement and concrete strengths is not well understood.

Materials such as clay, sand and fly ash may not add strength to a backfill directly, but can improve the long term strength of a backfill/cement mixture. Also, well-graded granular materials (wide range of particle sizes) can improve the initial strength of a backfill by reducing its initial porosity.

In Saskatchewan, many potash mine tailings include insoluble materials such as clay, quartz, and anhydrite (Johnson et al., 1984). These materials have little effect on the backfill behaviour until they make up about 30% of the backfill. At higher quantities, the behaviour of the backfill is dominated by the insolubles rather than the salt grains.

Spiers et al. (1989) have examined the addition of small quantities of anhydrite (2-3%) and large grains of salt to granular halite. They noted that the anhydrite had little effect on the mechanical behaviour (creep) of the granular halite. The large grains, however, reduced the overall compaction rate of the backfill, but not the rate of the finer grained matrix. They suggest that the mass fraction of large grains to fine matrix grains should not exceed 20%, otherwise the components can interact mechanically and will impede compaction in the matrix. This content of 'non-compacting' particles is similar to that noted by Johnson et al. (1984).

6.2 Materials

Backfill additives have two general applications within a mine. For mining applications a backfill additive is included as a small percentage of all backfill placed in a mine (i.e. cement is often included as 3-8% of the total backfill volume). In structural applications, backfill additives are used for engineering purposes such as the construction of retaining walls or bulkheads. For the latter, volumes are much reduced and structures often have specific requirements (i.e. support strength) allowing larger amounts of additive to be used.

The requirements for a backfill additive for general use throughout the mine are as follows:

a) high efficiency/cost ratio; this is a somewhat qualitative measure which relates the benefits (strength, reduced initial porosity) an additive provides, to its cost.

b) availability; the material should be locally available in the quantities required. The greater the transport required, the higher the cost of the additive and the lower its efficiency/cost ratio.

The primary requirement for a backfill additive for structural use (i.e. specific locations within the mine) is rapid strength development. Ideally, the backfill/additive mixture should develop a Unconfined Compressive Strength (σ_c) within the range of pillar materials in 3 to 6 months.

In the case of mining application, reduction of volumetric creep within backfill, combined with required gain in strength in 2 to 4 years, may satisfy the requirement.

Two types of cement were examined initially; ordinary Portland Cement (Type 10) and cement Fondu. Cement Fondu is a high alumina cement (HAC), which has high early strength (1-2 days) and moderate heat of hydration. It cannot be used for structural purposes under conditions of temperatures greater than 33°C and/or 100% humidity and it must be prepared with a water/cement ratio (by volume) of less than 0.4.

Seven sand mixture samples were obtained from the Sussex Silica quarry near Denison-Potacan in New Brunswick. These were mixed in equal proportions (by weight) for use in testing. A grain size curve for the mixed sample is shown in Figure 6.1. The sand mixture has particles ranging up to about 15 mm in diameter. For σ_c and compaction testing, all of the grains of 6 mm were removed from the mixture in order to keep the ratio of the diameter of the test sample to the largest particle size above 10. The grain size curve for the tested sand mixture is also shown in Figure 6.1

The backfill materials were obtained from the Denison-Potacan processing mill in early 1986. The backfill is primarily halite (NaCl) (approx. 98-99%) with some sylvite (KCL) (approx. 1-2%). The grain size distribution of the backfill is shown in Figure 6.1.

The brine used for concrete preparation and to add moisture to compaction tests was process brine, also obtained from the DPPC plant. It is assumed to be fully saturated with respect to both halite and sylvite.

The specific gravities of DPPC halite backfill, the sand mixture and the cements are 2.14, 2.65, and 3.10, respectively. Because materials with varying specific gravities were combined during the test programs, reporting of backfill 'denseness' has been done in terms of porosity. Porosity was calculated as:

$$n = \frac{(G_{sb} - \gamma)}{G_{sb}} \tag{6.1}$$

where: n = porosity

G_{sb} = bulk specific gravity

γ = density (g/cc)

FIGURE 6.1

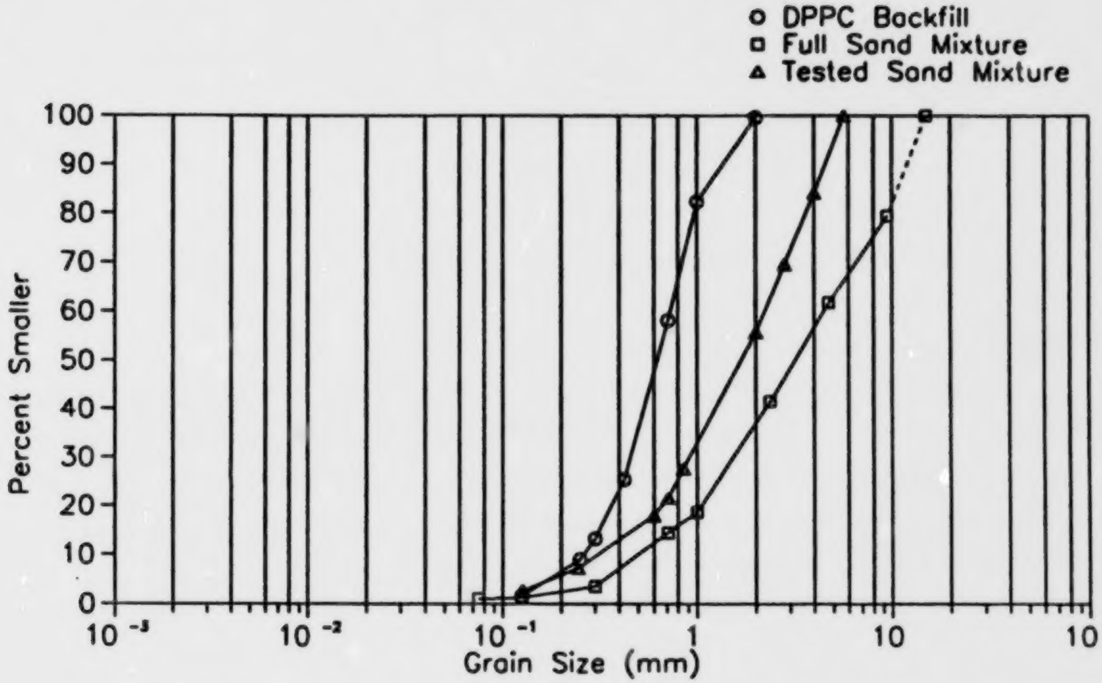

Grain size distributions of DPPC halite backfill, full silica sand mixture, and tested silica sand mixture.

Bulk specific gravity was calculated as:

$$G_{sb} = \sum_{i=1,j} \frac{V_t - V_i}{V_t} * G_{si} \tag{6.2}$$

where: i = material number
j = number of materials
V_t = total volume
V_i = volume of material 'i'
G_{si} = specific gravity of material 'i'

6.3 Test Program

Four properties were examined:

a) initial porosity;

b) strength of mining backfill (low cement contents (3-10%));

c) compaction behaviour;

d) strengths of structural backfill (high cement contents (15-30%)).

Porosity of backfill/sand mixes was tested by mixing 5000 g of backfill (with 2.5% moisture) with 0 to 10% sand by weight (also with 2.5% moisture). The backfill and sand mixtures were poured into a 20 cm diameter plexiglass cylinder. The depth of the mixture was measured and the density calculated by:

$$\gamma = \frac{M_b + M_s}{\pi \cdot r^2 \cdot h} \tag{6.3}$$

where: γ = density
M_b = Mass of backfill
M_s = Mass of sand
r = cylinder radius (10 cm)
h = depth of backfill/sand mixture

Porosity was calculated using Equation (6.1).

After the initial porosity was measured, the mixture was vibrated on a vibrating table for 1 minute and a final porosity calculated. No load was applied to the surface of the backfill.

The compaction tests were performed in 1-D, oedometer style cells (Figure 6.2). The tests were performed on standard DPPC backfill material (2.5% moisture) with 5 and 10% sand by weight at 0.5 MPa. The results were compared to similar tests performed on backfill alone.

The backfill/brine/cement mixtures for mining backfill were examined by preparing test cylinders of salt concrete made with 70% backfill, 3, 7 and 10% cement and 27, 23 and 20% brine (by volume). The test cylinders were allowed to cure for 7 to 28 days and then tested for UCS.

The backfill/brine, brine/cement and backfill/brine/cement mixtures for structural backfill were examined by preparing test cylinders of salt concrete with 60% backfill, 15 to 30% cement and 25 to 10% brine (by volume). The cylinders were tested for UCS as soon as they could be removed from the cardboard molds and had dried after 6-7 days.

6.4 Results

6.4.1 Mixture of Backfill and Sand

The initial porosities of the backfill/sand mixtures decreased with increasing sand content (Table 6.1; Figure 6.3). The final porosities showed a similar rate of decrease in porosity, indicating that both the backfill and the sand vibro-compact in a similar manner.

Table 6.1: Porosities of Backfill/Sand Mixtures

Sand Content (%)	Initial Porosity	Final Porosity
0	0.65	0.61
2	0.63	0.60
5	0.62	0.58
7	0.61	0.58
10	0.61	0.57
15	0.60	0.56
20	0.60	0.56

FIGURE 6.2

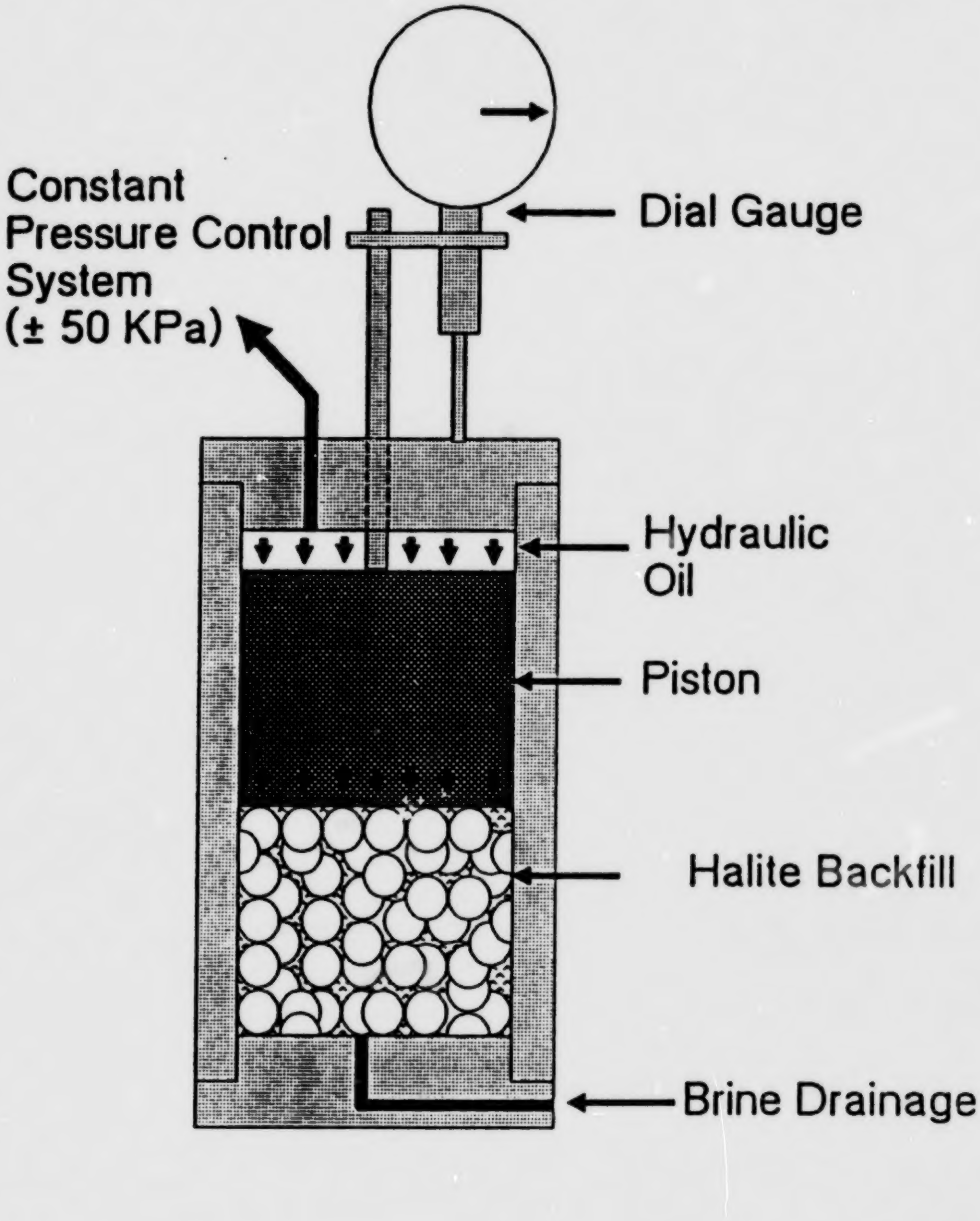

1-D oedometer used for compaction testing of DPPC backfill and halite backfill/sand mixes.

FIGURE 6.3

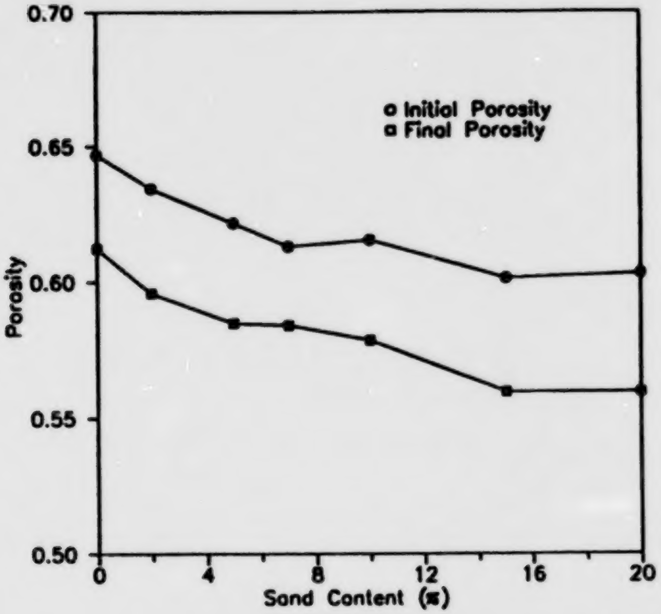

Porosities of DPPC halite backfill/sand mixes before (initial) and after (final) vibro-compacting for 1 minute.

FIGURE 6.4

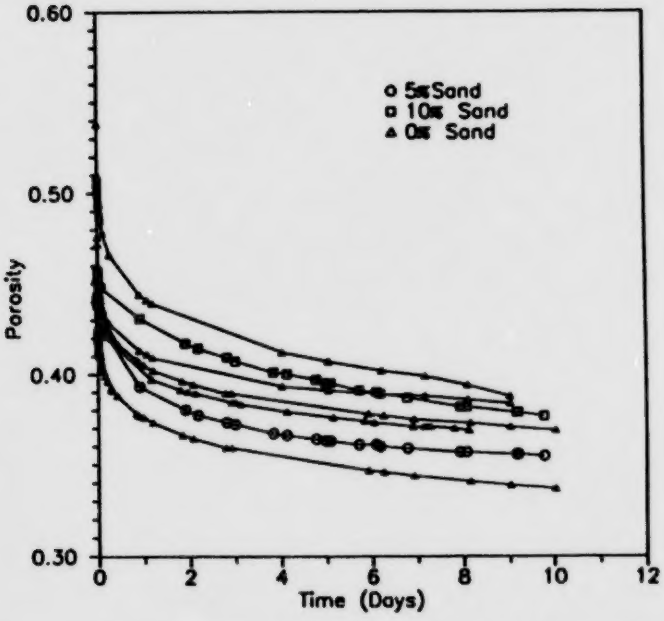

Compaction curves for DPPC halite backfill and halite backfill with 5 and 10% sand added. All tests were performed with material at 2.5% moisture content under 0.5 MPa.

It should be noted that the porosities achieved (both initial and final) are considerably higher than in situ placement porosities (about 0.35 to 0.4). Laboratory conditions have not taken into account the stresses encountered in backfill due to self-weight and mine vehicle transit. As well, the initial moisture content of freshly placed backfill is higher than 2.5% and this is also likely to decrease initial porosities. However, the relative effects of adding a well-graded granular material to the poorly graded DPPC backfill in the laboratory should be similar in situ.

There was little noticeable difference in compaction behaviour between 'pure' halite backfill and backfill with 5 and 10% sand content (Figure 6.4). This agrees with the observations of Johnson et al. (1984) and Spiers et al. (1989), who suggested that backfill behaviour will only be dominated by 'non-creeping' materials when they make up greater than 20-30% of the backfill volume. The variations between the seven curves in Figure 6.4 is due to variations in initial porosity. This effect is dominantly an artifact of laboratory testing; materials with low initial porosities such as those noted in situ (approx. 0.4) display a much smaller dependence on initial porosity.

6.4.2 Mixture of Backfill, Brine and Cement

Results of the strength development for the mixture of halite backfill, brine and cement are shown in Figure 6.5. For all cement contents, the σ_c values tended to increase with age up to 14 to 21 days. The 28 day strengths of the 7 and 10% specimens have shown reduced strengths. It appears that the acidity of the brine attacked the lime in the hydrated cement paste causing a loss of strength. Cement less susceptible to acid attack (Type 50) was, therefore, substituted for Type 10. In some mixes, fly ash obtained locally, known as Detroit fly ash, was added as well.

Two properties were of interest; flowability of the pre-cured mix and strength of the cured saltcrete. The results are summarized in Tables 6.2, 6.3, 6.4 and 6.5 (all in % volume).

FIGURE 6.5

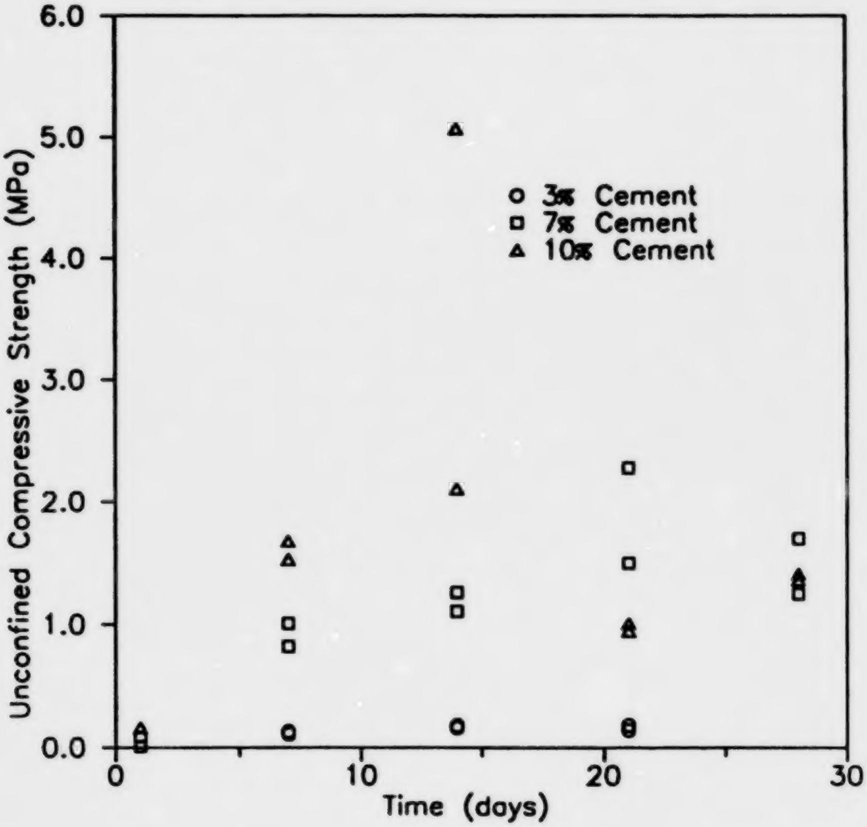

Strength development of DPPC halite backfill with 3, 5, and 10% Type 10 cement added.

Table 6.2: Backfill/Sand Aggregate with Water:Cement Ratio of 0.3

Backfill (%)	Sand (%)	Brine (%)	Cement (%)	Curing Time (days)	σ_c (MPa)
70	0	7.5	22.5	7	9.8
52.5	17.5	7.5	22.5	7	10.1
35	35	7.5	22.5	7	11.2

It appears that adding sand as an aggregate can increase the strength of the backfill, probably by reducing the overall porosity percentages. However, the strength increases are modest (only 1.4 MPa) over the range of sand percentages tested. Overall, the strengths listed in Table 6.2 are much higher than those noted previously. This is attributed to the low water:cement ratio and the high cement content.

While the low water:cement ratio gave the materials good strength properties, it also made them fairly stiff and likely not easily pumpable. In order to improve their flowability, a superplasticizing agent (silkament 300) was added in place of 5% of the brine/cement mixture. This greatly reduced the viscosity of the mix and should allow it to be pumped. The superplasticizer can also produce high strength, but retards set if added in too large a quantity.

Table 6.3: Backfill Aggregate with Various Water:Cement Ratios

Backfill (%)	Brine (%)	Cement (%)	Curing Time (days)	σ_c (MPa)
70	21	9	3	1.5,1.34
70	23	7	3	0.65
70	25	5	3	0.35
70	27	3	7	0.30

With lower cement contents (and higher water to cement ratios) the strengths are reduced. The results listed in Table 6.3 are shown in Figure 6.6. A material with a σ_c of about 1.3 to 2 appears to be possible with a cement content of about 9-10%. At lower cement contents (and higher brine contents), much of the brine will flow out of the backfill, removing the cement.

Because the water:cement ratios were much higher for these mixes, they all appeared easily pumpable, as they all could be poured from the mixing vessel into the concrete molds.

Table 6.4: Backfill Aggregate with Fly Ash and Various Water:Cement Ratios

Backfill (%)	Fly Ash (%)	Brine (%)	Cement (%)	Curing Time (days)	σ_c (MPa)
65	15	15	5	1	1.2
65	10	20	5	1	0.44
70	10	15	5	1	0.9

Table 6.5: Backfill Aggregate with Fly Ash and Various Water:Cement Ratios

Backfill (%)	Fly Ash (%)	Brine (%)	Cement (%)	Curing Time (days)	σ_c (MPa)
65	5	21	9	2	1.15
65	5	23	7	2	0.55
65	5	25	5	2	0.49

Fly ash appears to increase the strength of low cement (5%) backfill, provided it is added at more than 10% of the total volume (Table 6.4 and 6.5). At lower contents, it has little effect on the strength (Figure 6.7). All of these mixes appeared pumpable.

FIGURE 6.6

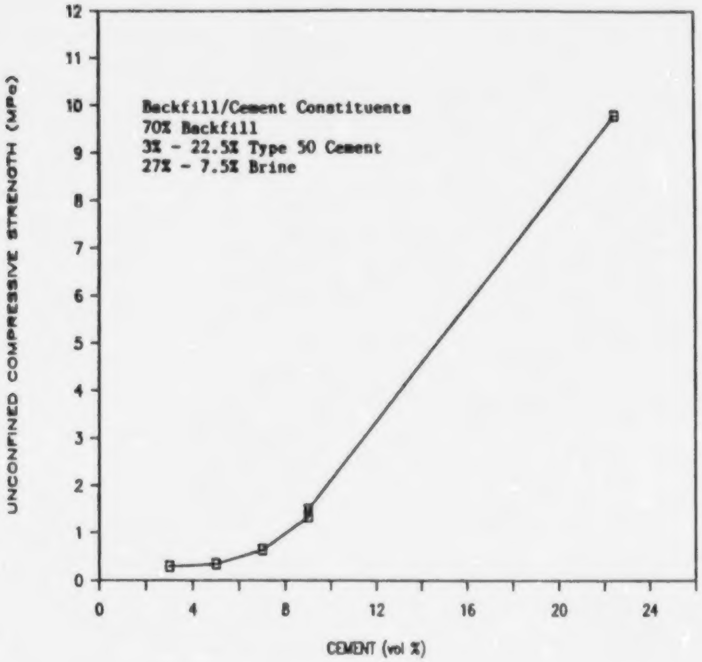

Unconfined Compressive Stength as a Function of Cement Content, DPPC Halite Backfill.

FIGURE 6.7

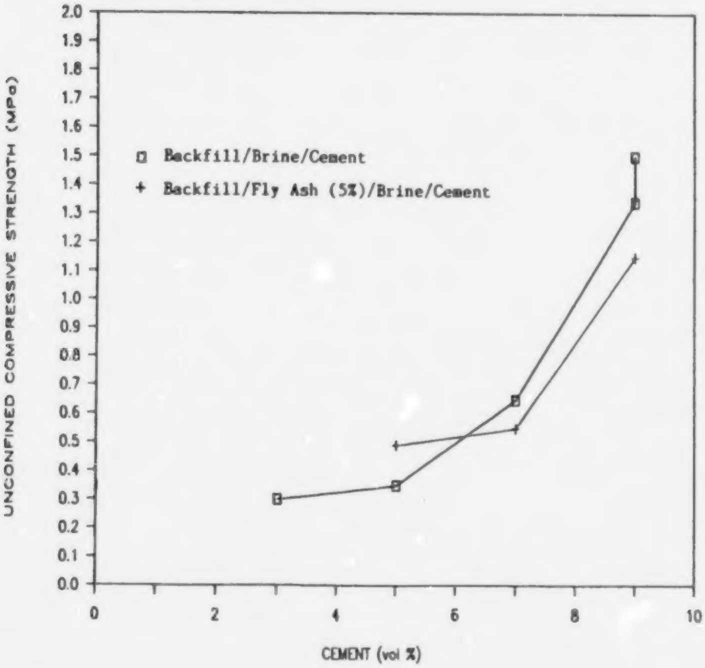

Unconfined Compressive Strength as a Function of Cement and Fly ash Content, DPPC Halite Backfill.

Fly ash is a material which can vary chemically (particularly alkali contents) depending on its source. If a particular fly ash is to be added to the backfill, samples of it should be tested as a backfill additive.

6.5 Conclusions

The conclusions which can be reached from this part of the study are as follows:

1. Incorporation of sand into the backfill can reduce its placement porosity, thereby reducing the total amount of closure and time to achieve overburden support.

2. Type 10 cement (Ordinary Portland cement) does not stand up to acid attack due to the lime created during hydration. The process brine used during this study resulted in a weakening of salt concrete.

3. The strength of engineered backfill is primarily a function of its cement content and water:cement ratio. It appears that a 9-10% cement content (by volume) will achieve a material with a UCS of 1.3-2 MPa. At lower cement contents, much of the cement is removed from between the grains of the backfill as the brine drains.

4. Additives such as silica sand and fly ash can increase the strength of the backfill provided they are added in high enough proportions. Silica sand should make up more than 25% of the backfill and fly ash more than 10% by volume to affect the strength.

5. All mixes with 65-70% aggregate and water:cement ratios of greater than 2 appear to be pumpable. At lower water:cement ratios, plasticizing agents may make the material flow more easily. However, these agents can also increase the set time or impede proper set altogether if they are added in excessive quantity.

SECTION 7.0

7.0 PARAMETRIC ANALYSIS OF IN SITU AND LABORATORY DATA ON SALT ROCKS

7.1 Introduction

Since the completion of Phase I of the project, additional research was devoted to the analysis of in situ and laboratory data and development of parameters for input into the numerical modelling process.

Included were:

a) the use of a different shear stress criterion in derivation of creep strain rate;

b) re-evaluation of initial in situ and laboratory data;

c) re-evaluation of parameters derived from in situ and laboratory data;

d) determination of corresponding input parameters.

7.2 Definition of Shear Stress Criterion

A shear stress criterion is a mathematical expression giving a specific combination of stress components in a body which will initiate and maintain a specific level of creep strain rate. In Phase I of the research project, **Tresca's criterion** was used in the numerical modelling. This was changed to **Von Mises criterion** in Phase II.

Tresca's Criterion is based on **maximum shear** from the theory of plasticity. According to this criterion, the maximum shear stress uniquely governs the level of creep strain rate.

The yield criterion is defined by the following equation (Valliappan, 1981):

$$\sigma_s = \sigma_1 - \sigma_3 \tag{7.1}$$

where: σ_s = deviatoric stress level
σ_1 = major principal stress
σ_3 = minor principal stress

The disadvantage of Tresca's criterion is that it implies that stresses in tension and compression have the same effect, which does not hold true for rocks. The criterion is not affected by the intermediate principal stress (σ_2).

Von Mises criterion is based on distortion energy theory. The Von Mises effective stress is defined as (Farmer, 1983; Jaeger & Cook, 1979):

$$\sigma_{eff} = \sqrt{3J_2} \tag{7.2}$$

where σ_{eff} = effective stress level
J_2 = second invariant of stress deviation
$J_2 = 1/6\,[(\sigma_1 - \sigma_2)^2 + (\sigma_2 - \sigma_3)^2 + (\sigma_3 - \sigma_1)^2]$
σ_1 = major principal stress
σ_2 = intermediate principal stress
σ_3 = minor principal stress

The advantage of this criterion is that it takes into account the intermediate principal stress (σ_2).

In the case of triaxial compression tests in the laboratory (i.e. creep tests) from which all of the creep data was obtained, the intermediate and minimum principal stresses are equal. Therefore, both criterions are the same and can be defined by equation (7.1). In situ, these two stresses are seldom equal. Under plain strain conditions, assuming $\sigma_2 = (\sigma_1 + \sigma_3)/2$, the value of effective stress σ_{eff}, as defined by Von Mises criterion, is $(\sqrt{3/2})\ \sigma_s$ as compared to Tresca's shear stress.

Examination of available published research literature showed that the Von Mises criterion was more widely accepted as compared to Tresca's criterion when used to predict the in situ behaviour of rock. However, neither of these criteria are perfect and alternative criteria are available such as maximum shear stress creep potential (Van Sambeek, 1986).

7.3 Re-evaluation of Original Parameters

The Rock Mechanics Station (Test Room) used for calibration in Phase I of the CANMET study was rerun using the Von Mises definition of effective stress, the same modelling parameters as in Phase I, and a restructured mesh (Figure 7.1). It was rerun on a SUN IV computer using the most current version of the numerical modelling program VISCOT as revised by Dr. L. Rothenburg of the University of Waterloo.

The material assigned to the mesh was sylvinite as in Phase I. The initial parameter values used for the rerun were as follows:

Reference Strain Rate : 3.0×10^{-11} s^{-1}
Reference Stress : 17.6 MPa
Exponent "n_1" : 1.0
Exponent "n_2" : 6.0
Young's Modulus : 5.453 GPa
Poisson's Ratio : 0.33
Unconfined Compressive Strength : 26.25 MPa
Tensile Strength : 1.65 MPa
Constant "M" : 53.8
Room Depth : 911 m
Field Stress Level : 20.0 MPa

Upon completion of the rerun, it was found that the predicted closure rates were 5.5 times greater than the measured in situ rates. The vertical and horizontal closure rates predicted were symmetrical at 6.2 cm/yr, compared to the in situ rate of 1.13 cm/yr (CANMET, 1987).

In comparing values of the creep parameters (i.e. σ_0, n_2) used in Phase I of the project to values found in more recently published research literature, a considerable difference was noted (note that the reference

FIGURE 7.1

DPPC VIRGIN GROUND OPENING

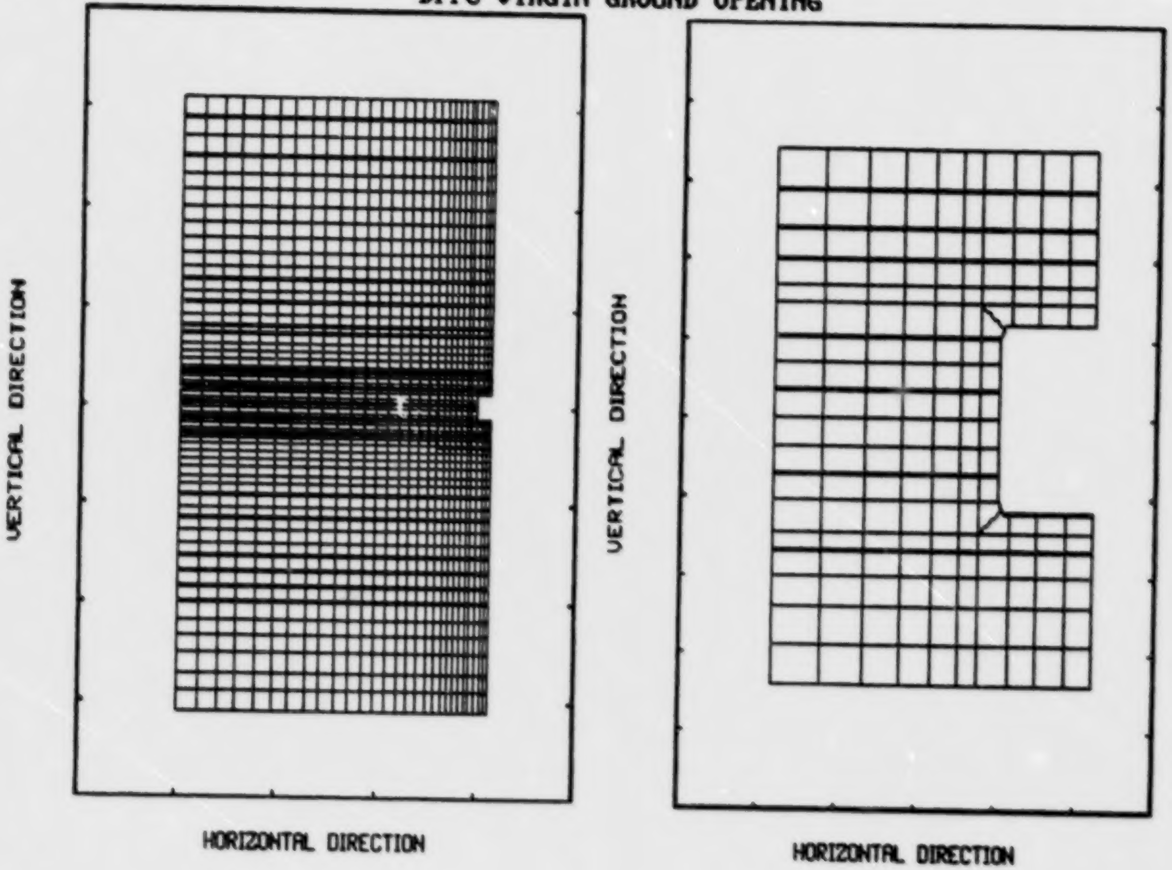

stress σ_0 was referred to as "2K" in Phase I of the project). Average values for the reference stress and the exponent "n_2" were found to be approximately 10.0 MPa, and 6.0 to 7.0, respectively.

According to modern theoretical views, creep in polycrystalline materials is primarily due to the presence of lattice defects and discontinuities in lattice orientations across grain boundaries. Impurities in natural materials and small quantities of brine in salt rock are additional imperfections that may enhance or possibly even control creep deformations. In general, the rate of creep depends on the nature of defects, their mobility under given conditions and the number of defects per unit volume of material (Rothenburg, 1988).

The full complexity of the mechanisms by which materials behave in creep has become apparent only in the last decade. What was once thought to be a simple mechanism has now revealed itself as a hierarchy of interacting mechanisms, each dominant over a certain range of stress, strain state, strain rate, temperature and microstructure. As a consequence of this, micromechanical materials modelling approach, deformation mechanism maps have been developed for metals, alloys and ceramics (Ashby and Brown, 1983). A similar map was proposed for salt as shown in Figure 7.2 (Munson, 1979). This map describes, in a general sense, currently perceived dominant mechanisms controlling the steady state creep of salt. In constructing the mechanism map, all mechanisms controlling these regimes are added together to describe the observed steady state creep. Because of the exponential nature of the models, only one mechanism dominates in a certain regime (Munson and Fossum, 1986).

As shown in Figure 7.2, only two mechanisms are thought to operate at ambient temperatures and within the regime of stresses under typical mining conditions: mechanism (2) and mechanism (5). This leads to the concept of a two-component creep law, reflecting a change of power law exponent at the level of stress between the two regions. This perception is consistent with observations from in situ where the long-term steady state strain rates tend to approach the level of between about 10^{-11} and 10^{-10} sec^{-1} around the opening.

FIGURE 7.2

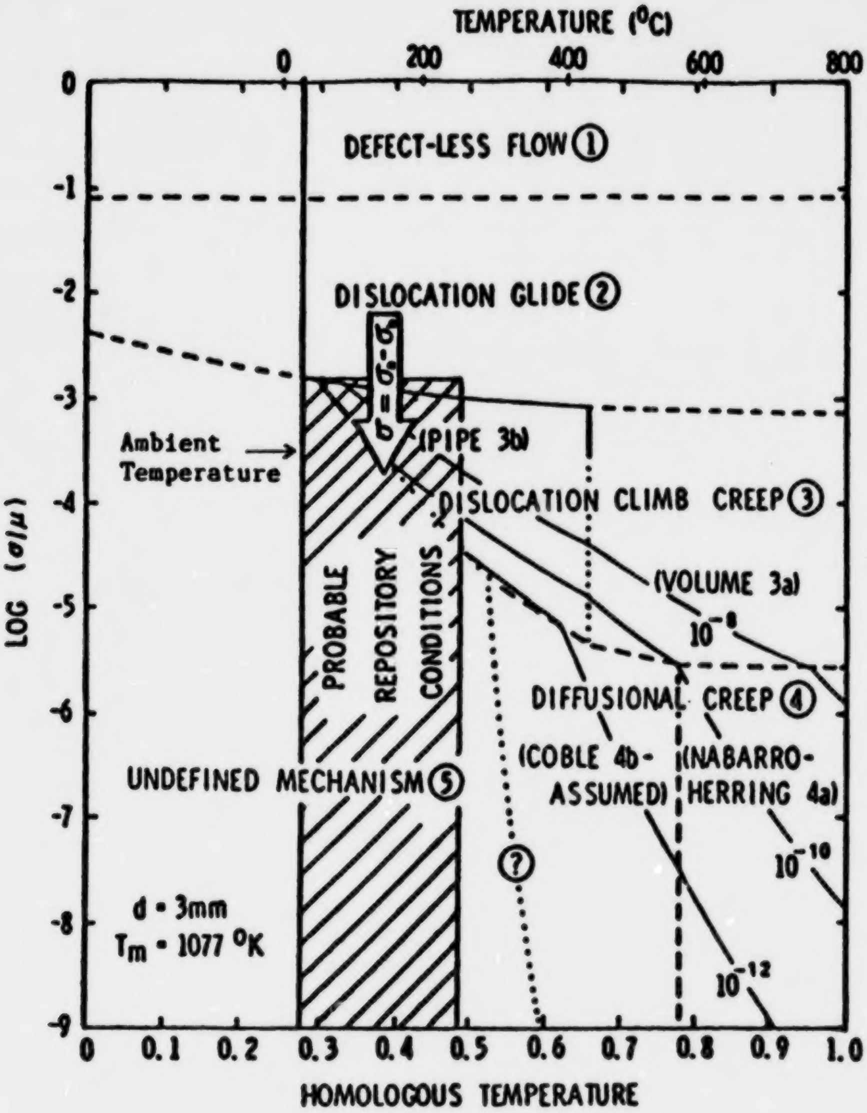

Deformation Mechanism Map for Salt
(After Munson, 1979).

Rothenburg (1988) statistically analyzed 34 creep tests on Palo Duro Salt with respect to the applicability of two steady state creep models:

- the single mechanism power law
- the steady state component of the multi-mechanism Munson-Dawson model (Munson and Dawson, 1982).

He found that the Munson-Dawson model gives a very good fit to the data and that only two creep mechanisms contribute to steady state creep at ambient temperatures (Figure 7.3). Furthermore, he found that mechanism (5) is governed by a power law with an exponent of 3. This is supported by the results of uniaxial creep tests at low stresses on Rocanville potash, performed by Lajtai et al. at the University of Manitoba (1988). Data obtained from the above report were plotted on scale in a log/log plane as shown in Figure 7.4 resulting in a fitted exponent "n_1" value of 3.0.

These new considerations raised doubts as to the validity of some of the parameters used in Phase I. To alleviate these doubts, an exercise was undertaken to re-evaluate the values of the creep parameters.

7.4 Determination of Exponent "n_2"

The initial step in reevaluating the parameters was to analyze the values determined by linear regression, particularly the value of exponent "n_2". Upon investigation, irregularities were found in the results of the creep tests performed at deviatoric stresses above 25.0 MPa.

Two distinct clusters of data points in this range of deviatoric stresses were present, with a difference in strain rates of approximately 1.0 x 10^{-8} (s^{-1}).

The value of the exponent "n_2" used in Phase I (i.e. n_o = 6.0) was determined to be lower than the values reported in published research literature.

FIGURE 7.3

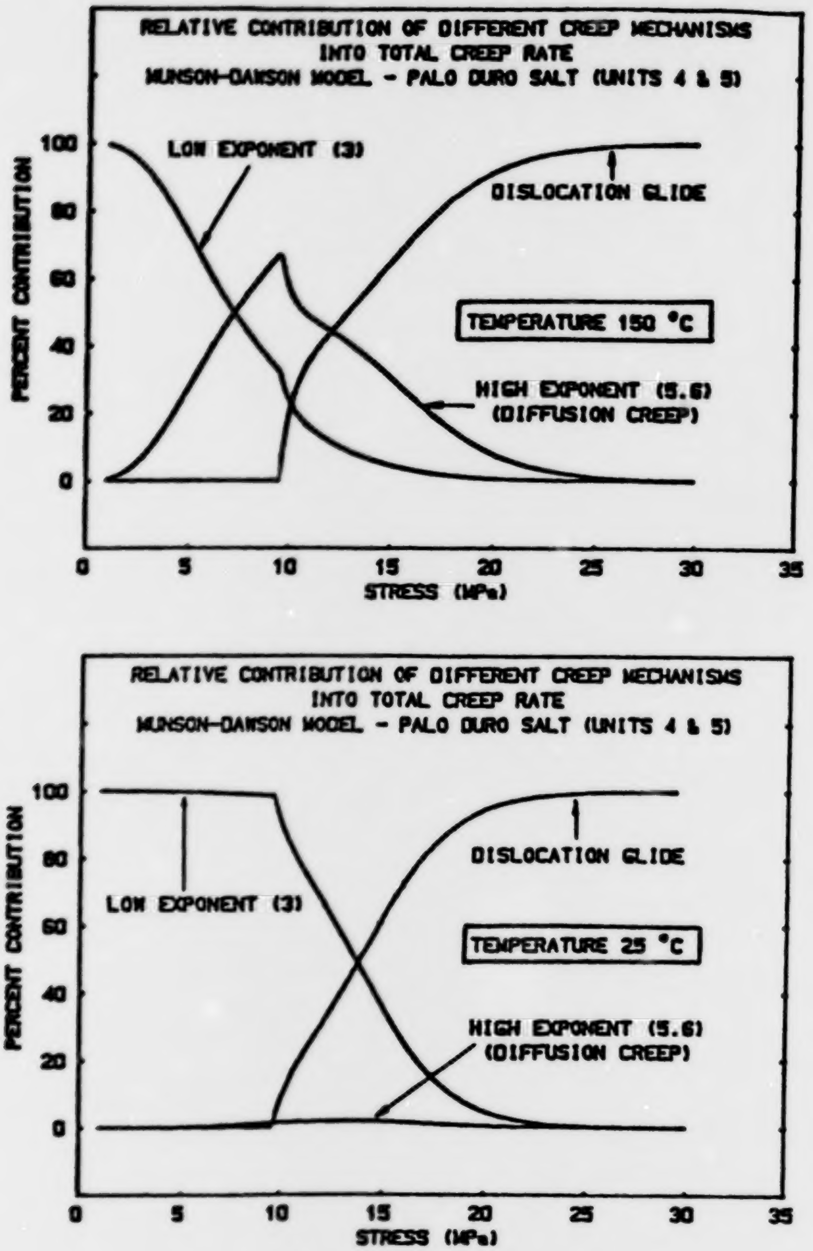

Components of Creep at High and Low Temperatures
(After Rothenburg) Palo Duro Salt, Units 4 and 5

FIGURE 7.4

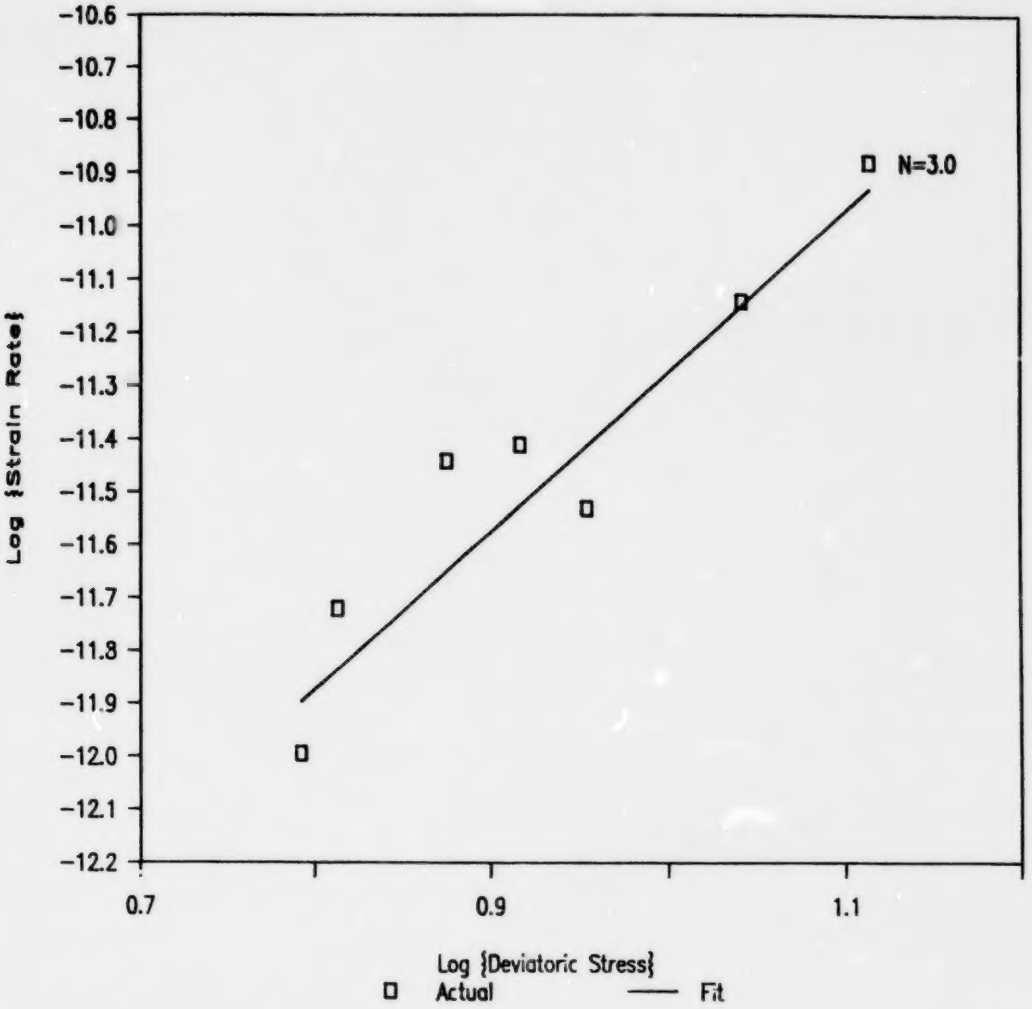

Exponential Fit of Rocanville Potash Tests

It was decided that the lower grouping of four data points was anomalous, therefore these points were removed from the linear regression analysis (Table 7.1).

The linear regression was conducted to fit the determined creep data to the following equation:

$$\dot{\epsilon} = A\,\sigma_{eff}^{\,n_2} \tag{7.3}$$

where $\dot{\epsilon}$ = strain rate
σ_{eff} = effective stress
A, n_2 = constants

The new analysis resulted in the exponent "n_2" equal to 6.9, and the constant "A" of 3.562×10^{-18} (s^{-1}), compared to the previous values of 5.8 and 1.018×10^{-16} (s^{-1}). Note that the linear regression fit of 5.8 was previously rounded to a value of 6.0 for modelling purposes.

7.5 Determination of Reference Parameters

The next step taken in the reevaluation was to determine the values of the reference stress and strain rate that would reproduce the in situ closure rate of 1.13 cm/yr. To accomplish this, a total of three numerical modelling runs were required to determine if a relationship existed between the closure rate and these reference parameters.

A reference stress (σ_0) was arbitrarily chosen for each of the three runs, and the reference strain rates ($\dot{\epsilon}_0$) were determined using equation (7.3).

The values of σ_0 and $\dot{\epsilon}_0$ along with the resultant steady-state closure rates obtained from the problems modelled are listed in the Table 7.2.

TABLE 7.1

DPPC CREEP PARAMETER DETERMINATION

MATERIAL: SYLVINITE

Deviatoric Stress (MPa)	Logarithmic Stress	Strain Rate (/s)	Logarithmic Strain Rate	Regression Output		
19.50	1.2900	1.70E-09	-8.7696	PHASE I FIT		
19.70	1.2945	5.97E-09	-8.2240	Constant		-15.9924
19.80	1.2967	1.60E-09	-8.7959	Std Err of Y Est		0.1959
20.00	1.3010	6.08E-09	-8.2161	R Squared		0.7057
20.00	1.3010	2.27E-09	-8.6440	No. of Observations		24
20.20	1.3054	5.65E-09	-8.2480	Degrees of Freedom		22
20.30	1.3075	5.55E-09	-8.2557			
20.60	1.3139	6.08E-09	-8.2161	X Coefficient(s)	5.8041	
20.70	1.3160	4.26E-09	-8.3706	Std Err of Coef.	0.7991	
21.10	1.3243	3.94E-09	-8.4045			
21.20	1.3263	6.29E-09	-8.2013			
21.70	1.3365	3.94E-09	-8.4045			
22.98	1.3614	8.10E-09	-8.0915			
23.50	1.3711	8.00E-09	-8.0969	PHASE II FIT		
23.70	1.3747	1.08E-08	-7.9666	Constant		-17.4483
24.80	1.3945	2.65E-08	-7.5768	Std Err of Y Est		0.1900
25.00	1.3979	9.10E-09	-8.0410	R Squared		0.7611
25.50	1.4065	2.93E-08	-7.5331	No. of Observations		20
26.40	1.4216	2.93E-08	-7.5331	Degrees of Freedom		18
27.60	1.4409	2.60E-08	-7.5850			
25.30	1.4031	1.09E-08	-7.9626	X Coefficient(s)	6.9115	
25.60	1.4082	1.15E-08	-7.9393	Std Err of Coef.	0.9128	
25.90	1.4133	1.14E-08	-7.9431			
27.00	1.4314	1.13E-08	-7.9469			

Note : the last four data points were not used in the Phase II Linear Regression Fit.

Table 7.2

Reference Stress (MPa)	Reference Strain Rate (s^{-1})	Steady-State Closure Rate (cm/yr)
11.5	7.39×10^{-11}	1.81
12.5	1.32×10^{-10}	2.47
13.5	2.24×10^{-10}	3.33

A linear regression was performed upon the logarithmic values to determine if a relationship exists between the reference stress (σ_o) and the steady-state closure rate.

The results of the linear regression (Table 7.3) show a definite relationship between the two parameters which is defined by the following equation:

$$\dot{U}_{ss} = 1.67 \times 10^{-4} \ \sigma_o^{3.8} \tag{7.4}$$

where $\dot{U}_{ss}$ = steady state closure rate (cm/yr)
σ_o = reference stress

Using this equation and the in situ steady-state closure rate of 1.13 cm/yr (CANMET, 1987), a value of 10.2 MPa was determined for the reference stress. The values obtained for n_2, A, and σ_o, were used in conjunction with equation (7.3) to determine a value of 3.24×10^{-11} for the reference strain rate ($\dot{\epsilon}_o$).

The Rock Mechanics Station problem was run once more using the parameters as listed in Section 7.3 with the following changes

Reference Stress : 10.2 MPa
Reference Strain Rate : 3.24×10^{-11} (s^{-1})
Exponent "n_2" : 6.9
Exponent "n_1" : 3.0

TABLE 7.3

DPPC CREEP PARAMETER DETERMINATION

MATERIAL: SYLVINITE

Deviatoric Stress (MPa)	Logarithmic Reference Stress	Closure Rate (cm/yr)	Logarithmic Closure Rate
11.50	1.0607	1.81	0.2577
12.50	1.0969	2.47	0.3927
13.50	1.1303	3.33	0.5224

```
           Regression Output:
                                      -3.7750
Constant                               0.0022
Std Err of Y Est                       0.9999
R Squared                                   3
No. of Observations                         1
Degrees of Freedom
                                       3.8011
X Coefficient(s)                       0.0442
Std Err of Coef.
```

With these new values, the problem was rerun using the numerical modelling program VISCOT. A steady state closure rate of 1.13 cm/yr was predicted which is in complete agreement with the actual in situ measurements.

The results of the final calibration run and two of the development runs are illustrated in Figures 7.5 to 7.8.

7.6 Determination of Properties for Remaining Materials

The final step in the reevaluation was to determine the material properties for the Upper Halite (UH), Lower Gradational Bed (LGB), Caprock Breccia and the Collapse Breccia.

Reference stress values of 14.16 MPa and 13.10 Mpa were determined by statistical analysis of laboratory data for the Upper Halite and Lower Gradational Bed as shown in Tables 7.4 and 7.5.

It was assumed as a result of similarity between the materials of the Sylvinite bed, the Upper Halite Bed and the Lower Gradational Bed that their creep behaviour was similar. Hence, the constants n_2 and $\dot{\epsilon}_0$ (determined for sylvinite) were used for the Upper Halite and the Lower Gradational Bed.

The mechanical material properties for the Caprock and Collapse Breccias were determined as described earlier in Section 4.0.

A summary of the properties recommended for the computer modelling is given in Table 7.6.

7.7 Summary of Parametric Analysis

The values of the new creep parameters determined by this analysis and used in modelling, produced results that were in close agreement with measured in situ behaviour. Therefore the values listed in Table 7.6 were used in any subsequent numerical modelling runs.

The form of the creep law used in the numerical modelling is as follows:

FIGURE 7.5

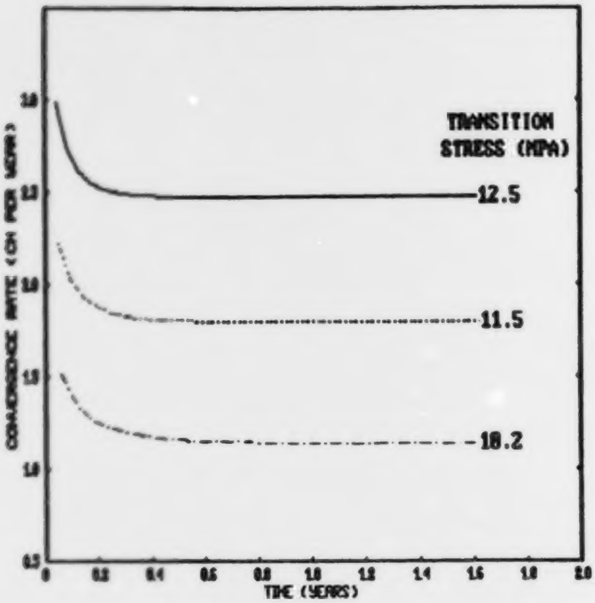

DPPC Virgin Ground Opening Roof to Floor Convergence Rates

FIGURE 7.6

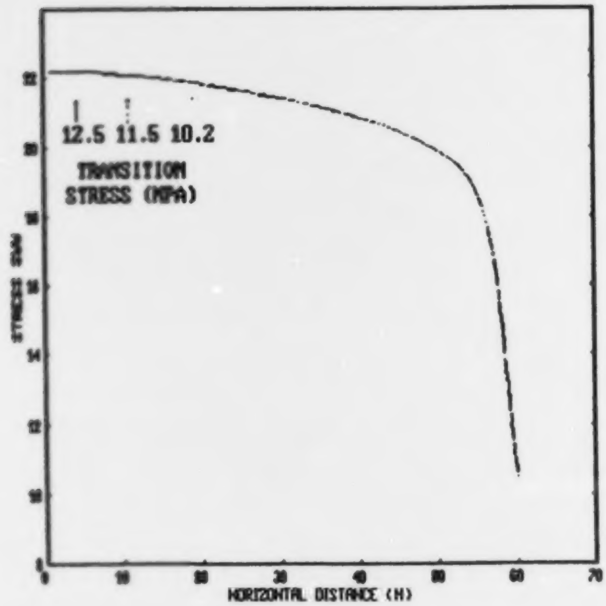

DPPC Virgin Ground Opening Vertical Stress Along Mid-Height of Pillar

FIGURE 7.7

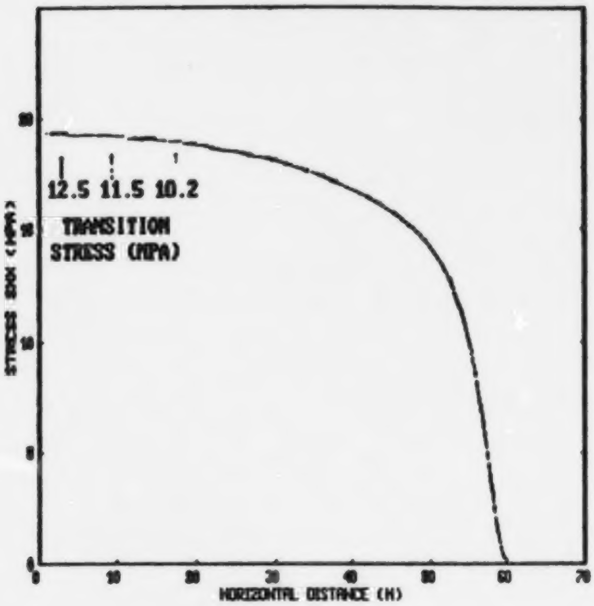

DPPC Virgin Ground Opening Horizontal Stress Along Mid-Height of Pillar

FIGURE 7.8

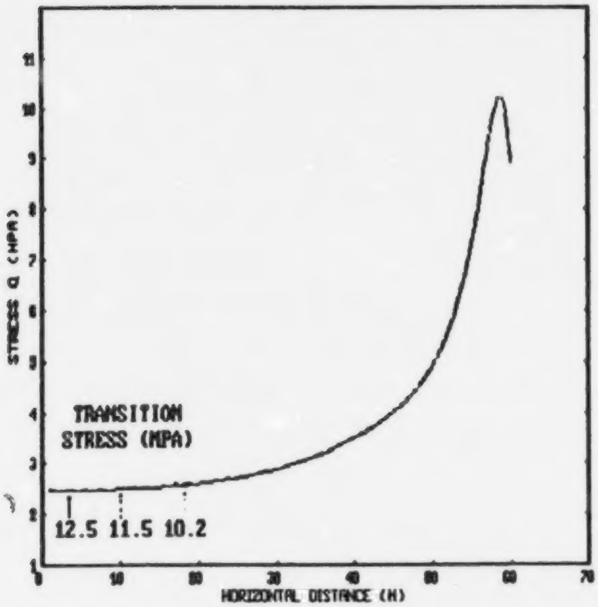

DPPC Virgin Ground Opening Effective Stress Along Mid-Height of Pillar

TABLE 7.4

DPPC CREEP PARAMETER DETERMINATION

MATERIAL: UPPER HALITE

Exponent "n_2": 6.9
Exponent "n_1": 3.0
Sigma "o" : 14.16
Strain Rate : 3.24E-11

Deviatoric Stress (MPa)	Actual Strain Rate (/s)	Logarithmic Strain Rate	Calculated Strain Rate (/s)	Logarithmic Strain Rate	Percent
26.50	3.93E-09	-8.4056	2.45E-09	-8.6108	97.617
27.60	1.93E-09	-8.7144	3.24E-09	-8.4895	102.650
25.50	3.42E-09	-8.4660	1.88E-09	-8.7258	97.022
26.50	3.75E-09	-8.4260	2.45E-09	-8.6108	97.853
24.40	1.22E-09	-8.9136	1.38E-09	-8.8601	100.604
31.80	3.90E-09	-8.4089	8.61E-09	-8.0650	104.265
				Mean............	100.002
				Standard Deviation.......	2.731

TABLE 7.5

DPPC CREEP PARAMETER DETERMINATION

MATERIAL: LOWER GRADATIONAL BED

Exponent "n_2": 6.9
Exponent "n_1" : 3.0
Sigma "o" : 13.10
Strain Rate : 3.24E-11

Deviatoric Stress (MPa)	Actual Strain Rate (/s)	Logarithmic Strain Rate	Calculated Strain Rate (/s)	Logarithmic Strain Rate	Percent
26.50	7.86E-09	-8.1046	4.18E-09	-8.3788	96.727
29.70	1.45E-08	-7.8386	9.18E-09	-8.0372	97.530
23.40	2.12E-09	-8.6737	1.77E-09	-8.7520	99.105
25.50	3.08E-09	-8.5114	3.20E-09	-8.4949	100.195
27.60	3.84E-09	-8.4157	5.53E-09	-8.2573	101.918
29.70	3.98E-09	-8.4001	9.18E-09	-8.0372	104.516
				Mean............	99.999
				Standard Deviation.......	2.637

$$\dot{\epsilon}_{ss} = e^{-\frac{Q}{R_i}\left(\frac{1}{T_i}-\frac{1}{T_R}\right)} \left| \begin{array}{ll} \dot{\epsilon}_{01}\left(\dfrac{\sigma_{eff}}{\sigma_{01}}\right)^{n_1} & \sigma_{eff} \leqq \sigma_0 \\ \\ \dot{\epsilon}_{02}\left(\dfrac{\sigma_{eff}}{\sigma_{02}}\right)^{n_2} & \sigma_{eff} > \sigma_0 \end{array} \right. \tag{7.5}$$

where $\dot{\epsilon}_{ss}$ = steady state strain rate

$\dot{\epsilon}_{01}, \dot{\epsilon}_{02}$ = reference strain rates

σ_{01}, σ_{02} = reference stresses

σ_{eff} = effective stress

σ_0 = critical effective stress

n_1, n_2 = exponents

Q = activation energy

R_i = ideal gas constant

T_i = in situ temperature

T_R = laboratory temperature

Equation 7.5 can also be written as follows:

$$\dot{\epsilon}_{ss} = \left| \begin{array}{ll} A_1\,\sigma_{eff}^{\,n_1} & \sigma_{eff} \leq \sigma_0 \\ A_2\,\sigma_{eff}^{\,n_2} & \sigma_{eff} > \sigma_0 \end{array} \right. \tag{7.5a}$$

and the corresponding parameters and constant are:

$$A_1 = e^{-\frac{Q}{R_i}\left(\frac{1}{T_i}-\frac{1}{T_R}\right)} \cdot \dot{\epsilon}_{01} \cdot \sigma_{01}^{-n_1}\left[\mathrm{MPa}^{-n_1}/\mathrm{s}\right] \tag{7.6}$$

$$A_2 = e^{-\frac{Q}{R_i}\left(\frac{1}{T_i}-\frac{1}{T_R}\right)} \cdot \dot{\epsilon}_{02} \cdot \sigma_{02}^{-n_2}\left[\mathrm{MPa}^{-n_2}/\mathrm{s}\right] \tag{7.7}$$

The statistical fits of the current creep law parameters for the three materials studied are illustrated in Figures 7.9 to 7.11. These figures also show that the current parameters offer much better fits than parameters used in Phase I. The better fit is as a result of the re-evaluation described above and provides a successful correlation of in situ measurements, laboratory analysis and theory for the purposes of numerical modelling.

TABLE 7.6

SUMMARY OF PARAMETRIC ANALYSIS

Property	Symbol	Units	Sylvinite Bed	Upper Halite Bed	Lower Gradational Bed	Caprock Breccia	Collapse Breccia	Source of Parameter		
								In Situ	Laboratory	Analysis
Density	γ	Kg/m^3	2050	2150	2100	2530	2650		X	
Young's Modulus	E	GPa	5.453	10.214	6.916	0.44	13.27		X	
Poisson's Ratio	ν	-	0.33	0.33	0.33	0.33	0.16		X	
Exponent n_2	n_2	-	6.9	6.9	6.9	-	-	X	X	X
Exponent n_1	n_1	-	3.0	3.0	3.0	-	-	X	X	X
Reference Strain Rate	$\dot{\epsilon}_o$	(/s)	3.24E-11	3.24E-11	3.24E-11	-	-	X	X	X
Reference Stress	σ_o	MPa	10.2	14.16	13.1	-	-	X	X	X
Unconfined Compressive Strength	σ_C	MPa	26.25	29.2	28.4	-	-		X	
Tensile Strength	σ_T	MPa	1.65	2.0	1.48	-	-		X	
Empirical Constant	M	-	53.8	500	34.2	-	-		X	
Cohesion	C	MPa	-	-	-	4.7	27.0		X	
Angle of Internal Friction	ϕ	degrees	-	-	-	32.5	24.5		X	

FIGURE 7.9

PARAMETRIC COMPARISON

Sylvinite Bed

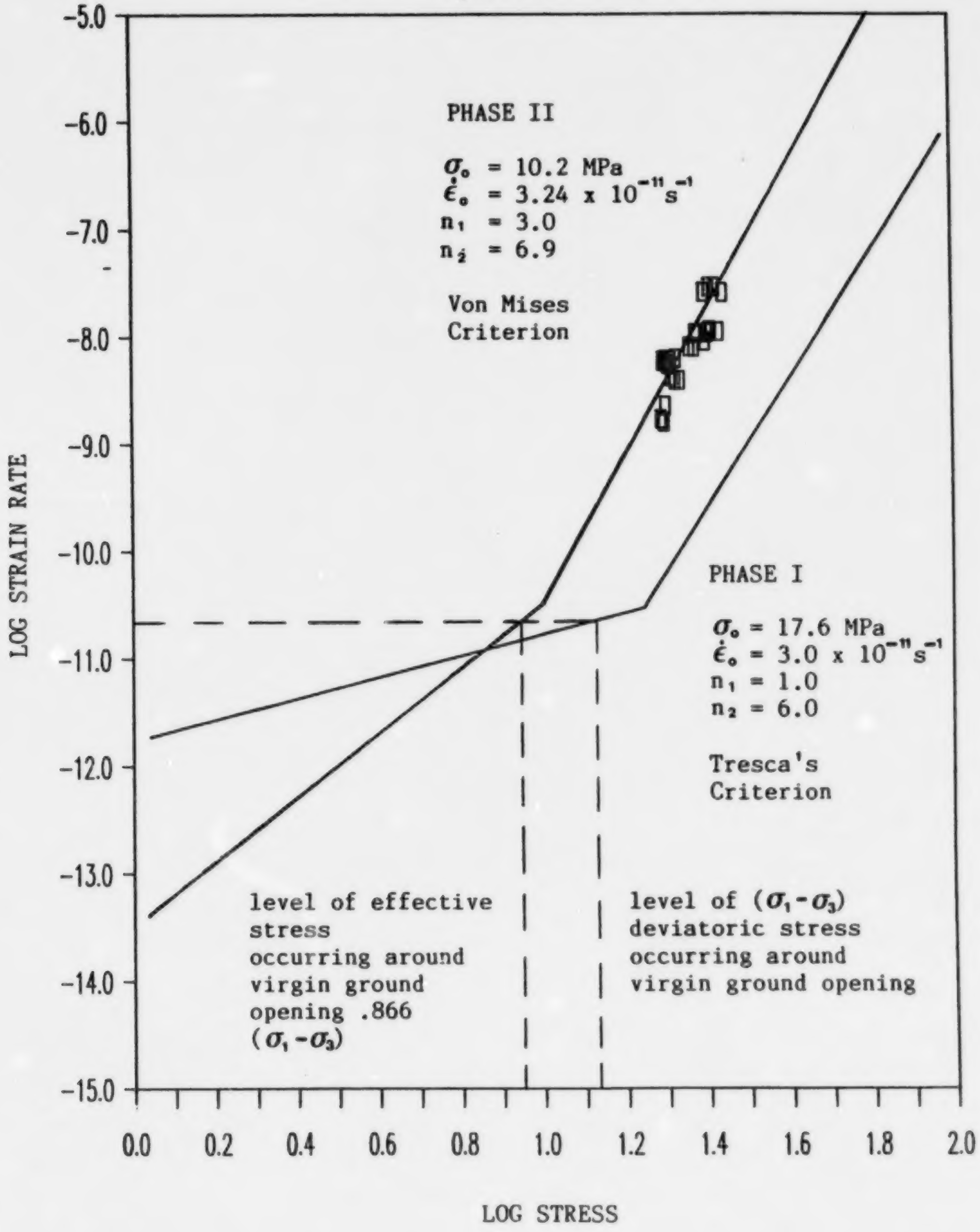

FIGURE 7.10

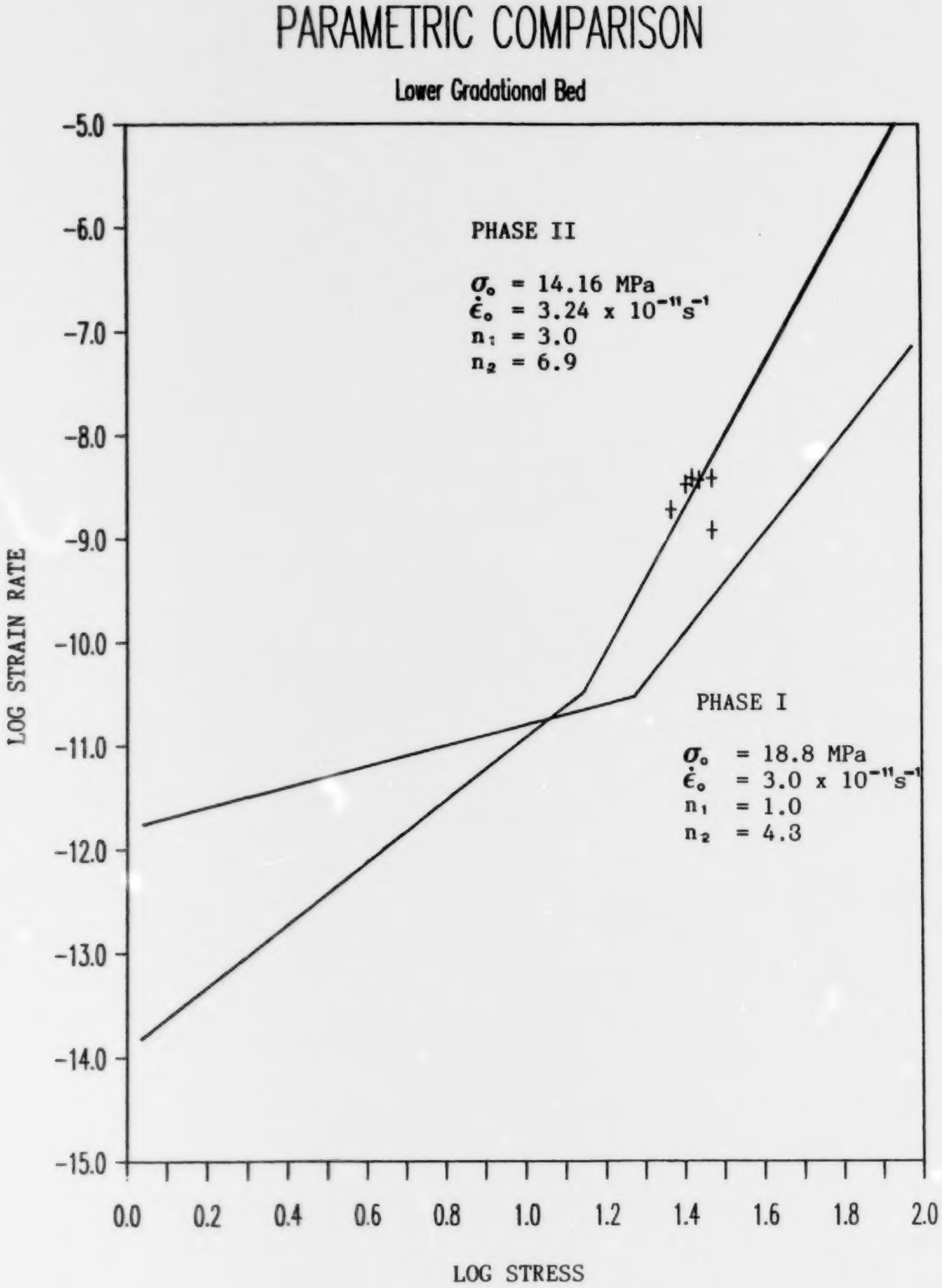

PARAMETRIC COMPARISON

Lower Gradational Bed

FIGURE 7.11

PARAMETRIC COMPARISON

Upper Halite

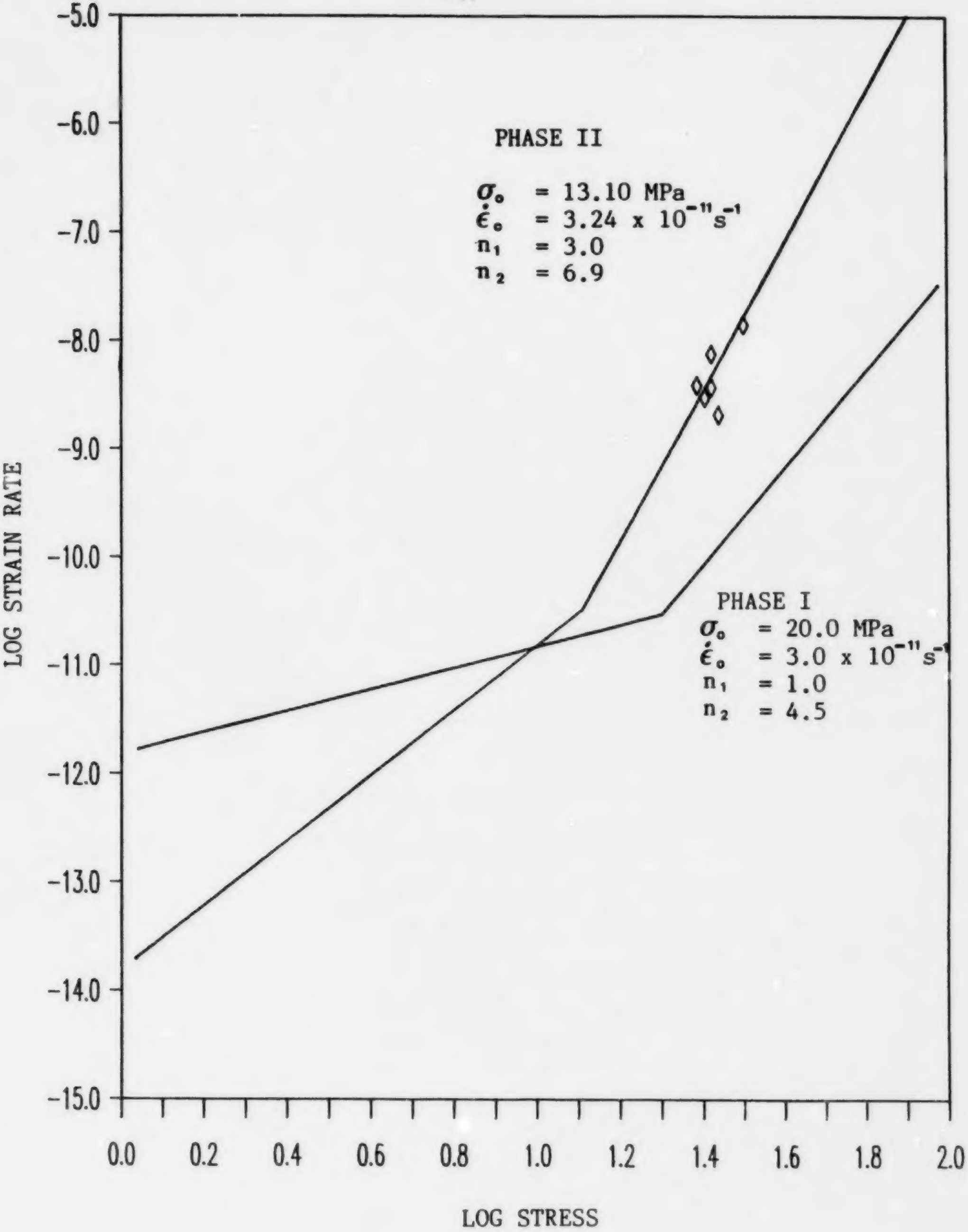

SECTION 8.0

8.0 NUMERICAL MODELLING OF DPPC MINE USING THE PROGRAM FLAC WITHOUT BACKFILL

8.1 Introduction

The program **FLAC** (Fast Langarian Analysis of Continua), written by ITASCA Consulting Group Inc., was used for two-dimensional modelling. The constitutive law used in this study was developed through joint effort of MPC and the University of Waterloo and incorporated into the program by ITASCA under a contract with Mraz Project Consultants Ltd.

8.2 Computational Procedure Used in FLAC to Predict Behaviour of Visco-Elastic/Plastic Material

FLAC is a two-dimensional microcomputer program that uses the explicit finite difference method (Itasca, 1987) to model a variety of geotechnical problems, including large-strain plasticity, time dependent creep, interfaces and support-structure interaction. FLAC is capable of analyzing plane strain, plane stress or axisymmetric problems.

The explicit finite difference method is a numerical technique for differentiating functions by employing arithmetic operations. It is a time-marching solution scheme in which the right-hand-sides of all equations consist of known values (Itasca, 1987). The time step is chosen small enough so that information cannot physically propagate from one zone of the grid to the next within that time step. As equilibrium is approached, the time step automatically increases, but still satisfies the condition. Initially, strain increments produced by known nodal velocities and the stresses as a result of the strain are derived for each zone according to the governing constitutive law. Subsequently, the nodal forces as a result of the new stresses are derived, and the velocities resulting from the forces are calculated. The co-ordinate system is then updated, and the calculation cycle is repeated until a state of equilibrium is reached. FLAC uses a form of dynamic relaxation built into the code to reach a state of equilibrium.

The operation of the numerical model is as follows:

1. Determine and construct geometry.
2. Apply material properties, stress states, and boundary conditions.
3. Bring system to elastic equilibrium.
4. Modify mesh (i.e. excavation) and bring back to elastic equilibrium.
5. Start time stepping problem to equilibrium or for a particular time period.
6. Repeat steps 4 and 5 as many times as desired (i.e. sequential mining).

8.3 Capabilities of FLAC

Finite element programs are more common in engineering than finite difference programs. However, FLAC has several advantages over finite element programs. It handles non-linear material models in almost the same calculation time as small-strain linear problems (i.e. finite element) and large grid distortions. Furthermore, the explicit formulation and mixed-discretization scheme (Marti and Cundall, 1982) ensure that plastic collapse and flow are modelled very accurately. The explicit method is ideal for geomechanics problems that consist of several stages because it is capable of modelling each stage sequentially as in reality.

8.4 Verification of FLAC

8.4.1 Comparison of Analytical and Numerical Solutions

A numerical solution obtained using FLAC was compared to the analytical solution for closure of an infinitely long cylindrical cavity. The numerical solution was obtained using a uniform stress field under virgin ground conditions. Sylvinite material properties were used in the analysis. The material properties for sylvinite are listed in Table 7.6.

A comparison of the analytical and FLAC solutions for the closure rate of a circular opening is shown in Figure 8.1. The analysis shows very good correlation. Similarly, good matches between analytical and numerical

FIGURE 8.1

FLAC VERIFICATION RUN

Closure Rate of Circular Opening

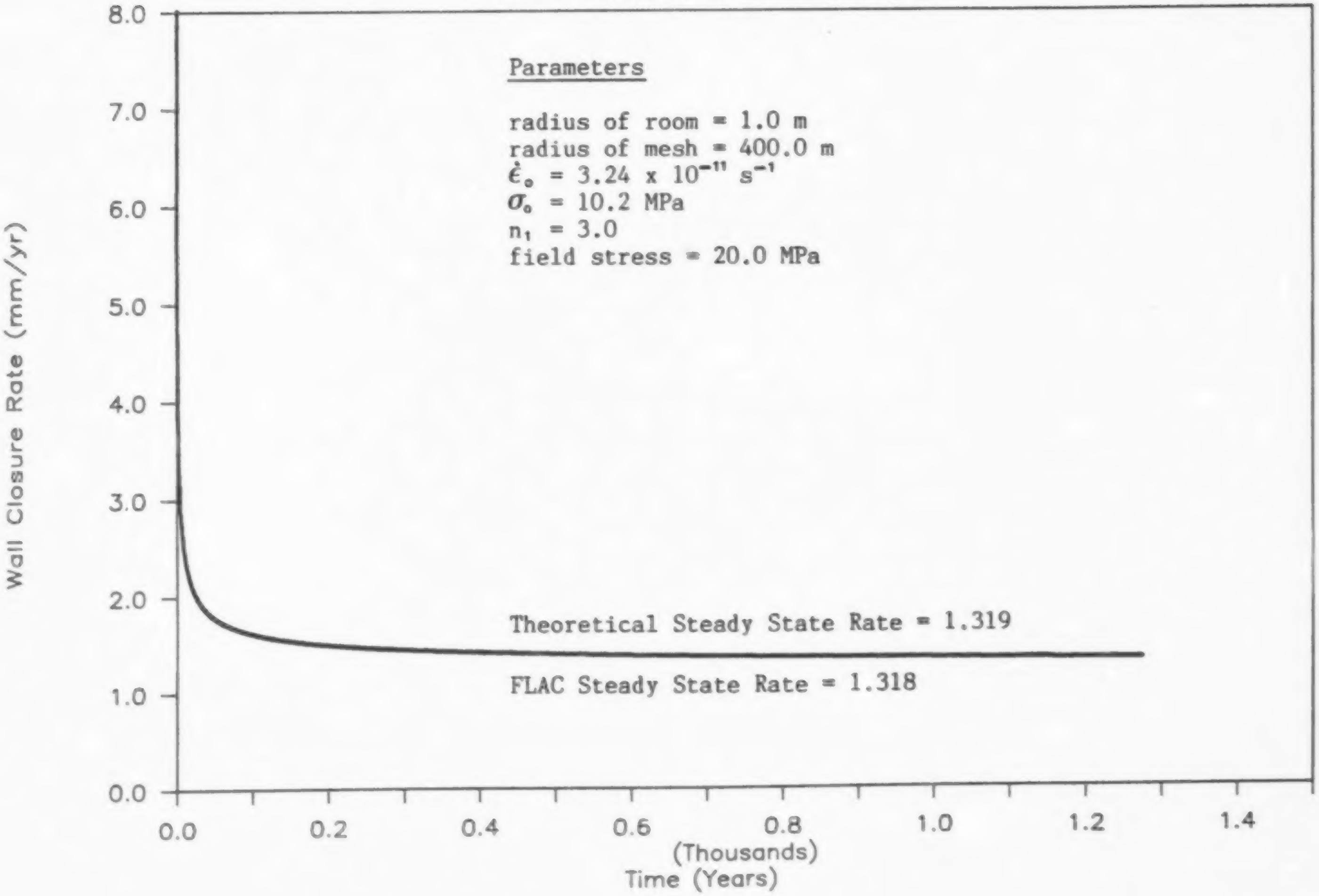

FIGURE 8.2

FLAC VERIFICATION RUN

Radial Stress Around Opening

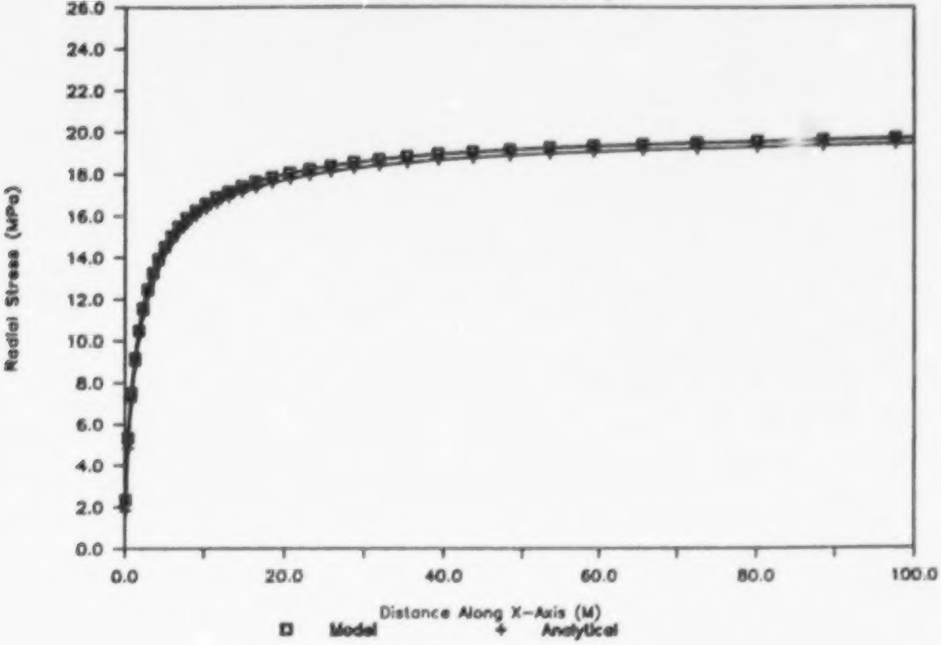

FIGURE 8.3

FLAC VERIFICATION RUN

Circumferential Stress Around Opening

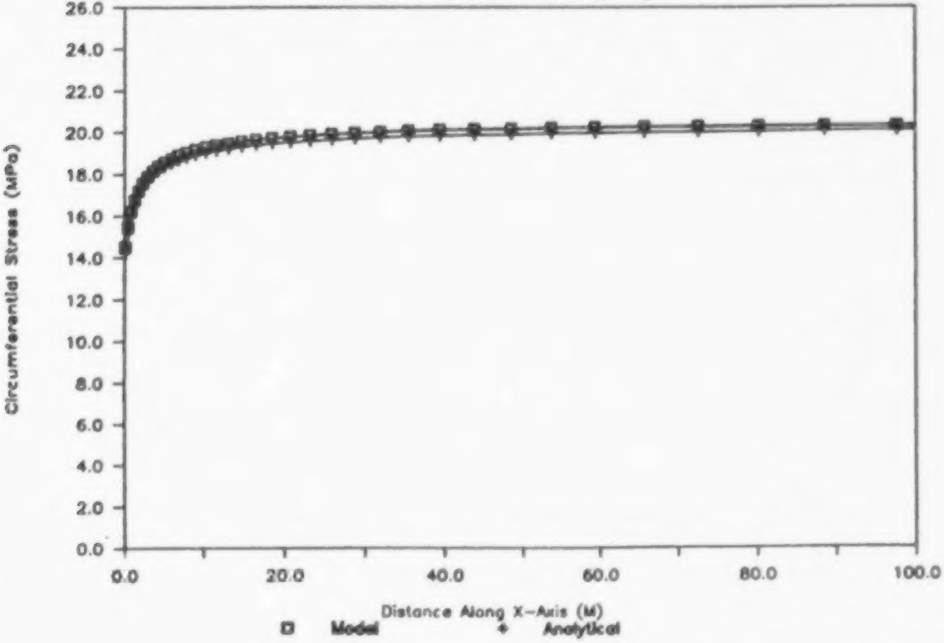

solutions are shown in Figures 8.2 and 8.3 for the radial and circumferential stresses, respectively.

8.4.2 Benchmark Against Numerical Models

The exercise described as the "Second WIPP Benchmark Problem" (Morgan et al., 1981) was used to benchmark FLAC. This problem has been identified by some as the most thorough benchmark exercise to date for thermomechanical codes performing analyses related to nuclear waste isolation studies (Hart et al., 1987).

This exercise was performed specifically for the WIPP Salt Testing Program and emphasised the verification of codes containing a salt creep constitutive model (ITASCA, 1988). However, the exercise also covered other material behaviours not specific to salt, such as the behaviour of interbedded materials, slip along discontinuities and temperature-dependent conductivity. Thus, the WIPP exercise provided the means to verify the accuracy of several thermal-mechanical features in FLAC.

8.5 Calibration of FLAC

8.5.1 Calibration Against the Virgin Ground Test Room

Prior to using FLAC as a predictive tool for mine design, FLAC was calibrated against in situ data from the virgin ground Test Room (refer to Figure 3.1 for location). In situ measurements for roof and wall closure were accumulated over a period of almost four years in the Test Room. Using the material properties and the constitutive law derived in this study, behaviour of the test room was simulated.

The material properties used to calibrate FLAC against the test room are summarized in Table 7.6. The constitutive law that governs material behaviour is defined by equation (7.5). Outputs of this calibration run are shown in Figures 8.4 to 8.14.

FIGURE 8.4

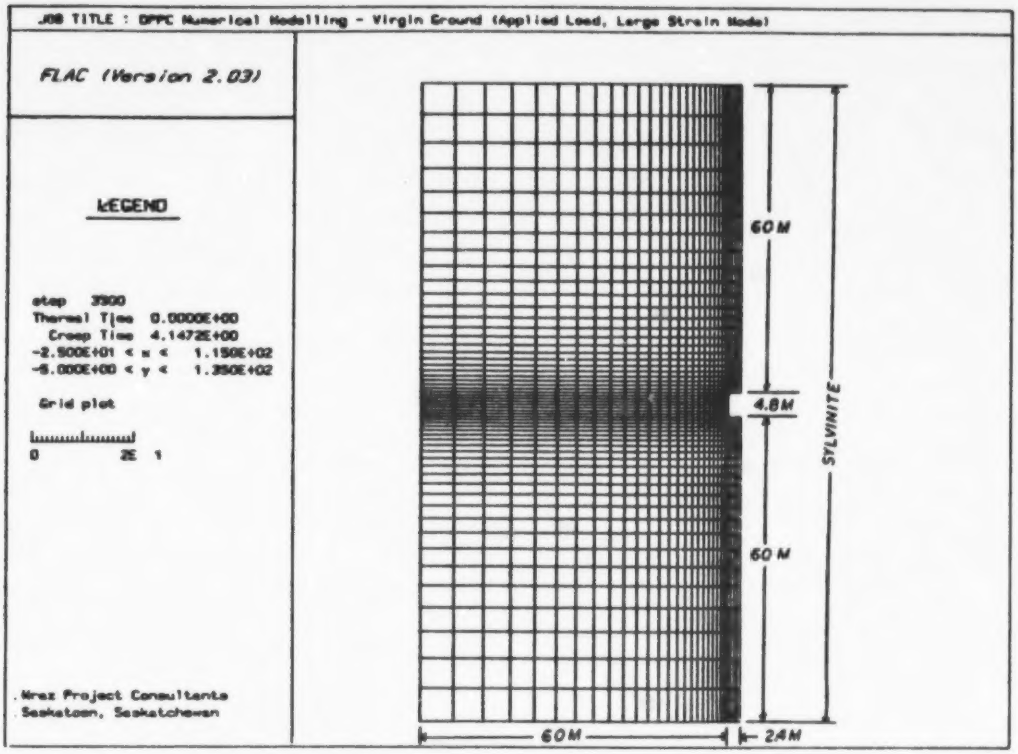

FIGURE 8.5

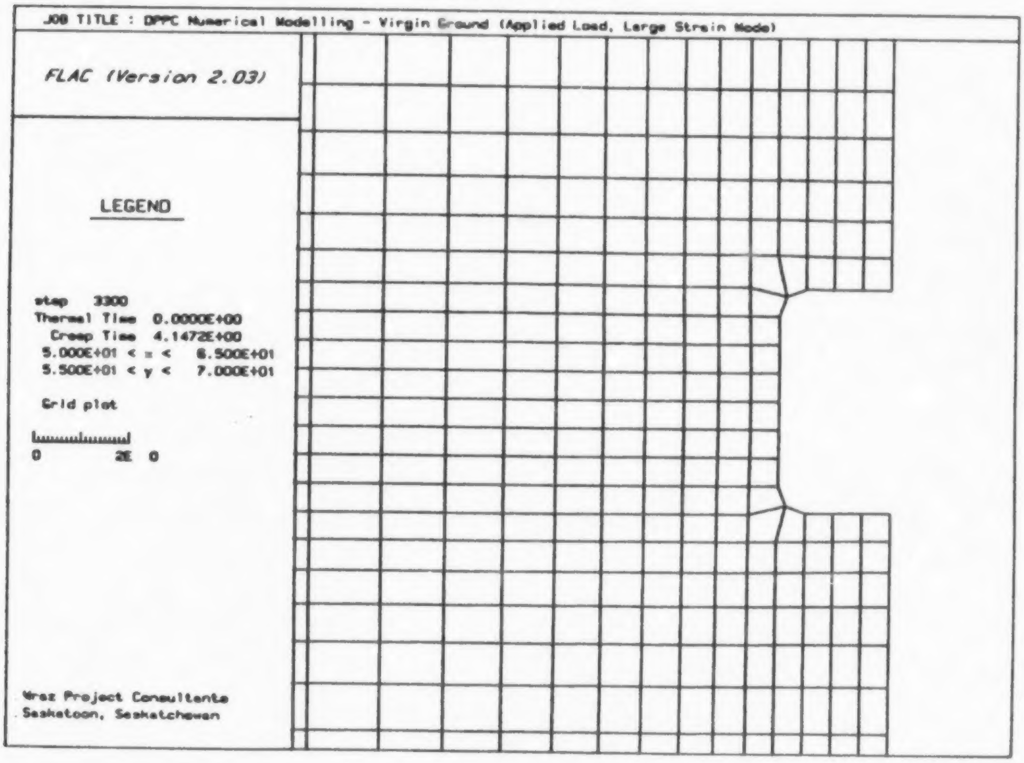

FIGURE 8.6

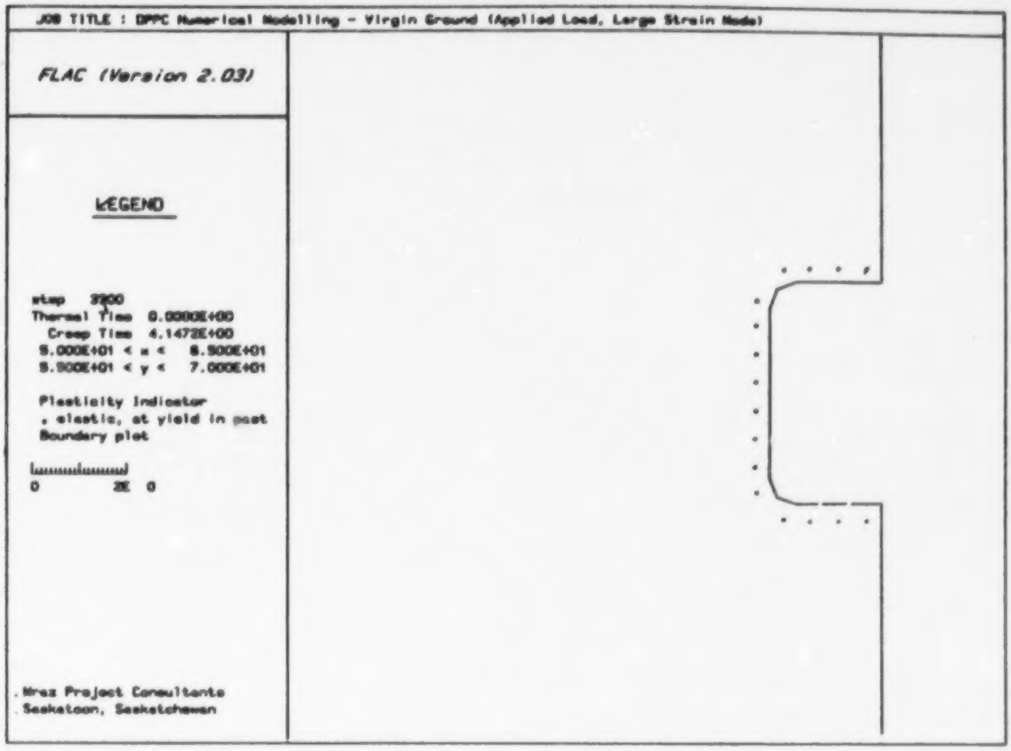

FIGURE 8.7

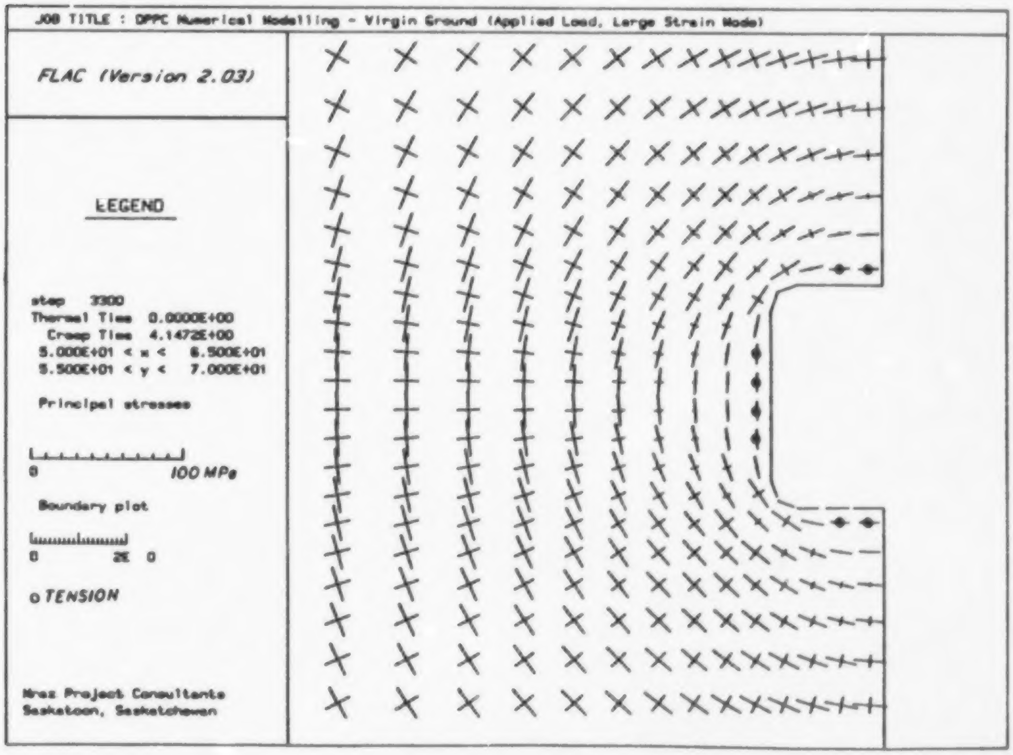

FIGURE 8.8

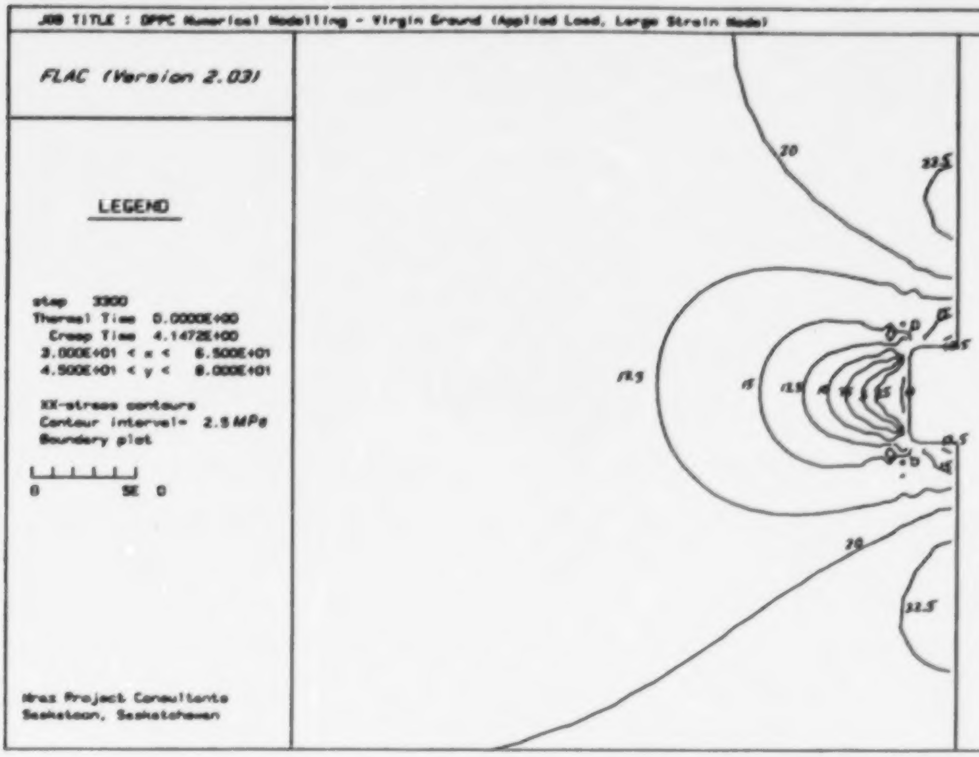

FIGURE 8.9

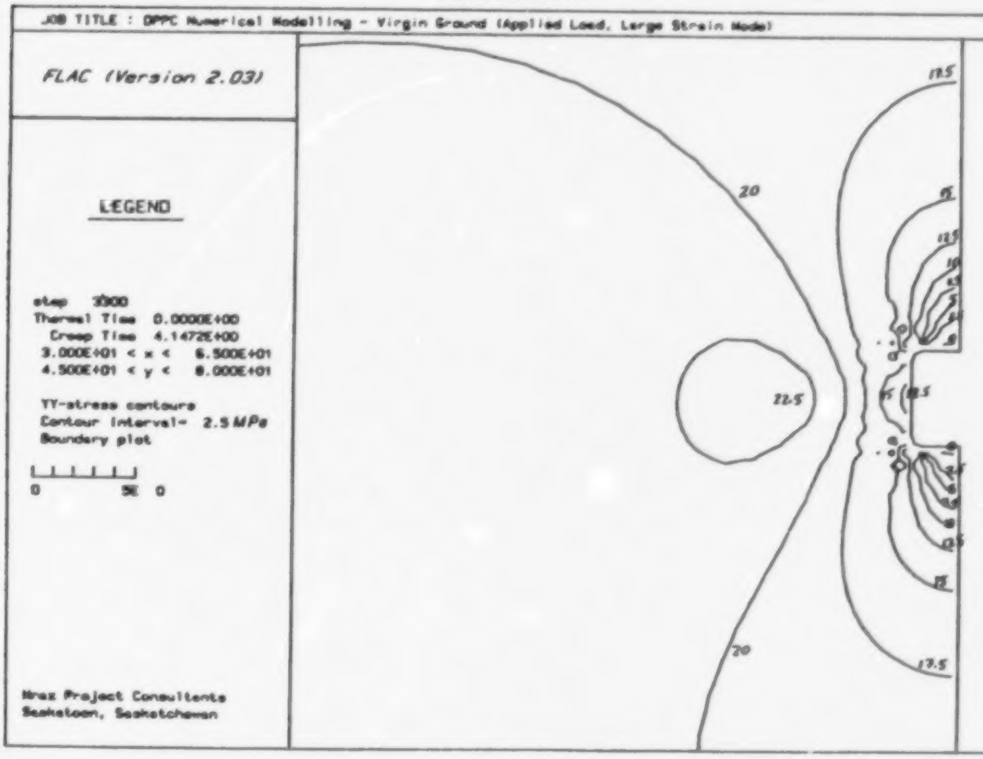

FIGURE 8.10

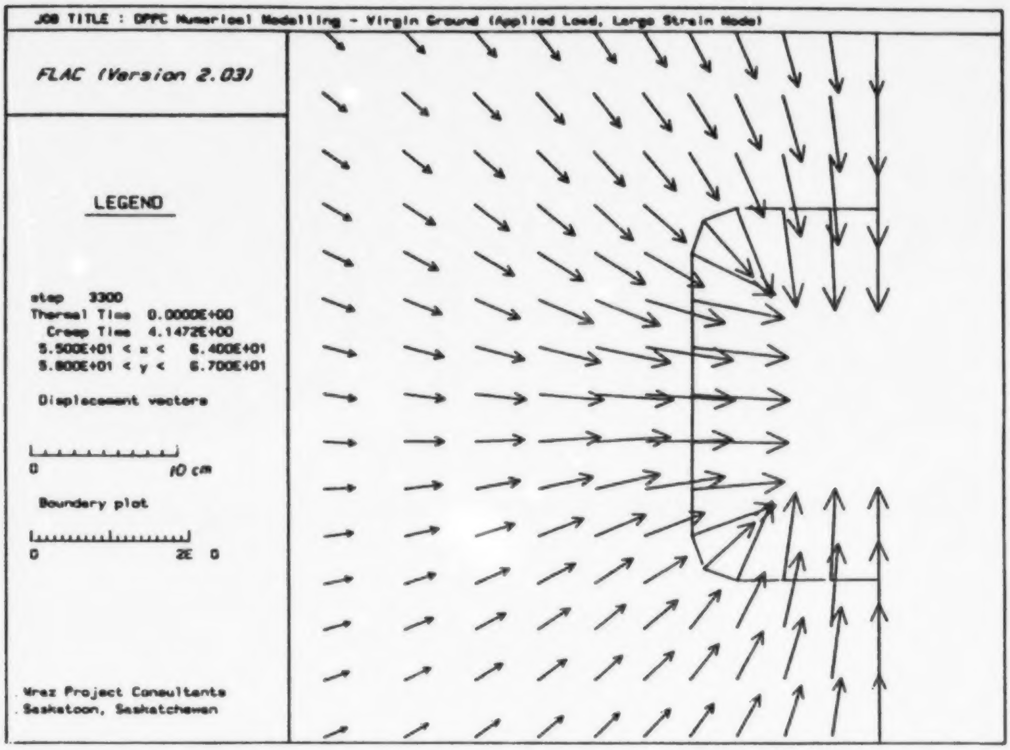

FIGURE 8.11

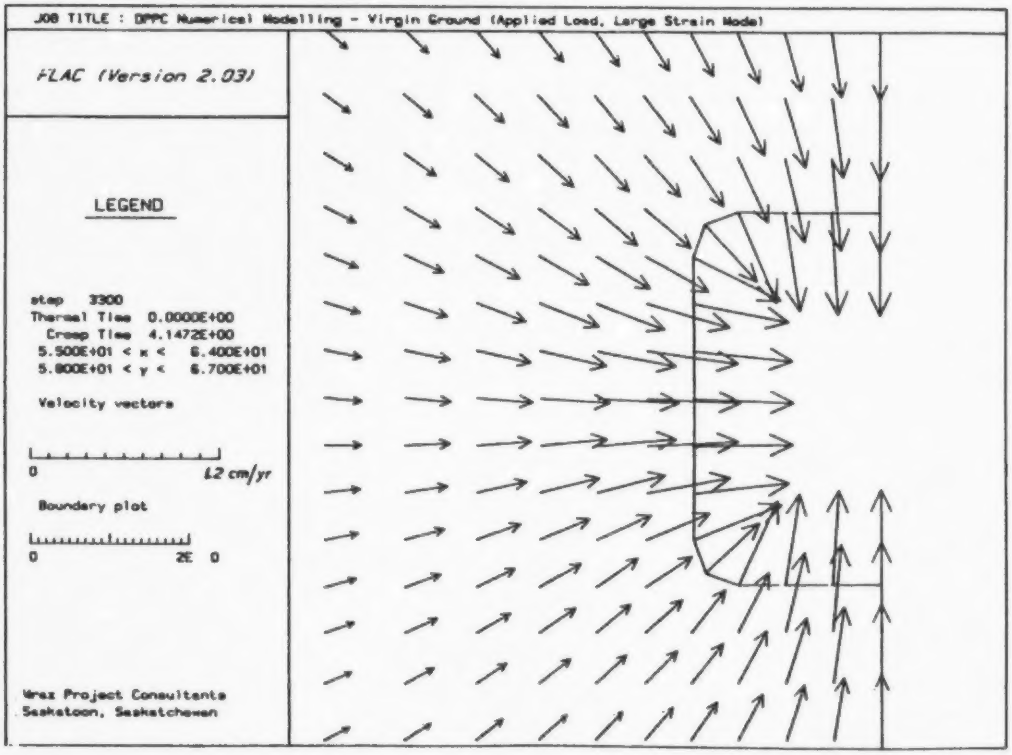

FIGURE 8.12

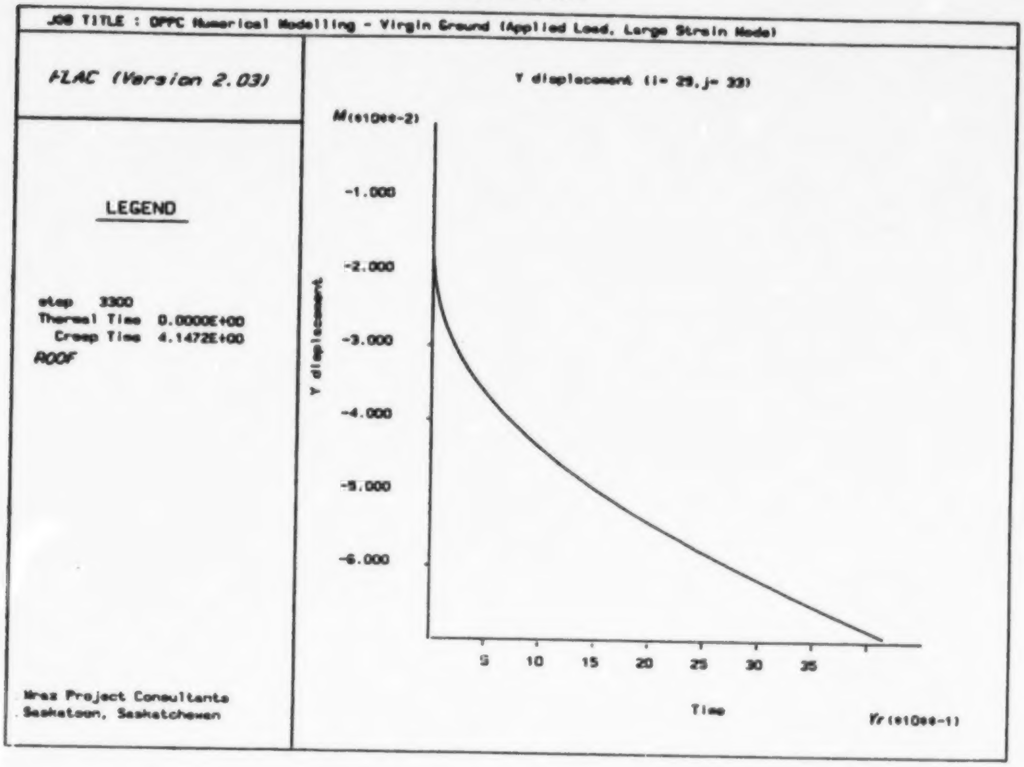

JOB TITLE : OPPC Numerical Modelling - Virgin Ground (Applied Load, Large Strain Mode)

FLAC (Version 2.03)

LEGEND

step 3300
Thermal Time 0.0000E+00
Creep Time 4.1472E+00
ROOF

Mraz Project Consultants
Saskatoon, Saskatchewan

FIGURE 8.13

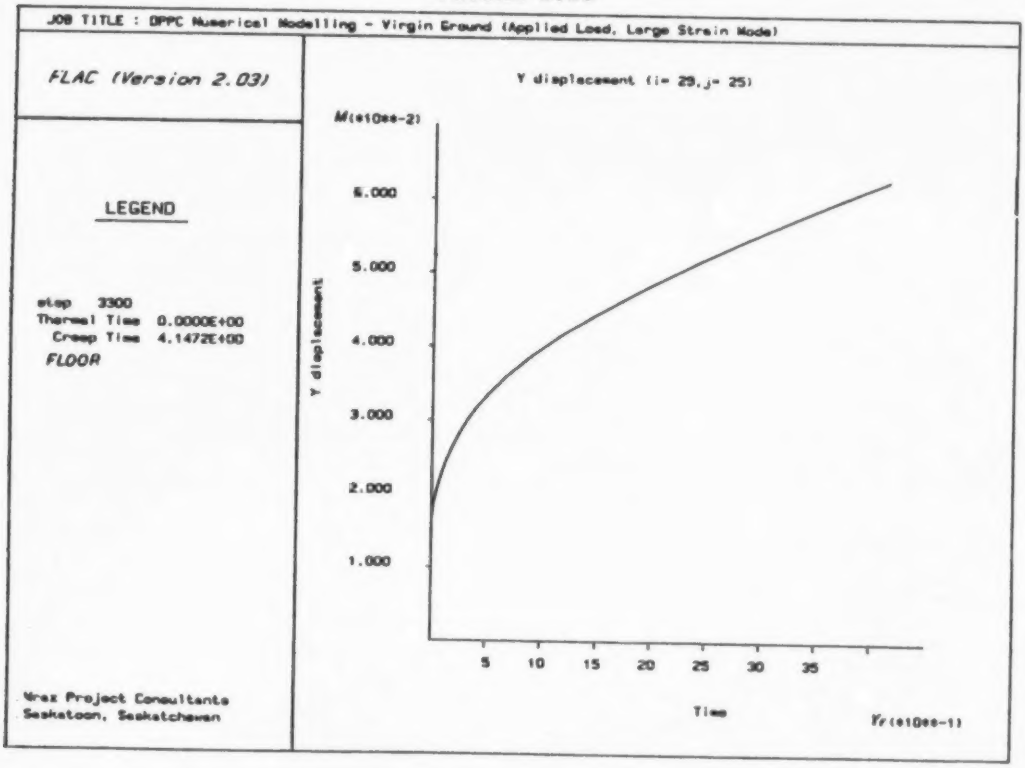

JOB TITLE : OPPC Numerical Modelling - Virgin Ground (Applied Load, Large Strain Mode)

FLAC (Version 2.03)

LEGEND

step 3300
Thermal Time 0.0000E+00
Creep Time 4.1472E+00
FLOOR

Mraz Project Consultants
Saskatoon, Saskatchewan

FIGURE 8.14

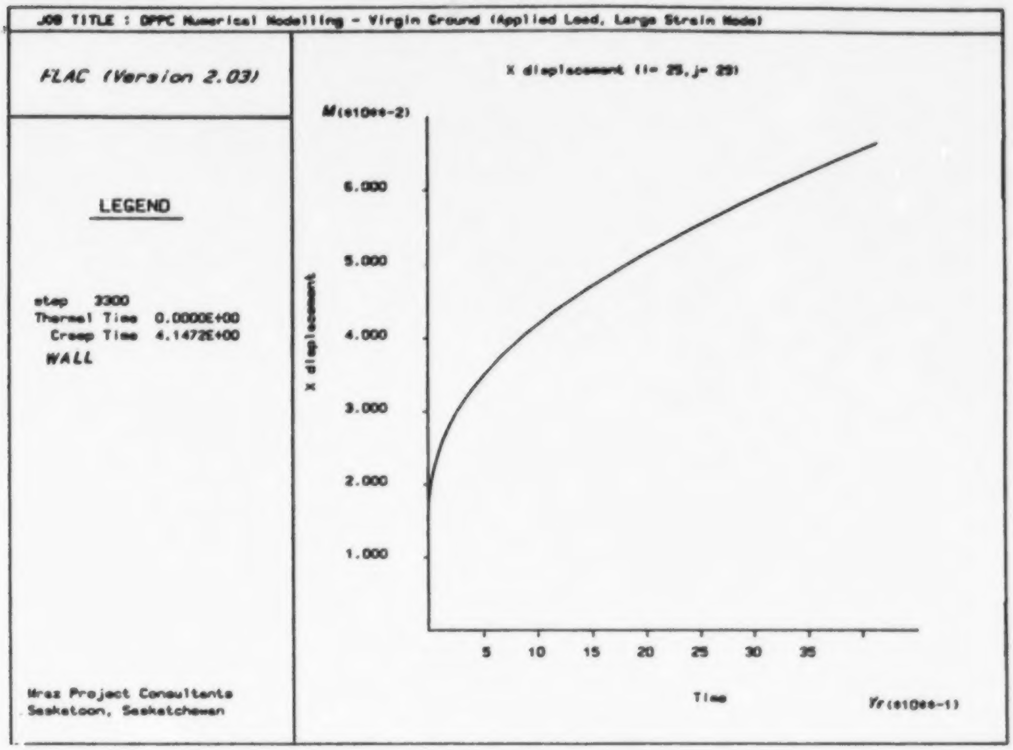
JOB TITLE : OPPC Numerical Modelling - Virgin Ground (Applied Load, Large Strain Mode)
FLAC (Version 2.03)
LEGEND
step 3300
Thermal Time 0.0000E+00
Creep Time 4.1472E+00
WALL
Mraz Project Consultants
Saskatoon, Saskatchewan
X displacement (i= 25, j= 29)
M(*10^-2)
6.000
5.000
4.000
3.000
2.000
1.000
X displacement
5
10
15
20
25
30
35
Time
Yr(*10^-1)

FIGURE 8.15

FLAC COMPARISON

Vertical Closure

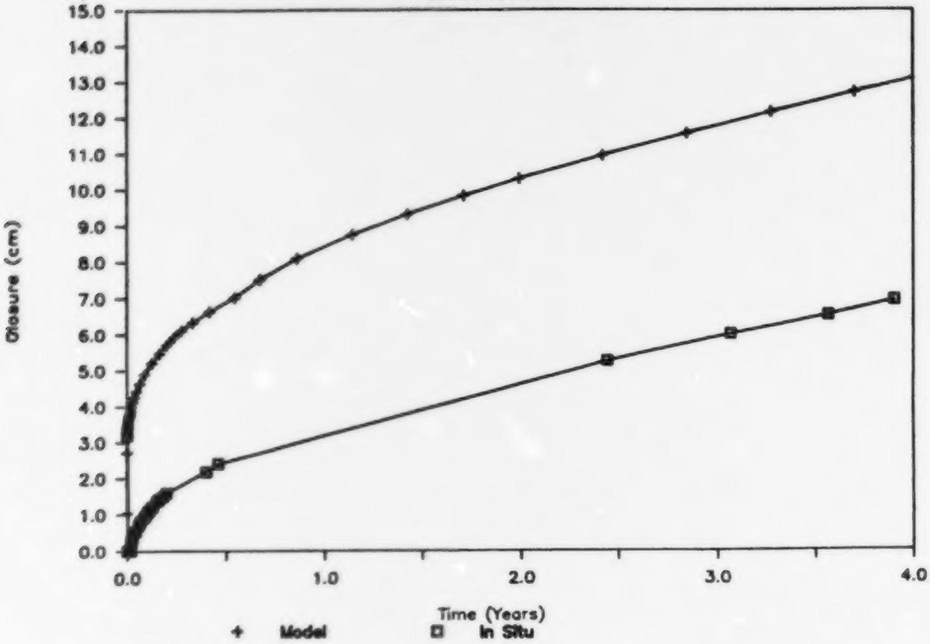

FIGURE 8.16

FLAC COMPARISON

Horizontal Closure

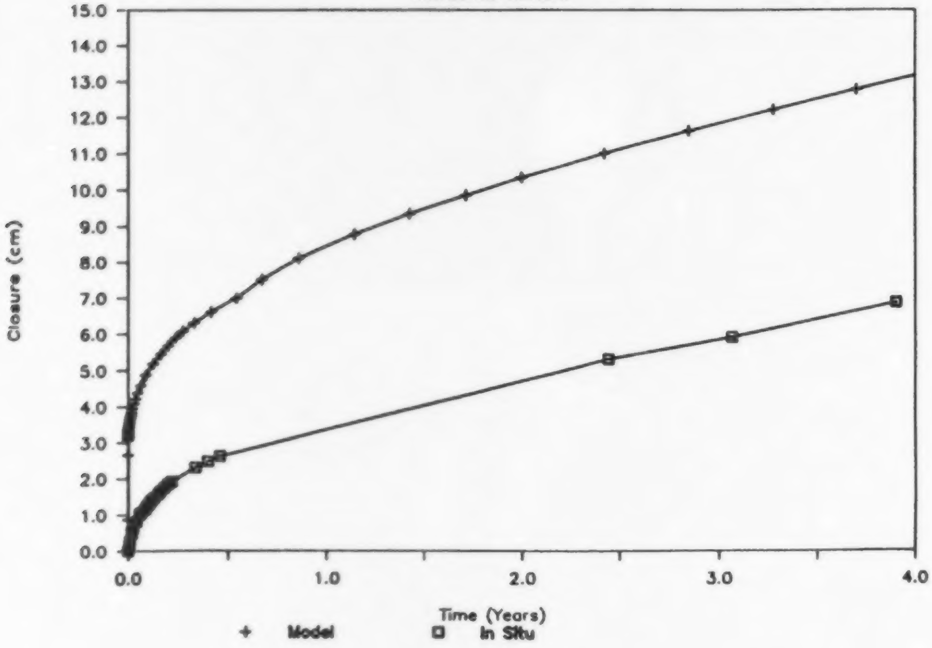

FIGURE 8.17

FLAC COMPARISON

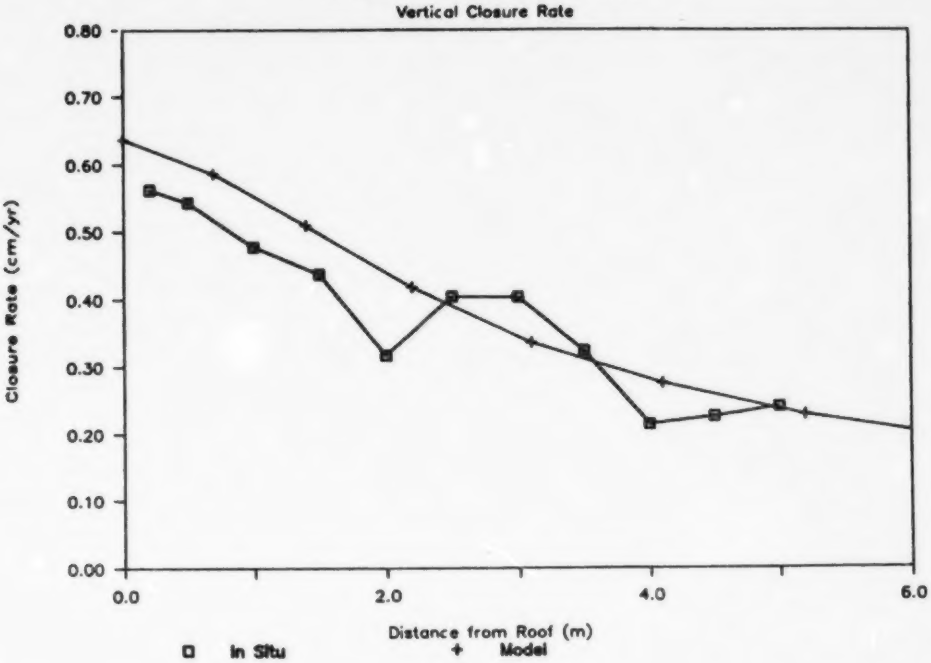

FIGURE 8.18

FLAC COMPARISON

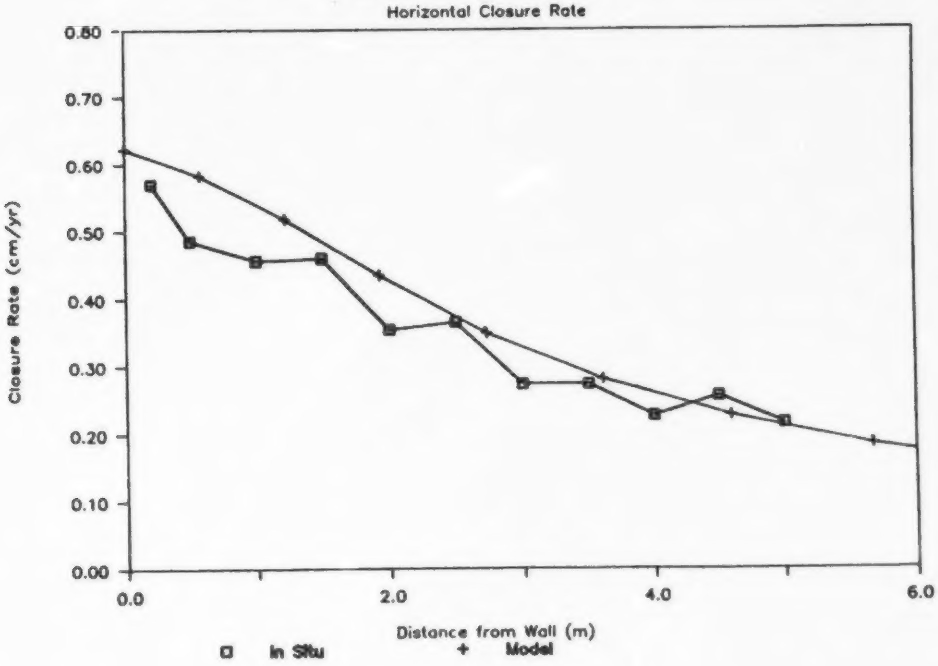

A comparison between the in situ data for vertical and horizontal closure and the numerical solution is shown in Figures 8.15 and 8.16, respectively. The in situ measurements do not reflect the portion of closure that occurs between mining of the room and installation of instrumentation (i.e. transient closure). Otherwise, good correlation is shown between the in situ measurements and the modelled closures.

A comparison between the in situ measurements for vertical and horizontal closure rates and the rates predicted by FLAC are shown in Figures 8.17 and 8.18, respectively. Good correlation between in situ rates and the modelled rates are shown.

8.5.2 Calibration Against the Three Room Entry (12826/12827/12828) System

This numerical modelling run simulated the mining of the three room entry system (12826, 12827, 12828). Rooms 1, 2 and 3 correspond to Entries 12826, 12827 and 12828, respectively.

The objective of this run was to compare and calibrate predicted closures and stress levels with that of in situ data reported in Section 3.4.3.

Outputs from the numerical simulation are shown in Figures 8.19 to 8.45. The material properties used to calibrate FLAC against the three room entry system are summarized in Table 7.6. The constitutive law used is defined by Equation 7.5.

A comparison between the in situ measurements and the modelling results for vertical stress in the yield pillar between Entries 12826 and 12827 is shown in Figure 8.43. Similarly, comparisons of in situ and predicted horizontal and vertical closures are shown in Figures 8.44 and 8.45, respectively.

Several types of pressure cells were utilized in obtaining in situ vertical stress measurements in the yield pillar between Entries 12826 and 12827 (see Section 3.0 for details). The numerical simulation predicted

FIGURE 8.19

JOB TITLE : DPPC Numerical Modelling - Three Room Calibration (Stage #1)

FLAC (Version 2.03)

LEGEND

step 4311
Thermal Time 0.0000E+00
Creep Time 5.1231E-01
$-5.000E+00 < x < 1.650E+02$
$-3.500E+01 < y < 1.350E+02$

Grid plot

0 2E 1

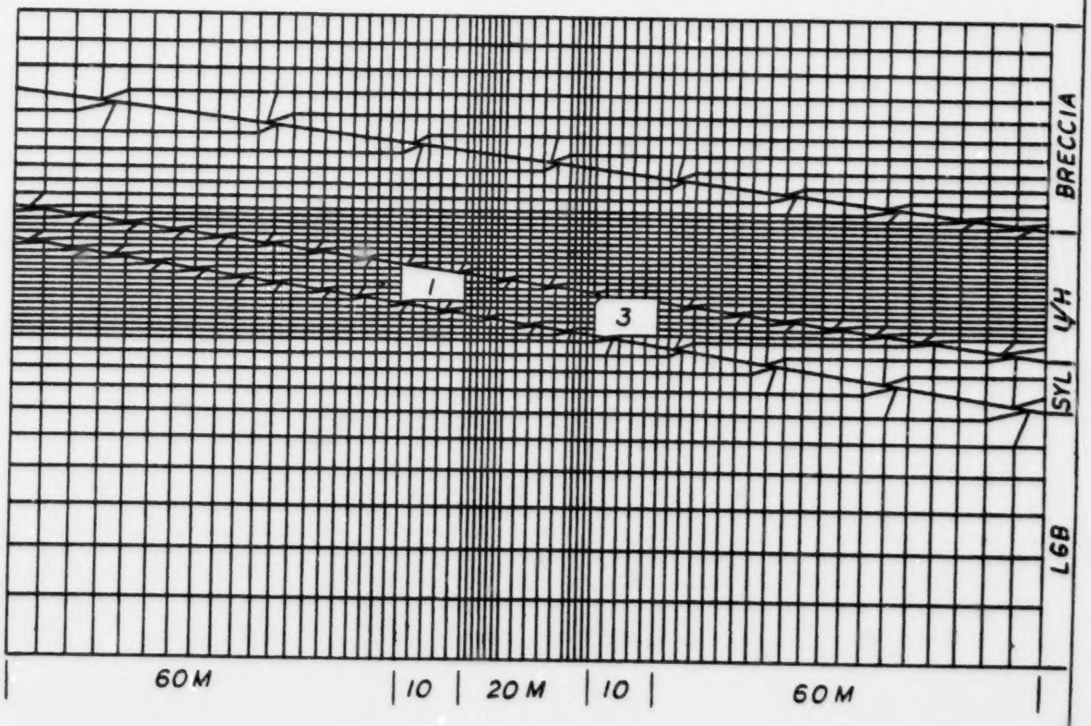

. Mraz Project Consultants
. Saskatoon, Saskatchewan

FIGURE 8.20

JOB TITLE : DPPC Numerical Modelling - Three Room Calibration (Final)

FLAC (Version 2.03)

LEGEND

step 12000
Thermal Time 0.0000E+00
Creep Time 5.0010E+00
-5.000E+00 < x < 1.650E+02
-3.500E+01 < y < 1.350E+02

Grid plot

0 2E 1

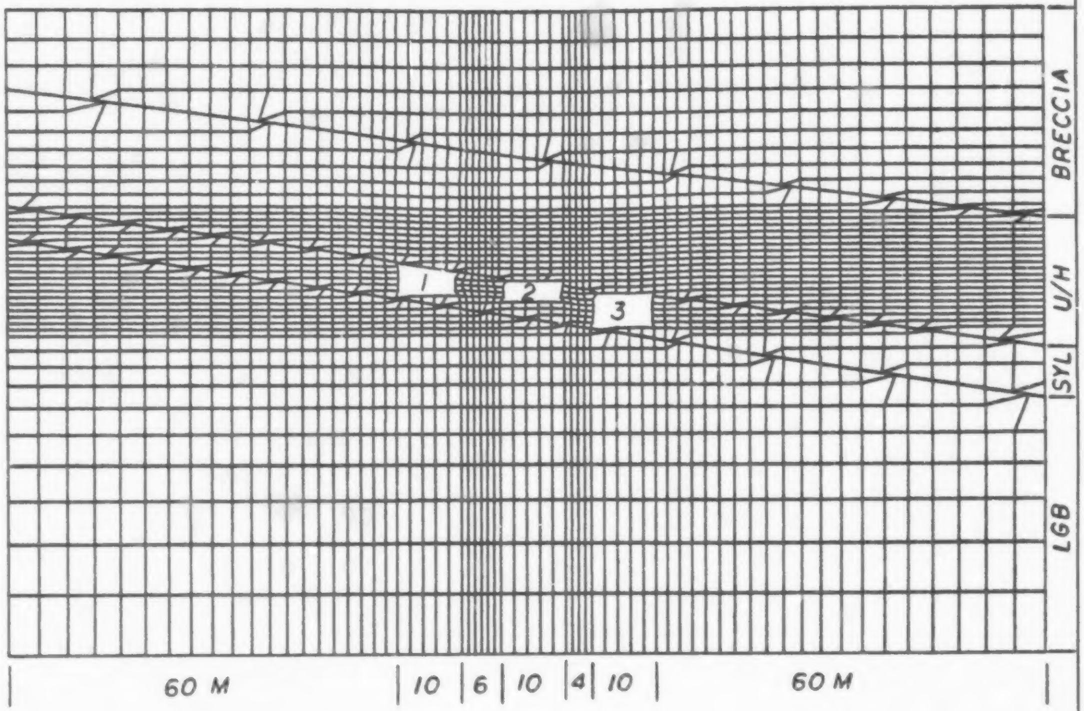

Mraz Project Consultents
Saskatoon, Saskatchewan

FIGURE 8.21

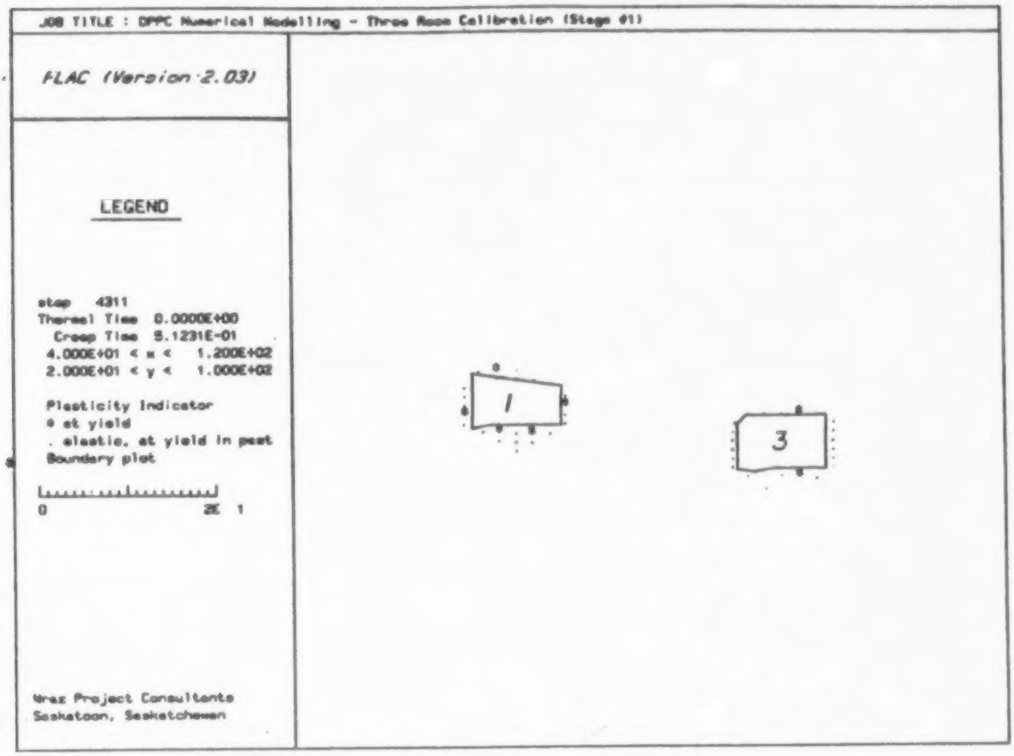

```
JOB TITLE : DPPC Numerical Modelling - Three Room Calibration (Stage #1)

FLAC (Version 2.03)

LEGEND

step   4311
Thermal Time  0.0000E+00
  Creep Time  5.1231E-01
 4.000E+01 < x <   1.200E+02
 2.000E+01 < y <   1.000E+02

 Plasticity Indicator
 # at yield
 . elastic, at yield in past
 Boundary plot

0                    2E  1

Wrax Project Consultants
Saskatoon, Saskatchewan
```

FIGURE 8.22

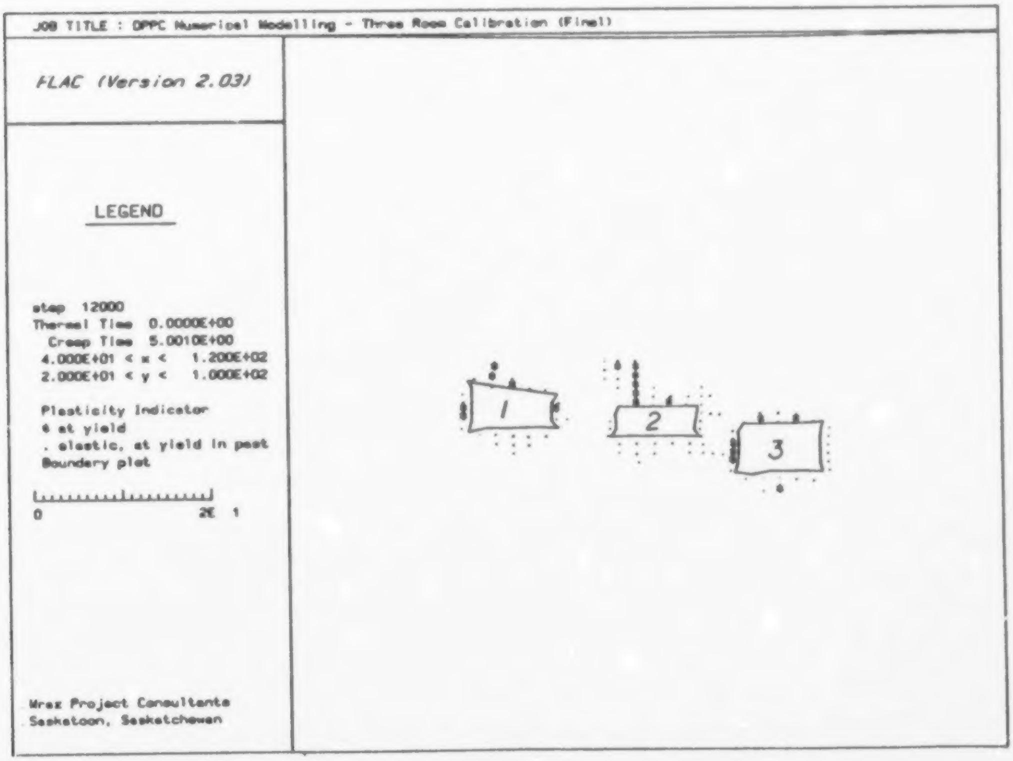

```
JOB TITLE : DPPC Numerical Modelling - Three Room Calibration (Final)

FLAC (Version 2.03)

LEGEND

step  12000
Thermal Time  0.0000E+00
  Creep Time  5.0010E+00
 4.000E+01 < x <   1.200E+02
 2.000E+01 < y <   1.000E+02

 Plasticity Indicator
 # at yield
 . elastic, at yield in past
 Boundary plot

0                    2E  1

Wrax Project Consultants
Saskatoon, Saskatchewan
```

FIGURE 8.23

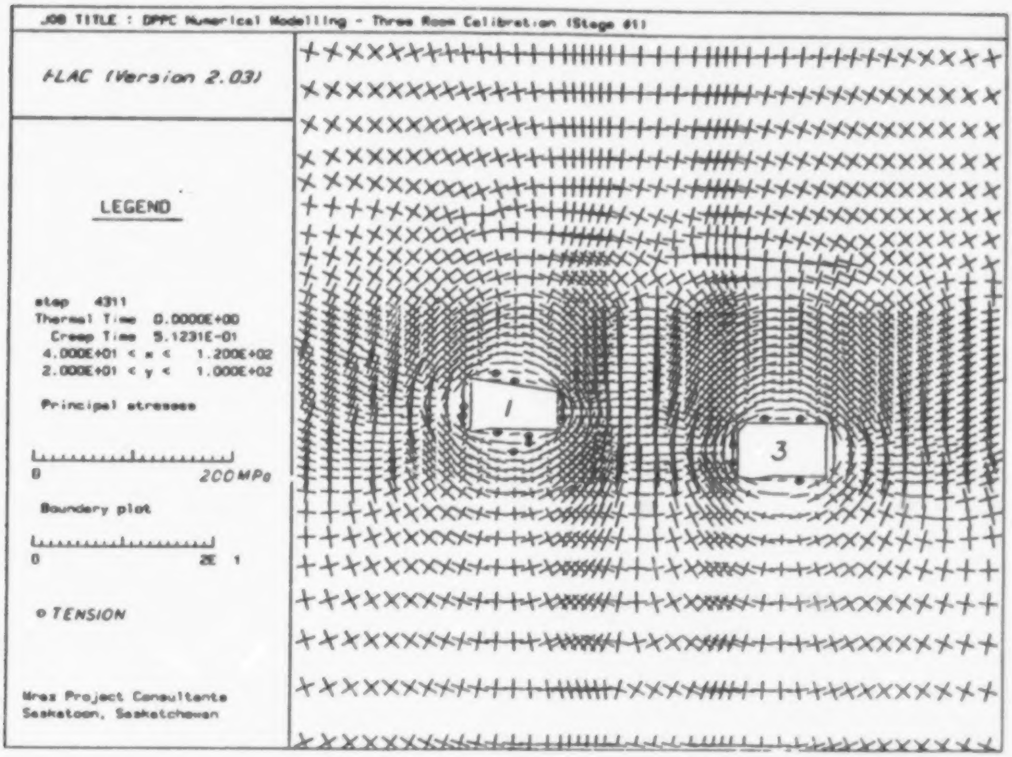

FIGURE 8.24

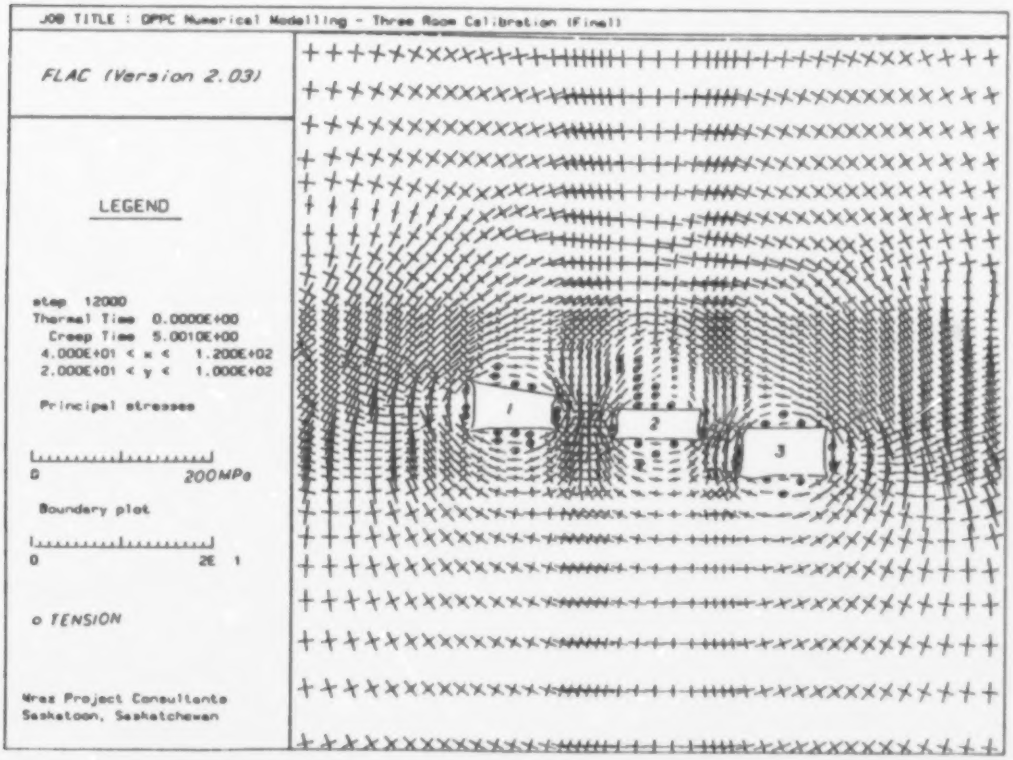

FIGURE 8.25

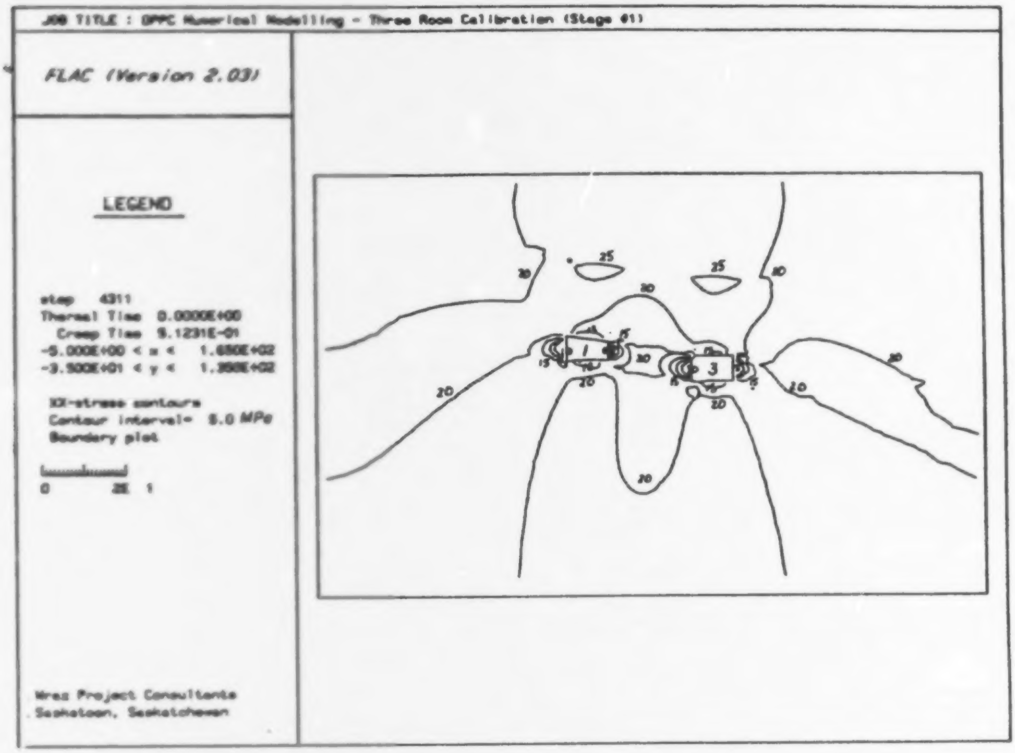

```
JOB TITLE : DPPC Numerical Modelling - Three Room Calibration (Stage #1)

FLAC (Version 2.03)

LEGEND

step   4311
Thermal Time  0.0000E+00
  Creep Time  5.1231E-01
-5.000E+00 < x <   1.650E+02
-3.500E+01 < y <   1.350E+02

 XX-stress contours
 Contour interval=  5.0 MPa
 Boundary plot

0         2E  1

Wroz Project Consultants
Saskatoon, Saskatchewan
```

FIGURE 8.26

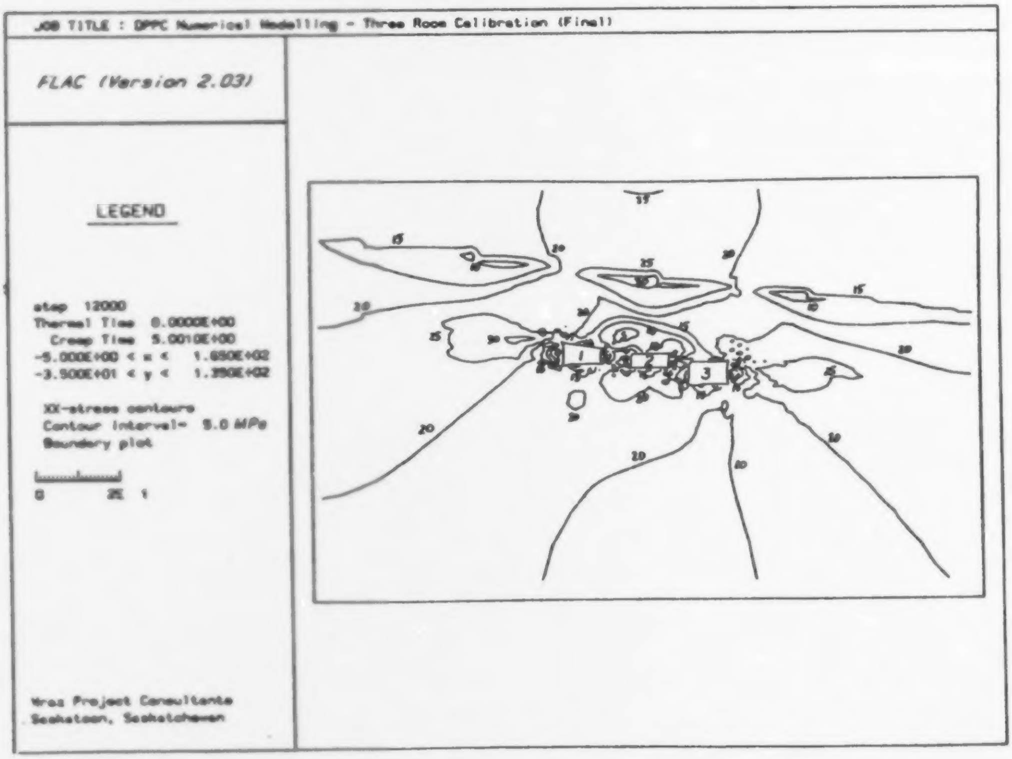

```
JOB TITLE : DPPC Numerical Modelling - Three Room Calibration (Final)

FLAC (Version 2.03)

LEGEND

step  12000
Thermal Time  0.0000E+00
  Creep Time  5.0010E+00
-5.000E+00 < x <   1.650E+02
-3.500E+01 < y <   1.350E+02

 XX-stress contours
 Contour interval=  5.0 MPa
 Boundary plot

0         2E  1

Wroz Project Consultants
Saskatoon, Saskatchewan
```

FIGURE 8.27

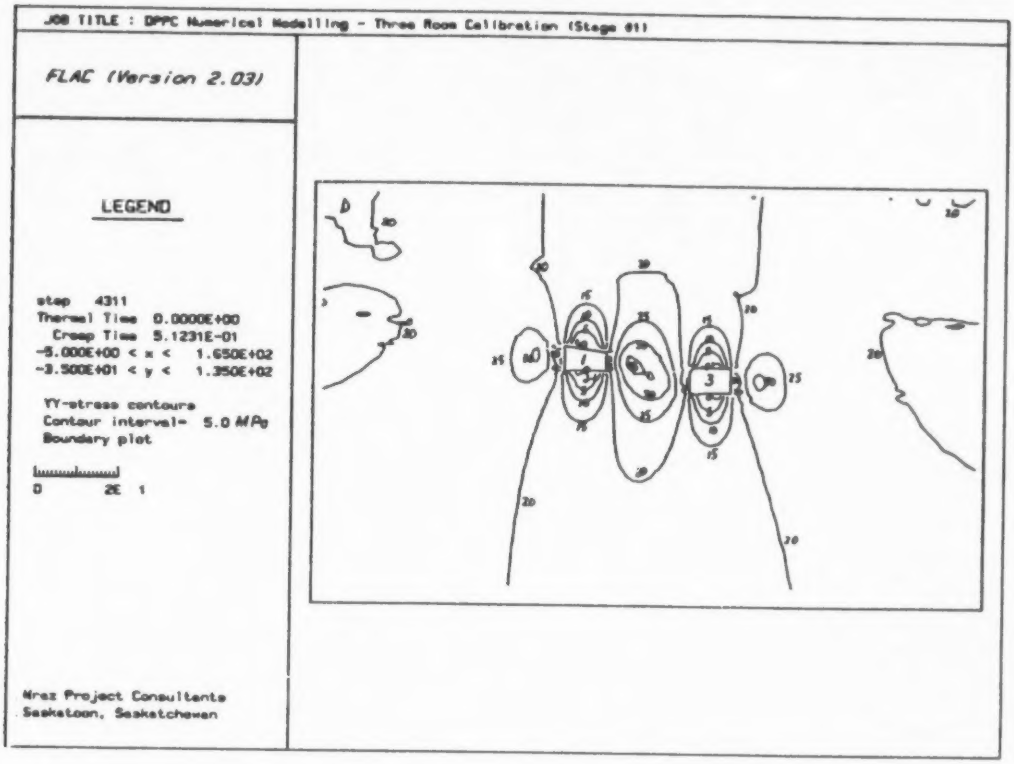

FIGURE 8.28

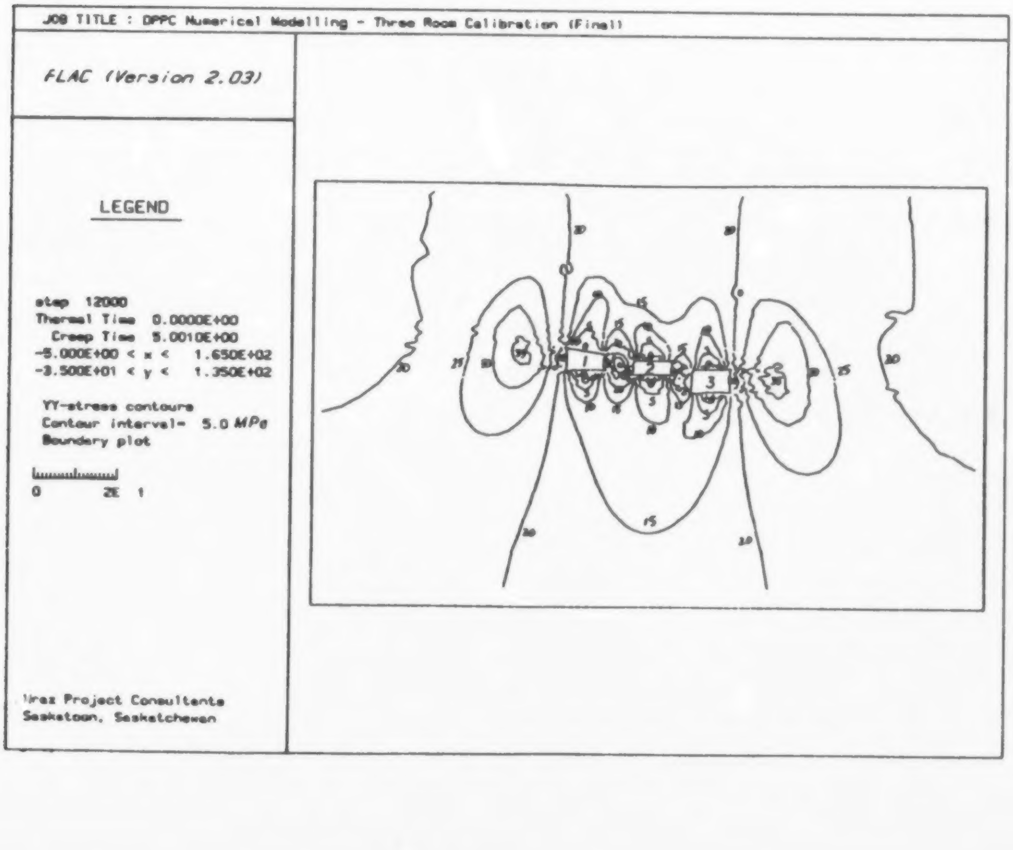

FIGURE 8.29

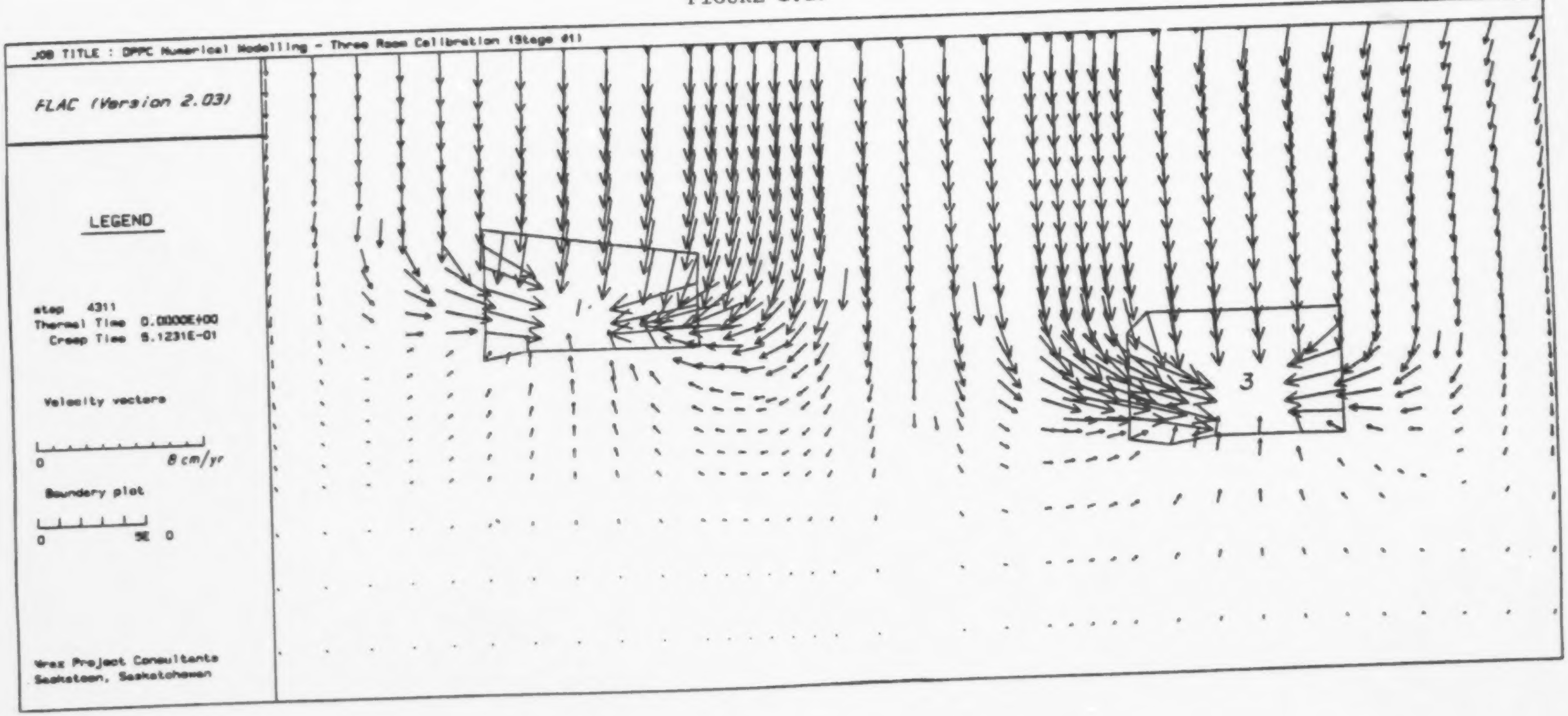
JOB TITLE : DPPC Numerical Modelling - Three Room Calibration (Stage #1)
FLAC (Version 2.03)
LEGEND
step 4311
Thermal Time 0.0000E+00
Creep Time 5.1231E-01
Velocity vectors
0
8 cm/yr
Boundary plot
0
5E 0
Wrex Project Consultants
Saskatoon, Saskatchewan
1
3

FIGURE 8.30

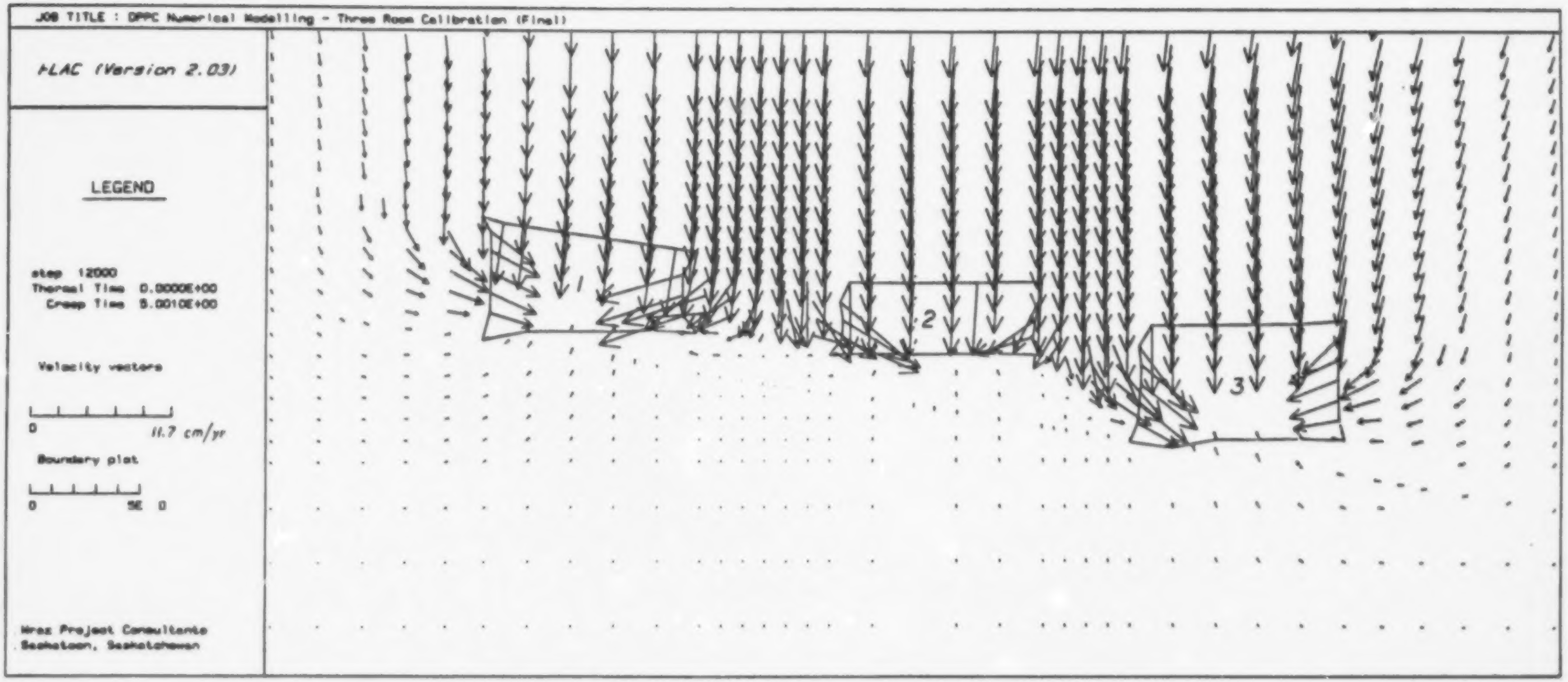
JOB TITLE : DPPC Numerical Modelling - Three Room Calibration (Final)
FLAC (Version 2.03)
LEGEND
step 12000
Thermal Time 0.0000E+00
Creep Time 5.0010E+00
Velocity vectors
0
11.7 cm/yr
Boundary plot
0
5E 0
Mraz Project Consultants
Saskatoon, Saskatchewan
1
2
3

FIGURE 8.31

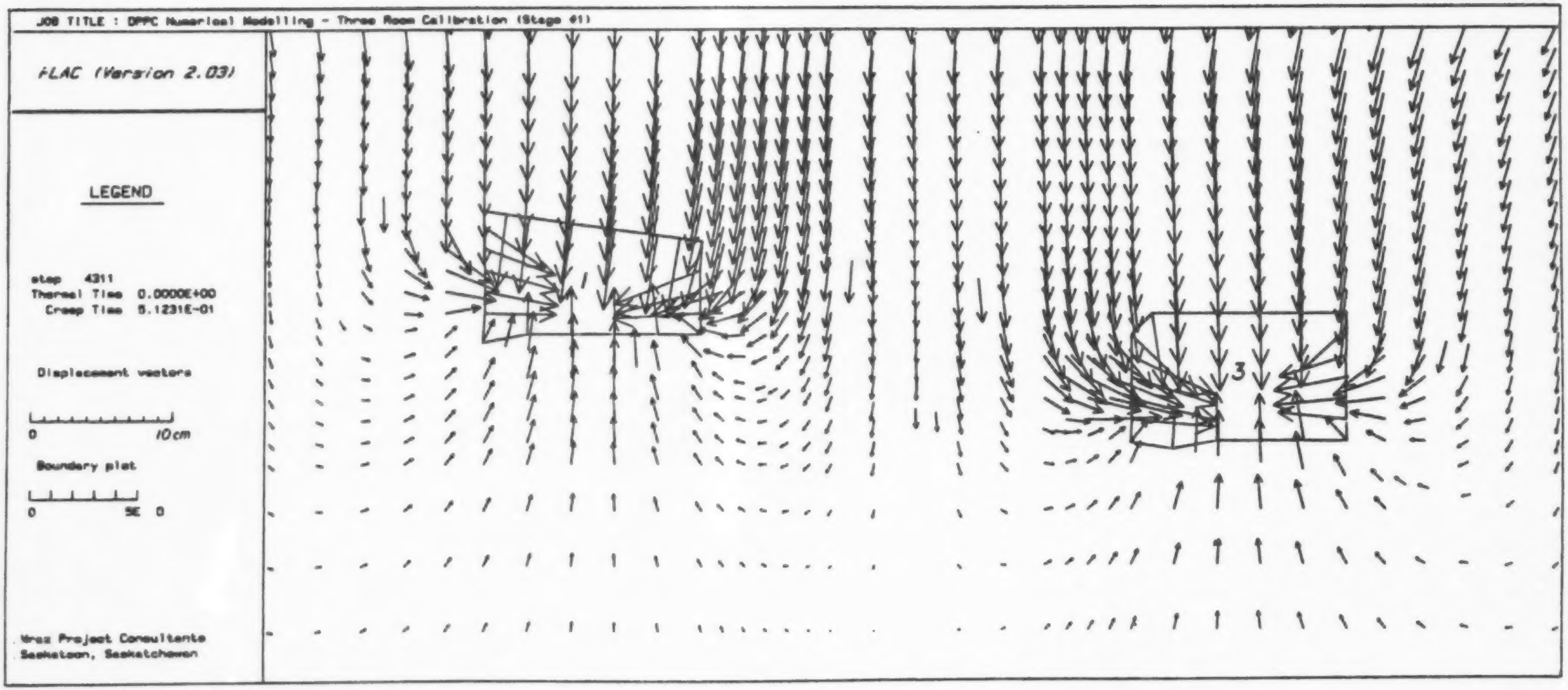
JOB TITLE : DPPC Numerical Modelling - Three Room Calibration (Stage #1)
FLAC (Version 2.03)
LEGEND
step 4311
Thermal Time 0.0000E+00
Creep Time 5.1231E-01
Displacement vectors
0
10cm
Boundary plot
0
5E 0
Mraz Project Consultants
Saskatoon, Saskatchewan
3

FIGURE 8.32

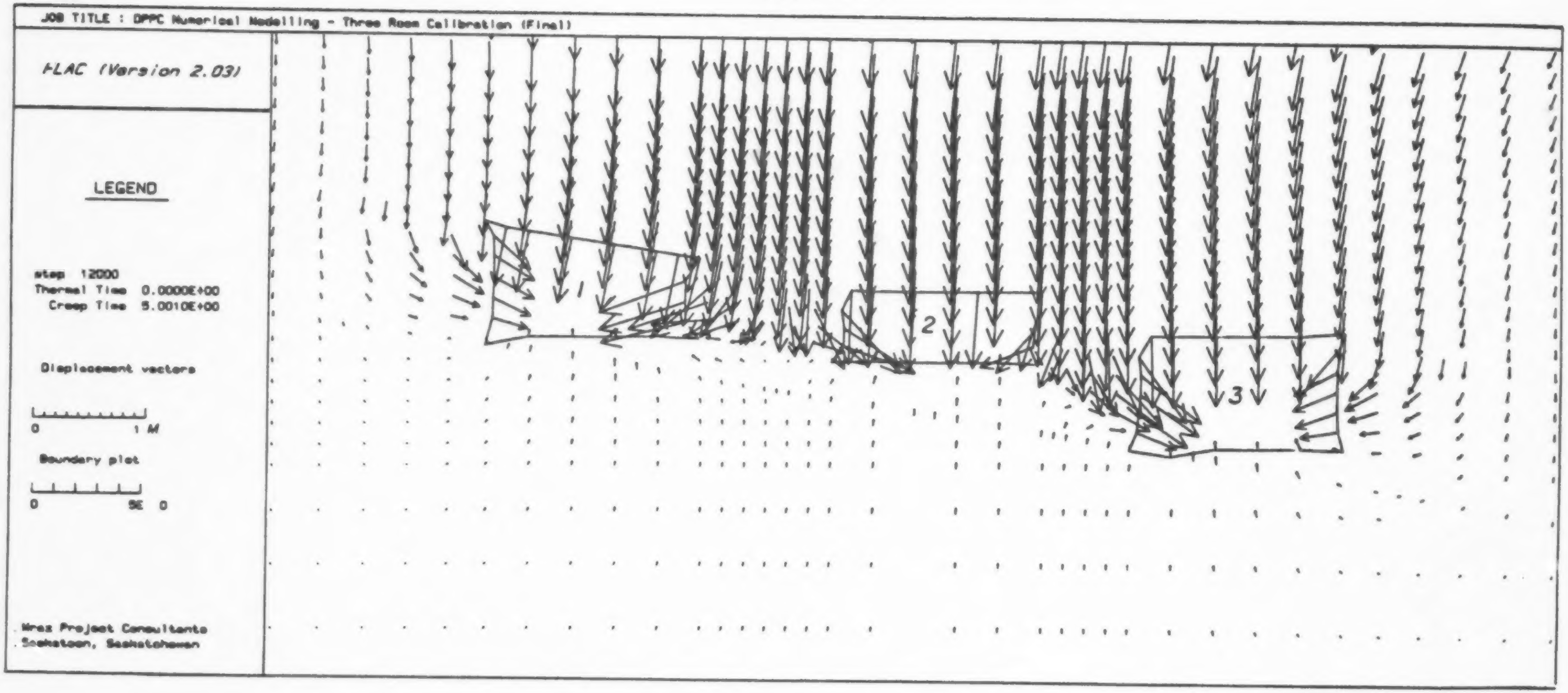
JOB TITLE : DPPC Numerical Modelling - Three Room Calibration (Final)
FLAC (Version 2.03)
LEGEND
step 12000
Thermal Time 0.0000E+00
Creep Time 5.0010E+00
Displacement vectors
0
1 M
Boundary plot
0
5E 0
Wroz Project Consultants
Saskatoon, Saskatchewan
1
2
3

FIGURE 8.33

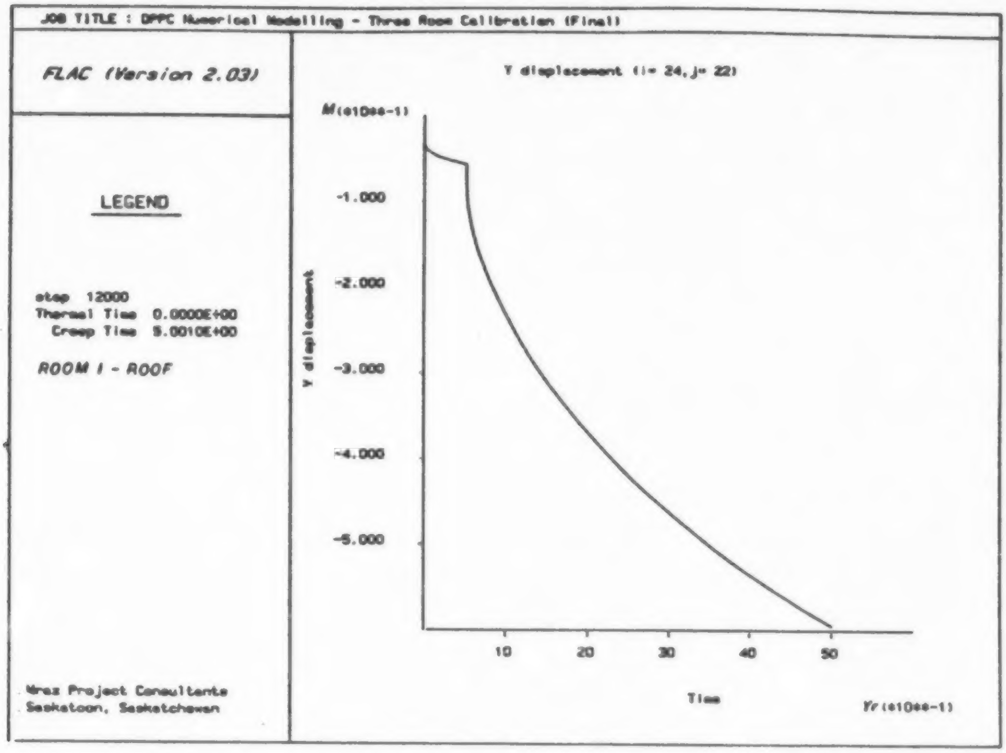

FIGURE 8.34

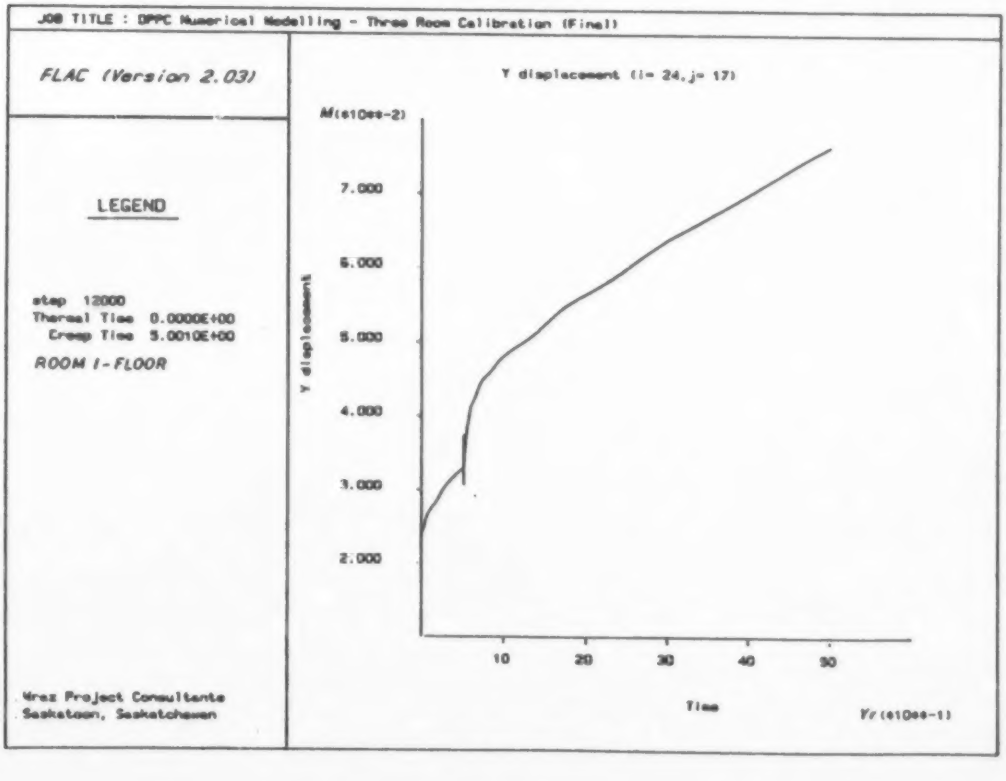

FIGURE 8.35

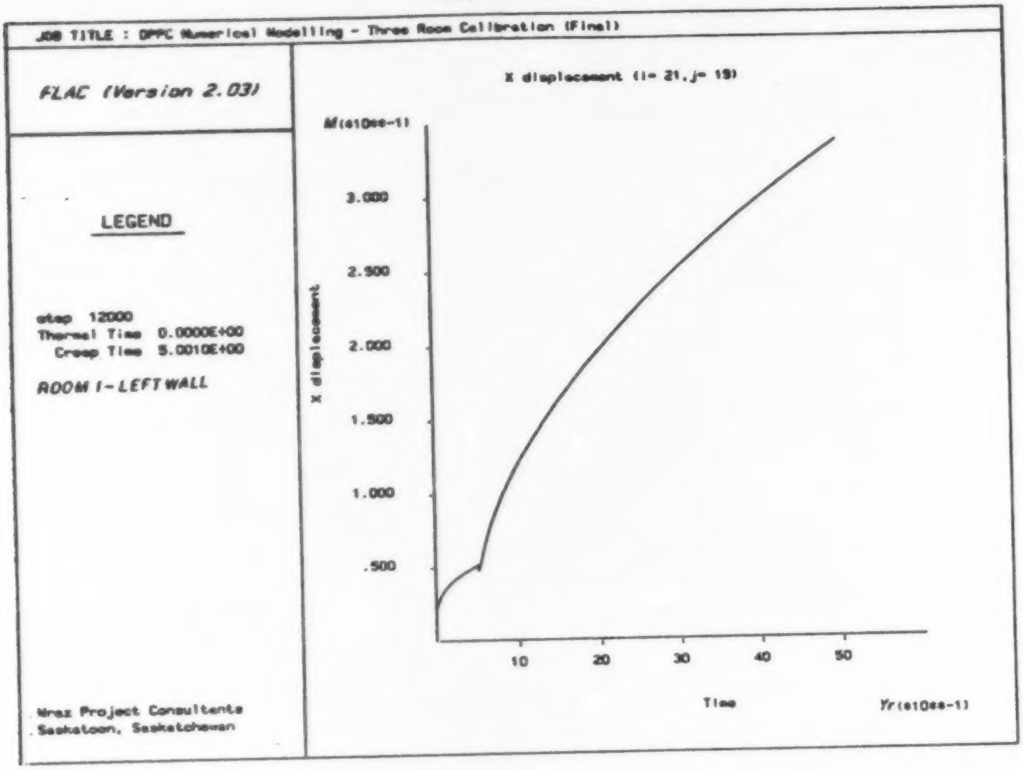

FIGURE 8.36

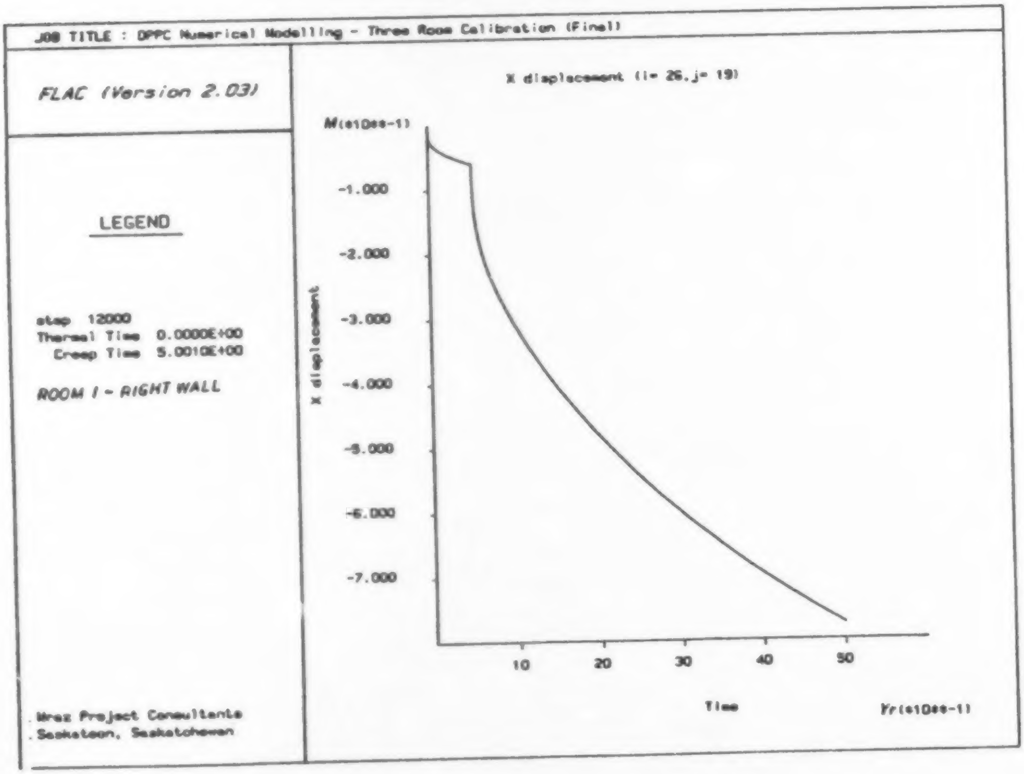

FIGURE 8.37

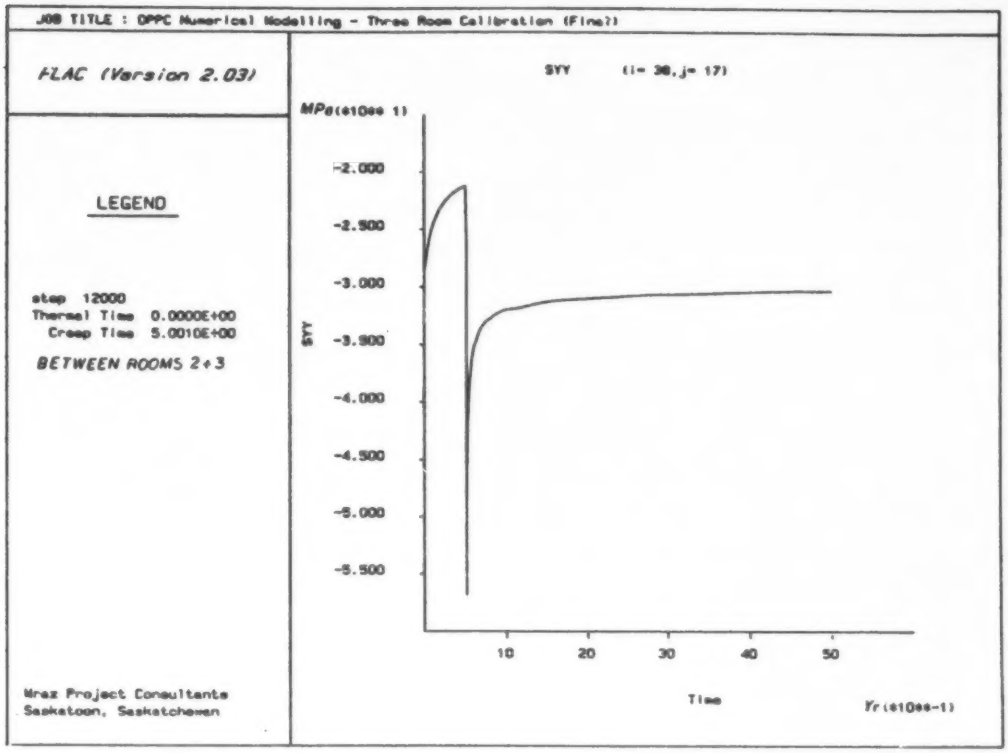

FIGURE 8.38

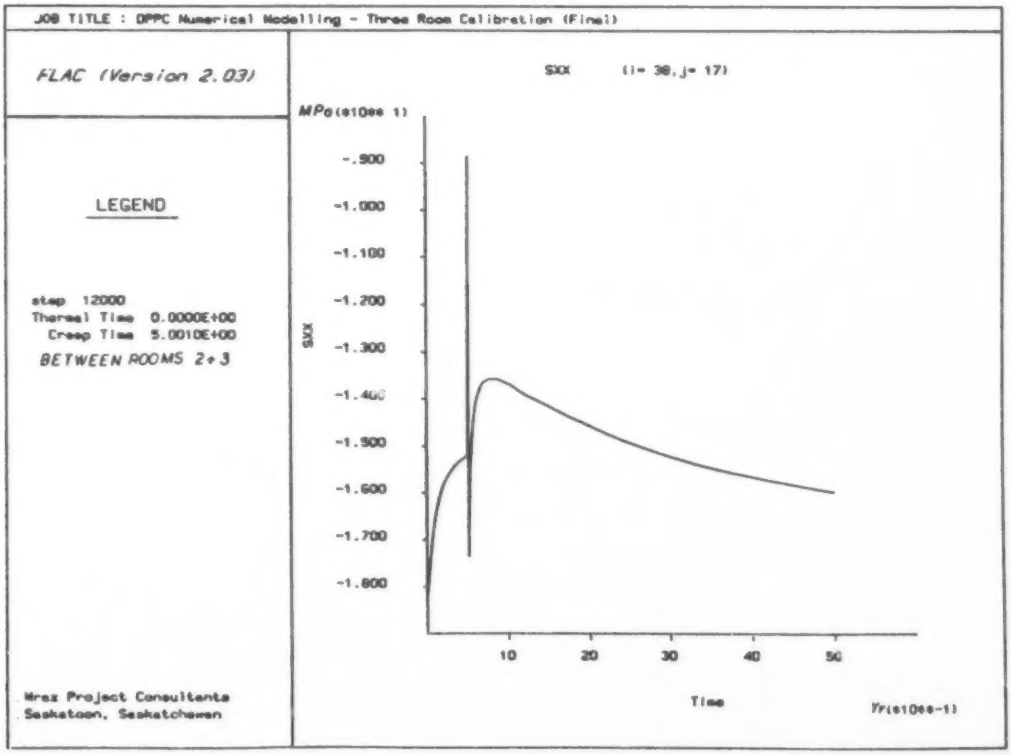

FIGURE 8.39

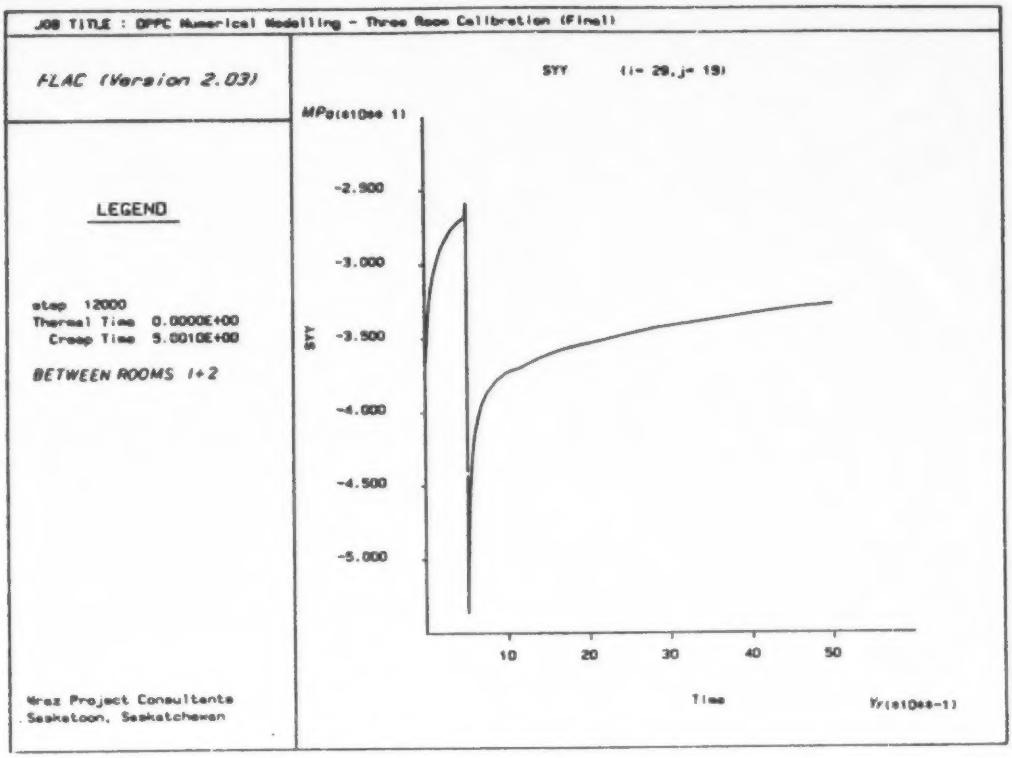

FIGURE 8.40

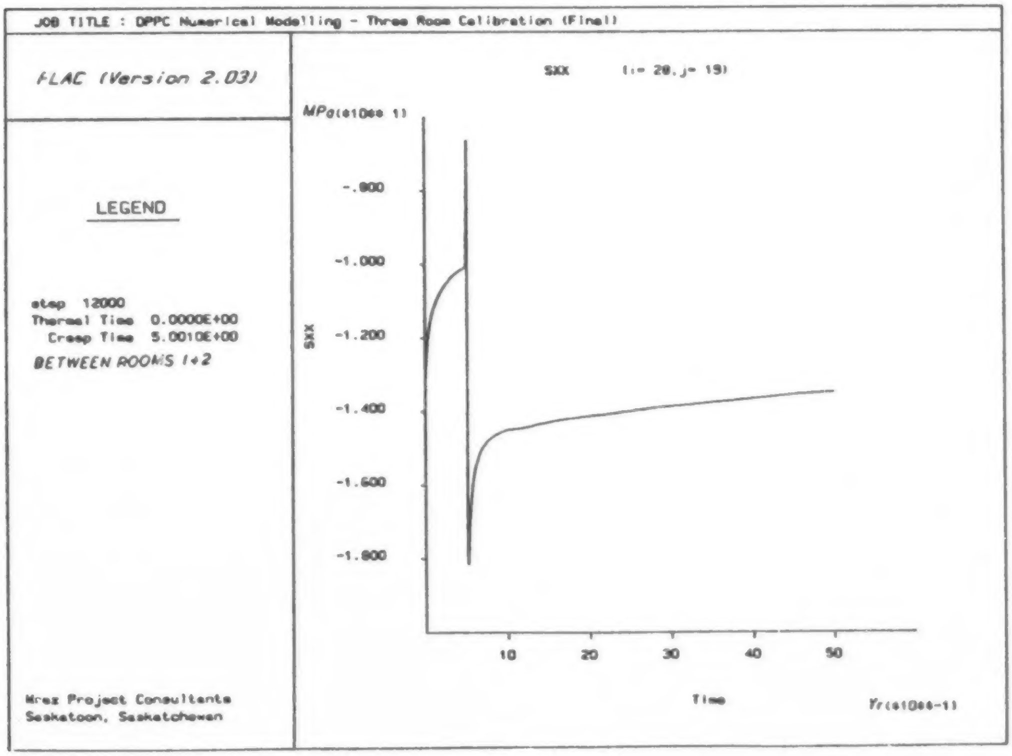

FIGURE 8.41

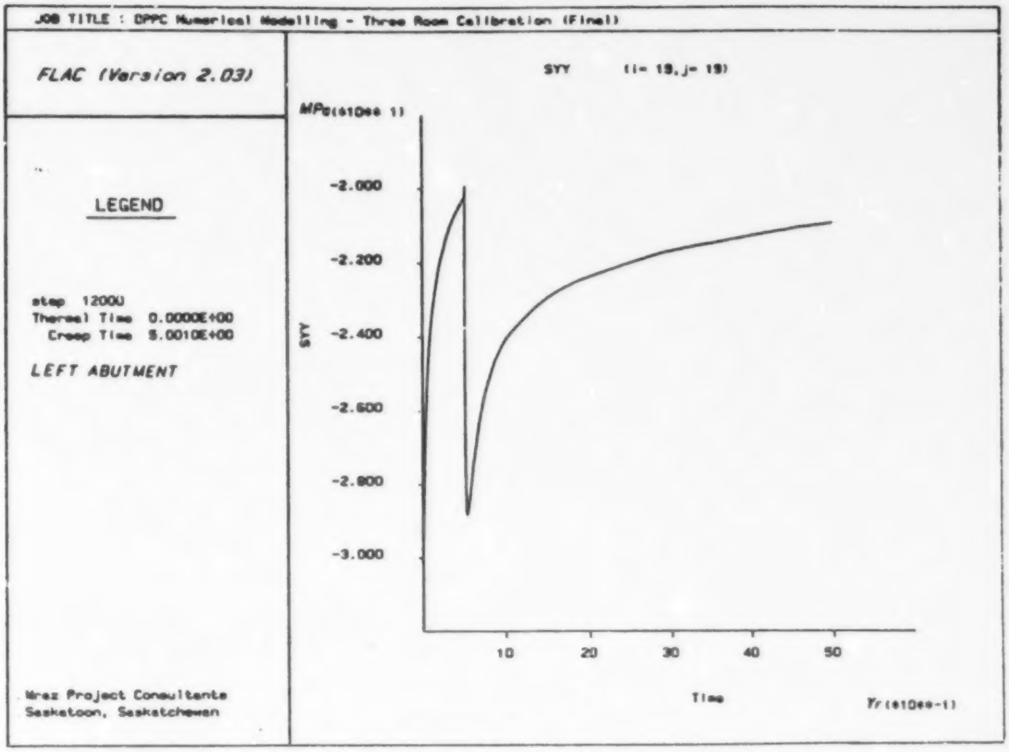

FIGURE 8.42

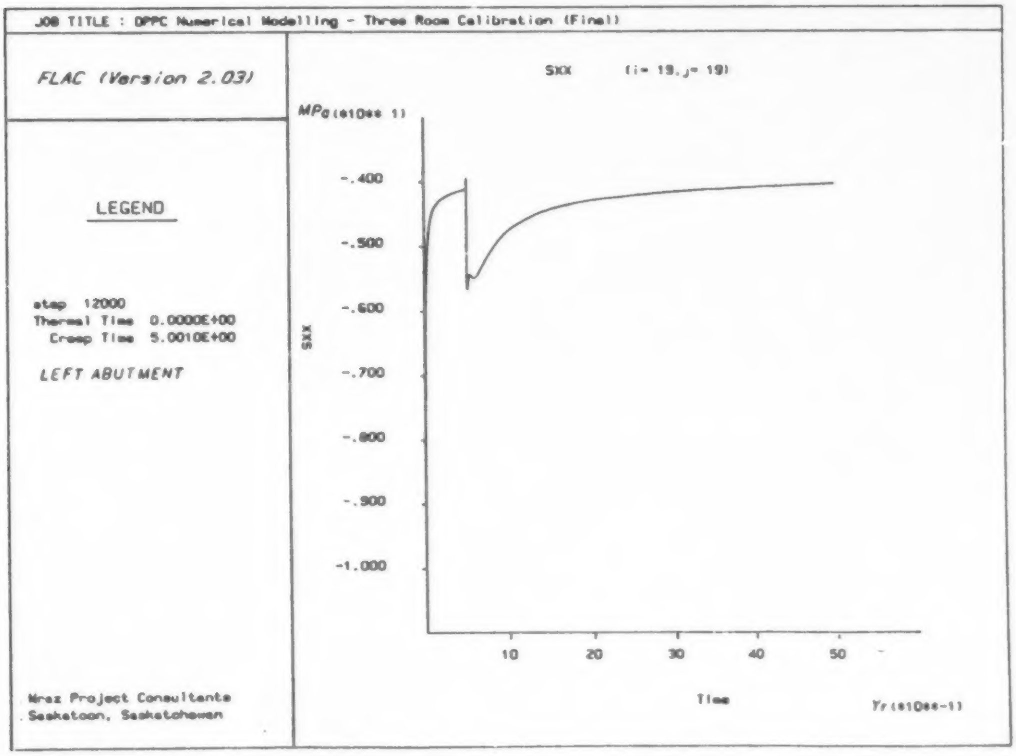

FIGURE 8.43

DPPC 12826 3–ENTRY CALIBRATION

Vertical Stress in Yield Pillar

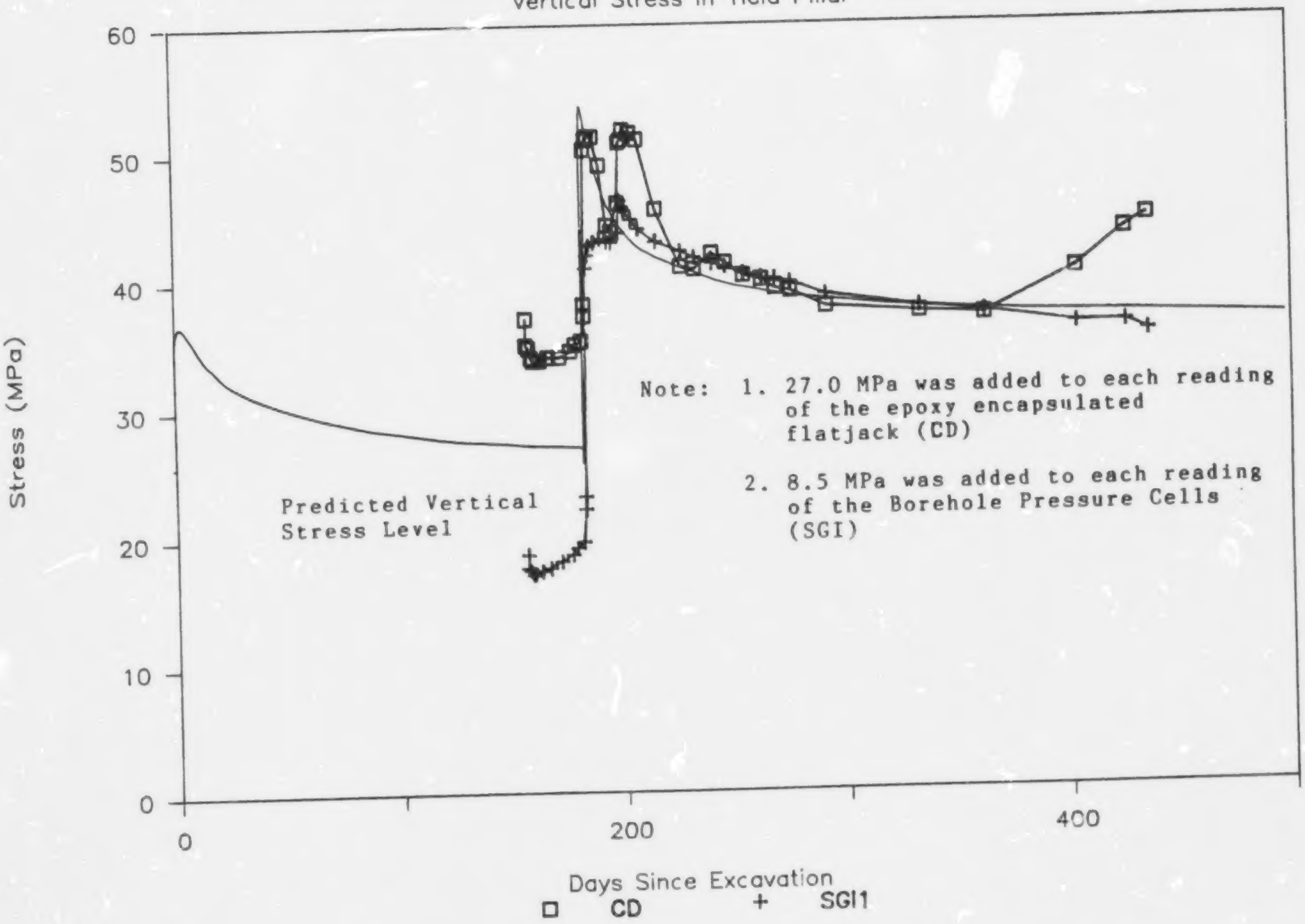

Note: 1. 27.0 MPa was added to each reading of the epoxy encapsulated flatjack (CD)

2. 8.5 MPa was added to each reading of the Borehole Pressure Cells (SGI)

FIGURE 8.44

ROOM 12826 3—ENTRY CALIBRATION

Horizontal Closure

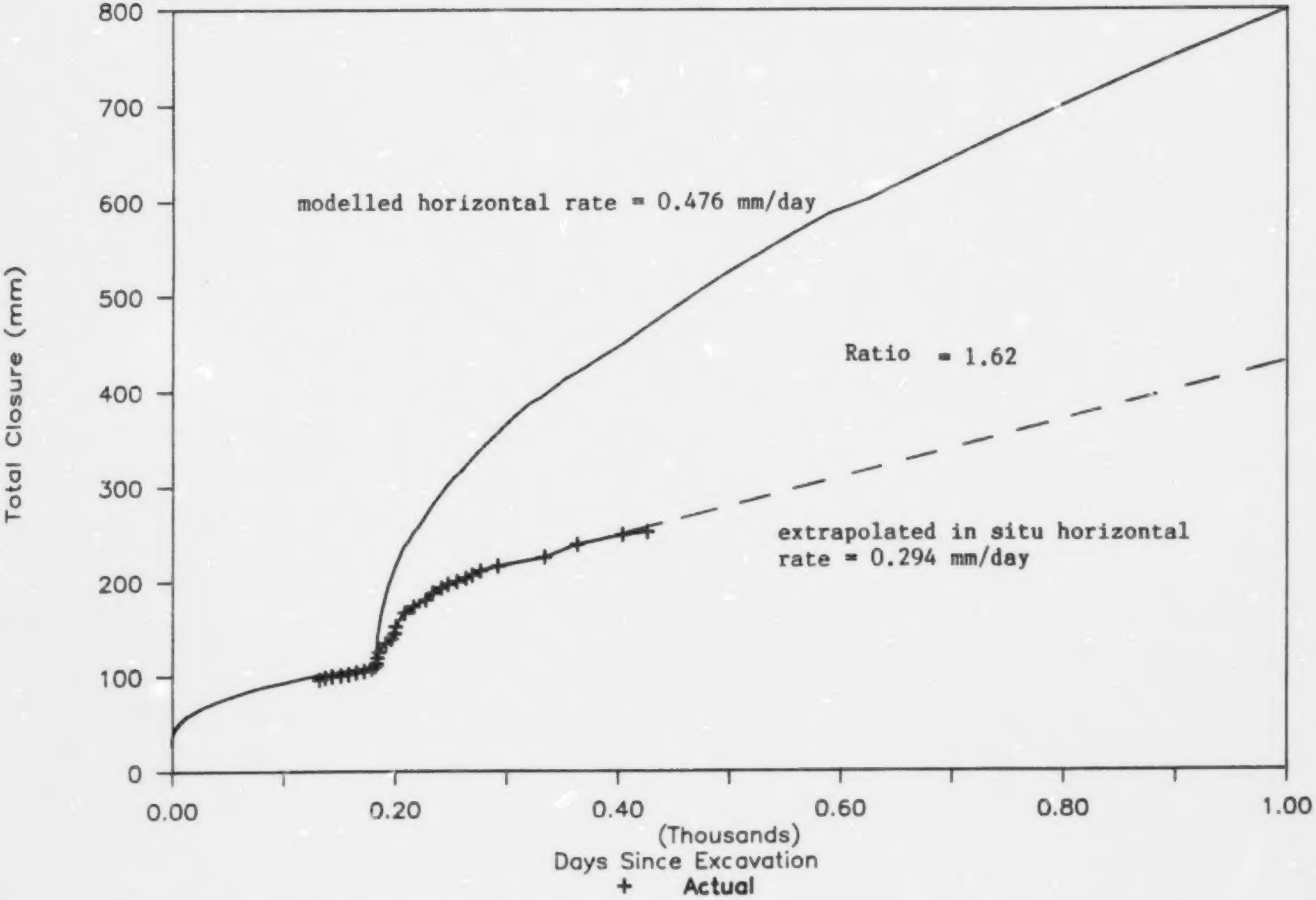

FIGURE 8.45

ROOM 12826 3–ENTRY CALIBRATION

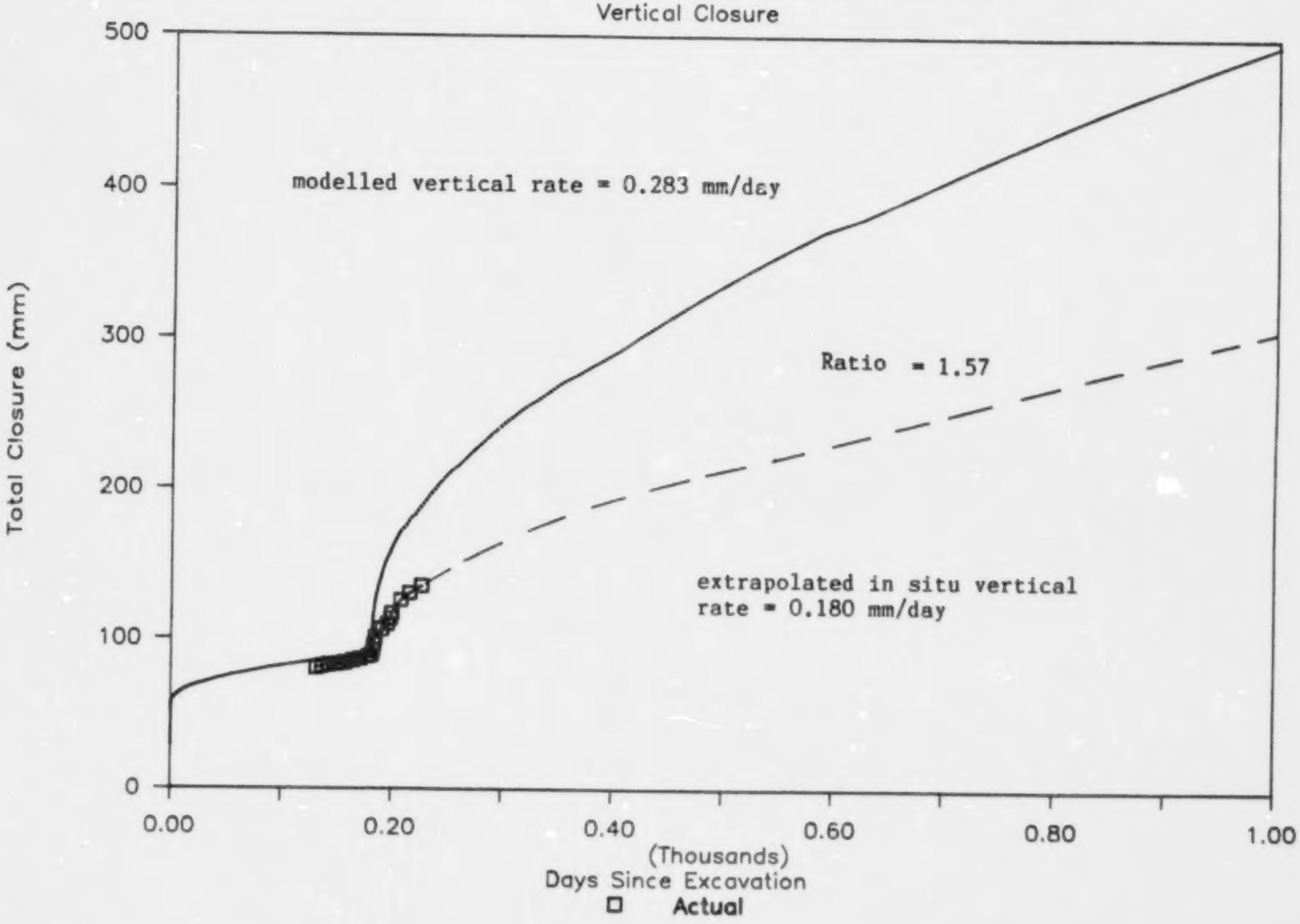

higher vertical stress levels than any of the pressure cells installed in the yield pillar measured (Figure 3.30). Upon further investigation, it was discovered that if a fixed amount of stress was added to each reading of a particular pressure cell the resulting curve was in close agreement with the predicted vertical stress path. This phenomenon is shown in Figure 8.43 for two different types of pressure cells.

Each individual pressure cell shown in Figure 8.52 required a different amount of stress added to its reading for it to be in agreement with the predicted stress levels. This is because each cell measures a different type of stress. The epoxy encapsulated flat jack cell is measuring a uniaxial stress. The borehole pressure cell is measuring a biaxial stress and indicating a mean stress.

The predicted stress path is in good agreement with the actual stress path. The difference between the predicted and the measured vertical stress levels is likely due to the fact that the model did not account for the loss of yielded material adjacent to the walls. The middle opening (12827) was also modelled as one excavation, but was actually excavated with two separate passes which is why the in situ data contains two stress peaks. As well, no provision was made for the clay seams, although FLAC is capable of handling discontinuities.

A comparison of the closure rates has shown that the predicted steady state closure rates were approximately 1.6 times greater than the extrapolated in situ closure rates. Investigation of the closure rates immediately after excavation (i.e. days 209 to 253) of Entry 12827 shows good agreement between predicted and actual rates (Table 8.1). After this time period the predicted horizontal rate is 2.5 times that of the measured rate.

The above differences indicate that further study is required to determine methods of modelling yielded regions around the openings, as well as discontinuities, such as clay seams.

TABLE 8.1

COMPARISON OF PREDICTED AND ACTUAL CLOSURE RATES
FOR THREE ROOM ENTRY SYSTEM (12826, 12827 & 12828)

Days Since Excavation Time Period (Days)	Modelled Closure Rate (um/day)		Actual Closure Rate (um/day)	RATIO
209-253 44 days	Horizontal	1391	1518	0.92
	Vertical	843	1007	0.84
253-452 199 days	Horizontal	918	362	2.54
209-452 243 days	Horizontal	1003	571	1.76

Note : Vertical closure rates are not compared after Day 253 because in situ vertical closure measurements are not available after this date.

8.6 FLAC Outputs and Analyses

The objective of the computer analysis in Phase II of the project was to perform an assessment of standard mining panel geometries, pillar variations, sequential backfill placement and second pass mining geometries.

Using the computer program FLAC, analysis of existing mining geometries and planned geometries were simulated to evaluate their performance. The analyses were used to identify potentially unfavourable stress conditions and potential failure zones. The amount of closure and the accompanying closure rates were used to investigate the overall rock mass behaviour in response to the closure/stress events produced by mining.

The following mining geometries were evaluated using FLAC:

Pillar Run, 10 m x 30 m Room
Pillar Run, 20 m x 30 m Room
Pillar Run, 30 m x 30 m Room
Virgin Ground, 30 m x 30 m Room
Two Room Sequence (Stopes 11200 and 11240)
Three Room Entry System
Nine Room Sequence
Cut and Fill, 2 - 12 m Stopes
Cut and Fill, 3 - 10 m Stopes
Bauer Fold

Due to the volume of material contained in these runs only the modelled meshes are illustrated (Figures 8.46 to 8.54), except for the Two Room Sequence which is presented in detail (Figures 8.55 to 8.76).

FIGURE 8.46

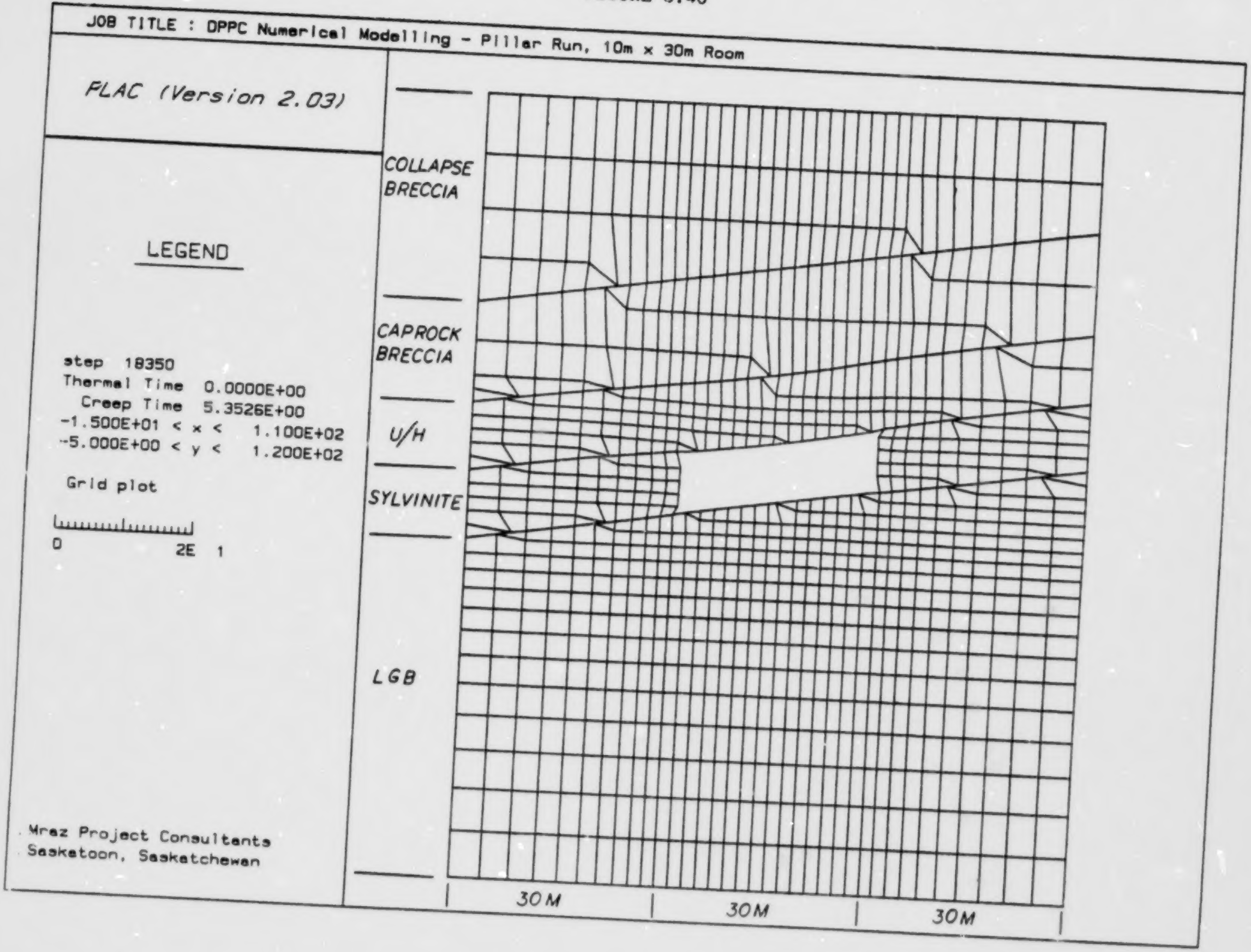
JOB TITLE : DPPC Numerical Modelling - Pillar Run, 10m x 30m Room
FLAC (Version 2.03)
LEGEND
step 18350
Thermal Time 0.0000E+00
Creep Time 5.3526E+00
-1.500E+01 < x < 1.100E+02
-5.000E+00 < y < 1.200E+02
Grid plot
0
2E 1
Mraz Project Consultants
Saskatoon, Saskatchewan
COLLAPSE BRECCIA
CAPROCK BRECCIA
U/H
SYLVINITE
LGB
30M
30M
30M

FIGURE 8.47

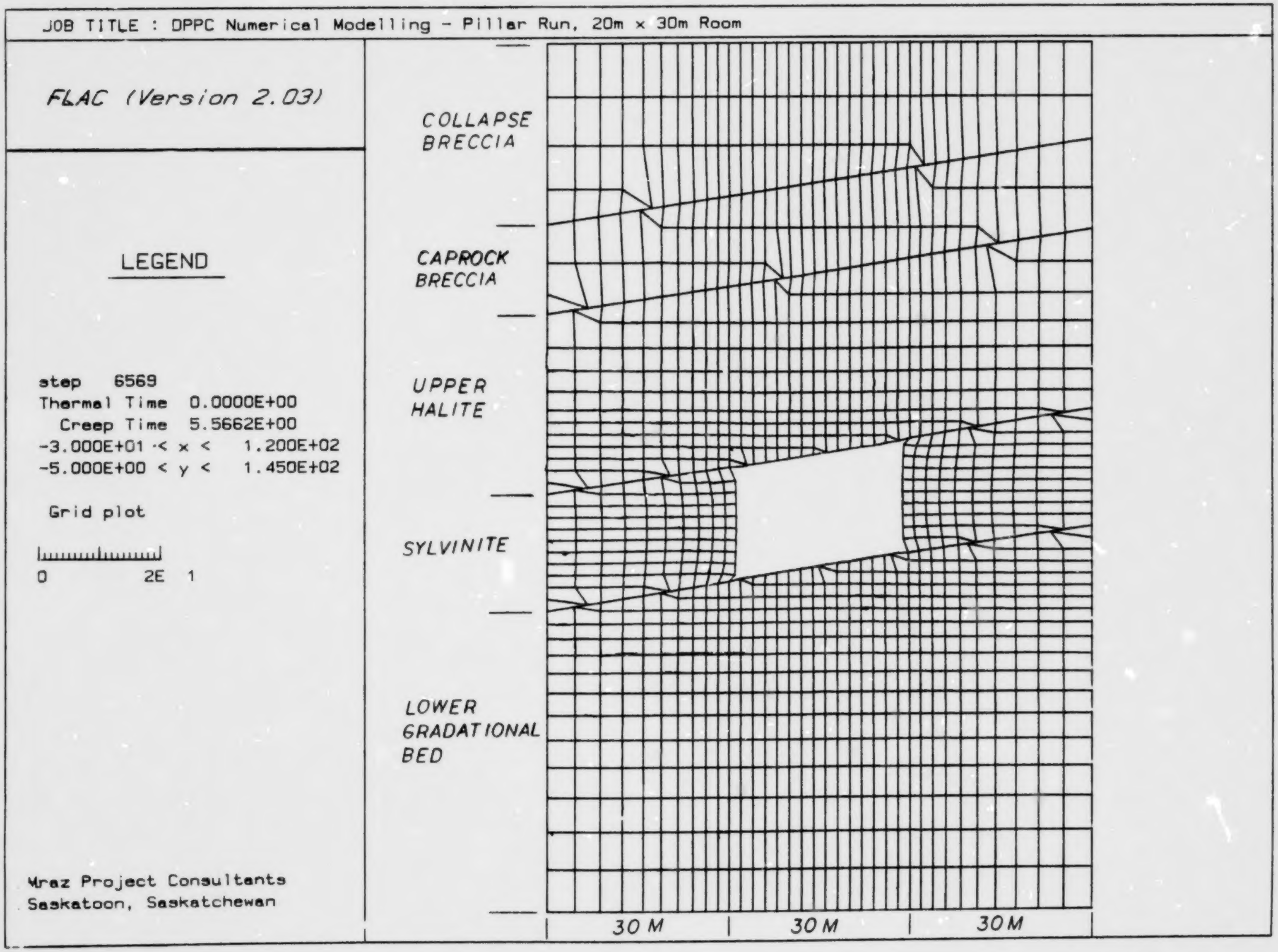
JOB TITLE : DPPC Numerical Modelling - Pillar Run, 20m x 30m Room
FLAC (Version 2.03)
LEGEND
step 6569
Thermal Time 0.0000E+00
Creep Time 5.5662E+00
-3.000E+01 < x < 1.200E+02
-5.000E+00 < y < 1.450E+02
Grid plot
0 2E 1
Mraz Project Consultants
Saskatoon, Saskatchewan
COLLAPSE BRECCIA
CAPROCK BRECCIA
UPPER HALITE
SYLVINITE
LOWER GRADATIONAL BED
30 M
30 M
30 M

FIGURE 8.48

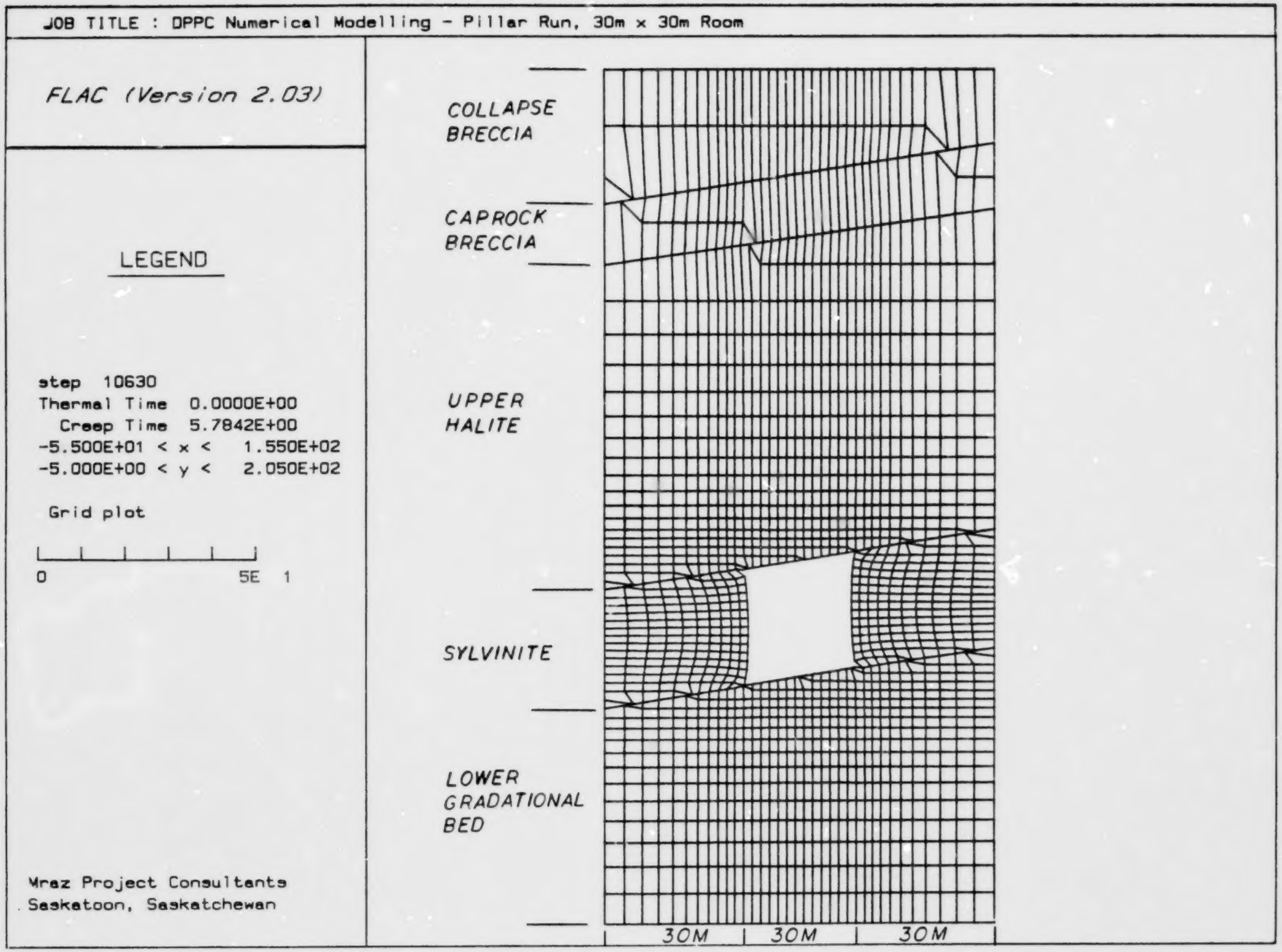
JOB TITLE : DPPC Numerical Modelling - Pillar Run, 30m x 30m Room
FLAC (Version 2.03)
LEGEND
step 10630
Thermal Time 0.0000E+00
Creep Time 5.7842E+00
-5.500E+01 < x < 1.550E+02
-5.000E+00 < y < 2.050E+02
Grid plot
0
5E 1
Mraz Project Consultants
Saskatoon, Saskatchewan
COLLAPSE BRECCIA
CAPROCK BRECCIA
UPPER HALITE
SYLVINITE
LOWER GRADATIONAL BED
30M
30M
30M

FIGURE 8.49

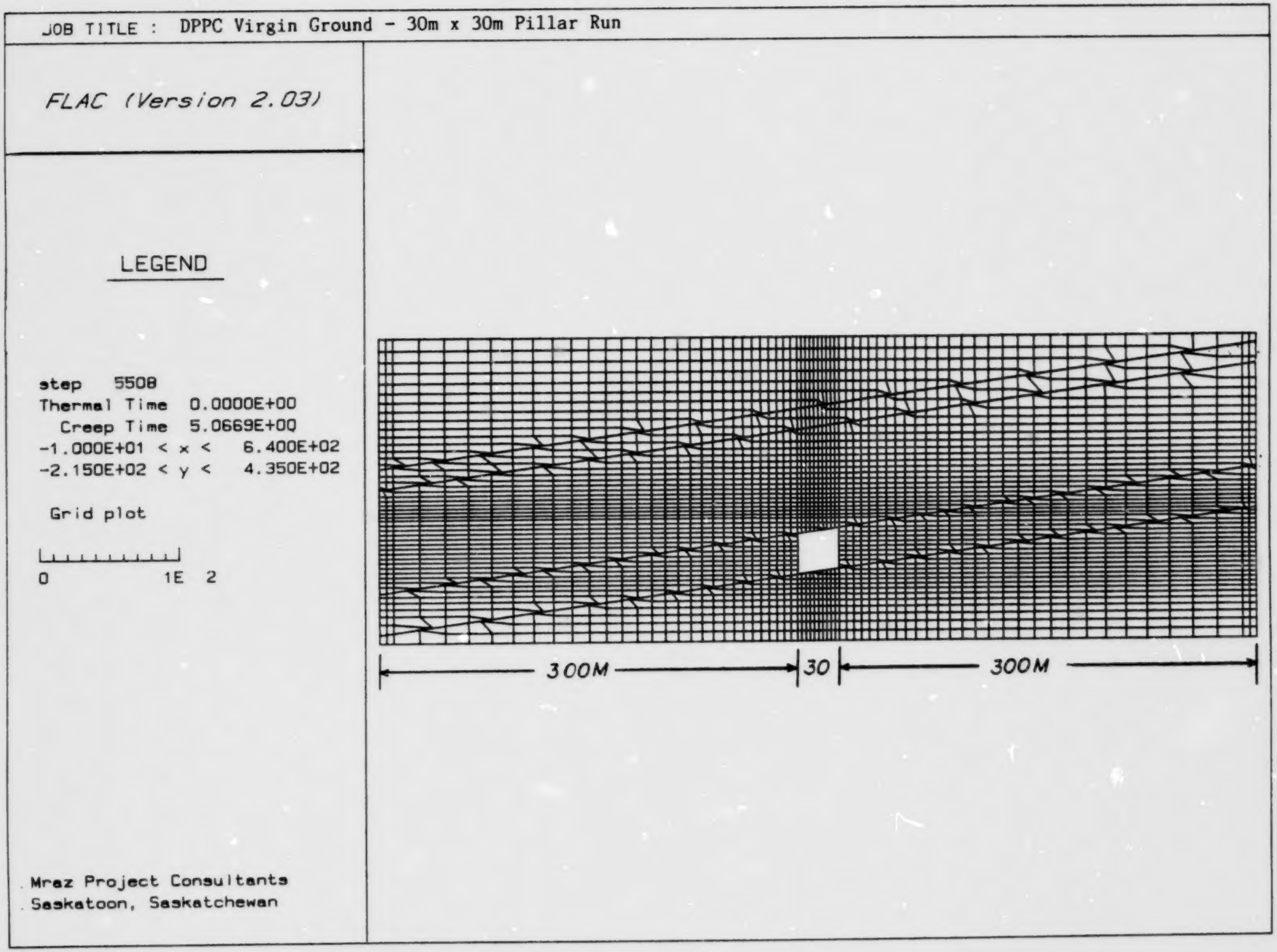

JOB TITLE : DPPC Virgin Ground - 30m x 30m Pillar Run

FLAC (Version 2.03)

LEGEND

step 5508
Thermal Time 0.0000E+00
Creep Time 5.0669E+00
-1.000E+01 < x < 6.400E+02
-2.150E+02 < y < 4.350E+02

Grid plot

Mraz Project Consultants
Saskatoon, Saskatchewan

FIGURE 8.50

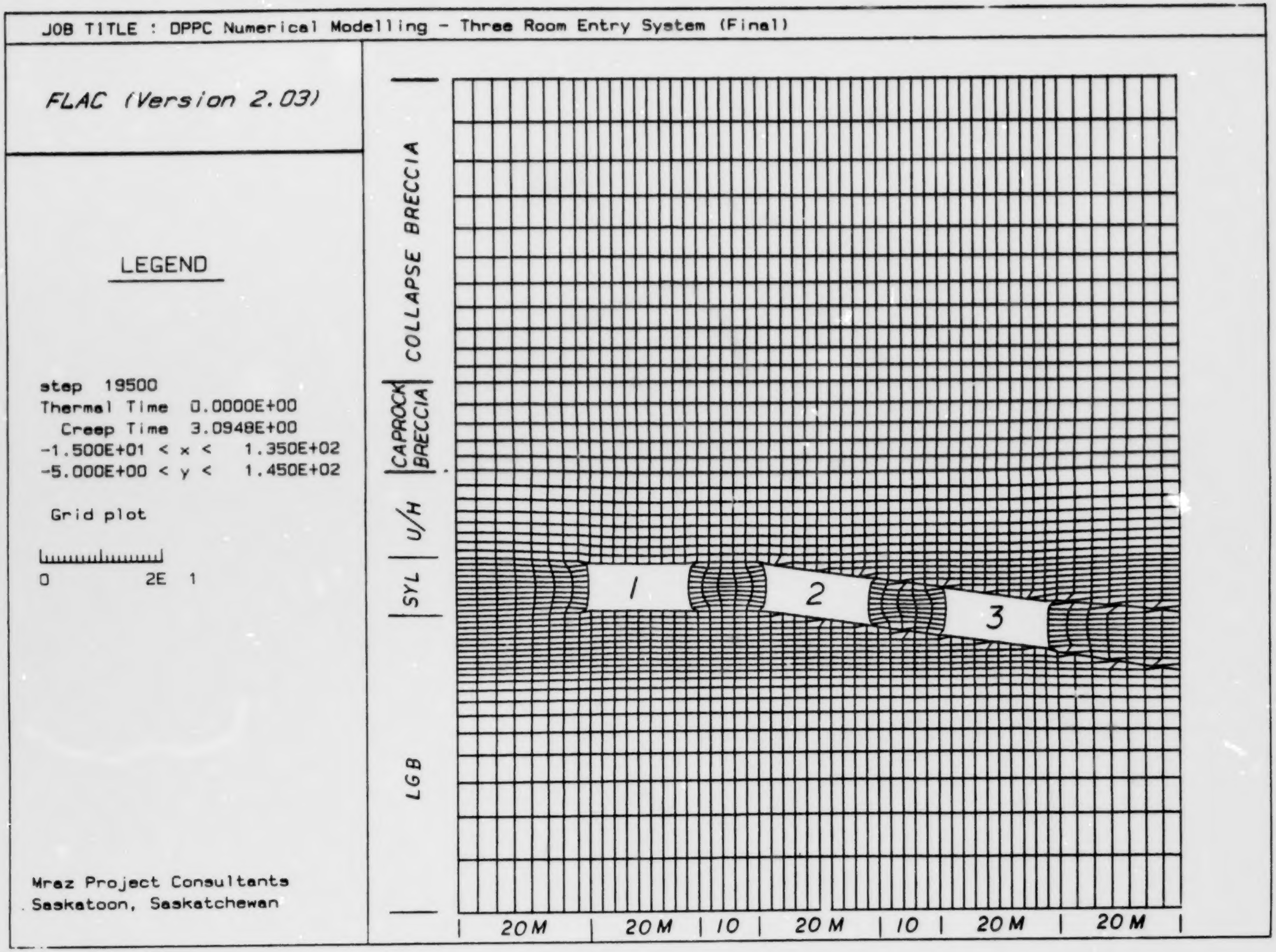
JOB TITLE : DPPC Numerical Modelling - Three Room Entry System (Final)
FLAC (Version 2.03)
LEGEND
step 19500
Thermal Time 0.0000E+00
Creep Time 3.0948E+00
-1.500E+01 < x < 1.350E+02
-5.000E+00 < y < 1.450E+02
Grid plot
0 2E 1
Mraz Project Consultants
Saskatoon, Saskatchewan
COLLAPSE BRECCIA
CAPROCK BRECCIA
U/H
SYL
LGB
1
2
3
20M
20M
10
20 M
10
20 M
20 M

FIGURE 8.51

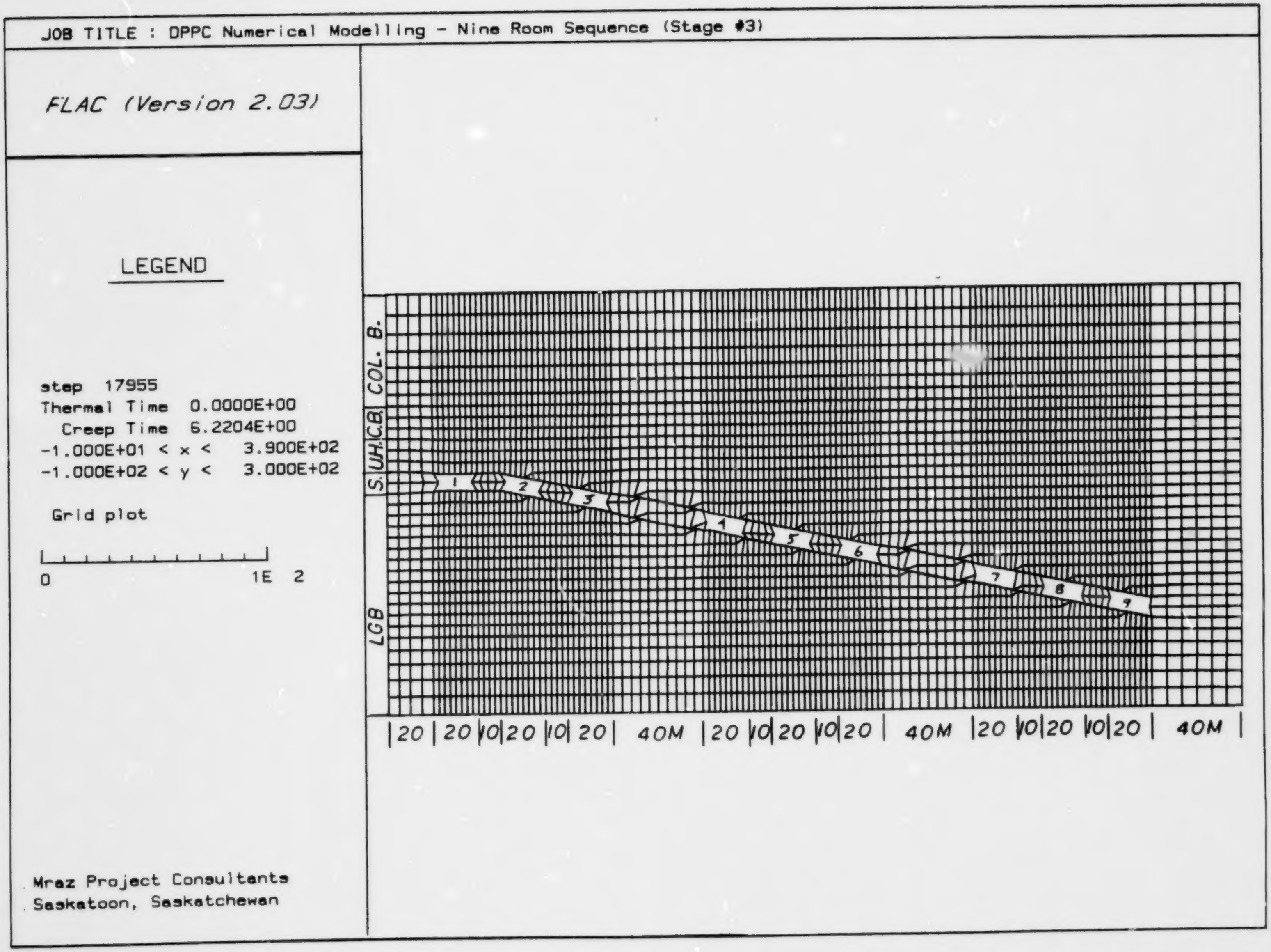

JOB TITLE : DPPC Numerical Modelling - Nine Room Sequence (Stage #3)

FLAC (Version 2.03)

LEGEND

step 17955
Thermal Time 0.0000E+00
Creep Time 6.2204E+00
-1.000E+01 < x < 3.900E+02
-1.000E+02 < y < 3.000E+02

Grid plot

Mraz Project Consultants
Saskatoon, Saskatchewan

0
1E 2
COL. B.
UH.C.B.
S.
LGB
1
2
3
4
5
6
7
8
9
|20 |20 |10|20 |10| 20| 40M |20 |10|20 |10|20 | 40M |20 |10|20 |10|20 | 40M |

FIGURE 8.52

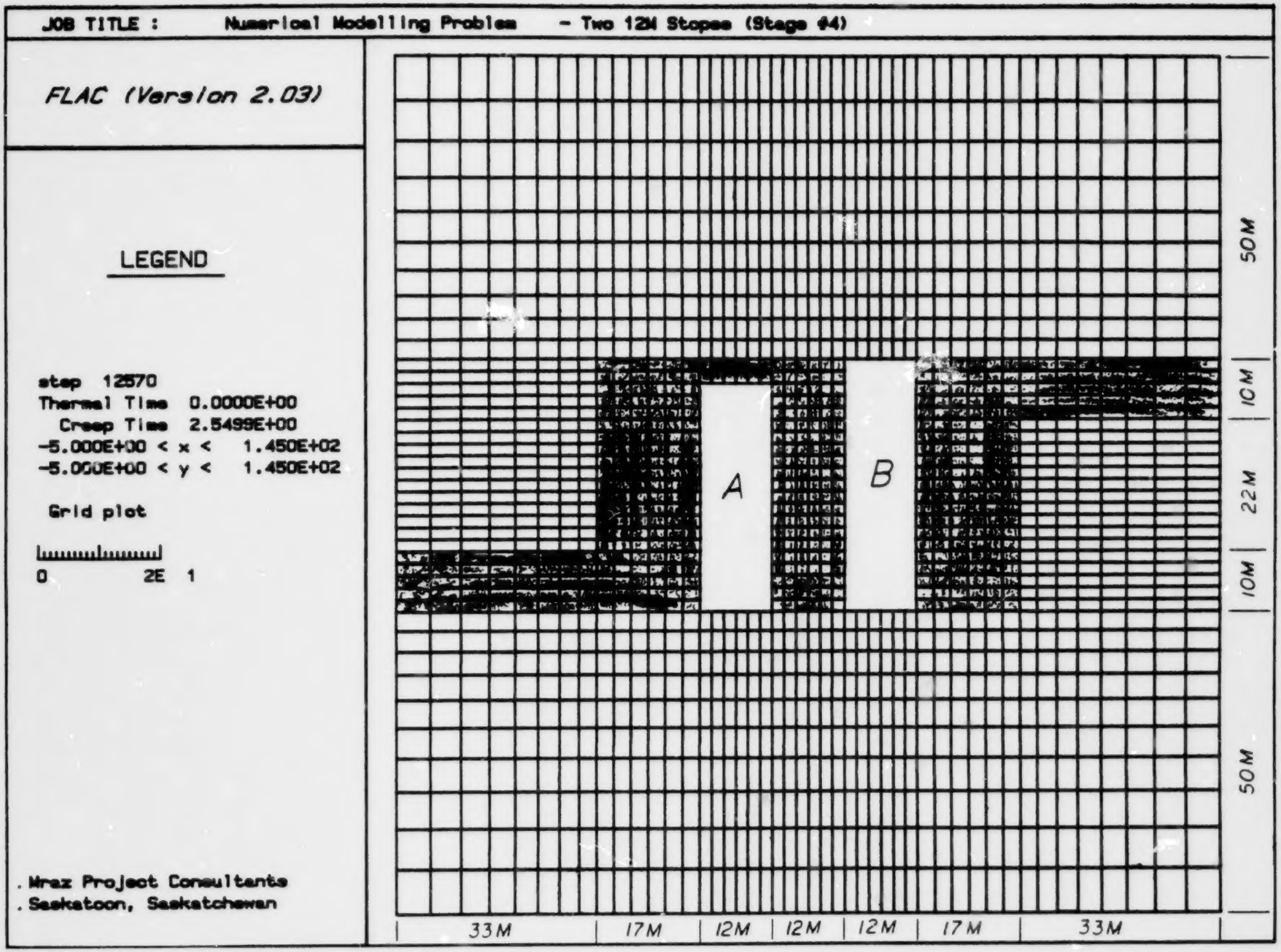
JOB TITLE : Numerical Modelling Problem - Two 12M Stopes (Stage #4)
FLAC (Version 2.03)
LEGEND
step 12570
Thermal Time 0.0000E+00
Creep Time 2.5499E+00
-5.000E+00 < x < 1.450E+02
-5.000E+00 < y < 1.450E+02
Grid plot
0 2E 1
. Mraz Project Consultants
. Saskatoon, Saskatchewan
A
B
50M
10M
22M
10M
50M
33M
17M
12M
12M
12M
17M
33M

FIGURE 8.53

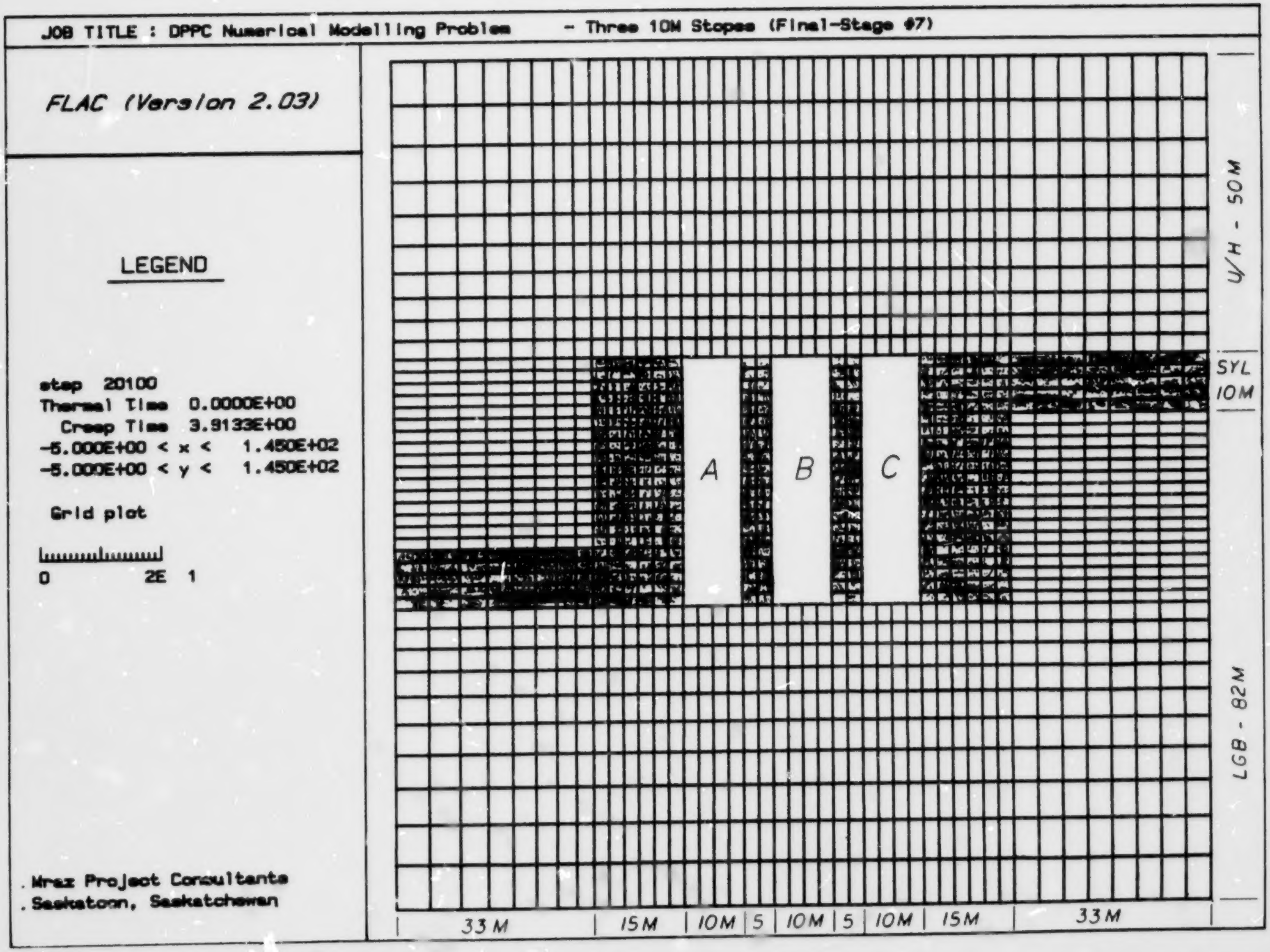
JOB TITLE : DPPC Numerical Modelling Problem - Three 10M Stopes (Final-Stage #7)
FLAC (Version 2.03)
LEGEND
step 20100
Thermal Time 0.0000E+00
Creep Time 3.9133E+00
-5.000E+00 < x < 1.450E+02
-5.000E+00 < y < 1.450E+02
Grid plot
0 2E 1
. Mraz Project Consultants
. Saskatoon, Saskatchewan
A
B
C
U/H - 50M
SYL 10M
LGB - 82M
33 M
15M
10M
5
10M
5
10M
15M
33M

FIGURE 8.54

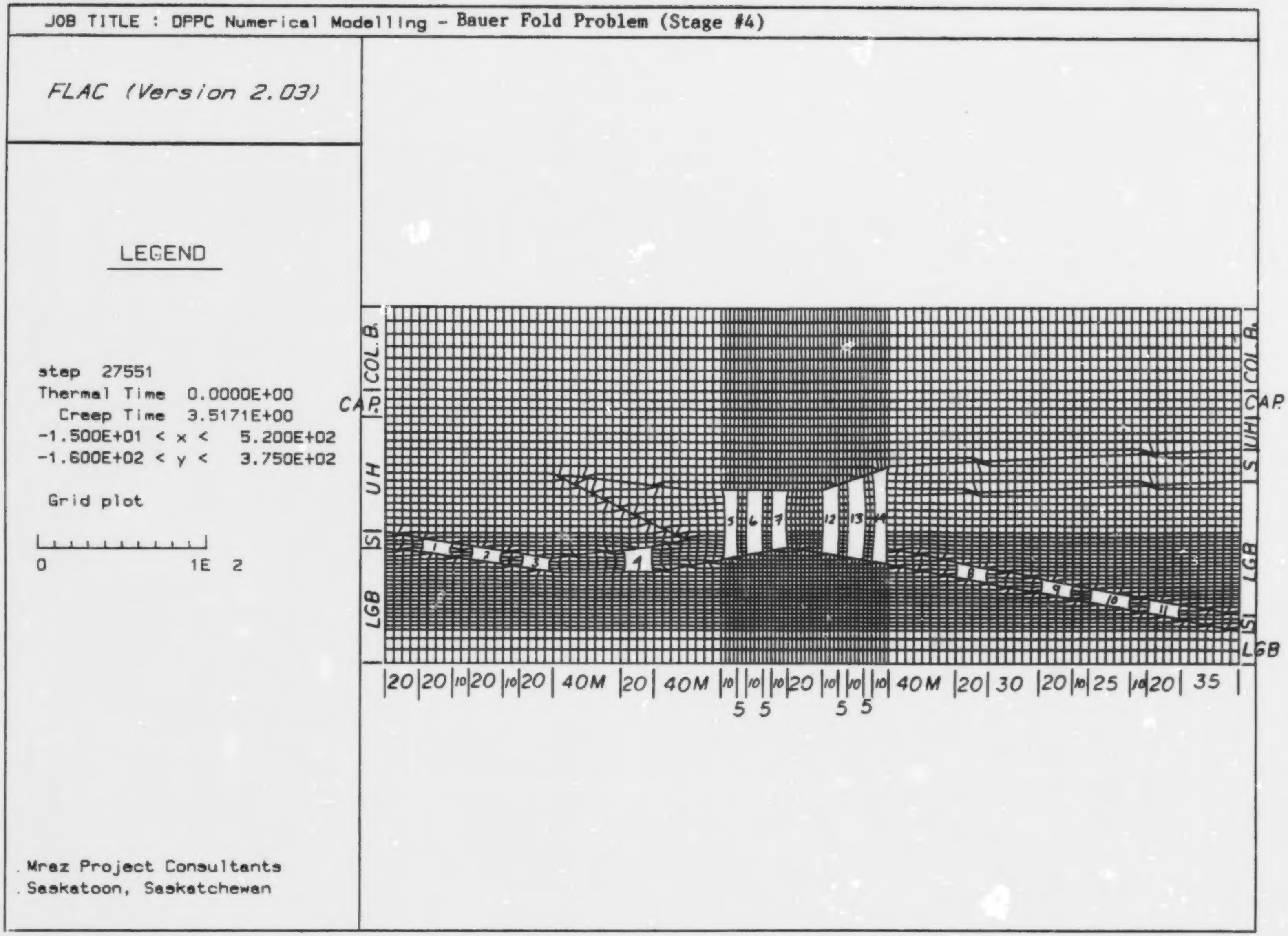

JOB TITLE : DPPC Numerical Modelling - Bauer Fold Problem (Stage #4)

FLAC (Version 2.03)

LEGEND

step 27551
Thermal Time 0.0000E+00
Creep Time 3.5171E+00
-1.500E+01 < x < 5.200E+02
-1.600E+02 < y < 3.750E+02

Grid plot

0 1E 2

. Mraz Project Consultants
. Saskatoon, Saskatchewan

COL.B.
CAP.
UH
S
LGB
COL.B.
CAP.
UH
S
LGB
S
LGB
1
2
3
4
5
6
7
12
13
14
8
9
10
11
20 20 10 20 10 20 40M 20 40M 10 5 10 5 10 20 10 5 10 5 10 40M 20 30 20 10 25 10 20 35

8.6.1 Two Room Sequence (Stopes 11200 and 11240)

This numerical modelling run simulated the mining of a two room sequence. Rooms 1 and 2 correspond to Stopes 11200 and 11240, respectively. Note that Stope 11200 is the location of the backfill instrumentation room. The material properties and law used for this are previously mentioned.

The outputs from the numerical simulation are shown in Figures 8.55 to 8.76. This problem was modelled in three stages of mining, but only the initial and final stages are shown.

It should be noted that the predicted steady state convergence rate in Stope 11240 is about 800 micrometers/day (Figure 8.68) compared to the in situ measurement of about 300 micrometers per day (Section 3.4.2, Figure 3.20). This overprediction is due to the two-dimensional nature of this analysis, as well as the limited size of the modelling layout, which assumes an infinite repetition of this sequence.

FIGURE 8.55

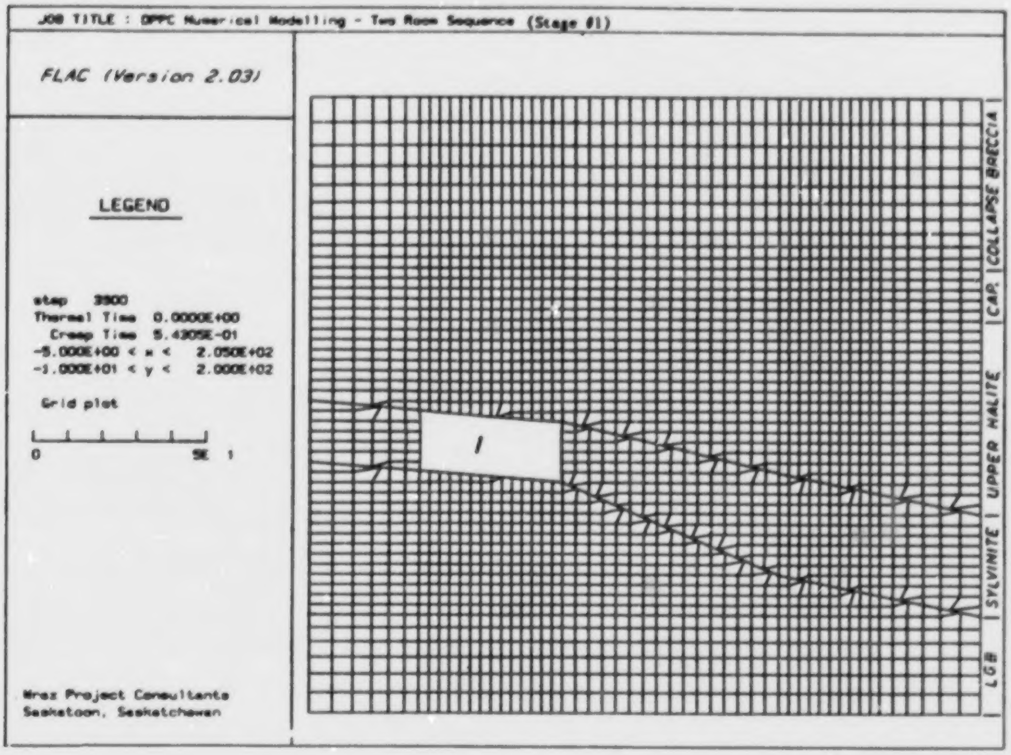

FIGURE 8.56

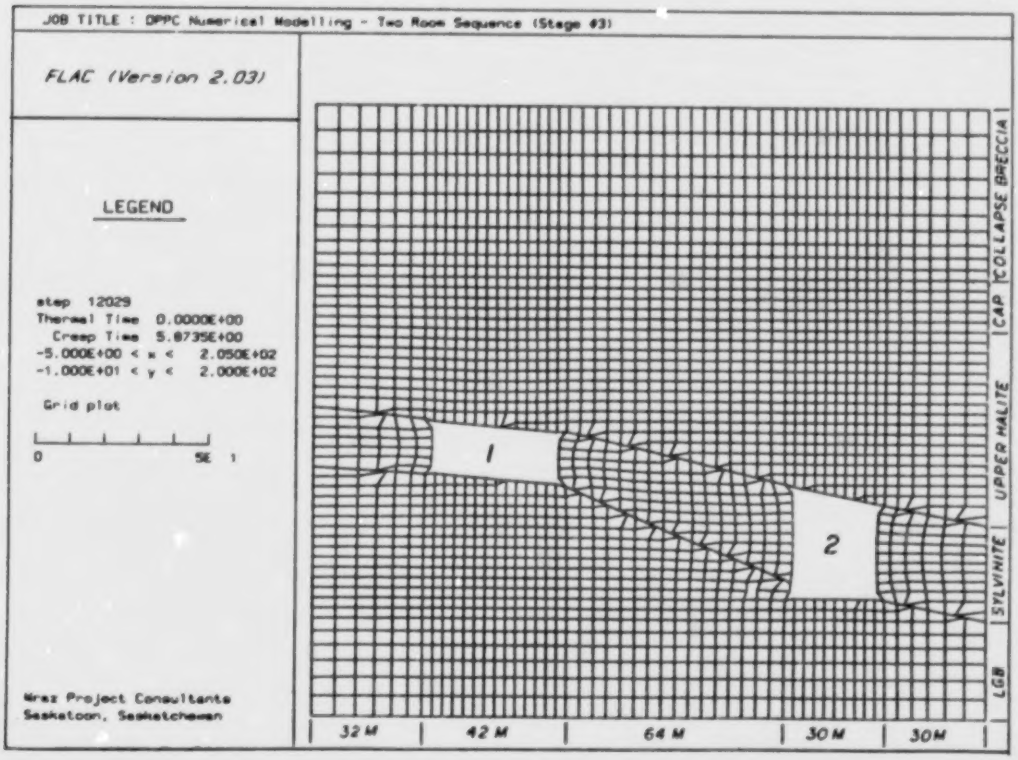

FIGURE 8.57

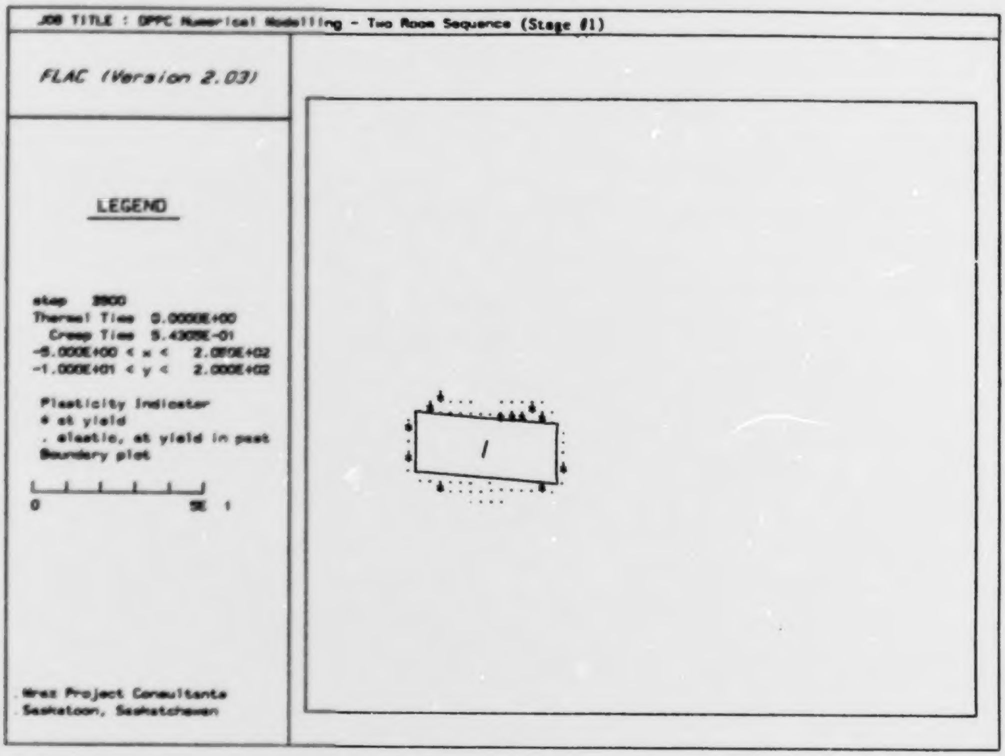

```
JOB TITLE : OPPC Numerical Modelling - Two Room Sequence (Stage #1)

FLAC (Version 2.03)

LEGEND

step   3900
Thermal Time  0.0000E+00
  Creep Time  5.4305E-01
-5.000E+00 < x <   2.050E+02
-1.000E+01 < y <   2.000E+02

 Plasticity Indicator
 * at yield
 . elastic, at yield in past
 Boundary plot

0                  5E  1

.Mraz Project Consultants
.Saskatoon, Saskatchewan
```

FIGURE 8.58

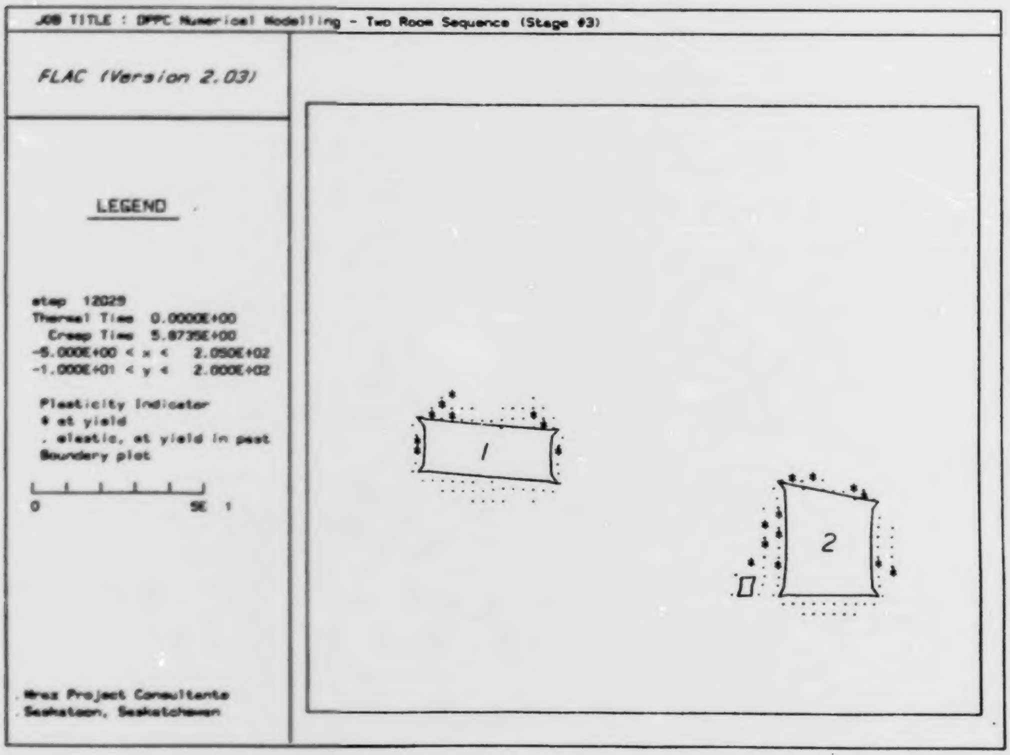

```
JOB TITLE : OPPC Numerical Modelling - Two Room Sequence (Stage #3)

FLAC (Version 2.03)

LEGEND

step  12029
Thermal Time  0.0000E+00
  Creep Time  5.8735E+00
-5.000E+00 < x <   2.050E+02
-1.000E+01 < y <   2.000E+02

 Plasticity Indicator
 * at yield
 . elastic, at yield in past
 Boundary plot

0                  5E  1

.Mraz Project Consultants
.Saskatoon, Saskatchewan
```

FIGURE 8.59

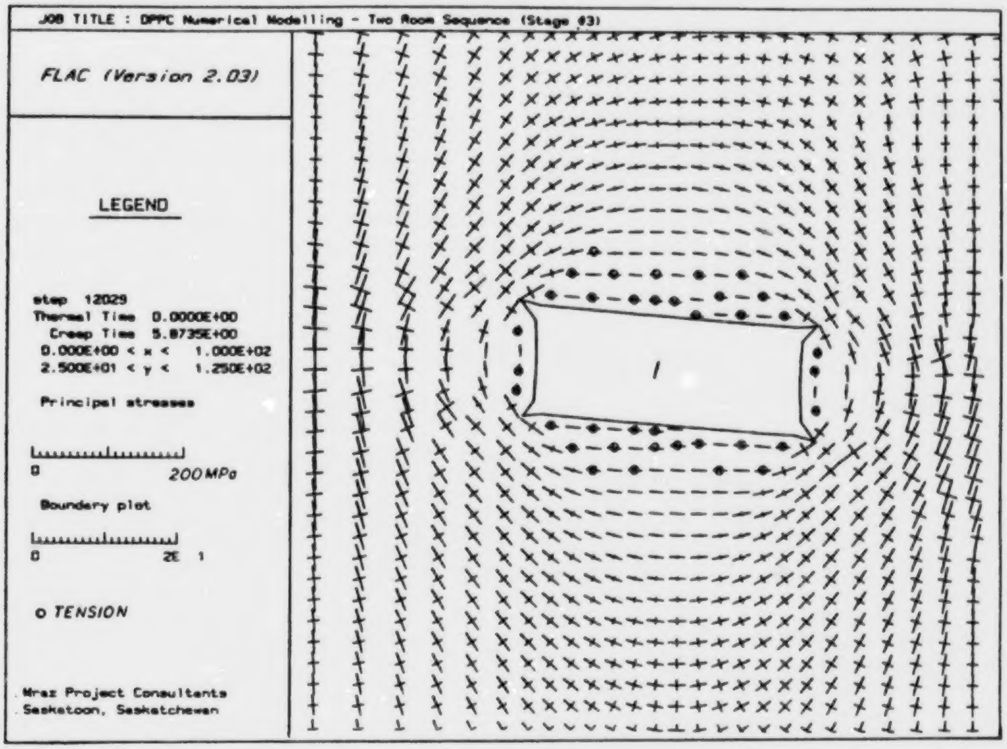

FIGURE 8.60

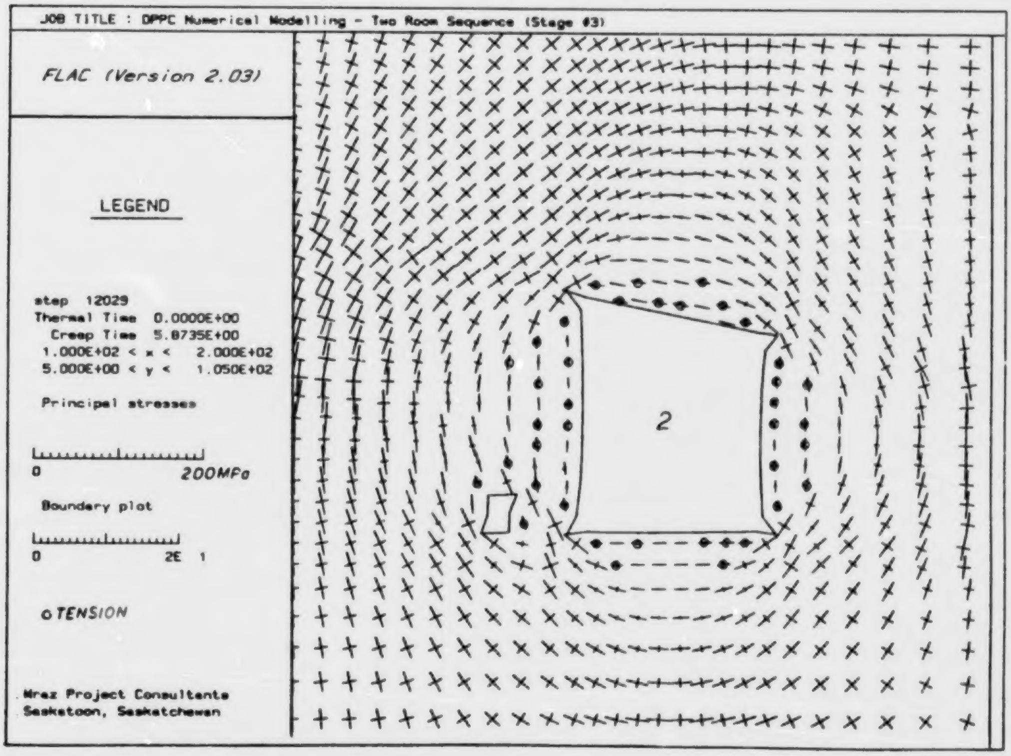

FIGURE 8.61

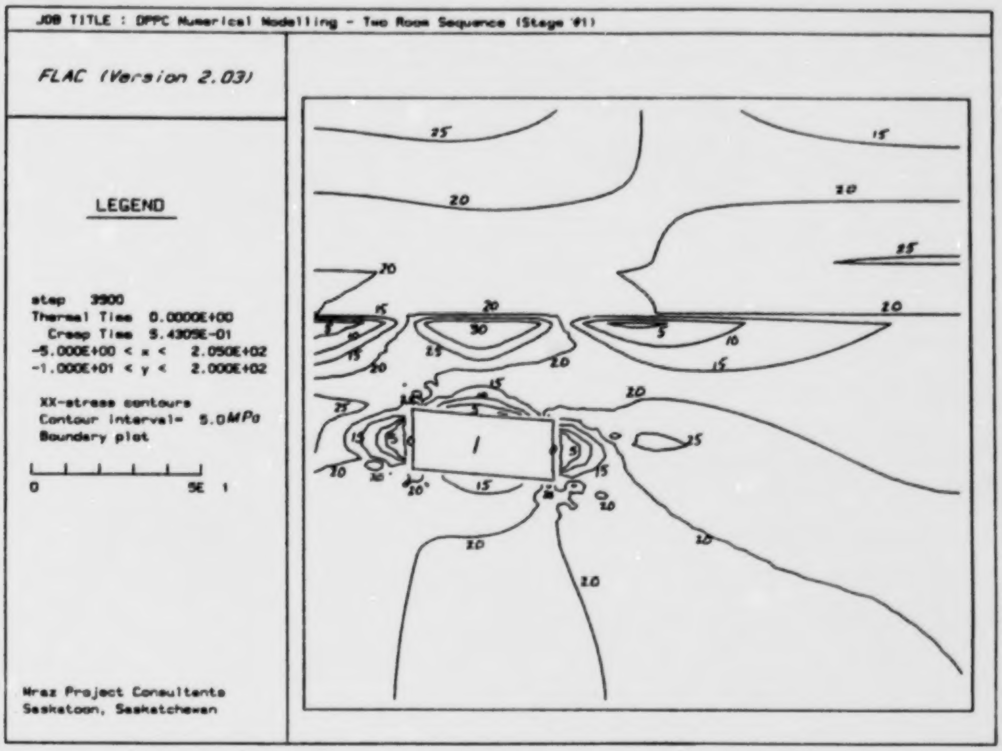

FIGURE 8.62

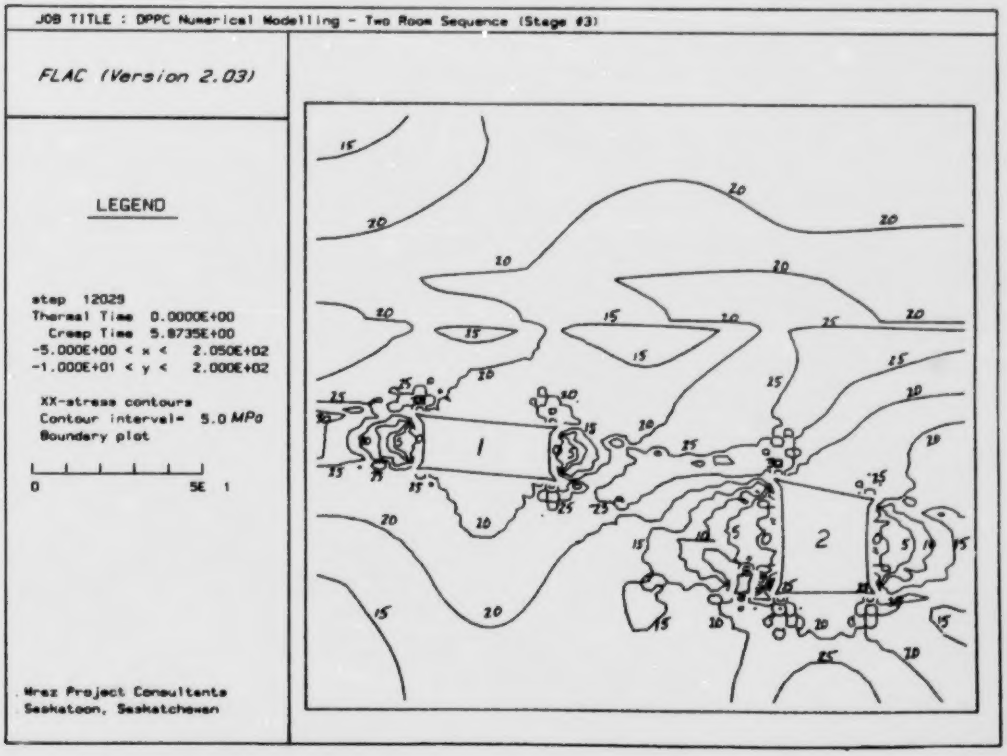

FIGURE 8.63

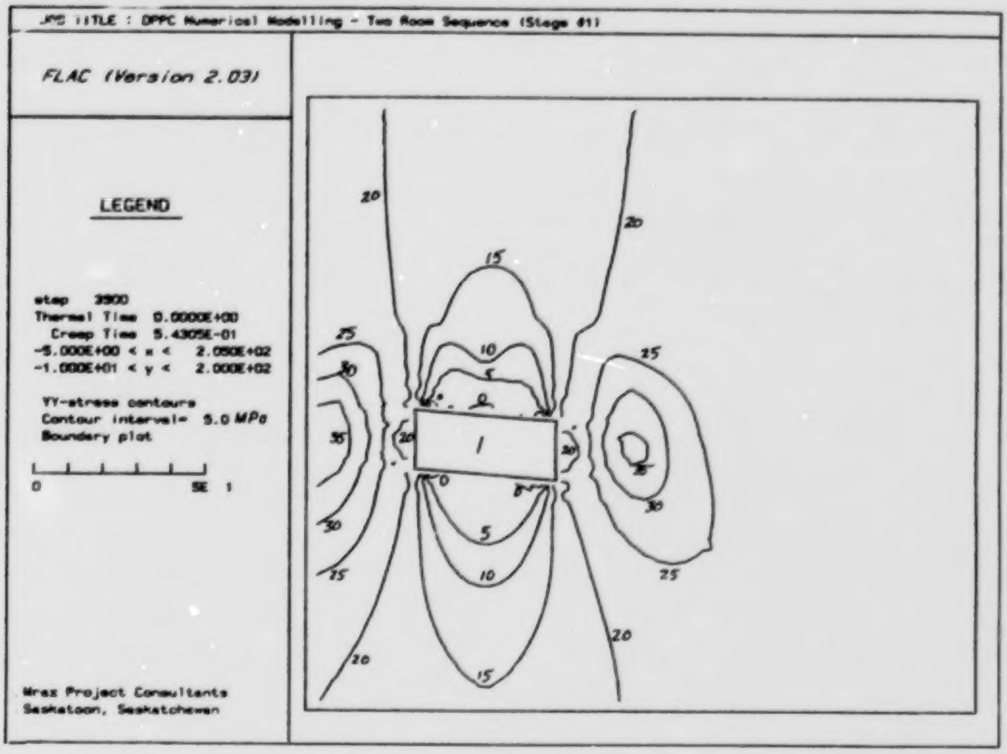

JOB TITLE : DPPC Numerical Modelling - Two Room Sequence (Stage #1)

FLAC (Version 2.03)

LEGEND

step 3900
Thermal Time 0.0000E+00
Creep Time 5.4305E-01
-5.000E+00 < x < 2.050E+02
-1.000E+01 < y < 2.000E+02

YY-stress contours
Contour interval= 5.0 MPa
Boundary plot

Mraz Project Consultants
Saskatoon, Saskatchewan

FIGURE 8.64

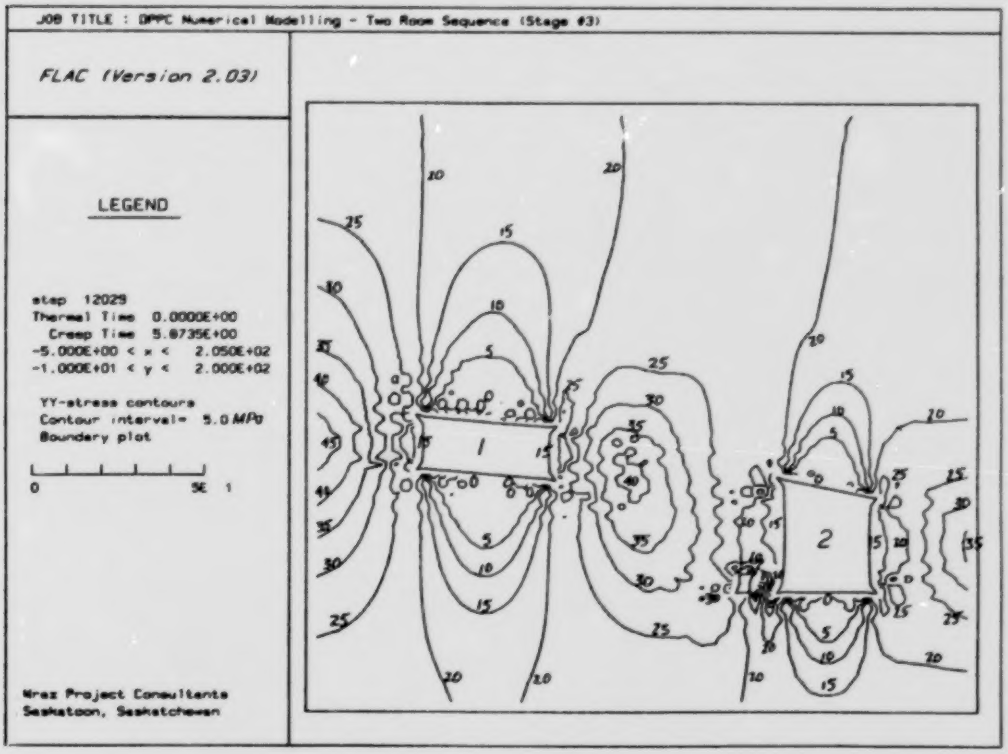

JOB TITLE : DPPC Numerical Modelling - Two Room Sequence (Stage #3)

FLAC (Version 2.03)

LEGEND

step 12029
Thermal Time 0.0000E+00
Creep Time 5.8735E+00
-5.000E+00 < x < 2.050E+02
-1.000E+01 < y < 2.000E+02

YY-stress contours
Contour interval= 5.0 MPa
Boundary plot

Mraz Project Consultants
Saskatoon, Saskatchewan

FIGURE 8.65

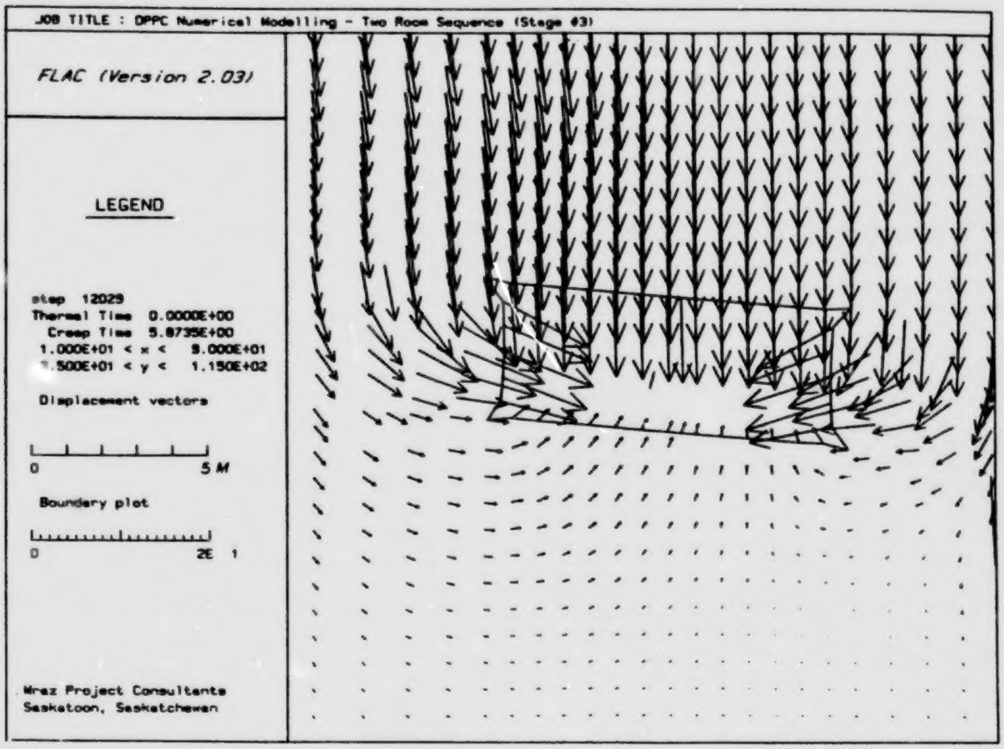

FIGURE 8.66

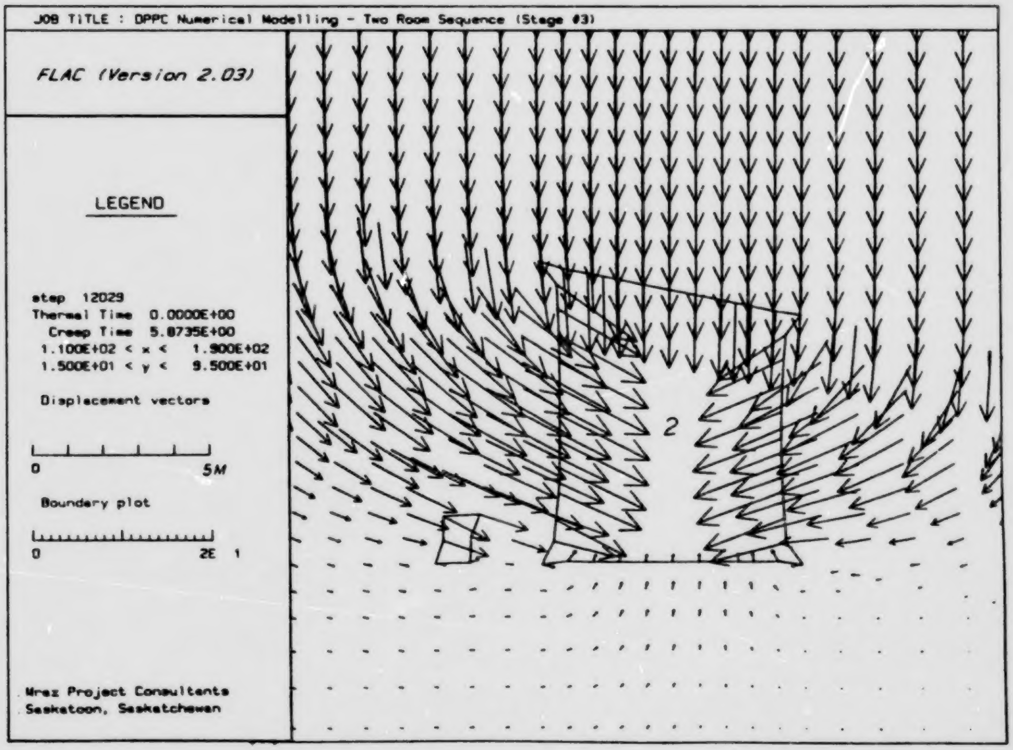

FIGURE 8.67

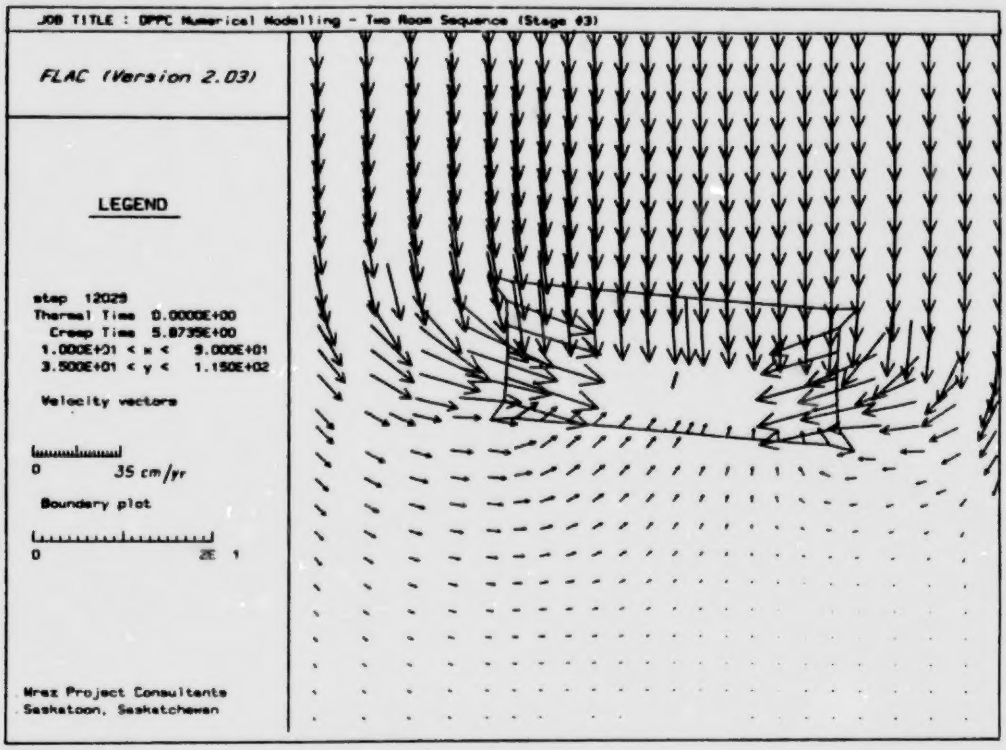

FIGURE 8.68

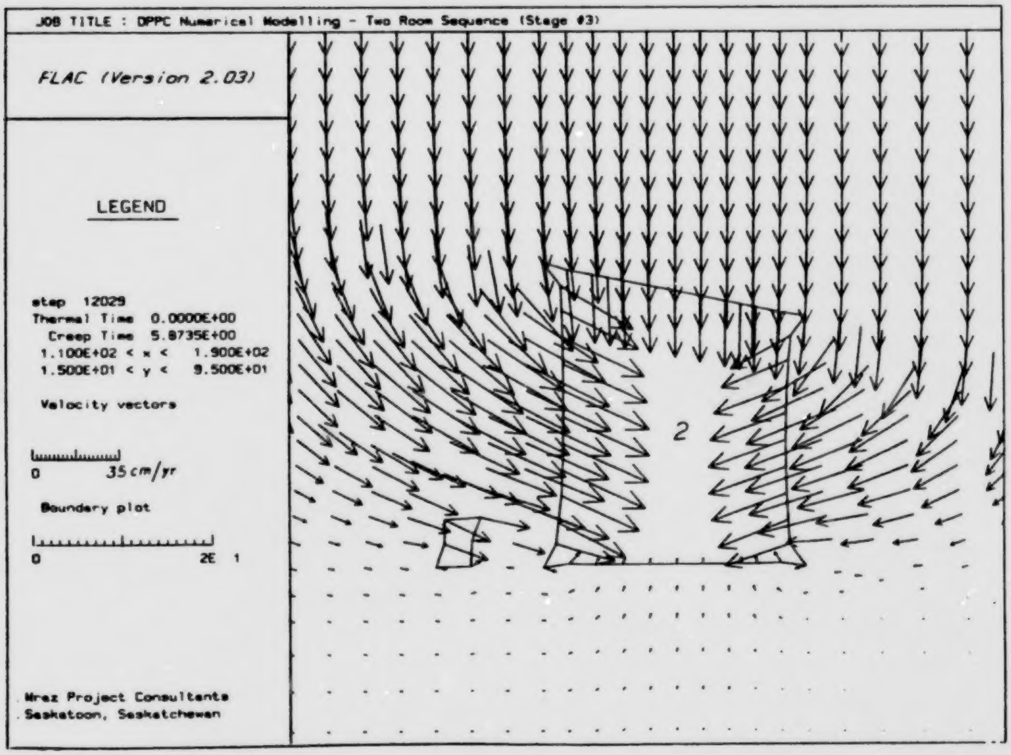

FIGURE 8.69

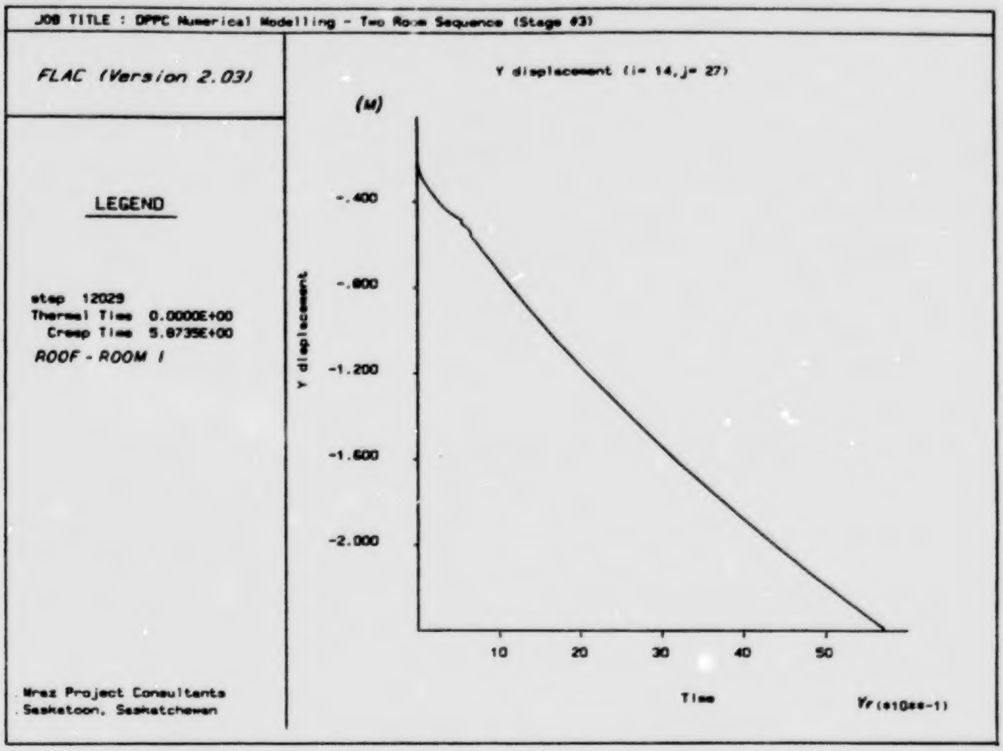

FIGURE 8.70

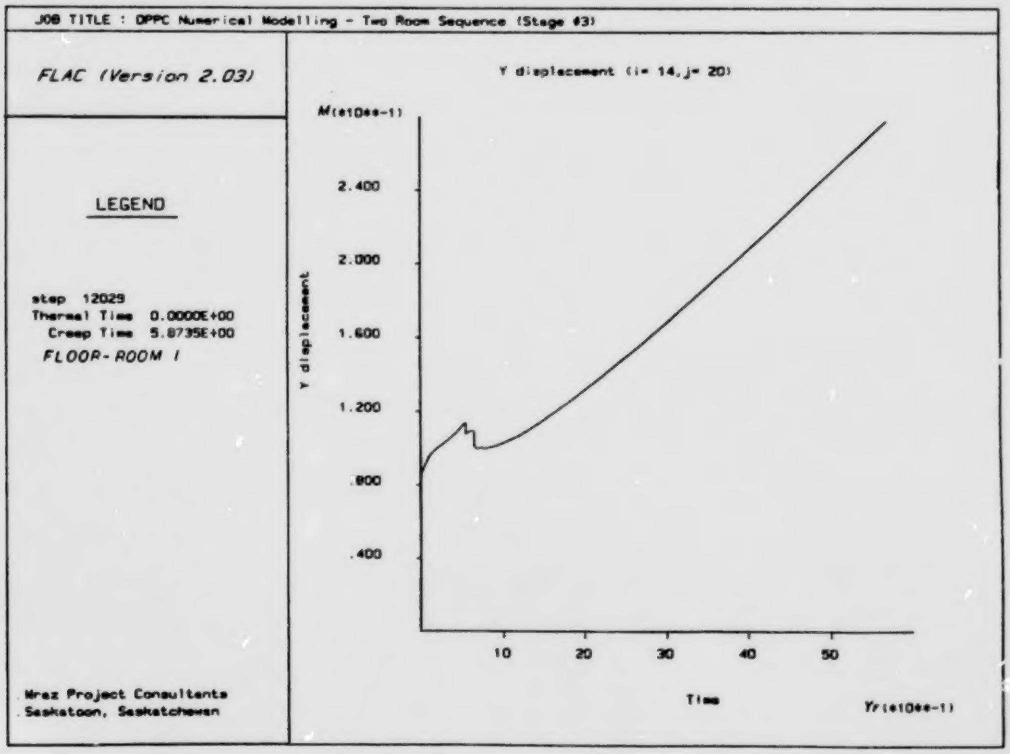

FIGURE 8.71

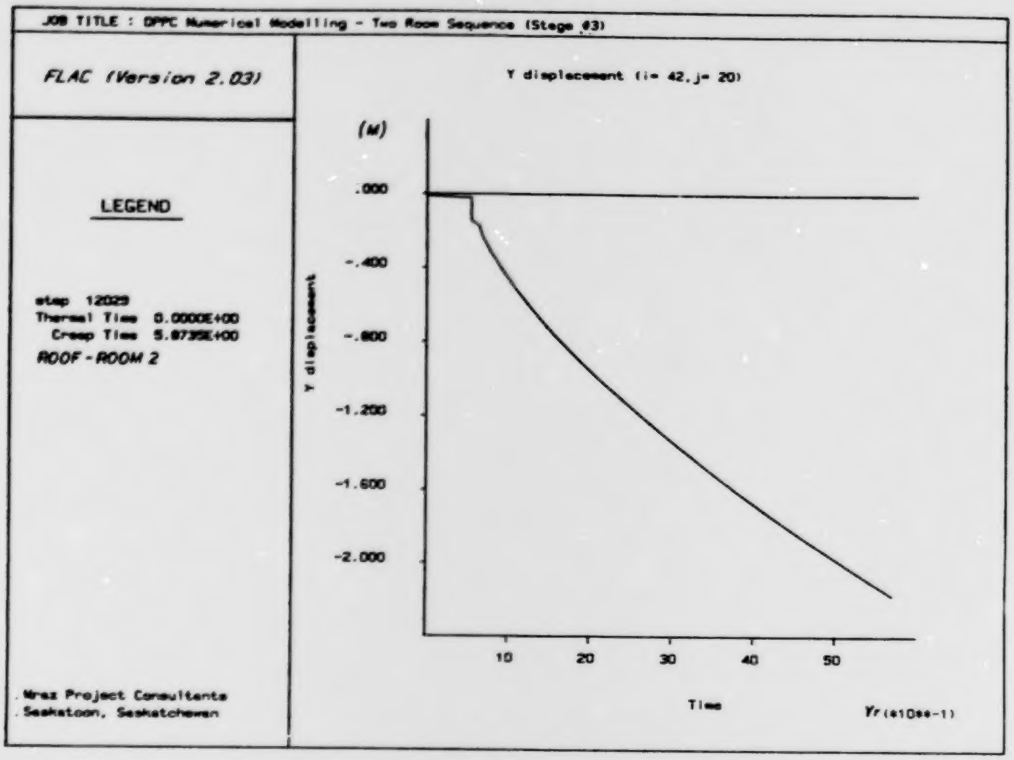

FIGURE 8.72

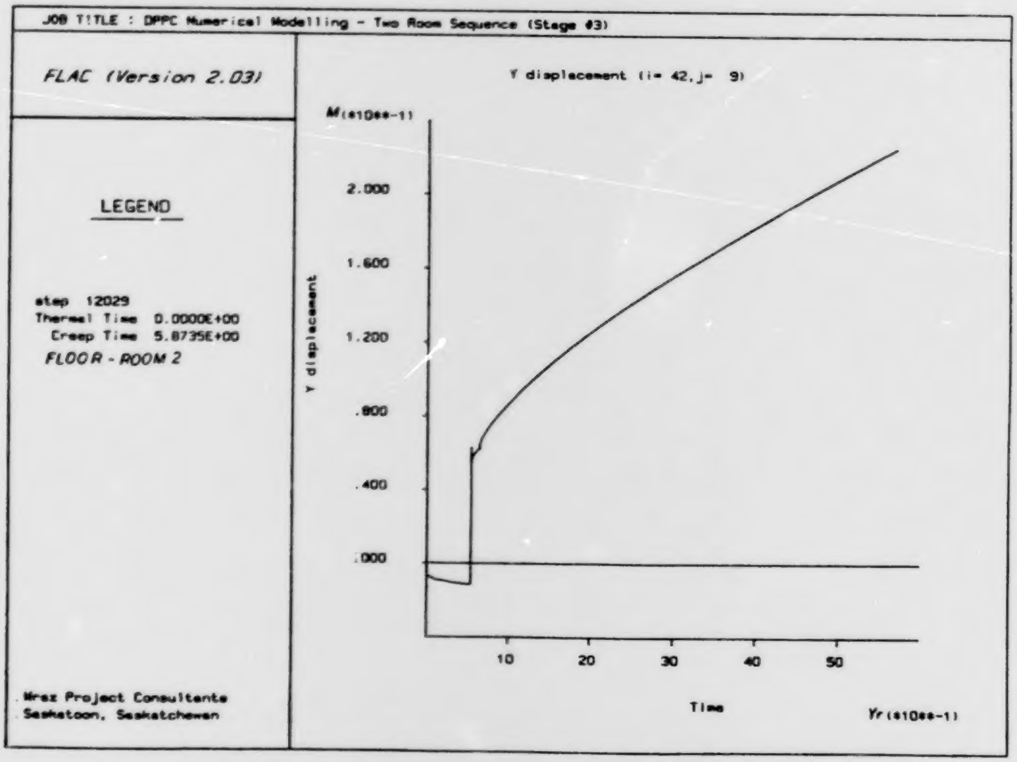

FIGURE 8.73

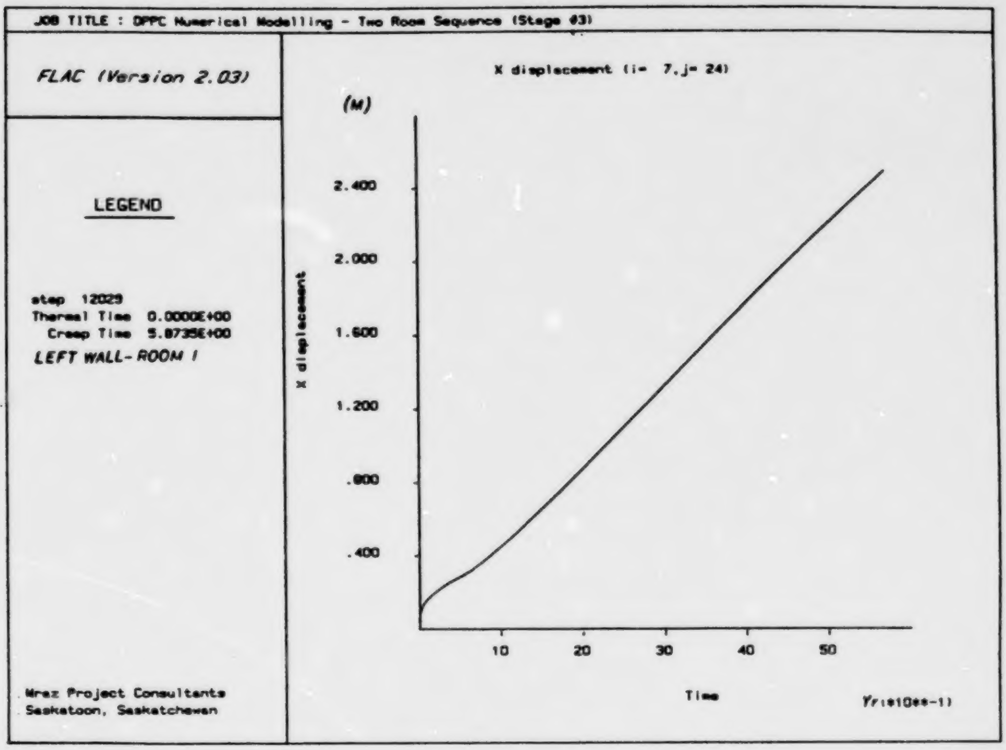
JOB TITLE : DPPC Numerical Modelling - Two Room Sequence (Stage #3)

FLAC (Version 2.03)

LEGEND

step 12029
Thermal Time 0.0000E+00
Creep Time 5.8735E+00
LEFT WALL- ROOM I

.Mraz Project Consultants
.Saskatoon, Saskatchewan

FIGURE 8.74

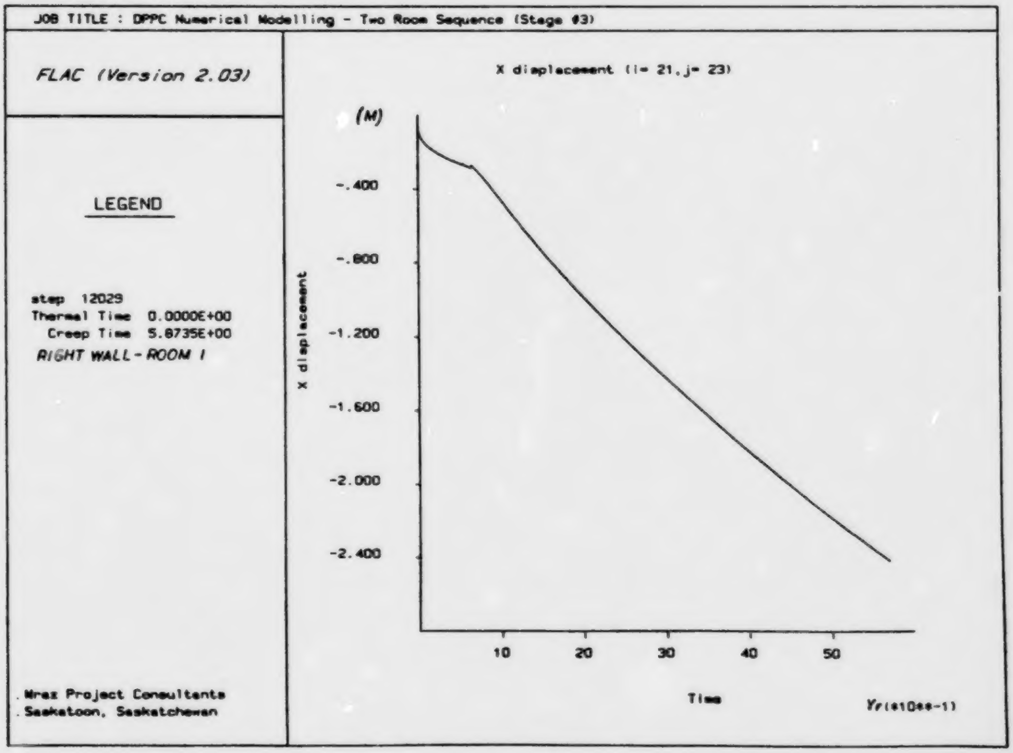
JOB TITLE : DPPC Numerical Modelling - Two Room Sequence (Stage #3)

FLAC (Version 2.03)

LEGEND

step 12029
Thermal Time 0.0000E+00
Creep Time 5.8735E+00
RIGHT WALL- ROOM I

.Mraz Project Consultants
.Saskatoon, Saskatchewan

FIGURE 8.75

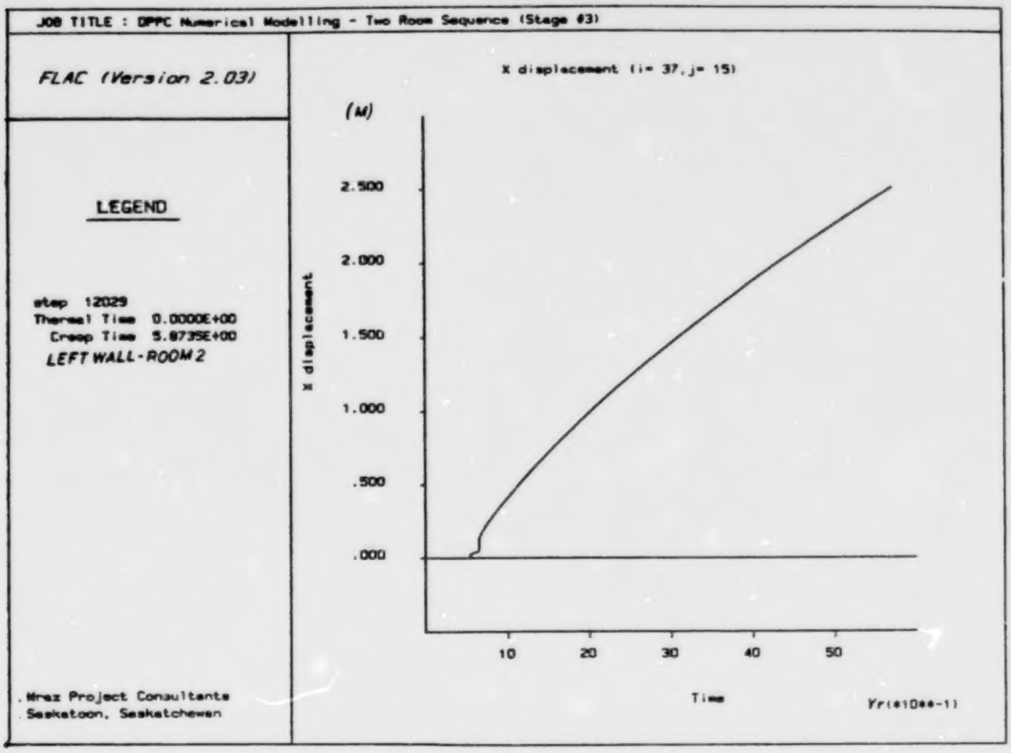

FIGURE 8.76

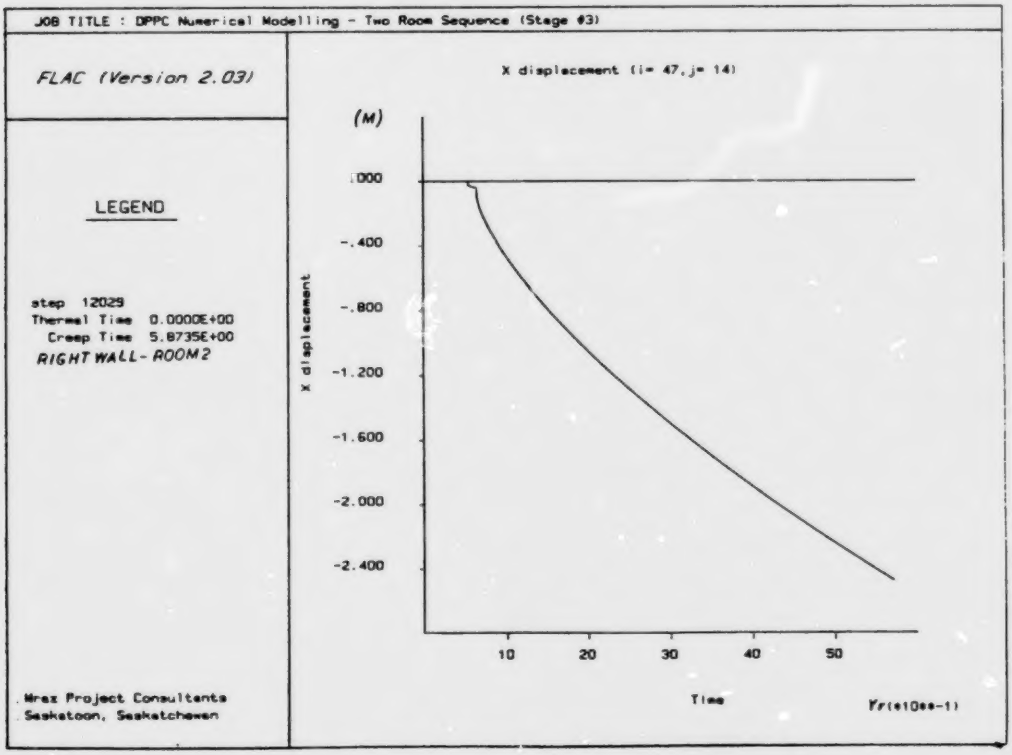

8.7 Results of FLAC Numerical Simulations

In the performing these numerical simulations, the following points were identified:

1. Satisfactory agreement between predicted and actual closure measurements in virgin ground openings (Sections 8.5.1 and 8.5.2) were obtained using the proposed properties summarized in Table 7.6 and the constitutive law for intact rock defined by Equation 7.5.

2. The convergence rates for high mining stopes were overpredicted due to the two-dimensional nature of the analysis and the limited size of modelling layout (Section 8.6.1). The convergence rate predictions for multiple room sequence (i.e. 9 room sequence) were in much closer agreement with in situ measurements.

3. Potential problems in regard to failure in the roof were identified if the salt cover was too thin.

4. Substantial slabbing and sloughing of the pillars, especially in large stopes were evident. Scaling and rib pillar bolting may be necessary in the case of stopes greater than 10 metres high.

5. In every case studied, the need for good roof bolting practices and regular roof inspections was evident.

6. Horizontal and vertical stress levels were found to be at safe levels at the top of the salt in regard to the hydrostatic water pressure of 9 MPa in each problem.

7. In none of the cases was the stability of the bearing pillars inadequate.

8. The yield pillars in development entries (Section 8.5.2) appeared to be slightly overloaded requiring more time for proper stress relief, but yielding sufficiently enough to allow uniform convergence of the roof.

This overload is likely exaggerated by the fact that the program does not account for yielded, fractured or dilated rock in pillars. A slight reduction in thickness of yielding pillars in development entries would reduce loading, decrease stiffness, and decrease the time required for stress relief, and possibly improve roof conditions. Further investigation into this topic is required before any final conclusions can be drawn.

9. Some tensile stresses develop in the roof of each geometry investigated, during the history of the runs.

Generally, the stress distributions observed in each problem indicate that the mining geometries investigated support the overburden load adequately and can be accepted as good design from the point of view of the overall mine stability. However, a great deal of attention must be paid to securing the roofs of individual stopes through the use of good bolting practices, sequence of excavations and, where required, backfill.

SECTION 9.0

9.0 NUMERICAL MODELLING OF DPPC MINE USING THE PROGRAM FLAC WITH BACKFILL

9.1 Introduction

A major objective of this study was to develop a constitutive law for halite backfill and incorporate that law into the numerical modelling programs that were to be used for this analysis. The program FLAC was used for two-dimensional modelling. Therefore, the code was modified to incorporate the backfill constitutive law by ITASCA under contract with Mraz Project Consultants Ltd.

9.2 Computational Procedure in FLAC to Predict Behaviour of Halite Backfill

It was determined by this study that three mechanisms govern the compaction creep of halite backfill in the laboratory. The three mechanisms are pressure solution, particulate sliding, and cataclasis.

In situ conditions will ultimately govern which mechanism dominates the compaction creep of halite backfill. Stresses and temperatures encountered in situ will be low for long periods of time before room closure begins to transfer roof and pillar loads onto the backfill. Pressure solution will, therefore, be the dominant in situ compaction creep mechanism.

This condition justifies the use of only the low rate regime portion of the compaction creep equation (5.10) which simplifies to the following:

$$\dot{\epsilon}_v = \dot{\epsilon}_{os} \left(\frac{\sigma_m}{\sigma_{os}}\right)^{m_1} \qquad (9.1)$$

where

$$\sigma_{os} = CD^{m_3} \qquad (9.2)$$

$$m_1 = a_1 D + b_1 \qquad \text{for } D < 0.74 \qquad (9.3)$$

$$m_1 = 3.0 \qquad \text{for } D \geq 0.74$$

$$D = \gamma_d / \gamma_f \qquad (9.4)$$

and parameters are the same as defined in Section 5.0

The constants used in the numerical modelling were as follows:

$\dot{\epsilon}_{0B} = 1.0 \times 10^{-6}\ (s^{-1})$
$C = 94.6$ MPa
$m_3 = 7.41$
$a_1 = 11.5$
$b_1 = -5.5$
$\gamma_f = g/cm^3$

Note that, if it is necessary, the high rate regime of the compaction creep equation is available in the FLAC program and can be used in the same manner as the low rate regime by simply applying the correct modelling parameters outlined in Section 5.0.

The method of modelling the halite backfill differs substantially from the way intact material is handled within the FLAC program. Intact material is divided into zones which form a grid that defines the geometry to be modelled. Each element interacts with the surrounding zones, and its behaviour is governed by a constitutive law. A backfilled room is modelled as a bulk material and is not divided into several elements, but is treated as a single zone. The reason for treating backfill in this manner is strictly due to time restraints. If backfill was modelled in the same manner as intact material, a simple problem would take a prohibitive amount of time to solve.

The manner in which the backfill constitutive law is utilized in a numerical modelling problem is as follows:

1. The problem is run to the desired time, at which backfilling is to take place, in the same manner as outlined in Section 8.0.
2. The area (ie. room) which is to be backfilled is defined by specifying the grid points that outlines the boundary of the area. Note that the entire room is backfilled, and the space between the top of the backfill and ceiling is factored into the "average" density.
3. Bulk material properties are assigned to the backfilled zone.
4. The problem is then restarted allowing the elastic response to be solved before the constitutive law governing compaction creep is initiated.

5. The degree of compaction and the increase in stresses within the backfill is determined in response to room closure using the constitutive law.
6. The mean (compaction) stress is determined within the backfill and is then converted into a back pressure which is applied against the boundary of the backfilled area.
7. This cycle is repeated until a predetermined amount of time has passed, at which point the problem is analyzed.

As the run progresses, the backfill densifies and the closure rate of the backfilled area decreases. When the backfill reaches total densification, its behaviour is then governed by the constitutive law (Equation 7.5) that defines the behaviour of intact materials. The properties used for the backfill when it is completely densified are the same properties used for the Upper Halite.

9.3 Analysis of Backfilling Method

At present, DPPC is using a method of dry backfill placement, but has recently investigated and initiated a method of hydraulic backfill placement, as outlined in Section 2.0.

The two methods of backfill placement were simulated by assigning a specific value of initial backfill density for each placement method. The initial densities assigned were 1.26 g/cc and 1.4 g/cc for dry and hydraulic backfill placement methods respectively.

The geometry and geology of the Test Stope (Figure 9.1) were used to investigate the response of the backfill and the surrounding materials to the two placement methods. The Test Stope was excavated and the problem run to 1.36 years before emplacement of the halite backfill. The problem was run to approximately twenty years after backfill placement for each placement method. Histories of the vertical and horizontal stresses 2.5 metres into the pillar for both placement methods are illustrated in Figures 9.2 to 9.5. Vertical and horizontal closures for each method are shown in Figures 9.6 to 9.11.

FIGURE 9.1

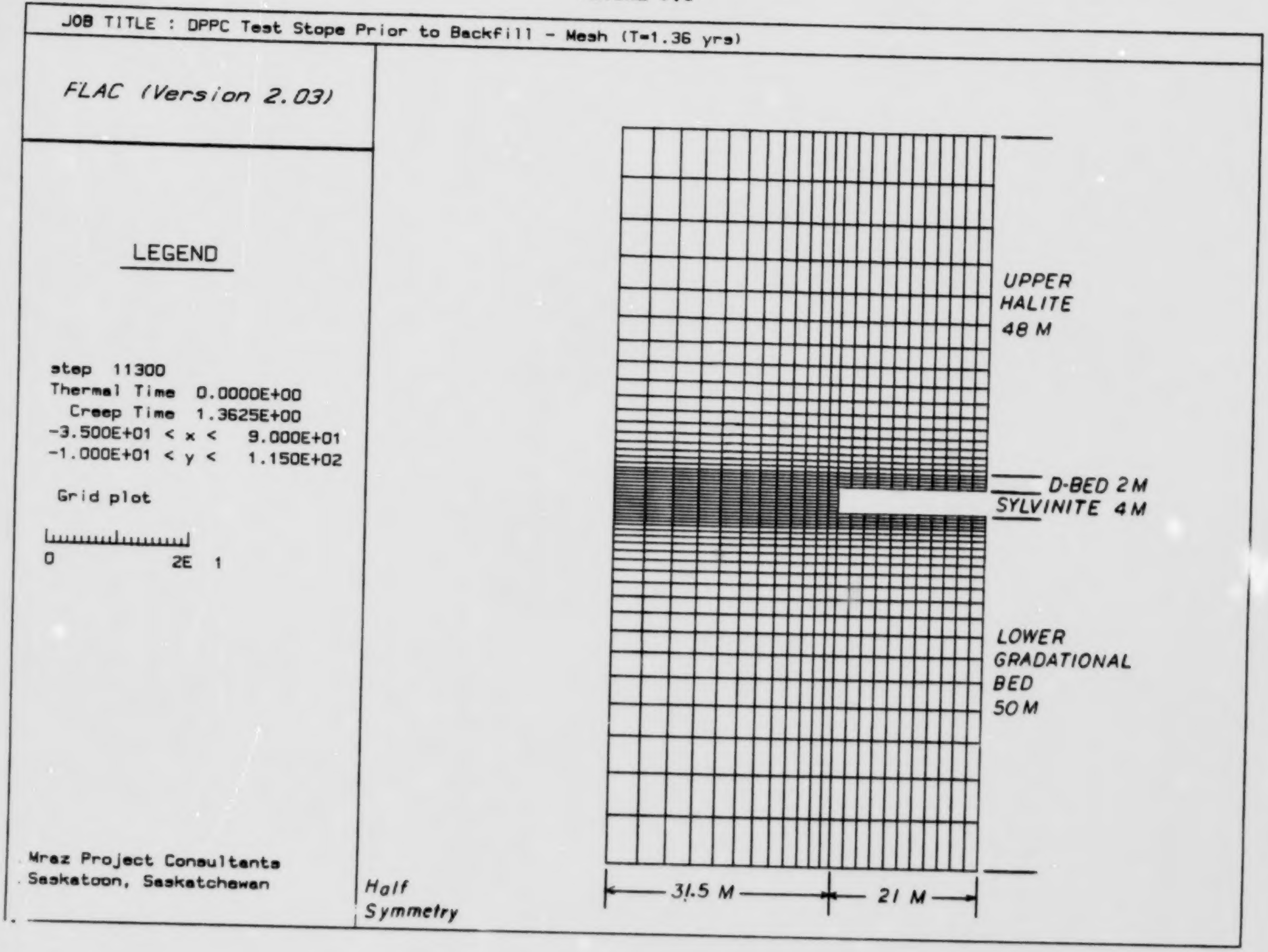
JOB TITLE : DPPC Test Stope Prior to Backfill - Mesh (T=1.36 yrs)
FLAC (Version 2.03)
LEGEND
step 11300
Thermal Time 0.0000E+00
Creep Time 1.3625E+00
-3.500E+01 < x < 9.000E+01
-1.000E+01 < y < 1.150E+02
Grid plot
0
2E 1
Mraz Project Consultants
Saskatoon, Saskatchewan
Half Symmetry
UPPER HALITE 48 M
D-BED 2 M
SYLVINITE 4 M
LOWER GRADATIONAL BED 50 M
31.5 M
21 M

FIGURE 9.2

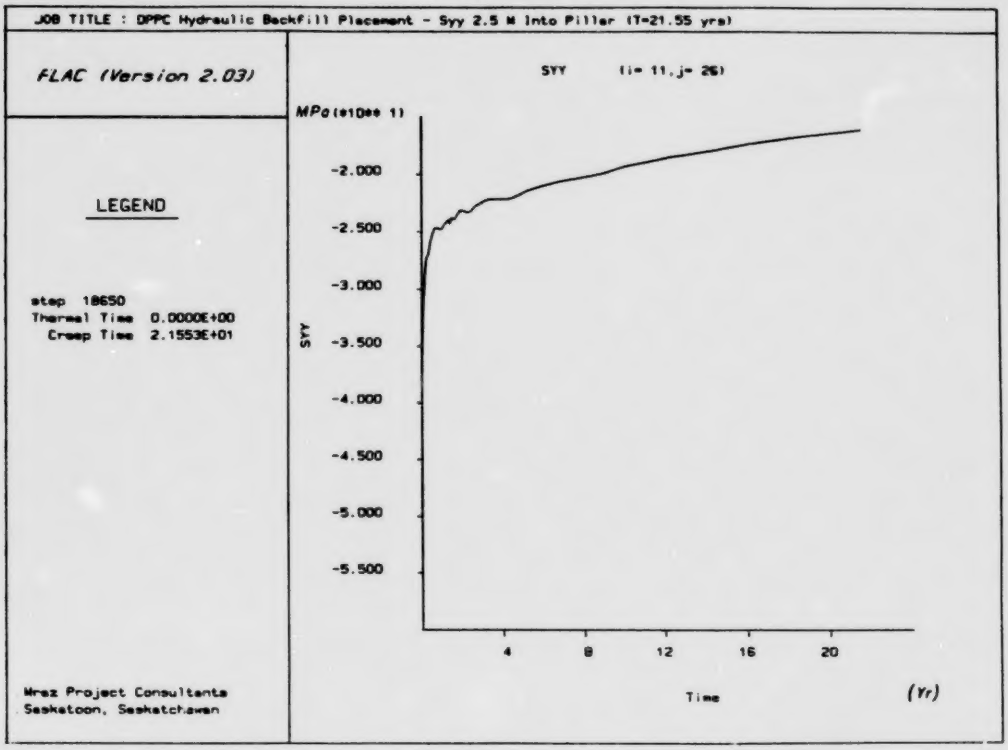

FIGURE 9.3

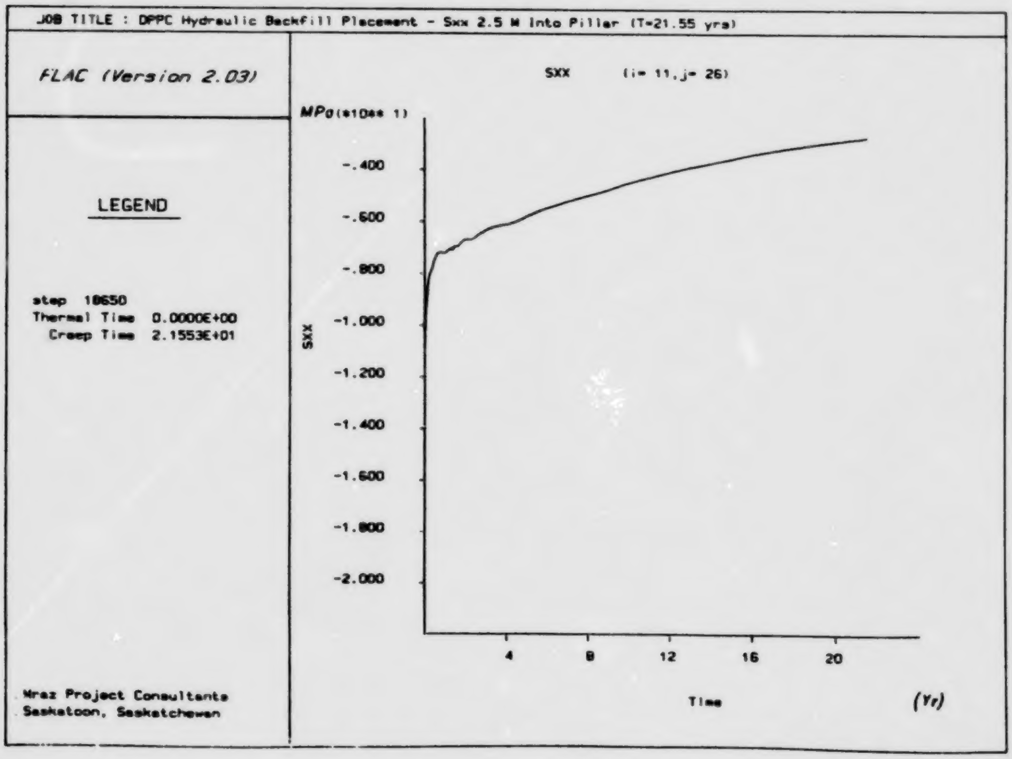

FIGURE 9.4

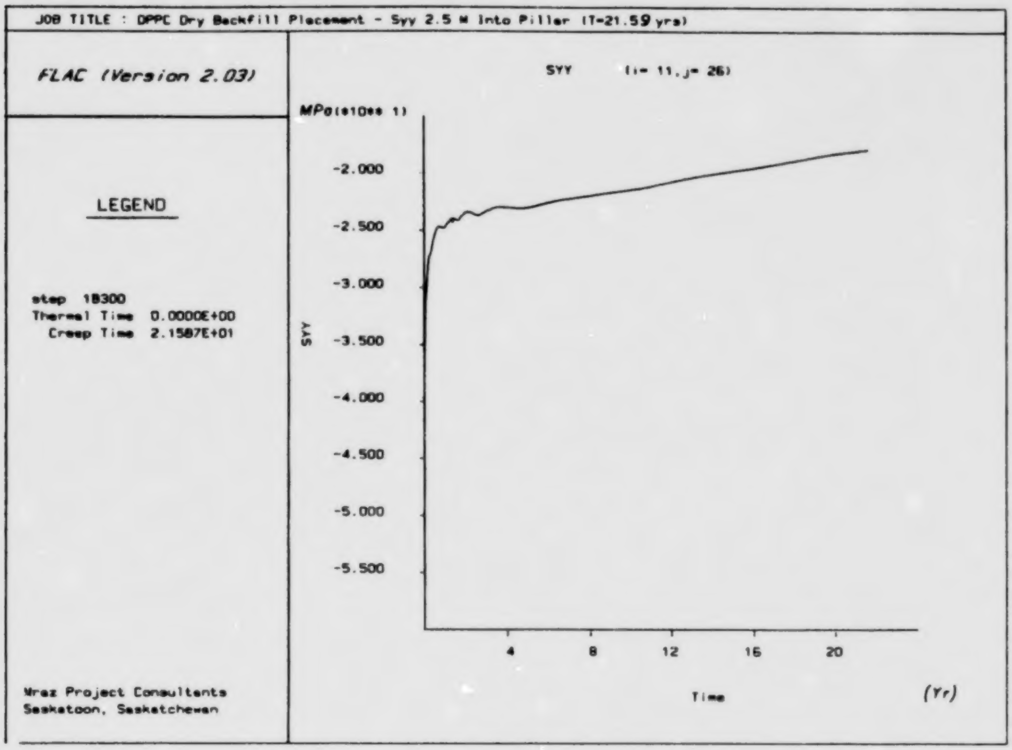

FIGURE 9.5

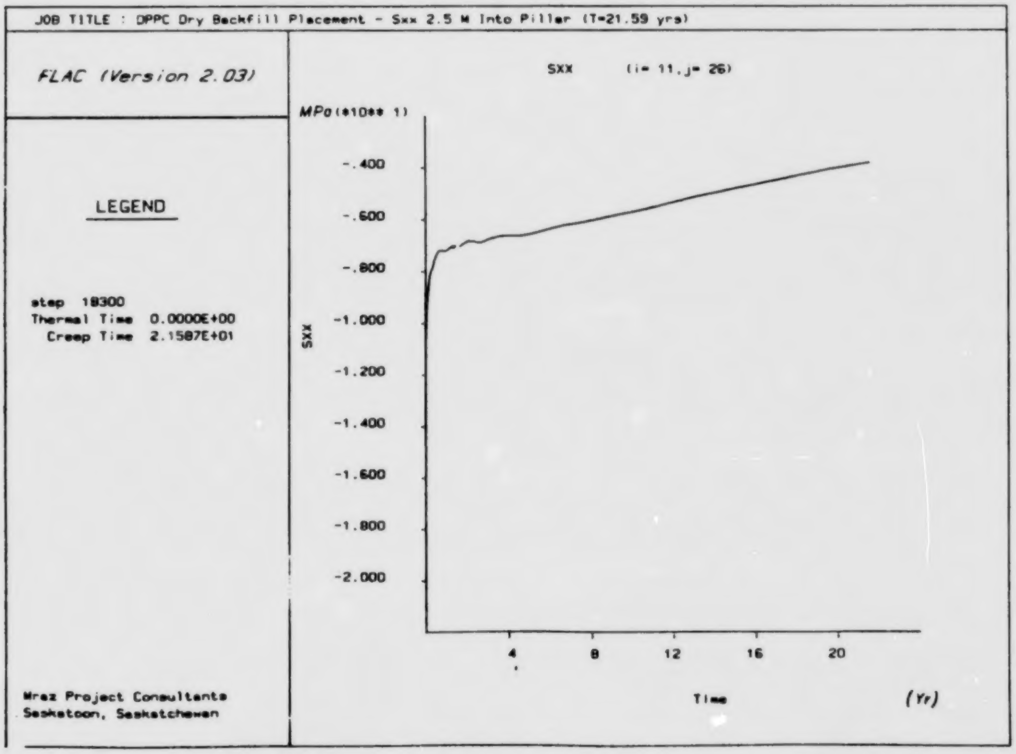

FIGURE 9.6

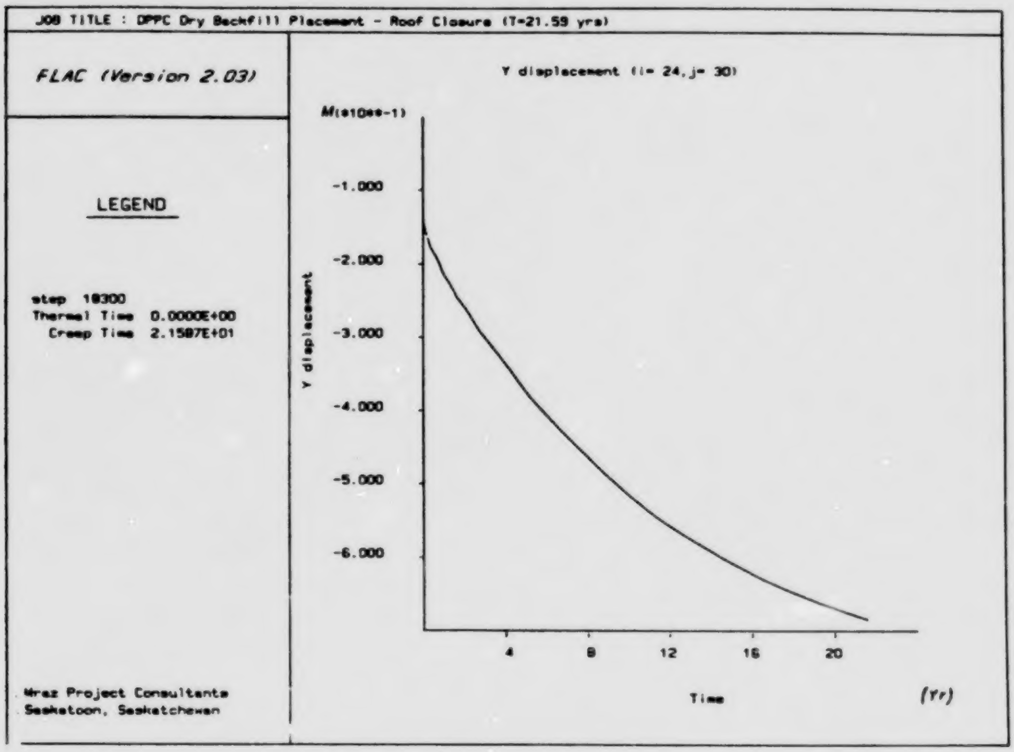

FIGURE 9.7

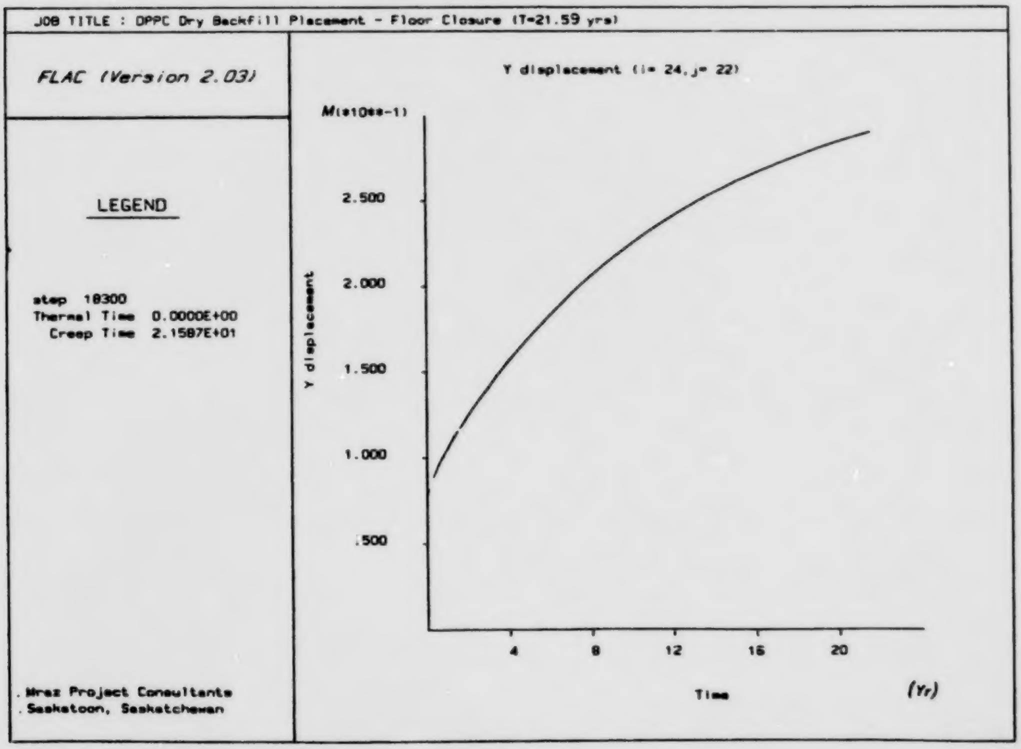

FIGURE 9.8

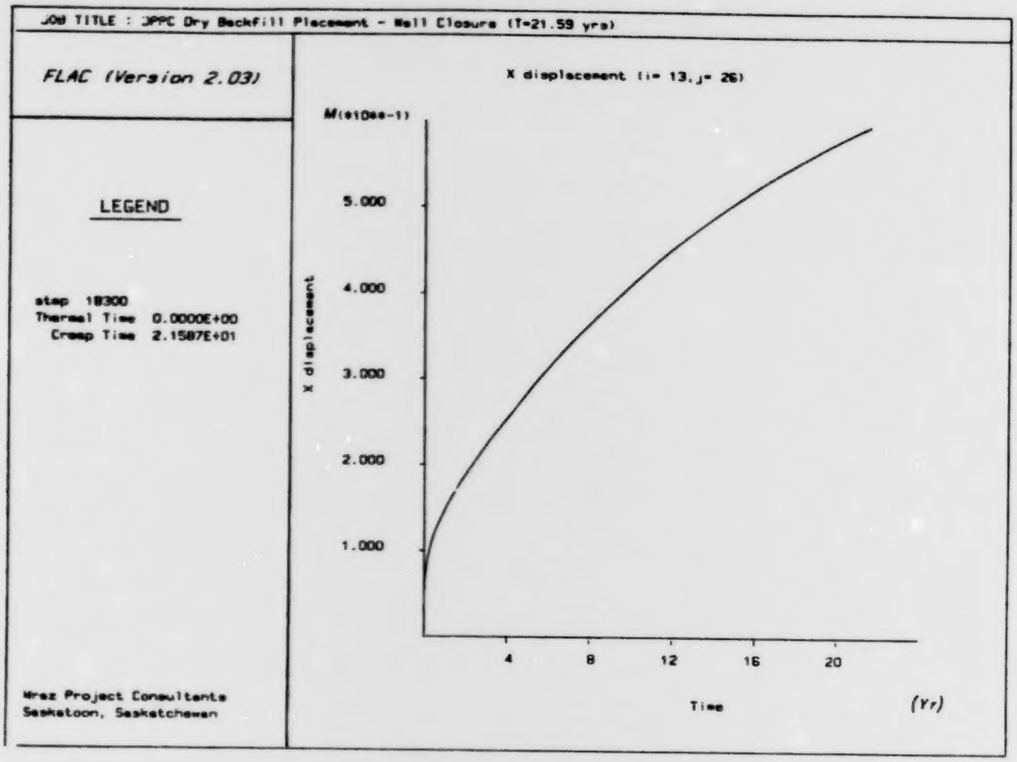

FIGURE 9.9

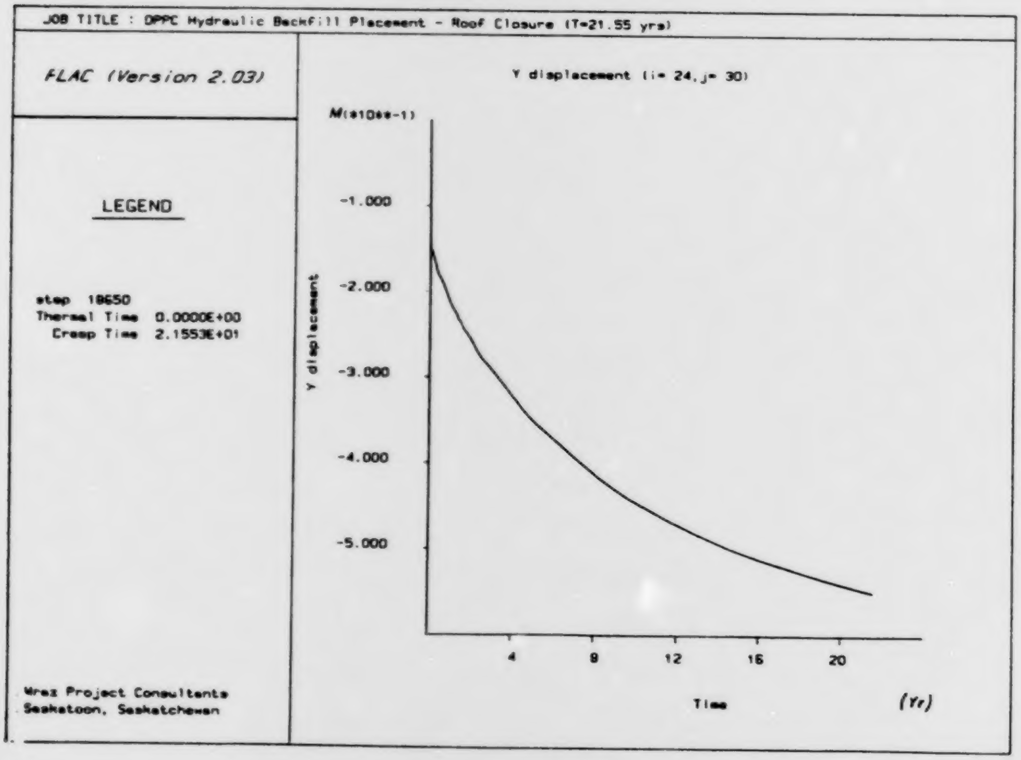

FIGURE 9.10

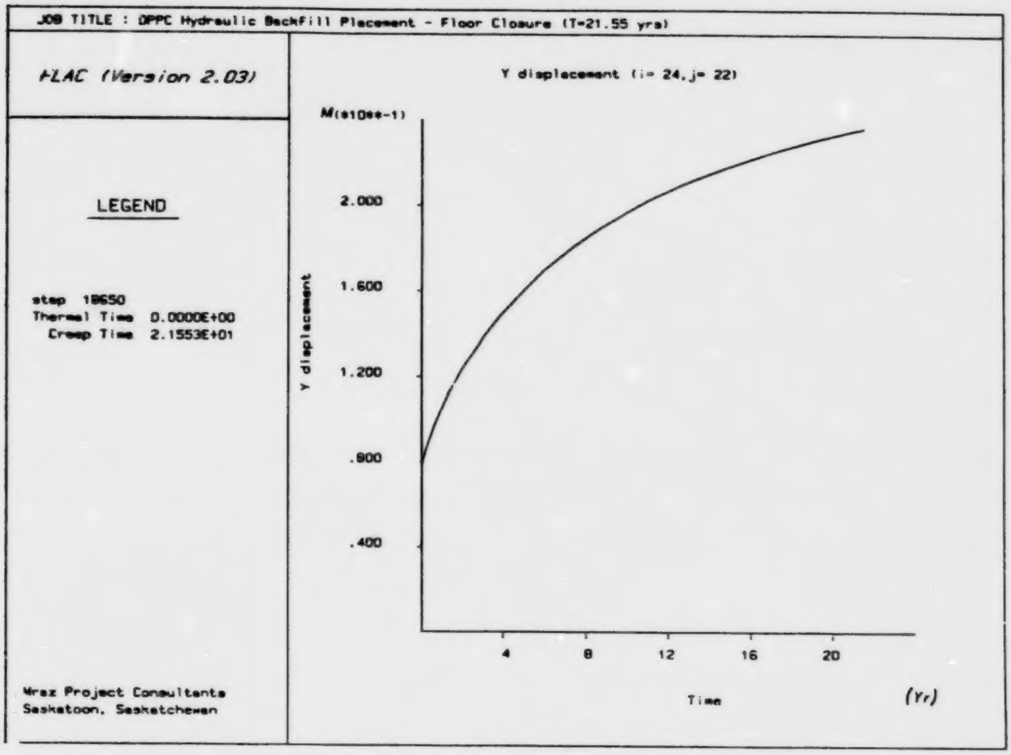

FIGURE 9.11

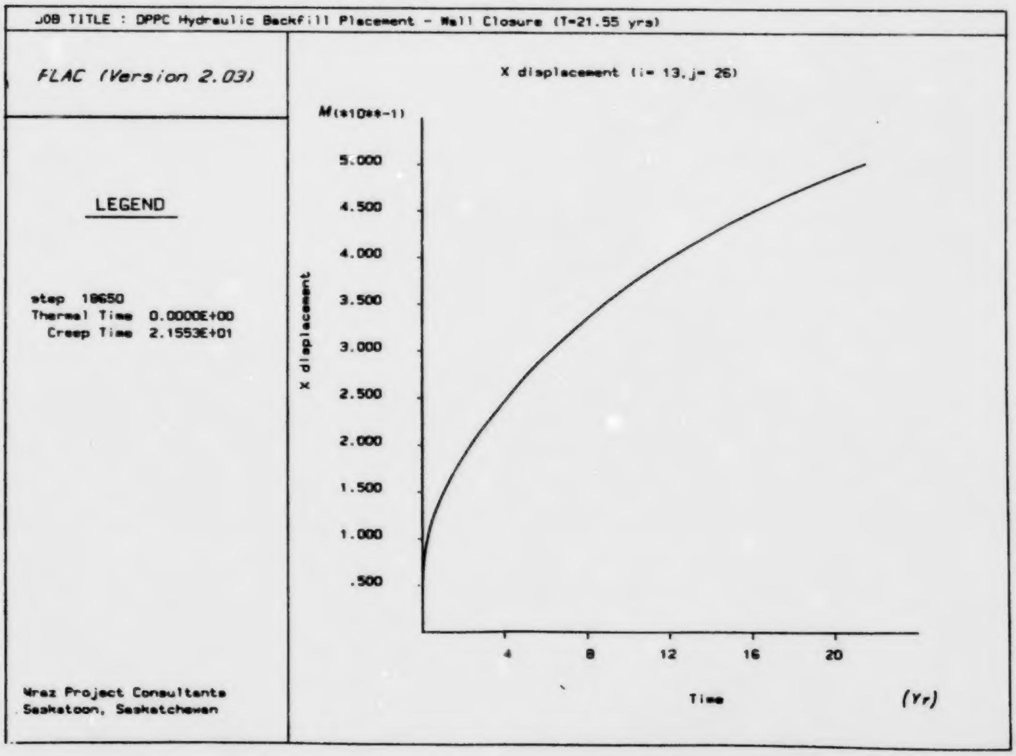

Comparison of the closure rates and stresses within the backfill are summarized in Tables 9.1 and 9.2.

Upon examining stresses in the pillar (Figures 9.2 to 9.5), it was observed that the initial transfer of load from the pillars is more rapid for the test stope backfilled hydraulically. After a period of approximately 5 years, the rate of stress transfer appears equal for both placement methods. However, there is a difference of about 2-3 MPa, both horizontally and vertically, between the two placement methods as a result of the quicker load transfer in response to initial densities when compared at the same point in time.

The horizontal and vertical closure rates for the hydraulically filled test stope were about 40% slower after 20 years than the rates encountered in the stope filled using the dry placement method (Table 9.1).

The failure state of halite backfill in the test stope was investigated for each backfill placement method (Table 9.2). The major principal stress was compared to the yield stress to determine the failure state within the backfill. The exponential failure envelope defined by Equation 5.25 was used to determine the yield stress.

Simulation of the dry placement method resulted in the backfill having no unconfined compressive strength or tensile strength according to Equations 5.19 and 5.5, because the minimum degree of consolidation (ie. 0.7 fractional density) was not obtained after 20 years. The yield stress is exceeded by the major principal stress during the entire time of the simulation, which indicates that the backfill is in a state of constant failure and will provide minimal overburden support.

Modelling of the hydraulic placement method indicated that the backfill developed unconfined compressive strength and a tensile strength within 10 years of backfill emplacement. It appears that the backfill is capable of providing overburden support about 10 years after placement. This is demonstrated by the fact that the yield stress is not exceeded by the major principal stress.

TABLE 9.1

SUMMARY OF CLOSURE RATES FOR BACKFILL PLACEMENT METHODS

Time Since Excavation (Yrs)	Placement Method	Vertical Closure Rate (cm/yr)	Horizontal Closure Rate (cm/yr)	Ratio Horizontal to Vertical	Comments
1.36	-	6.25	8.76	1.40	- just prior to backfill placement
21.55	Hydraulic	0.83	1.69	2.03	- 20.19 years after backfill placement Initial density = 1.4 g/cc
21.59	Dry	1.25	2.16	1.73	- 20.23 years after backfill placement Initial density = 1.26 g/cc

TABLE 9.2

FAILURE STATE OF HALITE BACKFILL IN TEST STOPE

Method of Backfill Placement : Dry Placement (Initial Density = 1.26 g/cc)
Time of Backfill Placement : 1.36 years after Test Stope excavation

Time Since Placement (Yr)	Area of Excavation (m^2)	Density (g/cc)	Fractional Density	Stress XX (MPa)	Stress XY (MPa)	Stress YY (MPa)	Minor Principal Stress (MPa)	Major Principal Stress (MPa)	Unconfined Compressive Strength (MPa)	Tensile Strength (MPa)	Yield Stress (MPa)
0.000	72.56	1.260	0.589	0.000	0.000	0.000	0.000	0.000	0.000	0.000	0.000
0.100	72.41	1.263	0.590	-0.013	-0.001	-0.033	-0.013	-0.033	0.000	0.000	0.000
0.163	72.32	1.264	0.591	-0.021	-0.001	-0.051	-0.021	-0.051	0.000	0.000	0.000
0.257	72.17	1.267	0.592	-0.035	-0.002	-0.082	-0.034	-0.082	0.000	0.000	0.000
0.332	72.08	1.269	0.593	-0.043	-0.000	-0.103	-0.043	-0.103	0.000	0.000	0.000
0.444	71.95	1.271	0.594	-0.055	-0.004	-0.132	-0.055	-0.132	0.000	0.000	0.000
0.519	71.86	1.272	0.594	-0.063	-0.005	-0.152	-0.063	-0.152	0.000	0.000	0.000
0.743	71.60	1.277	0.597	-0.087	-0.007	-0.211	-0.087	-0.211	0.000	0.000	0.000
1.005	71.28	1.283	0.600	-0.121	-0.009	-0.290	-0.120	-0.290	0.000	0.000	0.000
2.920	69.24	1.321	0.617	-0.369	-0.027	-0.884	-0.367	-0.885	0.000	0.000	0.000
4.439	67.81	1.348	0.630	-0.591	-0.045	-1.421	-0.588	-1.423	0.000	0.000	0.000
9.917	63.94	1.430	0.668	-1.493	-0.122	-3.638	-1.486	-3.645	0.000	0.000	0.000
20.225	60.14	1.520	0.710	-3.013	-0.245	-7.585	-3.000	-7.598	0.000	0.000	0.000

Method of Backfill Placement : Hydraulic Placement (Initial Density = 1.4 g/cc)
Time of Backfill Placement : 1.36 years after Test Stope excavation

Time Since Placement (Yr)	Area of Excavation (m^2)	Density (g/cc)	Fractional Density	Stress XX (MPa)	Stress XY (MPa)	Stress YY (MPa)	Minor Principal Stress (MPa)	Major Principal Stress (MPa)	Unconfined Compressive Strength (MPa)	Tensile Strength (MPa)	Yield Stress (MPa)
0.000	72.56	1.400	0.654	0.0000	0.0000	0.0000	0.000	0.000	0.000	0.000	0.000
0.095	72.43	1.403	0.656	-0.0307	-0.0019	-0.0746	-0.031	-0.075	0.000	0.000	0.000
0.165	72.33	1.404	0.656	-0.0527	-0.0039	-0.1275	-0.052	-0.128	0.000	0.000	0.000
0.260	72.20	1.407	0.657	-0.0860	-0.0061	-0.2068	-0.086	-0.207	0.000	0.000	0.000
0.335	72.12	1.409	0.658	-0.1043	-0.0075	-0.2533	-0.104	-0.254	0.000	0.000	0.000
0.410	72.04	1.410	0.659	-0.1227	-0.0092	-0.2996	-0.122	-0.300	0.000	0.000	0.000
0.510	71.93	1.412	0.660	-0.1477	-0.0113	-0.3615	-0.147	-0.362	0.000	0.000	0.000
0.768	71.64	1.418	0.663	-0.2233	-0.0165	-0.5436	-0.222	-0.544	0.000	0.000	0.000
1.066	71.31	1.425	0.666	-0.3146	-0.0229	-0.7640	-0.313	-0.765	0.000	0.000	0.000
3.072	69.61	1.459	0.682	-0.8408	-0.0653	-2.0550	-0.837	-2.058	0.000	0.000	0.000
4.838	68.46	1.484	0.693	-1.2640	-0.1047	-3.1150	-1.258	-3.125	0.000	0.000	0.000
10.018	66.13	1.536	0.718	-2.3430	-0.1985	-5.9050	-2.332	-5.916	-0.614	0.037	-5.203
20.188	63.88	1.590	0.743	-3.6320	-0.2919	-9.5600	-3.618	-9.574	-2.914	0.175	-16.366

The hydraulic backfill placement method results in a higher initial density, allowing quicker load transfer to the backfill from the pillars. As a result, the backfill reaches a point of densification at which it can provide support to the overburden. The dry backfill placement method results in a lower initial density which results in slower load transfer and densification. Extrapolation of the results indicates that the backfill would not provide overburden support until 25 years after dry backfill placement.

The development time for overburden support within halite backfill is a major concern being addressed by this study. Hydraulic placement of backfill offers earlier development of overburden support than the dry placement method, which potentially allows second pass mining to be initiated within a more acceptable time period.

9.4 Numerical Simulation of Second Pass Mining

Second pass mining was investigated by simulating a two room sequence corresponding to Stopes 11200 and 11240 (Figure 9.12). This sequence was chosen because Stope 11200 is the location of the backfill instrumentation room.

The initial geometry (ie. Stopes 11200 and 11240) was excavated instantaneously and allowed to run to about 1.0 year. Both stopes were then backfilled simulating hydraulic placement (ie. initial density = 1.4 g/cc) and run to specific times at which second pass mining was performed (Figure 9.13). Second pass mining performed 5 and 10 years after backfill placement were the two scenarios investigated.

Horizontal and vertical pillar stresses were recorded for both scenarios. Stress histories are illustrated in Figures 9.14 to 9.21 for the second pass mining 5 years after backfilling, and in Figures 9.22 to 9.29 for second pass mining 10 years after backfill placement. Horizontal and vertical closures in Stopes 11200, 11240, and the Second Pass Stope are shown in Figures 9.30 to 9.53 for both scenarios. A summary of the mining and backfilling sequence and the subsequent closure rates for each scenario is tabulated in Table 9.3. Movement of the rock mass in response to second pass

FIGURE 9.12

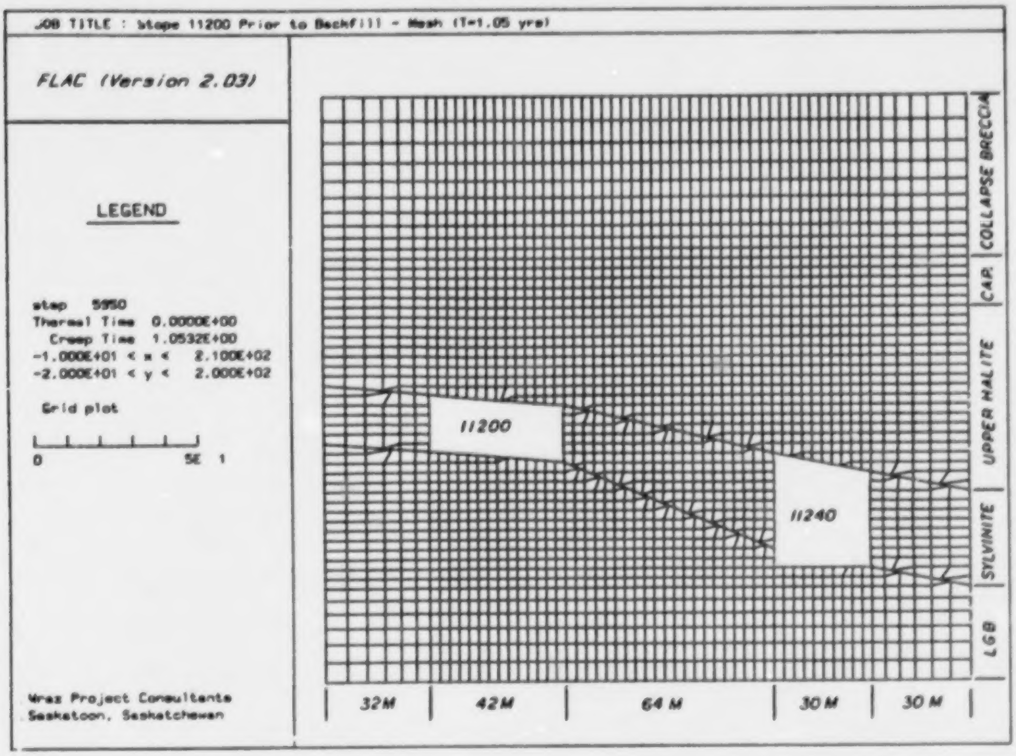

JOB TITLE : Stope 11200 Prior to Backfill - Mesh (T=1.05 yrs)

FLAC (Version 2.03)

LEGEND

step 5950
Thermal Time 0.0000E+00
Creep Time 1.0532E+00
-1.000E+01 < x < 2.100E+02
-2.000E+01 < y < 2.000E+02

Grid plot

Mraz Project Consultants
Saskatoon, Saskatchewan

FIGURE 9.13

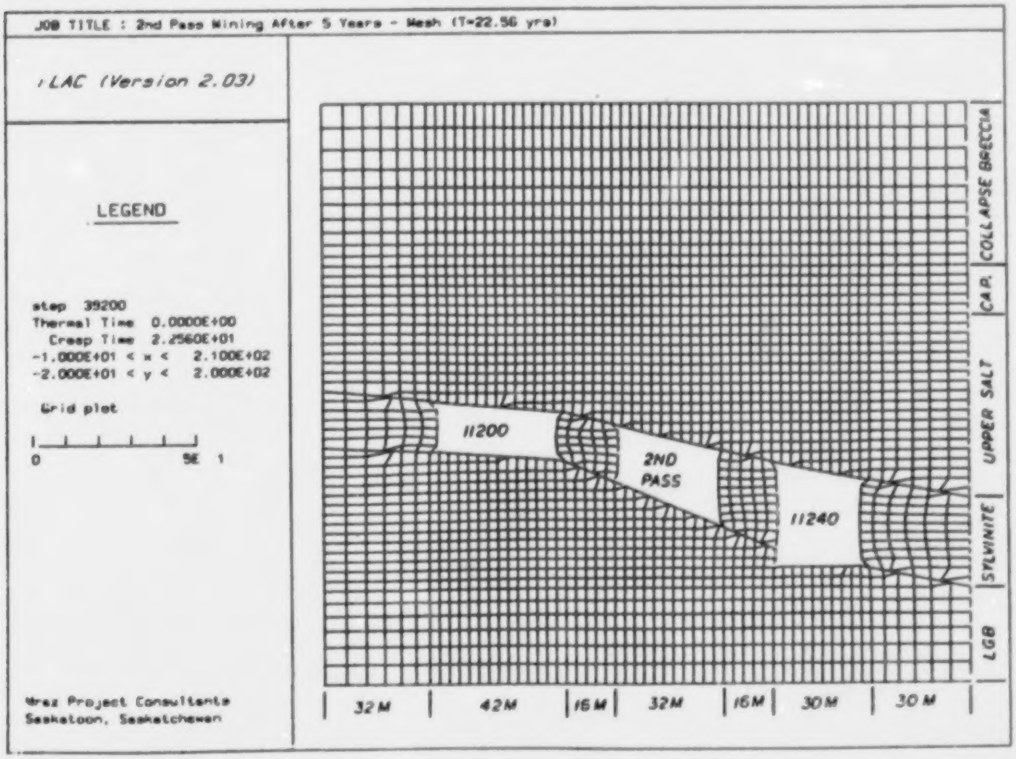

JOB TITLE : 2nd Pass Mining After 5 Years - Mesh (T=22.56 yrs)

FLAC (Version 2.03)

LEGEND

step 39200
Thermal Time 0.0000E+00
Creep Time 2.2560E+01
-1.000E+01 < x < 2.100E+02
-2.000E+01 < y < 2.000E+02

Grid plot

Mraz Project Consultants
Saskatoon, Saskatchewan

FIGURE 9.14

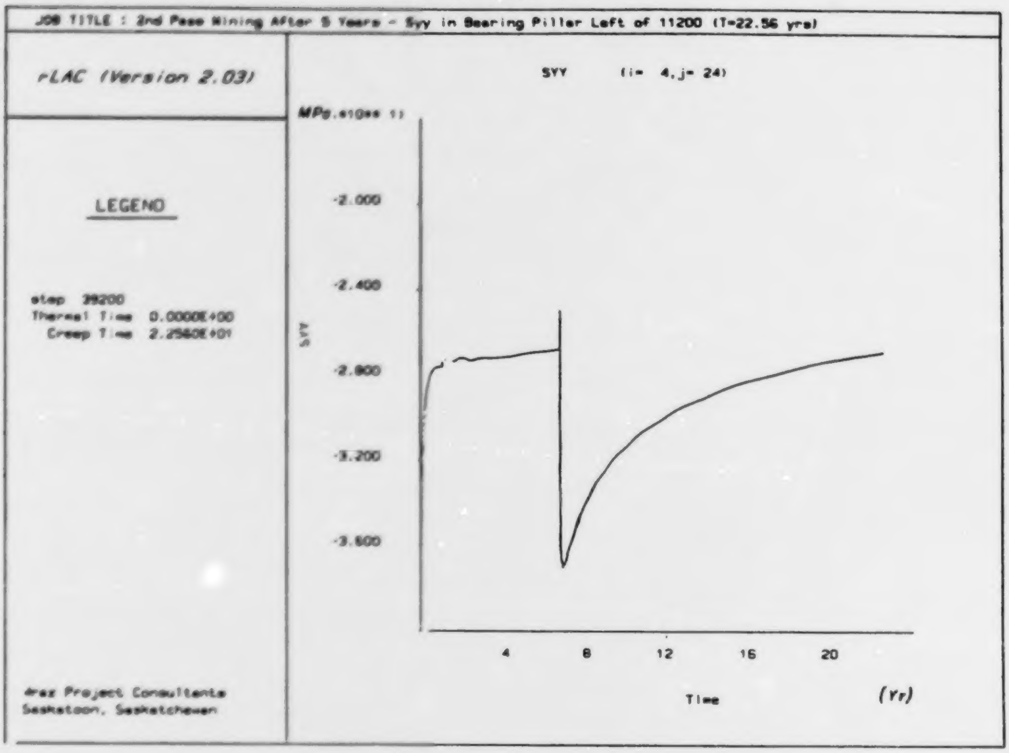

JOB TITLE : 2nd Pass Mining After 5 Years - Syy in Bearing Piller Left of 11200 (T=22.56 yrs)

FLAC (Version 2.03)

LEGEND

step 39200
Thermal Time 0.0000E+00
Creep Time 2.2560E+01

Mraz Project Consultants
Saskatoon, Saskatchewan

FIGURE 9.15

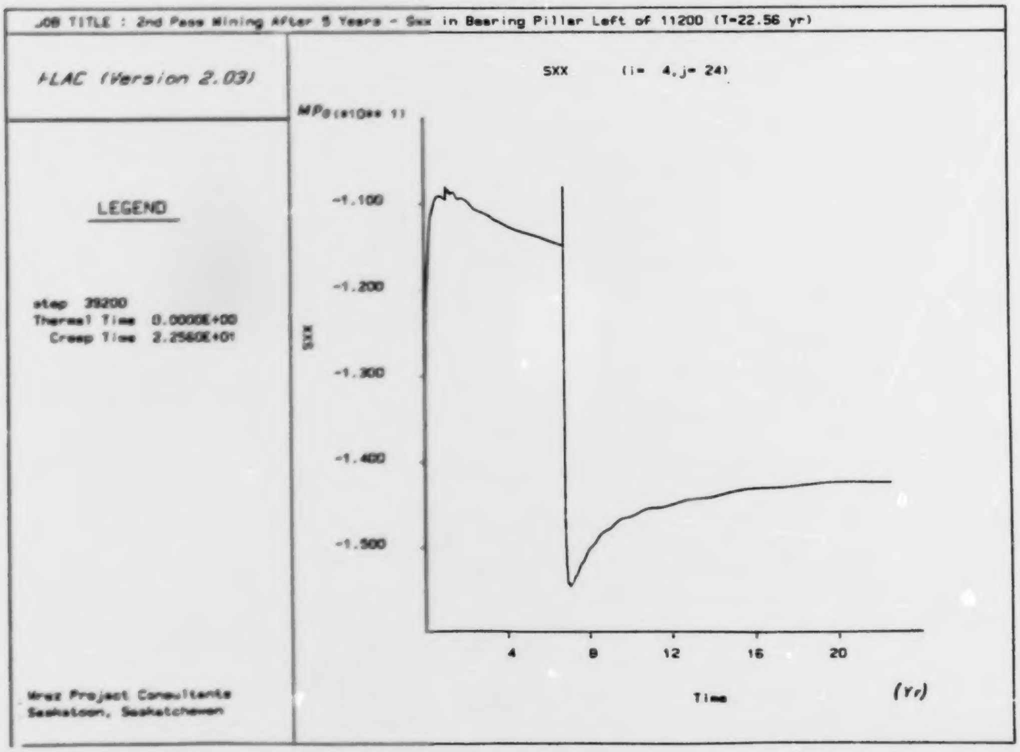

JOB TITLE : 2nd Pass Mining After 5 Years - Sxx in Bearing Piller Left of 11200 (T=22.56 yr)

FLAC (Version 2.03)

LEGEND

step 39200
Thermal Time 0.0000E+00
Creep Time 2.2560E+01

Mraz Project Consultants
Saskatoon, Saskatchewan

FIGURE 9.16

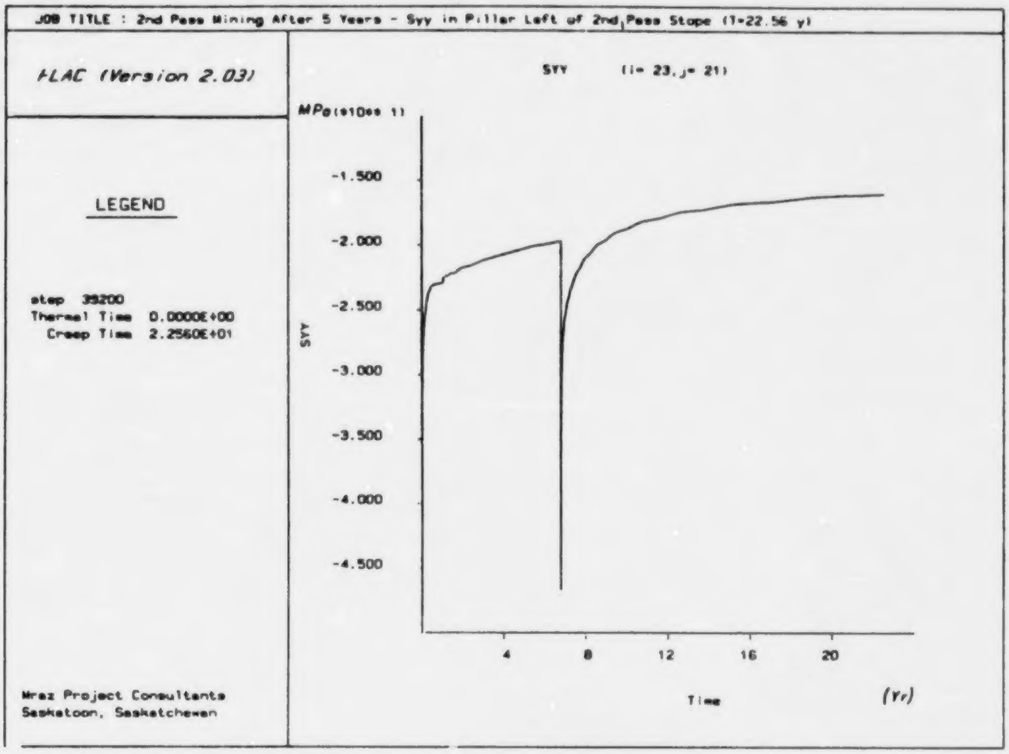

FIGURE 9.17

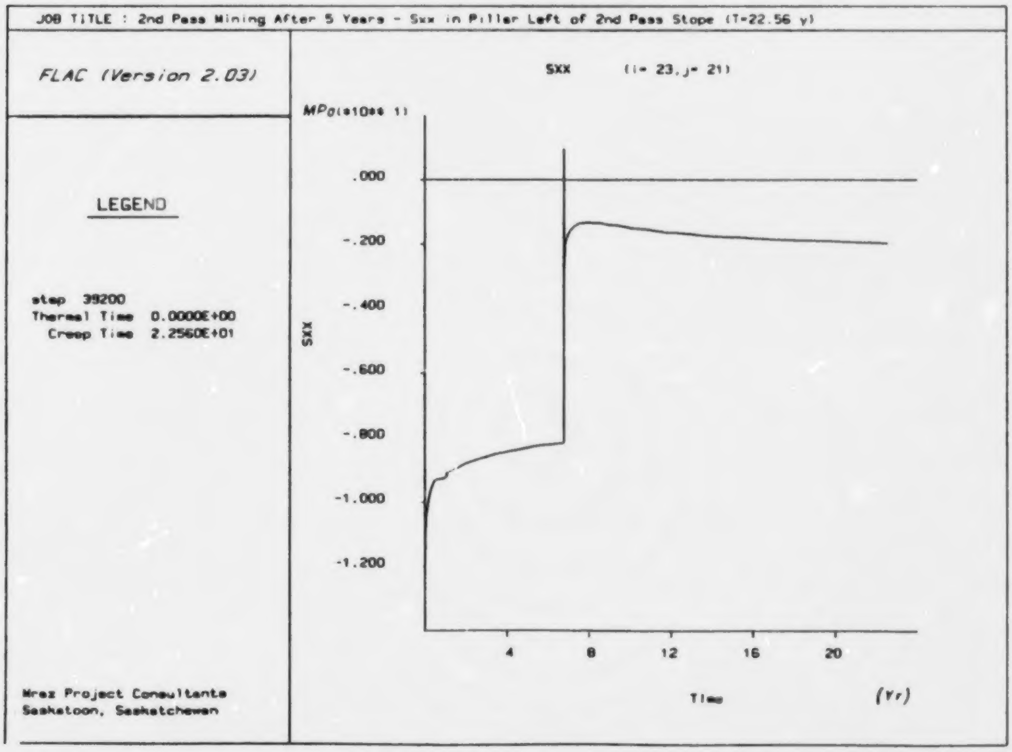

FIGURE 9.18

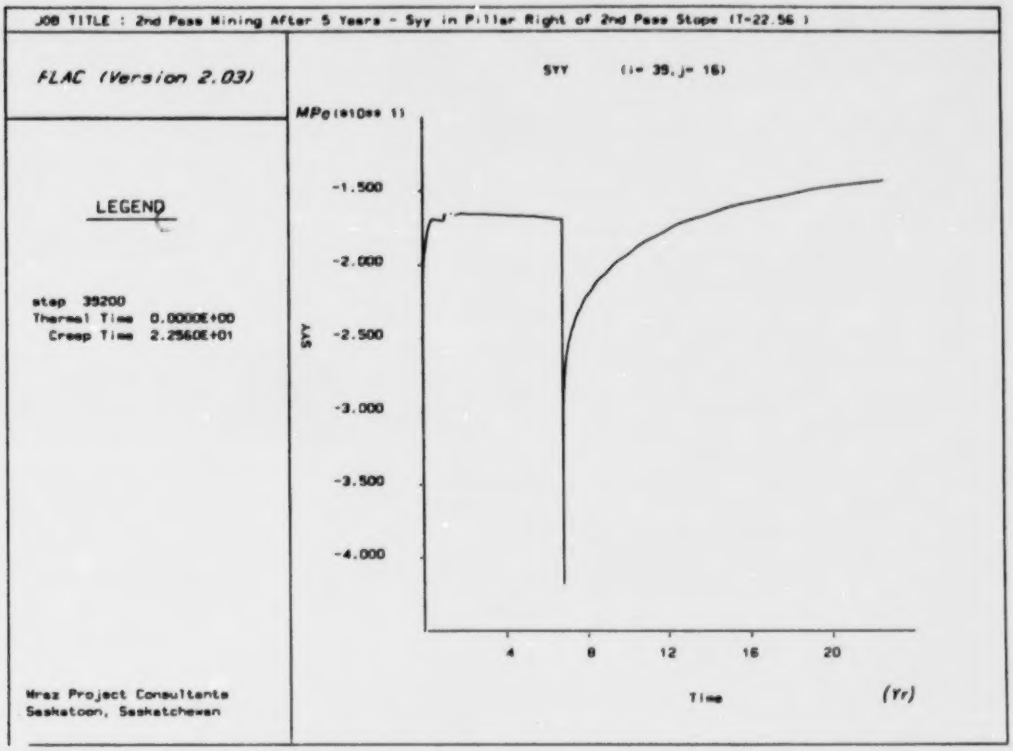

JOB TITLE : 2nd Pass Mining After 5 Years - Syy in Pillar Right of 2nd Pass Stope (T=22.56)

FLAC (Version 2.03)

LEGEND

step 39200
Thermal Time 0.0000E+00
Creep Time 2.2560E+01

Mraz Project Consultants
Saskatoon, Saskatchewan

FIGURE 9.19

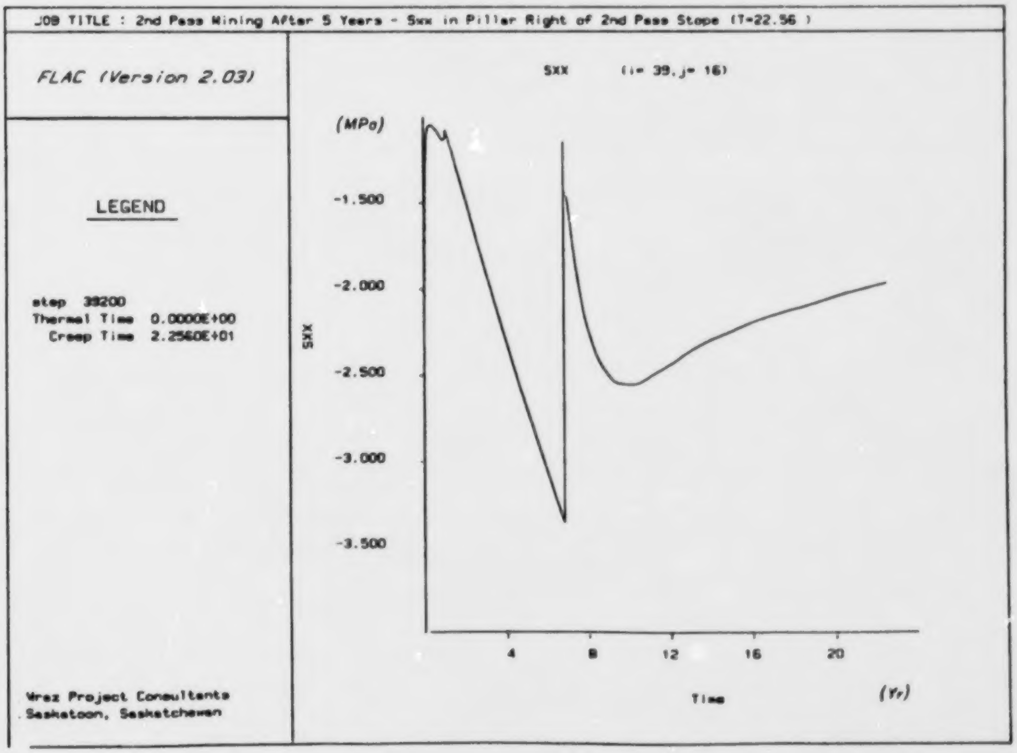

JOB TITLE : 2nd Pass Mining After 5 Years - Sxx in Pillar Right of 2nd Pass Stope (T=22.56)

FLAC (Version 2.03)

LEGEND

step 39200
Thermal Time 0.0000E+00
Creep Time 2.2560E+01

Mraz Project Consultants
Saskatoon, Saskatchewan

FIGURE 9.20

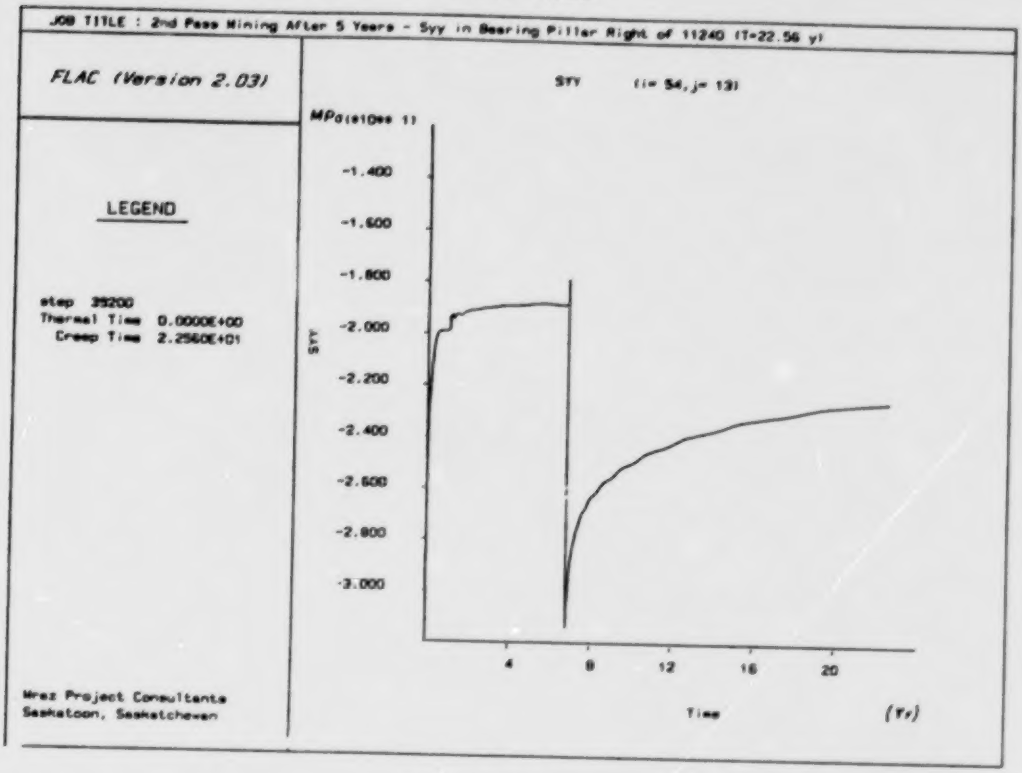

FIGURE 9.21

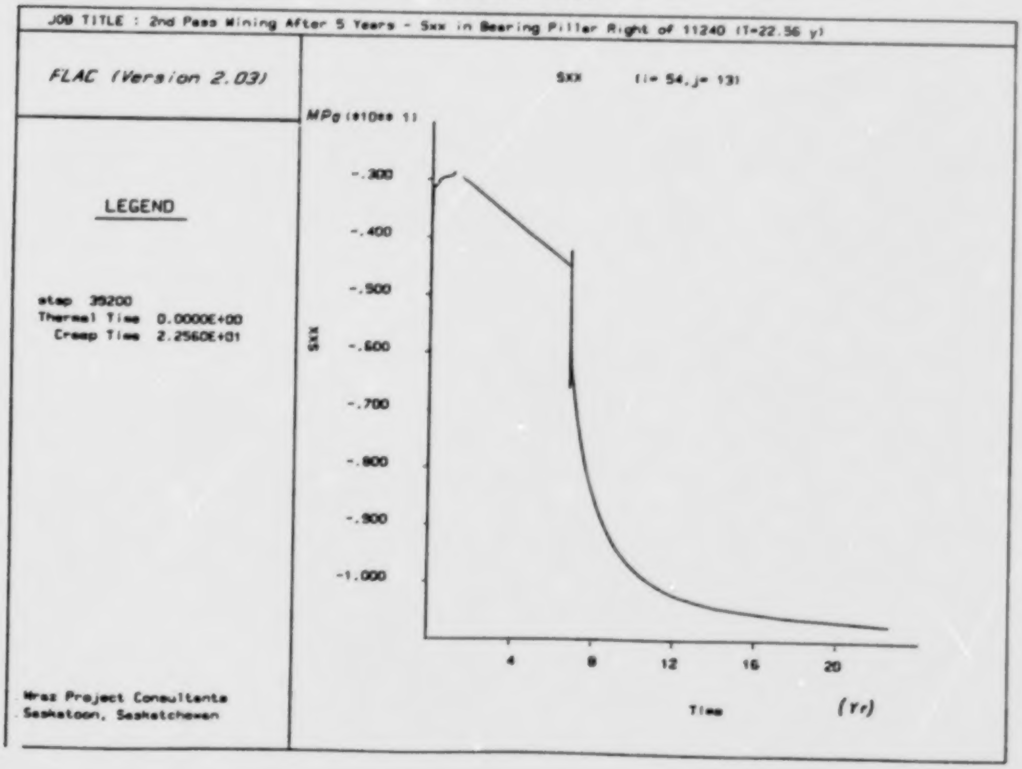

FIGURE 9.22

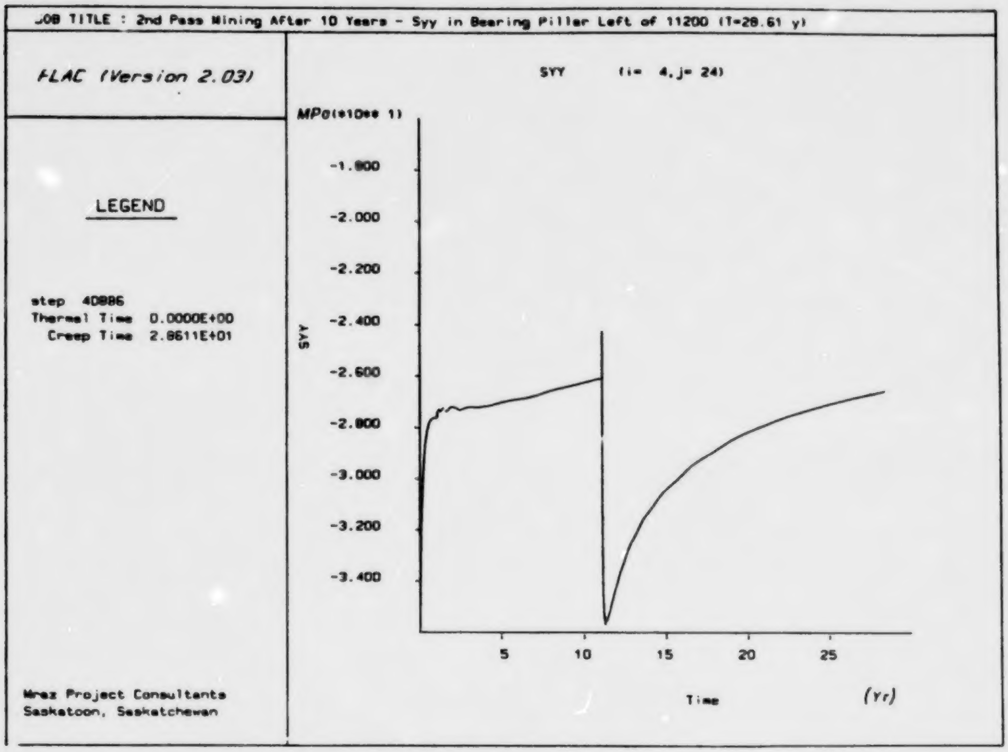

FIGURE 9.23

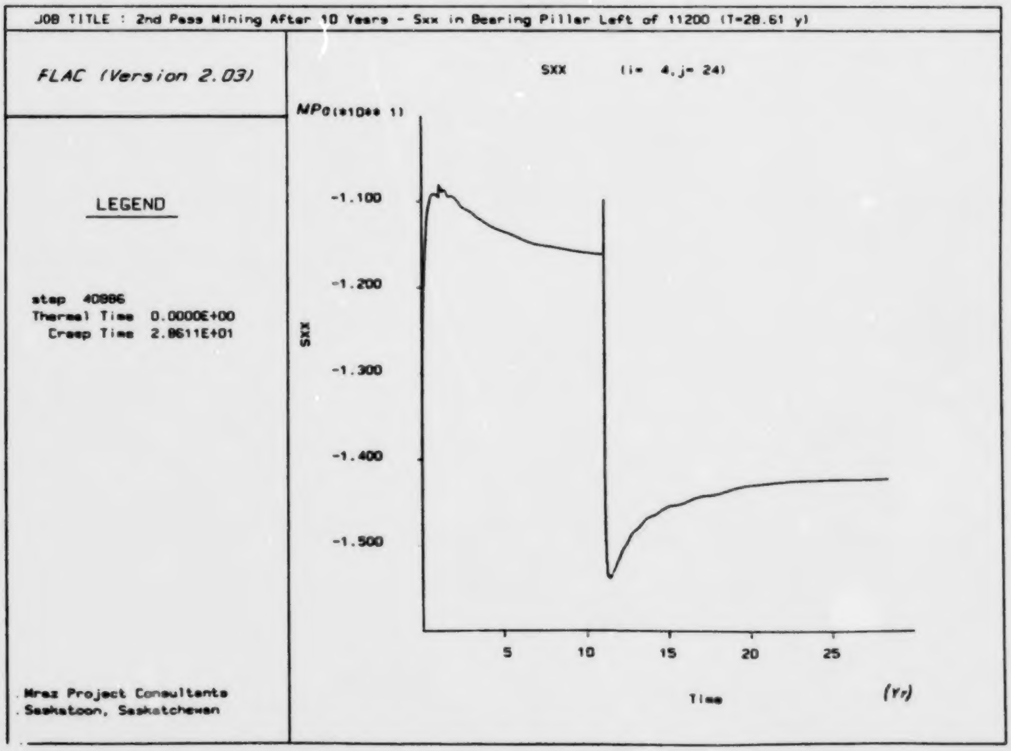

FIGURE 9.24

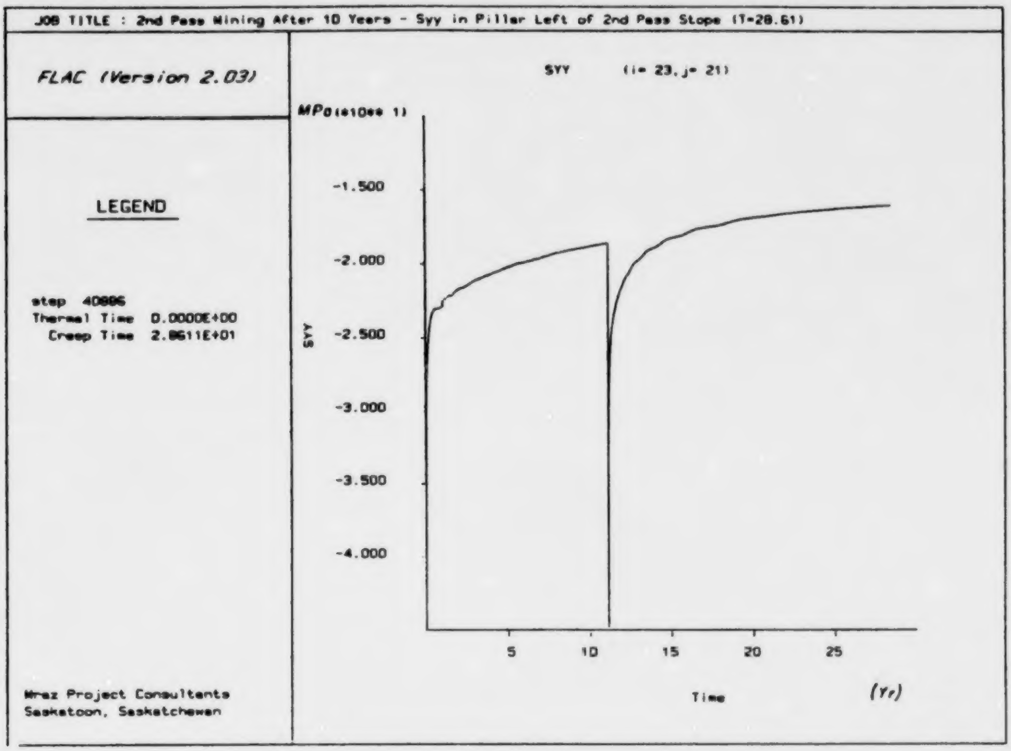

FIGURE 9.25

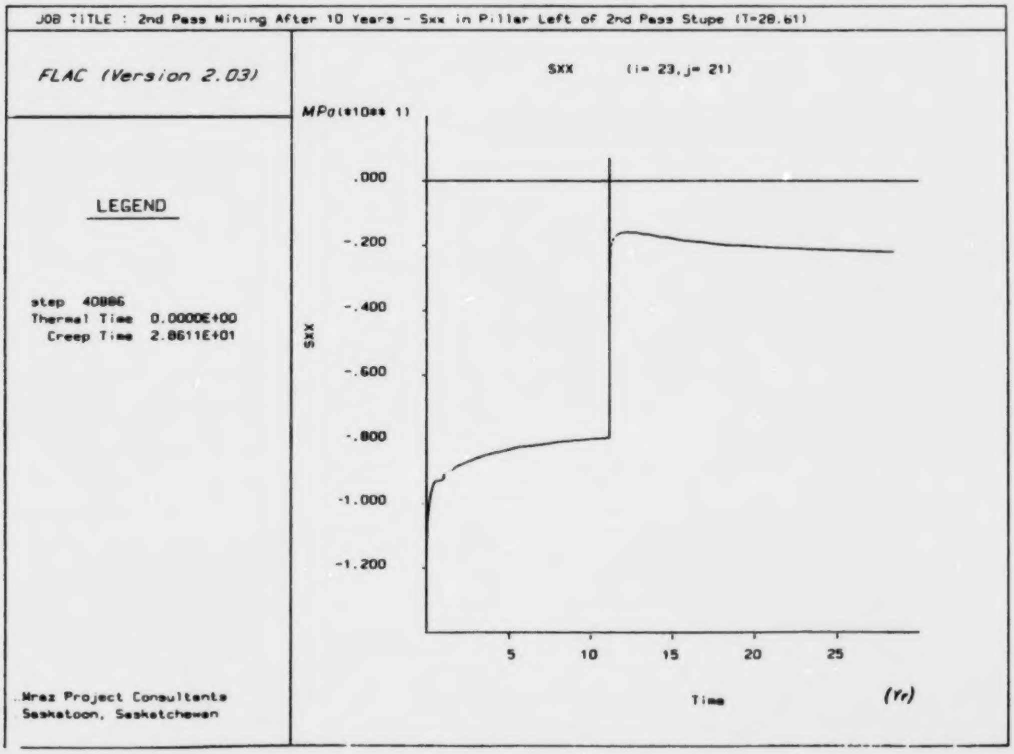

FIGURE 9.26

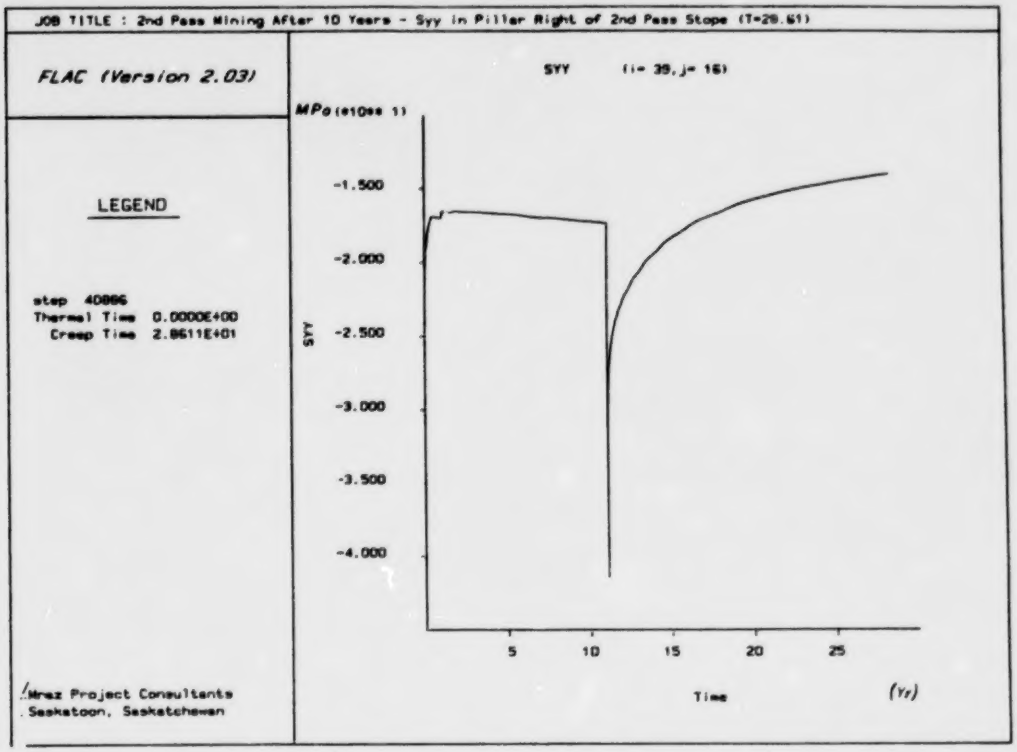

FIGURE 9.27

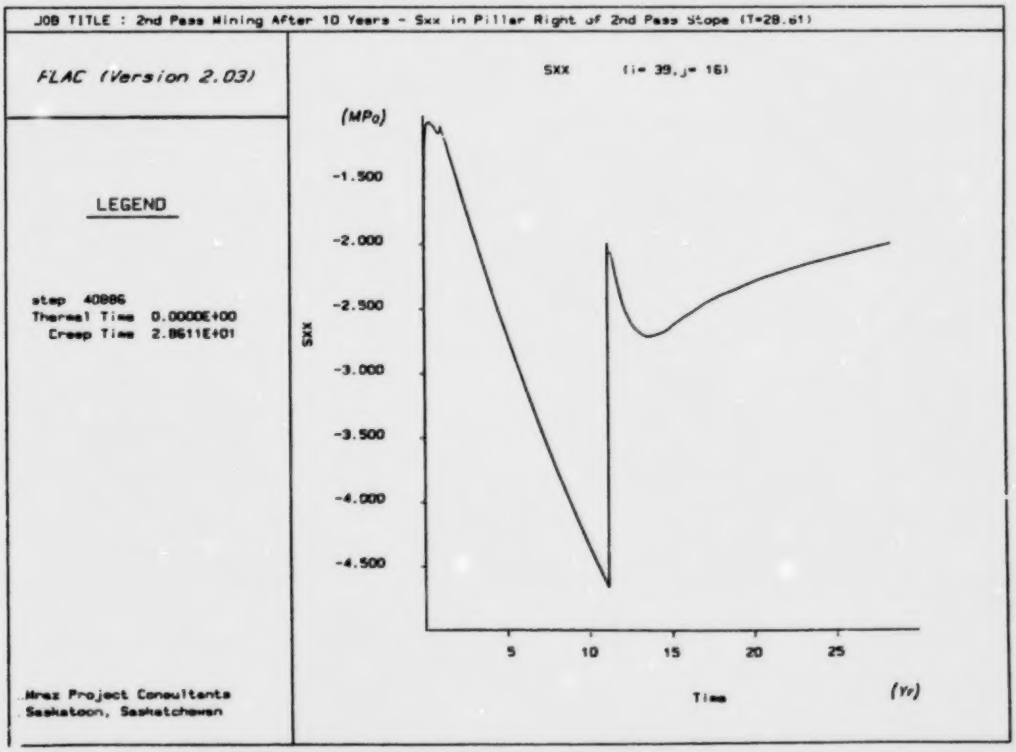

FIGURE 9.28

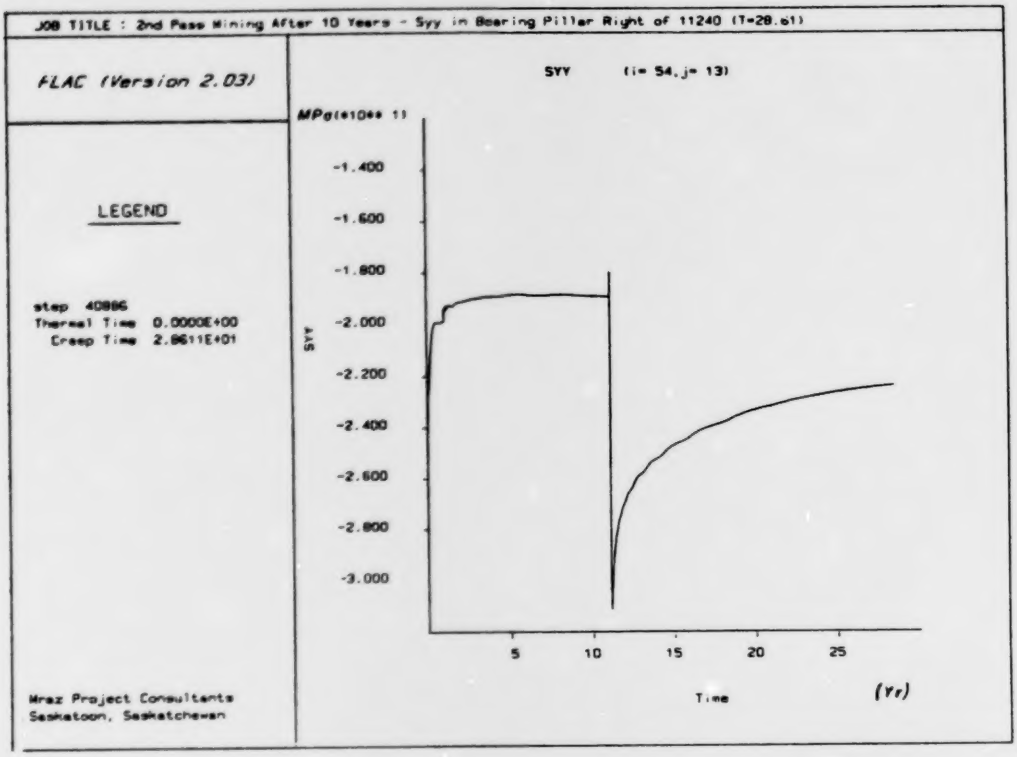

FIGURE 9.29

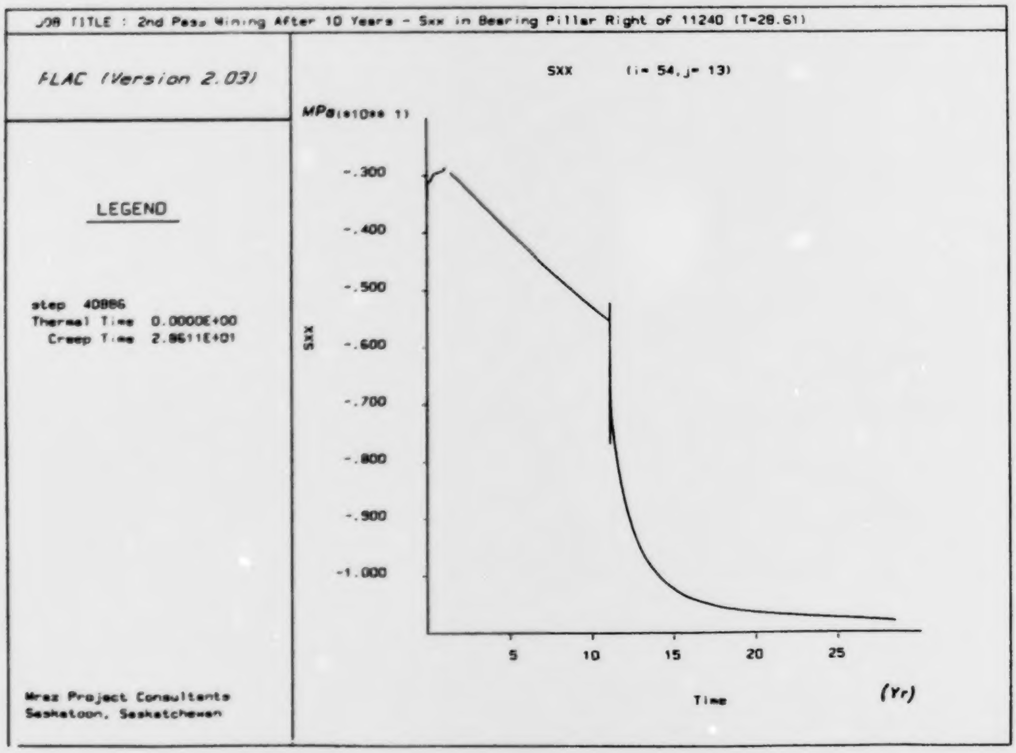

FIGURE 9.30

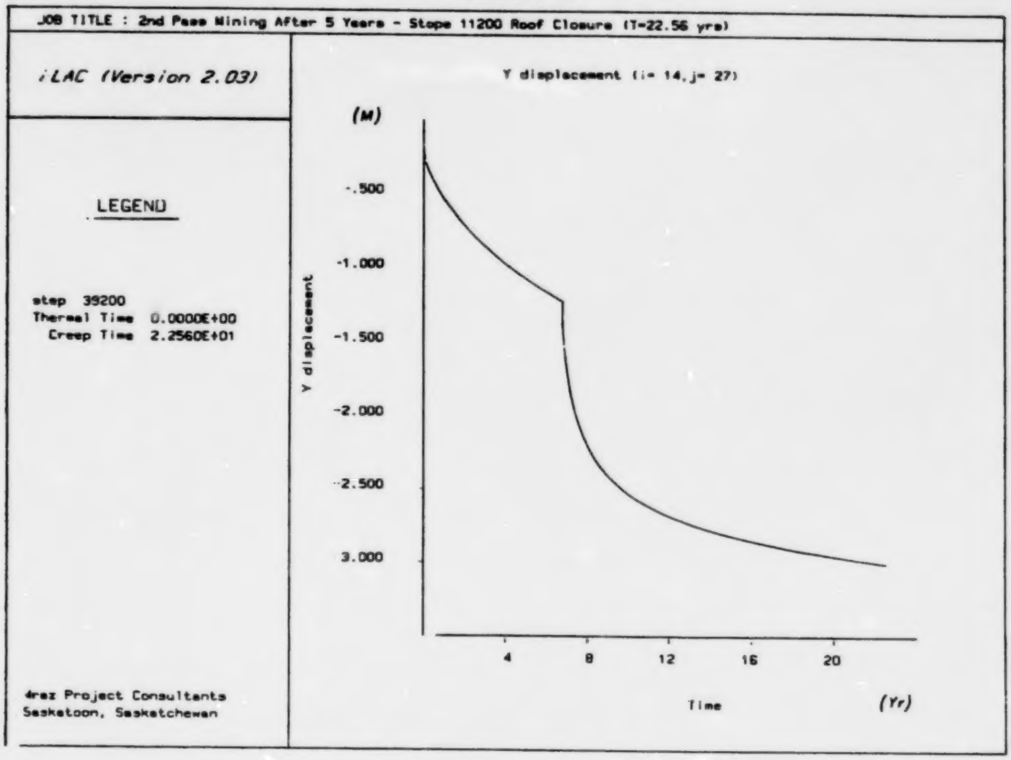
JOB TITLE : 2nd Pass Mining After 5 Years - Stope 11200 Roof Closure (T=22.56 yrs)

FLAC (Version 2.03)

LEGEND

step 39200
Thermal Time 0.0000E+00
Creep Time 2.2560E+01

Mraz Project Consultants
Saskatoon, Saskatchewan

FIGURE 9.31

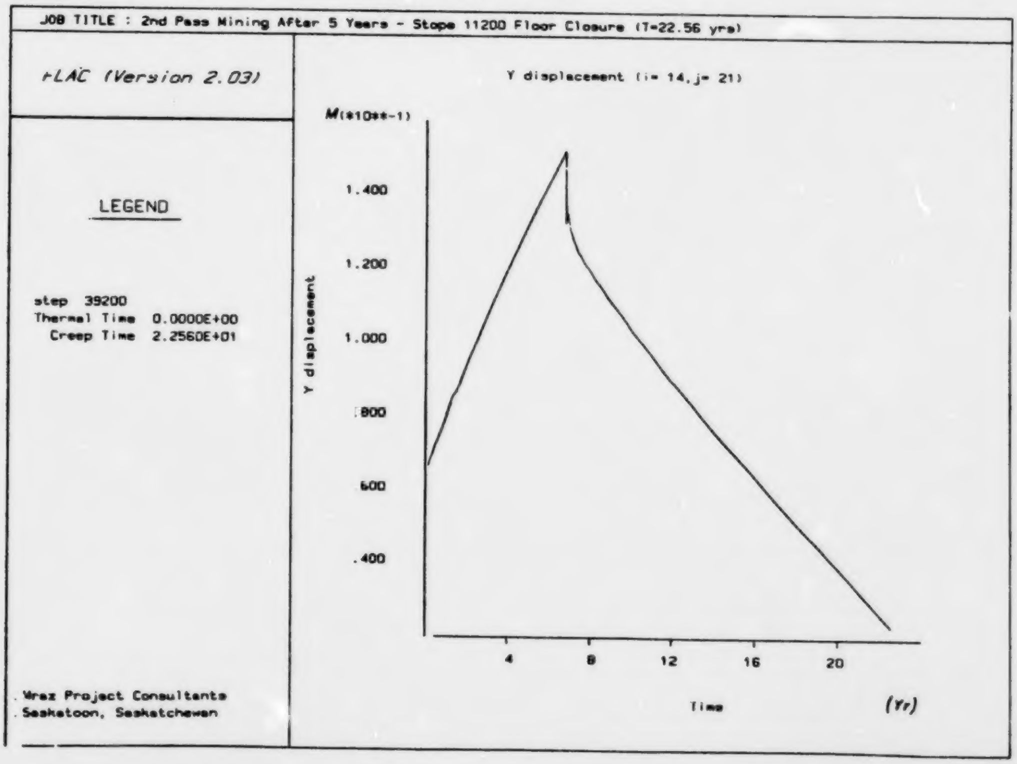
JOB TITLE : 2nd Pass Mining After 5 Years - Stope 11200 Floor Closure (T=22.56 yrs)

FLAC (Version 2.03)

LEGEND

step 39200
Thermal Time 0.0000E+00
Creep Time 2.2560E+01

Mraz Project Consultants
Saskatoon, Saskatchewan

FIGURE 9.32

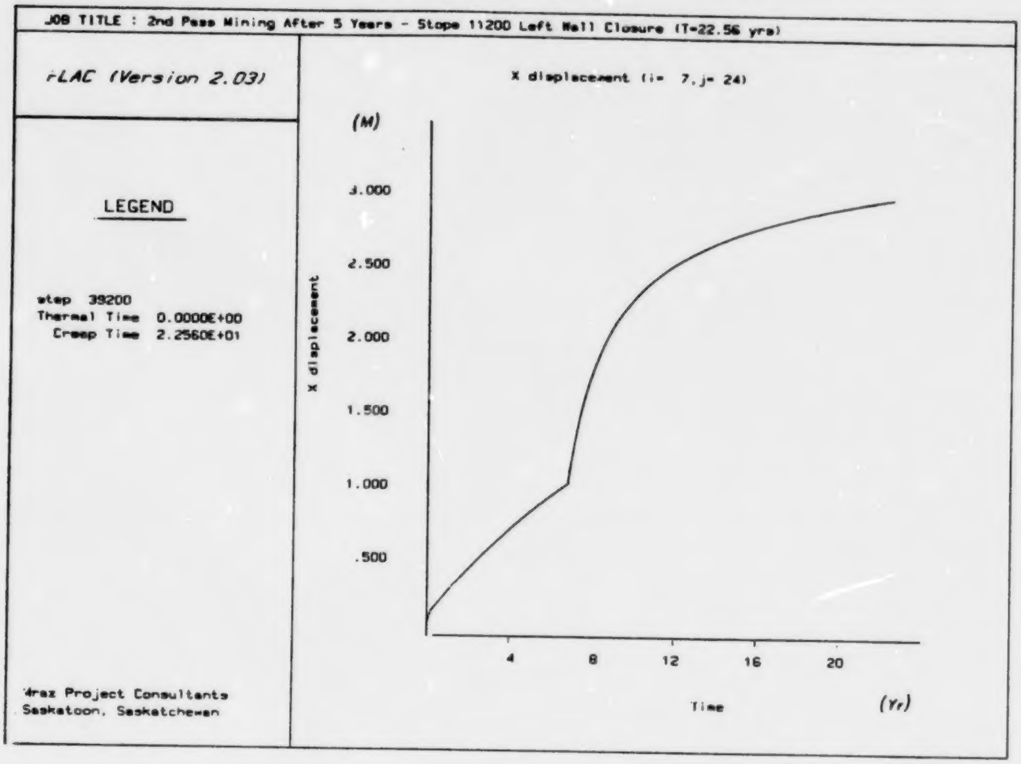

FIGURE 9.33

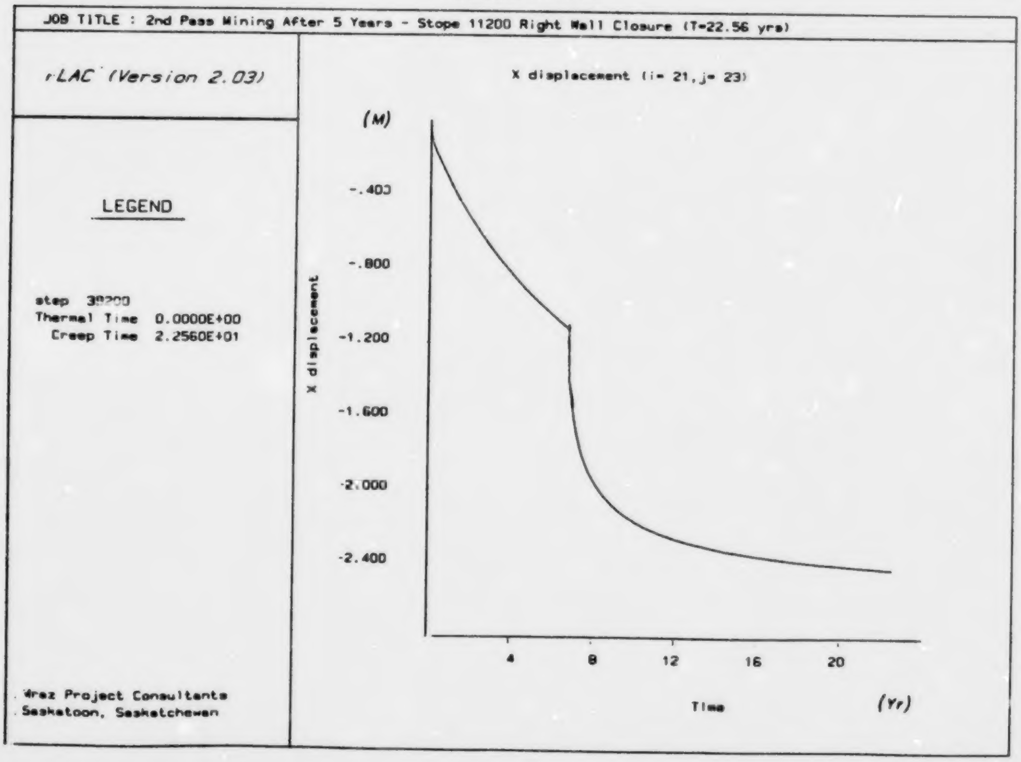

FIGURE 9.34

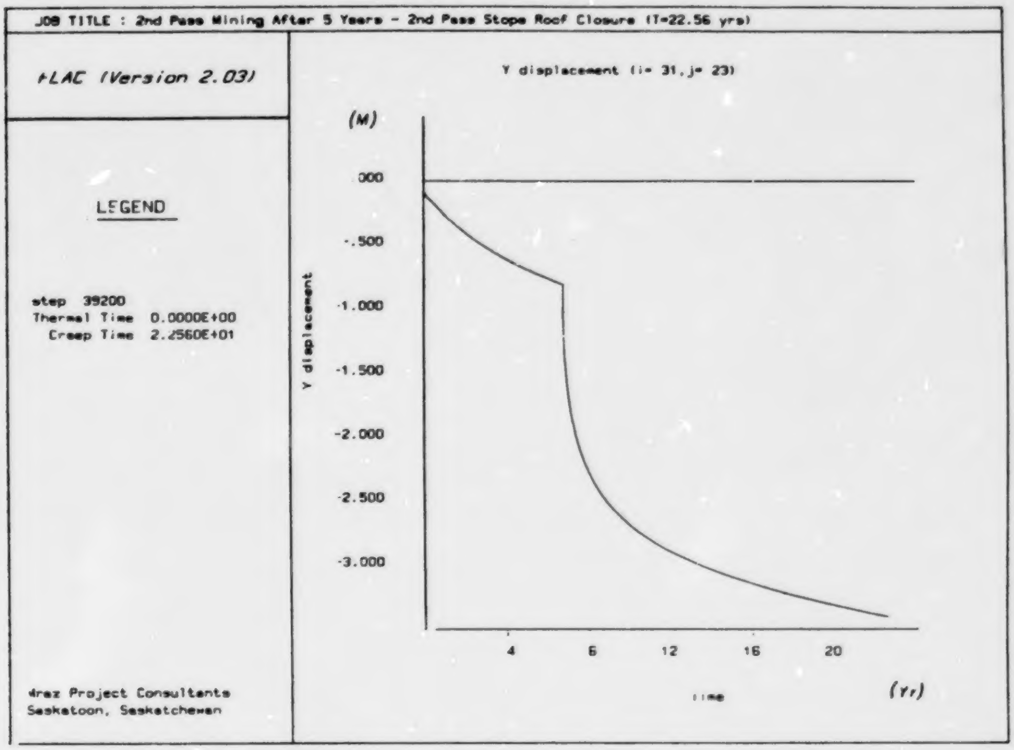

JOB TITLE : 2nd Pass Mining After 5 Years - 2nd Pass Stope Roof Closure (T=22.56 yrs)

FLAC (Version 2.03)

LEGEND

step 39200
Thermal Time 0.0000E+00
Creep Time 2.2560E+01

Mraz Project Consultants
Saskatoon, Saskatchewan

FIGURE 9.35

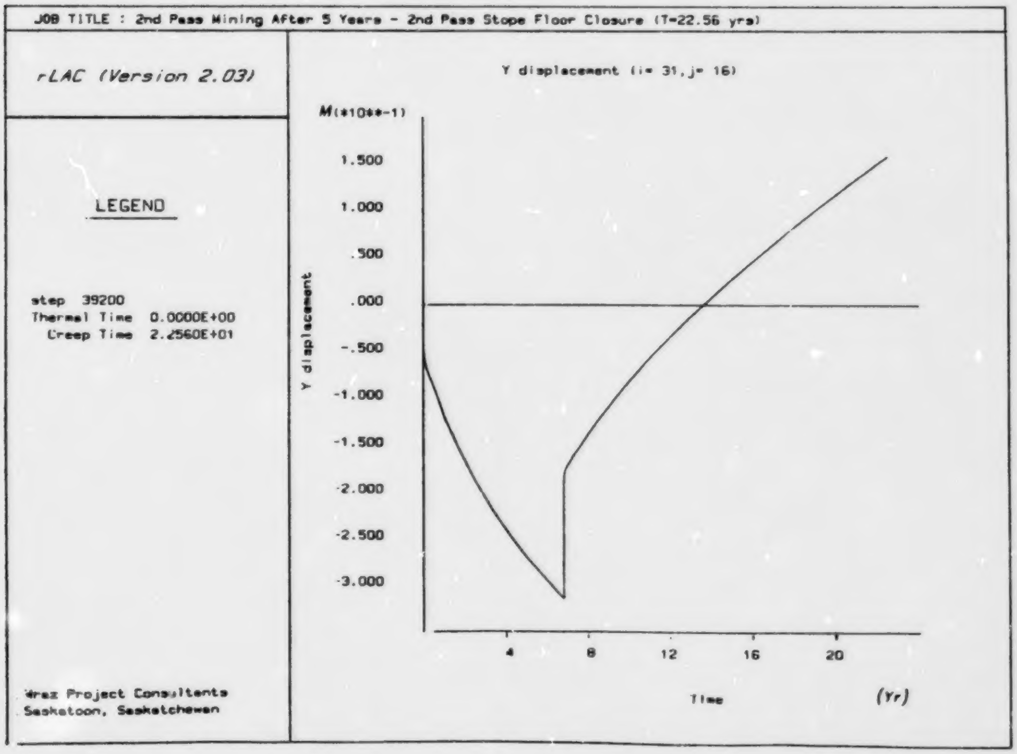

JOB TITLE : 2nd Pass Mining After 5 Years - 2nd Pass Stope Floor Closure (T=22.56 yrs)

FLAC (Version 2.03)

LEGEND

step 39200
Thermal Time 0.0000E+00
Creep Time 2.2560E+01

Mraz Project Consultants
Saskatoon, Saskatchewan

FIGURE 9.36

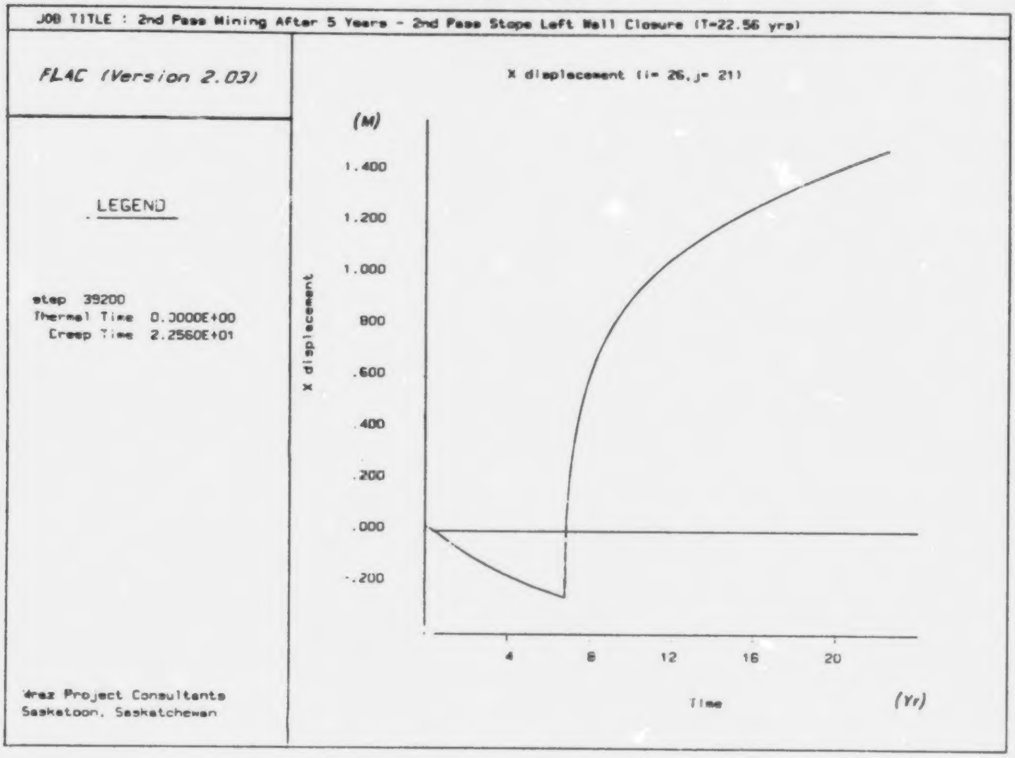

FIGURE 9.37

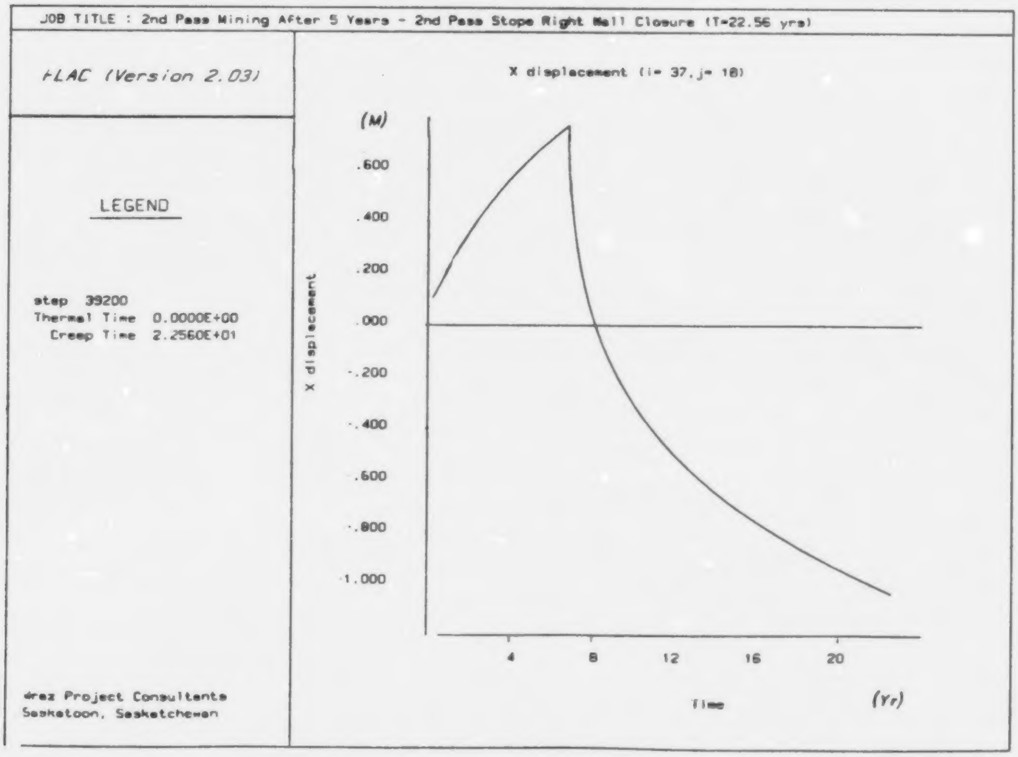

FIGURE 9.38

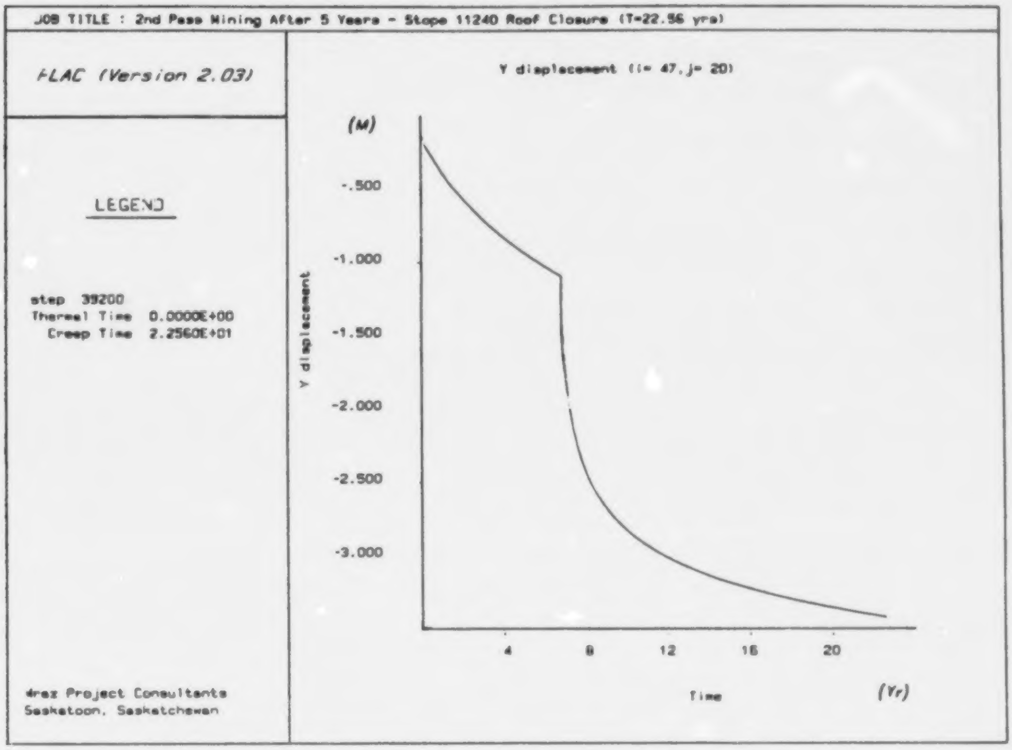

FIGURE 9.39

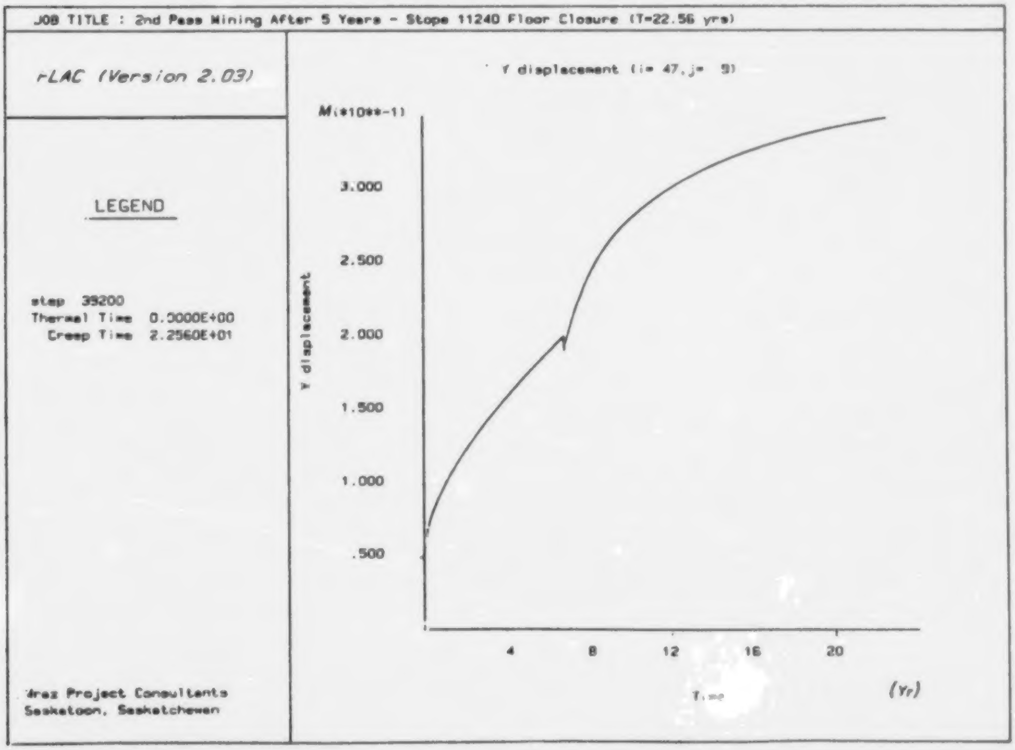

FIGURE 9.40

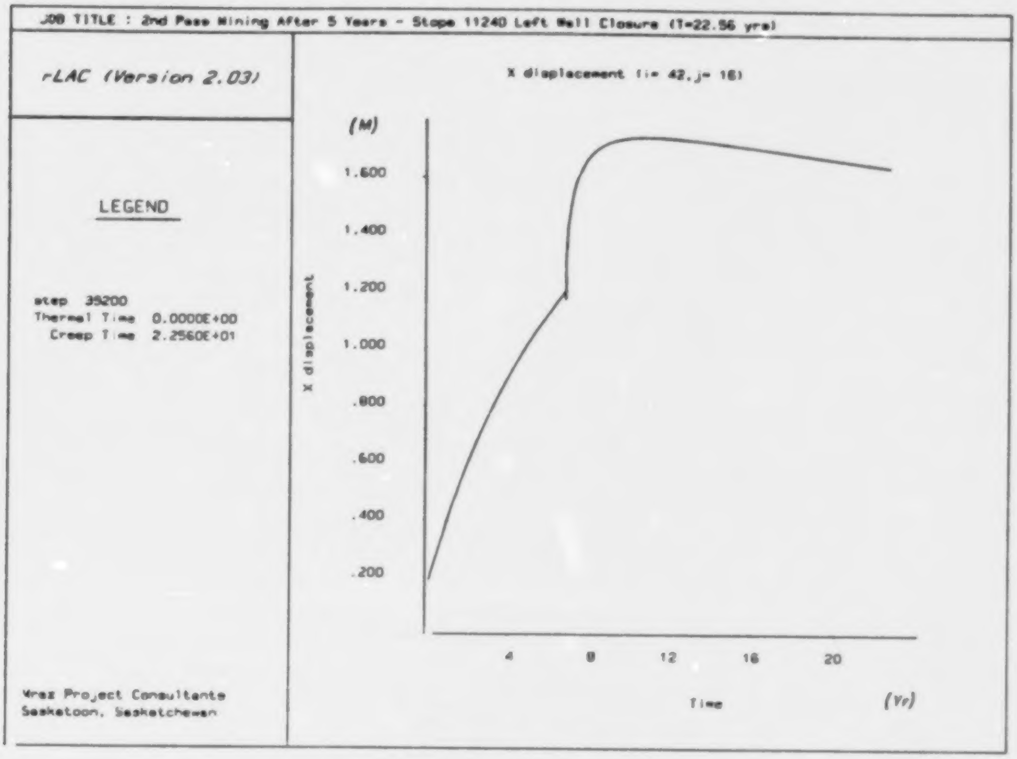

FIGURE 9.41

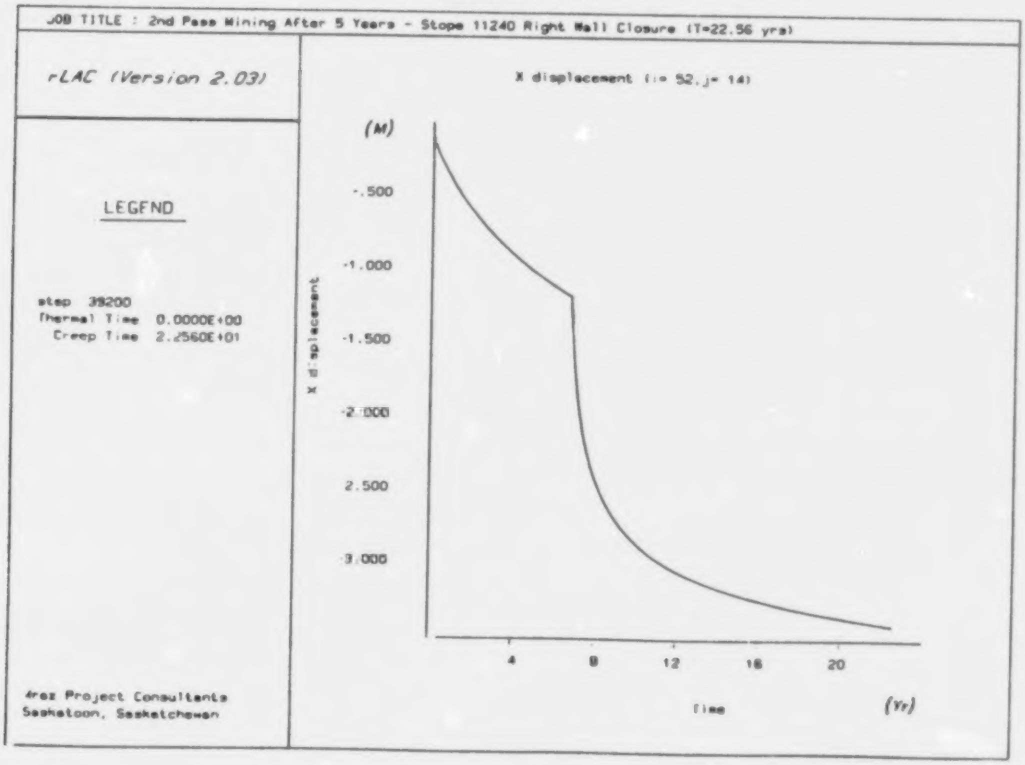

FIGURE 9.42

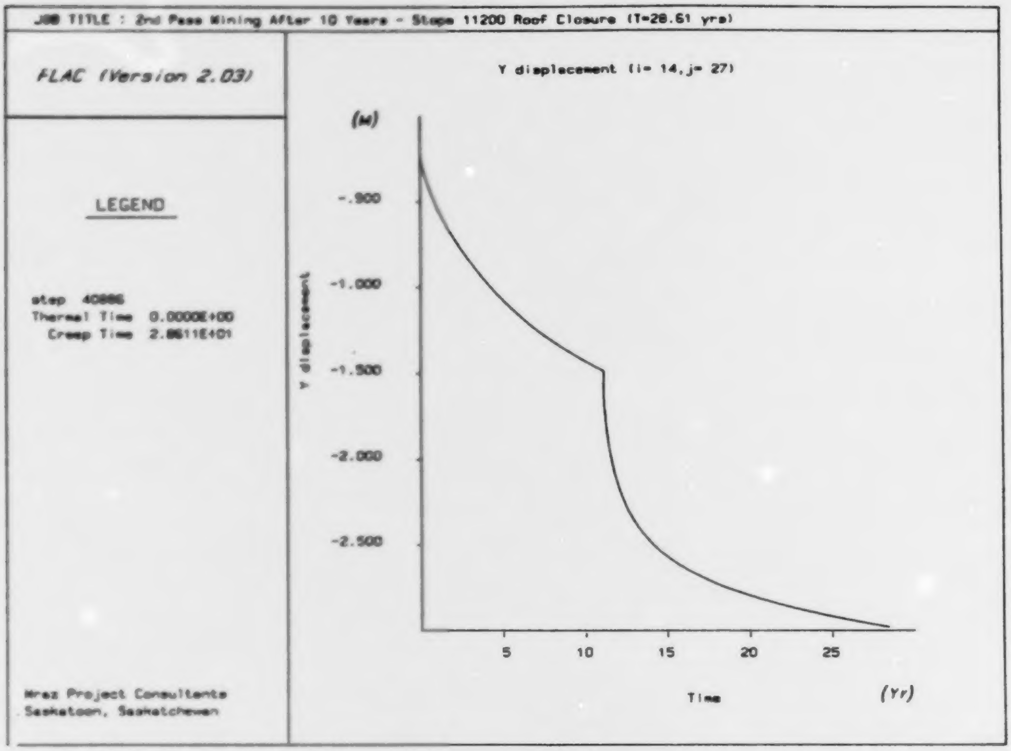

FIGURE 9.43

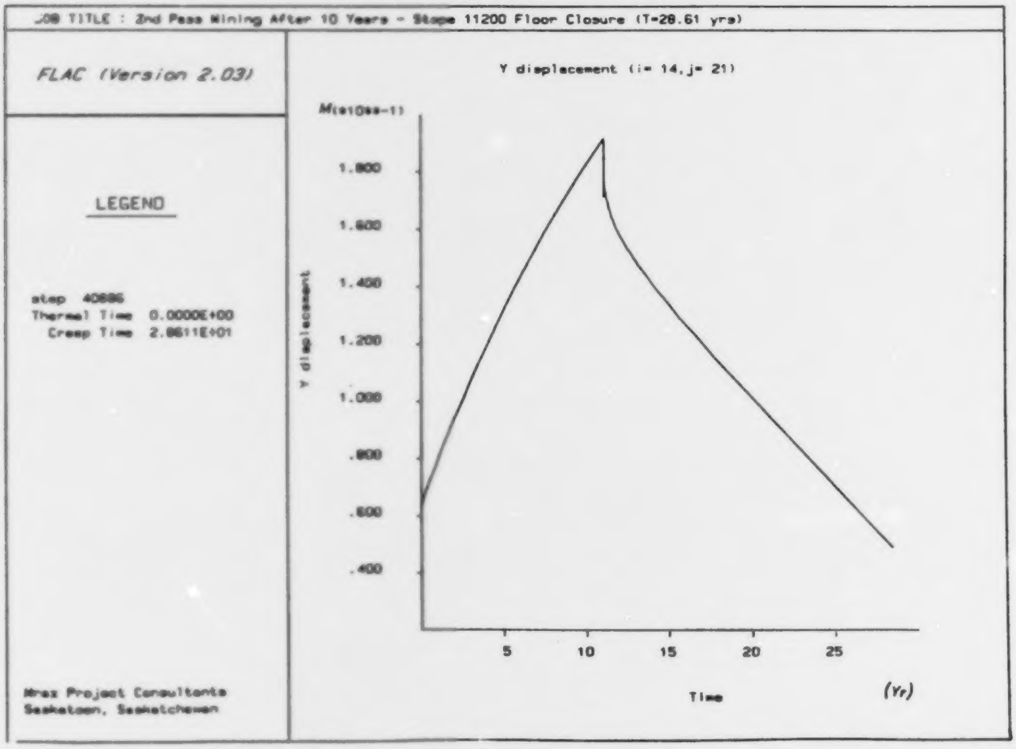

FIGURE 9.44

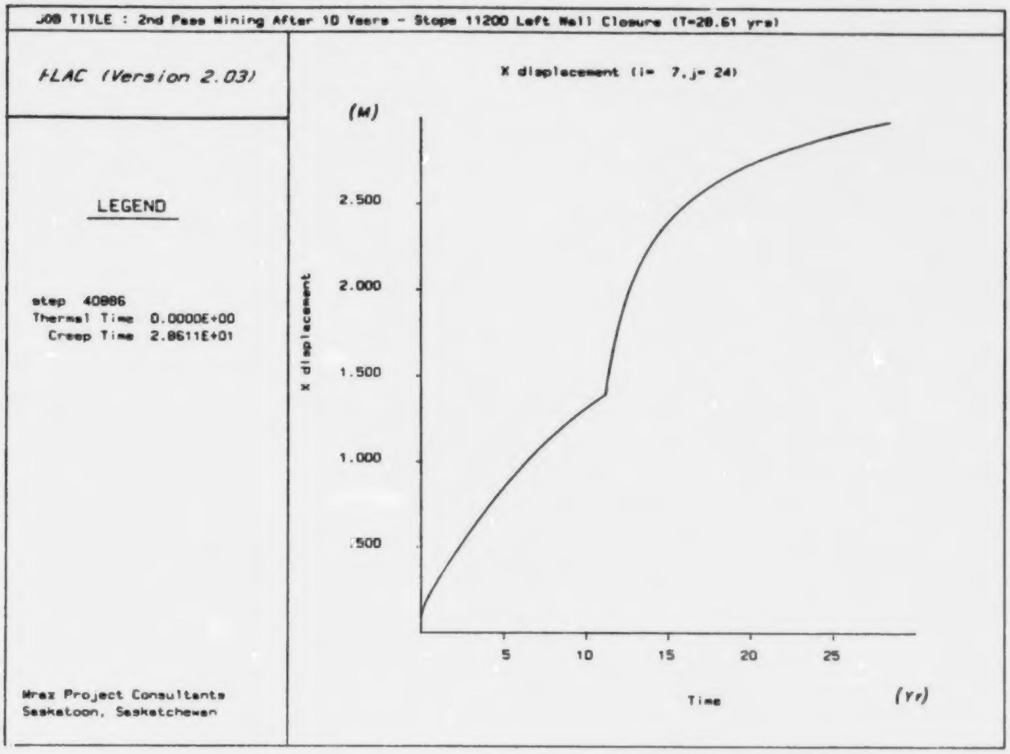

FIGURE 9.45

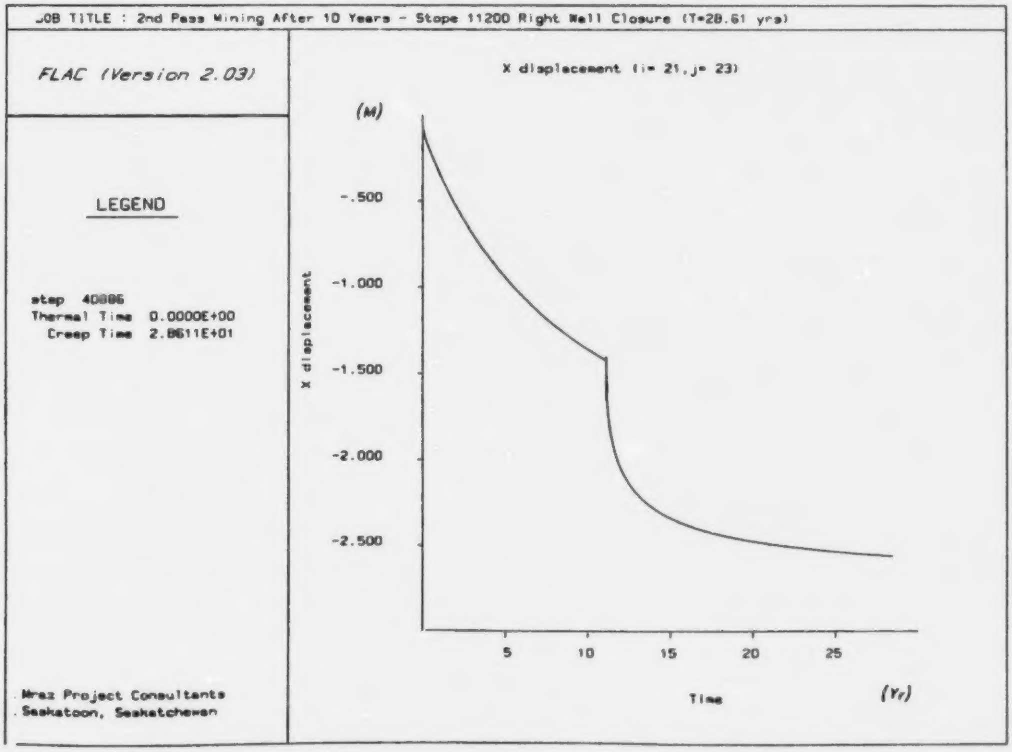

FIGURE 9.46

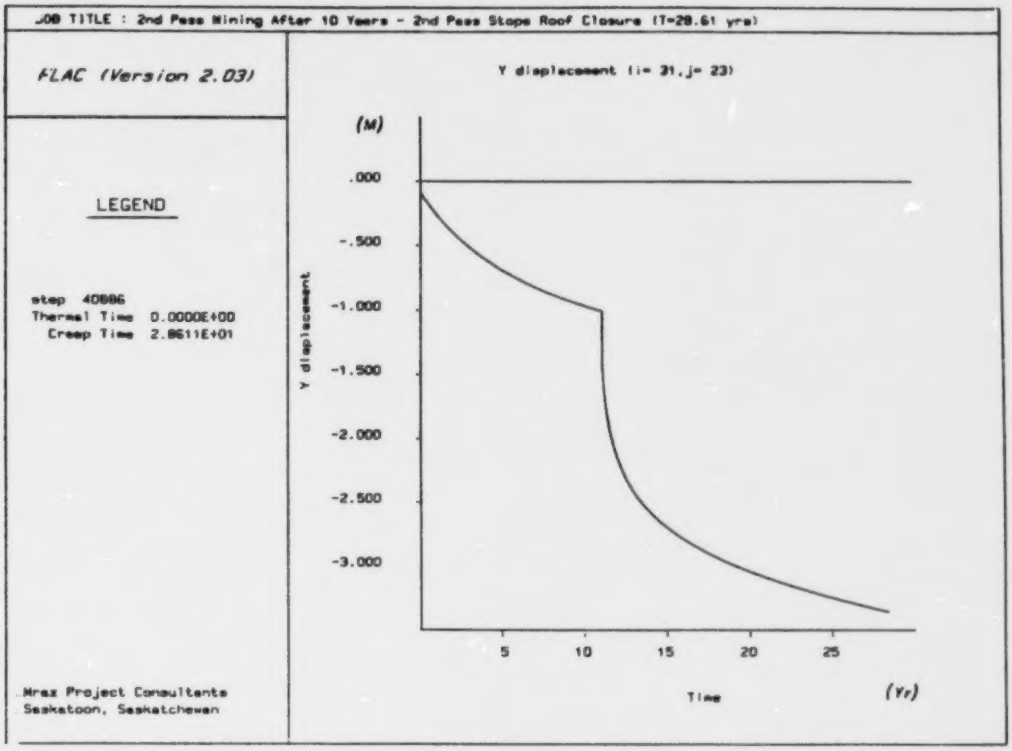

FIGURE 9.47

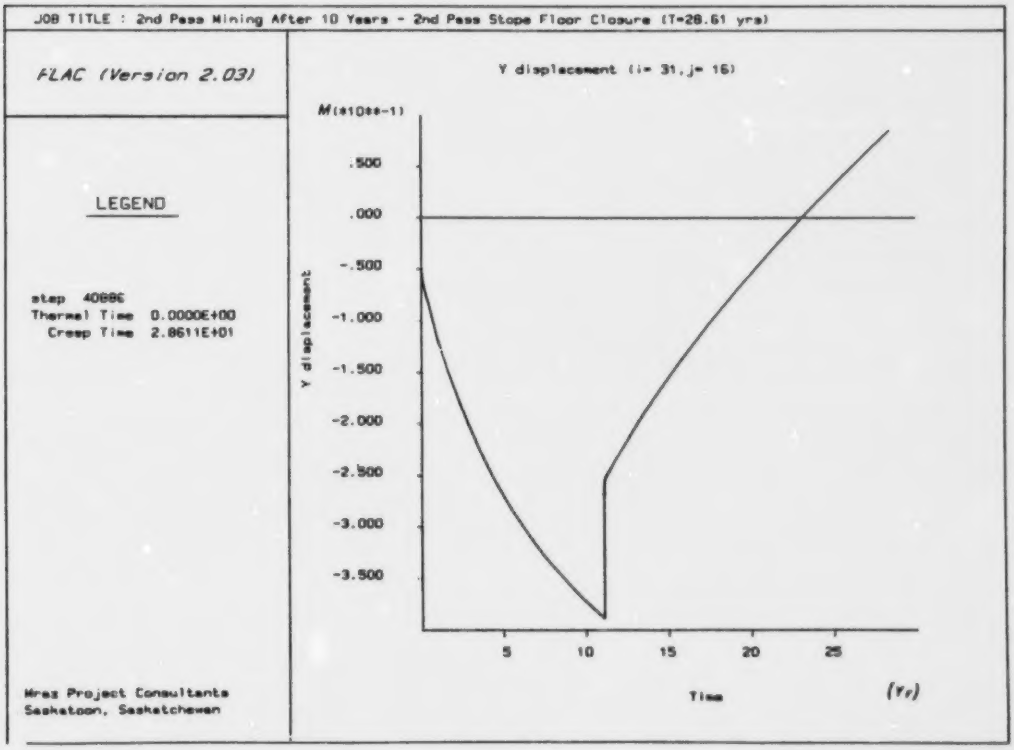

FIGURE 9.48

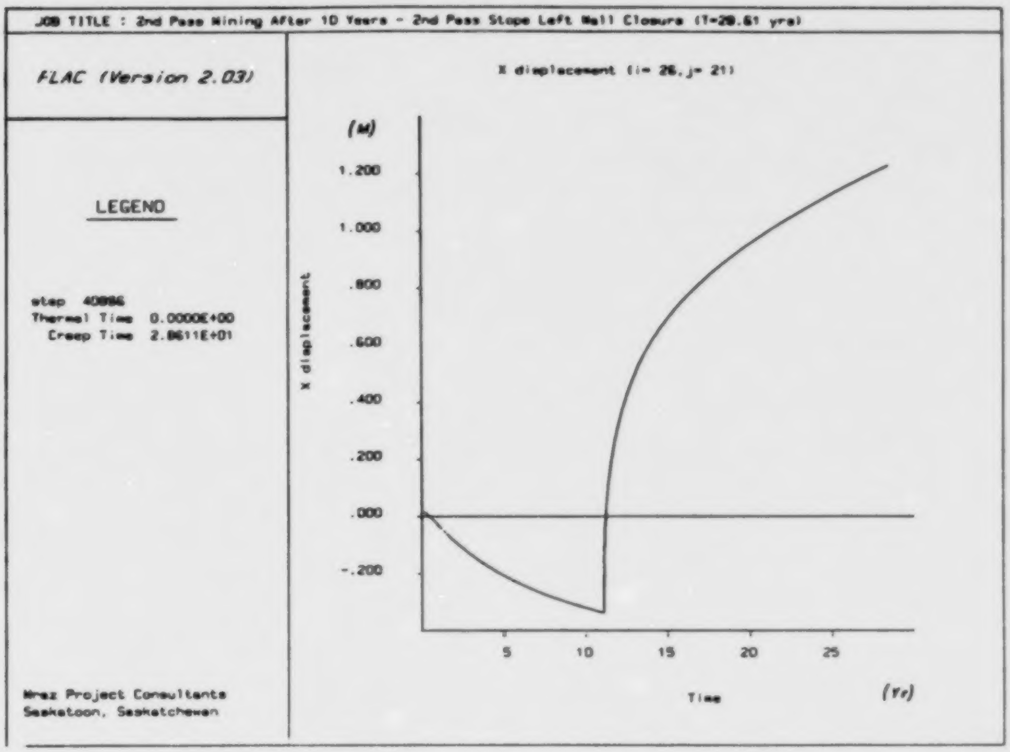

FIGURE 9.49

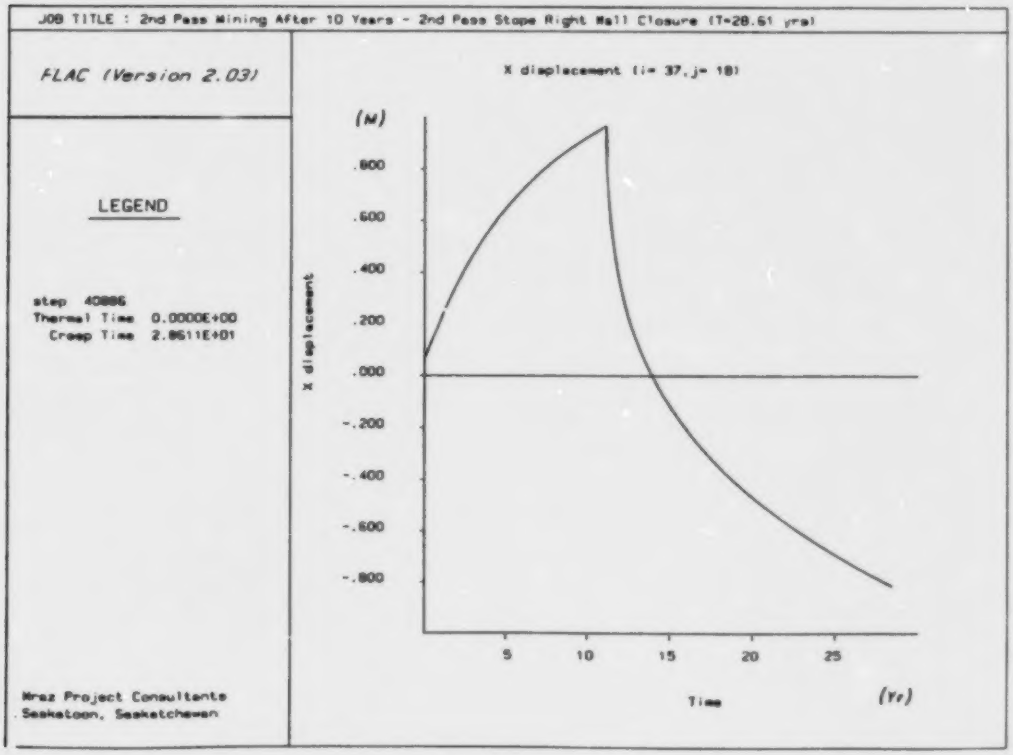

FIGURE 9.50

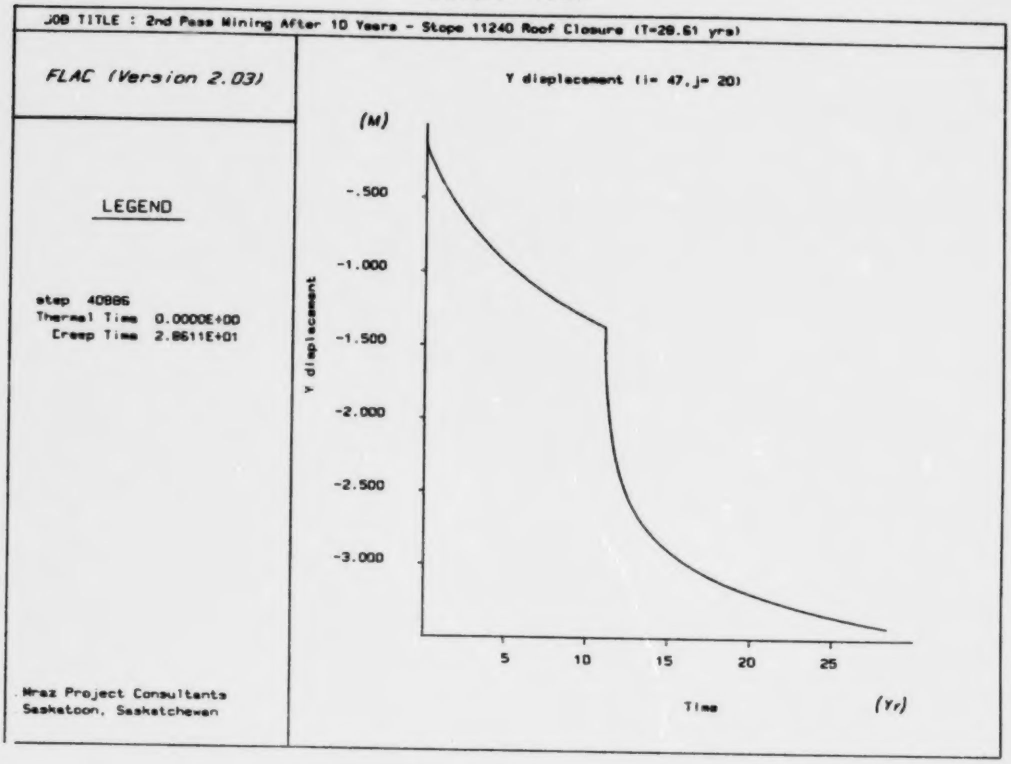

FIGURE 9.51

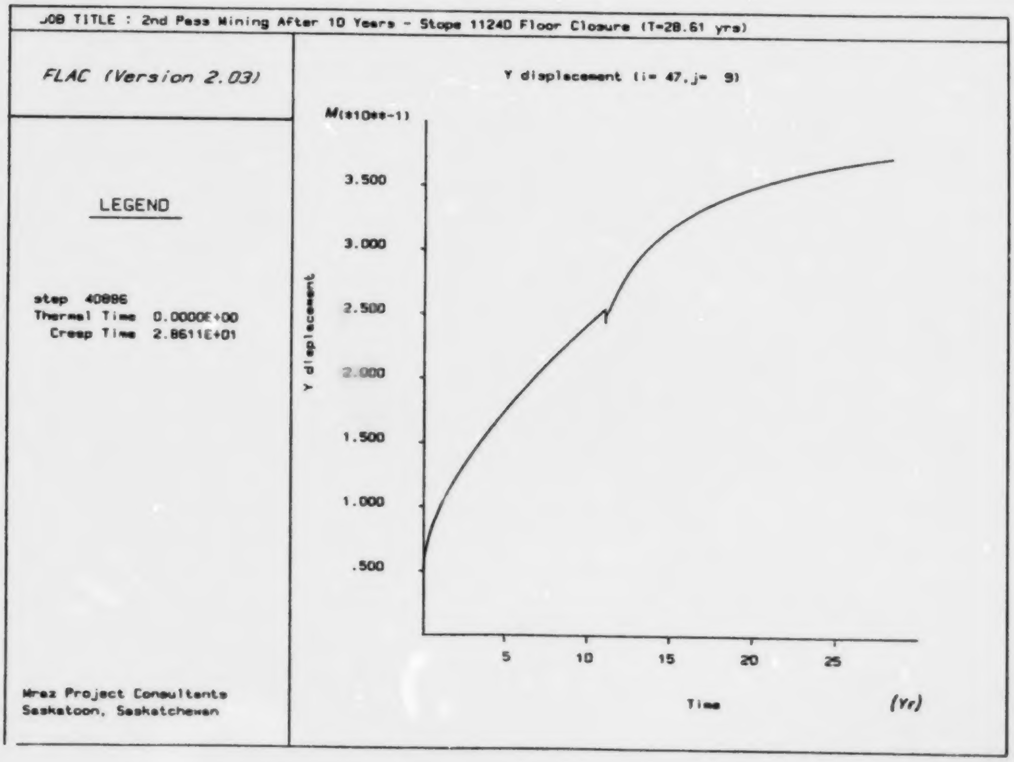

FIGURE 9.52

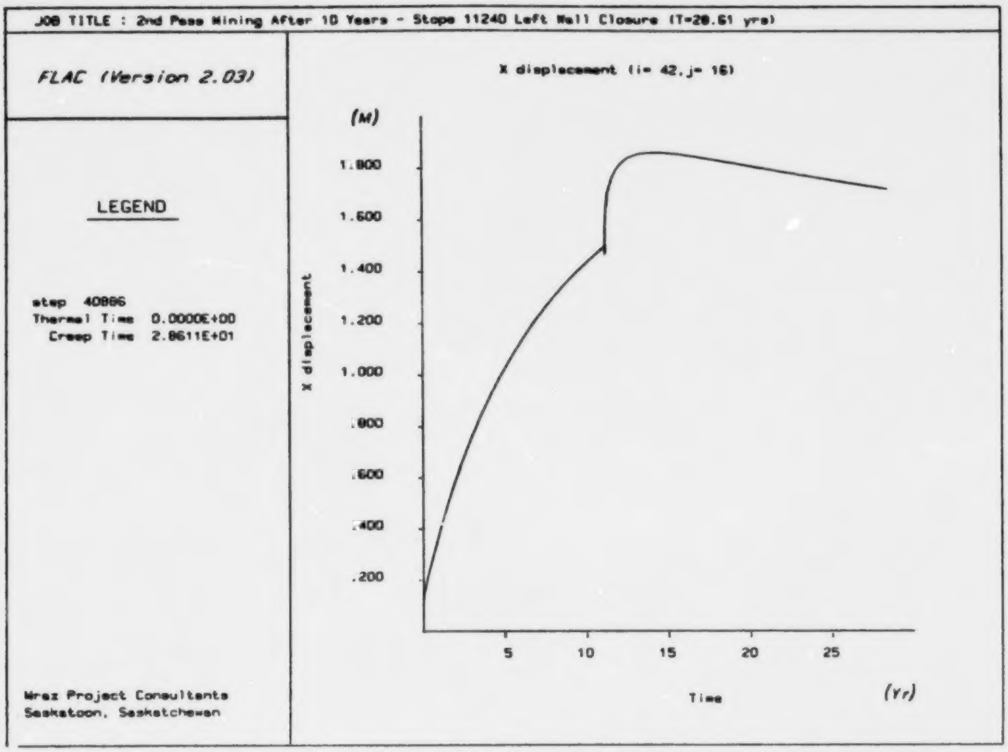

FIGURE 9.53

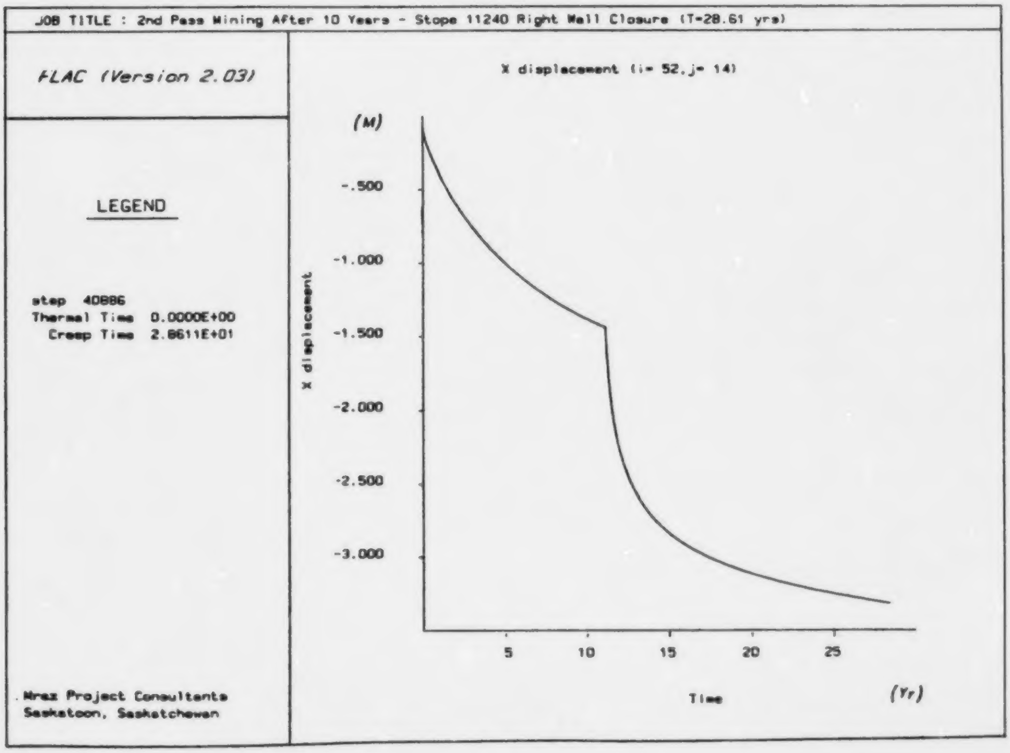

TABLE 9.3

SUMMARY OF MINING AND BACKFILLING SEQUENCE AND SUBSEQUENT CLOSURE RATES

Time Since Excavation (Yrs)	Stope	Vertical Closure Rate (cm/yr)	Horizontal Closure Rate (cm/yr)	Ratio Horz. to Vert.	Comments
1.05	11200	25.33	39.24	1.55	- 1.05 years after instantaneous excavation of both stopes
	11240	25.51	49.66	1.95	- just prior to backfill placement
6.81	11200	9.20	19.42	2.11	Scenario #1 - 5.76 years after backfill placement
	11240	9.84	17.82	1.81	- just prior to 2nd pass mining
22.56	11200	1.62	3.33	2.05	- 15.75 years after 2nd pass mining - floor of Stope 11200 moving towards 2nd pass stope
	2nd Pass	3.80	7.11	1.87	- left wall of stope 11240 moving towards 2nd pass stope
	11240	2.89	1.51	0.52	
11.13	11200	5.54	12.30	2.22	Scenario #2 - 10.08 years after backfill placement
	11240	6.52	10.56	1.62	- just prior to 2nd pass mining
28.61	11200	1.31	2.91	2.22	- 17.48 years after 2nd pass mining - floor of Stope 11200 moving towards 2nd pass stope
	2nd Pass	4.73	6.11	1.29	- left wall of stope 11240 moving towards 2nd pass stope
	11240	2.37	1.01	0.43	

mining is shown by velocity vectors for each scenario in Figures 9.54 and 9.55. Stress states within the backfill are summarized and compared to a failure criterion (Equation 5.25) in Tables 9.4 to 9.6 and Figures 9.56 to 9.59.

The stress plots (Figures 9.19 to 9.29) have shown very little difference in horizontal or vertical pillar stresses between the two different scenarios. The expected trends of stress relief were observed in both cases. The vertical stresses in the yield pillar about 15 years after second pass mining are lower than the stresses observed just prior to second pass mining. It could be expected that vertical stresses in the yield pillars would be higher after second pass mining, if the backfill does not provide any support. Therefore, the lower stresses would indicate that the backfill is providing some overburden support. It can also be concluded that the rock mass is behaving as if a lower extraction ratio existed because the backfilled rooms behave as intact material 15 years after second pass mining.

The closure graphs (Figures 9.30 to 9.53) and closure rates (Table 9.3) show the expected trends. Placement of backfill in Stopes 11200 and 11240 decreases the closure rates gradually. Closure rates 5 years after backfilling are approximately 1.6 times greater than the rates 10 years after backfill placement. Closure rates after second pass mining are slightly slower when second pass mining is performed 10 years after backfill placement due to the higher degree of backfill densification. A vertical closure rate of about 100 micro-metres per day, 15 years after excavation, in the second pass stope is in very good agreement with VELMINA predictions for both cases (Section 10.0).

It was observed (Figures 9.54 and 9.55) that the floor of Stope 11200 and the left wall of Stope 11240 moved towards the second pass stope in both scenarios. This indicates that the backfilled rooms are reflecting intact material behaviour and are providing overburden support. Note that this differential movement in the yield pillars could possibly lead to shearing.

FIGURE 9.54

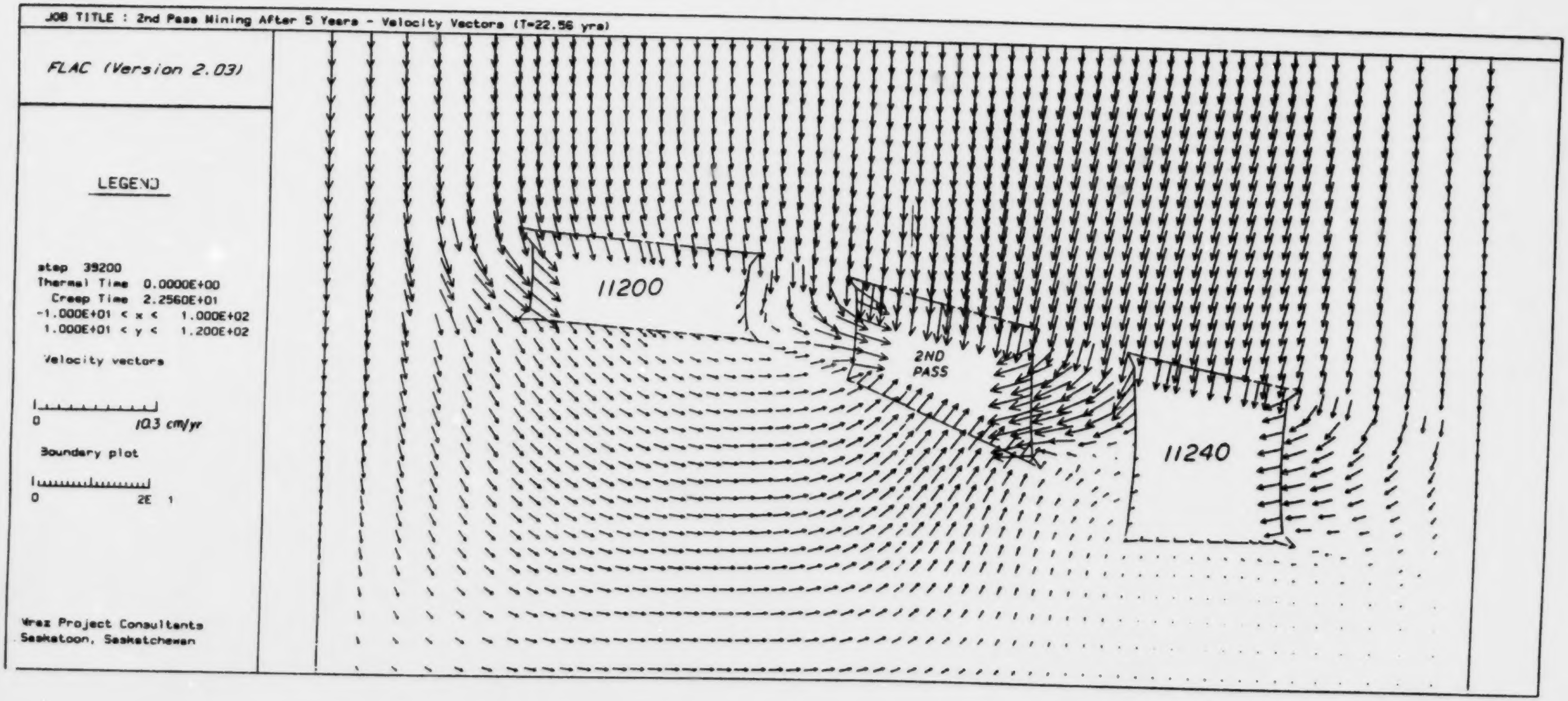
JOB TITLE : 2nd Pass Mining After 5 Years - Velocity Vectors (T=22.56 yrs)
FLAC (Version 2.03)
LEGEND
step 39200
Thermal Time 0.0000E+00
Creep Time 2.2560E+01
-1.000E+01 < x < 1.000E+02
1.000E+01 < y < 1.200E+02
Velocity vectors
0
10.3 cm/yr
Boundary plot
0
2E 1
Mraz Project Consultants
Saskatoon, Saskatchewan
11200
2ND
PASS
11240

FIGURE 9.55

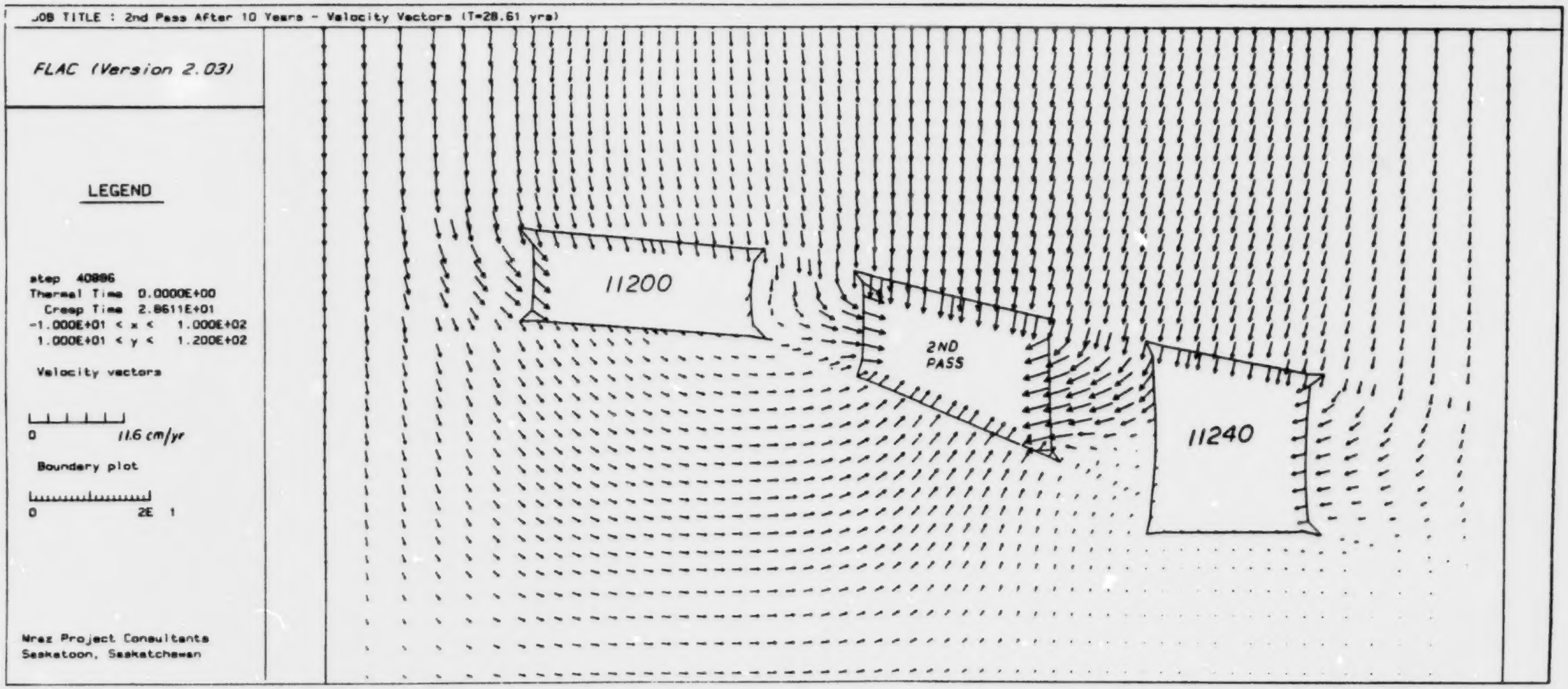
JOB TITLE : 2nd Pass After 10 Years - Velocity Vectors (T=28.61 yrs)
FLAC (Version 2.03)
LEGEND
step 40886
Thermal Time 0.0000E+00
Creep Time 2.8611E+01
-1.000E+01 < x < 1.000E+02
1.000E+01 < y < 1.200E+02
Velocity vectors
0
11.6 cm/yr
Boundary plot
0
2E 1
Mraz Project Consultants
Saskatoon, Saskatchewan
11200
2ND PASS
11240

TABLE 9.4

FAILURE STATE OF HALITE BACKFILL PROIR TO SECOND PASS MINING

Sequence : Stope 11200 & 11240 Before Second Pass Mining

Time (yrs)	Stope	Room Area (m^3)	Density (g/cc)	Fractional Density	Stress XX (MPa)	Stress XY (MPa)	Stress YY (MPa)	Minor Principal Stress (MPa)	Major Principal Stress (MPa)	Unconfined Compressive Strength (MPa)	Tensile Strength (MPa)	Yield Stress (MPa)
1.0532	11200	722.2	1.4	0.65	-0.004	0.002	0.003	0.004	-0.005	0.000	0.000	0.000
	11240	954.5	1.4	0.65	-0.004	0.001	0.004	0.004	-0.004	0.000	0.000	0.000
1.0533	11200	722.1	1.4	0.65	-0.002	0.002	0.005	0.006	-0.003	0.000	0.000	0.000
	11240	954.5	1.4	0.65	-0.003	0.001	0.005	0.005	-0.003	0.000	0.000	0.000
1.0571	11200	722.1	1.4	0.65	-0.002	0.002	0.004	0.004	-0.003	0.000	0.000	0.000
	11240	954.3	1.4	0.65	-0.004	0.001	0.005	0.005	-0.004	0.000	0.000	0.000
1.0987	11200	721.5	1.401	0.65	-0.005	0.001	-0.012	-0.005	-0.013	0.000	0.000	0.000
	11240	953.6	1.401	0.65	-0.002	0.000	0.005	0.005	-0.002	0.000	0.000	0.000
1.1812	11200	720.3	1.403	0.66	-0.010	0.000	-0.045	-0.010	-0.045	0.000	0.000	0.000
	11240	952.0	1.404	0.66	-0.060	-0.001	0.004	0.004	-0.060	0.000	0.000	0.000
1.3289	11200	718.3	1.407	0.66	-0.019	-0.004	-0.105	-0.019	-0.105	0.000	0.000	0.000
	11240	949.4	1.407	0.66	-0.126	-0.002	0.001	0.001	-0.126	0.000	0.000	0.000
1.6745	11200	713.9	1.416	0.66	-0.044	-0.012	-0.239	-0.044	-0.240	0.000	0.000	0.000
	11240	943.5	1.416	0.66	-0.278	-0.006	-0.006	-0.006	-0.278	0.000	0.000	0.000
2.6104	11200	703.3	1.437	0.67	-0.131	-0.031	-0.576	-0.129	-0.578	0.000	0.000	0.000
	11240	929.9	1.437	0.67	-0.678	-0.012	-0.022	-0.022	-0.678	0.000	0.000	0.000
4.9562	11200	682.5	1.481	0.69	-0.409	-0.081	-1.366	-0.402	-1.373	0.000	0.000	0.000
	11240	904.0	1.478	0.69	-1.614	-0.022	-0.076	-0.076	-1.614	0.000	0.000	0.000
6.8143	11200	669.9	1.509	0.71	-0.649	-0.117	-1.963	-0.638	-1.973	0.000	0.000	0.000
	11240	889.0	1.503	0.70	-2.281	-0.027	-1.370	-1.369	-2.282	0.000	0.000	0.000
8.9715	11200	658.2	1.536	0.72	-0.929	-0.153	-2.617	-0.915	-2.631	-0.614	0.037	-3.284
	11240	875.4	1.526	0.71	-2.976	-0.033	-0.224	-0.224	-2.976	-0.188	0.021	-0.877
11.129	11200	648.9	1.558	0.73	-1.197	-0.186	-3.231	-1.180	-3.248	-1.551	0.097	-6.333
	11240	864.6	1.546	0.72	-3.586	-0.004	-0.329	-0.329	-3.586	-1.039	0.062	-2.759

TABLE 9.5

FAILURE STATE OF HALITE BACKFILL AFTER SECOND PASS MINING

Sequence : Stope 11200 & 11240 - Second Pass Mining After 5 Years

Time (yrs)	Stope	Room Area (m^3)	Density (g/cc)	Fractional Density	Stress XX (MPa)	Stress XY (MPa)	Stress YY (MPa)	Minor Principal Stress (MPa)	Major Principal Stress (MPa)	Unconfined Compressive Strength (MPa)	Tensile Strength (MPa)	Yield Stress (MPa)
6.0143	11200	668.5	1.512	0.71	-1.930	-0.358	-3.462	-1.850	-3.542	0.000	0.000	0.000
	11240	887.1	1.506	0.70	-3.692	-0.013	-1.877	-1.877	-3.692	0.000	0.000	0.000
6.0143	11200	667.7	1.514	0.71	-0.557	-0.382	-2.207	-0.472	-2.291	0.000	0.000	0.000
	11240	886.1	1.508	0.70	-2.199	-0.015	-0.367	-0.367	-2.199	0.000	0.000	0.000
6.0143	11200	667.6	1.514	0.71	-0.558	-0.392	-2.214	-0.470	-2.302	0.000	0.000	0.000
	11240	886.0	1.508	0.70	-2.201	-0.013	-0.370	-0.370	-2.201	0.000	0.000	0.000
6.0145	11200	667.1	1.515	0.71	-0.560	-0.422	-2.247	-0.460	-2.347	0.000	0.000	0.000
	11240	885.6	1.509	0.71	-2.210	-0.007	-0.382	-0.382	-2.210	0.000	0.000	0.000
6.015	11200	666.3	1.517	0.71	-0.562	-0.467	-2.306	-0.444	-2.423	0.000	0.000	0.000
	11240	884.9	1.51	0.71	-2.223	-0.001	-0.406	-0.406	-2.223	0.000	0.000	0.000
6.0187	11200	663.5	1.524	0.71	-0.552	-0.596	-2.531	-0.386	-2.697	-0.102	0.006	-0.035
	11240	882.3	1.515	0.71	-2.269	0.005	-0.502	-0.502	-2.269	0.000	0.000	0.000
6.0241	11200	661.6	1.528	0.71	-0.546	-0.673	-2.694	-0.352	-2.888	-0.273	0.016	-1.332
	11240	880.3	1.518	0.71	-2.315	0.006	-0.573	-0.573	-2.315	0.000	0.000	0.000
6.036	11200	659.0	1.534	0.72	-0.530	-0.770	-2.927	-0.304	-3.153	-0.528	0.032	-1.709
	11240	877.0	1.524	0.71	-2.400	-0.003	-0.679	-0.678	-2.400	-0.102	0.006	-1.105
6.0669	11200	655.0	1.543	0.72	-0.529	-0.911	-3.278	-0.255	-3.553	-0.912	0.055	-2.279
	11240	871.0	1.534	0.72	-2.614	-0.045	-0.842	-0.840	-2.615	-0.528	0.032	-2.902
6.9705	11200	645.7	1.566	0.73	-0.545	-1.227	-4.188	-0.170	-4.563	-1.891	0.113	-3.173
	11240	855.8	1.561	0.73	-3.282	-0.216	-1.262	-1.239	-3.305	-1.678	0.101	-6.004
7.3755	11200	626.7	1.613	0.75	-0.793	-1.791	-6.334	-0.264	-6.862	-3.893	0.234	-6.259
	11240	829.2	1.611	0.75	-4.814	-0.652	-2.216	-2.061	-4.969	-3.808	0.228	-14.040
7.8546	11200	613.6	1.648	0.77	-1.200	-2.111	-8.073	-0.603	-8.670	-5.384	0.323	-10.703
	11240	813.5	1.643	0.77	-5.914	-0.971	-3.027	-2.731	-6.210	-5.171	0.310	-21.270
8.6668	11200	600.6	1.683	0.79	-1.860	-2.367	-10.090	-1.228	-10.722	-6.875	0.412	-17.676
	11240	799.1	1.672	0.78	-7.021	-1.298	-4.050	-3.563	-7.508	-6.406	0.384	-28.686
10.191	11200	587.5	1.721	0.80	-2.832	-2.541	-12.510	-2.205	-13.137	-8.493	0.510	-27.771
	11240	785.2	1.702	0.80	-8.087	-1.653	-5.453	-4.656	-8.884	-7.684	0.461	-38.200
12.915	11200	576.1	1.755	0.82	-3.963	-2.568	-15.040	-3.397	-15.606	-9.942	0.596	-39.637
	11240	773.2	1.728	0.81	-8.874	-2.009	-7.197	-5.859	-10.212	-8.791	0.527	-48.402
15.072	11200	570.9	1.771	0.83	-4.545	-2.535	-16.410	-4.026	-16.929	-10.623	0.637	-45.908
	11240	767.6	1.741	0.81	-9.147	-2.184	-8.258	-6.474	-10.931	-9.345	0.561	-53.092
18.217	11200	565.7	1.787	0.84	-5.148	-2.477	-17.910	-4.684	-18.374	-11.305	0.678	-52.763
	11240	762.0	1.753	0.82	-9.331	-2.355	-9.513	-7.065	-11.779	-9.856	0.591	-59.272
22.56	11200	561.1	1.802	0.84	-5.745	-2.384	-19.400	-5.341	-19.804	-11.943	0.717	-59.610
	11240	756.8	1.766	0.83	-9.416	-2.505	-10.880	-7.538	-12.758	-10.410	0.625	-64.515

TABLE 9.6

FAILURE STATE OF HALITE BACKFILL AFTER SECOND PASS MINING

Sequence : Stope 11200 & 11240 - Second Pass Mining After 10 Years

Time (yrs)	Stope	Room Area (m^3)	Density (g/cc)	Fractional Density	Stress XX (MPa)	Stress XY (MPa)	Stress YY (MPa)	Minor Principal Stress (MPa)	Major Principal Stress (MPa)	Unconfined Compressive Strength (MPa)	Tensile Strength (MPa)	Yield Stress (MPa)
11.129	11200	647.7	1.561	0.73	-2.501	-0.479	-4.000	-2.405	-4.976	-1.670	0.101	-9.559
	11240	862.9	1.549	0.72	-5.097	-0.021	-2.272	-2.272	-5.097	-1.167	0.070	-7.371
11.129	11200	646.7	1.563	0.73	-1.002	-0.542	-3.557	-0.969	-3.670	-1.764	0.106	-6.237
	11240	861.0	1.551	0.72	-3.479	-0.022	-0.629	-0.629	-3.479	-1.252	0.075	-4.136
11.129	11200	646.4	1.564	0.73	-1.006	-0.574	-3.507	-0.961	-3.712	-1.806	0.108	-6.305
	11240	861.5	1.551	0.72	-3.487	-0.016	-0.642	-0.642	-3.487	-1.252	0.075	-4.175
11.129	11200	645.6	1.566	0.73	-1.090	-0.636	-3.667	-0.941	-3.816	-1.891	0.113	-6.428
	11240	860.8	1.552	0.73	-3.504	-0.009	-0.675	-0.675	-3.504	-1.295	0.078	-4.362
11.13	11200	644.8	1.568	0.73	-1.085	-0.690	-3.755	-0.917	-3.923	-1.977	0.119	-6.528
	11240	860.0	1.554	0.73	-3.560	-0.007	-0.714	-0.714	-3.560	-1.380	0.083	-4.653
11.133	11200	643.3	1.571	0.73	-1.083	-0.781	-3.914	-0.882	-4.115	-2.104	0.126	-6.670
	11240	858.7	1.556	0.73	-3.546	-0.005	-0.703	-0.703	-3.546	-1.465	0.088	-5.030
11.142	11200	641.1	1.577	0.74	-1.075	-0.902	-4.172	-0.832	-4.415	-2.360	0.142	-6.987
	11240	856.4	1.56	0.73	-3.602	-0.007	-0.900	-0.900	-3.602	-1.636	0.098	-5.752
11.149	11200	640.0	1.58	0.74	-1.067	-0.961	-4.309	-0.804	-4.572	-2.488	0.149	-7.119
	11240	855.1	1.563	0.73	-3.637	-0.011	-0.965	-0.965	-3.637	-1.764	0.106	-6.226
11.158	11200	638.7	1.583	0.74	-1.066	-1.021	-4.456	-0.782	-4.740	-2.615	0.157	-7.269
	11240	853.5	1.566	0.73	-3.693	-0.022	-1.036	-1.036	-3.693	-1.891	0.113	-6.724
11.172	11200	637.3	1.586	0.74	-1.072	-1.092	-4.625	-0.763	-4.934	-2.743	0.165	-7.420
	11240	851.4	1.569	0.73	-3.777	-0.040	-1.121	-1.120	-3.778	-2.019	0.121	-7.272
11.197	11200	635.3	1.591	0.74	-1.079	-1.187	-4.861	-0.737	-5.203	-2.956	0.177	-7.682
	11240	848.4	1.575	0.74	-3.912	-0.074	-1.245	-1.243	-3.914	-2.275	0.136	-8.240
11.238	11200	632.6	1.598	0.75	-1.089	-1.316	-5.203	-0.704	-5.580	-3.254	0.195	-8.035
	11240	843.9	1.583	0.74	-4.125	-0.134	-1.425	-1.418	-4.132	-2.615	0.157	-9.607
11.316	11200	628.6	1.608	0.75	-1.120	-1.498	-5.724	-0.676	-6.168	-3.680	0.221	-8.594
	11240	837.3	1.596	0.75	-4.479	-0.241	-1.697	-1.676	-4.500	-3.169	0.190	-11.028
11.495	11200	621.7	1.626	0.76	-1.224	-1.706	-6.656	-0.609	-7.191	-4.447	0.267	-9.916
	11240	826.7	1.616	0.76	-5.123	-0.440	-2.179	-2.112	-5.190	-4.021	0.241	-15.602
11.887	11200	613.3	1.649	0.77	-1.440	-2.096	-7.910	-0.820	-8.530	-5.427	0.326	-12.352
	11240	814.9	1.64	0.77	-5.920	-0.716	-2.816	-2.659	-6.085	-5.043	0.303	-20.601
12.491	11200	601.3	1.681	0.79	-1.940	-2.435	-9.835	-1.249	-10.526	-6.790	0.407	-17.658
	11240	800.3	1.67	0.78	-7.028	-1.806	-3.848	-3.505	-7.355	-6.321	0.379	-28.146
13.653	11200	590.0	1.696	0.79	-2.607	-2.639	-11.920	-1.906	-12.621	-7.429	0.446	-23.746
	11240	787.7	1.713	0.80	-7.997	-1.436	-5.059	-4.474	-8.582	-8.153	0.489	-39.232
15.978	11200	578.4	1.740	0.82	-3.752	-2.718	-14.458	-3.101	-15.101	-9.643	0.579	-36.798
	11240	775.2	1.724	0.81	-8.846	-1.818	-6.783	-5.724	-9.905	-8.621	0.517	-47.086
19.982	11200	568.7	1.770	0.83	-4.837	-2.635	-16.980	-4.290	-17.527	-10.921	0.655	-48.766
	11240	764.8	1.747	0.82	-9.313	-2.162	-8.802	-6.880	-11.235	-9.601	0.576	-57.074
24.297	11200	563.0	1.796	0.84	-5.548	-2.519	-18.720	-5.083	-19.185	-11.688	0.701	-56.872
	11240	758.5	1.762	0.82	-9.428	-2.361	-10.360	-7.407	-12.381	-10.240	0.614	-63.335
28.611	11200	559.3	1.800	0.84	-6.060	-2.411	-19.950	-5.653	-20.357	-12.199	0.732	-62.743
	11240	754.2	1.772	0.83	-9.441	-2.405	-11.590	-7.000	-13.223	-10.666	0.640	-67.254
32.925	11200	556.6	1.816	0.85	-6.469	-2.321	-20.860	-6.104	-21.225	-12.540	0.752	-67.206
	11240	750.9	1.779	0.83	-9.438	-2.572	-12.600	-8.000	-14.038	-10.964	0.650	-69.097

FIGURE 9.56

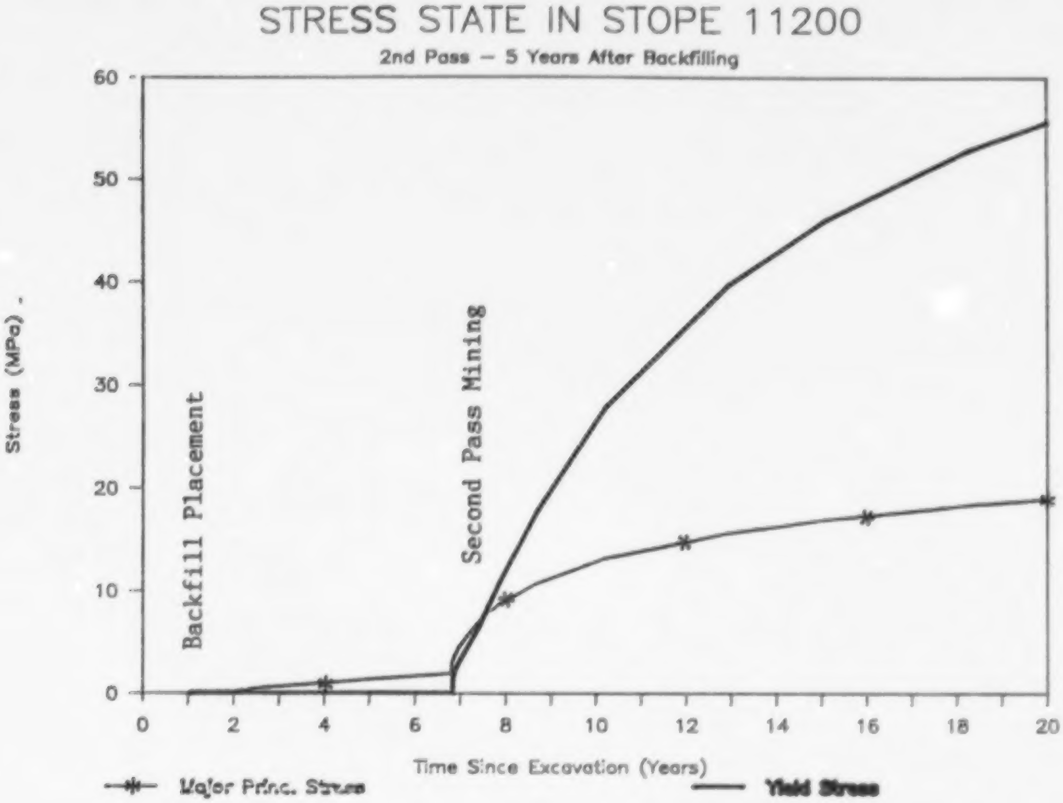

FIGURE 9.57

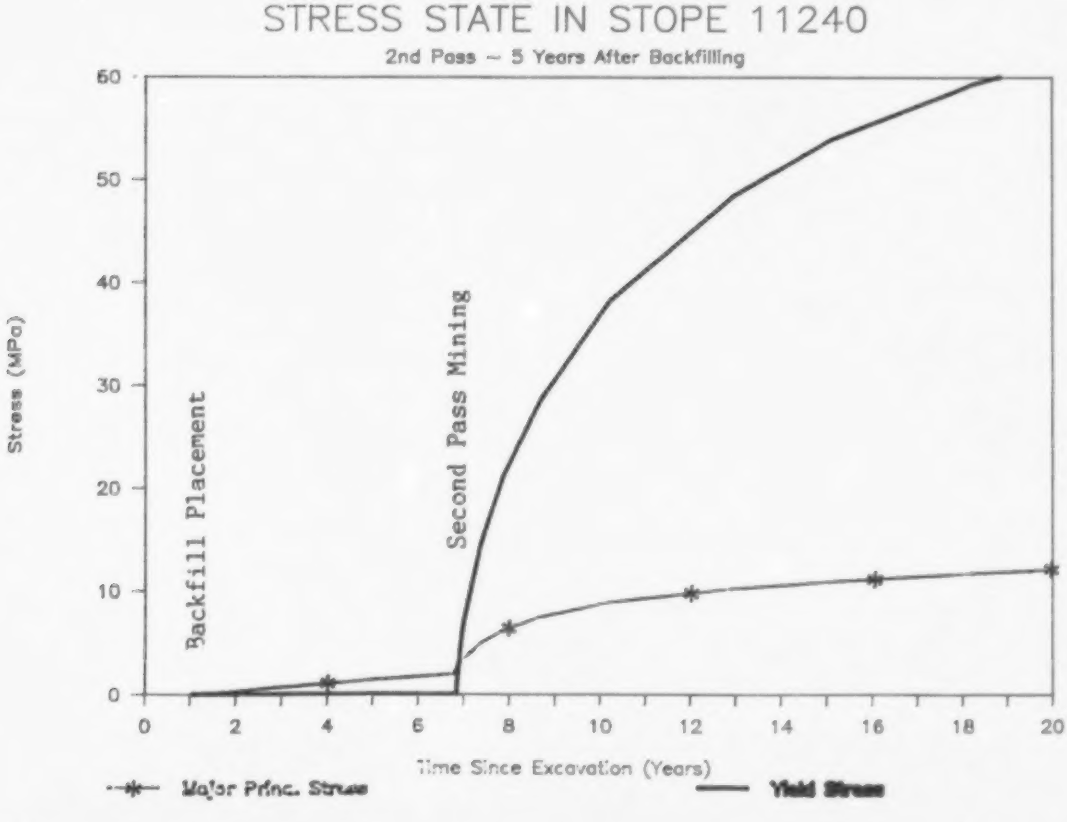

FIGURE 9.58

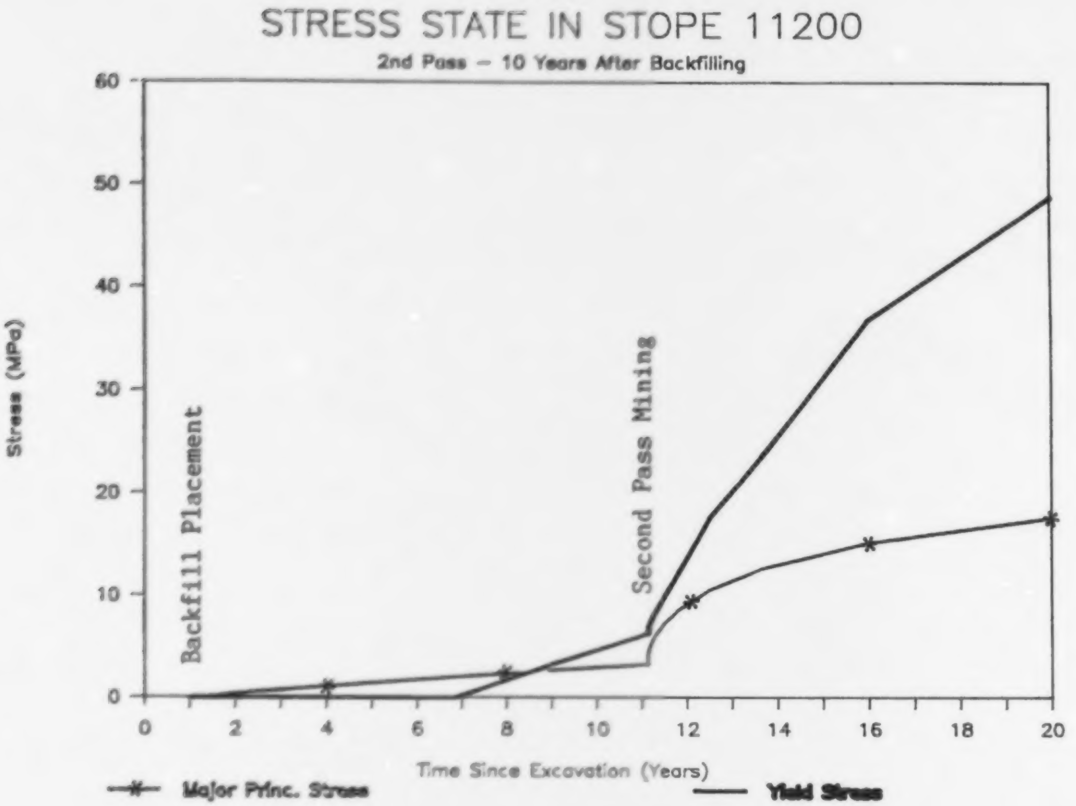

FIGURE 9.59

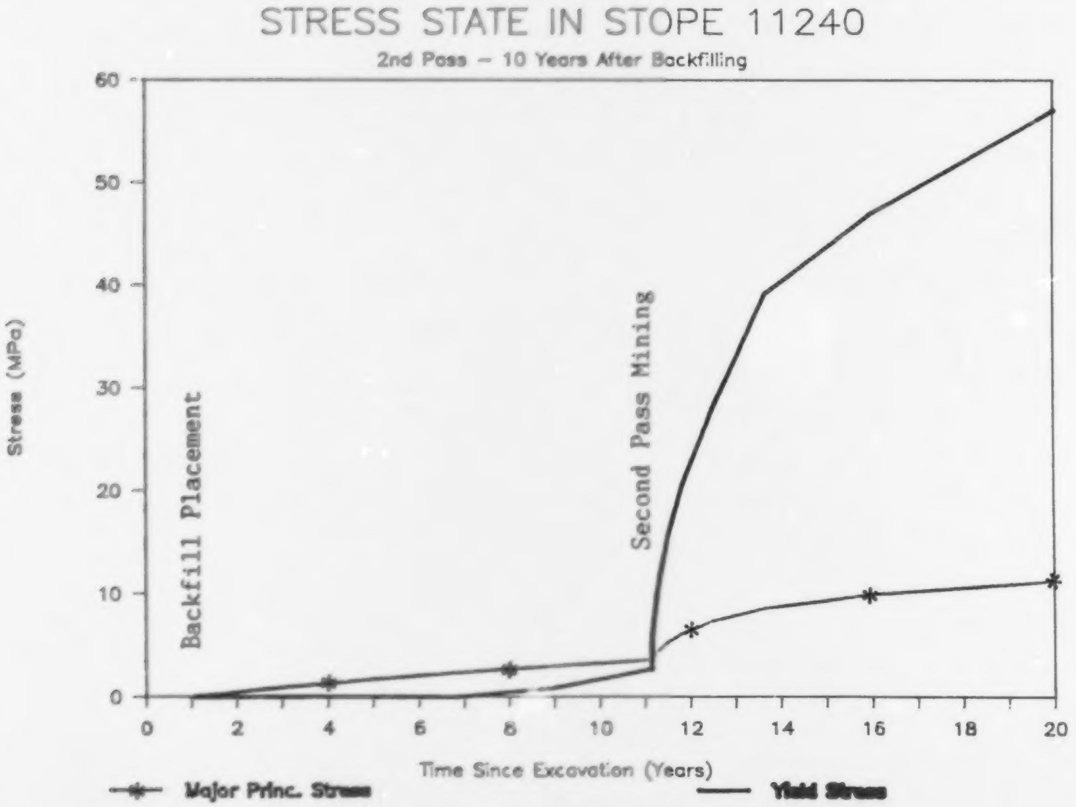

Upon investigation of the stress states within the backfill, it was observed that the backfill develops little or no unconfined compressive and tensile strength for about 8 years after placement, and is in a state of failure until this strength development has occurred. Comparing the yield stress to the major principal stress in the backfill indicates that the backfill does not provide adequate overburden support until at least 10 years after placement. Figures 9.56 and 9.57 show that the backfill in Stopes 11200 and 11240 would be in a state of failure if second pass mining was performed 5 years after backfill placement. Figures 9.58 and 9.59 illustrate that the backfill in Stopes 11200 and 11240 would be able to provide overburden support (ie. not in a state of failure) or be very close to the degree of densification at which support would be possible. The analysis of the stresses indicates that the backfill would provide overburden support and second pass mining of the pillars would be possible between 10 and 15 years after backfill placement.

9.5 Results of FLAC Numerical Simulations With Backfill

Based on the numerical simulations, the following conclusions can be drawn:

1. Backfill placed hydraulically will provide overburden support sooner than backfill placed using the dry method, allowing potential second pass mining to begin at an earlier date.
2. Based on the geometries investigated, backfill placed hydraulically does not start developing strength until approximately 8 years after placement.
3. Hydraulically placed backfill will not provide adequate overburden support for second pass mining until at least 10 years after backfill placement.

Generally, it can be concluded that stopes should be backfilled using the hydraulic placement method, and second pass mining can be considered after 10 to 15 years following the backfill placement.

SECTION 10.0

10.0 NUMERICAL MODELLING OF DPTC MINE USING COMPUTER PROGRAM VELMINA

10.1 Introduction

The three-dimensional modelling was done using the program VELMINA (Visco-Elastic Mine Analysis) written by Dr. L. Rothenburg. The program was designed for three-dimensional analysis of large-scale mining layouts that involve large numbers of rooms and pillars in visco-elastic rock. From a technical perspective, the program is an implementation of the Displacement Discontinuity method for visco-elastic media. Various implementations of the Displacement Discontinuity method for elastic rock were successfully used for mine planning and design since early sixties.

In general terms, representation of a mining layout in the Displacement Discontinuity method can be compared to a view of a mine from a distance that is much larger compared to sizes of rooms and pillars in the mine. From this distance the mine openings would appear as a set of discontinuities in the host rock. If one is to trace displacements of rock along a line crossing the mining plane, the impression would be that displacements are discontinuous across the mine. The Displacement Discontinuity Method is a mathematical idealization of that situation.

In all existing implementations of the Displacement Discontinuity method for hard rock mining, pillars are described in terms of equivalent gross properties like gross elastic stiffness, collapse loads, etc. From a computational point of view, a typical pillar in the mine is represented by a set of elements that support the roof. Such elements can "feel" only stress normal to the roof and deform in response to this stress only. Deformational and strength properties of a pillar are, on the other hand, dependent on confining stresses within the pillar. The latter are not a part of the analysis and the relationship between the stress directly involved in computations and confining stresses in pillars must be established a priori. Ideally, a series of finite element analyses is required for this purpose. However, in the current hard rock practice, this step is frequently ignored and equivalent pillar properties are assigned, neglecting confining stresses in pillars. When pillars creep, determination of confining stresses in pillars is unavoidable since creep rates in pillars are dramatically affected by confining stresses.

The current mathematical formulation (Appendix A) expressed in the VELMINA code is a rigorous implementation of the Displacement Discontinuity method for a linearly visco-elastic host rock outside of the mining seam. In-seam rock properties can be described by an arbitrary non-linear steady state creep law. Computational efficiency is achieved for a "bi-linear" creep law with individual exponents pertaining to each branch. Pillars can also be assigned non-linear elasto-visco-plastic properties (i.e. creep, limiting load and strain-softening). Both transient and steady state conditions can be determined. Determination of transient response requires considerable computing effort. Multi-level mining and sequential excavation can also be analyzed. The capability to model sequential excavation includes placement of backfill in selected areas.

Mathematical formulation of VELMINA assumes homogeneous material properties outside of mining horizons. Relatively thin layered inclusions in the host rock can be accommodated in analysis. The number of such layers is currently limited to seven. Incorporation of layered inclusions increases computing time and memory requirements dramatically.

Non-linear creep properties of host rock outside of mining planes cannot be modelled directly and equivalent linear properties must be assigned when necessary. However, the program has a capability of doing an iterative analysis to determine matching equivalent linear properties for a specified non-linear creep law of the host rock.

The entire mining layout is discreditized into a series of rectangular elements that can represent either a mined-out area or a part of a pillar. Each element is associated with a distinct set of material properties. For elements representing pillars with visco-elastic properties, a ratio of vertical to effective stress is assigned.

The ratios of vertical to effective stress are assigned based on finite element analysis of pillars. Although it is technically possible to assign effective to vertical stress ratios for individual elements of pillars, this is not feasible in practical applications. To cope with this difficulty VELMINA has a set of built-in functions that assign effective to vertical stress ratios to every element based on the distance of the element from the edge of the pillar. These functions were developed based on extensive finite element study of pillars of rectangular cross-section with different width to height ratios. In case of openings of other shapes, a separate finite element study is required.

The automatic assignment of effective to vertical stress ratio and determination of equivalent linear viscosity for out-of-seam material are the most significant elements of VELMINA. These are described in Appendix A together with other technical aspects of VELMINA. As well, verification of the code based on comparison of its performance in conditions of plane strain with results of finite element computations is presented.

10.2 Simulation of 1988 Mining Layout

The status of mining excavations in late 1988 is shown in Figure 10.1. The first mining panel, Panel 10, has been only partly mined out due to the problems associated with geological complexities. Panel 11 is being currently mined and most of the mining in 1989 has been concentrated in the northern part of this panel. Panel 12 has been under development. In order to reflect the complexity of the ore body correctly in the computer simulation, an **ore thickness** sub-routine has been generated. The ore thickness information has been extracted from a DPPC ore thickness isopach map and entered into the sub-routine for future use.

Since VELMINA requires a uniform mesh, the size of elements must be chosen carefully in order to properly represent the excavations within the ore zone. The size of the element selected for the simulation of Panels 10, 11 and 12 is 7.67 m by 7.67 m. This element size represented the best compromise for simulation of various rooms, stopes and pillars within the three panels.

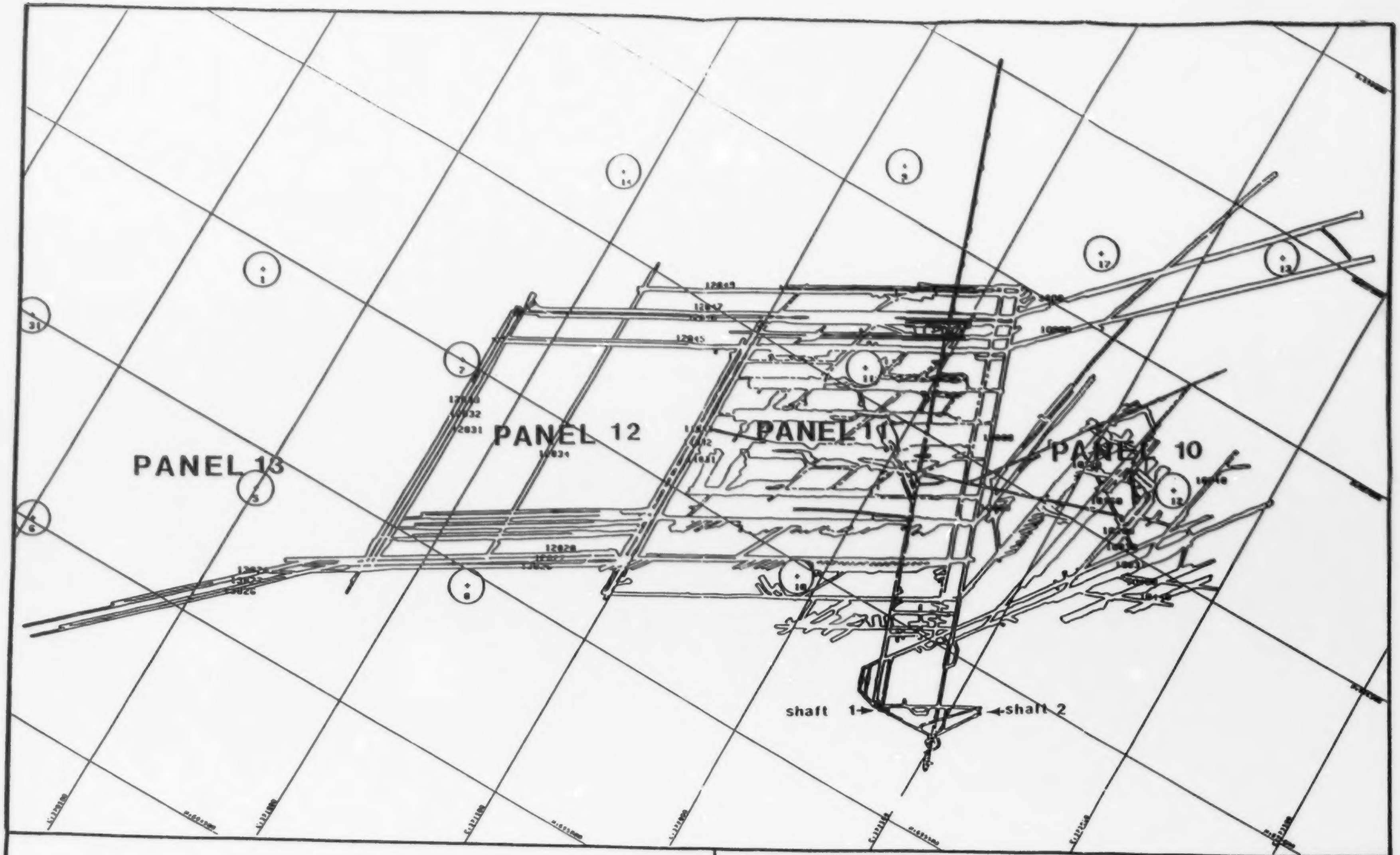

DENISON
POTACAN
POTASH
COMPANY

TITLE:
CLOVER HILL MINE
GENERAL MINE PLAN

SCALE: NTS

FIGURE: 10.1

The first geometry investigated was Panel 10 and 11 as shown in Figure 10.2. The mesh consisted of 30,000 elements. Figure 10.3 shows the information pertaining to the mining height. The mine development openings which were excavated to the height of 4 metres are shown in green colour. The elements shown in light blue colour represent mining stopes which were excavated to the full height of the ore thickness as per the ore thickness sub-routine. The results of this run are shown in Figures 10.4 to 10.8. Figure 10.11 includes steady state subsidence rate contours based on the assumption that the overburden is an orthotropic continuum and the surface a flat horizontal plane at the level of shaft collar.

10.3 Verification of Input Parameters

The behavioural laws and input parameters used in VELMINA were the same as those used in FLAC as described in Sections 8.0 and 9.0. In order to verify that these are valid for VELMINA runs, the results of the Panel 10 and 11 run were compared to the various in situ measurements.

The locations of the two convergence stations described in Section 3.4.2 are shown in Figure 10.9. It shows a good agreement between the predicted and in situ convergence rates.

The pressure cells located in the north pillar of rock mechanics station in Stope 11200 have been described in Sections 3.4.1 and 3.5.2. The comparison of readings from three undamaged vertical cells and the VELMINA prediction of the stress within the pillar is included in Figure 10.10. It would appear that the cells located within the **high exponent** region reflect the stress reasonably close. The cell located in the centre of the pillar, in the **low exponent** region apparently did not reach full pressure before the power was disconnected.

The comparison of predicted and measured subsidence rates is included in Figures 10.11 to 10.13. In comparing the two sets of subsidence rate profiles, it must be realized that VELMINA simulates steady state conditions. In reality, in 1988, the mining has been ongoing in Panel 11 with all of its transient effects including the increased rates of convergence in the vicinity

FIGURE 10.2

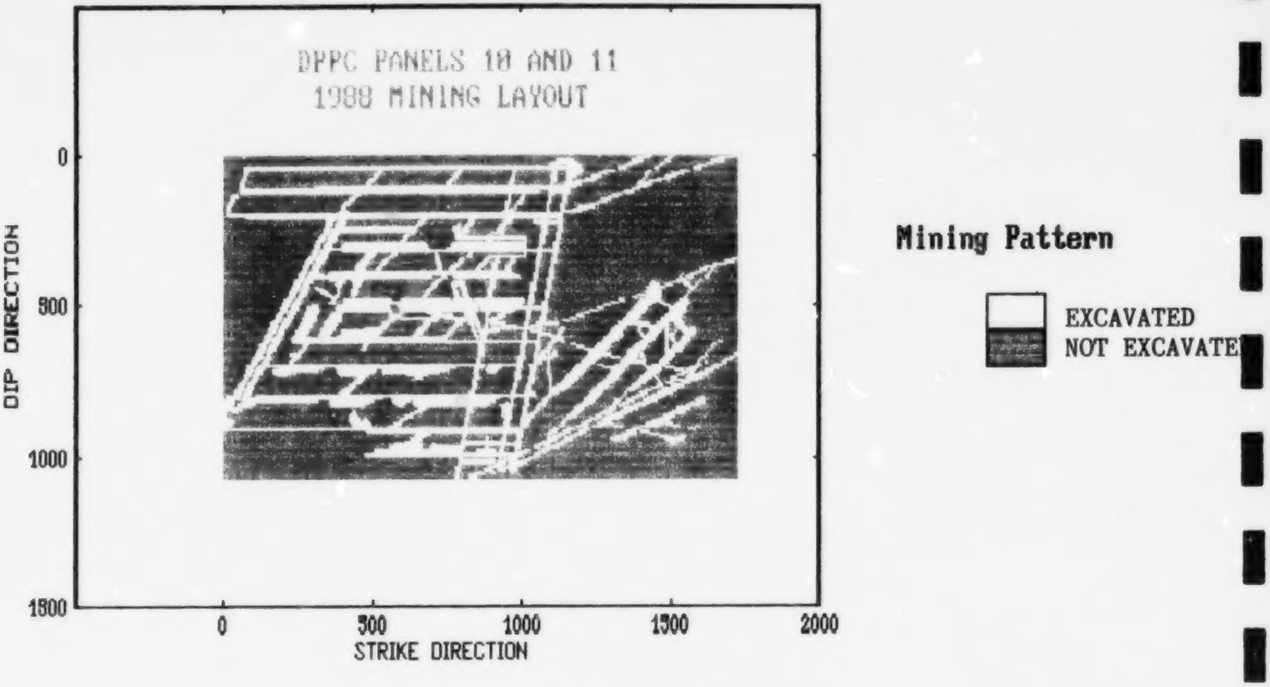

FIGURE 10.3

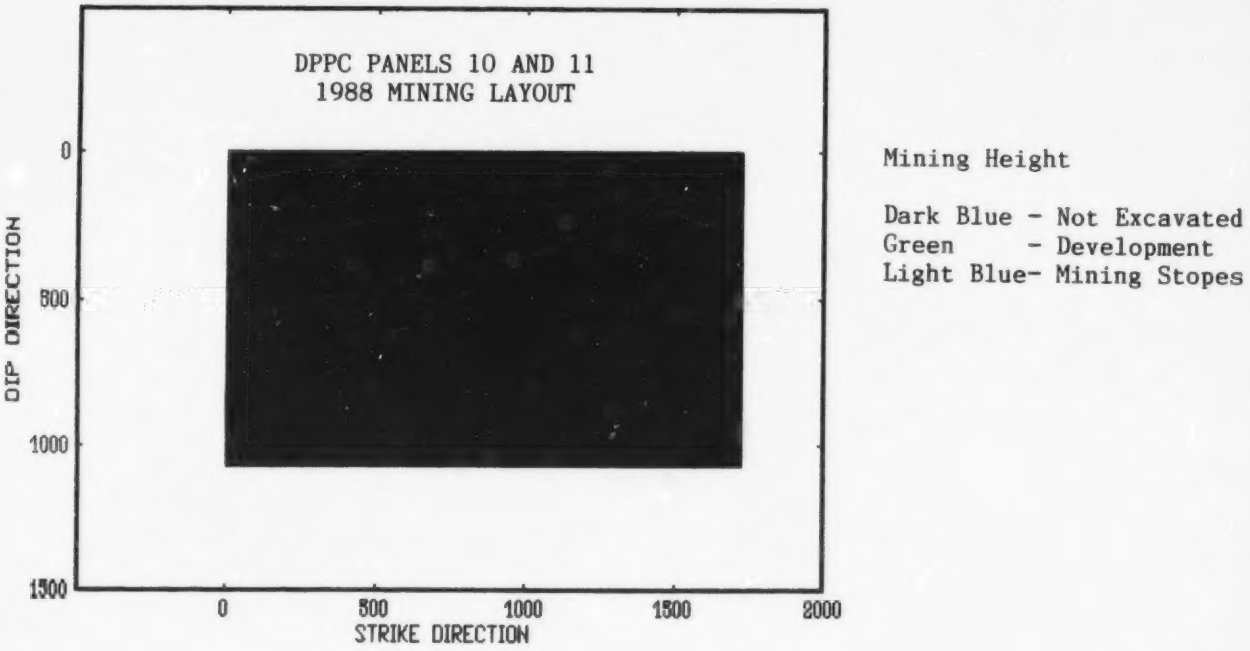

FIGURE 10.4

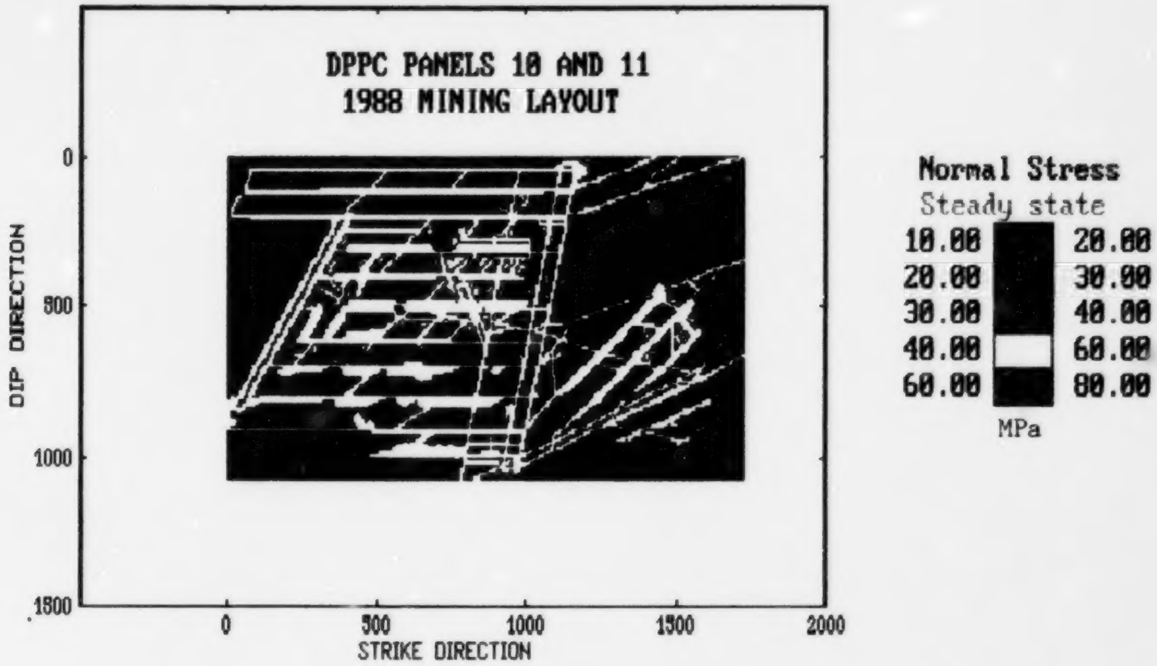

FIGURE 10.5

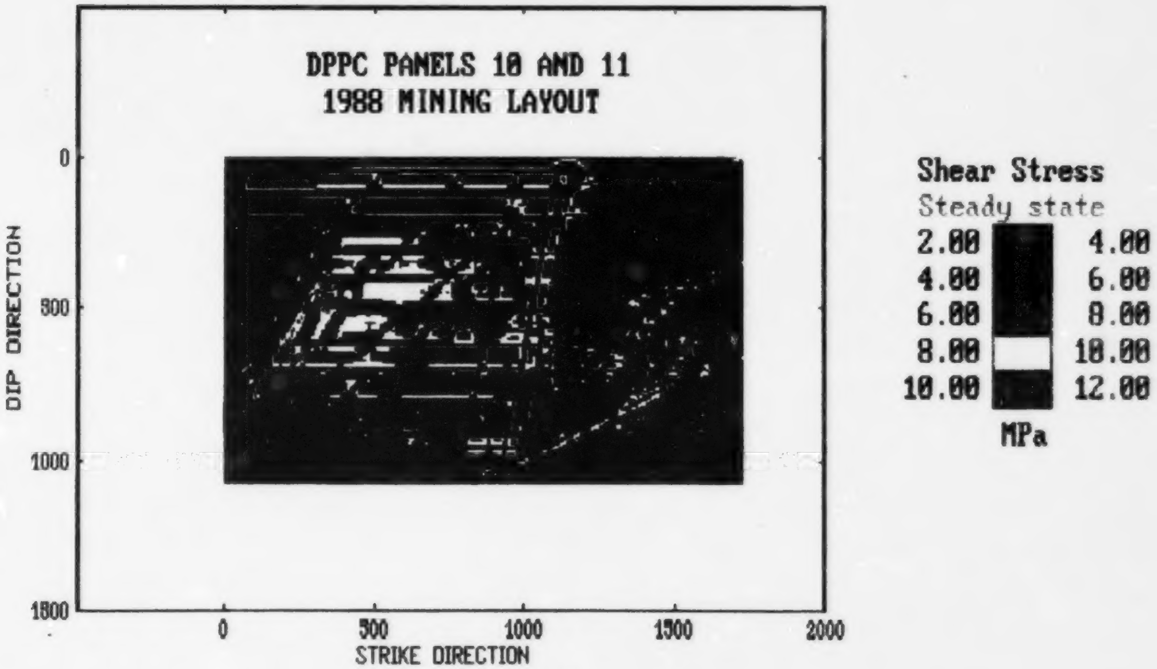

FIGURE 10.6

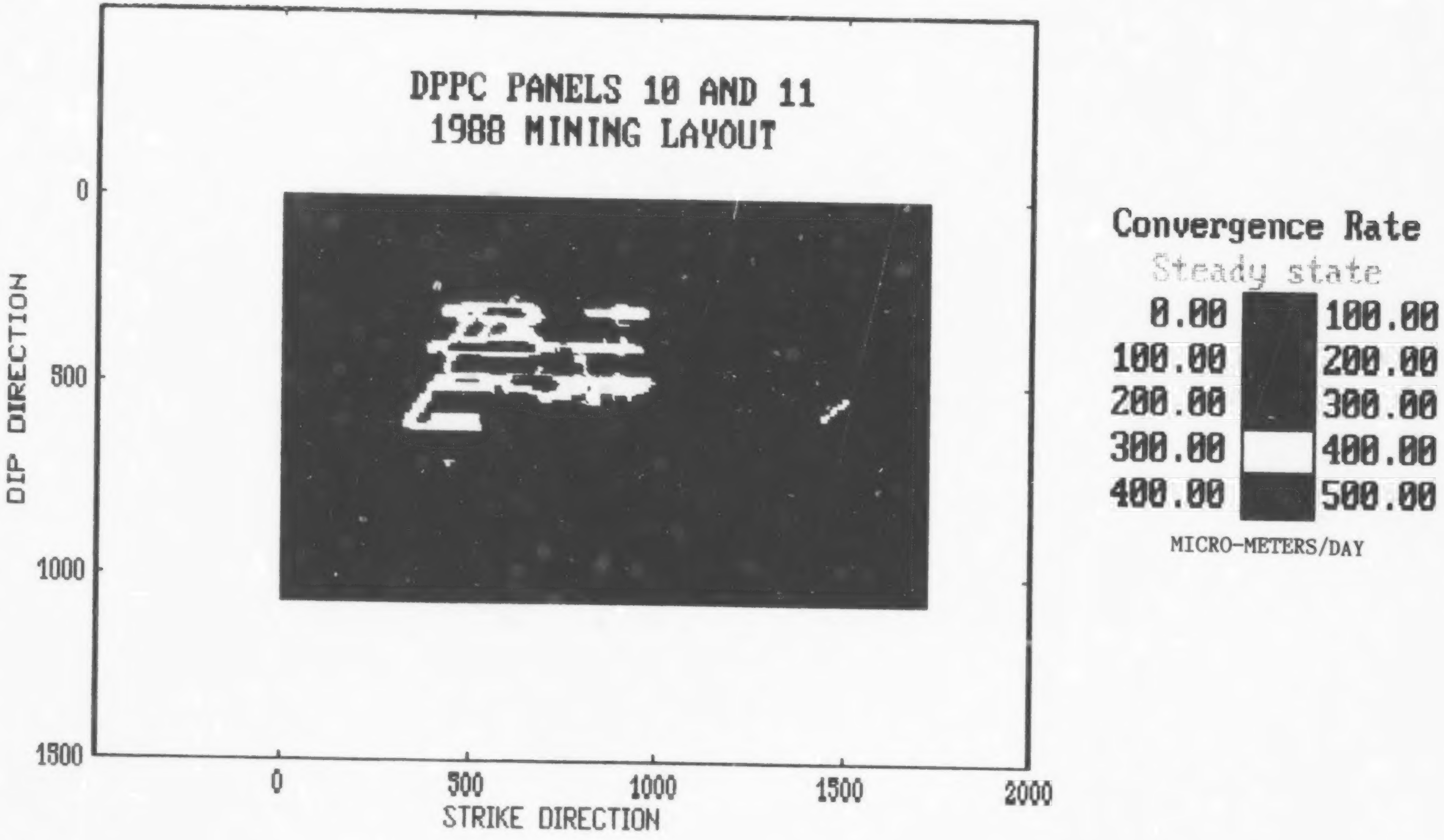
DPPC PANELS 10 AND 11
1988 MINING LAYOUT
DIP DIRECTION
0
500
1000
1500
STRIKE DIRECTION
0
500
1000
1500
2000
Convergence Rate
Steady state
0.00 100.00
100.00 200.00
200.00 300.00
300.00 400.00
400.00 500.00
MICRO-METERS/DAY

FIGURE 10.7

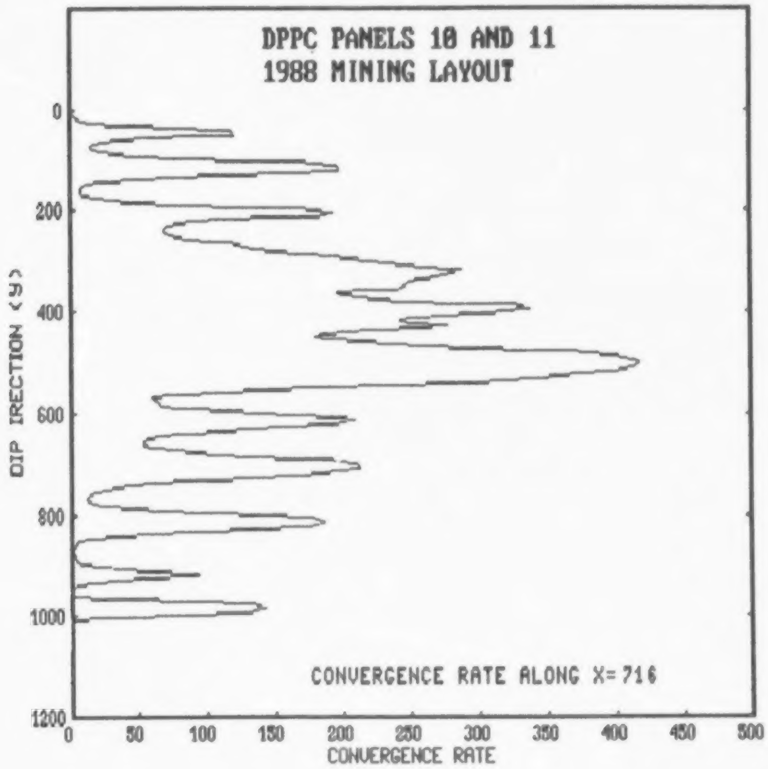

FIGURE 10.8

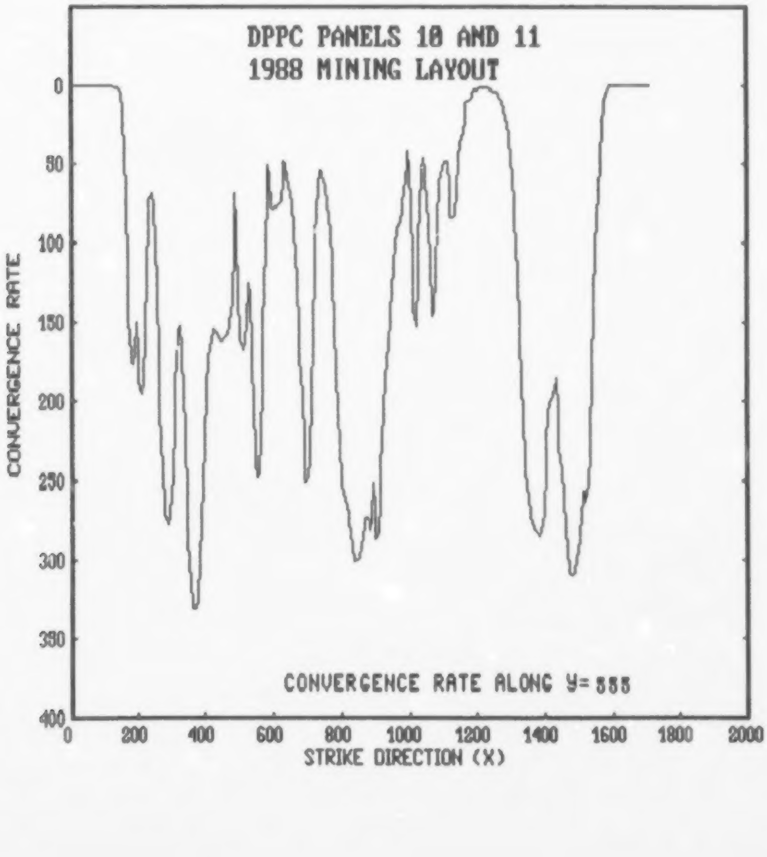

FIGURE 10.9

DPPC PANEL 11

1988 MINING LAYOUT SHOWING CONVERGENCE STATIONS

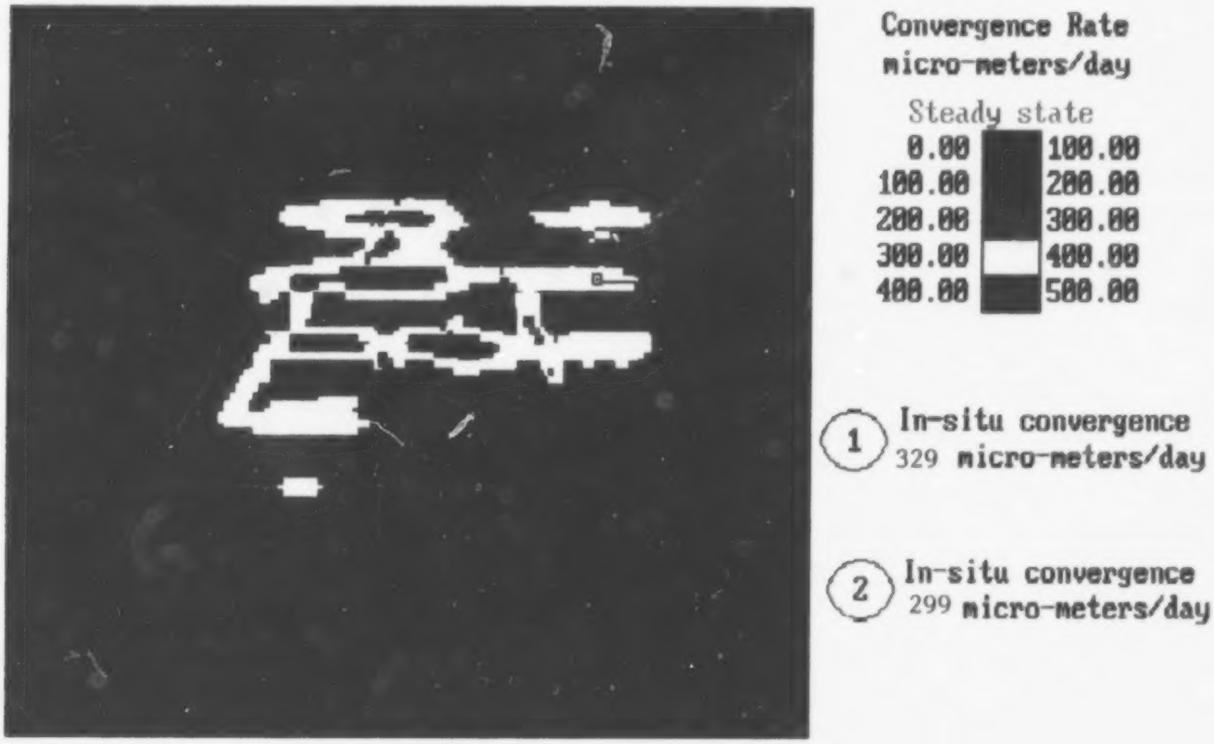

① In-situ convergence 329 micro-meters/day

② In-situ convergence 299 micro-meters/day

FIGURE 10.10

VERTICAL STRESS IN NORTH PILLAR,
ROCK MECHANICS STATION IN STOPE 11200

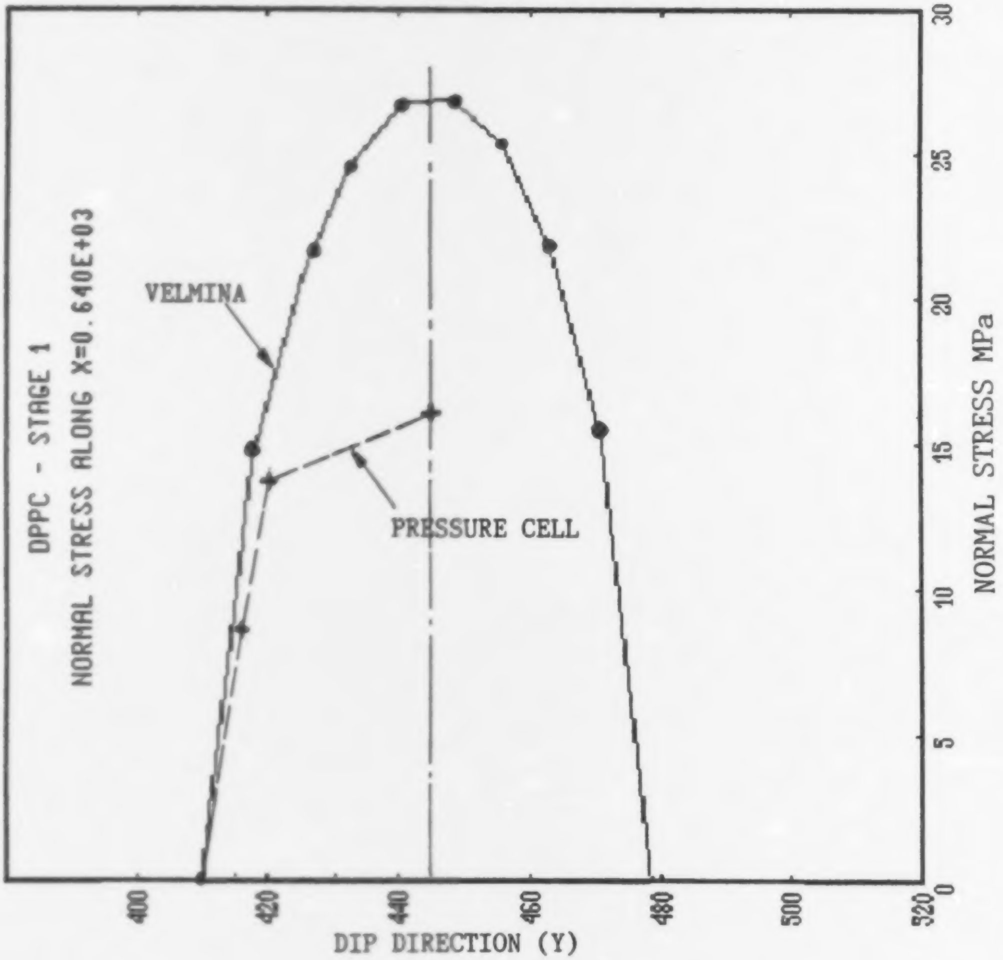

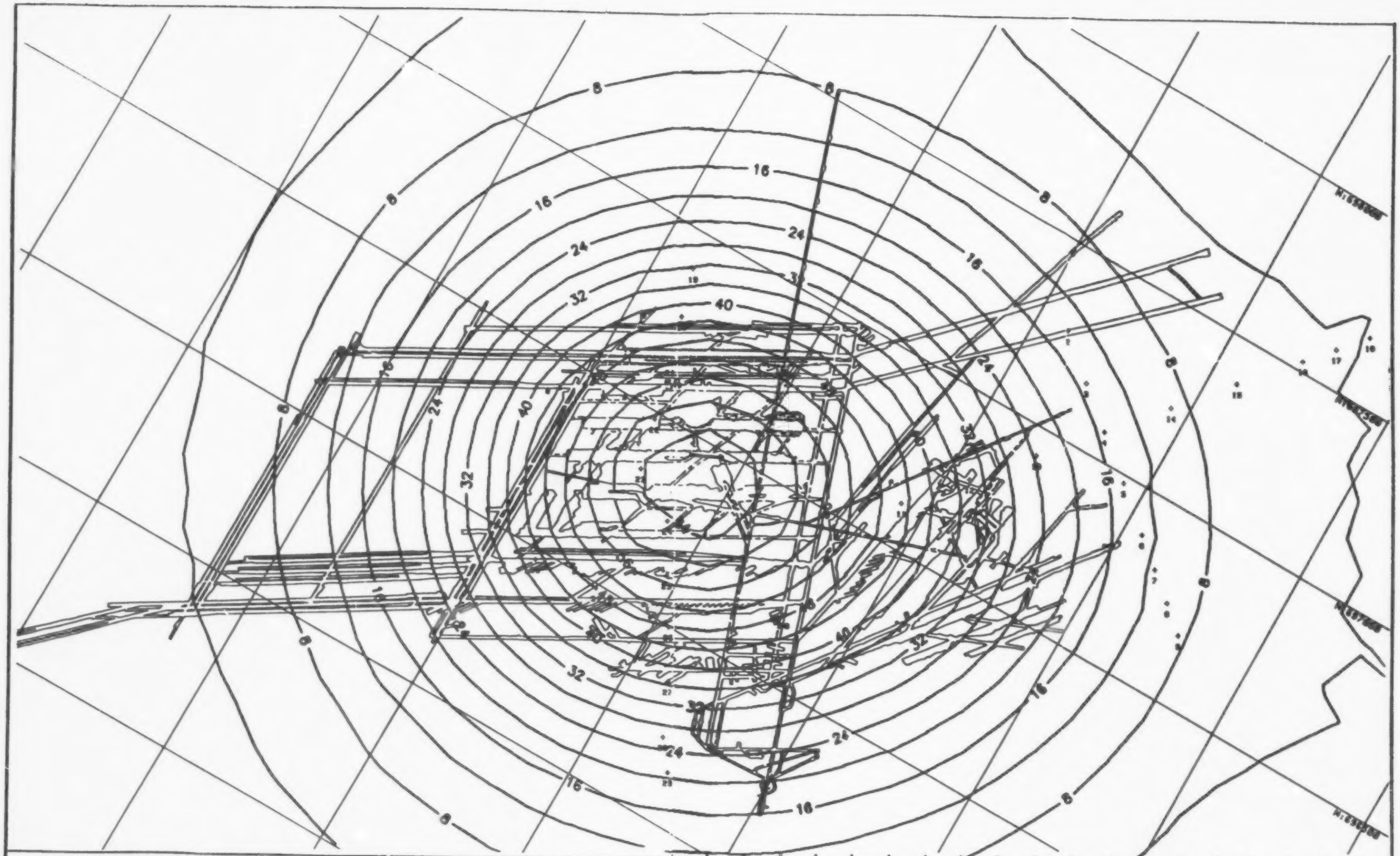

DENISON
POTACAN
POTASH
COMPANY

TITLE: PANLES 10, 11 and 12, 1988 MINING LAYOUT
SHOWING VELMINA STEADY-STATE SUBSIDENCE
RATE FOR LARGE BASE CASE
IN MICRO-METRES PER DAY

SCALE: NTS

FIGURE: 10.11

FIGURE 10.12

SUBSIDENCE RATE, 1987–88

NORTH–SOUTH SECTION

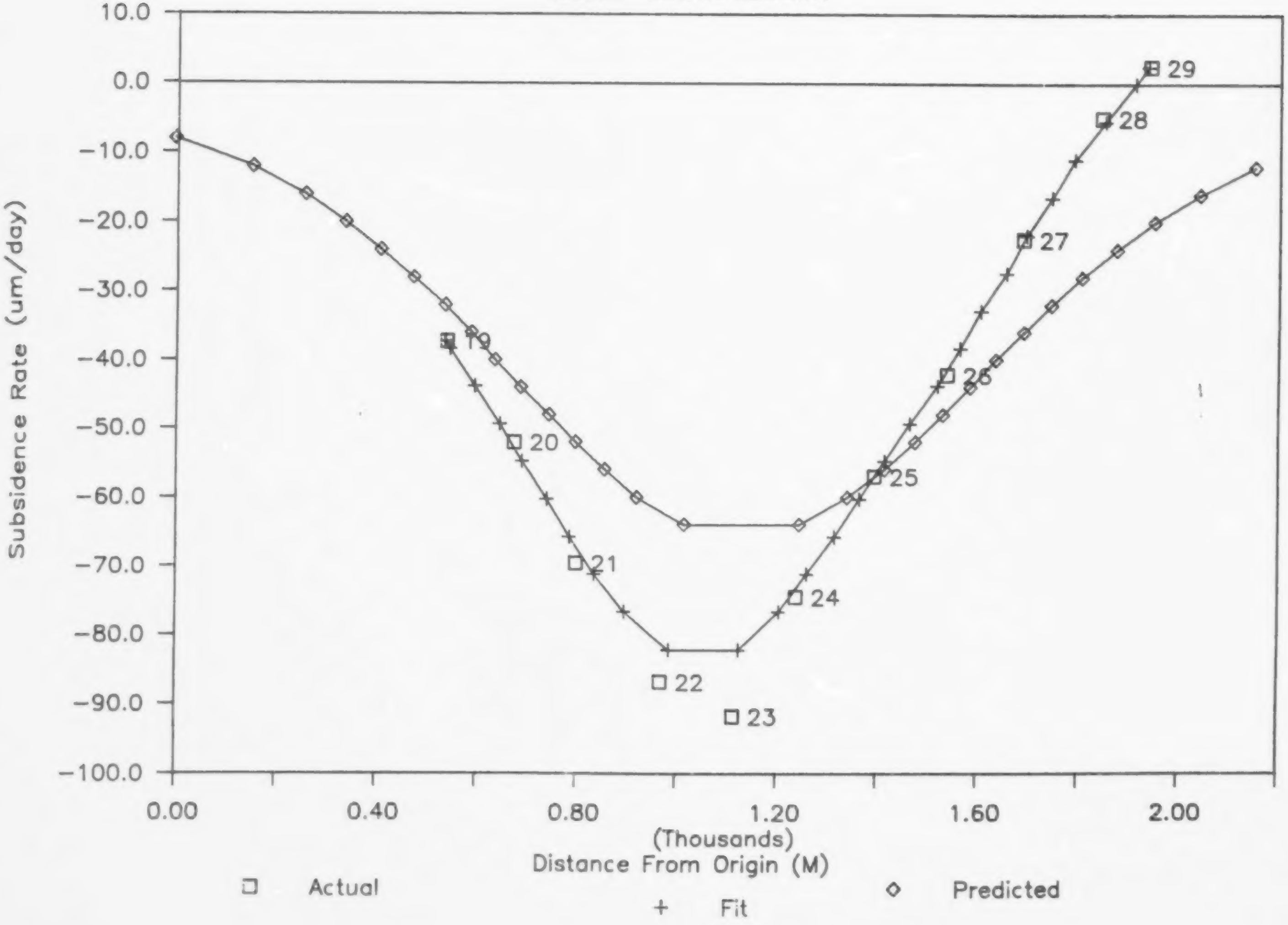

FIGURE 10.13

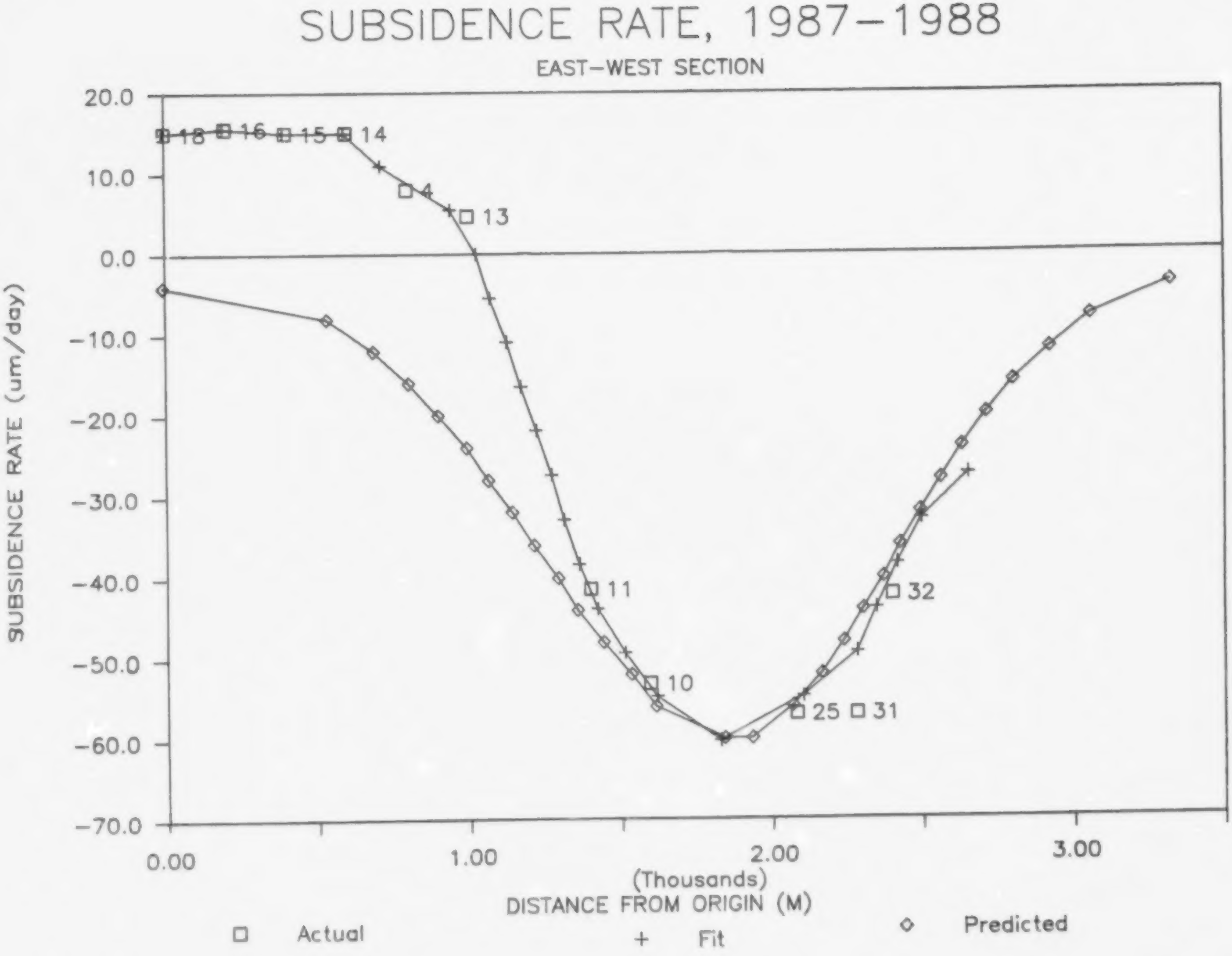
SUBSIDENCE RATE, 1987–1988
EAST–WEST SECTION
SUBSIDENCE RATE (um/day)
20.0
10.0
0.0
−10.0
−20.0
−30.0
−40.0
−50.0
−60.0
−70.0
0.00
1.00
2.00
3.00
(Thousands)
DISTANCE FROM ORIGIN (M)
18
16
15
14
4
13
11
10
25
31
32
□ Actual
+ Fit
◇ Predicted

of the point of maximum subsidence. Based on that and the fact that a continuum has been assumed rather than nonuniform strata, the in situ subsidence data compare with the predicted steady state rates very well.

In terms of absolute numbers, the convergence rates are the most reliable data in verifying the computer simulation. In spite of mining disturbances at the time of measurements, the predicted and measured convergence rates compare well and confirm validity of the input parameters and material laws used. The fact that the subsidence rates, and to some extent vertical stress measurements, compare well with the predicted values increases the level of confidence in this modelling.

10.4 Simulation of Combined Excavation of Panels 10, 11 and 12

The mesh for the combined excavation of Panels 10, 11 and 12 consisted of 60,000 elements. The ultimate mining layout of Panel 12 was based on the current DPPC mining plan as developed for this area. The overall mesh is shown in Figure 10.14, the detail of Panel 11 in Figure 10.15, the detail of Panel 12 in Figure 10.16 and a detailed example of the mesh in Figure 10.17. The results of the analysis are included in Figures 10.18 to 10.26. By comparing Figure 10.20 with Figure 10.6, it was determined that the maximum convergence rates in Panel 12 would be about twice the maximum convergence rates currently experienced in Panel 11.

10.5 Simulation of Backfill in Panels 10, 11 and 12

The behavioural law and properties used for simulation of backfill in this analysis were as tabulated in Section 9.0. The mesh (Figures 10.14) and the steady state stress conditions (Figure 10.18) from the previous analysis were used. The initial backfill placement density was assumed to be 1.4 g/cm^3 (D = 0.65). The results are included in Figures 10.27 to 10.34. Figures 10.27 to 10.31 show the density distribution at 6 years, 11 years, 16 years, 21 years and 26 years. The degree of densification at various points within the layout (Figure 10.32) over time is shown in Figure 10.33. The convergence rates at various points over time are shown in Figure 10.34.

FIGURE 10.14

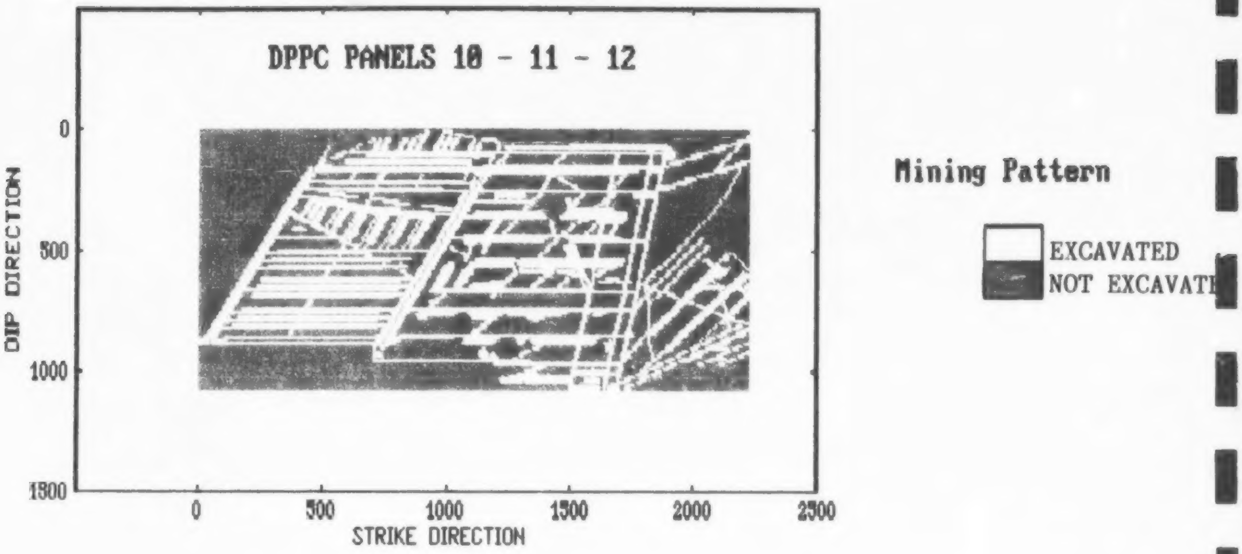

FIGURE 10.15

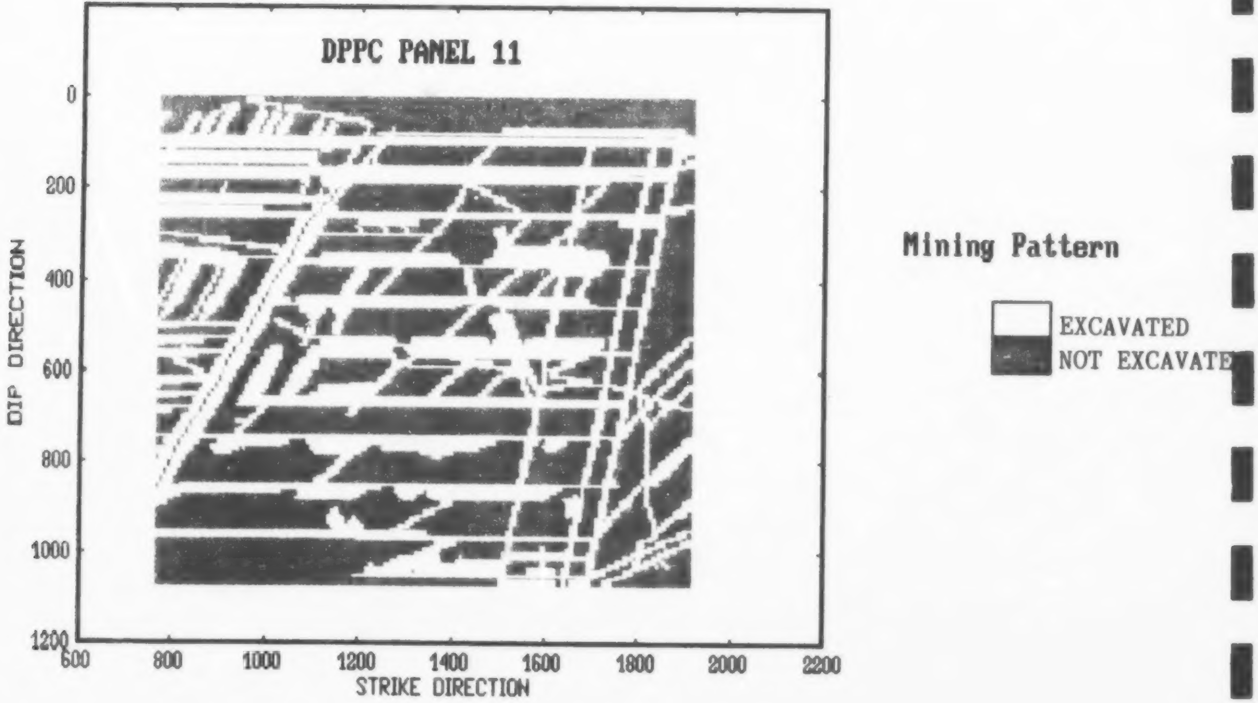

FIGURE 10.16

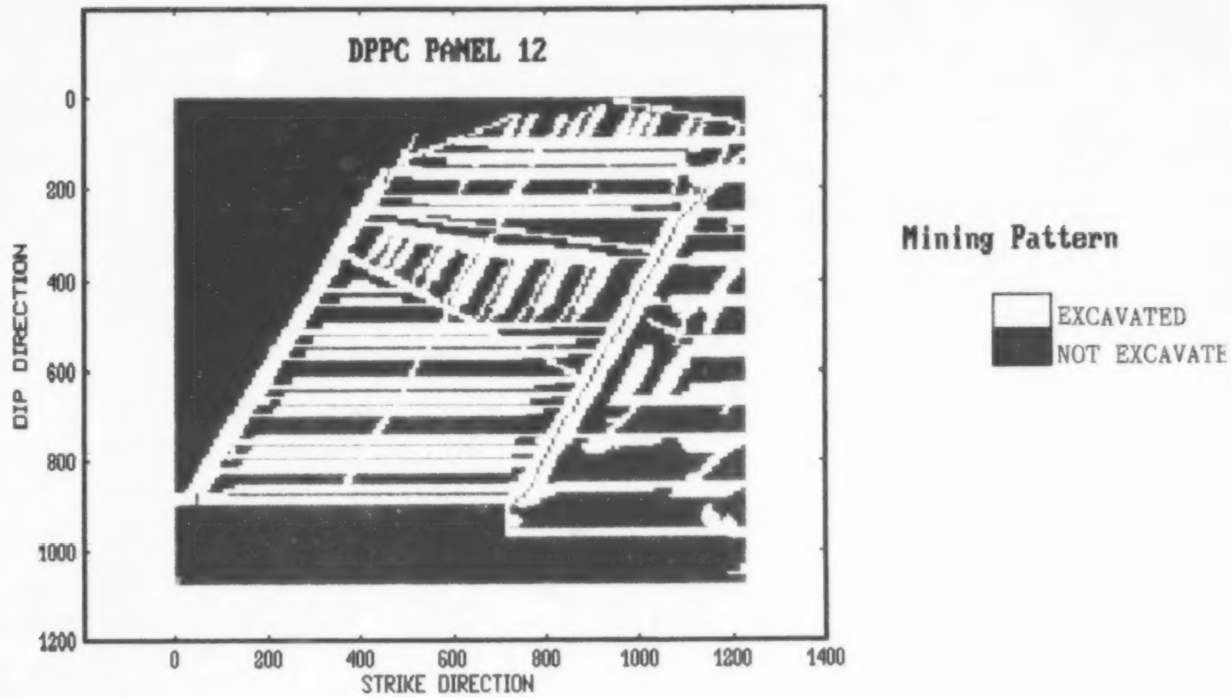

FIGURE 10.17

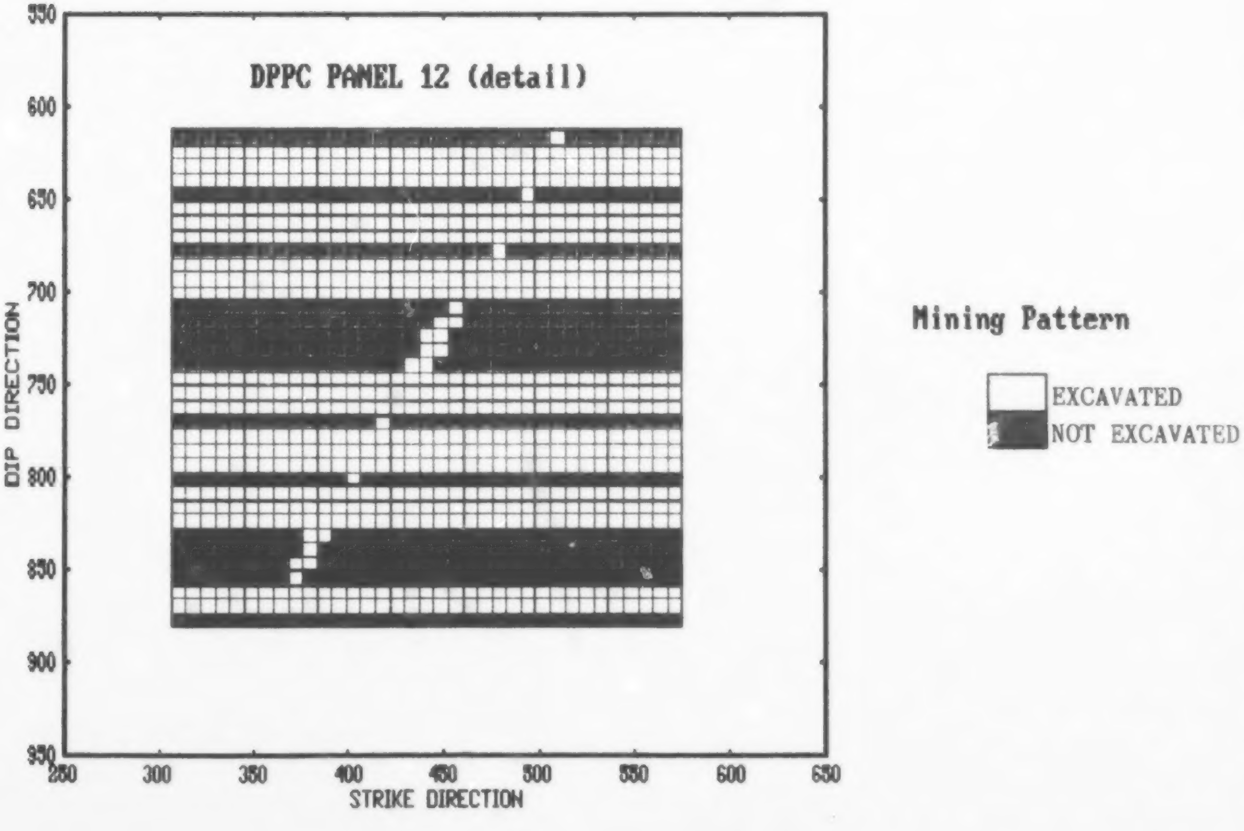

FIGURE 10.18

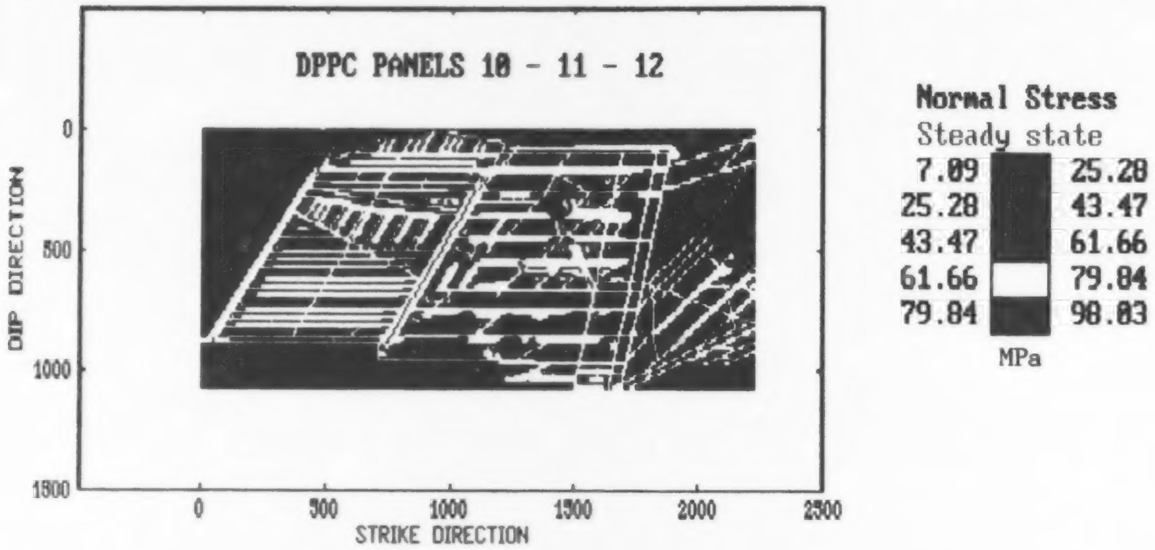

FIGURE 10.19

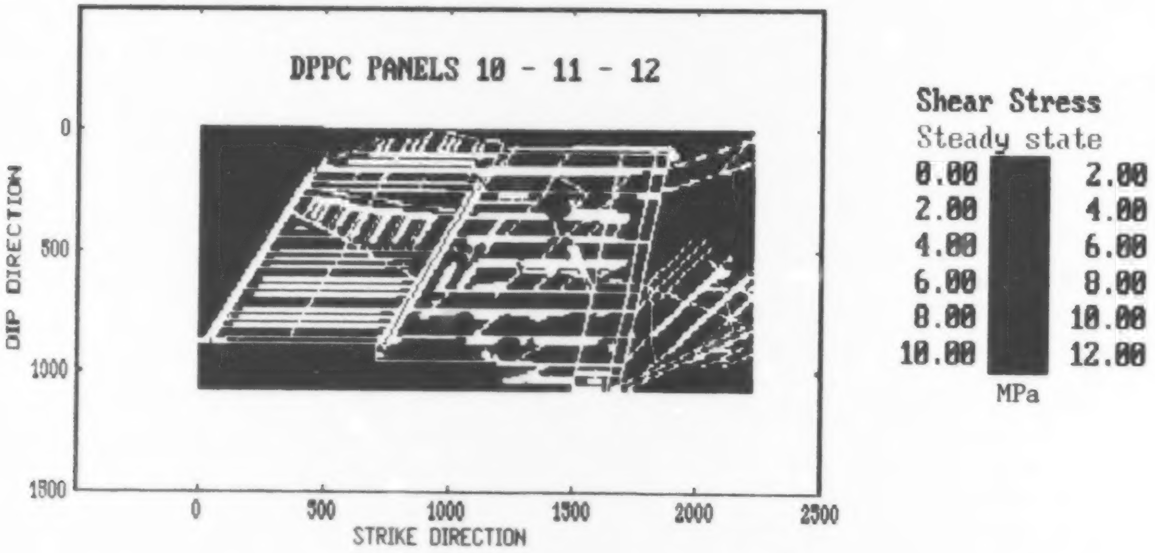

FIGURE 10.20

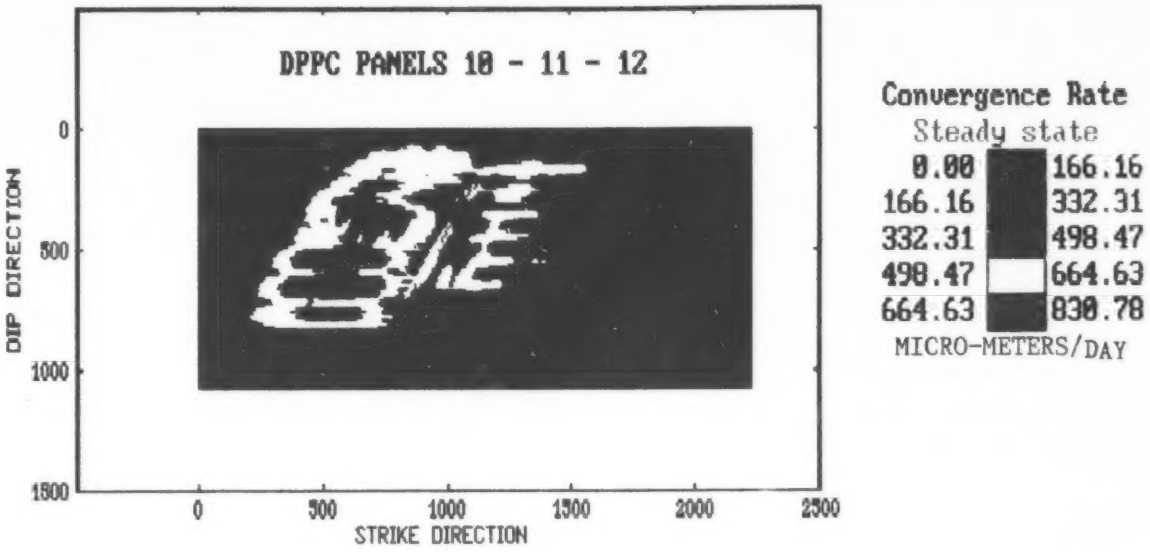

FIGURE 10.21

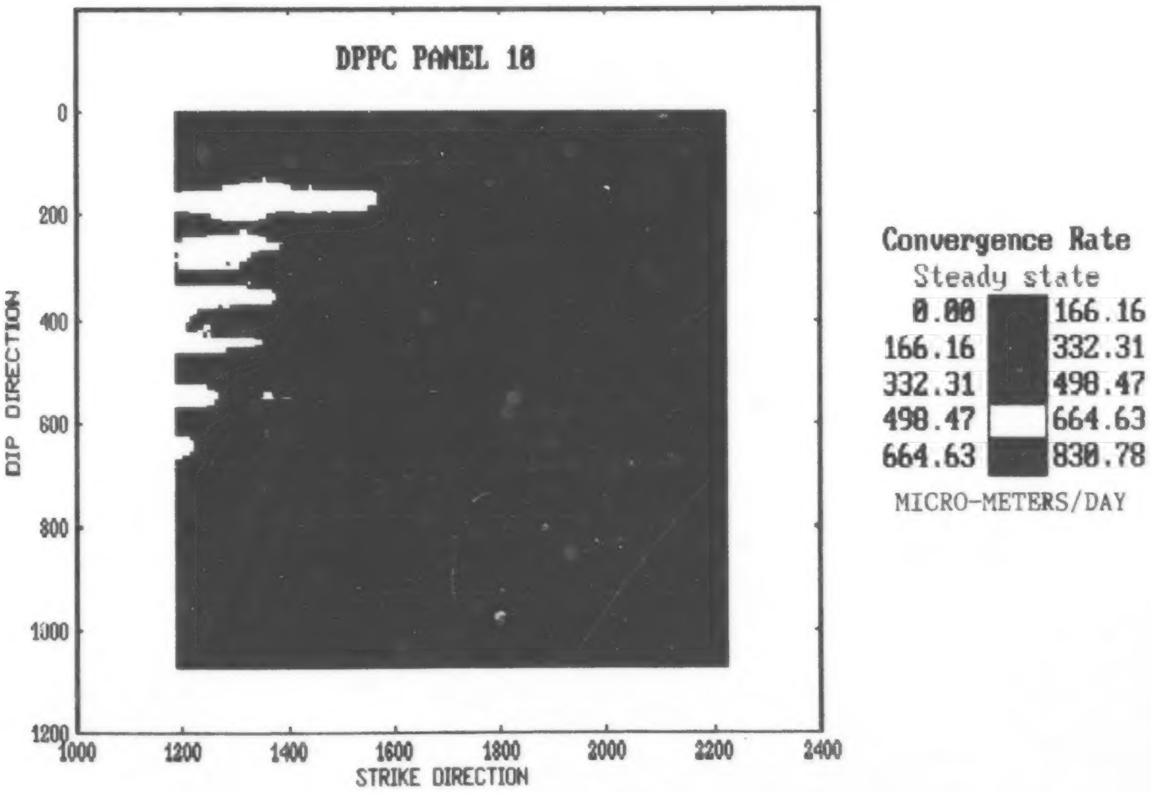

FIGURE 10.22

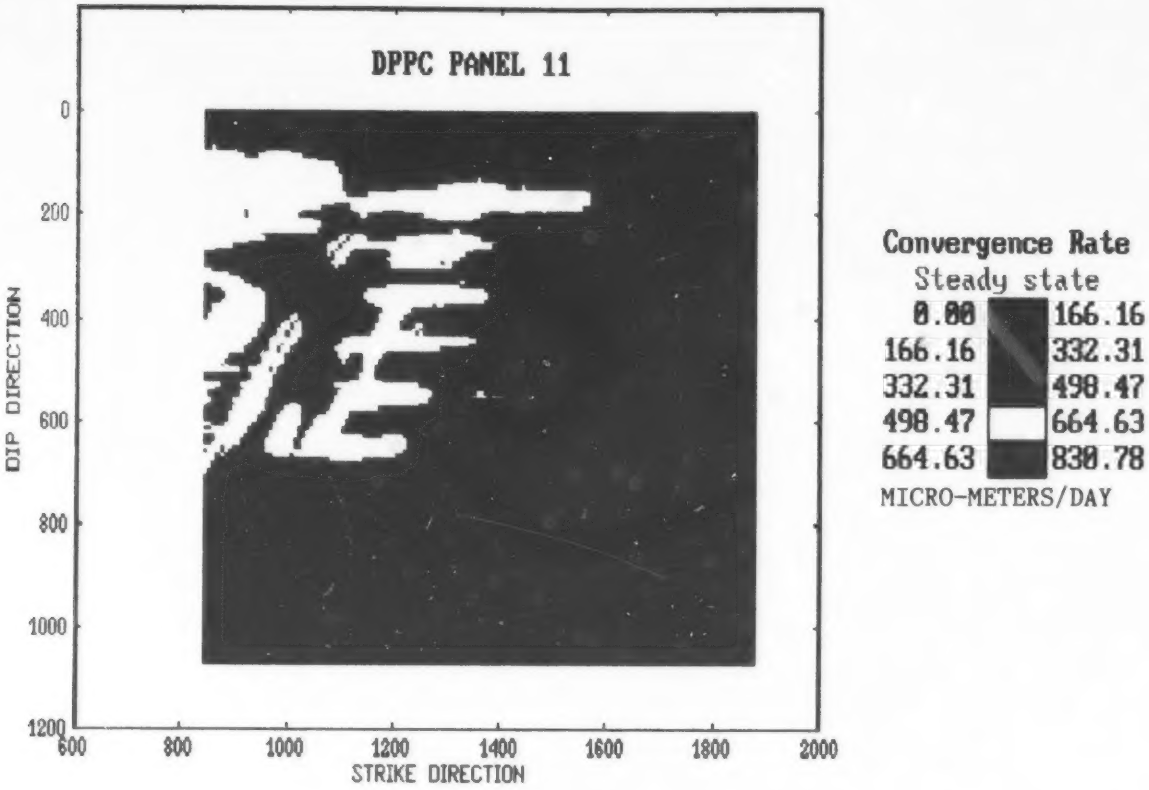

FIGURE 10.23

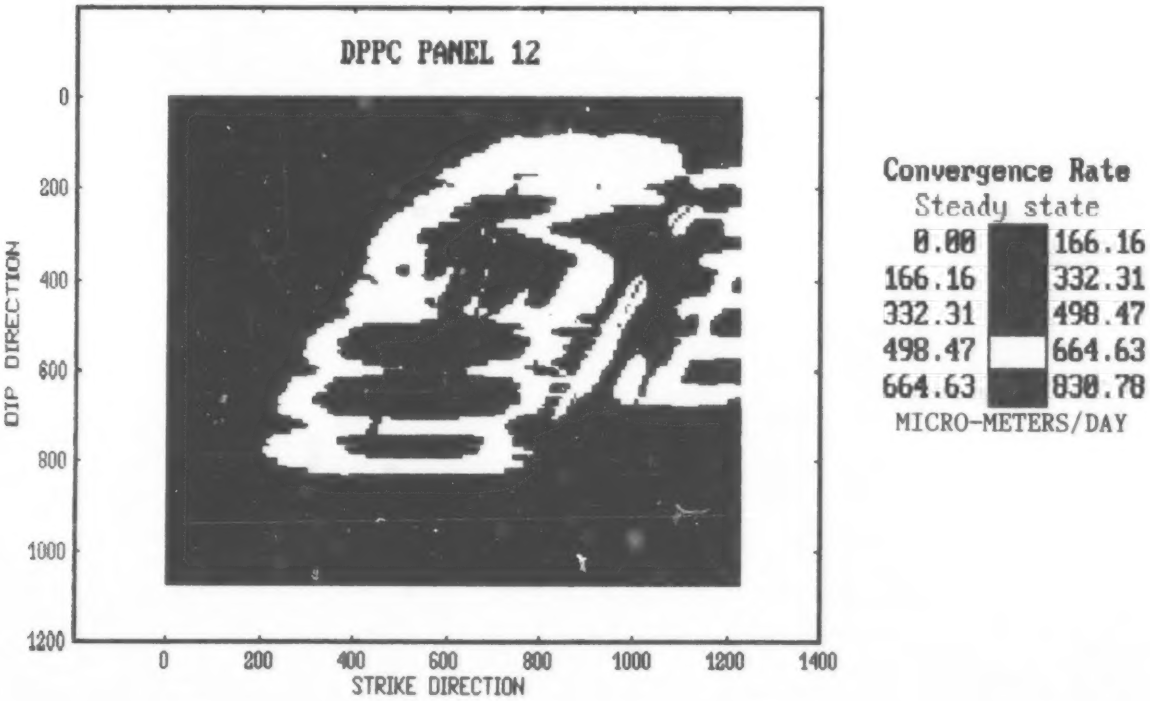

FIGURE 10.24

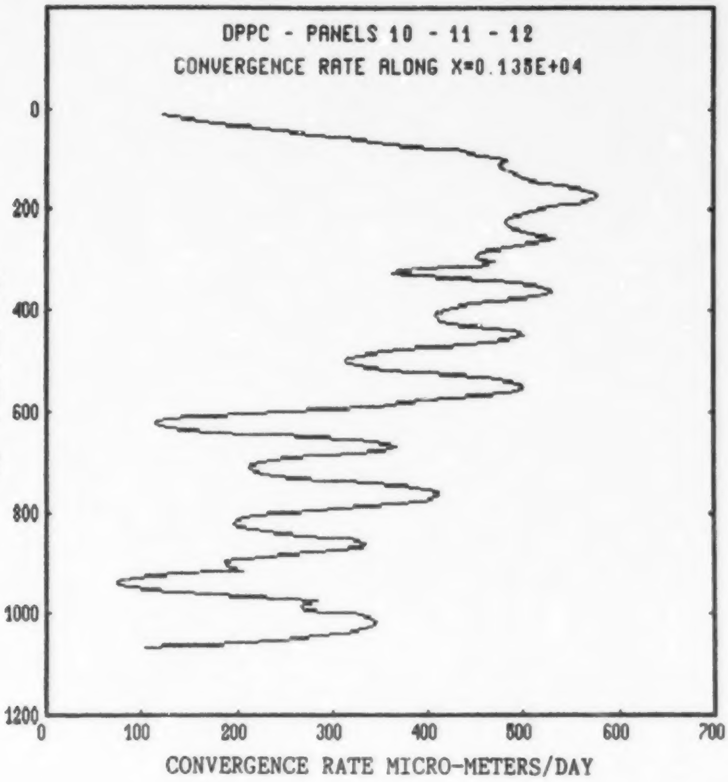

FIGURE 10.25

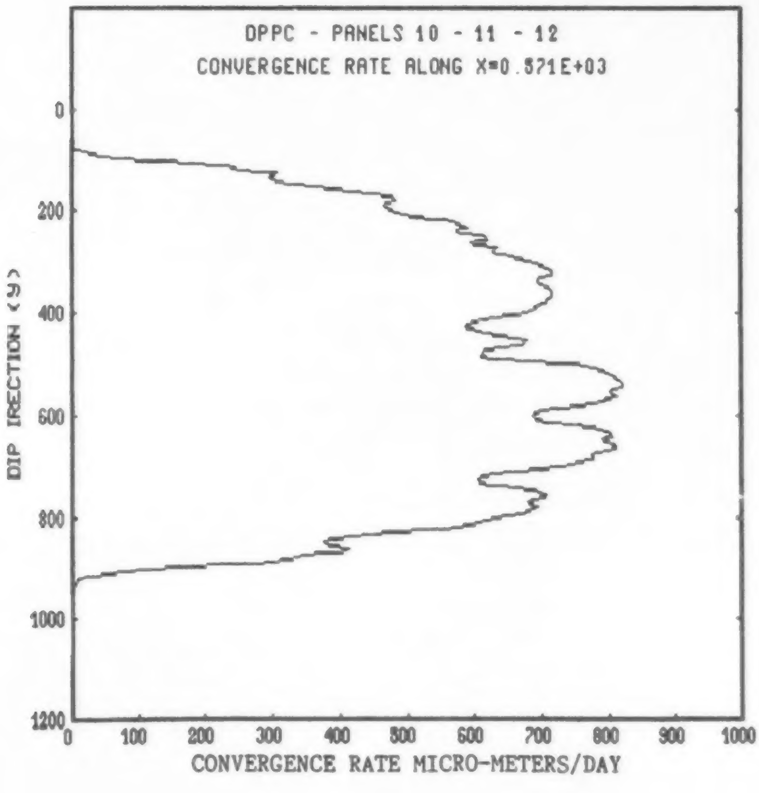

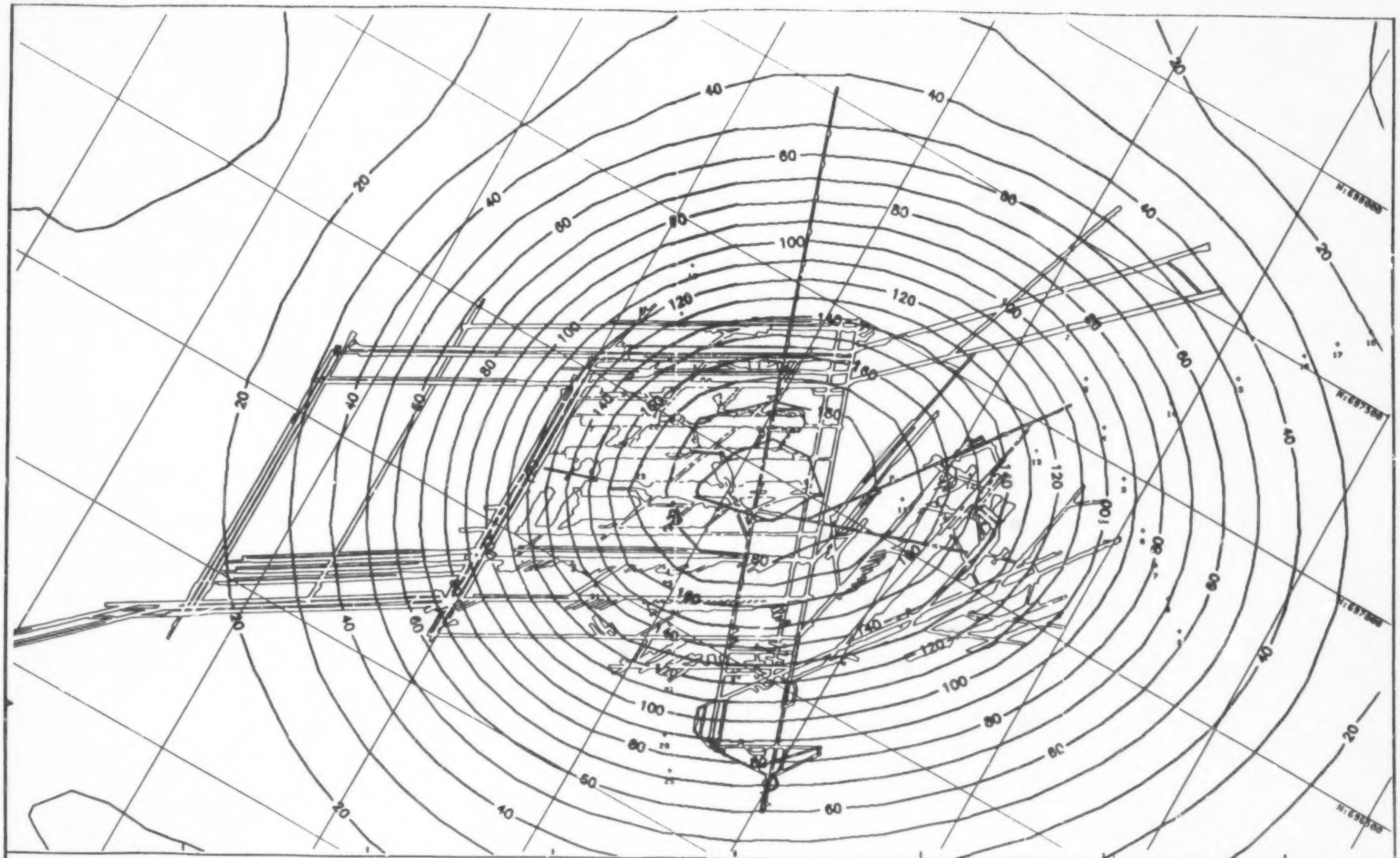

DENISON
POTACAN
POTASH
COMPANY

TITLE: PANELS 10, 11 and 12, 1988 MINING
LAYOUT SHOWING VELJINA STEADY-STATE
SUBSIDENCE RATE
IN MICRO-METRES PER DAY

SCALE: NTS

FIGURE: 10.26

FIGURE 10.27

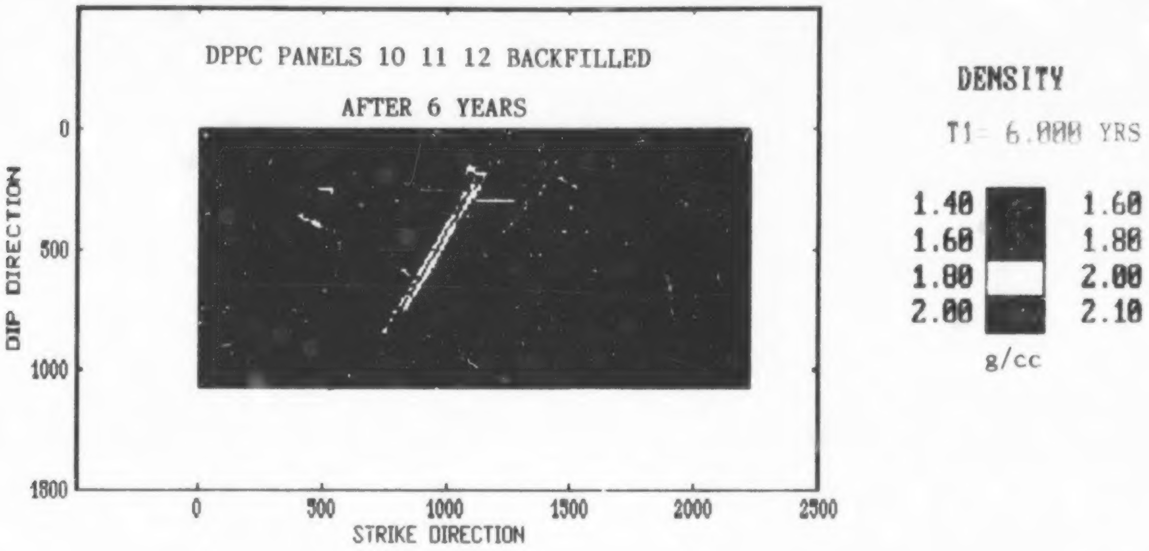

FIGURE 10.28

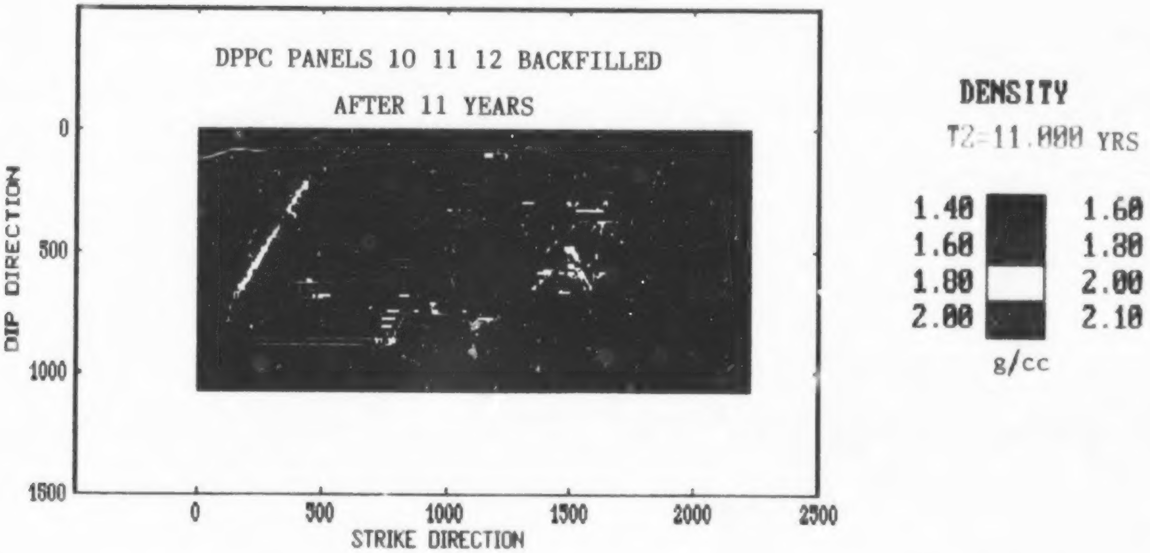

FIGURE 10.29

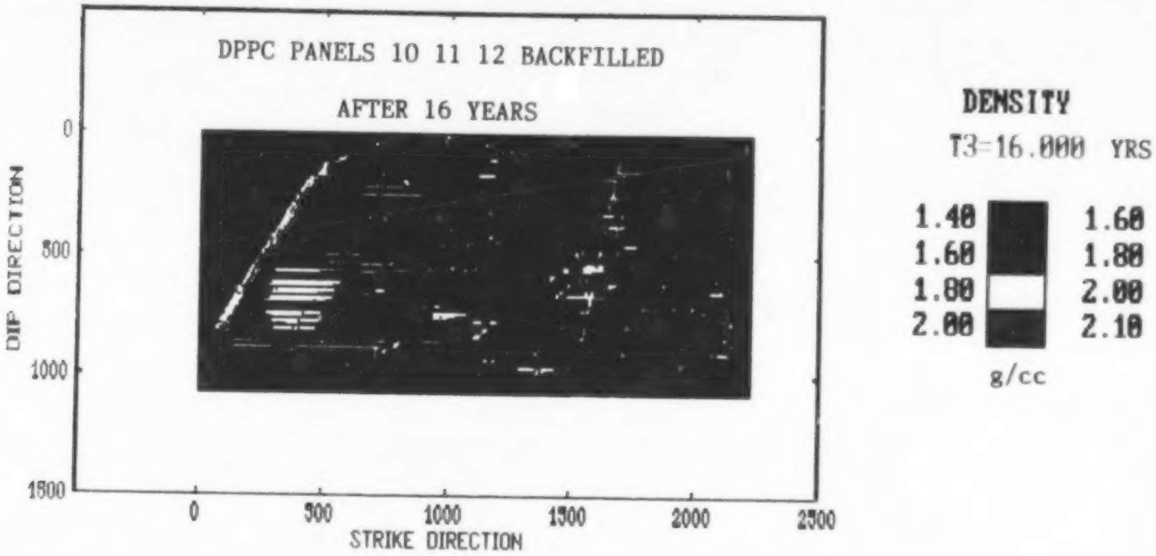

FIGURE 10.30

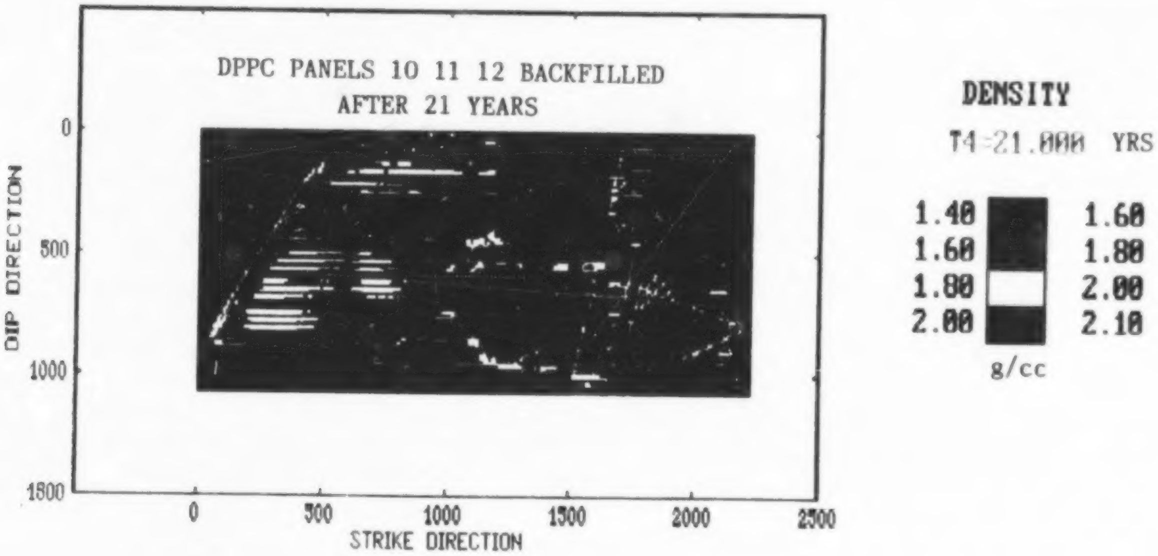

FIGURE 10.31

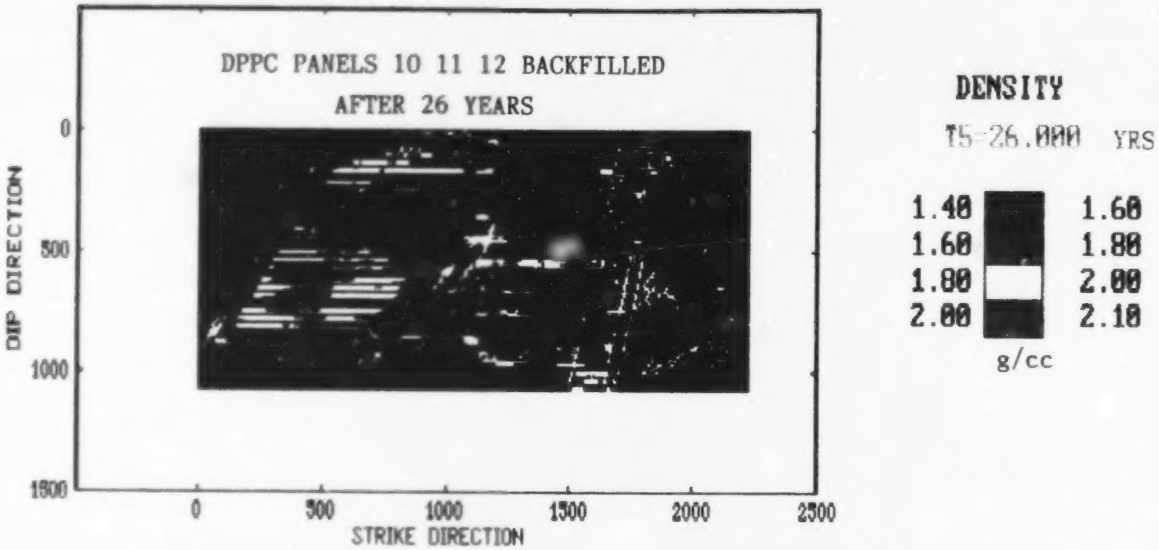

FIGURE 10.32

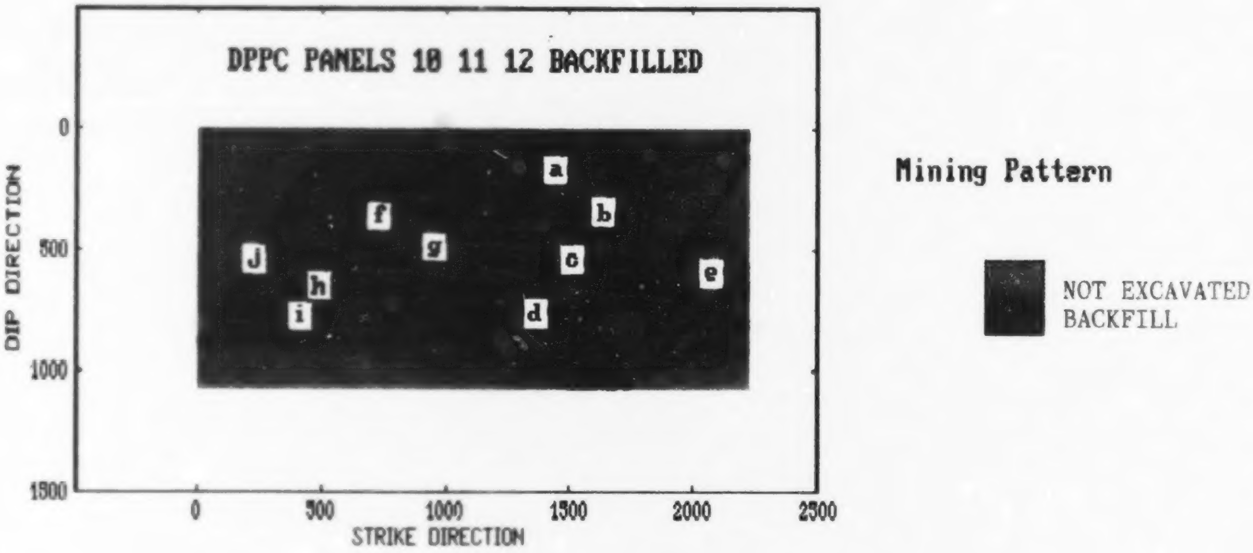

FIGURE 10.33

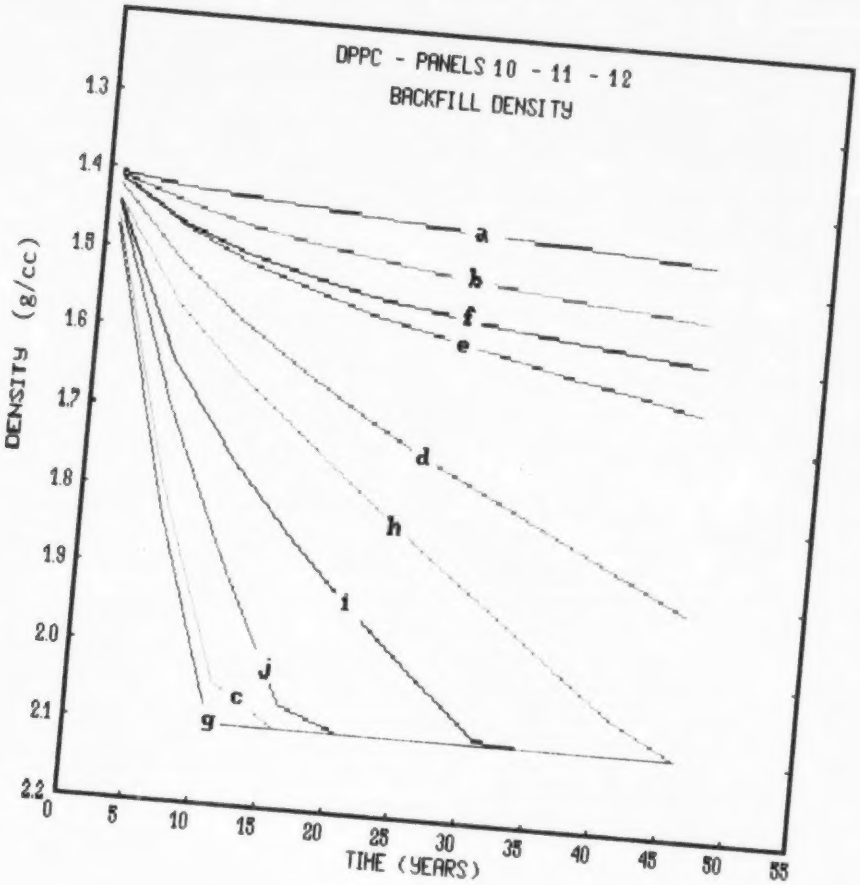
DPPC - PANELS 10 - 11 - 12
BACKFILL DENSITY
DENSITY (g/cc)
1.3
1.4
1.5
1.6
1.7
1.8
1.9
2.0
2.1
2.2
0
5
10
15
20
25
30
35
40
45
50
55
TIME (YEARS)
a
b
f
e
d
h
i
j
c
g

FIGURE 10.34

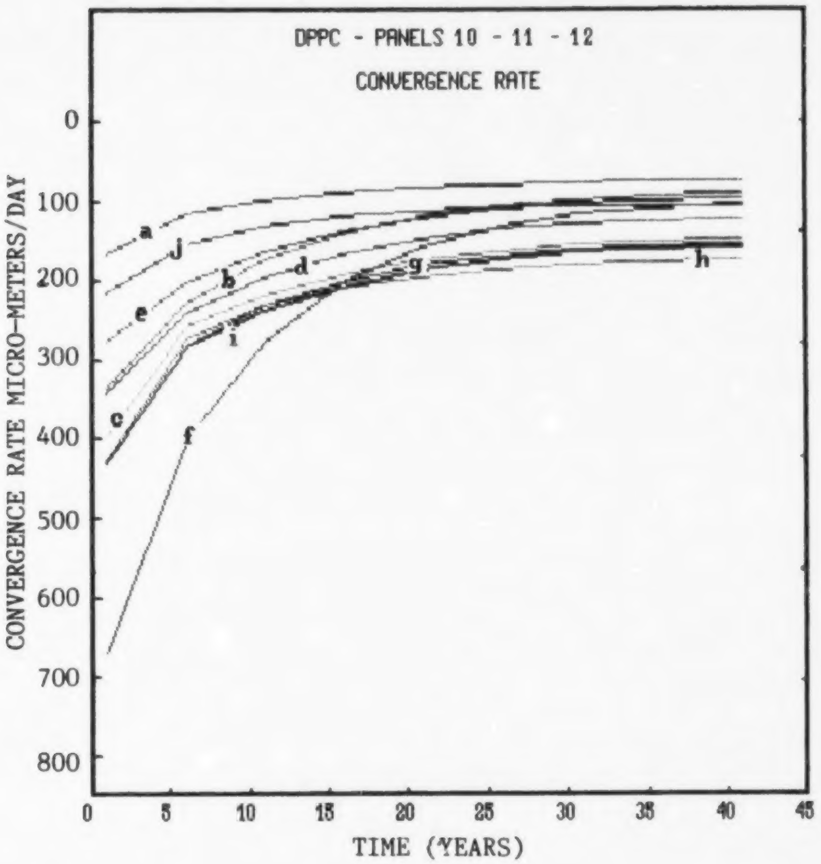
DPPC - PANELS 10 - 11 - 12
CONVERGENCE RATE
CONVERGENCE RATE MICRO-METERS/DAY
0
100
200
300
400
500
600
700
800
TIME (YEARS)
0
5
10
15
20
25
30
35
40
45
a
j
e
b
d
g
h
i
c
f

In situ placement of backfill in a stope is gradual, but for simplicity and modelling purposes, backfill placement is considered instantaneous. The effect of this simplification is negligible, because the response of backfill during the time it takes to backfill a stope is insignificant, with little change in its density (Figure 10.33).

In the analysis, it was simulated that the entry systems of the three panels were backfilled. In situ, backfilling of entry systems will seldomly occur for they will be required for travelways. However, the effect of backfilling the entry systems on the overall stress conditions and convergence rates would be insignificant. The degree of influence entry systems have on the behaviour of the rock mass when compared to large mining stopes can be neglected.

10.6 Simulation of Secondary Mining in Panels 10, 11 and 12

Based on the previous run, it was assumed that the secondary excavation in the pillars would be possible after about 10 years of backfill consolidation, assuming the initial placement density of 1.4 g/cm^3 (D = 0.65). The mesh of the secondary excavation layout is shown in Figure 10.35 and the results are included in Figures 10.36 to 10.41. The comparison of Figure 10.38 with Figure 10.6 shows that the maximum convergence rates would be similar to those currently experienced in Panel 11. Also, the convergence rate for Stope 11200 predicted by the FLAC analysis is in good agreement with the rates predicted by VELMINA. Thus, it can be concluded that potential secondary mining in backfilled panels 10, 11 and 12, 10 years after backfilling is feasible.

In both the two and the three dimensional analyses, secondary mining of pillars was instantaneous, 10 years after backfilling of primary stopes. Instantaneous excavation reduces the support capability of the pillars immediately, transferring the load to backfilled stopes and the remnant pillars. The rapid load transfer increases convergence rates of backfilled stopes causing an increase in compaction rates which leads to rapid densification of backfill and support of overburden. If the backfill has not

FIGURE 10.35

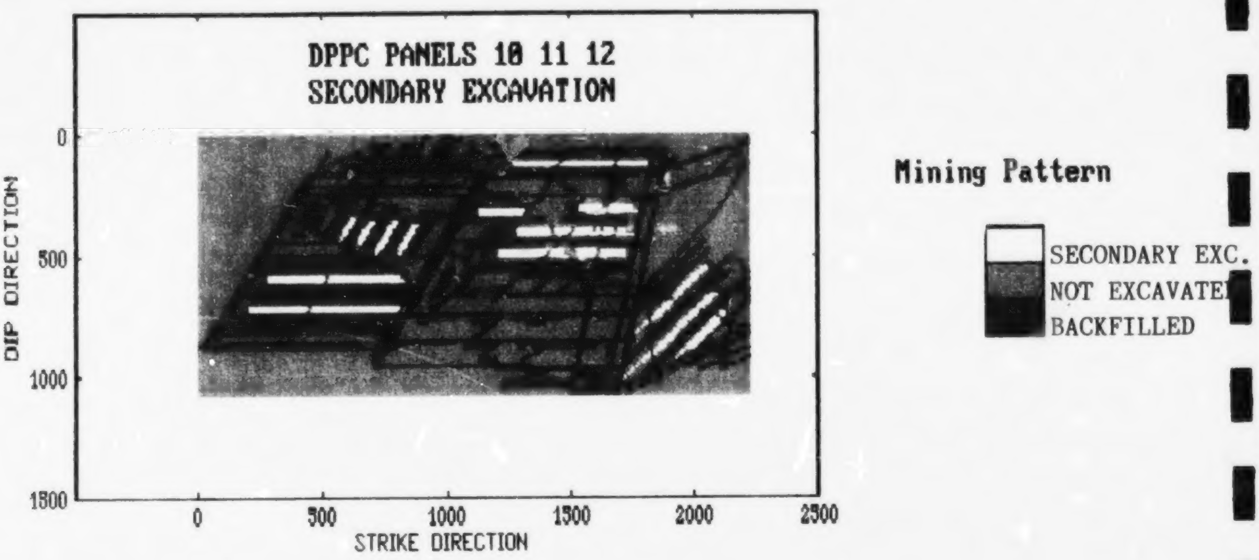

FIGURE 10.36

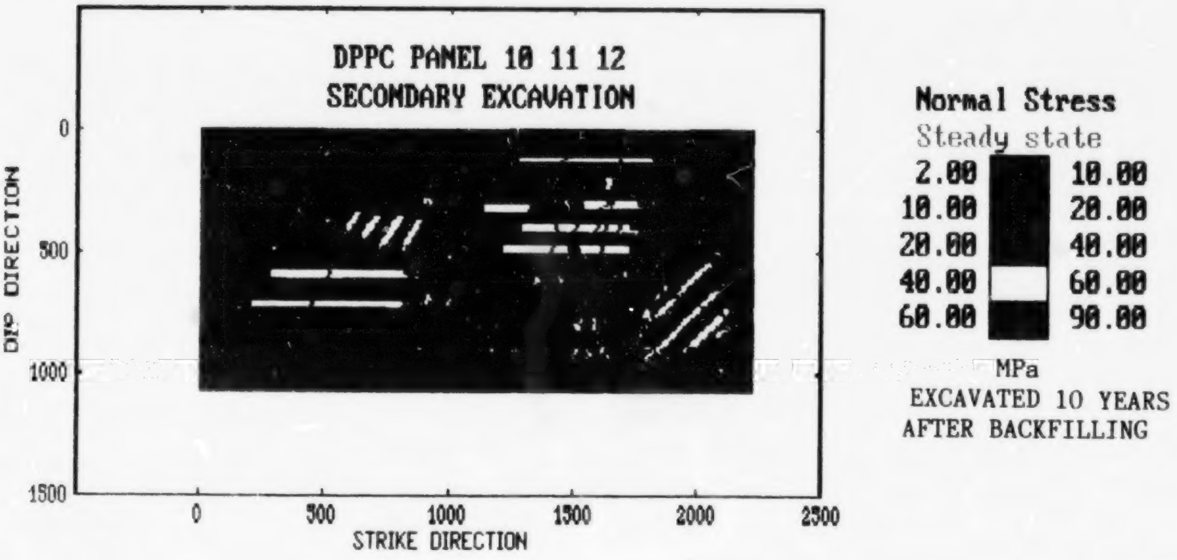

FIGURE 10.37

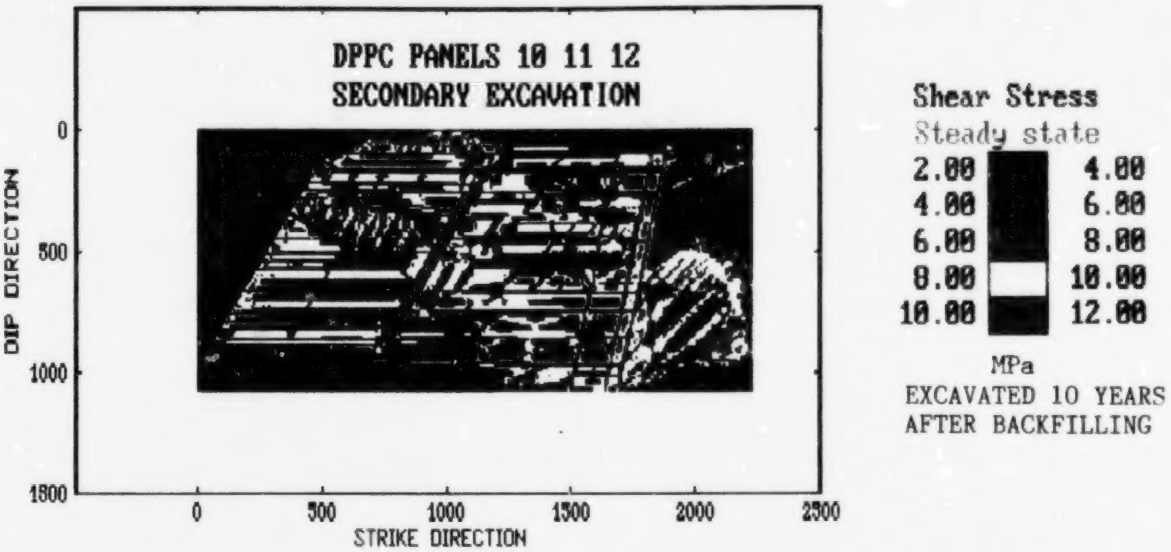

FIGURE 10.38

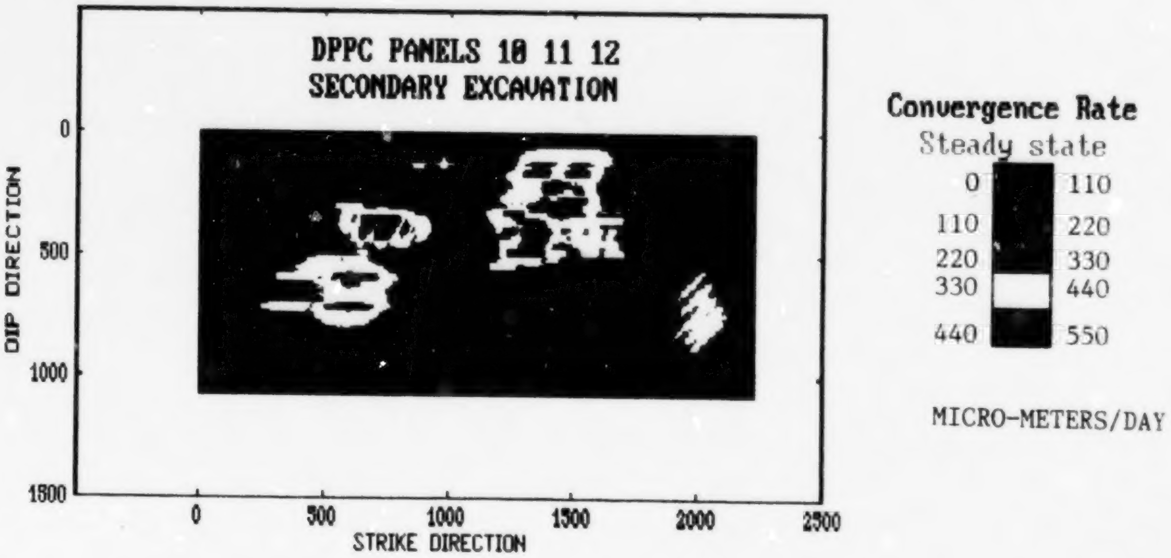

FIGURE 10.39

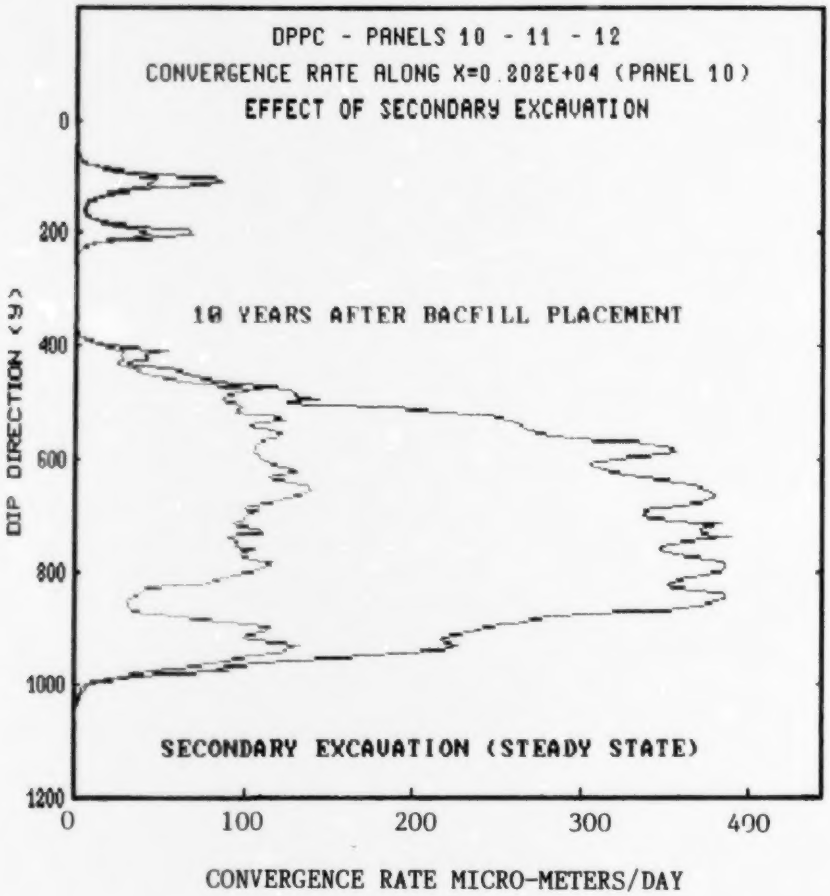
DPPC - PANELS 10 - 11 - 12
CONVERGENCE RATE ALONG X=0.202E+04 (PANEL 10)
EFFECT OF SECONDARY EXCAVATION
10 YEARS AFTER BACFILL PLACEMENT
SECONDARY EXCAVATION (STEADY STATE)
DIP DIRECTION (y)
0
200
400
600
800
1000
1200
0
100
200
300
400
CONVERGENCE RATE MICRO-METERS/DAY

FIGURE 10.40

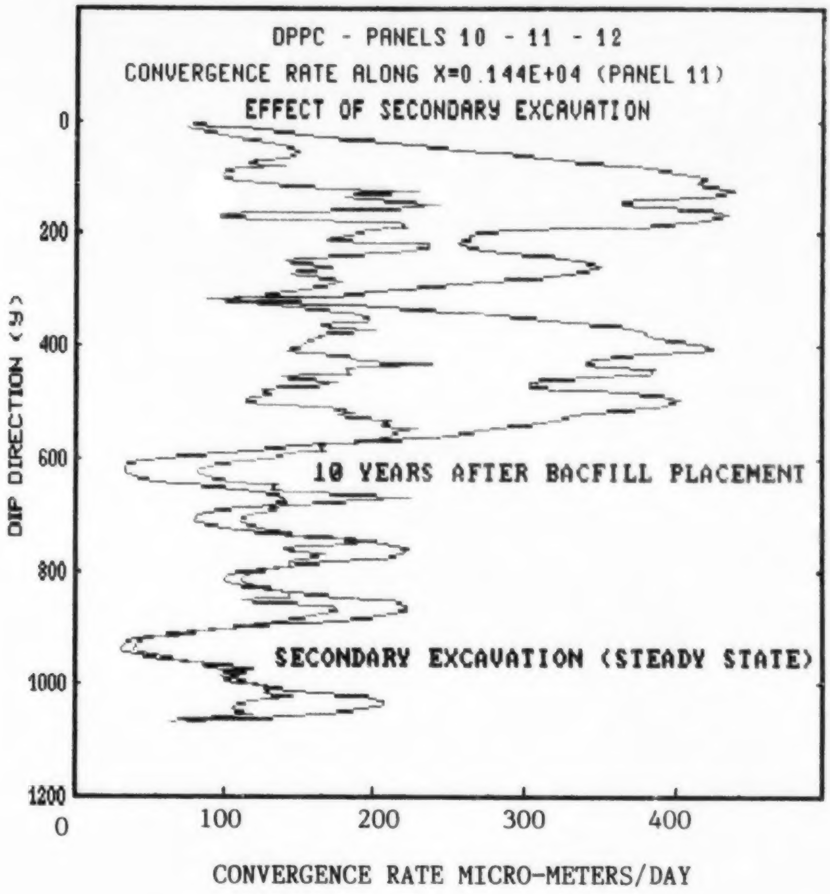
DPPC - PANELS 10 - 11 - 12
CONVERGENCE RATE ALONG X=0.144E+04 (PANEL 11)
EFFECT OF SECONDARY EXCAVATION
10 YEARS AFTER BACFILL PLACEMENT
SECONDARY EXCAVATION (STEADY STATE)
DIP DIRECTION (y)
0
200
400
600
800
1000
1200
0
100
200
300
400
CONVERGENCE RATE MICRO-METERS/DAY

FIGURE 10.41

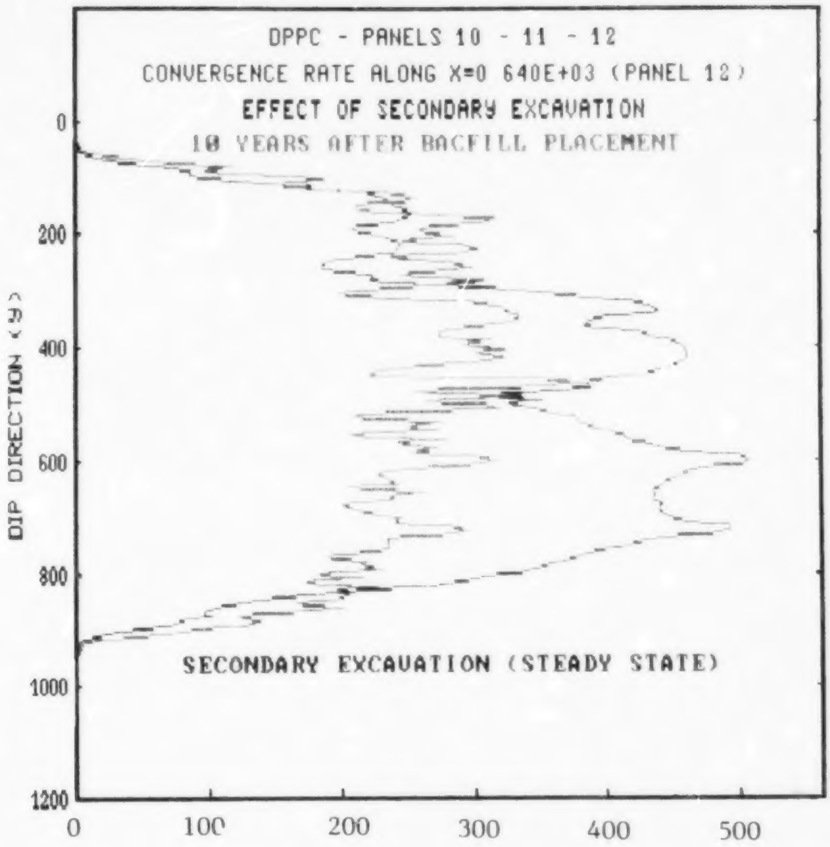

CONVERGENCE RATE MICRO-METERS/DAY

reached a required state of densification (i.e. fractional density > 0.7; Section 5.0), at the time of secondary mining, the load transfer will lead to failure.

In situ, secondary mining of pillars will occur gradually which will decrease support capabilities of pillars over an extended period of time instead of immediately. The gradual load transfer to backfilled stopes and remnant pillars will increase convergence rates and compaction rates, but over an extended period of time. The slightly increased compaction rate will potentially allow the backfill to reach a state of densification in which it can support overburden without failure (fractional density > 0.7). Hence, secondary mining could begin prior to 10 years after backfilling, which would accelerate compaction of backfill to a state at which it would competently support overburden strata.

SECTION 11.0

11.0 CONCLUSIONS AND RECOMMENDATIONS

11.1 Conclusions

1. The current method of dry backfill placement limits the initial net placement density to 1.26 g/cm^3 (0.6 fractional density), due to the inability to fill the stopes and rooms entirely. The feasibility study prepared by Denison-Potacan and underground trials indicate that the hydraulic backfill placement method is more efficient and will provide higher initial placement density.

2. Monitoring of strain rates in the roof and the wall of the Stope 11200, 42 metres wide and approximately 15 metres high, revealed two distinct strain rate intervals. In the roof, the strain rates within the interval from 0 to 7.5 metres were about an order of magnitude faster than the strain rates beyond 7.5 metres. Similarly, the strain rates within the interval of 0 to 15 metres in the wall were about an order of magnitude faster than the strain rates beyond 15 metres. The high strain rate interval within the roof (Figure 3.39) is attributable to development of separations (fractures) within the elliptical segment of "active opening" and the possible presence of geological planes of weakness (i.e. clay seams, etc.). The interval from 0 to 15 metres in the wall is clearly in the "high stress exponent" regime, while the interval beyond 15 metres is in the "low stress exponent" regime.

3. The oriented pressures measured by grouted flatjack cells in Stope 11200 show expected trends. Unfortunately, most of the instrumentation cables were severed by a ground fall and can no longer be monitored. The pressure in two flatjacks located in the centre of the pillar that continued to be monitored after the ground fall continued to rise as expected. Grouted pressure cells showed poor performance with pressure measurements being highly erratic. Subsequently, potash encapsulated pressure cells were installed showing good results to date.

4. The backfill pressure cells located within the backfill in Stope 11200 registered only a gravity load indicating that, within the time interval measured, no support was offered by backfill to the mine.

5. The convergence stations installed in Panel 11 recorded an average convergence rate of about 100 millimetres per year. This rate appeared to be quite uniform over the time period monitored indicating that the panel is converging at a steady state rate.

6. The instrumentation installed in the 3-entry system of Panel 12 indicated that the proposed 3-room layout provides a stress relief protection for the centre entry.

7. The maximum surface subsidence rate measured was 33.6 millimetres per year.

8. Based on the examination of laboratory behaviour, the following mechanisms are thought to dominate the volumetric creep deformation in halite backfill:
   (a) pressure solution at stresses of less than 2 MPa and volumetric strain rates of less than $10^{-6}s^{-1}$;
   (b) particulate sliding at volumetric strain rates above $10^{-6}s^{-1}$;
   (c) cataclasis upon a sudden imposition of stress.

   Based on the assumption that cataclasis is unlikely to operate in situ, an empirical two mechanism power law has been proposed and fitted to the experimental data.

9. Based on laboratory experiments, it was concluded that backfill with a fractional density of less than 0.7 has little or no unconfined strength, and that the uniaxial compressive strengths of backfill can be defined as a linear function of fractional density.

10. The stiffness of halite backfill was determined as a bulk measurement of the total instantaneous deformation, both recoverable elastic and non-recoverable cataclastic, the material undergoes when subjected to a deviatoric stress. The apparent stiffness was measured from the stress strain curves at 50% of the uniaxial compressive strength. The test results indicate that there is an exponential relationship between the apparent stiffness and density of backfill, and that backfill with fractional density of less than 0.7 has very little or no stiffness.

11. Triaxial brittle strength of backfill increases with density. The Mohr-Coloumb criterion was fitted to the brittle strength data and both the cohesion and the angle of internal friction could be defined as a linear function of density.

12. Mixing of sand into the halite backfill will reduce its initial placement porosity, thereby, reducing the total amount of consolidation required to achieve support.

13. Addition of cement into the halite backfill will decrease initial porosity and achieve early strength. Addition of 10% cement by volume results in a uniaxial compressive strength of about 2 MPa.

14. A parametric analysis of in situ and laboratory data on DPPC salt rocks, using Von Mises criterion, yielded new values for the creep parameters used in numerical modelling under this study. This produced results that were in close agreement with measured in situ behaviour of excavations.

15. The two-dimensional microcomputer program FLAC was used for all plane strain analyses. As part of this study, a numerical solution using FLAC was compared to the analytical solution for an infinitely long cylindrical cavity in a homogeneous continuum under a uniform stress field. A good correlation was obtained for closure rates as well as the radial and circumferential stresses.

16. The program VELMINA was used for three-dimensional analysis of all large scale mining layouts. The VELMINA code is a rigorous implementation of the displacement discontinuity method for visco-elastic medium and it was verified against the finite element code VISCOT. In order to confirm that the material laws and input parameters used in FLAC are valid for VELMINA, the existing mining geometry in Panel 10 and 11 (total existing mining geometry) was modelled by VELMINA and the results compared to the in situ convergence rate measurements. This comparison shows a very good agreement between the in situ convergence rates and the convergence rates predicted by VELMINA.

17. The steady state subsidence rates predicted by VELMINA were compared to the actual subsidence rates measured and a very good correlation was found. This is an indication that the strata over the DPPC mining area are subsiding correctly, without extensive bridging.

18. Numerical modelling of mine geometries with halite backfill was performed using both FLAC and VELMINA programs assuming the initial placement density of 1.4 g/cm^3 (fractional density of 0.65). Modelling indicated that the secondary mining of pillars may be possible 10 to 15 years after the initial placement of backfill, provided that the fractional placement density of backfill is 0.65 or higher. The effect of modelling backfill placement instantaneously is negligible because there is little change in backfill density during the time it takes to backfill a stope. However, gradual excavation, as in situ, of secondary mining stopes opposed to instantaneous excavation (i.e. numerical modelling) offers a potential reduction in the time to secondary mining. Gradual mining will potentially produce accelerated compaction of backfill resulting in backfilled stopes with overburden support capabilities which would allow earlier exploitation of pillars.

11.2 Recommendations

1. The initial average placement density of backfill in all future stopes should be 1.4 g/cm^3 (0.65 fractional density) or more. In order to achieve this initial placement density it is recommended to change from dry placement to hydraulic placement of halite backfill.

2. Wherever possible the open spaces in the existing backfilled stopes should be hydraulically backfilled to achieve an average backfill density of no less than 1.4 g/cm^3.

3. At least one set of backfill pressure cells should be placed in several backfilled stopes to monitor the backfill performance in the future.

4. The functional instrumentation in Stope 11200 should be reconnected and monitored regularly to collect long term data on backfilled stope.

5. The three-dimensional program VELMINA should be used for modelling large mining layouts in the future. Two-dimensional modelling can be handled by the program FLAC.

6. Continue monitoring subsidence and expand the array of subsidence stations over Panel 12.

7. Further investigation of engineered backfill using cement is warranted. It is recommended to investigate if the cement content could be reduced through use of a flocculant.

8. The results of this study indicate that the secondary mining in backfilled areas may be possible within 10 to 15 years after the backfill placement. It is recommended that this conclusion be confirmed through long term monitoring of backfilled areas. The samples of compacted backfill should be taken from selected locations annually and tested in order to obtain a long term history of in situ backfill behaviour.

9. Investigation of the effect upon backfilled stopes of sequential excavation of a secondary mining stope versus instantaneous excavation, as used in this study, is warranted. It is recommended that both two and three dimensional modelling of this situation be performed.

SECTION 12.0

12.0 REFERENCES

Ashby, M.R., and Brown, L.M., Perspectives in Creep Fracture, Pergamon Press, 1983.

Baar, C.A., 1977. Applied Salt Rock Mechanics I. Elsevier Scientific Publishing Co., Amsterdam, Netherlands.

Beddoes, R.J., 1984. Determination of Engineering Properties of Salt for Backfilling in Underground Potash Mines. Prepared by RE/SPEC Inc., Calgary, for the Canadian Centre for Mineral and Energy Technology, Project No. 310104.

Beddoes, R.J., Streisel, J.J., and Roulston, B.V. July 1989. Implementation of an Integrated Rock Mechanics Programme for Cut and Fill Potash Mining. Potash Company of America, Division of Rio Algom Ltd., Sussex, New Brunswick.

Burton, B., 1977. Diffusional Creep of Polycrystalline Materials. Trans Tech Publications, Aedermannsdorf, Switzerland. 119 p.

CANMET, 1987. Use of Backfill in New Brunswick Potash Mines. Prepared by Denison Potacan Potash Co., Mraz Project Consultants Ltd, and University of Waterloo, for the Canada Centre for Mineral and Energy Technology, Dept. of Energy Mines and Resources. Five Volumes.

Carter, N.L., and Hansen, F.D., 1983. Creep of Rocksalt. Tectonophysics, vol. 92, pp. 375-383.

Craig, R.F., 1978. Soil Mechanics. Van Nostrand Reinhold Co. Ltd., Scarborough.

Dusseault, M.B., Rothenburg, L., and Mraz, D.Z., 1987. The Design of Openings in Salt Using a Multiple Mechanism Viscoplastic Law. Proceedings of the 28th US Symposium on Rock Mechanics, Tuson, Arizona. pp. 633-642.

Evans, H.E., 1984. Mechanisms of Creep Fracture. Elsevier Applied Science Publishers, New York. 319 p.

Farmer, I.W., 1983. Engineering Behaviour of Rocks, 2nd Edition. Chapman and Hall Ltd., New York.

Fordham, C.J., 1988. Behaviour of Granular Halite for Use as a Backfill in Potash Mines. Phd Thesis, University of Waterloo, Waterloo, Ontario.

Fordham, C.J., Dusseault, M.B., and Mraz D., 1988. Strength Development in Halite Backfill. Proceedings of the 41st Canadian Geotechnical Conference, Waterloo, Ontario. pp. 194-200.

Hart, R.D., Larig, L.J., Board, M., Mack, M.G., and Wahi, K. March 1987. A Review of Thermomechanical Analysis Methodologies for NNWSI, BWIP and SRP. ITASCA Consulting Group Report, US Nuclear Regulatory Commission, Contract No. NRC-02-85-002.

Holcomb D.J., and Hannum, D.J., 1982. Consolidation of Crushed-Salt Backfill Under Conditions Appropriate to the WIPP Facility. Report No. SAND82-0630, Prepared by Sandia National Laboratory, Albequerque, NM for U.S. Dept. of Energy.

Holcomb D.J., and Shields, M., 1987. Hydrostatic Creep Consolidtion of Crushed Salt with Added Water. Prepared by Sandia National Laboratory, Albequerque, NM for the U.S. Dept. of Energy, Contract No. DE-AC04-76DP00789.

Horton, C.A.P., 1976. Grain Boundary Sliding and its Accommodation During Creep of Polycrystalline Materials, in Grain Boundaries, Proceedings of the Institution of Metallurgists Spring Residential Conference, Jersey. pp. E1-E6.

IT Corp., 1987. Laboratory Investigation of Crushed Salt Consolidation and Fracture Healing. Report no. BMI/ONWI-631, Prepared for the Office of Nuclear Waste Isolation, Battelle Memorial Institute, Columbus, OH.

ITASCA Consulting Group, Inc. 1987. FLAC: Fast Langarian Analysis of Continua, User Manual, Version 2.0. Minneapolis, MN.

ITASCA Consulting Group, Inc. 1988. Thermal-Mechanical Benchmark Testing of FLAC, US Nuclear Regulatory Commission Division of Waste Management Contract No. NRC-02-85-002.

Jaeger, J.C., and Cook, N.G.W., Fundamentals of Rock Mechanics, Chapman & Hall, Third Edition 1979.

Johnson, R.F., Lamb, K.N., Hart, R.T., Reid, K.W., 1984. Investigation of the Physical and Chemical Characteristics of Potash Tailings in Saskatchewan. Prepared by Potash Corporation of Saskatchewan, Saskatoon, for Canada Centre for Mineral and Energy Technology, Project No. 350204.

Kappei, G., 1986. Geotechnical Investigations on Backfill Materials in the Asse Salt Mine. Presented at the US/FRG Workshop on Sealing and Backfilling of a Salt Repository, Albuquerque, N.M., Sept. 23-25, 1986.

Kelsall, P.C., and Nelson, J.W., 1983. Geologic and Engineering Characteristics of Gulf Region Salt Domes Applied to Underground Storage and Mining. In Proceedings of the Sixth International Symposium on Salt, vol. 1. B.C. Schreiber and H.L. Harner eds. The Salt Institute, Alexandria, VA., pp. 519-544.

Kilborn Limited & Canadian Mine Services Ltd. October 1982. Denison Potacan Potash Company New Brunswick Potash Project Feasibility Report, Volume III.

Lajtai, E.Z. and Duncan, E.J. The Mechanism of Deformation and Fracture in Potash Rock, Final Report for CRD Project 0038997, University of Manitoba, 1988.

Langdon, T.G., 1973. Grain Boundary Sliding in a Magnesium Alloy and Pure Aluminium, in Third International Conference on the Strength of Metals and Alloys, Vol. 1. The Metals Society, London. pp. 222-226.

Marti, J., and Cundall, P.A. 1982. Mixed Discretization Procedure for Accurate Solution of Plasticity Problems. International Journal of Numerical Methods. England. pp. 129-139.

Morgan, H.S., Krieg, R.D., and Matalucii, R.V. 1981. Comparative Analysis of Nine Structural Codes Used in the Second WIPP Benchmark Problem. Sandia Report SAND81-1389.

Munson, D.E., Preliminary Deformation Mechanism Map for Salt, SAND79---76, Sandia National Laboratories Report, 1979.

Munson, D.E., and Dawson P.R., A Transient Creep Model for Salt During Stress Loading and Unloading, SAND82-0962, Sandia National Laboratories, Albuquerque, New Mexico, 1982.

Munson, D.E., and Fossum, A.F., Comparison Between Predicted and Measured South Drift Closures at WIPP Using a Transient Creep Model for Salt, 27th US Rock Mechanics Symposium, Alabama, 1986.

Pfeifle, T.W., Senseny, P.E., and Mellegard, K.D., 1987. Influence of Variables on the Consolidation and Unconfined Compressive Strength of Crushed Salt. Report no. BMI/ONWI-627, prepared by RE/SPEC Inc. for the Office of Nuclear Waste Isolation, Battelle Memorial Institute, Columbus, OH.

Poirier, J.P., 1985. Creep of Crystals. Cambridge University Press, Cambridge, England. 260 p.

Pufahl, D.E., and Yoshida, R.T., 1982. A Study of Potash Tailings: Properties and Behaviour for Total Extraction Mining. Prepared by University of Saskatchewan Civil Engineering for Potash Corporation of Saskatchewan.

Raj, R., 1982. Creep in Polycrystalline Aggregates by Matter Transport through a Liquid Phase. Journal of Geophysical Research, vol. 87, no. B6, pp. 4731-4739.

Raj, R., and Chyung, 1981. Solution-Precipitation Creep in Glass Ceramics. Acta Metallurgica, vol. 29, pp. 159-166.

Rothenburg, L., Constitutive Behaviours of Salt Rock and Thermo-Mechanical Aspects of Waste Package Performance in Bedded Salt, report for Stone and Webster Engineering Corporation under contract with United Stated Department of Energy, 1988.

Rutter, E.H., 1976. The Kinetics of Rock Deformation by Pressure Solution. Philosophical Transactions of the Royal Society of London A, vol 283, pp. 203-219.

Sjaardema, G.D., and Krieg, R.D., 1987. A Constitutive Model for the Consolidation of WIPP Crushed Salt and Its Use in Analyses of Backfilled Shaft and Drift Configurations. Report SAND87-1977 Prepared by Sandia National Laboratories, Albuquerque, N.M. under contract DE-AC04-76DP00789.

Sklenicka, V., Pahutova, M., and Cadek, J., 1973. Grain Boundary Behaviour in Creep of a Dispersion Strengthened Aluminium Alloy, in Third International Conference on the Strength of Metals and Alloys, Vol. 1. The Metals Society, London, pp. 207-212.

Skrotzki, W, and Haasen, P., 1984. The Role of Cross Slip in the Steady State Creep of Salt, in the Proceedings of the Second Conference on the Mechanical Behaviour of Salt, H.R. Hardy Jr., and M. Langer eds. Hanover Germany, pp. 83-88.

Spiers, C.J., Peach, C.J., Brzesowsky, R.H., Schutjens, P.M.T.M., Liezenberg, J.L., and Zwart, H.J., 1989. Long Term Rheological and Transport Properties of Dry and Wet Salt Rocks. Final Report to the Commission of the European Communities, CEC Contract no. FI1W-0051-NL.

Terzaghi, K., and Peck, R.B., 1967. Soil Mechanics in Engineering Practice. John Wiley and Sons Ltd., New York. 729 pp.

Theissing E.M., Hest-Wardenier, P.v., and de Wind, G., 1978. The combining of Sodium Chloride and Calcium Chloride by a number of Different Hardened Cement Pastes. Cement and Concrete Research, vol. 8, pp. 683-691.

Valliappan, S., 1981. Continuum Mechanics Fundamentals. A. A. Balkema, Rotterdam.

Van Sambeek, L.L., May 1986. Creep of Rock Salt Under Inhomogeneous Stress Conditions. Coloardo School of Mines, Golden, Colorado.

Wakely, L.D., Scheetz, B.B., Grutzeck, M.W., and Roy, D., 1981. Characterization of Samples of a Cement Borehole Plug in Bedded Evaporites from Southeastern New Mexico. Cement and Concrete Research, vol. 11, pp. 131-142.

Waugh, D.C.E., and Urquhart, B.R., 1983. The Geology of Denison-Potacan's New Brunswick Potash Deposit. In Proceedings of the Sixth International Symposium on Salt, Vol. 1. B.C. Schreiber and H.L. Harner eds. The Salt Institute. Alexandria, VA. pp. 85-113.

Wayment, W.R., 1978. Backfilling with Tailings-A new Approach. In Proceedings of the 12th Canadian Rock Mechanics Symposium; Mining with Backfill. Canadian Institute of Mining and Metallurgy, Sudbury, May 23-25, 1978.

Yost, F.G., and Aronson, E.A., 1987. Crushed Salt Consolidation Kinetics. Prepared by Sandia National Laboratories, Albequerque, NM for the U.S. Dept. of Energy, Contract No. DE-AC04-76DP00789.

APPENDIX A
TECHNICAL ASPECTS OF VELMINA CODE

A.1 Technical Aspects of VELMINA Code

As was mentioned previously, the basic formulation in the VELMINA code assumes linearly visco-elastic behaviour of host rock outside of the mining horizon. This assumption makes it possible to use the entire mathematical apparatus of the Displacement Discontinuity Method for linearly viscous materials by using the well-known formal analogy between displacement fields in linearly elastic incompressible solids and velocity fields in a Newtonian (linearly viscous) fluid.

The origin of the analogy between behaviour of incompressible elastic solids and Newtonian fluids is related to the fact that in a linearly viscous media strain rate $\dot{\epsilon}_{ij}$ is related to stress deviator σ'_{ij} as follows:

$$\dot{\epsilon}_{ij} = \sigma'_{ij}/2\mu \tag{A.1}$$

where μ is dynamic viscosity. The above relationship implies incompressibility to flow $\dot{\epsilon}_{kk} = 0$ since $\sigma'_{kk} = 0$. The previous relationship is mathematically equivalent to generalized Hooke's law for an elastic material with Poisson's ratio $\nu = 0.5$ and shear modulus $G = \mu$. In this analogy, the strain rate $\dot{\epsilon}_{ij}$ corresponds to elastic strain ϵ_{ij}. Due to this formal correspondence, a velocity field in a linearly viscous fluid can be found by determining a displacement field in an incompressible linearly elastic for the same boundary conditions as in the original problem. As a result, the displacement discontinuity solutions of linear elasticity taken for $\nu = 0.5$ are sufficient to describe the discontinuity in velocities of viscous flow across the mining plane. In a sense, the described method can be referred to as the "Velocity Discontinuity Method".

A.1.1 The Velocity Discontinuity Method

Technical details of the VELMINA code can be best outlined for the case of direct steady state field around the mine. Further description follows rather standard logic of the displacement discontinuity method in application to mining.

Let the mining plane be subdivided into N "face elements" representing mine pillars and excavated areas. The steady state creep rate in the host rock is discontinuous in crossing the mining plane from roof to floor of the mine. Let the magnitude of the rate discontinuity associated with element i at location r_i be d_i. As a result of this discontinuity in flow rates, the material at locations r_k corresponding to centres of other "face elements" flows with the rate $\dot{u}_k = d_i F(r_i - r_k)$, where F is a function representing the displacement discontinuity of linear elasticity computed for $\nu = 0.5$ (Wardle, 1980). Vertical stress at centres of face elements can also be computed in the same form with an appropriate influence function "S" [i.e. $\sigma_k = \dot{d}_i S(r_i - r_k)$], where σ_k represents stress normal to the face of the element at location r_k due to rate discontinuity $\dot{d}_i$ at r_i. The stress induced at location r_k as a result of all rate discontinuities is as follows:

$$\sigma_k = \sum_{j=1}^{N} \dot{d}_i S(r_i - r_j) \qquad \text{(A.2)}$$

The set of rate discontinuities $\dot{d}_i$ are unknown quantities and must be determined. In excavated areas, stresses induced by rate discontinuities must be negative of the in situ stress. In elements representing pillars, the roof-floor discontinuity rate $\dot{d}_i$ must be the same as the rate of pillar compression h. The latter is a function of stress σ_j at location r_j as well as r_j itself [i.e. $h_j = f(\sigma_j, r_j)$]. The set of equations for determining the rate discontinuities is as follows:

$$\sum_{i=1}^{N} \dot{d}_i S(r_i - r_j) + \sigma_j^o = 0 \qquad \text{for excavated areas} \qquad \text{(A.3)}$$

$$\dot{d}_j = f(\sigma_j, r_j)_i \; \sigma_j = \sum_{i=1}^{N} \dot{d}_i S(r_i - r_j) + \sigma^o_j \qquad \text{for pillars} \qquad \text{(A.4)}$$

where σ^o_j is the in situ stress normal to the mining plane. The above system of N equations for N unknown rate discontinuities is solved iteratively.

A.1.2 Mathematical Model of Pillars

In the described formulation, the mechanical response of pillars is essentially represented by a mathematical model reflected in the relationship $h_j = f(\sigma_j, r_j)$. By its physical nature, the function $f(\sigma, r)$ describes the steady state compression rate of an element of a pillar that is under normal stress σ and is located at position r in the mine. In actual applications, it is assumed that $f(\sigma, r)$ depends only on the location within the pillar itself and is independent on arrangement of other pillars in the mine. With this assumption $f(\sigma, r)$ can be derived by doing finite element analysis of a single pillar. The method for deriving $f(\sigma, r)$ is described in the following paragraphs.

Consider first a long pillar of height H and width B that can be analyzed by Finite Element Method (FEM) in plane strain approximation. Let x refer to a coordinate describing the location within the pillar and selected in such a way that x = 0 in the middle of the pillar. Assume for simplicity that the material of the pillar follows a single mechanism power law. The vertical compression rate of the pillar h(x) at the location x can be given in the form

$$h(x) = \int_0^H \dot{\epsilon}_{yy}(x,y)\,dy \tag{A.5}$$

The strain rate in VELMINA is computed according to the following relationship

$$\dot{\epsilon}_{ij} = \dot{\epsilon}_o \frac{3}{2} \frac{\dot{\sigma}_{ij}}{\sigma_{eff}} \left[\frac{\sigma_{eff}}{\sigma_o}\right]^M \tag{A.6}$$

where $\dot{\epsilon}_o$, σ_o, M are material constants, $\sigma_{eff} = \left[\frac{3}{2}\sigma'_{ij}\sigma'_{ij}\right]$, and different exponents can be used for effective stresses above and below σ_o .

Determination of vertical compression h required the knowledge of stress distributions in pillars and further integration over the height of the pillar. Stresses σ_{xx} and σ_{xy} averaged over the height of the pillar were determined from series of finite element runs on rectangular and circular pillars and were expressed as ratios σ_{xx}/σ_{yy} and σ_{xy}/σ_{yy}, where σ_{yy} refers to stress at mid-height of the pillar at distance x from its center. A total of 96 FEM analyses were carried out for exponent values M = 1, 2, 3, 4, 5, 6 and pillar widths/height ratio B/H = 1.250, 1.875, 2.500, 3.125, 3.750, 4.375, 5.000, 5.625. Data was generalized in analytical form to arrive at functions σ_{xx}/σ_{yy} (x/B,B/H,M) required to determine the steady state compression rate of pillars. Some of these average ratios involved in (A.6) are illustrated in Figures A.1 and A.2.

Based on the study of stress distributions in infinitely long and circular pillars, the procedure implemented in VELMINA for describing confining stresses in rectangular pillars is as follows.

For each element, a subroutine GEOMETRY determines minimum and maximum distances of the element from excavated areas. Vertical creep rate is computed according to the relationship:

$$h/H = \dot{\epsilon}_0 \frac{3}{2} \frac{\sigma'_v}{\sigma_{eff}} \left[\frac{\sigma_{eff}}{\sigma_0}\right]^M \qquad (A.7)$$

The stress-independent ratio $\frac{\sigma'_v}{\sigma_{eff}}$ taken by linearly interpolating between values corresponding to circular and infinitely long pillars is as follows:

$$\frac{\sigma'_v}{\sigma_{eff}} = \left[\frac{\sigma'_v}{\sigma_{eff}}\right]_{circular} (B/L) + (1 - B/L) \left[\frac{\sigma'_v}{\sigma_{eff}}\right]_{infinite} \qquad (A.8)$$

where B is the minimum distance between excavated areas along the line crossing given elements and, similarly, L is the maximum distance between excavated areas. The effective stress σ_{eff} is computed by determining average confining stresses ratios σ_{xx}/σ_{yy}, σ_{xy}/σ_{yy}, σ_{xz}/σ_{yy}, and σ_{zz}/σ_{yy} at minimum distances from the excavated areas based on functions determined for infinitely long pillars. As Figure A.2 suggests, the difference between these ratios for infinitely long and circular pillars is small. Henceforth, it is possible to interpolate between infinitely long and circular pillars although this is not currently implemented in VELMINA.

FIGURE A.1

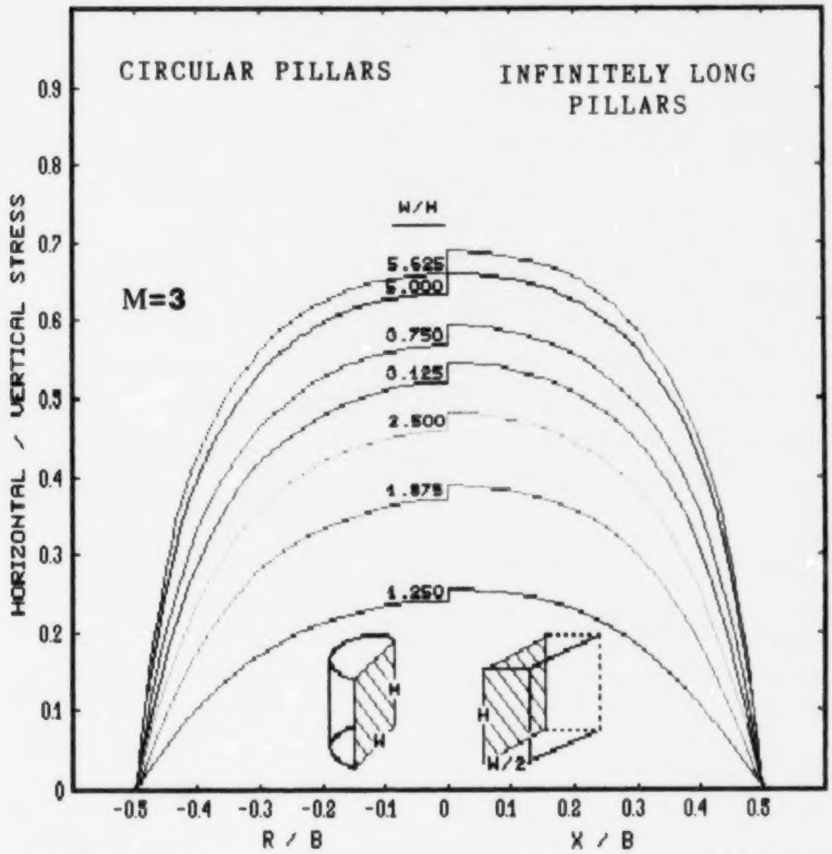

DISTRIBUTION OF HORIZONTAL/VERTICAL STRESS RATIOS
PILLARS OF DIFFERENT WIDTH TO HEIGHT RATIOS

FIGURE A.2

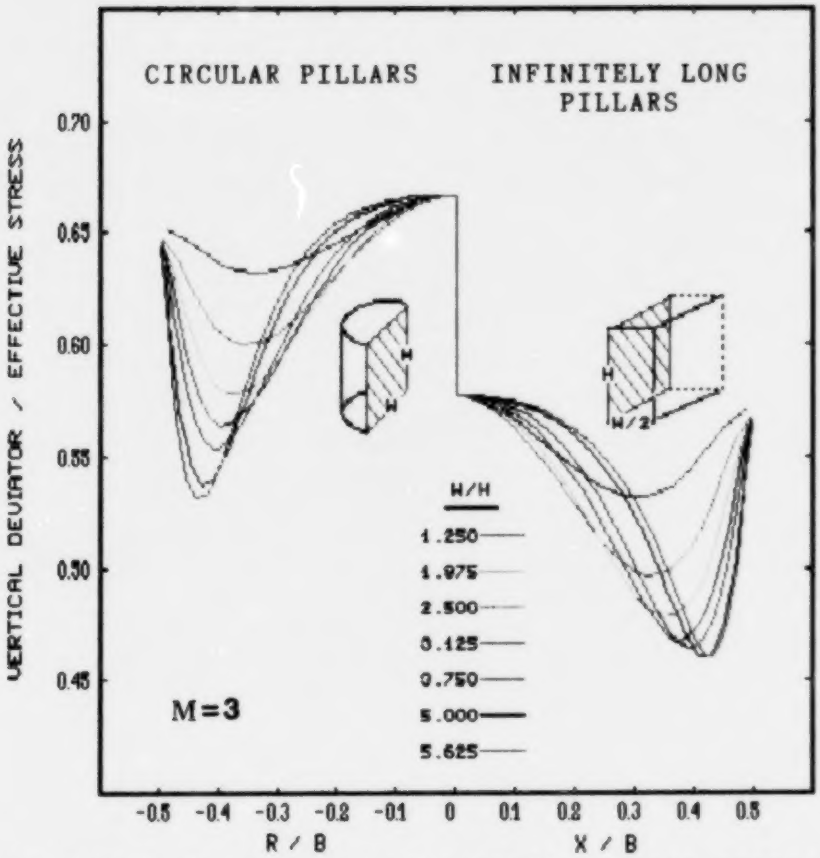

DISTRIBUTION OF VERTICAL DEVIATOR/EFFECTIVE STRESS RATIOS
PILLARS OF DIFFERENT WIDTH TO HEIGHT RATIOS

FIGURE A.3

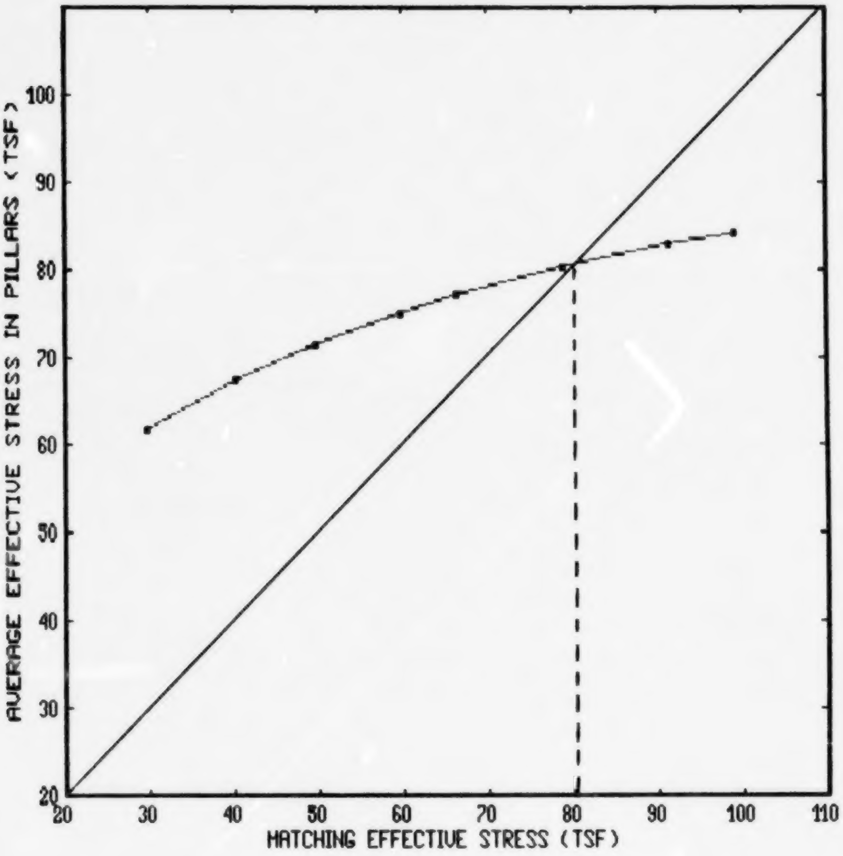

Average Effective Stress In Pillar vs Matching Effective Stress

A.1.3 Determination of Equivalent Linear Viscosity

Observations on many finite element computations that involve non-linear creep suggest that both in pillars and in areas adjacent to pillars there is a tendency to equalize shear stress. This effectively minimizes differences in creep rates in different areas on the mine. In VELMINA, the equivalent viscous properties of the roof are assigned in such a way that vertical strain rates in pillars and the roof are equal on average. If σ_{eff} is the effective stress computed for some element, the associated effective strain rate is $\dot{\epsilon}_{eff} = \dot{\epsilon}_o (\sigma_{eff} / \sigma_o)^M$ and linear dynamic viscosity μ is calculated to match this rate for this σ_{eff}. This computation is done for every element and average of viscosities computed in this way is taken over the entire layout. The problem is reanalysed until $\overline{\mu}$ does not change from iteration to iteration. This procedure is rather laborious and used rarely. In practice, an initial assessment of average effective stress in pillars is done by computing vertical stresses from tributary areas, then the average effective stress in pillars is assessed based on geometry-related vertical to effective stress ratios. Dynamic viscosity is then assigned to match creep rates at this effective stress. After the first iteration with the initially assessed viscosity, new $\overline{\sigma}_{eff}$ is calculated. In two iterations, one can determine a relationship between the matching stress and $\overline{\sigma}_{eff}$ and interpolate linearly to determine a point when the average effective stress and the matching stress for calculation of the equivalent viscosity become equal. A relationship between the matching stress and the average effective stress for a test program described in the next section is illustrated in Figure A.3.

A.2 Test Problem

Performance of VELMINA can be assessed by comparing its results with results of FEM calculations. Figure A.4 illustrates an infinite room sequence of three 60 ft by 80 ft high pillars with 120 ft by 80 ft pillars in between. Steady state stresses for this layout were determined using FEM code VISCOT and compared with the same layout, Figure A.5, analyzed by VELMINA. In this run VELMINA's periodic boundary condition option was used. Figure A.6 illustrates a very favourable comparison of loads on pillars computed by VISCOT and VELMINA. Closure rates, illustrated in Figure A.7, match very

FIGURE A.4

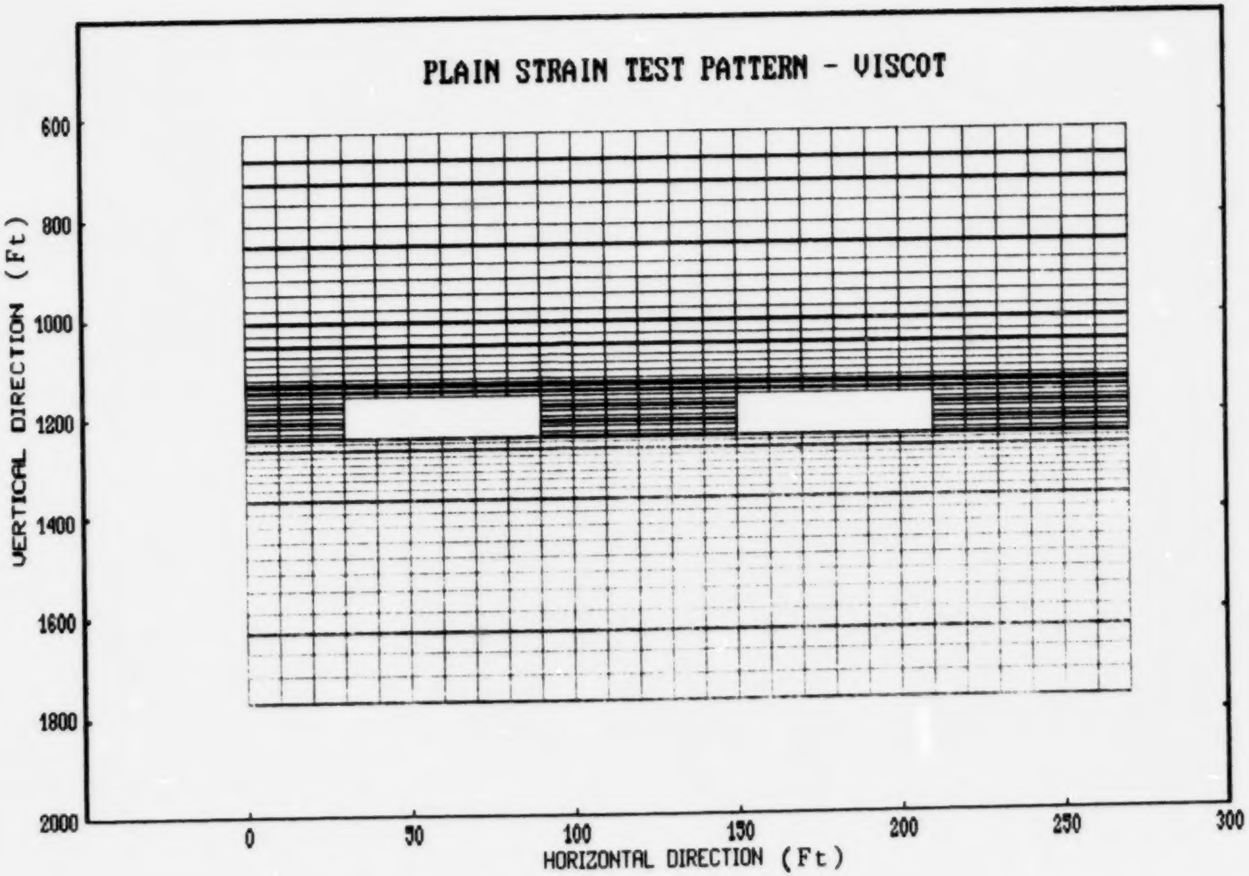
PLAIN STRAIN TEST PATTERN - VISCOT
VERTICAL DIRECTION (Ft)
1600
1800
2000
HORIZONTAL DIRECTION (Ft)

FIGURE A.5

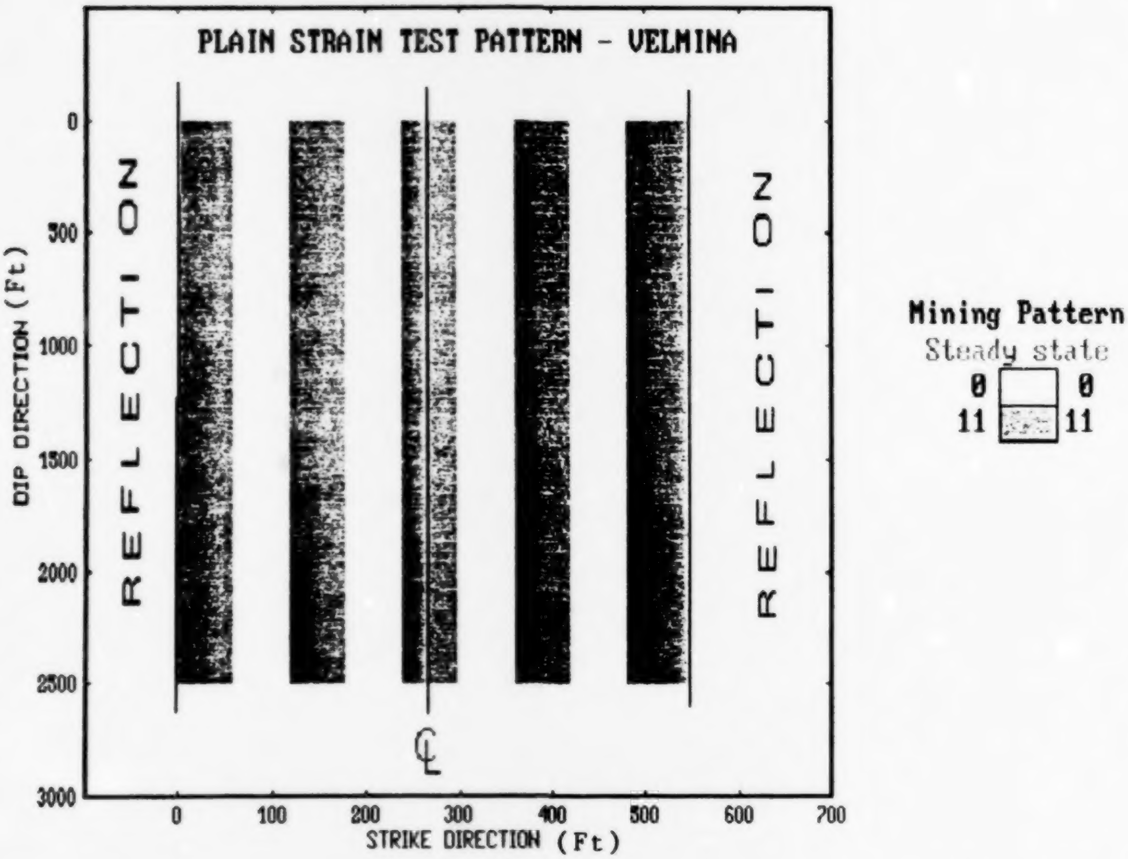
PLAIN STRAIN TEST PATTERN - VELMINA
DIP DIRECTION (Ft)
0
500
1000
1500
2000
2500
3000
STRIKE DIRECTION (Ft)
0
100
200
300
400
500
600
700
REFLECTION
REFLECTION
℄
Mining Pattern
Steady state
0
0
11
11

FIGURE A.6

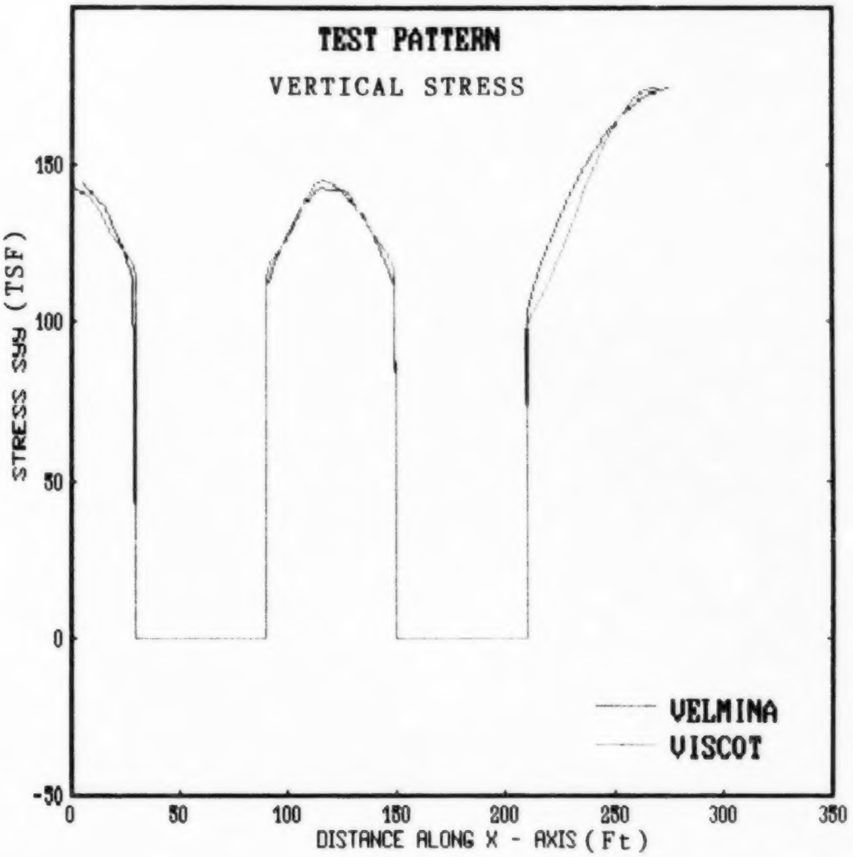
TEST PATTERN
VERTICAL STRESS
STRESS Syy (TSF)
150
100
50
0
-50
0
50
100
150
200
250
300
350
DISTANCE ALONG X - AXIS (Ft)
VELMINA
VISCOT

FIGURE A.7

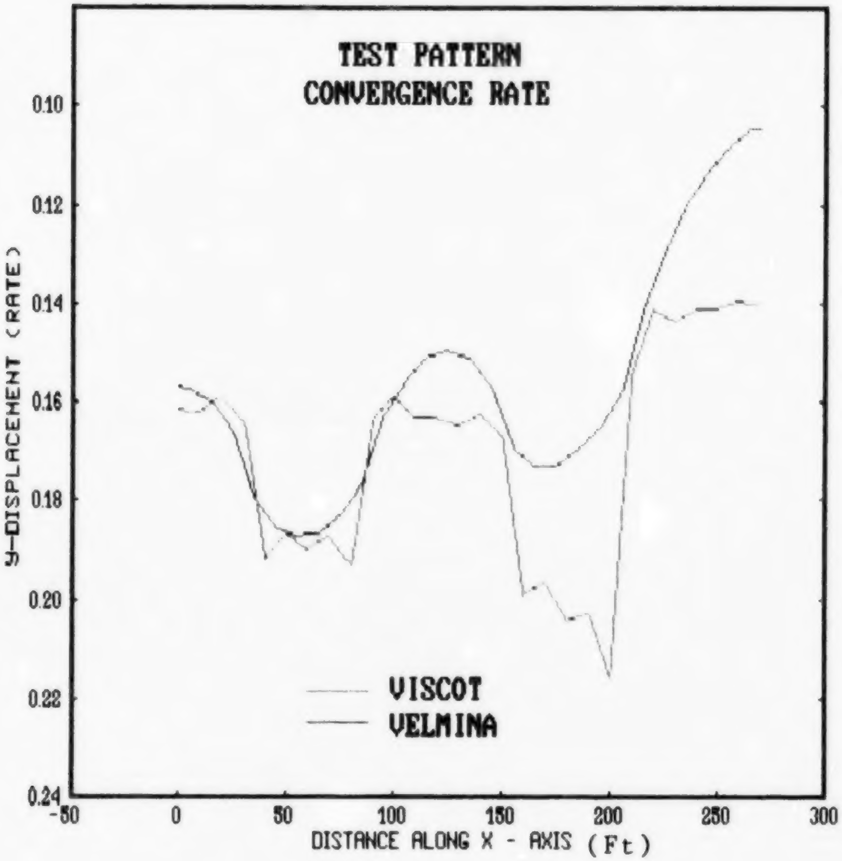
TEST PATTERN
CONVERGENCE RATE
y-DISPLACEMENT (RATE)
0.10
0.12
0.14
0.16
0.18
0.20
0.22
0.24
-50
0
50
100
150
200
250
300
DISTANCE ALONG X - AXIS (Ft)
VISCOT
VELMINA

FIGURE A.8

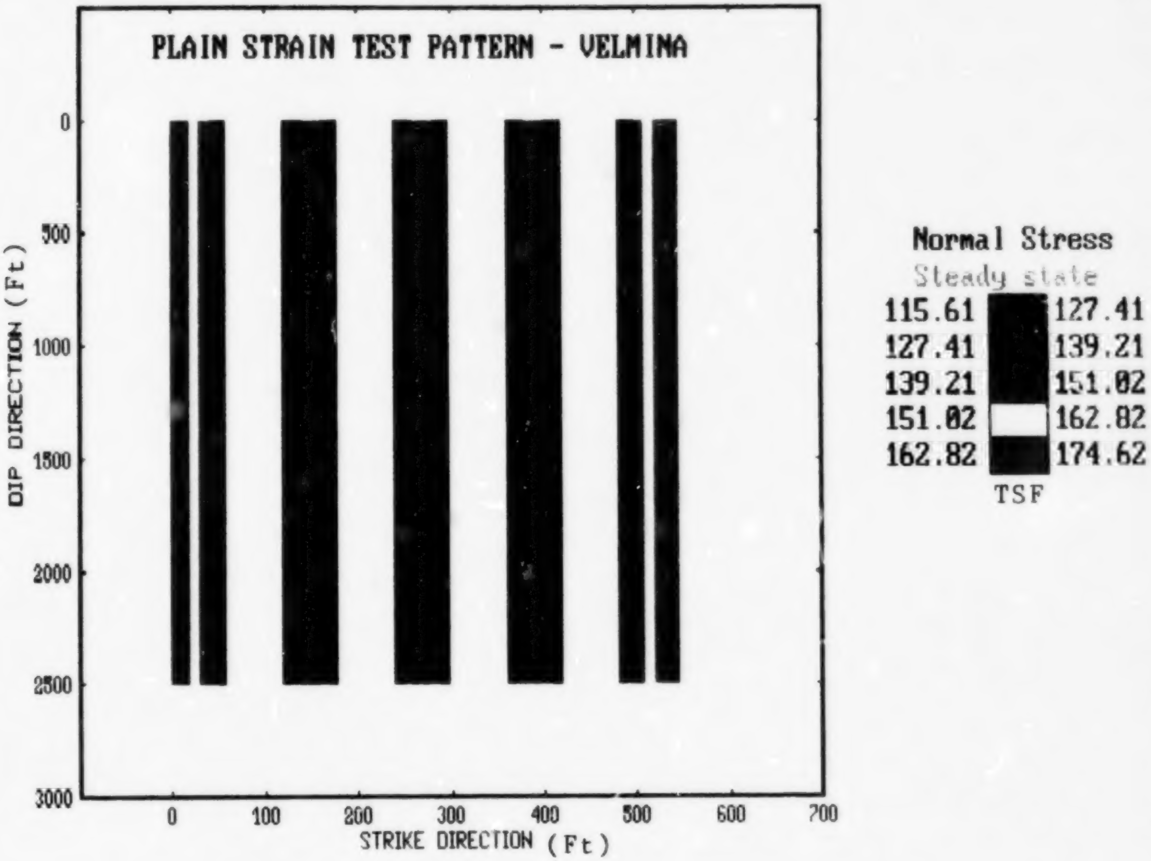
PLAIN STRAIN TEST PATTERN - VELMINA
DIP DIRECTION (Ft)
0
500
1000
1500
2000
2500
3000
STRIKE DIRECTION (Ft)
0
100
200
300
400
500
600
700
Normal Stress
Steady state
115.61 127.41
127.41 139.21
139.21 151.02
151.02 162.82
162.82 174.62
TSF

closely in the area of small pillars and match "on average" near the large pillar. This match of closure rates on average is inherent in the formulation of the code since equivalent linear stiffnesses are used in computations. Work is underway to accommodate true non-linear behaviour of material in the roof.

APPENDIX B

NUMERICAL MODELLING WITH VISCOT

B.1 Introduction

The program VISCOT was initially written by INTERA Consultants for the Office of Nuclear Waste Isolation in the United States. Modifications were made to the program by Dr. L. Rothenburg of the University of Waterloo. VISCOT is a non-linear, transient, thermal stress finite element code designed to determine the visco-elastic, visco-plastic or elasto-plastic deformation of a rock mass due to mechanical and thermal loading.

In the original VISCOT code, an error in handling an out-of-plane stress component was present. The error affected the time it took a problem to reach steady state and was not critical. This error was corrected for the current version, and several new features that improve VISCOT were introduced into the code. A function for automatic initial timestep selection and control and a bulk pressure correction to prevent the phenomenon of "shear locking" were added.

These modifications and subsequent verification of the program VISCOT were a necessity for the study. It was necessary to have a verified version of VISCOT for the following reasons:

1. VISCOT was used to derive a series of functions that would predict the mechanical response and the steady-state compression rate of pillars, which was subsequently implemented into the program VELMINA.

2. VISCOT was used to verify and assess the performance of the numerical models, VELMINA and FLAC, that were used extensively for this study.

3. VISCOT was used to re-evaluate the material properties and creep parameters that were used in Phase I, and subsequently determined the correct values to be used in Phase II of the study.

B.2 Finite Element Method of Numerical Modelling

Finite element is a numerical technique for solving a system of equations over a given domain. It is similar to the finite difference method in that an approximate solution is sought at a finite number of points (i.e. nodes). However, the continuum is divided into a number of elements which are joined at a discrete number of points along their boundaries.

By using the physical properties of the continuum and the appropriate constitutive law, a set of simultaneous equations can be obtained. The set of equations is in the form of a large banded global matrix. The matrix is solved for each timestep until a state of equilibrium is reached.

B.3 Technical Limitations

The disadvantages that occur using **VISCOT** (which make **FLAC** a more convenient program to use) are listed below:

- It is incapable of modelling discontinuities;
- The program does not easily permit sequential excavation or backfilling;
- Post and pre-processors are user unfriendly at present;
- Calculations are done assuming small strain mode (i.e. no coordinate updating);
- The global matrix limits the size of the problem that can be solved due to memory limitations.

B.4 Verification of VISCOT (Comparison of Analytical and Numerical Solutions)

A numerical solution obtained using VISCOT was compared to the analytical solution for closure of an infinitely long cylindrical cavity. The numerical solution was obtained using a uniform stress field under virgin ground conditions.

A comparison of the analytical and numerical solutions for the closure rate of a circular opening is illustrated in Figure B.1 Analysis shows very good correlation. Similarly, agreement between the two solutions is shown in Figures B.2 and B.3 for the radial and circumferential stresses, respectively.

FIGURE B.1

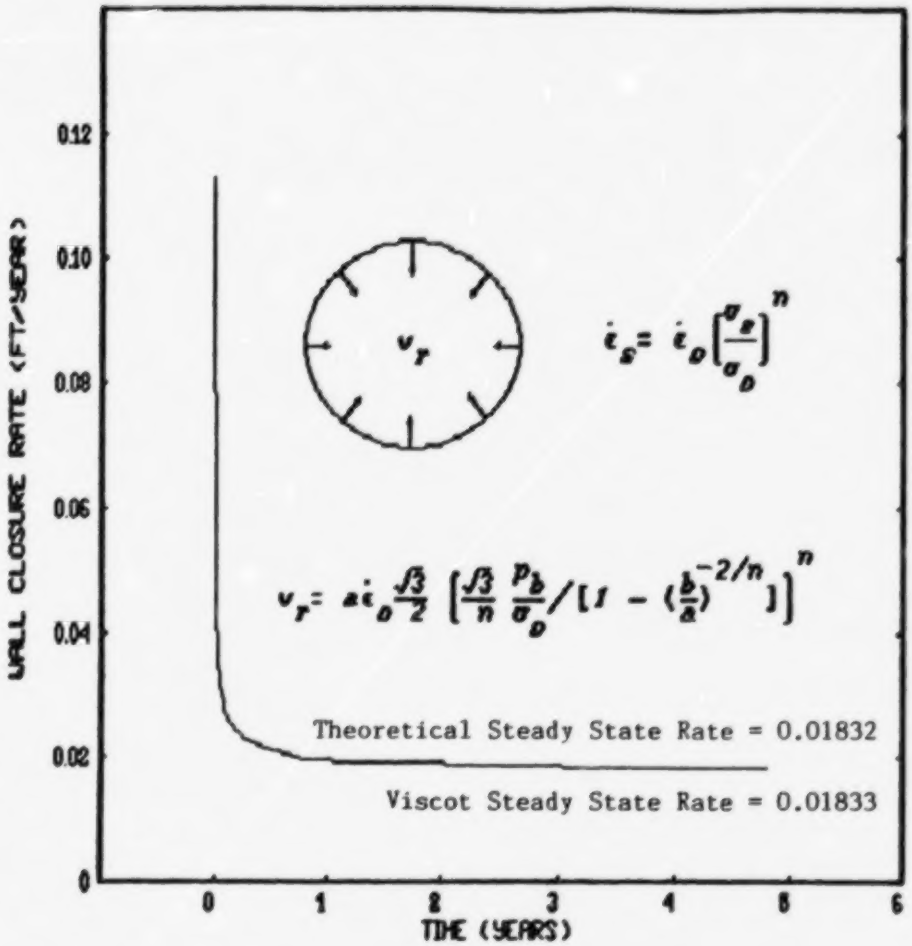

VISCOT Verification Run
Circular Opening in Uniform Stress Field
Closure Rate

FIGURE B.2

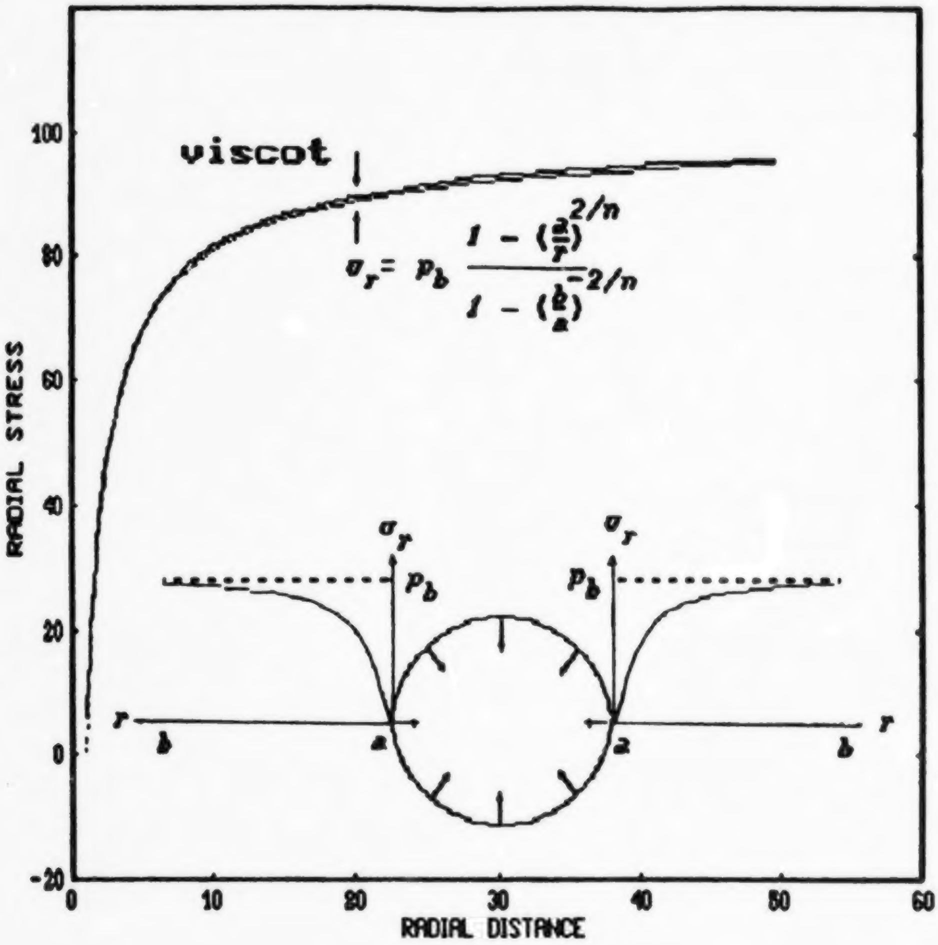

VISCOT Verification Run
Circular Opening in Uniform Stress Field
Radial Stress

FIGURE B.3

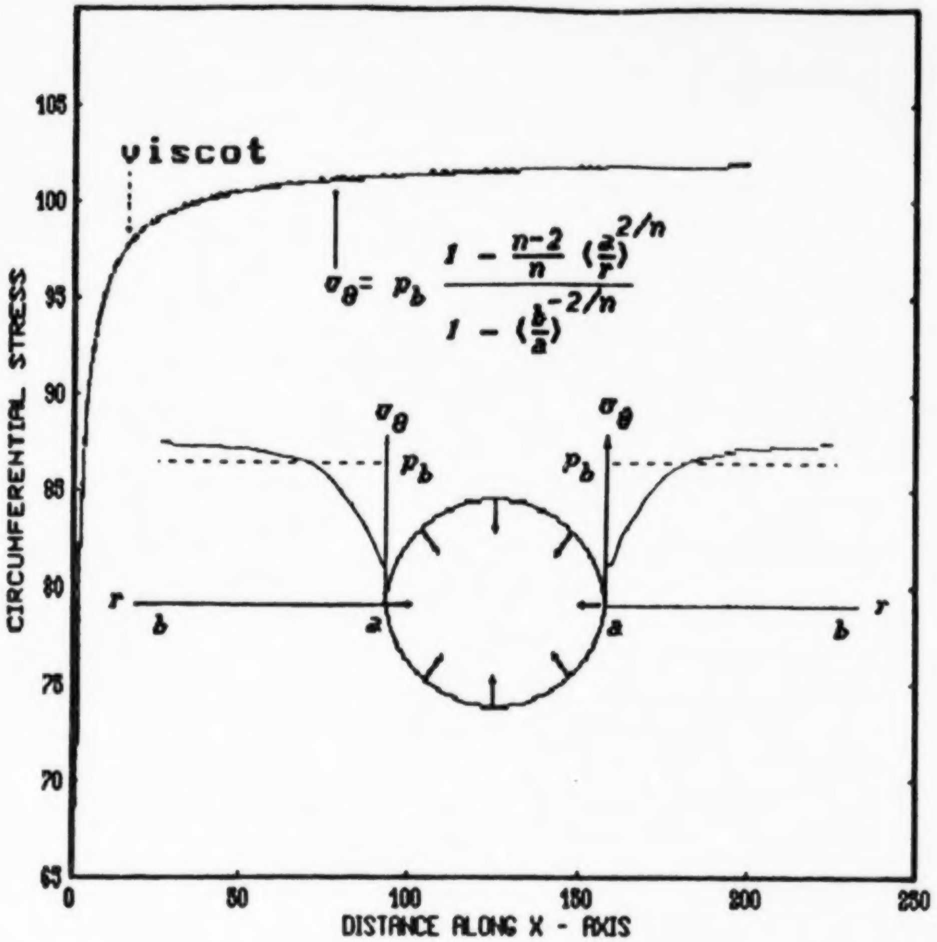

VISCOT Verification Run
Circular Opening in Uniform Stress Field
Circumferential Stress